PHYSICAL MECHANISMS CONTROLLING THE PRE-FAILURE STRESS-STRAIN BEHAVIOR OF FROZEN SAND

FINAL REPORT

by
Gregory Da Re
Charles C. Ladd
John T. Germaine

April, 2001

U.S. ARMY RESEARCH OFFICE
Contract Number DAAH04-96-1-0042

MASSACHUSETTS INSTITUTE OF TECHNOLOGY
Engineering and Environmental Mechanics Group
Department of Civil & Environmental Engineering
Cambridge, MA 02139-4307

APPROVED FOR PUBLIC RELEASE;
DISTRIBUTION UNLIMITED

MIT

DEPARTMENT OF CIVIL & ENVIRONMENTAL ENGINEERING

SCHOOL OF ENGINEERING
MASSACHUSETTS INSTITUTE OF TECHNOLOGY
Cambridge, Massachusetts 02139

20010503 111

REPORT DOCUMENTATION PAGE

Form Approved
OMB NO. 0704-0188

Public Reporting burden for this collection of information is estimated to average 1 hour per response, including the time for reviewing instructions, searching existing data sources, gathering and maintaining the data needed, and completing and reviewing the collection of information. Send comment regarding this burden estimates or any other aspect of this collection of information, including suggestions for reducing this burden, to Washington Headquarters Services, Directorate for information Operations and Reports, 1215 Jefferson Davis Highway, Suite 1204, Arlington, VA 22202-4302, and to the Office of Management and Budget, Paperwork Reduction Project (0704-0188,) Washington, DC 20503.

1. AGENCY USE ONLY (*Leave Blank*)	2. REPORT DATE	3. REPORT TYPE AND DATES COVERED
	30-Apr-2001	Final Report, 01 Apr 96 - 31 May 01

4. TITLE AND SUBTITLE
Physical Mechanisms Controlling the Pre-failure Stress-Strain Behavior of Frozen Sand

5. FUNDING NUMBERS
DAAH04-96-1-0042

6. AUTHOR(S)
Greg Da Re, John T. Germaine, Charles C. Ladd

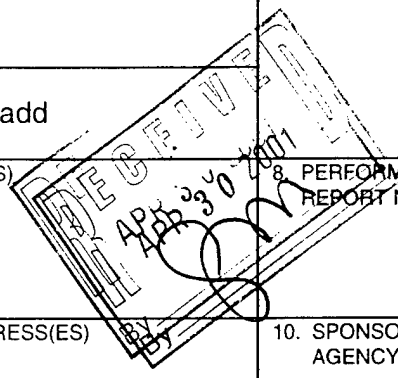

7. PERFORMING ORGANIZATION NAME(S) AND ADDRESS(ES)
Massachusetts Institute of Technology
77 Massachusetts Avenue
Cambridge, MA 02139

8. PERFORMING ORGANIZATION REPORT NUMBER

9. SPONSORING / MONITORING AGENCY NAME(S) AND ADDRESS(ES)
U. S. Army Research Office
P.O. Box 12211
Research Triangle Park, NC 27709-2211

10. SPONSORING / MONITORING AGENCY REPORT NUMBER
34905-GS.3

11. SUPPLEMENTARY NOTES

The views, opinions and/or findings contained in this report are those of the author(s) and should not be construed as an official Department of the Army position, policy or decision, unless so designated by other documentation.

12 a. DISTRIBUTION / AVAILABILITY STATEMENT

Approved for public release; distribution unlimited.

12 b. DISTRIBUTION CODE

13. ABSTRACT (*Maximum 200 words*)

The physical mechanisms controlling the pre-failure behavior of frozen sands are investigated in triaxial compression. The pre-failure behavior (ε_a<1%) is represented by the Young's modulus and upper yield stress. An experimental program conducted on a number of ice-saturated particulate systems investigated the dependency of these parameters on a number of testing variables. Results show that the Young's modulus varies significantly with particle modulus and increases slightly with particle volume fraction, but is independent of strain-rate and temperature. The development of stiffness also relies heavily on the coupling between phases for the transfer of shear stress. This coupling can take the form of an adhesional bond, or a frictional bond derived from particle angularity and surface roughness. Application of reinforcement theories for particulate composites has led to a new approach for predicting the Young's modulus of frozen sand. The upper yield stress behavior is controlled primarily by strain-rate, temperature, particle grain size, and for fully-bonded materials, is essentially independent of volume fraction and confinement. However, in the absence of an adhesional bond, surface roughness *and* confinement become important. The behavior of the upper yield stress can be explained by examining the influence of particles on cracks propagating through the ice matrix.

14. SUBJECT TERMS	15. NUMBER OF PAGES
frozen soil, Young's modulus, yield stress, triaxial testing, small strain, two-phase particulate systems, pre-failure behavior, strain rate, temperature.	354
	16. PRICE CODE

17. SECURITY CLASSIFICATION OR REPORT	18. SECURITY CLASSIFICATION ON THIS PAGE	19. SECURITY CLASSIFICATION OF ABSTRACT	20. LIMITATION OF ABSTRACT
UNCLASSIFIED	UNCLASSIFIED	UNCLASSIFIED	UL

Table of Contents

	Page
Report Documentation Page (SF298)	**i**
Table of Contents	**iii**
List of Figures	**ix**
List of Tables	**xx**
Nomenclature	**xxiii**
1. INTRODUCTION	**1**
1.1 PROBLEM STATEMENT	1
1.2 RESEARCH OBJECTIVES	4
1.3 ORGANIZATION	5
1.4 PUBLICATIONS AND REPORTS	8
1.5 STAFF AND ADVANCED DEGREES	9
1.6 ACKNOWLEDGEMENTS	10
1.7 REFERENCES	10
2. BACKGROUND AND COMPOSITE MATERIAL THEORY	**13**
2.1 INTRODUCTION	13
2.2 MECHANICAL BEHAVIOR OF POLYCRYSTALLINE ICE	14
2.2.1 Introduction	14
2.2.2 Structure of Polycrystalline Ice	14
2.2.3 Mechanisms of Deformation	15
2.2.4 Deformation and Failure Under Uniaxial Stress	18
2.2.4.1 Creep Under Constant Axial Stress	18
2.2.4.2 Deformation at Constant Strain Rate	20
2.2.4.3 Correspondence Principle	21
2.2.5 Continuum Behavior	22
2.2.5.1 Effect of Temperature	25
2.2.5.2 Effect of Confinement	27
2.2.5.3 Effect of Grain Size	27
2.2.6 Fracture Behavior	29

2.2.6.1 Compressive Fracture 30
2.2.6.2 Triaxial Behavior 36
2.3 MECHANICAL BEHAVIOR OF FROZEN SAND 36
2.3.1 Introduction 36
2.3.2 Structure of Frozen Sand 37
2.3.3 Mechanisms of Strength 38
2.3.3.1 Ice Strength 39
2.3.3.2 Soil Strength 40
2.3.3.3 Soil Skeleton-Ice Matrix Interactions 43
2.3.4 Strength and Deformation of Frozen Sand 45
2.3.4.1 Small Strain Behavior 48
2.3.4.2 Large Strain Behavior 56
2.3.4.3 Volumetric Strain Behavior 64

2.4 REINFORCEMENT THEORIES TWO-PHASE PARTICULATE-FILLED SYSTEMS 67
2.4.1 Introduction 67
2.4.2 Modulus of Particulate Composites 68
2.4.2.1 *Introduction* 68
2.4.2.2 *Theory of Dilute Suspensions* 69
2.4.2.3 *Mechanistic Models for Composite Materials* 71
2.4.2.4 *Effective Medium Models* 80
2.4.3 Limitations of Theoretical Models for Young's Modulus 90
2.4.4 Strength of Particulate Composites 93
2.4.4.1 *Introduction* 93
2.4.4.2 *Models for Strength in Tension and Compression* 94
2.4.5 Limitations of Theoretical Models for Strength 110

2.5 REFERENCES 114

3. LABORATORY EQUIPMENT 125
3.1 INTRODUCTION 125

3.2 LOW TEMPERATURE TESTING FACILITY 126

3.3 SPECIMEN TESTING APPARATUS 127
3.3.1 Introduction 127
3.3.2 MIT Automated High-Pressure Low-Temperature Triaxial Cell 128
3.3.3 Equipment Modifications 133
3.3.3.1 Introduction 133
3.3.3.2 Load Application 133
3.3.3.3 Temperature Control and Measurement 134
3.3.3.4 Strain Rate Control 136

3.4 DATA ACQUISTION SYSTEM 138
3.4.1 AD1170 Data Acquisition Card 138
3.4.2 Central Data Acquisition System 138

3.5 SMALL STRAIN MEASUREMENT SYSTEM 139
3.5.1 Introduction 139
3.5.2 Design Requirements 140
3.5.3 Mechanical Configuration 142
3.5.4 Signal Conditioning Unit 144
3.5.5 Mounting the Small Strain System on the Triaxial Specimen 146
3.5.6 LVDT Electrical Performance 146
3.5.6.1 Stability Characteristics 146
3.5.6.2 Effect of Temperature on LVDT Output 148
3.5.6.3 Effect of Pressure on LVDT Output 150
3.5.7 Proof Testing on Aluminum and PMMA 151
3.5.8 Evaluation of Technology on Soil 153
3.5.8.1 Tests on Resedimented Boston Blue Clay 153
3.5.8.2 Tests on Frozen Manchester Fine Sand 156

3.6 REFERENCES 158

4. MATERIALS AND SPECIMEN PREPARATION 161
4.1 INTRODUCTION 161

4.2 MATERIALS 161
4.2.1 Manchester Fine Sand 161
4.2.2 Polycrystalline Ice 163
4.2.3 Alternate Granular Materials 166
4.2.3.1 Industrial Quartz 166
4.2.3.2 Hydrophobic Manchester Fine Sand 166
4.2.3.3 Polymethylmethacrylate (PMMA) 169
4.2.3.4 Glass Beads 169

4.3 TRIAXIAL SPECIMEN PREPARATION TECHNIQUES 179
4.3.1 Introduction 179
4.3.2 Equipment and Procedures 179
4.3.3 Specimen De-airing and Saturation 182
4.3.4 Specimen Freezing 183
4.3.5 Trimming Procedures 185

4.4 REFERENCES 186

5. RESEARCH METHODOLOGY **189**

5.1 INTRODUCTION 189

5.2 VARIABLES INVESTIGATED 189
- 5.2.1 Introduction 189
- 5.2.2 Void Ratio/Relative Density 190
- 5.2.3 Confinement Level 191
- 5.2.4 Strain Rate 192
- 5.2.5 Temperature 194
- 5.2.6 Particle Modulus 195
- 5.2.7 Particle Grain Size 196
- 5.2.8 Interface Adhesion 197
- 5.2.9 Particle Roughness 199

5.3 GENERAL TESTING PROCEDURES 200
- 5.3.1 Frozen Testing Procedures 200

5.4 SUMMARY OF EXPERIMENTAL PROGRAM 203

5.5 DATA HANDLING 203
- 5.5.1 Data Collection 203
- 5.5.2 Data Reduction 207

5.6 REFERENCES 210

6. BEHAVIOR OF FROZEN SYSTEMS IN THE ELASTIC REGION **213**

6.1 INTRODUCTION 213

6.2 EVALUATION OF YOUNG'S MODULUS 213
- 6.2.1 Effect of Void Ratio/Relative Density 214
- 6.2.2 Effect of Confinement 218
- 6.2.3 Effect of Strain Rate 220
- 6.2.4 Effect of Temperature 223
- 6.2.5 Effect of Particle Modulus 225
- 6.2.6 Effect of Particle Grain Size 227
- 6.2.7 Effect of Interface Adhesion 230
- 6.2.8 Effect of Particle Roughness 233

6.3 DISCUSSION OF MECHANISMS CONTROLLING YOUNG'S MODULUS OF FROZEN SAND 235
- 6.3.1 Introduction 235
- 6.3.2 Summary of Observations on Young's Modulus 235
- 6.3.3 Development of Stiffness in Frozen Sand 240

6.4 COMPARISON OF EXPERIMENTAL DATA WITH MODELS FOR TWO-PHASE PARTICULATE-FILLED SYSTEMS 244
6.4.1 Introduction 244
6.4.2 Theory of Dilute Suspensions 246
6.4.3 Mechanistic Models for Composite Materials 248
6.4.4 Effective Medium Models 255
6.4.5 Evaluation of Composite Material Models 257

6.5 PREDICTION OF YOUNG'S MODULUS OF FROZEN SAND 260

6.6 REFERENCES 262

7. BEHAVIOR OF FROZEN SYSTEMS IN THE UPPER YIELD REGION 267
7.1 INTRODUCTION 267

7.2 EVALUATION OF UPPER YIELD STRESS 267
7.2.1 Effect of Void Ratio/Relative Density 268
7.2.2 Effect of Confinement 270
7.2.3 Effect of Strain Rate 273
7.2.4 Effect of Temperature 275
7.2.5 Effect of Particle Modulus 280
7.2.6 Effect of Particle Grain Size 281
7.2.7 Effect of Interface Adhesion 284
7.2.8 Effect of Particle Roughness 287

7.3 DISCUSSION OF MECHANISMS CONTROLLING THE UPPER YIELD BEHAVIOR OF FROZEN SAND 289
7.3.1 Introduction 289
7.3.2 Summary of Observations at the Upper Yield Stress 290
7.3.3 Development of Strength in Frozen Sand 295

7.4 PREDICTION OF THE UPPER YIELD BEHAVIOR OF FROZEN SAND 303

7.5 REFERENCES 307

8. CONCLUSIONS AND RECOMMENDATIONS 311
8.1 RESEARCH OVERVIEW 311

8.2 RESULTS AND CONCLUSIONS 313
8.2.1 Introduction 313
8.2.2 Summary of Important Variables 313

8.2.2.1 Effect of Void Ratio/Relative Density 313
8.2.2.2 Effect of Confinement 314
8.2.2.3 Effect of Strain Rate 315
8.2.2.4 Effect of Temperature 315
8.2.2.5 Effect of Particle Modulus 316
8.2.2.6 Effect of Particle Grain Size 317
8.2.2.7 Effect of Interface Adhesion 318
8.2.2.8 Effect of Particle Roughness 318
8.2.3 Conclusions on Young's Modulus 319
8.2.4 Conclusions on Upper Yield Behavior 321

8.3 RECOMMENDATIONS FOR FUTURE RESEARCH 323
8.3.1 Equipment Enhancement 323
8.3.2 Additional Investigations 325

8.4 REFERENCES 327

APPENDIX A Measurement of Ice Adhesion in the Laboratory 329
A.1 Introduction
A.2 Ice Adhesion Apparatus
A.3 Specimen Preparation
A.4 Testing Procedures and Data Handling
A.5 Summary of Adhesion Test Results
A.6 Measurement of Contact Angles
A.7 Bibliography

APPENDIX B Summary of Frozen Testing Program 345
B.1 Frozen Test Summary (Testing Conditions)
B.2 Frozen Test Summary (Engineering Properties)

List of Figures

		Page
Figure 2.1	Crystal structure of ice Ih showing the tetrahedral constituent unit: (a) view along the *c*-axis, (b) view along the basal plane layers. (Sanderson 1988)	15
Figure 2.2	Schematic of deformation processes within a grain during uniaxial loading: (a) elastic deformation by atomic bond deformation, (b) delayed elastic strain as a result of grain boundary sliding, (c) secondary creep by dislocation glide and climb, (d) crack formation due to dislocation pile-up at grain boundaries, (e) dynamic recrystallization leading to the formation of fresh grains. (Sanderson 1988)	16
Figure 2.3	Deformation behavior of polycrystalline ice: (a) complete creep curve for a constant stress test on ice that is initially isotropic, (b) complete stress-strain curve for a constant strain rate test at moderate strain rate. (Mellor 1980)	19
Figure 2.4	Alternative presentations of creep curves: (a) using a log-log plot of strain rate against time, (b) using a log-log plot of strain rate against strain. (Mellor 1980)	20
Figure 2.5	Stress-strain curves from uniaxial tension tests on polycrystalline ice at -7±1°C, A: $\dot{\varepsilon}=6.4\text{x}10^{-4}$ s^{-1}, B: $\dot{\varepsilon}=3.3\text{x}10^{-6}$ s^{-1}. (Hawkes and Mellor 1972)	21
Figure 2.6	Stress-strain rate data for uniaxial tests on polycrystalline ice specimens at -7°C. (Mellor 1980)	23
Figure 2.7	Temperature dependence of Young's modulus (E), shear modulus (G), and Poisson's ratio (μ), of granular ice where T_m is the melting point. (Sinha 1989)	24
Figure 2.8	Uniaxial loading of pure polycrystalline ice. Below a strain rate of 10^{-5} s^{-1} power law creep occurs with n=3. (Sanderson 1988 after Hallam 1986)	25
Figure 2.9	Experimental curve for logarithm of minimum strain rate plotted against the reciprocal of absolute temperature. (Mellor 1980 after Mellor and Testa 1969a)	26
Figure 2.10	Effect of confinement on the peak strength of bulk polycrystalline ice in triaxial compression at various strain rates at -11.5°C. (Sanderson 1988 from data of Jones 1982)	28

List of Figures

		Page
Figure 2.11	Peak unconfined compressive stress of polycrystalline ice at -5°C as a function of grain size at various strain rates between 10^{-7} s^{-1} to 10^{-3} s^{-1}. (Cole 1987)	29
Figure 2.12	High strain rate data for tensile loading of polycrystalline ice as a function of grain size. (Schulson et al. 1984)	32
Figure 2.13	Simple geometry for tensile propagation of a flaw of half-length *a* subjected to a stress σ	33
Figure 2.14	Model for crack propagation in a brittle solid in compression: (a) formation of wing cracks in tensile zones, (b) idealized model of wing crack formation for analytical treatment. (Sanderson 1988)	34
Figure 2.15	Linkage of a population of propagating wing cracks.	35
Figure 2.16	Two dimensional schematic of the structure of frozen sand. (adapted from Ting et al. 1983)	38
Figure 2.17	Proposed failure mechanism map for unconfined compressive strength for frozen Ottawa sand 20-30. (Ting et al. 1983)	39
Figure 2.18	Steady state line developed from six CIUC tests on compacted sand specimens. (Poulos et al. 1985)	41
Figure 2.19	Effect of initial state on the steady state line for Erksak 330/0.7 sand in triaxial compression. (Been et al. 1991)	42
Figure 2.20	Definition of the state parameter. (Been et al. 1991)	43
Figure 2.21	Overview of stress-strain behavior of frozen Manchester fine sand showing the effect of relative density and confinement at: (a) varying strain rate, and (b) varying temperature. (Andersen et al. 1995)	47
Figure 2.22	Effect of dry density on the Young's modulus and Poisson's ratio of frozen Ottawa 16-100 sand. (Baker and Kurfurst 1985)	50
Figure 2.23	Variation of Young's modulus of frozen Manchester fine sand with relative density at various confinement levels, temperatures, and strain rates. (Andersen et al. 1995)	51

List of Figures

		Page
Figure 2.24	Effect of confinement level on the upper yield stress for various frozen sands. (Andersen et al. 1995)	53
Figure 2.25	Variation of the upper yield stress of frozen Manchester fine sand with strain rate at varying temperature at all relative densities and confinement levels. (Andersen et al. 1995)	54
Figure 2.26	Variation of the upper yield stress of 30-100 Ottawa sand with strain rate at -30°C. (Parameswaran and Roy 1982)	54
Figure 2.27	Variation of upper yield stress of frozen Manchester fine sand and peak strength of polycrystalline ice with strain rate. (Andersen et al. 1995)	55
Figure 2.28	Types of stress-strain curves describing large strain behavior of frozen Manchester fine sand. (Swan et al. 1995)	57
Figure 2.29	Variation of peak strength of frozen sands with volume fraction in unconfined compression at various temperatures. (Swan 1994)	59
Figure 2.30	Effect of dry density on the unconfined compressive strength of frozen 16-100 Ottawa sand prepared using multiple sieve pluviation. (Baker and Konrad 1985)	59
Figure 2.31	Variation of peak strength of frozen Manchester fine sand with relative density and temperature at moderate strain rates ($\dot{\varepsilon}=3.5x10^{-5}$ s^{-1}) and low confinement (0.1 MPa). (Swan et al. 1995)	60
Figure 2.32	Effect of confinement on the peak strength of various frozen dense sands at $T \approx -10°C$. (Swan et al. 1995)	61
Figure 2.33	Variation of the unconfined compressive peak strength of dense frozen Lanzhou sand with strain rate at various temperatures (adapted from Zhu et al. 1988)	62
Figure 2.34	Peak strength and upper yield stress of frozen Manchester fine sand plotted against strain rate for conditions of: (a) low density and low confinement, and (b) high density and high confinement. (Swan et al. 1995)	62

List of Figures

		Page
Figure 2.35	Normalized rate of strain softening versus volumetric strain at varying relative densities, strain rates, and temperatures. (Swan et al. 1995)	64
Figure 2.36	Variation of the maximum rate of dilation for frozen Manchester fine sand with confinement at moderate strain rate at -10°C. (Swan et al. 1995)	66
Figure 2.37	Variation of the volumetric strain at 20% axial strain with relative density at various strain rates and temperatures for frozen Manchester fine sand at low confinement (σ_c = 0.1 MPa). (Swan et al. 1995)	66
Figure 2.38	Model references (a) Voigt, (b) Reuss, (c) Hirsch, (d) Counto.	72
Figure 2.39	Unit cube with inclusion of arbitrary shape. (Paul 1960)	74
Figure 2.40	Detail of Counto's (1964) composite material model.	76
Figure 2.41	Schematics of (a) the idealized microstructure, (b) the unit cell of the composite. (Ravichandran 1992)	77
Figure 2.42	Effective medium model.	81
Figure 2.43	Topological transformation of a two-phase microstructure.	88
Figure 2.44	Tensile strength of glass bead filled epoxy composites plotted against volume fraction. (Sahu and Broutman 1972)	95
Figure 2.45	Upper and lower bounds as measured and predicted by Nicolais and Narkis (1971). (data from Sahu and Broutman 1972)	96
Figure 2.46	Variation of the yield stress ratio as a function of volume fraction for different values of B. (Turcsanyi et al. 1988)	98
Figure 2.47	Unconfined compressive yield stress versus strain rate for different filler contents. (Ishai and Cohen 1968)	104
Figure 2.48	Typical stress-strain curves of filled and unfilled epoxy specimens in tension and compression for the same constant strain rate. (Ishai and Bodner 1970)	105

List of Figures

		Page
Figure 2.49	Compressive yield stress versus filler content for different strain rate levels illustrating model fit. (Ishai and Cohen 1968)	106
Figure 2.50	Compressive yield stress versus strain rate at various temperatures. (Moehlenpah et al. 1969)	107
Figure 2.51	Yield stress versus $a_T\dot{\varepsilon}$ for different concentrations of glass beads. T_{ref} = 24°C. (Nicolais and Narkis 1971)	107
Figure 2.52	Stress-strain curves for different concentrations of glass beads in a SAN matrix. T_{ref} = 48°C, $\dot{\varepsilon}$ = 0.0262 min^{-1}. (Nicolais and Narkis 1971)	113
Figure 2.53	Stress at the point of discontinuity (σ_D) versus temperature for different concentrations of glass beads. $\dot{\varepsilon}$ = 0.0262 min^{-1}. (Nicolais and Narkis 1971)	114
Figure 3.1	MIT Low Temperature Testing Facility (plan view).	127
Figure 3.2	MIT automated high-pressure low-temperature triaxial system.	129
Figure 3.3	High-pressure low-temperature triaxial chamber.	131
Figure 3.4	Triaxial chamber loading assembly.	135
Figure 3.5	Improvement in strain rate as a result of PID algorithm and system modifications: (a) slow strain rate ($\dot{\varepsilon}$ = $3x10^{-6}$ s^{-1}), (b) moderate strain rate ($\dot{\varepsilon}$ = $3.5x10^{-5}$ s^{-1}).	137
Figure 3.6	Schematic of yolks and mounting configuration.	143
Figure 3.7	Functional block diagram of signal conditioning unit.	145
Figure 3.8	LVDT stability with new signal conditioning system at 20°C (a) over 300 s, (b) over 24 hours.	147
Figure 3.9	LVDT stability as a function of temperature (a) over 300 s, (b) over 24 hours.	149
Figure 3.10	LVDT stability as a function of confining pressure (0-10 MPa) at T=20°C.	150

List of Figures

		Page
Figure 3.11	Stress-strain behavior of 6061 aluminum determined with the new MIT small strain measuring system.	152
Figure 3.12	Stress-strain behavior of PMMA determined with the new MIT small strain measuring system.	152
Figure 3.13	Undrained shear data on normally consolidated RBBC: (a) large strain region, 0.00-2.00%, (b) 0-0.05%, (c) small strain region, 0.00-0.005%, (d) 0.00-0.0005%. (Santagata 1998)	154
Figure 3.14	Repeatability of results on normally consolidated RBBC: stiffness versus logarithm of axial strain (σ'_{vc}=0.24, K_0-consolidation). (Santagata 1998)	155
Figure 3.15	Shear data on frozen MFS: (a) large strain region, 0.00-20.0%, (b) 0.00-2.00%, (c) small strain region, 0.00-0.02%, (d) 0.00-0.005%.	157
Figure 4.1	SEM image of untreated Manchester fine sand (a) Magnification 100X, (b) Magnification 300X.	162
Figure 4.2	Grain size distributions for Manchester fine sand, industrial quartz, PMMA powder, and small glass beads.	164
Figure 4.3	Thin section of typical untested polycrystalline ice.	165
Figure 4.4	SEM image of 2010 industrial quartz (a) Magnification 100X, (b) Magnification 300X.	167
Figure 4.5	Schematic of quartz mineral surface.	168
Figure 4.6	SEM image of hydrophobic Manchester fine sand (a) Magnification 100X, (b) Magnification 300X.	170
Figure 4.7	SEM image of PMMA powder (a) Magnification 100X, (b) Magnification 300X.	171
Figure 4.8	SEM image of small glass beads with various levels of treatment (a) untreated (Magnification 100X), (b) untreated (Magnification 300X), (c) hydrophobic (Magnification 100X), (d) hydrophobic (Magnification 300X), (e) surface roughened (Magnification 100X), (f) surface roughened (Magnification 300X) (g) hydrophobic surface roughened (Magnification 100X), (h) hydrophobic surface roughened (Magnification 300X).	173

List of Figures

		Page
Figure 4.9	SEM image of large glass beads with various levels of treatment (a) untreated (Magnification 75X), (b) untreated (Magnification 150X), (c) surface roughened (Magnification 75X), (d) surface roughened (Magnification 150X).	177
Figure 4.10	Frozen specimen preparation mold detail.	180
Figure 4.11	Multiple sieve pluviation technique.	181
Figure 4.12	Frozen specimen de-airing/saturation apparatus.	183
Figure 4.13	Freezing cap detail.	184
Figure 5.1	Comparison between on-specimen axial strain LVDT's showing (a) *excellent* agreement, (b) *good* agreement, (c) *fair* agreement, and (d) *poor* agreement.	210
Figure 6.1	Effect of void ratio on Young's modulus of frozen systems at -10°C at varying confining pressures and strain rates; (a) Manchester fine sand, (b) 2010 industrial quartz, (c) PMMA, (d) small and large glass beads.	215
Figure 6.2	Effect of relative density on Young's modulus of frozen Manchester fine sand at -10°C.	216
Figure 6.3	Variation of Young's modulus with ACDT agreement for Manchester fine sand at -10°C at varying confining pressures and strain rates (includes data from Andersen 1991 and Swan 1994).	217
Figure 6.4	Effect of confinement on Young's modulus of frozen systems at -10°C at varying void ratios and confining pressures; (a) Manchester fine sand, (b) hydrophobic Manchester fine sand (c) 2010 industrial quartz, (d) PMMA, (e) small and large glass beads, (f) polycrystalline ice.	219
Figure 6.5	Effect of strain rate on Young's modulus of frozen systems at -10°C at varying void ratios and confining pressures; (a) Manchester fine sand, (b) hydrophobic Manchester fine sand (c) 2010 industrial quartz, (d) PMMA, (e) small and large glass beads, (f) polycrystalline ice.	222

List of Figures

		Page
Figure 6.6	Effect of temperature on Young's modulus of frozen systems at varying void ratios, confining pressures and strain rates; (a) Manchester fine sand, (b) hydrophobic Manchester fine sand (c) 2010 industrial quartz, (d) PMMA, (e) polycrystalline ice.	224
Figure 6.7	Effect of particle modulus on Young's modulus of frozen systems at -5°C and -10°C at varying confining pressures and strain rates.	227
Figure 6.8	Comparison of Young's modulus of PMMA system with that of polycrystalline ice at varying void ratios, confining pressures, and strain rates.	228
Figure 6.9	Effect of particle size on Young's modulus of frozen quartz based systems at -5°C and -10°C at varying void ratios, confining pressures, and strain rates.	229
Figure 6.10	Effect of interface adhesion on Young's modulus results at -10°C at varying void ratios, and strain rates for (a) Manchester fine sand, (b) small and large glass beads.	232
Figure 6.11	Effect of particle roughness on Young's modulus of small and large glass bead systems at -10°C at varying void ratios, confining pressures, and strain rates.	234
Figure 6.12	Variation of Young's modulus with relative density at varying temperatures for all confining pressures and strain rates. (adapted from Andersen et al. 1995)	237
Figure 6.13	Variation of Young's modulus of frozen sand with particle modulus at -10°C at varying void ratios, confining pressures, and strain rates.	238
Figure 6.14	Interaction diagram for the influence of particle roughness and interface adhesion on the composite Young's modulus of frozen systems at -10°C.	241
Figure 6.15	Proposed mechanism map for Young's modulus of frozen sand.	244
Figure 6.16	Comparison of dilute suspension models to experimental data on quartz and PMMA-based systems at -10°C at varying confining pressures and strain rates.	247

List of Figures

		Page
Figure 6.17	Comparison of Voigt, Reuss, and Hirsch models to experimental data for quartz-based systems at -10°C at varying confining pressures and strain rates for (a) V_p=0.00-1.00, (b) V_p=0.50-0.70.	249
Figure 6.18	Comparison of Voigt, Reuss, and Hirsch models to experimental data for PMMA-based systems at -5°C and -10°C for V_p=0.50-0.70 at varying confining pressures and strain rates.	251
Figure 6.19	Comparison of Paul, Ishai, and Counto models to experimental data at -10°C at varying confining pressures and strain rates for (a) quartz-based systems, V_p=0.00-1.00, (b) quartz and PMMA-based systems, V_p=0.50-0.70.	252
Figure 6.20	Comparison of Hashin-Shtrikman, Voigt, Reuss, and BNC models to experimental data at -10°C at varying confining pressures and strain rates for (a) quartz based-systems, V_p=0.00-1.00, (b) quartz and PMMA-based systems, V_p=0.50-0.70.	254
Figure 6.21	Comparison of Mori-Tanaka, GSCM, Field Theory, and BNC models to experimental data at -10°C at varying confining pressures and strain rates for (a) quartz-based systems, V_p=0.00-1.00, (b) quartz and PMMA-based systems, V_p=0.50-0.70.	256
Figure 6.22	Design chart for estimation of the composite modulus of frozen sand based on BNC model.	261
Figure 7.1	Effect of void ratio on the upper yield stress of frozen systems at -10°C at varying confining pressures and strain rates (a) Manchester fine sand, (b) 2010 industrial quartz, (c) PMMA, (d) small glass beads.	269
Figure 7.2	Effect of confinement on the upper yield stress of frozen systems at -10°C at varying void ratios and strain rates (a) Manchester fine sand, (b) hydrophobic Manchester fine sand, (c) 2010 industrial quartz, (d) PMMA, (e) small glass beads (regular and hydrophobic), (f) polycrystalline ice.	271
Figure 7.3	Effect of confinement for hydrophobic surface roughened small glass beads tested at -10°C at varying strain rates.	272
Figure 7.4	Effect of confinement on the strain at the upper yield stress (strain at peak stress for polycrystalline ice) at -10°C at varying void ratios and strain rates.	274

List of Figures

		Page
Figure 7.5	Effect of strain rate on the upper yield stress of untreated frozen systems at -5°C and -10°C at varying void ratios and confining pressures (a) Manchester fine sand, (b) 2010 industrial quartz, (c) PMMA, (d) glass beads (e) polycrystalline ice.	276
Figure 7.6	Temperature dependence of Manchester fine sand at slow, moderate, and fast strain rates.	278
Figure 7.7	Effect of temperature on the upper yield stress of frozen systems for slow and moderate strain rates at varying void ratios and confining pressures (a) Manchester fine sand, (b) hydrophobic Manchester fine sand, (c) 2010 industrial quartz, (d) PMMA, (e) polycrystalline ice.	279
Figure 7.8	Effect of particle modulus on the upper yield stress of frozen systems at -10°C at varying void ratios and confinements (a) slow rate ($3x10^{-6}$ s^{-1}), (b) moderate rate ($3.5x10^{-5}$ s^{-1}).	281
Figure 7.9	Effect of particle size on the upper yield stress of the frozen systems tested at slow (dark symbols) and under moderate (open symbols) strain rates (a) at -5°C, (b) -10°C.	282
Figure 7.10	Effect of interface adhesion (hydrophobic coating) on the upper yield stress of frozen systems at -10°C at varying void ratios and confining pressures for (a) Manchester fine sand, (b) small glass beads, (c) large glass beads.	285
Figure 7.11	Effect of particle roughness on the upper yield stress of hydrophobic glass bead systems at -10°C at varying void ratios and confining pressures for (a) small glass beads, (b) large glass beads.	289
Figure 7.12	Upper yield stress of frozen Manchester fine sand and peak strength of polycrystalline ice. Ice data from Hawkes and Mellor 1972, Jones 1982. (adapted from Andersen et al. 1995)	292
Figure 7.13	Effect of adhesional bonding and influence of confinement on frozen systems of small glass beads at -10°C at varying void ratios.	298
Figure 7.14	Effect of surface roughness and influence of confinement on frozen systems of small glass beads at -10°C at varying void ratios.	299

List of Figures

		Page
Figure 7.15	Comparison of 2010 industrial quartz, PMMA and small glass beads at -10°C at varying void ratios and confining pressures showing the effect of particle shape (K_{Ic}).	301
Figure 7.16	Comparison of 2010 industrial quartz and Manchester fine sand at -10°C at varying void ratios and confining pressures showing the effect of particle size.	302
Figure 7.17	Proposed mechanism map for the upper yield stress of frozen sand.	303
Figure 7.18	Comparison of yield model (Equation 7.4) and experimental data for Manchester fine sand at -2°C to -25°C using parameters given in Table 7.9. (data at T≤-10°C from Andersen et al. 1995)	306
Figure 7.19	Comparison of upper yield model (Equation 7.4) and experimental data at -5°C and -10°C at varying void ratios and confining pressures for (a) 2010 industrial quartz, (b) PMMA, (c) small glass beads, (d) polycrystalline ice.	307

List of Tables

		Page
Table 2.1	Prior measurements of Young's modulus on saturated frozen sand. (Andersen et al. 1995)	50
Table 3.1	Summary of calibration details for devices used.	130
Table 3.2	Summary of measured testing temperatures from previous experimental programs on frozen Manchester fine sand. (Andersen et al. 1995)	136
Table 3.3	Improvement in temperature control in current testing program.	136
Table 3.4	Transducer characteristics as measured by the central data acquisition system. (adapted from Sheahan et al. 1991)	139
Table 5.1	Summary of research approach for variables investigated during current research program.	190
Table 5.2	Number of tests performed for all materials at each confining pressure investigated.	192
Table 5.3	Range of strain rates examined during testing program	194
Table 5.4	Number of tests performed for each material for each temperature investigated.	195
Table 5.5	PMMA testing program.	196
Table 5.6	Industrial quartz testing program.	197
Table 5.7	Interface adhesion testing program.	198
Table 5.8	Materials examined for effects of particle roughness.	199
Table 5.9	Summary of triaxial compression experimental program on frozen specimens.	204
Table 6.1	Summary of void ratio range and number of tests for each material investigated at -10°C.	214
Table 6.2	Summary of variation of Young's modulus with ACDT agreement for Manchester fine sand at -10°C at all void ratios, confining pressures, strain rates.	217

List of Tables

		Page
Table 6.3	Summary of the mean Young's modulus and standard deviation for each material type at -10°C at varying void ratios, confining pressures, and strain rates (excluding "poor" tests).	218
Table 6.4	Summary of confinement levels investigated for each material type at -10°C at varying void ratios and strain rates.	220
Table 6.5	Summary of Young's modulus obtained at low ($\sigma_c \leq 2$ MPa) and high confinements for each material type at -10°C at varying void ratios and strain rates.	220
Table 6.6	Summary of the Young's modulus obtained for each material type at the two strain rates investigated at -10°C at varying void ratios and confining pressures.	221
Table 6.7	Summary of the Young's modulus obtained for each material type at the various temperatures investigated.	225
Table 6.8	Summary of the Young's modulus obtained for each material type at -5°C and -10°C at varying void ratios, confining pressures, and strain rates.	226
Table 6.9	Summary of the variation of Young's modulus with particle size at -5°C and -10°C at varying void ratios, confining pressures, and strain rates.	230
Table 6.10	Summary of the effect of interface adhesion on the Young's modulus of Manchester fine sand and glass bead systems at -10°C at varying void ratios, confining pressures, and strain rates.	231
Table 6.11	Summary of the effect of particle roughness on the Young's modulus of glass bead systems at -10°C and moderate strain rate at varying void ratios and confining pressures.	234
Table 6.12	Summary of comparison of experimental data with predictive models for two-phase particulate systems at -10°C.	259
Table 7.1	Summary of the effect of void ratio on the upper yield stress of each material tested at -10°C.	268

List of Tables

		Page
Table 7.2	Summary of upper yield stress obtained at low ($\sigma_c \leq 2$ MPa) and high confinements for each material type tested at -10°C for varying void ratios.	273
Table 7.3	Summary of strain rate dependency (power law exponent) for each material type at -5°C and -10°C at varying void ratios and confining pressures.	277
Table 7.4	Summary of temperature dependence for each material type investigated.	278
Table 7.5	Summary of the effect of particle modulus on the upper yield stress of frozen systems at -10°C at varying confining pressures.	281
Table 7.6	Summary of the effect of particle size dependence of the upper yield stress of the frozen systems tested at -5°C and -10°C at the slow ($\dot{\varepsilon}=3.0\text{x}10^{-6}$ s^{-1})and moderate ($\dot{\varepsilon}=3.5\text{x}10^{-5}$ s^{-1}) strain rates.	283
Table 7.7	Summary of the effect of interface adhesion on the upper yield stress of Manchester fine sand and glass bead systems at -10°C.	286
Table 7.8	Summary of the effect of particle roughness on the upper yield stress of hydrophobic glass bead systems at -10°C.	288
Table 7.9	Summary of fitting coefficients for Equation 7.4 for frozen systems investigated.	305

Nomenclature

Abbreviations/Acronyms:

AC	Alternating Current
ACDT	Alternating Current Displacement Transducer
ADC	Analog-to-Digital Converter
ASTM	American Society for Testing and Materials
BNC	Bache and Nepper-Christensen
CIDC	Isotropically Consolidated Drained shear test, Compression
CIUC	Isotropically Consolidated Undrained shear test, Compression
CL	Clay of Low Plasticity
COV	Coefficient of Variation
CRREL	Cold Regions Research and Engineering Laboratory
DAC	Digital-to-Analog Converter
DC	Direct Current
DCDT	Direct Current Displacement Transducer
FRS	Frozen Test Specimen
FT	Field Theory
GSCM	Generalized Self Consistent Model
HPLC	High-Pressure Liquid Chromatography
IC	Integrated Circuit
LTTF	Low Temperature Testing Facility
LVDT	Linear Voltage Displacement Transducer
MFS	Manchester Fine Sand
MRD	Maximum Rate of Dilation
MTM	Mori-Tanaka Method
NRSS	Normalized Rate of Strain Softening
OCR	Overconsolidation Ratio
PC	Personal Computer
PID	Proportional-Integral-Derivative
PMMA	Polymethylmethacrylate
PVC	Pressure Volume Controller
RBBC	Resedimented Boston Blue Clay
SAN	Styrene-Acrylo-Nitrile copolymer
SD	Standard Deviation
SEM	Scanning Electron Micrograph
SHANSEP	Stress History and Normalized Soil Engineering Properties
SM	Silty Sand
SP	Poorly Graded Sand
TX	Triaxial
USCS	Unified Soil Classification System
WLF	Williams-Landel-Ferry

Symbols (English):

a	Half-length of crack
a_T	WLF shift factor
A	Constant depending on crystal type (Arrhenius equation)
A	Temperature dependent constant
A_i	Area of inclusion or filler material
A_m	Area of matrix material
B	Temperature dependent constant
c	Inclusion volume fraction
C	Temperature dependent constant
C_{ax}	Coefficient relating volume change due to base flexure to applied axial load
C_c	Coefficient of concavity
C_f	Filler concentration
cs	centistokes
C_u	Coefficient of uniformity
C_x	Contiguity of phase x
d	Grain size
d_{50}	Mean grain diameter
d_{III}	Volume fraction weighted average grain size
D	Temperature dependent constant
D_r	Relative density
e	Void ratio
E	Young's modulus
E_c	Young's modulus of the composite
E_i	Young's modulus of the inclusion
E_{ice}	Young's modulus of ice
E_m	Young's modulus of the matrix
E_{MAX}	Maximum Young's modulus
E_p	Young's modulus of particle
E_{so}	Theoretical stiffness
E_u	Undrained stiffness
f_x	Volume fraction of phase x
f_{xc}	Continuous volume fraction of phase x
f_{xIII}	Volume fraction of phase x in EIII body
F	Force
F_{ax}	Change in axial force during shear
G	Specific gravity
G_c	Shear modulus of the composite
G_m	Shear modulus of the matrix
$G_{U/L}$	Upper and lower bound for shear modulus (Hashin and Shtrikman 1963)
k	Self crowding factor
K	Relative change of the matrix strength due to the presence of particles
K_0	Coefficient of lateral earth pressure at rest
K_1	Fitting coefficient for particle size
K_{1c}	Fracture toughness

K_2	Fitting coefficient for particle shape
K_c	Bulk modulus of the composite
K_m	Bulk modulus of the matrix
$K_{U/L}$	Upper and lower bound for bulk modulus (Hashin and Shtrikman 1963)
l	Length of wing cracks
L	Length of wing crack divided by the half length of the crack
LR	Leakage rate
m	Modulus ratio
n	Power law exponent
N_A	Number of grains per unit area
NC	Normally consolidated
p	Particle aspect ratio
p'	Average effective stress ($[\sigma'_{11}+\sigma'_{33}]/2$)
q	Shear stress
Q	Deviator stress
Q_a	Activation energy
Q_{ice}	Peak strength of ice
Q_p	Peak strength
Q_{uy}	Upper yield stress
r	Mean particle radius
R	Ratio of inclusion diameter to matrix diameter
R	Universal gas constant (= 8.314 J mol^{-1} K^{-1})
S	Degree of saturation
S	Strength reduction or concentration factor
S_i	Ice saturation
t	Time
T	Temperature
T_g	Glass transition temperature
V_p	Particle volume fraction
V_s	Volume fraction of sand
V_s	Volume of solids
V_t	Total volume
w_c	Water content
w_i	Ice content
Z	Empirical fitting parameter (Hirsch 1962)
$Z_{0.05}$	Value exceeded by the standard normal variable with a probability of 0.05

Symbols (Greek):

α	Coefficient of friction
α	Non-dimensional constant
α_m	Molecular relaxation coefficient
β	Bias term
β	Coefficient (Sanderson 1988)
χ	Non-dimensional parameter (Ravichandran 1992)

$\delta\varepsilon$	Elastic strain increment
Δ_f	Flaw separation length
Δt	Change in time
ΔV_s	Volume change of specimen
ε	Error term
$\dot{\varepsilon}$	Strain rate
ε_a	Axial strain
ε_{min}	Minimum strain rate
ε_N	Critical strain for nucleation
ε_v	Volumetric strain
ϕ	Degree of roughness
ϕ_m	Curve fitting parameter (Lewis and Nielsen 1970)
γ_d	Dry density
γ_t	Total density
λ	Ratio of confining stress to compressive stress
$\underline{\log \beta}$	Empirical log bias
η_c	Viscosity of suspension
η_m	Viscosity of matrix
μ	Coefficient of friction
μ	Poisson's ratio
ν	Poisson's ratio
ρ_{max}	Maximum dry density
ρ_{min}	Minimum dry density
ρ_p	Particle density
σ	Stress
$\sigma_{11}, \sigma_{22}, \sigma_{33}$	Principal stresses
σ'_N	Compressive stress at which cracks nucleate under compression
σ'_{vc}	Effective vertical consolidation stress
σ^2	Variance
σ_a	Matrix-bead adhesion
σ_b	Stress carried by beads at failure
σ_c	Confining stress
σ_D	Stress at point of discontinuity
σ_N	Tensile stress required to nucleate cracks in tension
σ_{oct}	Mean octahedral stress
σ_y	Yield stress
σ_{yc}	Compressive yield stress of composite
σ_{ym}	Tensile yield stress of matrix
σ_{yt}	Tensile yield stress of composite
τ	Frictional stress transferred to the matrix
ψ	State parameter

CHAPTER 1

INTRODUCTION

1.1 PROBLEM STATEMENT

The effective design of foundations for stable structures in Arctic regions requires detailed knowledge of the strength and deformation characteristics of frozen soils. In North America in particular, development of the permafrost regions is advancing rapidly and engineering design and construction principles need to be formulated that will ensure structural and environmental stability over the long term (Parameswaran and Jones 1981). However, the mechanical properties of frozen soil are perhaps the most variable and difficult of all geomaterials to understand and model (Andersen et al. 1995). The uncertainties regarding its stress-strain-time-temperature response consequently limits the greater use of frozen soil as a structurally effective material.

The importance of frozen ground engineering is not limited to the design of structures in the cold regions of the world. It also pertains to the use of artificial ground freezing as a construction aid to provide temporary support for excavations, tunnels, mine shafts, and buildings. Controlled ground freezing has also been shown to provide a viable and competitive alternative for providing temporary groundwater control for large open excavations. A major limitation to the greater use of artificial ground freezing is the difficulty in predicting the mechanical behavior of the resulting soil-ice material, and the influence of temperature on its behavior. Since frozen soils also have a distinct time dependent strength, the temporal development of stress and strain is also of interest (Bragg 1980).

Understanding and thus predicting the behavior of frozen soil systems is a complex problem owing to the complex interaction between the soil particles and the ice matrix. The mechanical behavior is also influenced by the intrinsic material properties such as moisture content, air bubbles, salts, organic matter, and grain size, and by externally imposed conditions such as strain rate, temperature, stress and strain history, and confining pressure. (Parameswaran and Jones 1981). Nevertheless, the mechanical

properties of frozen soils are gradually being defined through the independent effort of numerous researchers. In addition, there have been many new developments in the understanding of the behavior of the main components of frozen soil, especially in the behavior of polycrystalline ice. The rapid development of the science of composite materials has also allowed certain aspects of frozen soil behavior to be viewed from a more general standpoint, and compared with a vast selection of other composite materials (Ladanyi 1981).

Although much work has been done, much more remains before constitutive relations to model the stress-strain-time-temperature behavior of frozen soil can be developed. A qualitative understanding of basic frozen soil behavior is still, for the most part, lacking in the literature. A key to this understanding, as with soil and ice, is a knowledge of the physical mechanisms controlling the strength of the frozen soil system (Ting et al. 1983). Only after a basic understanding of the mechanisms governing the strength and stiffness generation of frozen sands can progress be made in modeling this material. Furthermore, since it has been shown that in most practical problems, soil undergoes only limited straining under working conditions (Jardine 1994), it is the pre-failure deformation behavior of soil that is generally of greatest interest for design. Therefore, in order to make accurate predictions of deformations around geotechnical structures, the stress-strain response in the pre-failure region of strain must be well understood (Santagata 1998). This usually requires characterization of the initial stiffness and yielding behavior of a geomaterial as a first step. Whereas the factors controlling the small strain response are well understood for clays, most of the current analyses for sands tend to be highly empirical (Jovicic and Coop 1997). A similar situation exists for frozen soils where the factors affecting the small strain behavior of frozen soils are only now starting to be quantified and understood. Much of the earlier work suffered from poor resolution of the axial strains needed to reliably quantify the small strain behavior.

The focus of this report is therefore to further the understanding of the physical mechanisms controlling the pre-failure stress-strain behavior of frozen sands. Although the results of many quantitative and qualitative analyses on the compressive strength behavior of a wide variety of frozen soils is available in the literature, the results fall short

of being able to predict the small strain response without having to resort to testing the material first (Joshi and Wijeweera 1989). In addition, a systematic approach to the investigation of the variables known to influence the mechanical behavior of frozen soils has for the most part been absent from the literature, yet is absolutely essential in uncovering the physical mechanisms operating in these materials.

Much of the work performed in this field at MIT over the last 10-15 years has focused on characterizing the behavior of a frozen sand in triaxial compression under a wide range of strain rates, confining pressures, relative densities, and temperatures. This has been performed with the aid of state of the art high-pressure, low-temperature triaxial testing equipment that has been continuously improved over the years. Recent improvements made to this equipment has alleviated many of the limitations and problems associated with the earlier equipment such as excessive compliance, lack of internal strain and force measurement, and inadequate temperature control. Advances in small strain measurement technology have allowed precise on-specimen measurements of strain which are absolutely essential for the reliable quantification of the initial stiffness and yielding characteristics of frozen sand (Da Re et al. 2000). This has led to the most comprehensive characterization of a frozen sand available in the literature as a function of the main testing variables (i.e. relative density, confinement, strain rate, temperature) from very small strains to very large strains.

With the behavior of a typical frozen sand in triaxial compression being well characterized, it is now possible to explore in greater depth other variables that have been postulated to be important to the strength and stiffness of a frozen sand. They include interfacial bonding and a variety of particle characteristics such as size, shape, stiffness, and roughness. Investigation of these fundamental parameters will greatly aid in our understanding of the mechanisms controlling the stress strain behavior of frozen sand and hopefully will assist in the development of improved modeling techniques for describing the small stain behavior of frozen sands.

1.2 RESEARCH OBJECTIVES

The work included in this report represents a continuation of MIT's commitment to frozen soil research and specifically on the physical mechanisms controlling the strength-deformation behavior of frozen sand. Historically, the approach taken was to conduct a comprehensive experimental program to precisely measure the behavior of a frozen natural sand over a wide range of conditions. Such was the approach taken by Andersen (1991) and Swan (1994) who, as a result of their exhaustive characterization of Manchester fine sand, have advanced the understanding of the behavior of frozen sand considerably. However, many questions still remain as to the underlying fundamental mechanisms that control the behavior of a typical frozen sand.

This research represents the next step that is required before constitutive relationships for frozen sand can be successfully developed. The main objective of this research is then to make progress in understanding the physical mechanisms controlling the pre-failure stress-strain behavior of frozen sand. Whereas previous researchers have focused on one material and a limited set of testing parameters, the work presented herein strictly focuses on the small strain or pre-failure behavior of frozen systems and investigates the importance of a number of more qualitative or subjective parameters. Attention is primarily given to the characterization of Young's modulus and the upper yield stress of frozen sand since these are important parameters in modeling efforts and ultimately to design.

The research pertaining to the Young's modulus has several goals: (1) to investigate the importance of particle modulus and the adhesional bond which exists between the ice matrix and soil particle, (2) to investigate further any dependency on strain rate and temperature, and (3) develop a practical methodology to predict the modulus of frozen sand. Similarly, for the upper yield region the specific goals are: (1) to investigate the role of particle size and adhesional bonding, (2) to determine the mechanisms why the upper yield stress of frozen sand is much higher than the peak strength of ice, and (3) to develop a practical methodology for predicting the upper yield stress.

The aforementioned research programs (i.e. Andersen 1991, Swan 1994) have already characterized the variation of Young's modulus and upper yield stress of a natural

sand as a function of relative density, confinement, strain rate, and temperature. This program addresses the role of the particle size, stiffness, roughness, shape, and interface adhesion in addition to the other four variables. The experimental results are expected to provide valuable insight into the significance of these variables, and then aid in developing a methodology for the prediction of Young's modulus and the upper yield stress, which together describe the most important features of the small strain behavior of frozen sand. Ultimately this work is aimed at providing a qualitative description of the mechanisms controlling the pre-failure behavior of frozen sand.

This program also seeks to enhance the technology available for investigating the small strain behavior of frozen geomaterials in the triaxial apparatus. This includes the development of a reliable, automated, high-performance triaxial testing system with improved strain rate and temperature control, and in particular the development of a versatile on-specimen device that can consistently and accurately measure very small axial strains over a relatively large range of deformation. These improvements have all contributed to the accuracy of the small strain measurements.

Lastly, the author hopes that the data obtained from this experimental program will be used by others in both the geotechnical and material science professions to further the understanding of the behavior of frozen sands and of particulate composite materials as well. In this way many of the uncertainties surrounding the development and design of particulate composite materials may eventually be alleviated.

1.3 ORGANIZATION

This report is organized as a series of eight chapters. It begins with an outline of the goals and objectives of the research, proceeds to give a comprehensive review of the relevant background information, continues with the details of the experimental program and of the equipment and materials used, and finally culminates with a presentation of the experimental data and a detailed analysis which represent the main contributions of this dissertation. All chapters are intended to be self-contained and hence relevant references are included at the end of each chapter. A summary of the purpose of each chapter and their general content follows.

Chapter 2 provides the pertinent background information needed to understand the materials investigated during the current research program. As such, this chapter is divided into three main parts. The first part gives a detailed description of both the continuum and fracture behavior of freshwater polycrystalline ice . The second part summarizes the state of knowledge on the mechanical behavior of frozen sand with much of the discussion focusing on its pre-failure behavior. Lastly, a comprehensive review of the many types of reinforcement theories for two-phase particulate composite materials is given to provide potential frameworks for explaining the elastic properties and yield behavior of frozen sand.

Chapter 3 provides a complete description of the experimental equipment used to perform the type of tests presented in this report. It begins with a brief overview of the Low Temperature Testing Facility (LTTF) and then proceeds to describe the MIT automated high-pressure low-temperature triaxial cell in detail, highlighting the improvements made to it during the course of this research. A description of the system used for data acquisition is also included, although the reader is referred to Sheahan (1991) for a more thorough treatment of this topic. The primary focus of this chapter is to describe the device that was developed for the measurement of small axial strains in the triaxial cell. The device, which features miniature LVDT's mounted on yokes that clamp to the specimen, has been instrumental in observing the levels of strain needed to accurately quantify the pre-failure behavior of frozen sand systems. The chapter also presents a quantitative description of the device's signal stability as a function of time, temperature and pressure, as well as the results of numerous proof tests designed to validate the mechanical design.

Chapter 4 discusses both the materials and specimen preparation techniques used during the experimental program. For each of the granular materials tested pertinent information such as the particle origin, mineralogical composition, grain size, and specific gravity is given. Scanning electron microscopy photographs are included to provide the reader with an idea of the particle shape and roughness. Details of the techniques used to prepare specimens of ice and frozen soil have been thoroughly outlined in an attempt to

standardize the process between this and future research programs such that reproducible results may be obtained.

As outlined in the previous section, the main goal of this research is to investigate the physical mechanisms affecting the pre-failure behavior of frozen sand. Chapter 5 outlines the research methodology employed to achieve this goal by elaborating on the reasons for choosing the variables and materials investigated. Also provided in a detailed explanation of the general testing procedures that were followed for each of the triaxial tests performed. This has been done in order to standardize the procedure as much as possible. Finally, Chapter 5 summarizes the experimental program and the data reduction and evaluation procedures that were used in analyzing the data that was obtained.

The following two chapters, Chapter 6 and Chapter 7, present the results of the experimental program designed to investigate the factors affecting the small strain behavior of frozen sand, namely the Young's modulus and upper yield stress. Chapter 6 addresses the first of these two parameters, the Young's modulus of frozen particulate systems. This chapter begins by presenting the effect that each of the variables and materials investigated have on the composite modulus. Due to the large number of parameters that have been examined, a separate section has been devoted to the discussion of each variable. Following the presentation of the data, a discussion of the mechanisms controlling the Young's modulus of frozen sand is given based on the information derived from the experimental program. A comparison of the experimental data with existing models for the prediction of the composite modulus of two-phase systems is provided. Finally, a methodology for the prediction of the Young's modulus of frozen sand is presented.

Chapter 7 is organized in much the same way as Chapter 6, but focuses on the upper yield properties of frozen systems instead. Following a similar examination of the data according to each of the various variables and materials investigated, a discussion of the mechanisms controlling the behavior and onset of this point is then given. As this point is very particular to frozen systems and ice, few predictive models exist for the description of this point. Hence, comparison with existing models is not possible. This

chapter concludes with a methodology that was developed for the prediction of the upper yield behavior in frozen materials.

Chapter 8 summarizes the main results obtained during the course of the research and presents a series of recommendations for future research in the study of the physical mechanisms controlling the small strain behavior of frozen sand.

Finally, a series of appendices have been included at the end of this report. Details regarding a series of tests that were performed to quantify the effectiveness of the hydrophobic coating at reducing ice adhesion are given in Appendix A. Appendix B contains a summary table of all the experimental results.

1.4 PUBLICATIONS AND REPORTS

The following is a list of publications and reports submitted/published under ARO sponsorship (Grant # DAAH04-96-1-0042):

Publications in Peer-Reviewed Journals:

Da Re, G., Germaine, J.T., Ladd, C.C. (2001), *"Physical Mechanisms Controlling the Initial Stiffness of Frozen Sand"*, Canadian Geotechnical Journal, in preparation.

Da Re, G., Germaine, J.T., Ladd, C.C. (2001), *"Physical Mechanisms Controlling the Upper Yield Stress of Frozen Sand"*, Canadian Geotechnical Journal, in preparation.

Da Re, G., Germaine, J.T., Ladd, C.C. (2001), *"Triaxial Testing of Frozen Sand: Equipment and Example Results"*, ASCE Journal of Cold Regions Engineering, in preparation.

Da Re, G., Ladd, C.C., Andersen, G.R., Swan, C.W., Germaine, J.T. (2001), *"Large Strain Behavior of Frozen Sand in Triaxial Compression"*, Canadian Geotechnical Journal, in preparation.

Da Re, G., Santagata, M.C., Germaine, J.T. (2000), *"LVDT-Based System for the Measurement of the Pre-failure Behavior of Geomaterials"*, ASTM Geotechnical Testing Journal, in print.

Theses:

Da Re, G. (2000), *"Physical Mechansims Controlling the Pre-failure Stress-Strain Behavior of Frozen Sand"*, Doctor of Philosophy Thesis, Massachusetts Institute of Technology, Cambridge, MA, 570p.

Conference Proceedings:

Da Re, G., Germaine, J.T., Ladd, C.C. (1999), *"Strain Rate and Temperature Dependency of the Modulus of Frozen Manchester Fine Sand"*, Proc. 2nd International Symposium on the Pre-failure Deformation Characteristics of Geomaterials, Torino, Italy, pp. 81-88.

Poster Presentations:

Da Re, G., Germaine, J.T., Ladd, C.C. (1998), *"The Mechanical Behavior of Frozen Sand at Small Strains under High Pressure Triaxial Conditions"*, Poster presented at the 7th International Conference on Permafrost, Yellowknife, Canada.

Da Re, G., Germaine, J.T., Ladd, C.C. (1998), *"The Mechanical Behavior of Frozen Manchester Fine Sand at Small Strains"*, Poster presented at MIT Materials Day 1998: Precision in Shape, Process Control, Structure, and Properties, Cambridge, MA.

1.5 STAFF AND ADVANCED DEGREES

Dr. Charles C. Ladd, Professor, and Dr. John T. Germaine, Principal Research Associate, served as co-principal investigators for the entire length of the project. Both are members of MIT's Department of Civil and Environmental Engineering. Dr. Germaine was mainly responsible for supervision of the equipment development and experimental work, while Professor Ladd administered the contract and was mainly responsible for supervising the analyses and reporting the results.

Gregory Da Re was a full-time graduate Research Assistant on the project from its inception to June, 2000. At that time he received a Doctor of Philosophy degree in Civil and Environmental Engineering. He has continued on with the project as a Post-Doctoral Research Associate until March, 2001 performing additional analyses and preparing publications.

The project involved a number of undergraduate students under MIT's Undergraduate Research Opportunities Program (UROP). They were Joon Suk Hor (Spring 1996), Monica Bhattacharya (Summer 1996), Audrey Alchin (Spring 1997), Janette Kelly (Spring 1997), Jared B. Jonas (Spring 1998), Welkin H. Pope (Summer 1998). All were supported using non-ARO funds.

1.6 ACKNOWLEDGEMENTS

The authors appreciate the support of *Dr. Russell Harmon* who acted as the program manager. The authors are also specially indebted to *Dr. David Cole* of CRREL whose expertise has been of considerable help in understanding the behavior of polycrystalline ice. Dr. Cole has also served on the Ph.D. committee of graduate students working on the prior and current ARO-sponsored projects. Dr. Branko Ladanyi, a world renowned expert on frozen soils and permafrost engineering and professor at Montreal's Ecole Polytechnique, served as the external examiner at the doctoral defense of Mr. Gregory Da Re. His help and guidance were invaluable to this project.

1.7 REFERENCES

1. Andersen, G.R. (1991), "Physical Mechanisms Controlling the Strength and Deformation Behavior of Frozen Sand", Sc.D Thesis, Department of Civil and Environmental Engineering, MIT, Cambridge, MA, 560 p.

2. Andersen, G.R., Swan, C.W., Ladd, C.C., Germaine, J.T. (1995), "Small-Strain Behavior of Frozen Sand in Triaxial Compression", *Canadian Geotechnical Journal*, v. 32, no. 3, pp. 428-451.

3. Bragg, R.A. (1980), "Material Properties for Sand-Ice Structural System", Ph.D. Thesis, Department of Civil and Sanitary Engineering, Michigan State University, East Lansing, MI, 281 p.

4. Da Re, G., Santagata, M.C., Germaine, J.T. (2000), "LVDT-Based System for the Measurement of the Pre-Failure Behavior of Geomaterials", *ASTM Geotechnical Testing Journal*, (in print).

5. Jardine, R.J. (1994), "One Perspective of the Pre-Failure Deformation Characteristics of Geomaterials", *Proc. International Symposium on the Pre-Failure Deformation Characteristics of Geomaterials,* Hokkaido, Japan, v.2, pp. 855-885.

6. Joshi, R.C., Wijeweera , H. (1989), "Compressive Strength of Find-Grained Frozen Soils", *Proc. Canadian Geotechnical Conference*, Winnipeg, Canada, pp. 92-102.
7. Jovicic, V. Coop, M.R. (1997), "The Stiffness of Coarse Grained Soil at Small Strains", *Geotechnique*, v.46, no. 2, pp. 357-362.

8. Ladanyi, B. (1981), "Mechanical Behavior of Frozen Soils", *Proc. International Symposium on Mechanical Behavior of Structured Media*, Ottawa, Canada, pp. 205-245.

9. Parameswaran, V.R. and Jones, S.J. (1981), "Triaxial Testing on Frozen Sand", *Journal of Glaciology*, v. 27, no. 95, pp. 147-155.

10. Santagata, M.C. (1998), "Factors Affecting the Initial Stiffness and Stiffness Degradation of Cohesive Soils", Ph.D. Thesis, Department of Civil and Environmental Engineering, MIT, Cambridge, MA, 336p.

11. Sheahan, T.C. (1991), "An Experimental Study of the Time-Dependent Undrained Shear Behavior of Resedimented Boston Blue Clay Using Automated Stress-Path Triaxial Equipment", Sc.D. Thesis, Department of Civil and Environmental Engineering, MIT, Cambridge, MA, 955 p.

12. Swan, C. (1994), "Physical Mechanisms Controlling the Deformation and Strength Behavior of Unfrozen and Frozen Manchester Fine Sand", Sc.D Thesis, Department of Civil and Environmental Engineering, MIT, Cambridge, MA, 1044 p.

13. Ting, J.M., Martin, R.T., Ladd, C.C. (1983), "Mechanisms of Strength for Frozen Sand", *ASCE Journal of Geotechnical Engineering*, v. 109, no. 10, pp. 1286-1302.

CHAPTER 2

BACKGROUND AND COMPOSITE MATERIAL THEORY

2.1 INTRODUCTION

Frozen soil, and specifically frozen sand, is a complex geomaterial whose mechanical properties have proved to be extremely difficult to understand and model. This is due to its behavior being governed by complex interactions between the sand skeleton and the pore ice matrix which continuously change with time as a function of temperature and stress level.

This complicated behavior has been a subject of interest to scientists and engineers since the early 1960's when development and exploitation of the north for purposes of national defense, as well as for petroleum and mining exploration, stimulated research on this subject. Although a complete understanding of frozen soil behavior is still lacking, a substantial amount of research exists on this topic spawned mainly by the activities just described.

The following discussion presents an overview of the micro and macro level mechanical behavior of polycrystalline ice and frozen sand and then introduces a number of reinforcement theories for two phase particulate systems that may be useful for describing the mechanical behavior of frozen sand. This Chapter begins with a review of the structure and mechanical behavior of polycrystalline ice, one of the two main components of frozen sand (Section 2.2). This knowledge is then used in conjunction with information of the behavior of unfrozen sand to understand the complex behavior of frozen sands at both small and large strains in Section 2.3. A review of some of the more promising composite material theories for modeling both the Young's modulus and yielding behavior of frozen sand follows in Section 2.4. Finally, Section 2.5 lists the references pertinent to the material presented in this chapter.

2.2 MECHANICAL BEHAVIOR OF POLYCRYSTALLINE ICE

2.2.1 Introduction

Ice is not purely elastic, viscous or plastic, and so does not readily lend itself to analysis via classical continuum mechanics. When a stress is applied to a specimen of ice, it displays a combination of responses: it shows an instantaneous elastic response, but also immediately begins to creep at a time-dependent rate. In addition, ice also has a low fracture strength causing it to sometimes behave as an extremely brittle material. If the applied stress is high enough, or is applied quickly, the ice will fail by brittle fracture rather than deform by ductile creep. Although both processes are a form of yield, they are quite different and hence must be treated by quite different formalisms.

As such it is convenient to divide the treatment of ice properties into two parts: continuum behavior which considers the elastic and plastic deformation behavior of the material without fracture or rupture; and fracture behavior which considers brittle processes. Although laboratory tests show an apparently smooth transition between ductile and brittle behavior, the two processes have quite different scaling properties which mean that they have to be treated separately.

2.2.2 Structure of Polycrystalline Ice

Many different forms of ice have been identified and they are generally classified according to their crystal type and orientation. This discussion focuses on the behavior of granular or polycrystalline ice. For a full description of the many types of ice found in nature and prepared in the laboratory, the reader is referred to Michel (1979).

The basic ice unit is the single crystal of ordinary Ice Ih, the most stable form of solid water encountered in typical engineering applications. The basic building structure of Ice Ih is a tetrahedron formed by the five oxygen atoms of five water molecules. Hexagonal rings form as three tetrahedrons combine by each sharing two oxygen atoms. These hexagonal rings of oxygen atoms lie in a slightly distorted plane that forms the basal plane and are symmetrical about the *c*-axis, defined as the axis normal to the basal plane (Figure 2.1). An ice crystal lattice consists of layers of these hexagonal rings bonded by relatively weak hydrogen bonds. The density of ice in this arrangement is 0.917 Mg/m^3 at

0°C (Mellor 1980) conferring the important property of positive buoyancy in water. Because the oxygen atoms are packed more densely along the basal plane than they are along the *c*-axis, ice crystals are naturally anisotropic. Shear applied parallel to this plane (easy glide) gives a strain rate about two orders of magnitude higher than that resulting from shear normal to the basal plane (hard glide) (Mellor 1980).

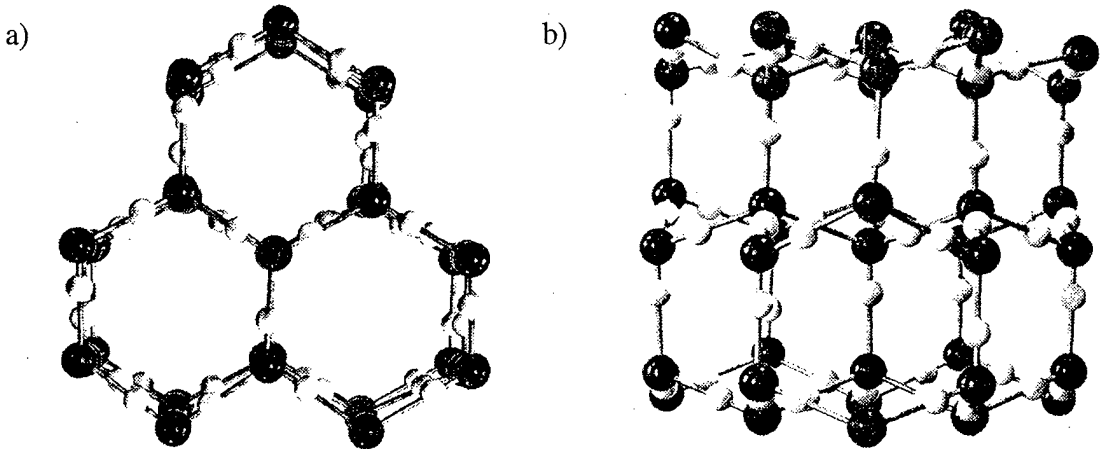

Figure 2.1: Crystal structure of Ice Ih showing the tetrahedral constituent unit: (a) view along the *c*-axis, (b) view along the basal plane layers. (Sanderson 1988)

Anisotropy of the monocrystal greatly influences the mechanical behavior of polycrystalline ice. Polycrystalline or granular ice is a conglomerate of randomly oriented crystals of ice, typically with a grain size of 1-3 mm (Sanderson 1988). It is the kind of ice normally found in glaciers, icebergs, and permafrost. If the crystal orientations are truly random, then the mechanical properties of the ice are statistically isotropic. Many laboratory studies on granular ice are carried out on ice formed by flooding fine snow crystals with cold water. This is known as T-1 ice. When T-1 ice is stressed the compliance of individual grains varies, depending partly on how the basal planes are oriented relative to the stress field. Recrystallization under prolonged deviatoric loading can take place so as to bring basal planes into closer coincidence with resolved shears, and consequently the crystal orientation ceases to be random (Mellor 1980).

2.2.3 Mechanisms of Deformation

An analysis of the microscopic deformational mechanisms occurring within polycrystalline ice (e.g., elastic strains, delayed elastic strain, tertiary creep) needs to consider the mechanics of individual crystal grains as they interact with each other. Figures 2.2a-e represent, schematically, the processes occurring within and around a single grain in a cylindrical specimen of polycrystalline ice under uniaxial compressive stress.

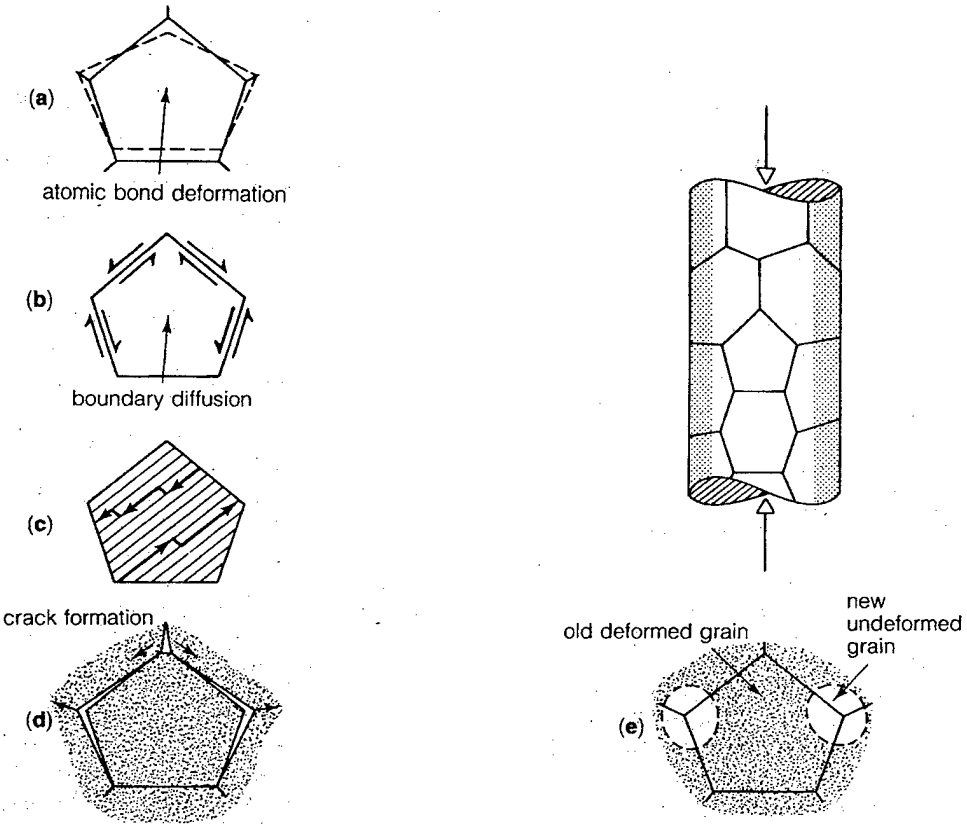

Figure 2.2: Schematic of deformation processes within a grain during uniaxial loading: (a) elastic deformation by atomic bond deformation, (b) delayed elastic strain as a result of grain boundary sliding, (c) secondary creep by dislocation glide and climb, (d) crack formation due to dislocation pile-up at grain boundaries, (e) dynamic recrystallization leading to the formation of fresh grains. (Sanderson 1988)

Elastic deformational processes involve the elastic straining of the hydrogen bonds holding the water molecules in the ice lattice (Figure 2.2a). As a specimen is subjected to an external compressive stress, grains initially deform in a purely elastic and reversible manner simply by the lengthening and shortening of atomic bonds as necessary to

accommodate the strain. Upon the removal of stress they return to their original position. Elastic deformations can be observed under all loading conditions so long as sufficient care is taken to make high quality measurements (Cole 1990).

Anelastic (delayed elastic) strains refer to time dependent elastic deformations in ice and play a significant role in primary (transient) creep. As a result of shear stresses generated between grains, sliding occurs at the grain boundaries, storing up additional elastic energy within the grain itself. Sliding generally occurs by the mechanism of diffusional flow, at a rate that depends on the grain size, since diffusion of matter must take place over a distance of the order of a grain facet (Figure 2.2b). Diffusional flow is associated with the motion of point vacancies through the crystal lattice and along grain boundaries. The sliding occurs in conjunction with an elastic deformation of the grain, but in the case of pure delayed elastic strain, no internal permanent deformation of the grain takes place. All of the atomic rearrangement processes occur at the boundary. This means that if the applied stress is relaxed, then the grain will eventually recover its original undeformed shape. To do so it must reverse all the sliding that has occurred. This must occur by diffusional flow and accounts for the reversibility of the anelastic strain. Duval (1978) observed anelastic deformations in monotonic creep tests upon removal of the load, and Cole (1990) observed anelastic deformations in cyclic tests as a hysteretic behavior. In monotonic loading and unloading creep tests the anelastic strain can be more than an order of magnitude greater than the corresponding elastic strain (Duval et al. 1983).

Plastic deformation mechanisms include those mechanisms which result in the irreversible rearrangement of the material within the grain such as dislocation climbing processes. Grain boundary sliding occurs in conjunction with diffusion of point defects and leads to Newtonian fluid type behavior. These mechanisms dominate the deformation behavior only at very low stresses or strain rates such as those associated with the flow of glaciers (Langdon 1973). Dislocation gliding leads to the slipping of adjacent sections of a given crystal, with dislocation climb occurring where necessary for compatibility (Figure 2.2c). Dislocations are linear defects in the crystalline lattice and travel at velocities which are linearly proportional to the shear stress acting on them. Research by Langdon (1973)

and Duval et al. (1983) suggest that dislocation glide and climb dominate the behavior of polycrystalline ice and are responsible for secondary creep. As a result of these processes, dislocations tend to pile up at grain boundaries. Eventually this may lead to the formation of cracks (Figure 2.2d) and accelerating strain rates. This is one cause of tertiary creep. Alternatively, especially at high temperatures, dynamic recrystallization may occur in regions of high dislocation density (Figure 2.2e). Instead of cracks forming, extensive rearrangement of dislocations occurs, resulting in the formation of a new, effectively dislocation-free grain.

Internal fracturing and cracking processes dominate the behavior of polycrystalline ice when the strain rates (or creep stresses) are too high or the temperatures are too low to allow for significant contributions from other deformational mechanisms. Cracking can result from the pile-up of dislocations at grain boundaries as described above, and from the elastic stresses developed from the anisotropy of the individual crystals. Cracking results in a volumetric component to the straining of the crystals and hence exhibits strong pressure sensitivity. Jones (1982) found that pressures in excess of 10-20 MPa at -11°C appear to be sufficient in suppressing internal fracturing activity at all strain rates.

2.2.4 Deformation and Failure Under Uniaxial Stress

Much of the information on the mechanical properties of ice is derived from laboratory tests that apply uniaxial stress in compression or tension. The basic tests are creep tests under approximately constant stress, and strength tests at an approximately constant strain rate. If these tests are carried to sufficiently large strains, they will exhibit the response illustrated in Figure 2.3.

2.2.4.1 Creep Under Constant Axial Stress

Figure 2.3a illustrates the results from a typical creep test on a specimen of polycrystalline ice. The conventional representation of this type of test data is a plot of strain as a function of time. The complete strain-time curve displays four distinct regions: (1) instantaneous elastic strain, (2) decelerating creep rate, or strain hardening (primary creep), (3) a period of transition or constant creep rate (secondary creep), and (4) an

accelerating creep rate, or strain softening (tertiary creep). The inflection point shown in Figure 2.3a gives the minimum strain rate for the applied stress, and also the failure strain. The strain at the inflection point has not yet been determined systematically, but it appears to be slightly less than 1% for typical stresses encountered in typical engineering applications.

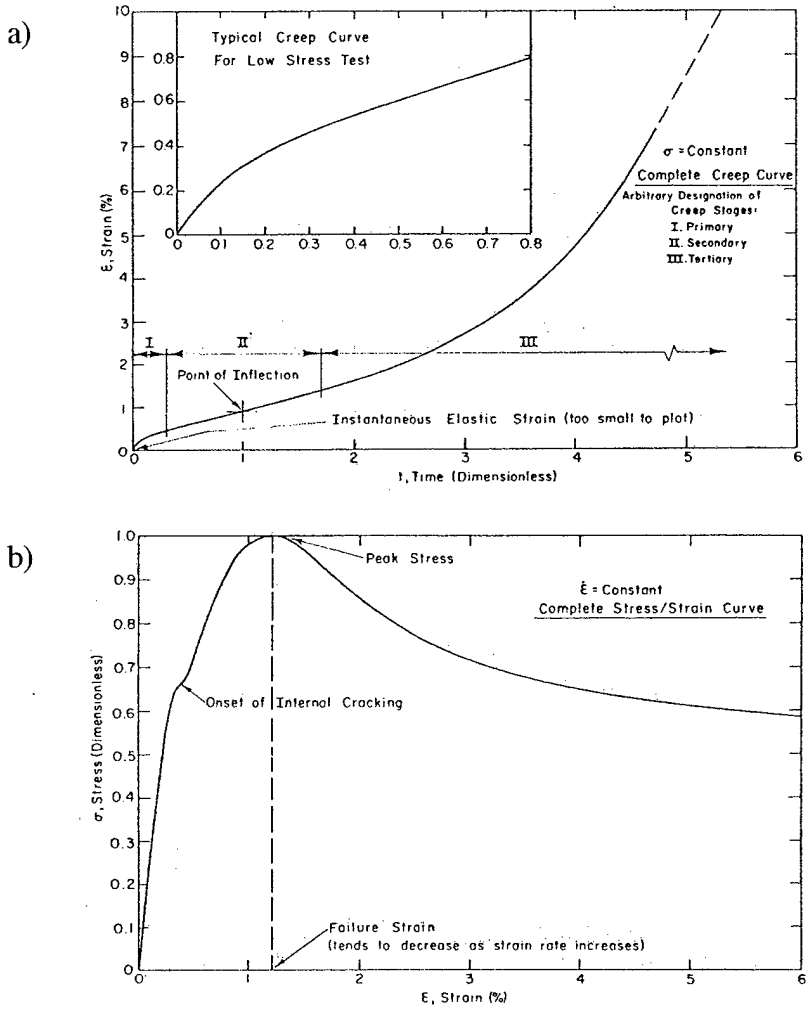

Figure 2.3: Deformation behavior of polycrystalline ice: (a) complete creep curve for a constant stress test on ice that is initially isotropic, (b) complete stress-strain curve for a constant strain rate test at moderate strain rate. (Mellor 1980)

Alternative presentations of creep data are also possible. One useful procedure is to plot strain rate against strain or against time using logarithmic scales. Such plots are

shown in Figure 2.4 and show immediately whether a minimum strain rate has been reached, thus helping to prevent the terminal strain rate from being accepted as the minimum secondary creep rate in tests terminated while still in decelerating creep.

The broken lines in Figures 2.3 and 2.4 show the uncertainty during tertiary creep. This arises partly from the practical difficulty of running uniaxial tests to large strains without undue distortion of the test geometry.

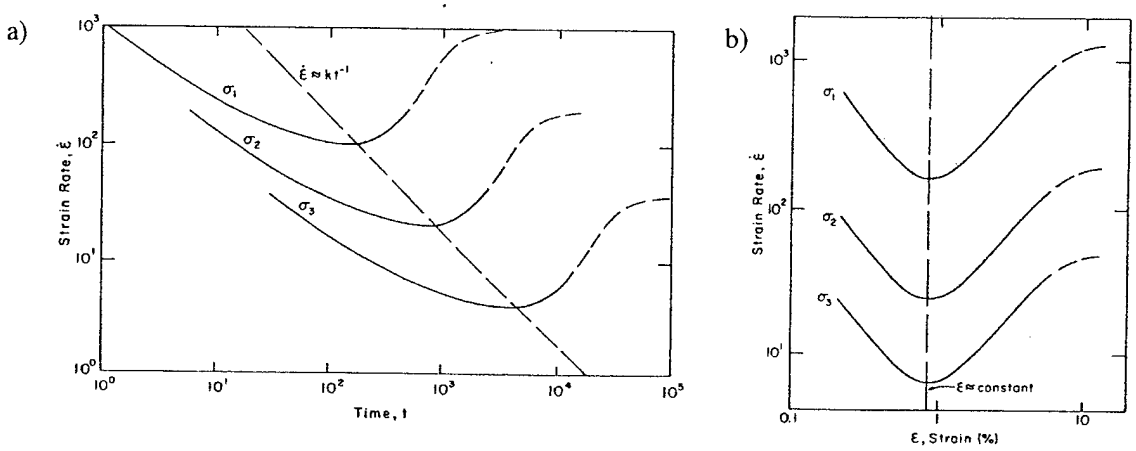

Figure 2.4: Alternative presentations of creep curves: (a) using a log-log plot of strain rate against time, (b) using a log-log plot of strain rate against strain. (Mellor 1980)

2.2.4.2 Deformation at Constant Strain Rate

Figure 2.3b illustrates results from a typical strength test which involves the application of a constant axial strain rate to a specimen of polycrystalline ice with or without confinement. The conventional presentation of data is a plot of stress as a function of strain. In general, the complete stress-strain curve displays: (1) a non-linear increase of stress with strain, the slope at the origin representing the initial tangent modulus, (2) an initial yield point signifying the onset of internal cracking (only detected with on-specimen strain measurement), (3) a peak where stress is a maximum and where the slope of the curve is zero, (4) a non-linear decrease in stress with strain and the slope gradually decreasing in magnitude to a value at some finite value of stress. The amount of post-peak strain softening increases at higher strain rates and lower temperatures and is also reduced by added confinement. However, in all cases of interest, there is a very

significant post-peak loss in the strength of polycrystalline ice having a grain size of about 1 mm (Swan et al. 1995).

Polycrystalline ice exhibits a different behavior in uniaxial tension than in compression. Figure 2.5 shows the stress-strain response of two constant strain rate tests performed by Hawkes and Mellor (1972). As illustrated in this figure, tensile specimens fail by brittle fracture even at relatively low strain rates.

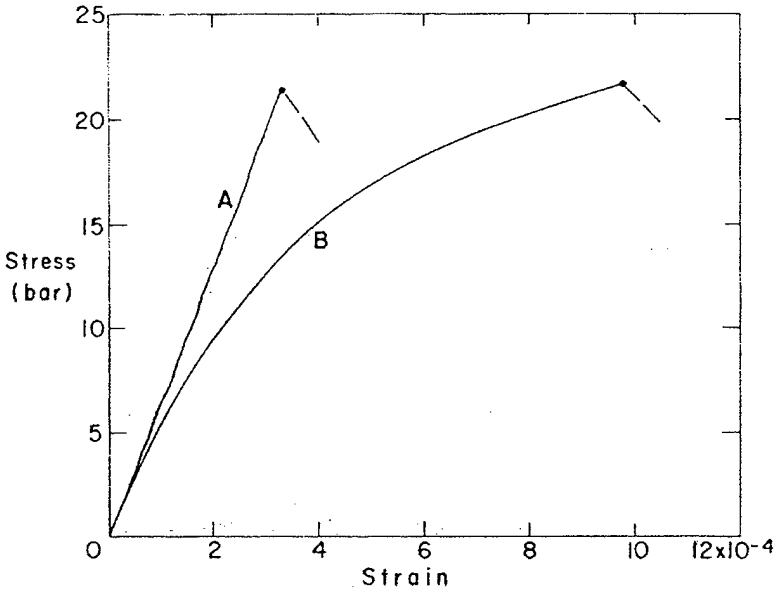

Figure 2.5: Stress-strain curves from uniaxial tension tests on polycrystalline ice at -7±1°C, A: $\dot{\varepsilon}=6.4\times10^{-4}$ s^{-1}, B: $\dot{\varepsilon}=3.3\times10^{-6}$ s^{-1}. (Hawkes and Mellor 1972)

2.2.4.3 Correspondence Principle

When samples of the same material are subjected to constant stress and constant strain rate tests, the same material properties should be revealed by each test. The stress-strain correspondence is a relationship between the applied stress and minimum strain rate in creep tests, and the peak strength and the applied strain rate in strength tests. The minimum strain rate ($\dot{\varepsilon}_{min}$) for a given stress is obtained on the log-log creep curve at the inflection point. The maximum stress for a given strain rate is obtained on the stress-strain curve by the peak stress (σ_{max}). Thus, each test gives a pair of σ–$\dot{\varepsilon}$ values for which $\sigma/\dot{\varepsilon}$ is a maximum. If both tests give the same information, a stress-strain plot for $(\sigma/\dot{\varepsilon})_{max}$ will be the same for both tests, at least where the yielding is predominately ductile. This is true so

long as the mechanical properties of the ice do not change under these two loading conditions. This relationship, between the minimum strain rate and the applied stress, is often referred to as the *flow law* of ice or *flow curve*.

The relationship is usually presented graphically as a log-log plot for tests at constant temperature (Figure 2.6). The linear portion of the flow curve, which represents the region where ice exhibits ductile behavior, is commonly called the region of power law creep and can be expressed by an equation of the form:

$$\dot{\varepsilon}_{min} = B\sigma^n \tag{2.1}$$

where the exponent n is between 3 and 4, and B is a temperature dependent constant that can be expressed in terms of the classical Arrhenius activation energy law (Section 2.2.5.1). As seen in Figure 2.6 the ductile region for compression extends to higher strain rates than that for uniaxial tension. At faster rates of straining power law breakdown occurs as the ice begins to behave in a more brittle manner with significant cracking and fracturing occurring during shear. Typically, a transition zone exists between the ductile and brittle regimes which involves attributes from both regions. Since the simple power relation does not fully describe this behavior, various alternative expressions have been used. The most common is the hyperbolic sine function as applied by Barnes et al. (1971).

2.2.5 Continuum Behavior

As previously mentioned, polycrystalline ice exhibits elastic, ductile, and brittle behavior. The discussion of the continuum behavior of polycrystalline ice is restricted to the elastic and ductile deformation behavior prior to the onset of fracture which is thought to occur at the initial yield point as shown in Figure 2.3b.

The elastic behavior of polycrystalline ice can be described in terms of the Young's modulus (E) and Poisson's ratio (ν or μ). These parameters in theory can be typically measured by applying a uniaxial stress (σ) to a specimen at time t_o. The instantaneous true elastic strain (ε_e) which occurs follows Hooke's Law:

$$\varepsilon_e = \frac{\sigma}{E} \tag{2.2}$$

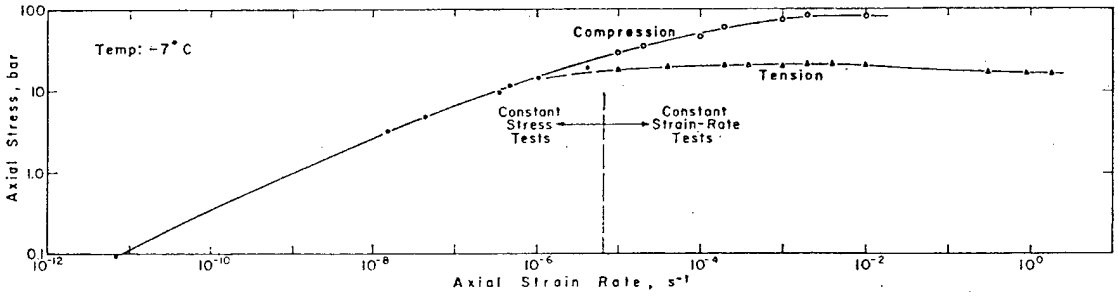

Figure 2.6: Stress-strain rate data for uniaxial tests on polycrystalline ice specimens at -7°C. (Mellor 1980)

The theoretical value of E for pure polycrystalline ice is thought to be about 9 GPa and is not strongly dependent on temperature (Sinha 1989). Using averaging techniques appropriate for a system of hexagonal crystals, Sinha (1989) computed the Young's modulus, shear modulus (G) and Poisson's ratio for granular ice over a temperature range of 0°C to -50°C. Figure 2.7 illustrates these results.

However, lower values for the Young's modulus of polycrystalline ice, in the region of 5-7 MPa, are often quoted in the literature from the results of static or monotonic loading tests. These lower values are usually attributed to time-dependent delayed elastic strain effects which manifest themselves from the moment the load is first applied. The deformation is not permanent, but reversible, and if the ice is suddenly unloaded it should, under ideal conditions, gradually recover all the deformation due to this delayed elastic strain process. This is why it is referred to as an elastic strain, even though it is manifested as a time-dependent process, and why it is sometimes confused with true elastic strain (Sanderson 1988).

The truly elastic properties are best measured by applying high-frequency oscillating pulses or vibrations which do not allow significant creep deformations to take place. Under these conditions the theoretical value of Young's modulus can be measured. Young's modulus is, however, quite strongly dependent on porosity, whether due to the inclusion of air or brine. At 10% porosity, E has a value of about 7 GPa (Weeks and Mellor 1984). Poisson's ratio for pure ice has been measured to be approximately 0.33±0.03 (Weeks and Assur 1967) ,though again, different values (somewhat higher) are sometimes quoted if creep deformations are significant. Sinha (1989) calculates Poisson's

ratio to be approximately 0.31, decreasing slightly with increasing temperature as shown in Figure 2.7.

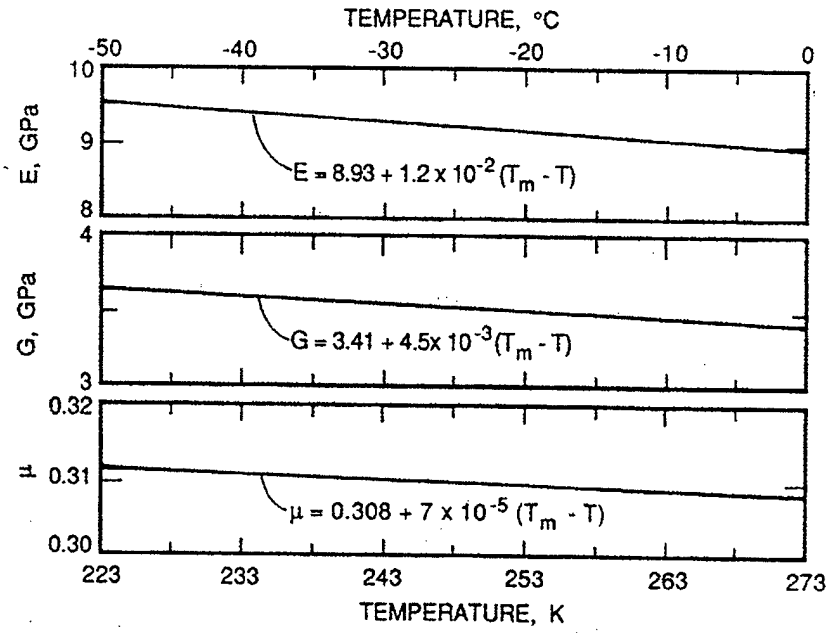

Figure 2.7: Temperature dependence of Young's modulus (E), shear modulus (G), and Poisson's ratio (μ), of granular ice where T_m is the melting point. (Sinha 1989)

The strength of a material is usually defined in terms of the maximum stress that can be reached when the material is loaded at either a constant strain rate or a constant stress rate. For polycrystalline ice at a constant temperature, this stress is strongly rate dependent and so its strength must be specified as a function of strain rate. This property was shown previously in Figure 2.6 and a simple power law relationship (Equation 2.1) was introduced to describe the strength of this material in the ductile region. A vast amount of experimental data, derived in both tension and compression, exists to confirm this equation for pure ice (Figure 2.8).

Over a wide range of strain rates (from 10^{-10} s^{-1} to 10^{-5} s^{-1}) the data in Figure 2.8 shows a clear and consistent slope of about 3 over a wide range of temperatures indicating that the power index in the flow law equation is approximately equal to 3. This is the index which is expected to be associated with creep by the mechanism of dislocation glide as discussed by Goodman et al. (1981).

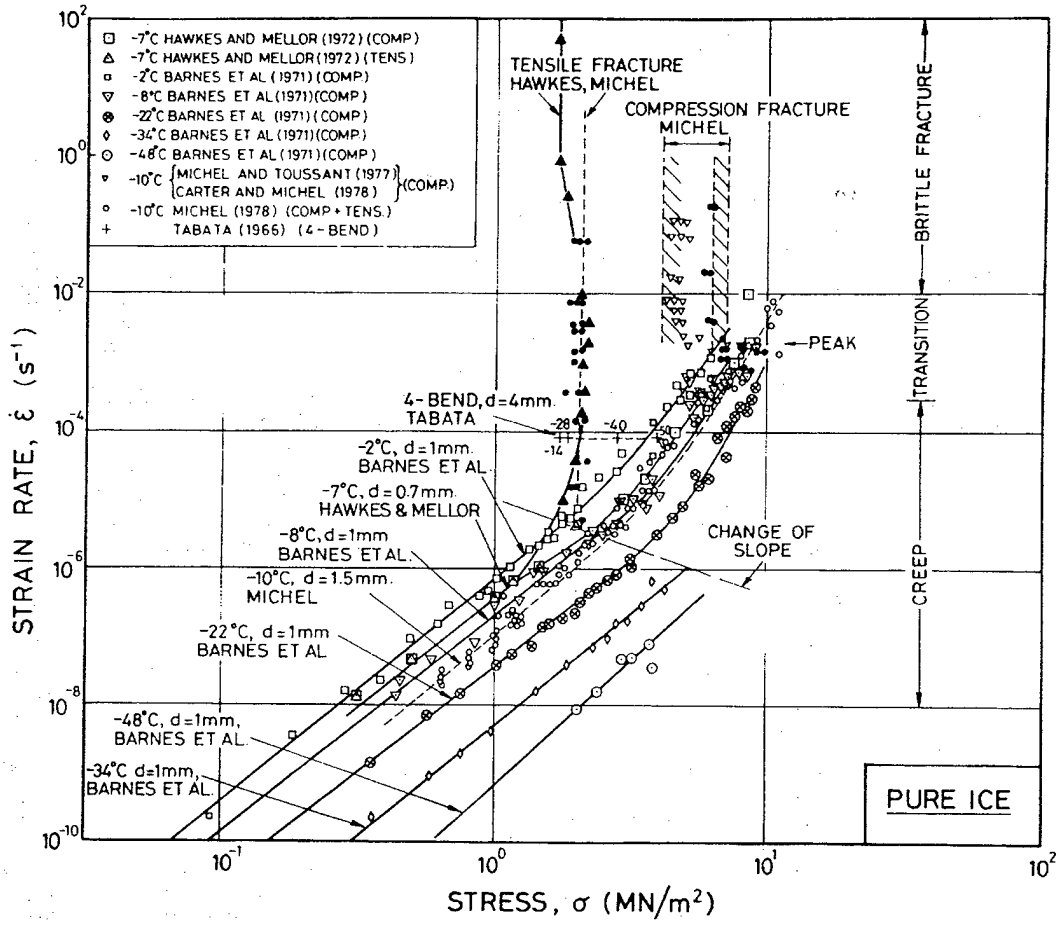

Figure 2.8: Uniaxial loading of pure polycrystalline ice. Below a strain rate of 10^{-5} s^{-1} power law creep occurs with n=3. Note: at stresses exceeding 5-10 MPa, a transition to brittle behavior occurs. (Sanderson 1988 after Hallam 1986)

2.2.5.1 Effect of Temperature

As Figure 2.8 shows, the strength of polycrystalline ice is dependent on temperature. Mellor and Testa (1969a) investigated this effect using constant stress tests and observed a decrease in the minimum strain rate ($\dot{\varepsilon}_{min}$) with a decrease in temperature (Figure 2.9). The trend is linear for temperatures below -10°C, but non-linear at higher temperatures. This trend with temperature can be well described by incorporating the classical Arrhenius activation energy law into the constant B in Equation 2.1 such that:

$$B = A \cdot \exp\left(-\frac{Q_a}{RT}\right) \tag{2.3}$$

where R = 8.314 J mol^{-1} K^{-1} (the universal gas constant), T is temperature in Kelvin (K), and Q_a is the activation energy. The constant A depends only on crystal type (i.e. granular ice vs. columnar ice). This formulation is based on the assumption that creep is a thermally activated process. For granular ice at temperatures below -10°C, the variation in the minimum strain rate with temperature can be described using a constant activation energy of about 70 kJ/mol. The non-linear behavior at higher temperatures indicates that the activation energy is changing, possibly due effects such as increased grain boundary melting. Thus, the Arrhenius equation may not be applicable at temperatures greater than -10°C for polycrystalline ice. A summary of the Arrhenius constants computed from tests on polycrystalline ice over a wide range of temperatures is given by Barnes et al. (1971).

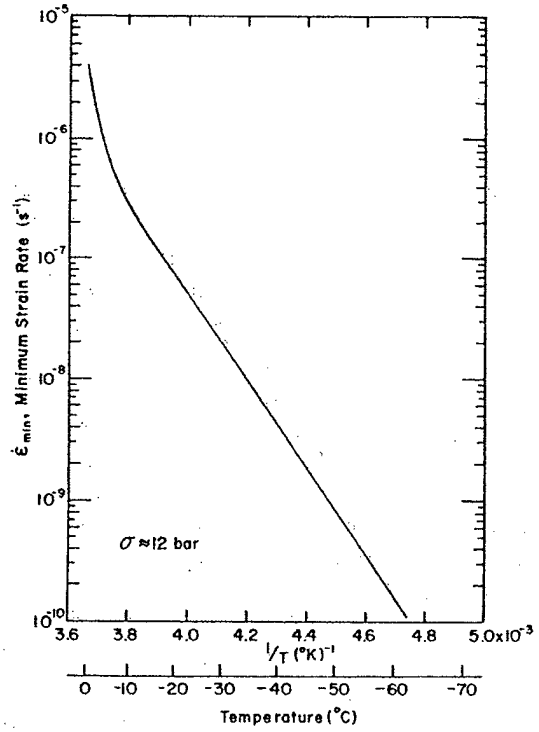

Figure 2.9: Experimental curve for logarithm of minimum strain rate plotted against the reciprocal of absolute temperature. (Mellor 1980 after Mellor and Testa 1969)

Incorporating Equation 2.3 above into the power law expression and using n=3 yields:

$$\dot{\varepsilon} = A \cdot \exp\left(-\frac{Q_a}{RT}\right) \cdot \sigma^3 \qquad (2.4)$$

The equation can of course be inverted to derive stress (strength) from strain rate:

$$\sigma = \left[\frac{1}{A}\cdot \exp\left(\frac{Q_a}{RT}\right)\dot{\varepsilon}\right]^{\frac{1}{3}} \tag{2.5}$$

At rates above about 10^{-5} s^{-1} the data in Figure 2.8 shows signs of power law equation breakdown. This is probably due to a gradual change in the deformation mechanisms which leads to polycrystalline ice exhibiting crack formation at higher rates of strain as already discussed.

2.2.5.2 Effect of Confinement

The application of confining pressure leads to the overall strengthening of isotropic polycrystalline ice, but the magnitude depends on the applied strain rate and applied stress level. For strain rates which encompass the ductile behavior of ice there is little effect, regardless of the confinement (Figure 2.10). At higher strain rates, where crack formation becomes important, increases in confining pressure can lead to significant strength gains. For confining pressures greater than about 20 MPa, fracture behavior is suppressed and the strength of ice becomes independent of the level of confinement and solely a function of strain rate (and temperature). Increased confinement is thought to increase the stress required to nucleate a crack, and increases the frictional resistance along cracks which develop (Jones 1982). Hence, this strengthening effect only becomes important when internal cracking becomes important, such as in the ductile-to-brittle regime of ice behavior. This is discussed in more detail a subsequent section dealing with the fracture behavior of polycrystalline ice. It should be noted that at high homologous temperatures, high confining pressures also contribute to pressure melting which has been shown to lead to a decrease in strength (Jones 1982).

2.2.5.3 Effect of Grain Size

The effects of grain size on the creep rate and strength of ice has received limited attention in the literature. Part of the reason lies in the difficulty in preparing ice grains smaller than about 0.5 mm in the laboratory since they tend to grow spontaneously, while grains larger than 10 mm are very large relative to typical specimen sizes.

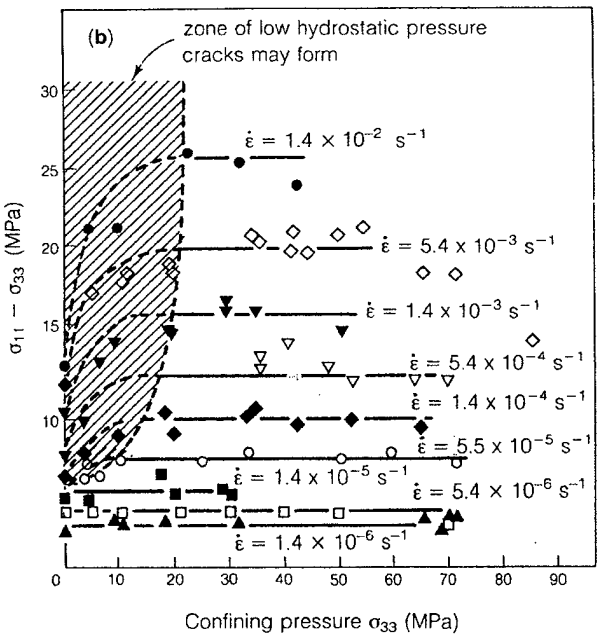

Figure 2.10: Effect of confinement on the peak strength of bulk polycrystalline ice in triaxial compression at various strain rates at -11.5°C. (Sanderson 1988 from data of Jones 1982)

A decrease in grain size from the coarse (10 mm) to the fine (1 mm) range has been shown to lead to an increase in strength (e.g., Cole 1987, Schulson et al. 1984), especially at strain rates in the ductile-to-brittle transition regime (Figure 2.11). In this region, a shift from a mechanism of crack nucleation based on dislocation pile-ups to a mechanism based on elastic anisotropy can be expected as the strain rate increases and the material becomes more brittle (Gold 1972). Thus, an increase in strength with decreasing grain size is not surprising. Internal cracking theories (e.g., Cole 1988, Shyam Sunder and Wu 1990) also predict an increase in strength with a decrease in grain size. However, it should be pointed out that Cole (1987) found a reversal of this grain size effect at very slow strain rates ($<5x10^{-6}\ s^{-1}$) and attributed this apparent change in behavior to dynamic recrystallization processes that intervene and serve to lower the peak stress. Similarly, a decrease in grain size from the fine (1 mm) to the ultra-fine ($<<1$ mm) range may result in a significant decrease in strength since finer grained specimens offer a greater number of potential nucleation sites for recrystallization to occur (Cole 1987).

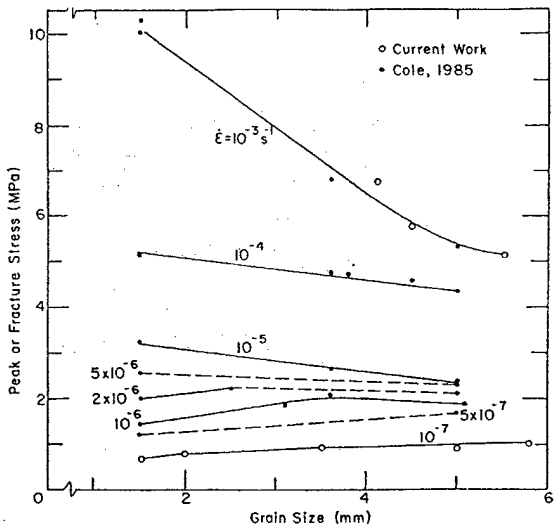

Figure 2.11: Peak unconfined compressive stress of polycrystalline ice at -5°C as a function of grain size at various strain rates between 10^{-7} s^{-1} to 10^{-3} s^{-1}. (Cole 1987)

2.2.6 Fracture Behavior

At a certain stage in the loading process, ice may display a gradual or sudden change of deformation mechanism and begin to exhibit brittle behavior due to crack formation instead of pure continuum creep and elasticity. The onset of fracture behavior (i.e. the initial yield point in the stress-strain curve) may be interpreted as being due to:

(a) the stress exceeding a certain level (under uniaxial compression this appears to be about 5-10 MPa; and under uniaxial tension it appears to be about 1-2 MPa),

(b) the strain rate exceeding a certain level. From Figure 2.8 this appears to lie in the region of 10^{-5} s^{-1} for uniaxial compression at -10°C,

(c) the strain in the material exceeding a certain critical level, generally 1% or more.

The most important distinction to make when discussing fracture behavior is that different processes control the *nucleation* of a crack and the *propagation* of the crack. A sample may contain pre-existing micro-cracks, or cracks may nucleate and develop during the loading process. However, if the stress field is insufficient to make these cracks propagate, then the specimen will not fail. The specimen may undergo a phase of accelerating creep but unless the fractures extend and link together, the sample will remain intact. Even if cracks do propagate under the prevailing stress field, they may do so at a

stable rate in which case it is necessary to investigate how far they must propagate before failure occurs (Sanderson 1988).

Although an applied load may induce the nucleation of very small micro-cracks, it may not be sufficiently large to propagate the crack. In this case, the load must be increased further to cause crack propagation. This fracture process is often referred to as being *propagation controlled.* This is a common phenomenon in fine grained samples of ice. After nucleation the sample may contain many cracks and show increased ductility and loss of stiffness due to their presence, but failure does not occur until they propagate. If however the applied load results in the formation of larger micro-cracks they may propagate the moment immediately after they nucleate. In this case the fracture process is *nucleation controlled.* If the cracks had existed before the load was applied they would have propagated at a lower load.

The distinction between the two controlling mechanisms depends on the size of the cracks when they nucleate. This in turn depends principally on the grain size of the ice. Although this is best demonstrated by the tensile fracture of ice, the following discussion concentrates on the compressive fracture of ice since it is more relevant to this work. The reader is referred to Sanderson (1988) for a complete discussion of the tensile and compressive fracture of polycrystalline ice.

2.2.6.1 Compressive Fracture

The nucleation of cracks under compressive stresses is generally due to the pile-up of dislocations at grain boundaries, and the relief of stress concentrations by parting along grain boundaries. However, cracks may also form across grains. These are referred to an trans-granular cracks.

Experimental evidence suggests that the onset of internal crack formation for low to moderate loading conditions is related simply to the total delayed elastic strain which is dependent on grain size (Sinha 1982). Sanderson (1988) discusses some of problems associated with applying this criterion to higher loading rates since it implies that the initial bearing capacity of ice is infinite. Furthermore, since delayed elastic strain takes a finite

time to develop, fractures would not be expected to nucleate immediately however high the applied stress is.

In order to resolve this problem, an alternative crack nucleation criterion is therefore required. Hallam (1986) proposed that crack nucleation under compressive stress occurs when the lateral tensile strain induced by Poisson expansion reaches a level defined as critical for tensile crack nucleation.

In tensile tests on polycrystalline ice, the stress for nucleation to occur shows a clear dependence on grain size as shown in Figure 2.12. The dependence can be well modeled by the following equation:

$$\sigma_N = \sigma_0 + \frac{k_1}{\sqrt{d}} \tag{2.6}$$

where σ_N is the tensile stress required to nucleate cracks in tension as a function of the grain size d and two constants σ_o and k_1. Equation 2.6 can be rewritten in terms of the critical strain for nucleation ε_N:

$$\varepsilon_N = \varepsilon_0 + \frac{k_2}{\sqrt{d}} \tag{2.7}$$

where the constants ε_o and k_2 are related to σ_o and k_1 by Young's modulus. Under a compressive stress σ_{11}, the lateral tensile strain ε_{22} is given by:

$$\varepsilon_{22} = -\nu\frac{\sigma_{11}}{E} \tag{2.8}$$

where ν is Poisson's ratio. Crack nucleation occurs when the lateral Poisson expansion strain ε exceeds the level ε_N defined in Equation 2.7. This leads directly to the following expression for the compressive stress σ'_N at which cracks nucleate under compression:

$$\sigma'_N = -\frac{\sigma_N}{\nu} = -\frac{1}{\nu}\left(\sigma_0 + \frac{k_1}{\sqrt{d}}\right) \tag{2.9}$$

with constants as defined previously. This implies that the stress required to nucleate a crack under compression is about three times that required in tension since $1/\nu \sim 3$. This is consistent with the data in Figure 2.8 where for fine grained polycrystalline ice, brittle tensile fracture occurs at about 1-2 MPa and brittle compressive fracture occurs at about 4-6 MPa.

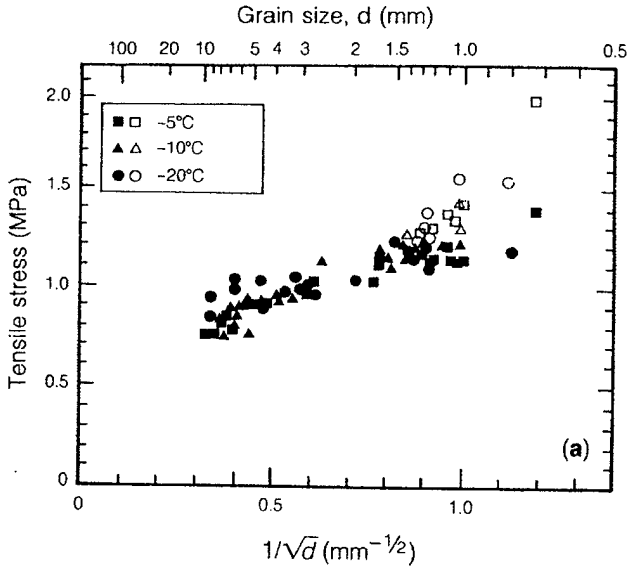

Figure 2.12: High strain rate data for tensile loading of polycrystalline ice as a function of grain size. Note: closed symbols indicate crack nucleation while open symbols indicate crack propagation. (Schulson et al. 1984)

The process of crack propagation under compressive stress does not always lead to failure. This is because the propagation of cracks in compression is generally a stable process, and final failure generally occurs by the linkage of a large number of cracks and not simply by the catastrophic propagation of a single crack such as that which occurs in tension.

The basic criterion for propagation uses linear elastic fracture mechanics, which was developed originally for more conventional engineering materials such as steel subjected to tensile stresses. The criterion states that a crack or flaw of length $2a$ in a material (Figure 2.13) will propagate unstably under a normal tensile stress (σ) if:

$$\sigma > \frac{K_{Ic}}{\sqrt{\pi a}} \tag{2.10}$$

where K_{Ic} is the fracture toughness of the material, and for truly elastic materials, is quite well behaved and easily measured. Ice is unfortunately substantially more complex owing to its creep properties. Under rapid loading conditions ice may be treated by simple linear elastic fracture mechanics, but under slower loading conditions ductile processes advancing the crack complicate the behavior. At slower rates of deformation the apparent

fracture toughness of ice is higher, that is, it displays higher strength. Nevertheless, the fracture toughness K_{Ic} of pure polycrystalline ice is approximately 0.115 MPa $m^{1/2}$ (Goodman 1979), although it shows some variations with loading rate and temperature as a result of the non-linear ductile processes discussed previously.

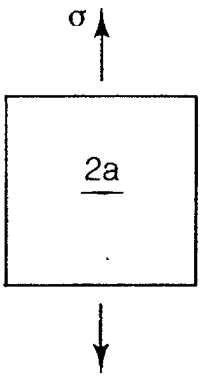

Figure 2.13: Simple geometry for tensile propagation of a flaw of half-length *a* subjected to a stress σ.

After nucleation of cracks at grain boundaries a specimen of ice under compression contains a wide variety of cracks, of length on the order of the grain size, lying at various angles clustered around the axis of loading. For the purposes of determining the stress at which a crack will propagate in compression, the system has been simplified as shown in Figure 2.14. It represents a single crack of length 2*a* inclined with respect to the principal compressive stress (σ_{11}) and subject to a lateral confining stress (σ_{33}).

As the load (stress) is applied, the crack tries to slide, and at a certain stress level tensile "wing cracks" form and the process of propagation begins (Figure 2.14a). This process has received widespread attention, particularly in the area of rock mechanics. Figure 2.14b shows a two-dimensional model of an idealized crack (Ashby and Hallam 1986). As the stress increases, wing cracks form and grow stably to a length *l*. This length can be related to the stress conditions and the mechanical properties of ice. The general result is:

$$K_{Ic} = \frac{\sigma_{11}\sqrt{\pi a}}{(1+L)^{3/2}}\left[1-\lambda-\mu(1+\lambda)-\frac{\sqrt{3}\lambda L}{\beta}\right]\cdot\left[\frac{\beta L}{\sqrt{3}}+\frac{1}{\sqrt{3}(1+L)^{1/2}}\right] \qquad (2.11)$$

where K_{Ic} is the fracture toughness, a is the half-length of the initial crack, l is the length of the wing cracks, $L = l/a$, $\lambda = \sigma_{33}/\sigma_{11}$ (the ratio of the confining stress to the axial stress), β is a coefficient (~0.4), and μ is the coefficient of friction across the crack.

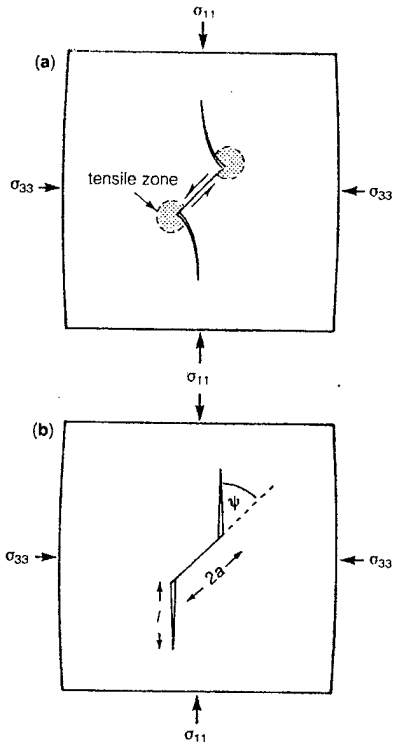

Figure 2.14: Model for crack propagation in a brittle solid in compression: (a) formation of wing cracks in tensile zones, (b) idealized model of wing crack formation for analytical treatment. (Sanderson 1988)

Rearranging and assuming simple uniaxial compression yields:

$$\sigma_{11} = 3.5 K_{Ic} \sqrt{\frac{l}{a^2}} \qquad (2.12)$$

A full explanation of the detailed physics behind this equation can be found in Ashby and Hallam (1986). Equation 2.12 then gives the compressive stress required to propagate wing cracks of length l in a specimen of polycrystalline ice.

For failure to occur in compression, linkage of a large number of propagating wing cracks needs to occur, although it is not clear exactly what degree of crack propagation will necessarily lead to complete failure of a specimen. However, if initial flaws are separated by some average distance of order Δ_f (Figure 2.15), it is likely that wing cracks

will have to propagate a distance of no more than half that distance before the specimen is so damaged that failure occurs.

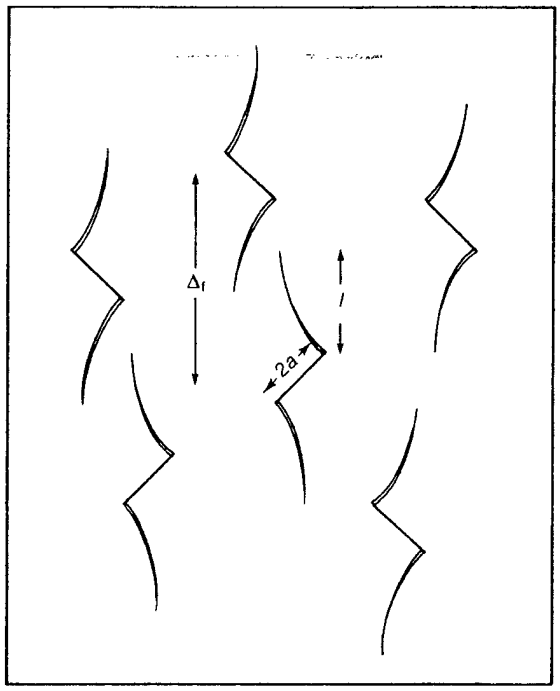

Figure 2.15: Linkage of a population of propagating wing cracks.

Adopting this criterion allows the nominal compressive failure stress (σ) to be derived from Equation 2.12 (Sanderson 1988):

$$\sigma \sim 3.5 \frac{K_{Ic}}{a} \sqrt{\frac{\Delta_f}{2}} \qquad (2.13)$$

Laboratory observations suggests that initial crack density may be of the order of one nucleated crack per grain (Cole 1986) such that $\Delta_f \sim d$, the grain diameter. Furthermore, assuming that $2a = 0.65d$, Equation 2.13 can be rewritten as:

$$\sigma \sim 7.6 \frac{K_{Ic}}{\sqrt{d}} \qquad (2.14)$$

This expression yields sensible results for the compressive strength of ice (Sanderson 1988).

2.2.6.2 Triaxial Behavior

As already pointed out, the application of a multiaxial confining pressure to ice has negligible effect in the ductile region. The same is not true of the fracture behavior of polycrystalline ice. Even a low lateral confining pressure can effectively inhibit fractures from propagating. This leads to a dramatic increase in the peak strength. This is well illustrated in Figure 2.10 in which cylindrical specimens of ice were deformed at a constant rate of strain in triaxial compression at varying degrees of confinement.

For low confining pressures, in the range up to about 20 MPa, the strength increases substantially with confining pressure as a result of internal cracking being suppressed. Above 25 MPa, however, the family of curves becomes essentially flat. Hence, a sufficiently high confining pressure causes pure creep where fracture is suppressed at all rates of applied strain.

The behavior of ice in the zone between pure uniaxial conditions and perfect constraint is represented by the shaded portion to the left of the plot in Figure 2.10. This zone is not well understood but can probably be treated by application of the generalized crack-propagation equation (Equation 2.11). The introduction of even a small confining pressure ($\lambda=\sigma_{33}/\sigma_{11}>0$ in Equation 2.11) is very effective in inhibiting the growth of wings cracks. This is obvious from Figure 2.14 since a lateral confining stress will tend to close any wing crack which has initiated.

2.3 MECHANICAL BEHAVIOR OF FROZEN SAND

2.3.1 Introduction

Frozen sand is a composite material made up of a sand particles within a matrix of ice. Its behavior results from a highly complex interaction between the skeleton of solid particles and the pore ice matrix that changes continuously with time as a function of temperature and applied stress. The rheological characteristics of frozen soils therefore are a direct result of the presence of ice as a matrix and internal bonding agent. Particle contact has an important influence on the behavior of highly-filled (dense) frozen soil systems, whereas in ice-rich materials, a significant portion of the particles are separated from each other by ice. Between these two extremes, its strength is a maximum because

of the synergistic interaction between the sand skeleton and ice matrix. The properties of ice are therefore responsible for many aspects of the unique behavior of frozen soils (Ladanyi 1981).

Although a complete understanding of frozen soil behavior is lacking, a substantial amount of research exists on the macro-structural behavior. However, the micro-structural interactions between the sand and pore ice, as well as the effect of unfrozen water and ice adhesion, are poorly understood. The following discussion provides a brief overview of the structure of typical frozen sand as well as hypotheses regarding the mechanisms contributing to frozen sand strength. A review of the state of knowledge on the macro-structural strength-deformation behavior is also presented.

2.3.2 Structure of Frozen Sand

Frozen sand is a natural particulate composite material. It is commonly recognized that it consists of four components: sand grains, ice within the pores between grains, a film of continuous unfrozen water at the ice-soil interface and at the ice grain boundaries, and air trapped within the pore ice. Its most important characteristic by which frozen sands differs from other similar materials, such as unfrozen sand and the majority of artificial particulate composites, is that it contains ice, whose behavior changes continuously with temperature and applied stress resulting in extremely complex behavior. This means that any physical parameter deduced by ordinary testing methods can hardly be regarded as a true material property, but is more likely to be a constant that only describes the observed behavior within a given tested region (Ladanyi 1981).

A conceptual structure of frozen sand is illustrated in Figure 2.16 (Ting et al. 1983). Effectively solid contacts exist between most particles in frozen coarse grained materials. The ice present within the pores of the soil is thought to be polycrystalline in nature with a random crystal orientation and a maximum ice grain size equal to the pore size or smaller. The amount of ice in the soil, or conversely the volume fraction of soil particles, the temperature, and the applied strain rate are perhaps the most important parameters that influence the behavior of frozen sand systems (Andersen et al. 1995).

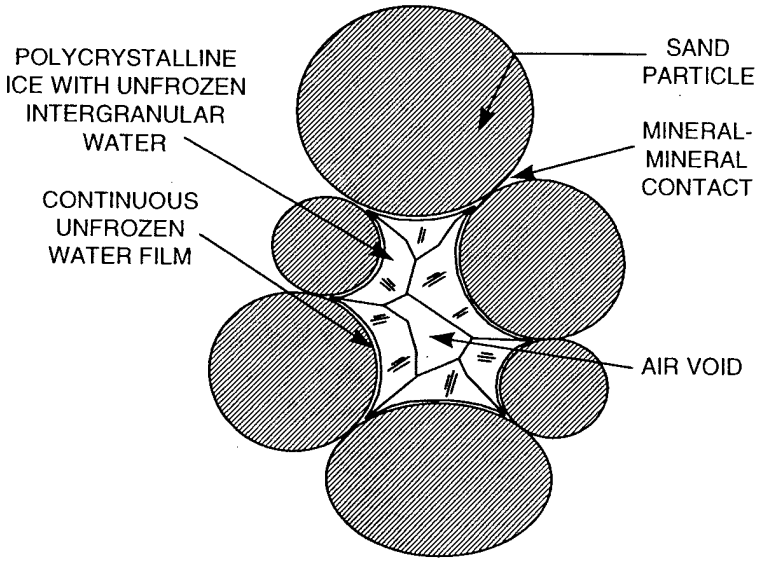

Figure 2.16: Two dimensional schematic of the structure of frozen sand. (adapted from Ting et al. 1983)

The unfrozen water film surrounding the sand grains is in equilibrium with the ice and strongly held to the particle surface by high intermolecular forces. The amount of water present in a frozen sand system depends upon the kind of sand minerals present, the specific surface area of the sand, temperature, and the concentration of impurities such as salt in the soil. As a result of this strongly adsorbed water film, probably no direct ice-to-sand grain contact exists (Ting 1983).

Air present in frozen soils contributes negligible resistance to the applied stress or deformation. However, much of the non-recoverable compressibility (i.e. consolidation) can be attributed to the presence of air in frozen soil (Tsytovich 1975).

2.3.3 Mechanisms of Strength

After studying the findings of earlier investigators on the shear behavior of frozen sands (e.g., Goughnour and Andersland 1968, Andersland and AlNouri 1970, Chamberlain et al. 1972, Alkire and Andersland 1973, Sayles 1973) as well as the results of their own investigations, Ting et al. (1983) hypothesized that the behavior of frozen sands is essentially controlled by the following three mechanisms: (1) pore ice strength, (2) soil strength, consisting of interparticle friction, particle interference, and dilatancy effects, and

(3) interactions between the ice matrix and soil skeleton. Ting et al. (1983) also proposed a failure mechanism map (Figure 2.17) in which the simultaneous presence of various mechanisms depends essentially on the volume fraction of sand in the ice-sand mixture.

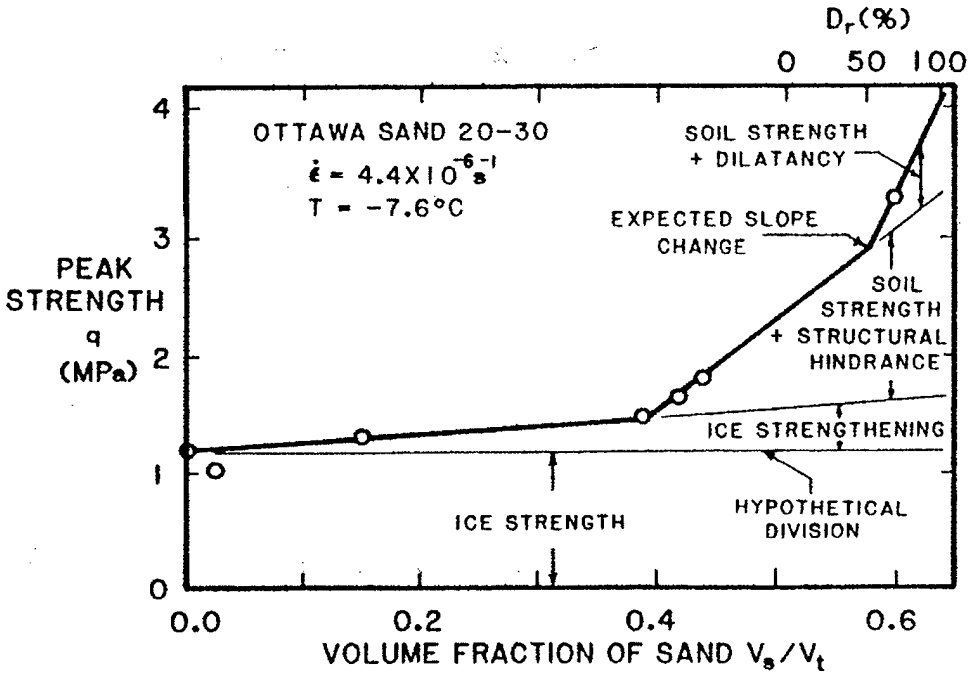

Figure 2.17: Proposed failure mechanism map for unconfined compressive strength for frozen Ottawa sand 20-30. (Ting et al. 1983)

2.3.3.1 Ice Strength

Ice strength is generally thought to be one of the most important factors affecting the behavior of frozen sands at small strains (e.g., Andersland 1989, Ting et al. 1983) since it provides a major portion of the initial resistance. While the actual type of ice with the pore structure of frozen sand is unclear, it is usually assumed to be polycrystalline in nature (Andersland 1989). Although the behavior of bulk polycrystalline ice is fairly well understood, it is very difficult to analytically assess the influence of grain size, grain orientation, confining stress level, stress state, and strain rate effects for the pore ice in frozen soil since loading conditions vary from pore to pore. Nevertheless, substantial insight into the behavior and strength of pore ice can be gained from an understanding of the structure and behavior of bulk polycrystalline ice.

A rather detailed description of the structure and behavior of polycrystalline ice has already been presented in Section 2.2 and will not be revisited here. Furthermore, a

discussion of the mechanisms responsible for strength generation in bulk ice has also been included in Section 2.2 and may also be applicable to the pore ice in frozen sand.

2.3.3.2 Soil Strength

Rowe (1962) postulated that the drained strength of dry cohesionless sands results from a frictional component due to sliding between grains that is constant, dilatancy effects resulting from the energy required because of expansion of the soil against a confining stress, and particle interference effects. These mechanisms are also valid for frozen ice-saturated sands except the inability to measure the effective stress in frozen soils makes it difficult to assess the contribution of the soil skeleton to the overall frozen soil strength. However, some insight into its relative importance can be obtained through laboratory testing and noting how the frictional characteristics of the soil skeleton affect the overall behavior.

When a two-phase granular mass (sand and water), consolidated under hydrostatic pressure, is subjected to shear stresses, its initially stable structure will either contract, if the density is low and/or the confining pressure is high, or it will expand (dilate) at high density and/or low confinement. If the specimen is saturated and volume changes during shear are prevented, shear will produce an increase in the porewater pressure in the first case and a decrease in the second case. This will result in a decrease of inter-granular (effective) stresses for contractive specimens and an increase for dilatant specimens, as long as cavitation of the porewater does not occur. Therefore, soil density, degree of confinement, and de-airing condition all have important effects on the stress-strain behavior of granular soils.

It has also been shown experimentally that the dense and loose sands sheared in drained or undrained conditions under identical vertical normal stresses tend to come to the same density (void ratio) and shear stress at large strains (Castro and Poulos 1977, Been and Jeffries 1985). This condition signifies a state of continuous deformation at constant volume and at constant shear and normal effective stress. The steady state of deformation is achieved only after all particle orientation has reached a statistically steady-state condition and after all particle breakage, if any, is complete so that the shear stress

needed to continue deformation remains constant (Poulos 1981). This concept of steady state of deformation forms the basis of critical state soil mechanics.

The steady state condition is often assume to be unique for a given sand and is characterized in *e*-log σ' space (i.e. void ratio after consolidation versus mean effective stress) or "state diagram" by a steady state line (SSL). The SSL for a particular soil defines a state where there is no additional volume change and no change in stresses in a specimen which has been sheared to large strains. Figure 2.18 shows a steady state line developed from a series of consolidated-undrained tests on compacted sand specimens.

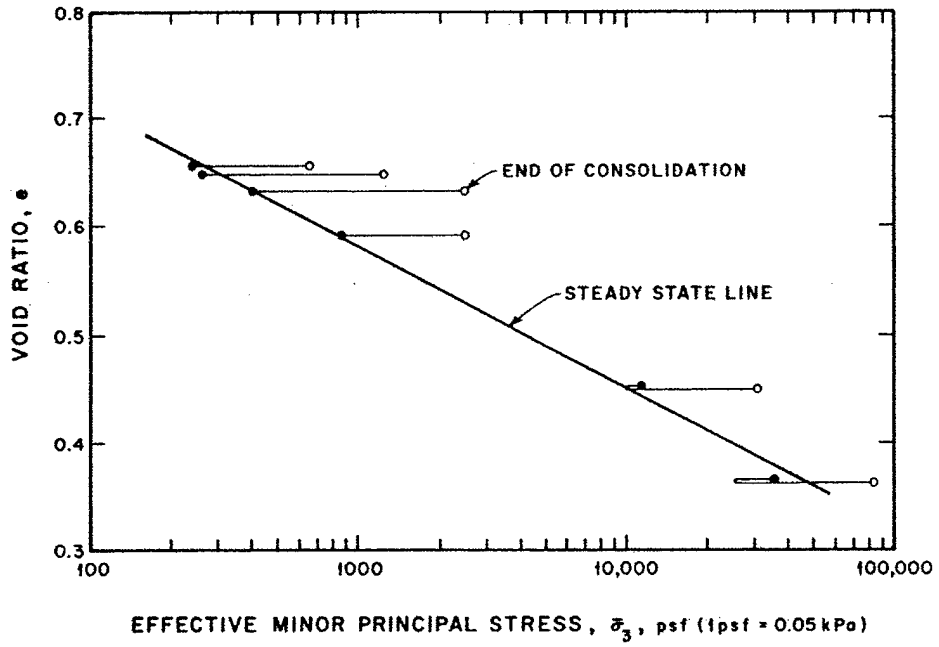

Figure 2.18: Steady state line developed from six CIUC tests on compacted sand specimens. (Poulos et al. 1985)

Poulos et al. (1985) claim that the steady state condition can be reached from either drained or undrained conditions and its position is extremely sensitive to the gradation and angularity of the sand. Therefore, the SSL is unique for a particular type of sand and independent of the testing conditions, or initial state. This is shown in Figure 2.19. The data presented in this figure were obtained from a triaxial compression testing program (Been et al. 1991) on one type of sand using different loading rates, drainage conditions, stress paths, and specimen preparation techniques. As shown in Figure 2.19, the SSL is actually a bilinear curve, becoming steeper at higher stresses. Been et al.

(1991) attributes the break in the SSL, which occurs at around 1 MPa for this particular sand, to the breakage of sand grains which results in a change in the sand's particle size distribution.

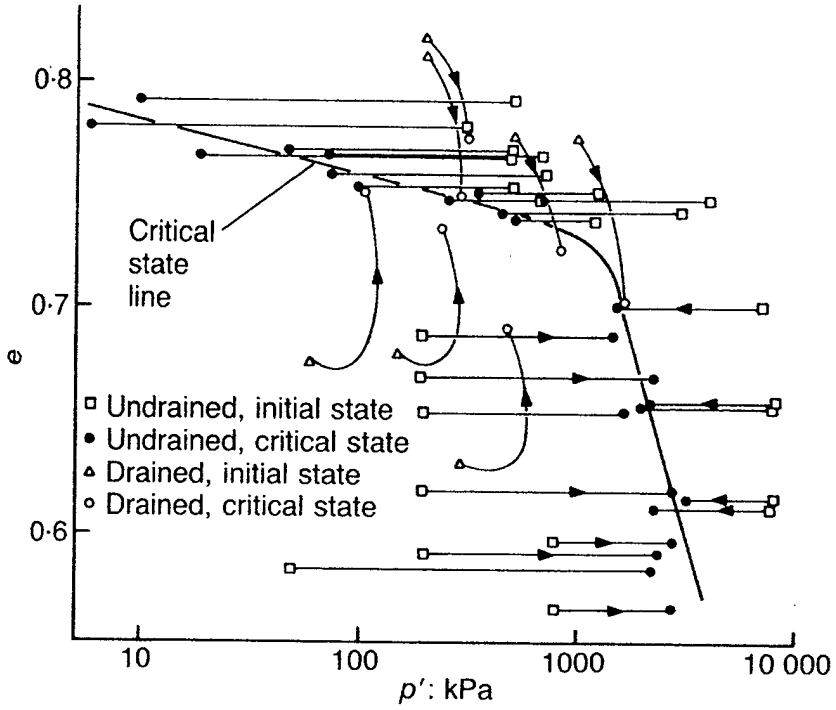

Figure 2.19: Effect of initial state on the steady state line for Erksak 330/0.7 sand in triaxial compression. Note: $p'=\sigma'_{oct}$. (Been et al. 1991)

Using the steady state line as a reference, Been and Jeffries (1985) introduced the concept of the state parameter (ψ) as a measure of the physical condition (state) of a sand in terms of its initial void ratio and the initial state of stress with respect to the conditions at the steady state. As illustrated in Figure 2.20, the ψ parameter is defined as the vertical distance from the initial state to the SSL expressed in units of void ratio. A sand which has an initial state that plot above the SSL has a $+\psi$ and will exhibit a contractive response during shear. Conversely, a sand which has an initial state that plots below the SSL has a $-\psi$ and will exhibit a dilative response during shear. The state parameter's usefulness lies in its ability to correlate various aspects of shear such as undrained shear strength and effective friction angles as a function of both changes in both void ratio and confining stress.

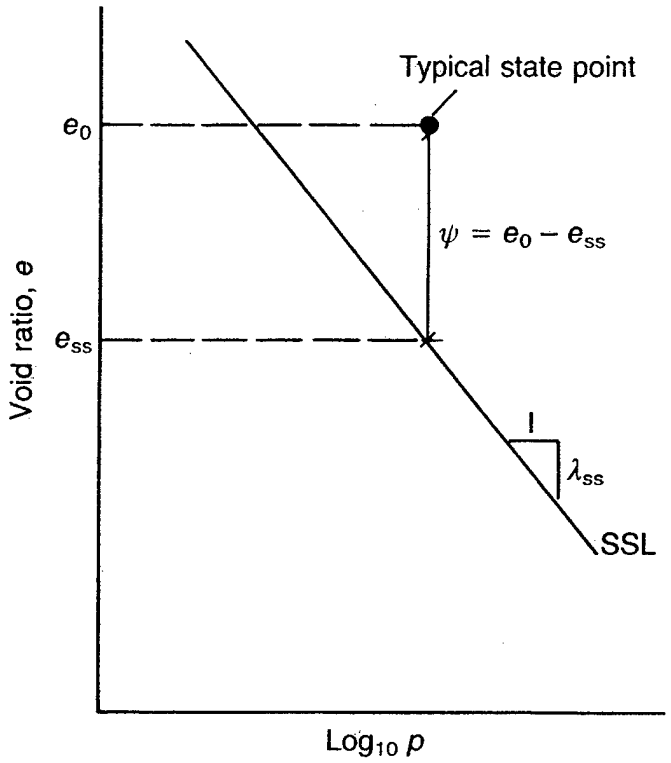

Figure 2.20: Definition of the state parameter. (Been et al. 1991)

If the same criterion is used in connection with a frozen sand, a $+\psi$ would only mean that the sand would not tend to dilate, so that its strength would be governed essentially by the strength of the pore ice, enhanced by the presence of the soil skeleton. On the other hand, a $-\psi$ would indicate that the overall shear strength would also contain a component due to dilatancy induced hardening, often referred to as dilatancy-hardening (Ladanyi and Morel 1990). This effect may only exist up to strains of about 1-2% at ordinary confining pressures and temperatures after which the pore ice starts to break in a brittle manner under combined tensile and shear stresses. These few comments suggest that a more complete understanding of the physical mechanisms controlling the strength-deformation behavior of frozen granular soils is needed.

2.3.3.3 Soil Skeleton-Ice Matrix Interactions

Generally, the strength of frozen granular soil exceeds the sum of the strength of pure granular ice and the undrained unfrozen soil strength. This may be due to such

mechanisms as ice strengthening (the effect of soil on the ice), soil strengthening (the effect of the ice on the soil), and tension in the unfrozen water film (Ting et al. 1983).

Strengthening of the ice matrix involves interaction between the ice and soil phases and can result from several different mechanisms. One possibility is that the ice within frozen soil may possess an altered structure having a higher strength than normally tested ice. Certainly the stress states and deformational constraints imposed on the ice grains in the pores differ from those in pure ice. Strengthening could also result from the strain rates in the ice matrix being greater than the average strain rate applied to the specimen. It is, however, very difficult to assess the importance of each of these mechanisms since the loading conditions in the pore ice probably varies in an unpredictable manner.

Soil strengthening results from the fact that the soil skeleton of the frozen soil system carries a portion of the applied load and thus an increased sand relative density increases the number of interparticle contacts which then must subsequently decrease the load on the ice. This could result in a stronger, less creep susceptible system. At high relative densities and low confining pressures, where dilatant behavior is expected, tensions are imposed on the ice as the soil skeleton wants to expand during shear. Assuming that the adhesional bond between the ice and the soil exceeds the interfacial stress (i.e. cleavage does not occur between the ice and soil), the tension in the pores induces a positive increment of effective stress which results in an increased overall strength. Goughnour and Andersland (1968) report that increasing the concentration of sand particles beyond 42% by volume leads to a rapid increase in strength with increasing sand density due to interparticle friction and dilatancy effects contributing to shear strength. At lower sand concentrations, strengths were observed to be only a little higher than those of pure ice (i.e. ice strengthening only). Structural hindrance may also enhance the strength of frozen sand. As load is applied to a frozen soil system, both the soil skeleton and ice matrix deform accordingly. Resistance to the movement of sand particles is provided by the usual interparticle friction and particle interference plus an added structural impedance from the ice matrix. This structural hindrance may greatly increase the shear resistance of the soil skeleton.

The presence of a tension at the soil-unfrozen water-ice interface due to some physico-chemical interaction could also provide a strengthening of the system if it increased the effective confining stress on the soil skeleton. The thickness, and therefore the amount of tension, of the unfrozen water film are determined by the soil mineralogy and the specimen temperature. Although measurements of pore water pressures (if possible) are needed to quantify this effect, it probably does not contribute significantly to the overall behavior of frozen soil, except possibly for conditions approaching the long term limiting strength (Ting et al. 1983).

Pressure melting, resulting from the application of hydrostatic or deviator stresses, also increases the amount of unfrozen water present (Chamberlain et al. 1972). It develops from stress concentrations on the ice component between soil particles and leads to unfrozen water flowing to regions of lower stress where it re-freezes.

The key to assessing the relative importance of the interactions between the ice matrix and the soil skeleton lies in understanding the nature of the tensile and shear adhesional strengths at the soil-ice interface. It is well known that substantial tensile and shear adhesion can develop between ice and silicate surfaces (Jellinek 1962). Whether this adhesional strength is significant in comparison with the strength of the pore ice in frozen soil still remains unknown. If the adhesional strength is less than the strength of the pore ice, then failure will probably occur at the ice-soil interface. If the adhesional strength is higher than the ice matrix strength then failure by entire system deformation is likely.

2.3.4 Strength and Deformation of Frozen Sand

The strength of a frozen soil is interrelated to its deformational characteristics. When strength is considered the term failure must be defined. A system that has been fractured by an applied stress has clearly reached its strength limit or failure point. However, when plastic flow or creep occurs the definition of failure often becomes arbitrary as to the amount of strain that is considered to represent failure. The term strength is often used to describe the maximum or peak stress that is observed when a soil is subjected to an increasing stress, although the residual strength is sometimes quoted which is the resistance the soil can withstand at large strains.

The stress-strain-strength behavior of frozen sand is most commonly investigated in the laboratory either via creep tests, where a constant deviator stress is applied to the test specimen, or by constant rate of deformation tests, where the test specimen is deformed at a constant rate. Relaxation tests, where an initial deformation is held constant and the reduction or relaxation of the stress is observed with time, may also be performed. At the present time, the most common method for investigating the strength of frozen sands is by performing uniaxial (unconfined) or triaxial compression tests.

Based on a number of early investigations, the strength and deformation behavior of frozen sands have been found to depend on numerous variables, the most important being the strain rate, temperature, level of confinement, relative density, degree of ice saturation, and the presence of ionic impurities. Although the last two variables can have a profound effect of the strength and deformation behavior of frozen sand, the following discussion restricts itself to the behavior of saturated (or nearly saturated) freshwater specimens since much of the data in the literature has been obtained for these conditions.

An overview of typical behavior of frozen sands is presented in Figure 2.21 (Andersen et al. 1995). Two stress-strain curves are plotted at each strain rate and temperature shown. One corresponds to specimens having a low relative density and low confining pressure. This represents a state of minimum frictional resistance of the sand skeleton. The other corresponds to specimens having a high relative density and high confining pressure, presumably reflecting maximum frictional resistance of the sand skeleton. Figure 2.21a shows the effect of increasing strain rate for specimens sheared at a constant temperature of -10°C. The strain rates investigated during that program were slow ($3x10^{-6}$ s^{-1}), moderate ($3.5x10^{-5}$ s^{-1}), and fast ($5x10^{-4}$ s^{-1}). Figure 2.21b shows the effect of decreasing test temperature (i.e. -10°C to -20°C) for specimens sheared at the moderate rate of strain.

All of the stress-strain curves in Figure 2.21 exhibit a very distinctive yield point as shown by the circles in the figure. This point represents the onset of highly non-linear behavior and the development of very significant plastic deformations (Andersen et al. 1995). In this discussion it will be referred to as the upper yield stress, rather than the

"initial yield" or "first yield" as is often done in the literature, to distinguish it from yielding (non-linear) behavior that actually begins at much lower levels of strain.

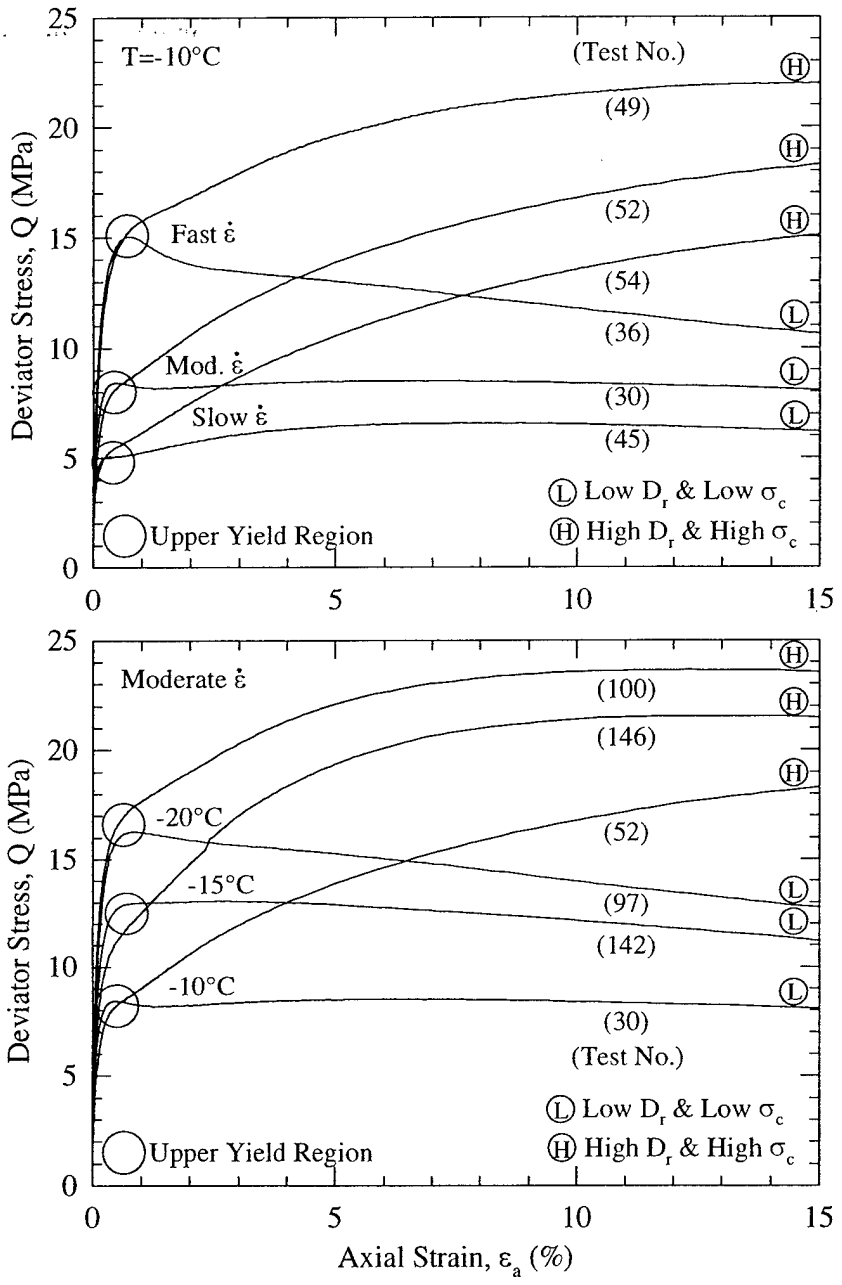

Figure 2.21: Overview of stress-strain behavior of frozen Manchester fine sand showing the effect of relative density and confinement at: (a) varying strain rate, and (b) varying temperature. (Andersen et al. 1995)

It is useful to divide the behavior of frozen sands into two parts: small strain behavior, which encompasses the initial response of the soil through to the upper yield point, and large strain behavior which describes the response at larger strains. A qualitative assessment of the stress-strain curves in Figure 2.21 shows that the behavior in the small strain region is largely unaffected by changes in relative density and confinement, which are variables that affect the frictional resistance of the sand skeleton. However, they have a tremendous effect on the behavior in the large strain region. In general, frozen sands may exhibit either post-upper yield strain hardening or strain softening depending on the frictional characteristics of the sand skeleton. Figure 2.21 also clearly shows that the upper yield stress is greatly affected by strain rate and temperature, two variables which are well known to greatly affect the strength of ice. Furthermore, strain rate and temperature also affect the post-upper yield strength gain.

In the following sections a detailed review of the small and large behavior of frozen soil in triaxial compression is presented. Volumetric strain behavior will also be discussed as it provides insight into processes reflecting both the sand skeleton and the ice matrix, and ultimately has been shown to influence the post-peak degree of strain softening (Swan et al. 1995).

2.3.4.1 Small Strain Behavior

As previously mentioned, the small strain region of frozen soil behavior extends to the upper yield point, typically occurring at levels of axial strain ranging from 0.3-1.0%. The small strain behavior of frozen soil in this range is described by the initial elastic response, characterized by Young's modulus and Poisson's ratio, and by the upper yield stress as defined previously.

Elastic Response

Recent improvements in measurement techniques combined with a number of experimental research works concerning various kinds of unfrozen geomaterials have confirmed that soil behaves as an elastic medium at small strains (Lo Presti 1994). Describing the elastic response of geomaterials typically involves quantifying the initial

tangent modulus (Young's modulus) and Poisson's ratio. Determination of these parameters from conventional laboratory compression tests requires specialized equipment capable of inducing and measuring very small deformations. Typically, the use of wave propagation techniques, resonant column, or on-specimen axial strain measurement devices are used for reliable determination of the elastic properties (Lo Presti 1994). A comprehensive review of the available techniques for local strain measurements is given by Scholey et al. (1995)

Young's moduli of ice-saturated cohesionless soils have been reliably measured only by a few programs. Kaplar (1963) determined the elastic parameters of Peabody gravelly sand and McNamara concrete sand using resonant beam techniques. Baker and Kurfurst (1985) used acoustic wave propagation, as well as on-specimen axial strain techniques, to measure the effect of relative density on the elastic properties of frozen Ottawa sand. More recently, Andersen et al. (1995) presented an extensive set of data on the Young's modulus of frozen Manchester fine sand measured with an on-specimen extensometer. Table 2.1 summarizes the results from these programs. The moduli reported in these programs were measured at stress levels corresponding to strains of less than 0.01%, which encompasses the linear range of stress-strain behavior observed for these soils. It is interesting to note that the actual sand type has a relatively minor effect on Young's modulus.

Young's modulus has been found to increase moderately with increasing dry density, and perhaps with increasing confining pressure. Baker and Kurfurst (1985) found the modulus to increase approximately 20% for an increase in relative density from 20% to 100% (Figure 2.22). A somewhat smaller variation was also reported by Andersen et al. (1995) as shown in Figure 2.23. Vinson (1978), however, measured a 60% increase in the complex shear modulus over a wide range in relative density.

Little information is available on the value and variation of Poisson's ratio for typical frozen sands. From Figure 2.22 (Baker and Kurfurst 1985) there appears to be a consistent increase in Poisson's ratio with increasing specimen density. It also is shown to increase with decreasing temperature in a manner similar to polycrystalline ice. However, both Kaplar (1963) and Shibata et al. (1985) present data that is in direct

contrast to that of Baker and Kurfurst (1985). Their results suggest that the Poisson's ratio of various frozen sands increase with increasing temperature. Clearly, additional research in this area is required before definitive statements can be made.

Reference	Material	Measurement Technique	Temperature (°C)	Young's Modulus (GPa)
Kaplar (1963)	Peabody gravelly sand	Resonant beam	-1.1 to -27.8	34.5 to 42.4
Kaplar (1963)	McNamara concrete sand	Resonant beam	-1.1 to -27.8	28.3 to 34.5
Baker & Kurfurst (1985)	Ottawa sand	Acoustic wave propagation	-3.2 to -10	27±3
Baker & Kurfurst (1985)	Ottawa sand	On-specimen extensometer	-10	23±9
Andersen et al. (1995)	Manchester fine sand	On-specimen extensometer	-9.6 to -25.4	26.5±4

Table 2.1: Prior measurements of Young's modulus on saturated frozen sand. (Andersen et al. 1995)

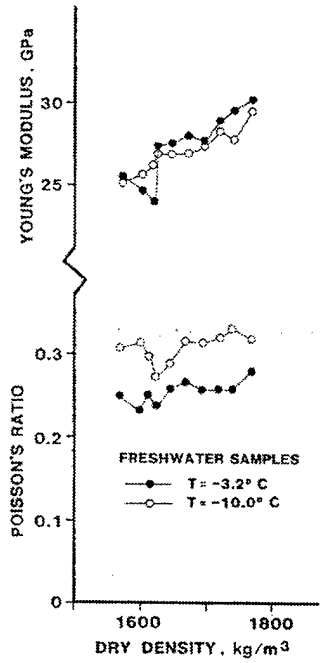

Figure 2.22: Effect of dry density on the Young's modulus and Poisson's ratio of frozen Ottawa 16-100 sand. (Baker and Kurfurst 1985)

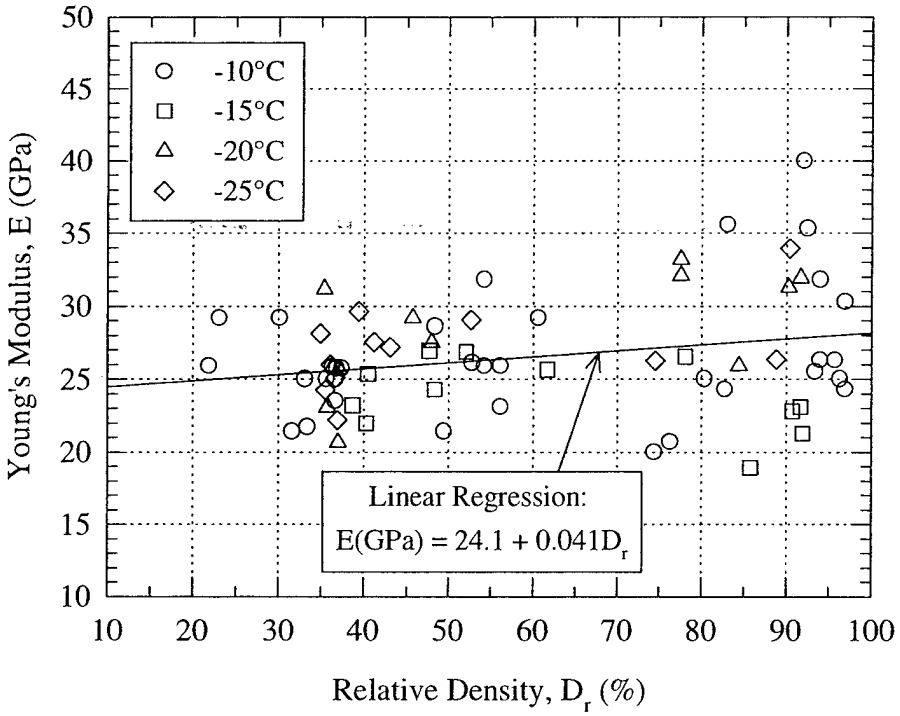

Figure 2.23: Variation of Young's modulus of frozen Manchester fine sand with relative density at various confinement levels, temperatures, and strain rates. (Andersen et al. 1995)

While many other programs (e.g., Parameswaran 1980, Zhu and Carbee 1984, Shibata et al. 1985) have reported values of modulus (tangent, secant, cyclic, 50% strength) for dense saturated sands, most are much lower than reported in Table 2.1. For temperatures ranging from -2°C to -15°C and strain rates from 10^{-7} to 10^{-2} s^{-1}, the reported values typically range from 0.1 to 8 GPa (Andersen et al. 1995). These measurements were made without reliable methods of measuring small axial strains (i.e. on-specimen extensometer) and hence are not representative of the initial stiffness properties. Modulus determinations made at higher levels of strain include nonlinear plastic deformations as the material deviates from strict linear-elastic behavior. These data also show a tendency for the modulus to increase with increasing strain rate, decrease with increasing confinement (although Vinson (1978) showed an opposite trend), and to increase with decreasing temperature. These trends are consistent with those observed by Andersen et al. (1995) for the yield offset stress for Manchester fine sand since this parameter, by definition, includes some non-linear deformations. Therefore, the writer

believes that Young's modulus, and perhaps Poisson's ratio, of frozen sand are most likely independent of strain rate, temperature, and possibly confining pressure. Conversely, relative density has been shown to have an influence on both the Young's modulus and Poisson's ratio (Figure 2.22 and Figure 2.23). This is supported by a simple two-phase composite material model first adapted for use on frozen sand by Andersen et al. (1995). This model also indicates that the modulus of the sand particles and the ice-silicate bond strength are much more important to the initial stress-strain response than is the density of the sand skeleton. This will be discussed in more detail in Section 2.4.

Upper Yield Stress

Limited data exists on the upper yield stress behavior because most researchers either did not use appropriate measuring techniques to adequately define the small strain behavior, or their discussions focused primarily on the peak stress rather than on the behavior at smaller strain levels.

Figure 2.24 plots the upper yield stress as a function of confining pressure for frozen sands tested by Sayles (1973), Chamberlain et al. (1972), Parameswaran and Jones (1981), and Andersen et al. (1995). All tests were performed at approximately -10°C except for the Sayles (1973) data, and all tests were performed on coarse-grained Ottawa sand except for the Andersen et al. (1995) data which are for Manchester fine sand. Figure 2.24 shows moderate to large pressure sensitivity for the coarse-grained sands as opposed to the slight decrease in the upper yield stress for the Manchester fine sand program. Coarse-grained sands and higher strain rates may cause earlier fracturing of the ice matrix, leading to a pressure sensitivity similar to that reported by Jones (1978, 1982) for polycrystalline ice. The data on Manchester fine sand indicates that confinement has little effect on the upper yield stress.

Andersen et al. (1995) also report no change in the upper yield stress for changes in relative density ranging from 20-100% on Manchester fine sand tested at -10°C. This is shown in Figure 2.25 and is consistent with the data reported by Baker and Konrad (1985) on coarse Ottawa sand tested under similar conditions.

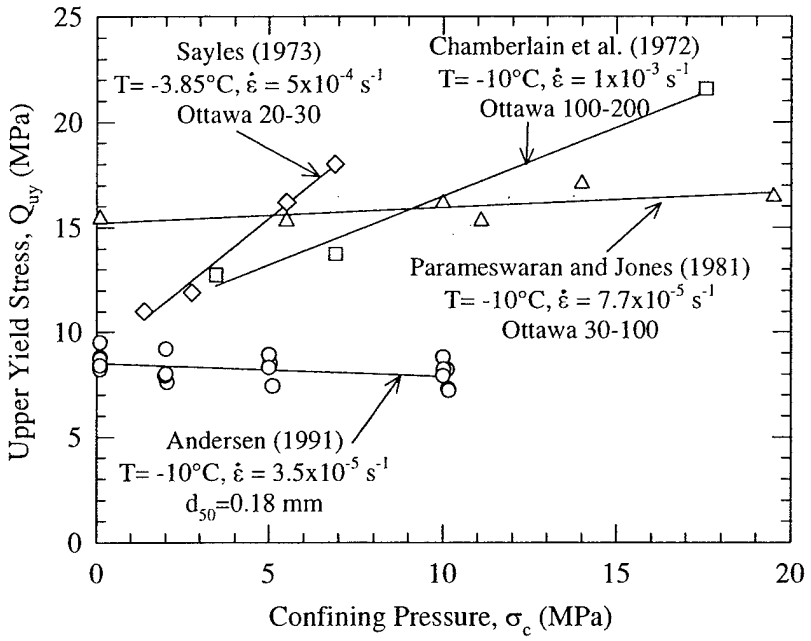

Figure 2.24: Effect of confinement level on the upper yield stress for various frozen sands. (Andersen et al. 1995)

Figure 2.25 also shows a significant trend for the upper yield stress to increase with increasing strain rate. This figure also shows the dependence of the upper yield stress with temperature. The strain rate dependency can be modeled using a power law relationship similar to that used for ice behavior. It takes the form of:

$$Q_{uy} = A(\dot{\varepsilon})^{\frac{1}{n}} \tag{2.15}$$

where A is a temperature dependent constant. The exponent *n* increases in a very consistent fashion with decreasing temperature from about 4.65 to 6.58 for temperatures varying from -10°C to -25°C (i.e. becoming less rate sensitive).

Data from uniaxial compression tests on frozen Ottawa sand at -30°C by Parameswaran and Roy (1982) also support this trend (Figure 2.26). They report a power law coefficient of 10.6 which indicates a lower rate sensitivity than for frozen Manchester fine sand. This may be attributed to their use of nominal strain rates, calculated from the crosshead speed, instead of the true strain rates experienced by the specimen.

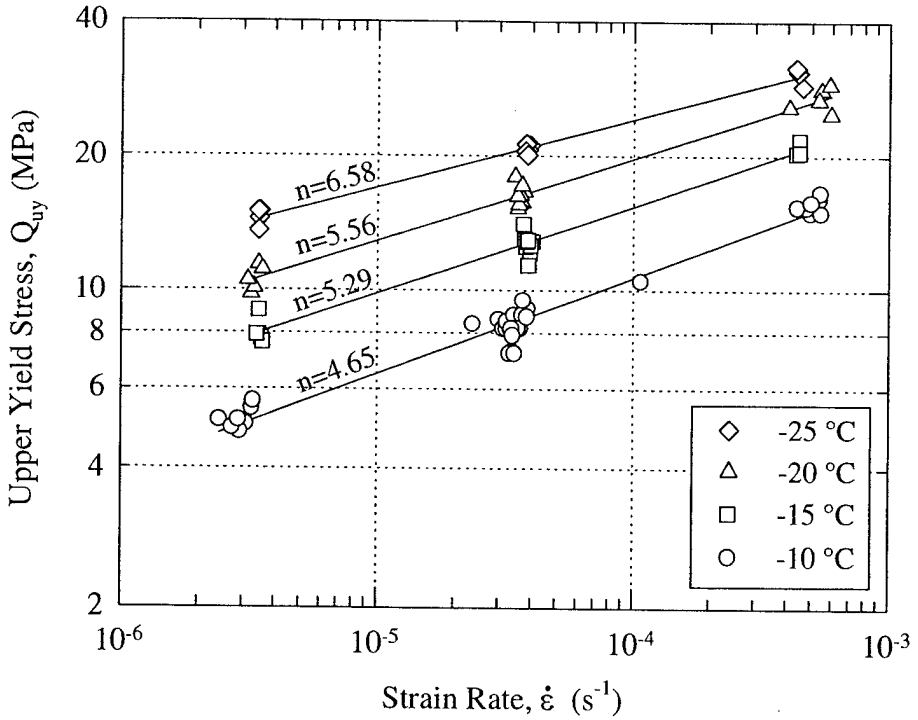

Figure 2.25: Variation of the upper yield stress of frozen Manchester fine sand with strain rate at varying temperature at all relative densities and confinement levels. (Andersen et al. 1995)

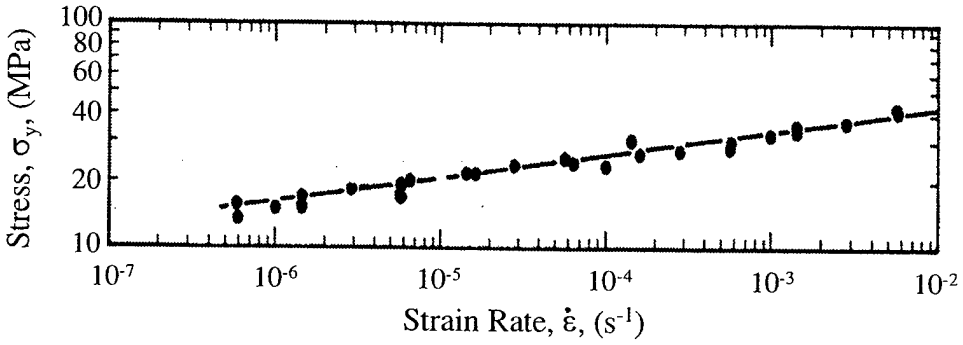

Figure 2.26: Variation of the upper yield stress of 30-100 Ottawa sand with strain rate at -30°C. (Parameswaran and Roy 1982)

With respect to the temperature dependence of the upper yield stress, Andersen et al. (1995) found that it can be expressed using a linear relationship of the form:

$$Q_{uy}(MPa) = C + D(T) \qquad (2.16)$$

where C and D are constants for a given strain rate. This reflects the basic trend illustrated in Figure 2.25 which is that the upper yield stress increases as the temperature decreases. However, the rate of strengthening with decreasing temperature is strain rate dependent, increasing with increasing strain rate.

From the information just presented the behavior of frozen sand in the upper yield region is qualitatively similar to that of polycrystalline ice. Various researchers have drawn analogies between the upper yield strength of frozen sand and the peak strength of bulk ice (e.g., Chamberlain et al. 1972, Sayles 1973, Parameswaran and Jones 1981, etc.). Figure 2.27 lends support to this analogy by comparing the peak strength of bulk polycrystalline ice from various test programs (e.g., Hawkes and Mellor 1972, Jones 1982) to the upper yield strength of frozen Manchester fine sand at various temperatures.

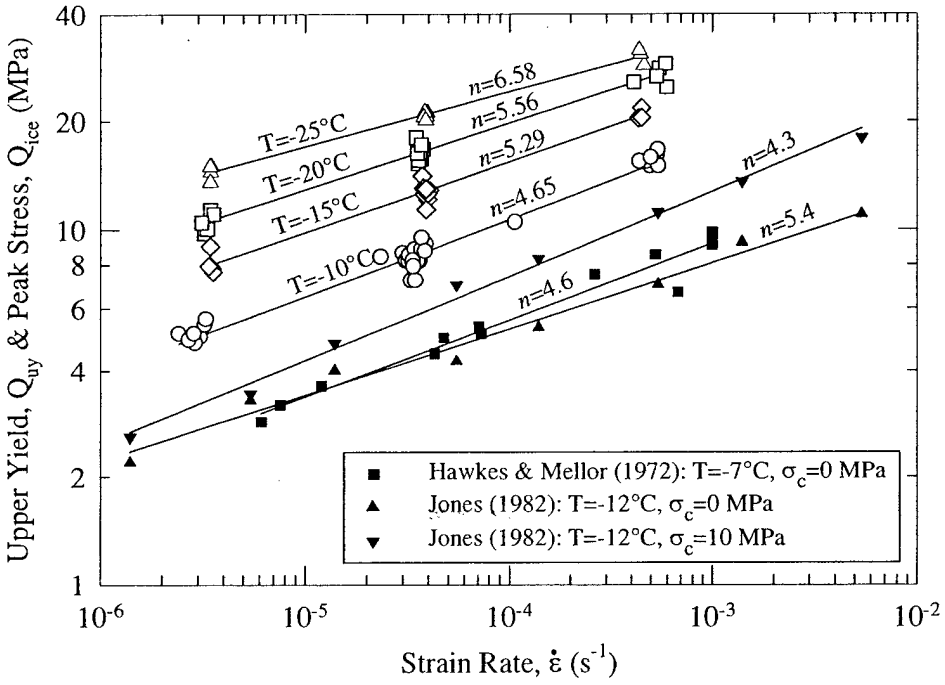

Figure 2.27: Variation of upper yield stress of frozen Manchester fine sand and peak strength of polycrystalline ice with strain rate. (Andersen et al. 1995)

As Figure 2.27 shows, the power law coefficients between the two materials are quite similar indicating qualitatively similar behavior. However, the magnitude of the upper yield stress at comparable temperatures is approximately double that of the strength of polycrystalline ice in unconfined compression. This may be attributed to the

strengthening effect of the sand particles even though the frictional characteristics of the sand skeleton seems to be unimportant as evidenced by the insensitivity of the upper yield stress to changes in relative density and degree of confinement. Furthermore, the strong dependence of the upper yield stress on the applied strain rate and temperature indicates that the structure of the sand skeleton probably does not play a significant role in controlling the behavior of frozen sand at this point (Andersen et al. 1995). In fact, the similarity in power law coefficients for the peak strength of polycrystalline ice and the upper yield stress of frozen sand over similar strain rates and temperatures suggests that similar physical mechanisms are at work in both systems. Therefore, it seems that the upper yield stress is essentially controlled by the strength of the ice matrix that has been effectively strengthened over the peak strength of bulk polycrystalline ice by the presence of the sand skeleton.

2.3.4.2 Large Strain Behavior

The previous section concluded that the upper yield stress of frozen sand varies with strain rate and temperature, and that this behavior is consistent with the general behavior of polycrystalline ice. However, at larger strains beyond the upper yield region, changes in sand density and confining pressure have a tremendous influence on the stress-strain behavior. This was shown previously in Figure 2.21. Moreover, these two parameters also affect the amount of volumetric straining that occurs at large strains (Swan et al. 1995). Since both sand density and the degree of confinement affect the frictional resistance of the sand skeleton, the behavior at large strains, and specifically the degree of post-upper yield strain softening or strain hardening, is controlled by the frictional characteristics of the sand skeleton.

In an effort to qualitatively characterize how changes in sand density and confining pressure affect the behavior at large strains, a classification system was developed by Swan et al. (1995) based on their results for frozen Manchester fine sand. The system uses four curve types as shown in Figure 2.28. Note that the stress-strain curves in Figure 2.28 are normalized by the upper yield stress.

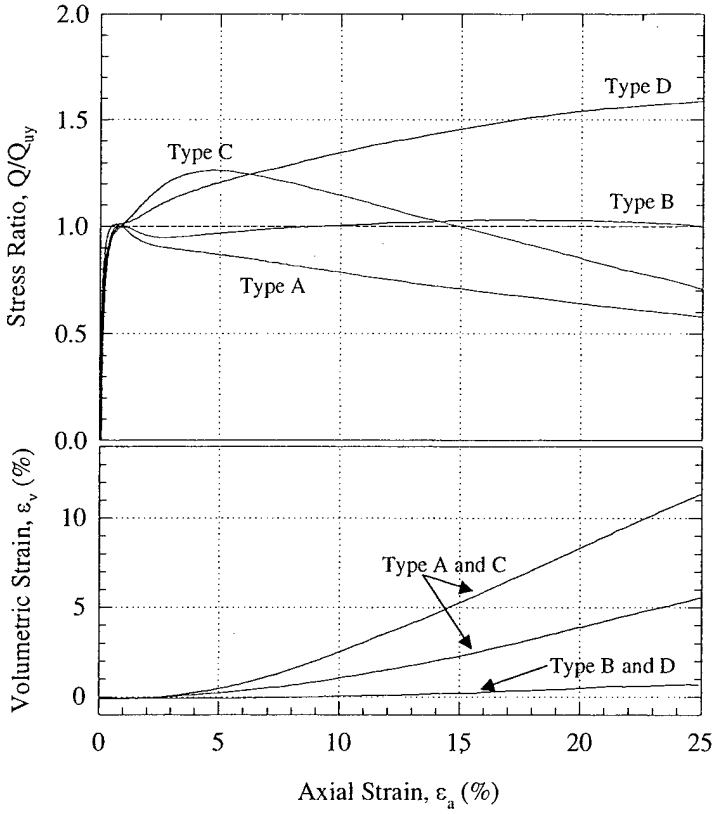

Figure 2.28: Types of stress-strain curves describing large strain behavior of frozen Manchester fine sand. Note: magnitude of stress ratio and rates of strain hardening/softening and dilation vary for each curve type. (Swan et al. 1995)

Briefly, Type C curves predominate at low confining pressures and are characterized by post-upper yield strain hardening to a peak strength at moderate strain levels, followed by significant strain softening and significant dilation. For loose sand sheared at higher strain rates and/or lower temperatures, this behavior switches to Type A curves. These curves have the peak strength coincident with the upper yield stress followed by significant strain softening and volumetric expansion with continued deformation. In contrast, Type D curves predominate at high sand densities and/or high confining pressures and are characterized by significant post-upper yield strain hardening to give a peak strength at large strains with minimal dilation. For loose sand sheared at higher strain rates and/or lower temperatures this behavior switches to Type B curves which are characterized by initial strain softening followed by strain hardening to produce

a system having a peak stress approximately equal to the upper yield stress and minimal dilation.

The following section presents a detailed analysis of the factors affecting the amount and nature of strengthening that occurs after reaching the upper yield stress. The analysis focuses on the effect of the relative density and confinement, but also discusses the impact of strain rate and temperature.

Post-Upper Yield Strengthening and Peak Strength

Sand content or relative density has a profound effect on the behavior of frozen sands at large strains. Unconfined compression tests by Goughnour and Andersland (1968) and Jones and Parameswaran (1983) are summarized in Figure 2.29. In the range of sand volume fractions from 0% (pure ice) to approximately 40%, a linear increase in peak strength above that of pure ice was found. At 40% by volume the rate of strengthening increases dramatically probably due to the sand particles coming in contact with one another. However, different methods of specimen preparation are often used to prepare specimens at low volume fractions which could account for the break in the curves shown in Figure 2.29.

Baker and Konrad (1985) found that the peak strength coincided with the upper yield stress (Figure 2.30) for specimens of low relative densities (D_r<65%) tested at -10°C at a strain rate of 1.67×10^{-4} s^{-1}. At higher relative densities, however, strain hardening occurred after the upper yield and the strength was strongly affected by sand density. Data by Swan et al. (1995) is presented in Figure 2.31 which plots the peak strength versus relative density for frozen Manchester fine sand at different temperatures. All tests at -10°C and -15°C had Type C curves and produced a well-defined linear increase in peak strength with increasing density. However, looser specimens at lower temperatures exhibited Type A behavior, similar to that found by Baker and Konrad (1985).

These data indicate that for test conditions that lead to strain hardening at large strains (Type C and D curves) there is a linear increase in the post-upper yield strength gain with increasing relative density. Furthermore, the rate of increase has been shown by

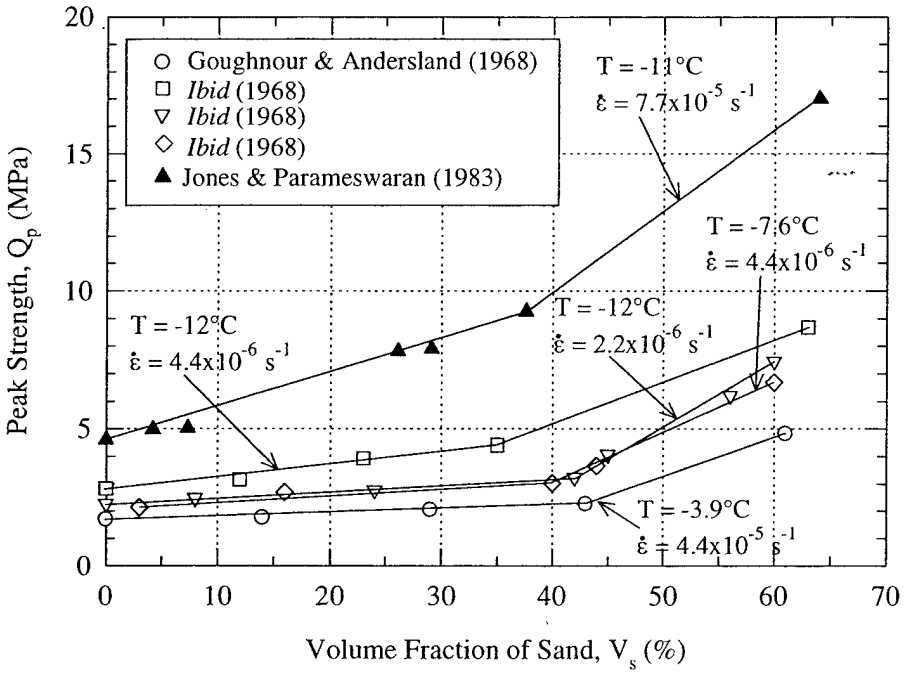

Figure 2.29: Variation of peak strength of frozen sands with volume fraction in unconfined compression at various temperatures. (Swan 1994)

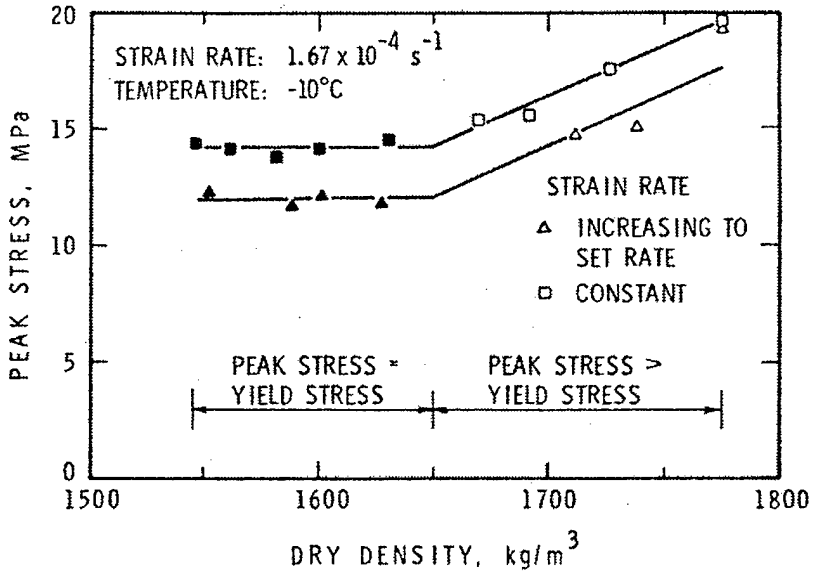

Figure 2.30: Effect of dry density on the unconfined compressive strength of frozen 16-100 Ottawa sand prepared using multiple sieve pluviation. (Baker and Konrad 1985)

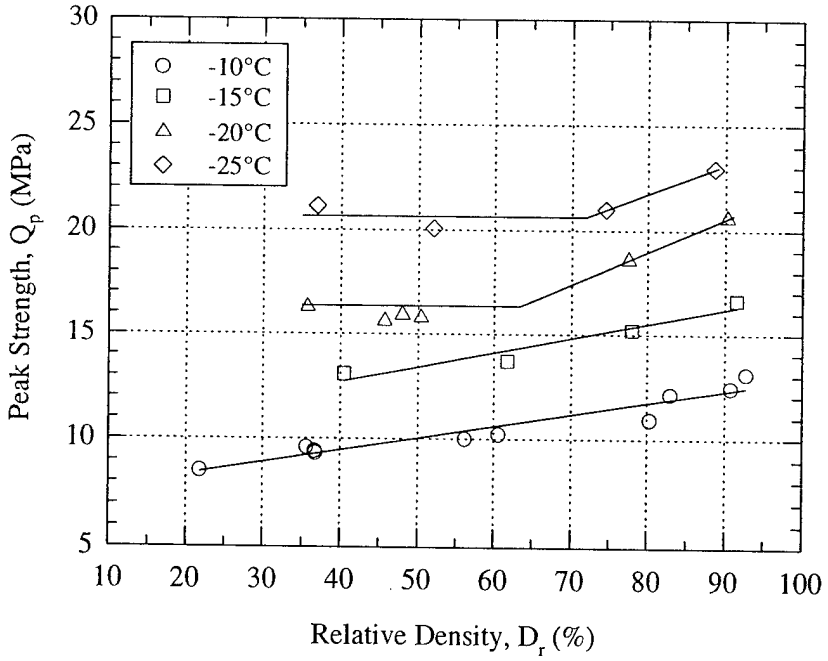

Figure 2.31: Variation of peak strength of frozen Manchester fine sand with relative density and temperature at moderate strain rates ($\dot{\varepsilon}$=3.5x10^{-5} s^{-1}) and low confinement (0.1 MPa). (Swan et al. 1995)

Swan et al. (1995) to be roughly independent of strain rate and temperature, but highly dependent on confinement.

Results from a number of testing programs (i.e. Chamberlain et al. 1972, Alkire and Andersland 1973, Parameswaran and Jones 1981, Shibata et al. 1985, Andersen et al. 1995) conducted on medium dense to dense sand at approximately -10°C over a wide range of strain rates show that increasing confining pressure generally leads to an increase in peak strength (Figure 2.32). In addition, Swan et al. (1995) found that the pressure sensitivity decreases for lower densities and for higher degrees of confinement. Furthermore, at very low sand densities, increases in strain rate and decreases in temperature produce Type A curves exhibiting zero pressure sensitivity as discussed previously.

The variation of the peak strength of a frozen sand with the applied strain rate can be described by a similar log-log relationship as that used to describe the strain rate variation in the upper yield stress. However, test results from Bragg and Andersland

(1980) and Zhu et al. (1988) show that above a certain strain rate, the strength of frozen sand may become insensitive to changes in strain rate in much the same way that polycrystalline ice does at fast strain rates. This effect is illustrated for dense frozen Lanzhou sand in unconfined compression in Figure 2.33 (Zhu et al. 1988).

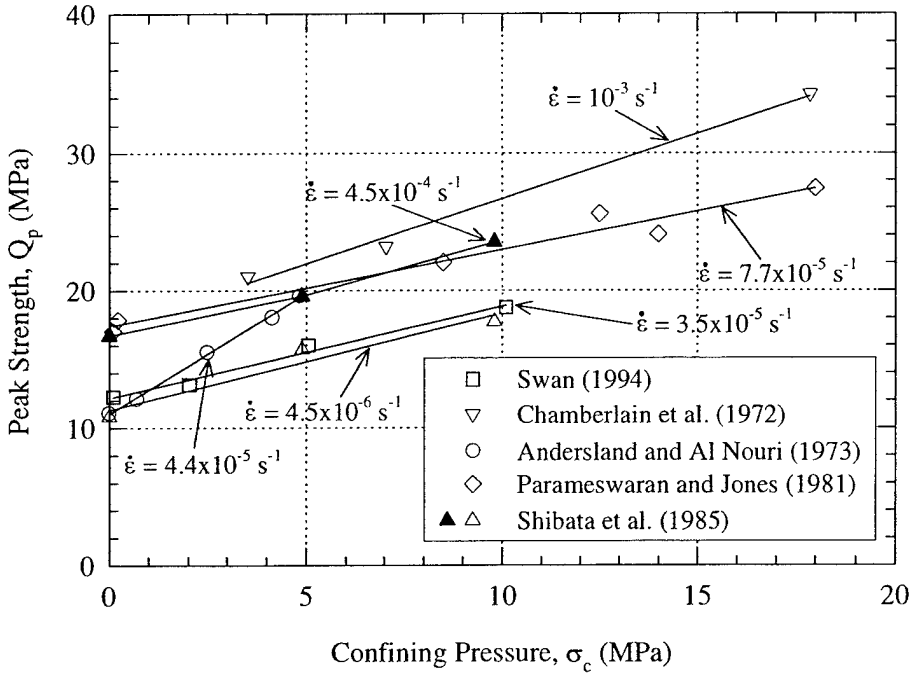

Figure 2.32: Effect of confinement on the peak strength of various frozen dense sands at T ≈ -10°C. (Swan et al. 1995)

However, an in-depth analysis of the large strain behavior of frozen Manchester fine sand by Swan et al. (1995) reveals that the peak strength and the post-upper yield strength gain varies in a complex fashion with relative density, confinement, strain rate, and temperature. As shown in Figure 2.34a, conditions of low density and low confinement lead to relatively little difference between the peak strength and the upper yield stress, while conditions of high density and confinement lead to the peak strength being much higher than the upper yield stress (Figure 2.34b). This comparison illustrates the extreme importance of comparing these two stresses since it was previously concluded that the upper yield stress is controlled by the behavior of the ice matrix and hence involves very little sand skeleton frictional resistance. It also shows that analysis of peak

strength data alone can lead to erroneous conclusions regarding the mechanisms controlling the large strain behavior of frozen sands (Swan et al. 1995).

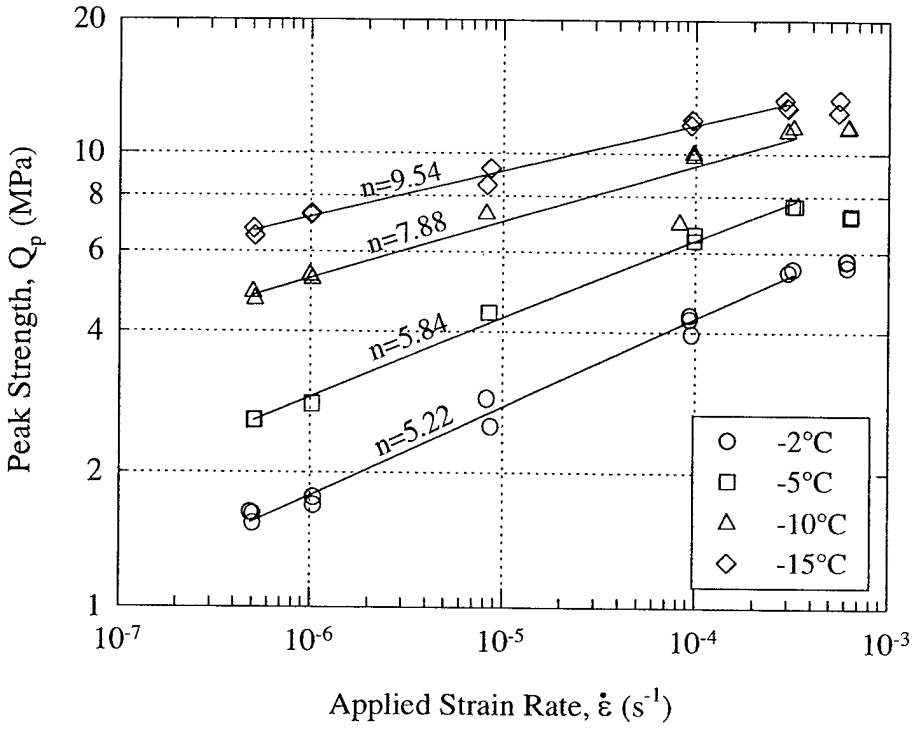

Figure 2.33: Variation of the unconfined compressive peak strength of dense frozen Lanzhou sand with strain rate at various temperatures (adapted from Zhu et al. 1988).

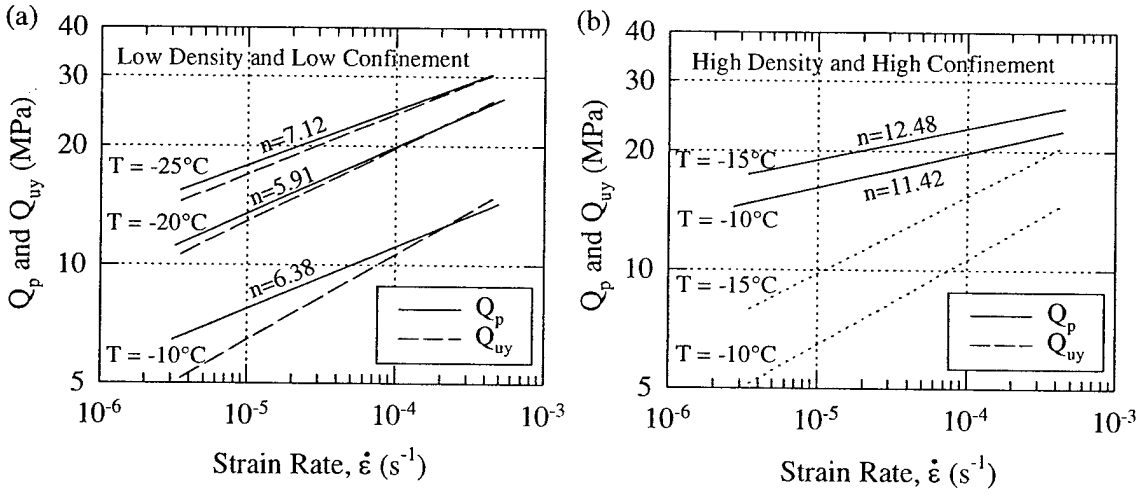

Figure 2.34: Peak strength and upper yield stress of frozen Manchester fine sand plotted against strain rate for conditions of: (a) low density and low confinement, and (b) high density and high confinement. (Swan et al. 1995)

Numerous programs have also studied the effects of temperature on the peak strength of frozen sands (e.g., Bragg and Andersland 1980, Parameswaran 1980, Zhu et al. 1988). In general, all programs show an increase in strength with decreasing temperature. This was illustrated in Figures 2.33 and 2.34. For the data presented in Figure 2.33 (Zhu et al. 1988), power law coefficients also increase with decreasing temperature with n values ranging from 5.22 to 9.54. In addition, the power law coefficient for the tests performed at -2°C (n=5.22) approaches that found for polycrystalline ice under similar conditions. Similar trends with temperature were also obtained by Swan et al. (1995). This may mean that the strength gain with temperature in frozen soil is mainly due to the increase in ice strength.

In summary, one can say that the frictional characteristics dominate at lower strain rates and higher temperatures, whereas fast shearing and low temperatures produces little post-upper yield strength gain except for dense sand at high confinement (Swan et al. 1995). This implies that estimation of the peak strength of frozen sands must incorporate the effects of all testing variables.

Post-Peak Strain Softening

Very few systematic studies quantifying the conditions leading to post-peak strain softening behavior are available in the literature even though it has important engineering implications. A detailed analysis, however, has been presented by Swan et al. (1995) whose testing program allowed a unique evaluation of the large strain behavior of frozen Manchester fine sand as a result of their use of lubricated end platens and precise measurement of volumetric strains.

The most significant result obtained from their analysis of the strain softening behavior of Manchester fine sand is that the strength loss is strongly related to the rate or amount of dilation. This was quantified by plotting the normalized rate of strain softening, $NRSS=[(Q_p-Q_{20})/Q_{uy}]/(\varepsilon_{20}-\varepsilon_p)$, versus the amount of dilation at 20% axial strain (ε_{v20}). Figure 2.35 presents this relationship and shows that the collective data, which cover a wide range of relative densities (35-95%) and confining pressures (0.1-10 MPa), have

relatively little scatter about the mean trend and furthermore, do not show a consistent deviation as a function of strain rate and temperature.

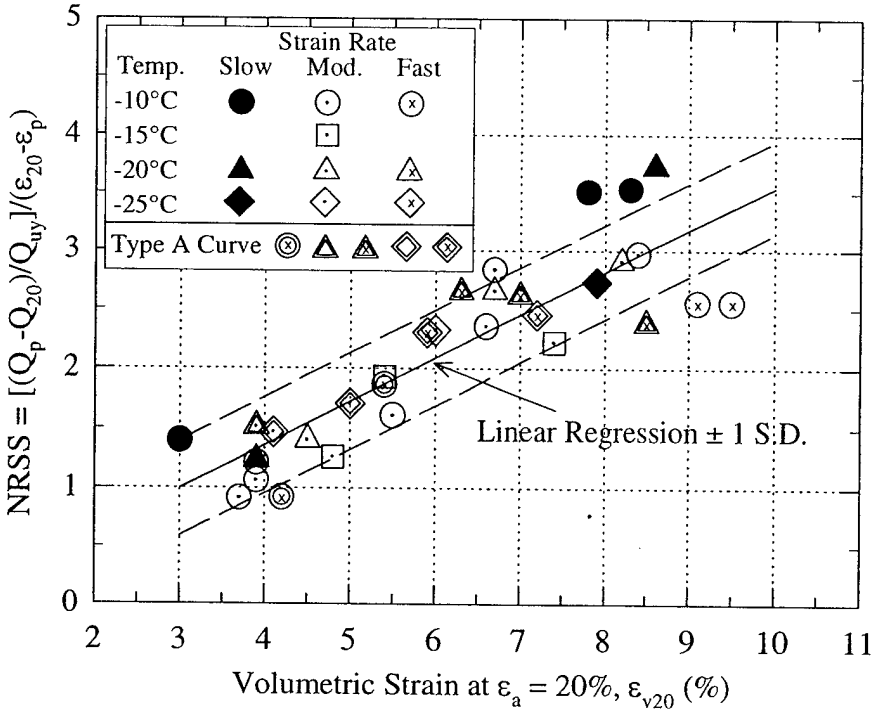

Figure 2.35: Normalized rate of strain softening versus volumetric strain at varying relative densities, strain rates, and temperatures. Note: Type A Curves at σ_c=0.1 MPa. (Swan et al. 1995)

2.3.4.3 Volumetric Strain Behavior

Very little information is available on the volumetric strain behavior of frozen sands. Shibata et al. (1985) quantified volumetric straining of Toyura sand under a range of confining pressures using lateral strain indicators. Swan (1994) and Youssef (1988) on the other hand used changes in confining cell fluid to monitor the amount of volumetric straining. All programs showed essentially zero volumetric strain at low axial strains up to the upper yield stress, and then varying amounts of volumetric expansion (dilation) that continues to increase with further straining. Figure 2.28, presented previously, illustrates that curve types B and D, or those which predominate at high confining pressures exhibit minimal dilation.

An ice-saturated system having a Poisson's ratio of less than 0.5 and sheared in triaxial compression can only undergo volumetric compression. Consequently, volumetric expansion (dilation) must reflect cracking or fracturing of the ice matrix or a loss of

bonding between the ice matrix and the sand particles. In other words, the onset of dilation suggests a decrease in the cohesive strength of the frozen sand system caused by damage to the ice matrix (Swan et al. 1995). Results from Youssef (1988), which performed triaxial tests on specimens of coarse Ottawa sand (20-30 mesh) at -5°C without using rubber membranes, support this conclusion. No increase in volume was recorded for these specimens suggesting that the confining fluid occupied the void gaps created by propagating cracks. This observation helps confirm that the formation of void gaps control the volumetric behavior of frozen sands subjected to triaxial stress conditions.

Two parameters for the quantification of volumetric strain behavior at large strains were developed by Swan et al. (1995): the maximum rate of dilation (MRD), which represents the maximum slope of the volumetric strain versus axial strain curve; and the volumetric expansion at 20% axial strain (ε_{v20}).

The maximum rate of dilation (MRD) is affected mainly by the amount of confinement as illustrated by Figure 2.36 for loose and dense specimens of Manchester fine sand. For this data set, the MRD equals 0.5±0.2 at low confinement (0.1 MPa) and drops to approximately 0.1 at high values of confinement (10 MPa). The MRD also increases with sand relative density at low confinement, but plays a very minor role at high confinement. Rate of strain and temperature have also been shown to have very little effect on the MRD for all values of confinement.

The ε_{v20} parameter follows the same basic trends at the MRD. This is shown in Figure 2.37 for low confinement. It is interesting to note that loose specimens at low confinement experience about twice as much dilation at 20% axial strain as unfrozen Manchester fine sand (Swan 1994). Hence, fracturing of the ice matrix must increase the dilation of frozen sand. More information of the volumetric behavior of Manchester fine sand can be found in Swan et al. (1995).

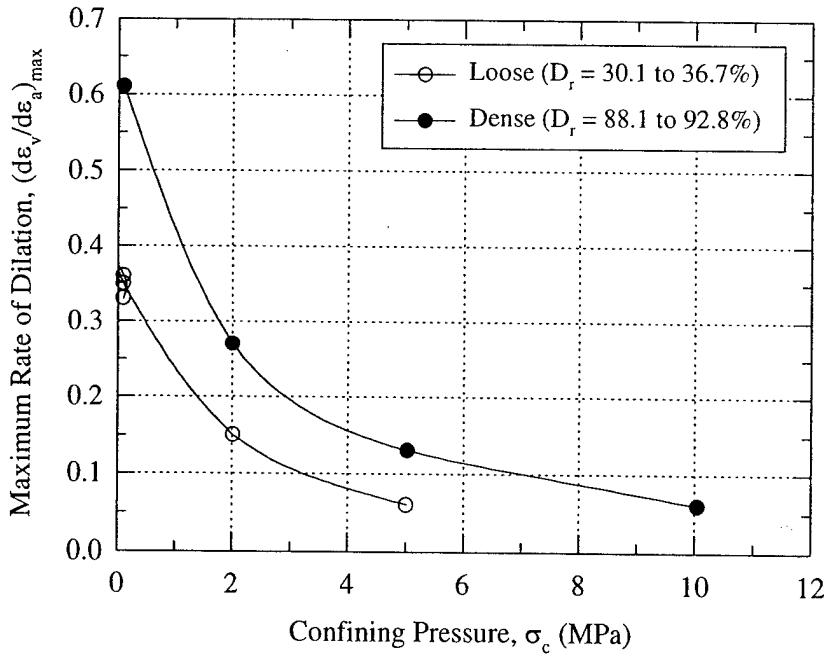

Figure 2.36: Variation of the maximum rate of dilation for frozen Manchester fine sand with confinement at moderate strain rate at -10°C. (Swan et al. 1995)

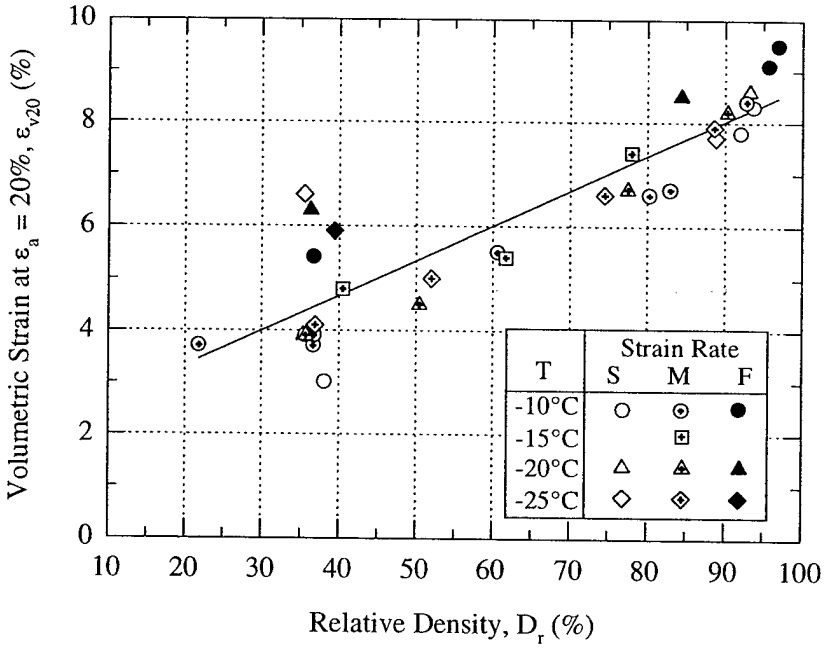

Figure 2.37: Variation of the volumetric strain at 20% axial strain with relative density at various strain rates and temperatures for frozen Manchester fine sand at low confinement (σ_c=0.1 MPa). (Swan et al. 1995)

2.4 REINFORCEMENT THEORIES FOR TWO-PHASE PARTICULATE-FILLED SYSTEMS

2.4.1 Introduction

This section present some techniques and models in the literature that describe the mechanical behavior of particulate-filled systems such as ice-saturated frozen sand. However, this is not a comprehensive and exhaustive review of the field since the contributions are scattered in journals of composite materials, applied mechanics, metallurgy, and polymer science. Rather this section should be regarded as a survey of the options available for modeling heterogeneous systems in terms of the mechanical properties and geometry of their constituents.

The term heterogeneous system or medium is defined as a mixture of discrete homogenous phases with well-known mechanical properties and behavior which form regions that are large enough to be regarded as a continuum. The following terminology is adopted. A heterogeneous medium consisting of an arbitrary number of phases is referred to as a *multiphase* medium. A special kind of multiphase medium is called a *suspension*, which is defined by the restriction that one phase is a matrix in which all other phases are embedded in the form of inclusions of any shape. They may be randomly dispersed in the matrix, or form a regular array. Ice-saturated frozen sand, a two-phase material, can hence be described as a suspension of sand particles in a matrix of ice. Finally, a *phase volume fraction* is the ratio of the volume of a phase to the volume of the multiphase body.

Prediction of the mechanical behavior of heterogeneous media is important for a number of reasons. Many of the high-performance materials in today's society are heterogeneous in nature (e.g., reinforced plastics, multiphase metal alloys, concrete). Composites offer unique combinations of better mechanical, physical, and electrical properties often unattainable from their individual constituents. For example, the addition of rigid particles to polymers or other matrices can produce a number of desirable effects such as an increase in stiffness, a reduction in the coefficient of thermal expansion, and an improvement in creep resistance and fracture toughness (Ahmed and Jones 1990a). Furthermore, the ability to predict the properties of a composite material is a prerequisite

for the rational design of materials having required properties. For example, the design of metal alloys will benefit from some knowledge of the relationship between the elastic constants of the constituent materials and those of the composite material (Paul 1960).

In principle, the effective properties of a composite material can be obtained by specifying the details of the micro-geometry (particle shape, packing geometry, and spacing), the distribution of surface loads, and the connectivity between the particle and matrix phase. The effective bulk response of the material can then be determined by taking volume averages, thereby relating the volume fraction of the constituents and their respective properties to the actual properties of the composite material. In practice, either simplifying assumptions must be introduced to make a general analysis tractable, or detailed numerical analyses must be performed for special cases. The various modeling approaches may be distinguished by the nature of the assumptions introduced to obtain tractable solutions to this problem.

In an effort to limit the scope of this review, it is useful to restrict attention to two component systems with inclusions of near spherical geometry embedded in a continuous matrix (suspension). This focus alleviates some of the theoretical and experimental problems associated with characterizing anisotropic materials. Therefore, the rest of this section is devoted to the presentation of techniques for predicting both the modulus (Young's, shear, or bulk) and the strength (or yield behavior) of two-phase composite materials. The following section (Section 2.4.2) deals specifically with models for the modulus of particulate composites. Having summarized the available models, their applicability and limitations will be discussed in Section 2.4.3. A similar structure is followed for the yield strength of particulate composites in Sections 2.4.4 and 2.4.5. These models will then be compared in subsequent chapters with experimental data obtained from frozen particulate systems.

2.4.2 Modulus of Particulate Composites

2.4.2.1 Introduction

A variety of approaches have been proposed to predict the Young's, shear, and bulk moduli of particulate-filled materials in terms of the properties and concentration

(volume fraction) of each of the constituent phases. In the prediction of the effective properties of a two-phase composite material, a key issue involved is the phase interaction. Owing to the difficulty of solving the problem rigorously for a medium in which there are many interacting inclusions, various methods have been developed to tackle this class of problems in an approximate manner. Moreover, the accurate prediction of the elastic moduli of particulate composite materials is problematic for many reasons, such as non-uniform particle distribution and irregular particle shape, which cannot readily be included in an exact solution (Fan et al. 1992). Consequently modeling approaches range from empirical curve fitting techniques to sophisticated analytical treatments.

The methods described below for the prediction of moduli of particulate two-phase composites may be broadly grouped into the following three categories: (1) theory of dilute solutions, (2) mechanistic models for composite materials, and (3) effective medium models. All of these approaches share two important assumptions: that the phase surfaces are assumed to be in direct contact and are either chemically or physically bonded so that slip does not occur at a phase interface, and that the overall average response of the composite to surface tractions (or deformations) is defined in terms of a representative volume element that encompasses the localized variations in the material response characteristics. These assumptions are appropriate for those properties associated with small deformation behavior and hence do not seriously affect the prediction of a composite modulus. The additional simplifying assumptions which distinguish the various models play a more significant role in establishing the validity, and hence applicability of the models (McGee and McCullough 1981).

2.4.2.2 Theory of Dilute Suspensions

A dilute suspension is defined as one in which the fractional volume of inclusions is very small. This allows interactions between inclusions to be neglected since it is generally assumed that the distance between inclusions is large. Accordingly, the field produced in and around an inclusion when either tractions or displacements are prescribed on the boundary of a suspension volume can be found from the boundary value problem of one inclusion embedded in an infinite matrix under similar boundary conditions. With

these assumptions the resulting stress-strain relations are determinate in terms of volume fractions and phase constants and are exact for vanishingly small volume fractions of inclusions.

Einstein (1956) first proposed in 1906 that the viscosity of a dilute two-phase suspension may in general be expressed in the form

$$\eta_c = \eta_m(1+\alpha c) \tag{2.17}$$

where η_c and η_m are the viscosity of the suspension and matrix respectively, c refers to the inclusion's volume fraction, and α is a non-dimensional constant which is dependent on matrix and inclusion material constants and inclusion geometry. Einstein determined that α is equal to 2.5 for rigid spheres in a viscous matrix. It has further been assumed that Equation 2.17 also holds for changes in a bulk material constant so that it can be rewritten as:

$$G_c = G_m(1+2.5c) \tag{2.18}$$

where G_c and G_m are the shear modulus of the composite and matrix, respectively. The range of validity of Equation 2.18 is usually not more than 1-2% for c (Hashin 1964). Furthermore, it assumes that the stiffening action of the inclusion is independent of its size and that it is the volume occupied by the inclusion and not its weight which is the important variable. Nevertheless, the primary importance of this equation is that it gives the slope of the G_c versus c curve at the origin for a suspension of finite fractional inclusion volume.

In extending Einstein's equation for dilute suspensions (Equation 2.18) to higher concentrations of inclusions, Mooney (1951) proposed a crowding theory for the viscosity of a monodisperse suspension which accounts for first-order interactions between particles:

$$G_c = G_m \exp\left(\frac{2.5c}{1-kc}\right) \tag{2.19}$$

where k is the self-crowding factor (volume occupied by the inclusions/true volume of the inclusions) predicted only approximately by the theory. For closely packed spheres, k=1.35. Equation 2.19 agrees with Einstein's equation at low volume fractions and also models other experimental data at higher volume fractions. From this it was concluded

that the interaction between spheres in suspension can be described by simple geometric crowding, and that the mutual disturbance of flow lines around two adjacent particles is of secondary importance.

For non-spherical particles the Mooney equation was subsequently modified by Brodnyan (1959):

$$G_c = G_m \exp\left(\frac{2.5c + 0.407(p-1)^{1.508} c}{1 - k\,c}\right) \tag{2.20}$$

where p is the aspect ratio of the particle ($1<p<15$). While this equation provided the best fit to the data Brodnyan had available at the time, it was far from exact as the experimental viscosity did not increase as fast as Equation 2.20 predicts.

2.4.2.3 Mechanistic Models for Composite Materials

In this second category of models for the prediction of moduli of two-phase particulate composites, the solutions range from approximate approaches, based on simplified mechanical models and on average stress (or strain) assumptions, to more sophisticated and rigorous variational methods involving the theory of linear elasticity.

The simplest possible approach for a two-phase system is the phase arrangements shown in Figure 2.38. This approach is based on the assumption that each phase component (or prescribed combination of phase components) is subject to either the same stress or the same strain. These simplifications in the internal distributions of stress (or strain) mitigates the influence of the shape, size, and packing of the phase components. The only descriptors that are retained are the elastic properties and volume fraction of the components. The classical results of Voigt (1910) and Reuss (1929) belong to this category. For the parallel arrangement shown in Figure 2.38a, Voigt assumed that each component was subject to the same strain. This assumption leads to the following combining rule on the elastic constants:

$$E_c = E_i\,c + E_m\,(1-c) \tag{2.21}$$

where E_c, E_i and E_m are the Young's modulus of the composite, inclusion, and matrix, respectively, and c is the volume fraction of inclusions as described previously. Alternatively, for the series arrangement shown in Figure 2.38b, Reuss assumed that each

phase component was subject to the same stress, resulting in the following combining rule on the compliance constants (1/E):

$$\frac{1}{E_c} = \frac{c}{E_i} + \frac{(1-c)}{E_m} \tag{2.22}$$

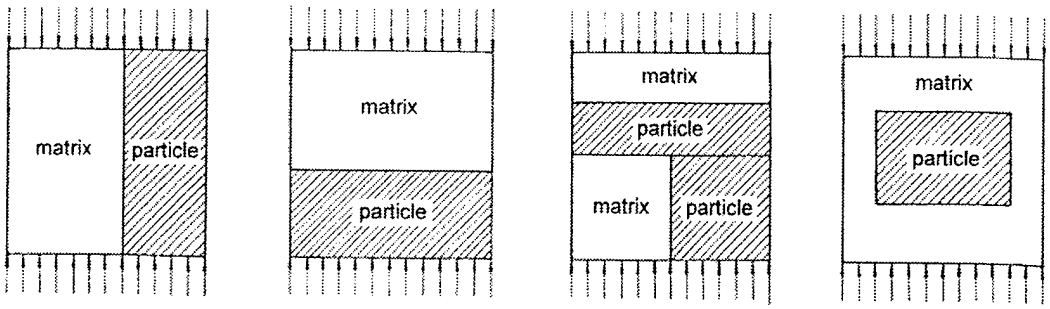

Figure 2.38: Model references (a) Voigt, (b) Reuss, (c) Hirsch, (d) Counto.

Examination of the Voigt and Reuss models presented above indicates that they represent extremes in material behavior. The Voigt (or constant strain) model attributes more significance to the stiffer phase, while the Reuss model emphasizes the more compliant phase. Equations 2.21 and 2.22 actually provide the upper and lower bound solutions for the composite modulus of a two-phase system for the special case where the Poisson's ratios of the constituent phases are equal. This result was obtained by Paul (1960) who derived a general solution for an elastic filler within an elastic matrix for an arbitrary phase geometry. Paul's treatment uses well-known elastic energy theorems in order to bound the strain energy and thus also the effective elastic modulus. The lower bound on E_c may be obtained by using the theorem of least work (minimum complementary energy), while the upper bound is obtained by the theorem of minimum potential energy. The main drawback of this approach lies in the assumption of non-interacting particles, which limits its representation to extreme filler contents (Ishai and Cohen 1967). While these bounds have the advantage of being exact, they are generally too far apart and often unable to adequately represent experimental data, especially if the ratio of the two moduli is greater than a factor of three (Fan et al. 1992). This implies that the assumption of either a state of uniform stress or uniform strain in the individual phases

of the filled systems is not sufficient to give a good estimate of the composite Young's modulus.

As a result of these shortcomings, numerous authors have proposed refinements or modifications to Equations 2.21 and 2.22. One of the first models to try to account for the complex stress distribution in the individual phases was proposed by Hirsch (1962) and may be written as:

$$\frac{1}{E_c} = \left(1 - \frac{2Z}{\pi}\right)\left(\frac{c}{E_i} + \frac{(1-c)}{E_m}\right) + \frac{2Z}{\pi}\left(\frac{1}{E_i\, c + E_m(1-c)}\right) \tag{2.23}$$

This model, illustrated in Figure 2.38c, is simply a weighted average of the first two models. The empirical parameter Z, which adjusts the relative proportions of material conforming to the upper and lower bound solutions, can be found by curve fitting the laboratory data. Hirsch (1962) recommends that a value of Z=0.785 be used in Equation 2.23 based on a series of tests on concrete systems. This essentially describes a solution which follows a curve based on the average value of the bounds given by Equations 2.21 and 2.22.

An approximate solution for a composite elastic modulus, which is neither an upper nor lower bound, has also been derived by Paul (1960). In the formulation of this model it is reasoned that since a filled composite material can be assumed to be uniform in the overall sense, it is therefore plausible to assume that the macroscopic stress and strain are reproduced in some average sense in a typical unit volume which consists of a single particle of inclusion material embedded in a cube of the matrix material. Therefore, in a typical cube assumed to be loaded over opposite faces by the force $F=(\sigma)(1)$, any cross section at a distance x from the end face will intersect an area A_m of matrix material and an area A_i of inclusion or filler material, as shown in Figure 2.39. Since the strain is uniform over such a cross section, the normal stress on area A_m will be $E_m\varepsilon$ and that on A_i will be $E_i\varepsilon$, where ε is the normal strain at the cross section. The total force on the cross section must equal the total applied force F, such that:

$$F = E_m\varepsilon\, A_m + E_i\varepsilon\, A_i = \varepsilon\left[E_m + (E_i - E_m)A_i\right] \tag{2.24}$$

If the total elongation of the cube is given by δ, where

$$\delta = \int_0^1 \varepsilon(x)dx = F\int_0^1 \frac{dx}{E_m + (E_i - E_m)A_i} \tag{2.25}$$

and if E_c is defined as the ratio of F/δ for a unit cube, it follows that:

$$\frac{1}{E_c} = \int_0^1 \frac{dx}{E_m + (E_i - E_m)A_i(x)} \tag{2.26}$$

For any particular distribution of inclusions, $A_i(x)$ is a well defined function of x and so Equation 2.26 gives an approximate value for E_c for any assumed distribution of the inclusion. If the inclusion is assumed to be of a cubic shape then it may be readily verified that the Young's modulus of the composite is given by:

$$E_c = E_m\left(\frac{1 + (m-1)c^{2/3}}{1 + (m-1)(c^{2/3} - c)}\right) \tag{2.27}$$

where m=E_i/E_m and c is defined as before. This solution also assumes that adhesion is maintained at the interface between the two constituent materials and that cross sections originally normal to the axis of the applied stress remain plane and normal to the axis.

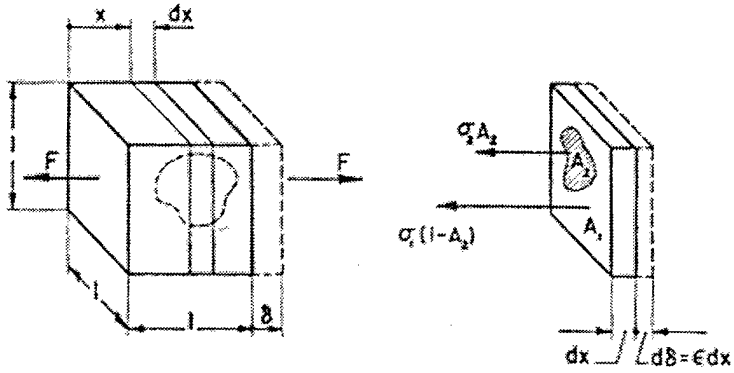

Figure 2.39: Unit cube with inclusion of arbitrary shape. (Paul 1960)

Using the same model, but solving for a uniform displacement at the boundary, results in the following formulation first proposed by Ishai (1965):

$$E_c = E_m\left(1 + \frac{c}{\frac{m}{(m-1)} - c^{1/3}}\right) \tag{2.28}$$

Ishai and Cohen (1967) showed that this approximate solution gave good results for both porous and filled epoxy composites in both tension and compression.

Counto (1964) also proposed a two-phase model, based on a similar geometric configuration, to predict the Young's modulus of concrete in compression. The Counto model considers the inclusion as a cylinder (or prism) placed in the center of a cylinder (or prism) of matrix material with both constituents having the same ratio of height to cross-sectional area. This arrangement is shown in Figure 2.38d. The deformational behavior of such a model can be determined by assuming that the stress applied to the concrete cylinder does not vary along the depth of the layers (AA'BB' or CC'DD'), and that for the combined material (BB'CC'), the strain in the direction of application of stress is the same as the strains in the inclusion and in the matrix (Figure 2.40). If a uniform stress σ_c is applied to the composite along the boundaries AA'DD' then it can be shown that:

$$\frac{\sigma_c}{E_m}\left(1-\sqrt{c}\right)+\frac{\sigma_c}{E_{im}}\sqrt{c}=\frac{\sigma_c}{E_c}\times 1 \tag{2.29}$$

or

$$\frac{1-\sqrt{c}}{E_m}+\frac{\sqrt{c}}{E_{im}}=\frac{1}{E_c} \tag{2.30}$$

where E_m, E_{im} and E_c are the Young's modulus of the matrix, combined material, and composite (AA'DD') respectively. E_{im} can be calculated as follows:

$$\frac{\sigma_m}{E_m}=\frac{\sigma_i}{E_i}=\frac{\sigma_c}{E_{im}} \tag{2.31}$$

where σ_m and σ_i are the stress on the matrix and inclusion respectively. Since the sum of the forces on the inclusion and matrix must equal the total force applied to the combined material BB'CC',

$$\sigma_m(1-\sqrt{c})+\sigma_i\sqrt{c}=\sigma_c\times 1 \tag{2.32}$$

A solution for the composite modulus (E_c) can be obtained by combining Equations 2.31 and 2.32 and solving for E_{im}, and then substituting the result in Equation 2.30:

$$\frac{1}{E_c}=\frac{1-\sqrt{c}}{E_m}+\frac{1}{\left(\frac{1-\sqrt{c}}{\sqrt{c}}\right)E_m+E_i} \tag{2.33}$$

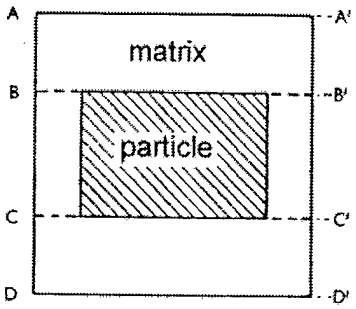

Figure 2.40: Detail of Counto's (1964) composite material model.

While the models of Paul, Ishai, and Counto offer more realistic results that cover a wide range of modulus ratios (m) and compositions, as well as more realistic boundary conditions, they still suffer from their failure to allow for the lateral effect which is especially important at high filler contents. Preliminary considerations (Andersen et al. 1995) indicate, however, that these cubic models are the best approximations for determining the composite modulus of a two-phase system since they mimic the composite behavior in an average sense despite ignoring the elastic interactions between phases, as well as averaging the stresses and strains over the individual phases.

Using a variation of the cubic model approach presented above, Ravichandran (1994) developed upper and lower bound expressions for the elastic properties of two-phase systems considering a unit cell representation of the material microstructure. In this model the microstructure of particulate filled matrix is idealized as a periodic arrangement of cubic inclusions distributed in a continuous matrix as illustrated in Figure 2.41a. Figure 2.41b illustrates the three-dimensional nature of the unit cell. Given this geometry, it can be shown that the volume fraction of the inclusion c is related to the non-dimensional parameter, $\chi=h/a$, as:

$$\chi = \left(\frac{1}{c}\right)^{1/3} - 1 \tag{2.34}$$

The approach basically involves dividing the unit cell into parallel and series elements and computing the resulting composite modulus. The elements are assumed to be loaded uniaxially in parallel and series are considered to experience isostrain and isostress loading conditions respectively. While strain compatibility and perfect bonding

are also assumed to exist, the effects of elastic interactions between particles, which may be important at large volume fractions, have been neglected. Depending on the sequence of element division, upper and lower bound solutions are obtained. The lower bound solution for composite modulus E_c is given by:

$$E_c = \frac{(\chi E_i E_m + E_m^2)(1+\chi)^2 - E_m^2 + E_i E_m}{(\chi E_i + E_m)(1+\chi)^2} \tag{2.35}$$

In an analogous fashion, the upper bound solution is given by:

$$E_c = \frac{\left[E_i E_m + E_m^2(1+\chi)^2 - E_m^2\right](1+\chi)}{(E_i - E_m)\chi + E_m(1+\chi)^3} \tag{2.36}$$

It should be noted that the above derivation has also been made on the condition of equivalence of Poisson's ratios of the inclusion and matrix phase.

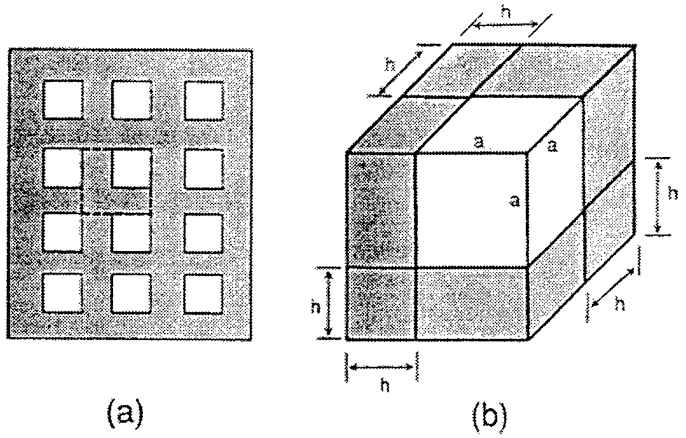

Figure 2.41: Schematics of (a) the idealized microstructure, (b) the unit cell of the composite. (Ravichandran 1992)

These simple expressions based on unit cell calculations were evaluated for a large number of composite systems by Ravichandran (1994) and were found to provide an improved prediction over the upper and lower bounds provided by Paul (1960). However upon closer inspection, the upper and lower bound solutions given in Equations 2.35 and 2.36 are simply the approximate solutions given in Equations 2.27 and 2.28 by Paul (1960) and Ishai (1965), respectively. Therefore, it seems that Ravichandran (1994) has arrived at the same solution using a different and possibly more rigorous approach.

Following the work of Paul (1960) and of Hashin (1962), Hashin and Shtrikman (1963) proceeded to solve the problem of predicting the effective composite elastic moduli of multiphase materials in terms of the elastic moduli and volume fractions of the constituent phases without making assumptions about phase geometry. Previous attempts at finding theoretical expressions for the effective composite elastic moduli, or other physical constants, have invariably been based on numerous simplifying assumptions concerning the geometrical form and physical behavior of phase regions. A more attractive approach consists of the use of variational principles in order to bound the strain energy and thus the composite modulus. Although such principles were used by Paul (1960), the bounds obtained were generally not close enough to provide a good enough estimate for the composite modulus even though an arbitrary phase geometry was assumed.

By considering a composite body consisting of n different elastic phases which may be regarded as quasi-homogeneous and quasi-isotropic, Hashin and Shtrikman derived improved expressions for the upper and lower bounds for the composite elastic moduli of multiphase materials by introducing new variational principles for non-homogeneous and isotropic elasticity. While a complete presentation of the procedure is beyond the scope of this review, the formulation involves calculation of the upper and lower limits for the bulk modulus K, and the shear modulus G. The upper and lower bounds, derived for the specialized case of two-phase materials, are given by the following equations (Hashin and Shtrikman 1963):

$$K_L = K_m + \frac{c}{\frac{1}{K_i - K_m} + \frac{3(1-c)}{3K_m + 4G_m}} \tag{2.37}$$

$$K_U = K_i + \frac{(1-c)}{\frac{1}{K_m - K_i} + \frac{3c}{3K_i + 4G_i}} \tag{2.38}$$

$$G_L = G_m + \frac{c}{\frac{1}{G_i - G_m} + \frac{6(K_m + 2G_m)(1-c)}{5G_m(3K_m + 4G_m)}} \tag{2.39}$$

$$G_U = G_i + \frac{(1-c)}{\frac{1}{G_m - G_i} + \frac{6(K_i + 2G_i)c}{5G_i(3K_i + 4G_i)}} \tag{2.40}$$

It has been shown (Hashin 1962) that Equation 2.37 is the exact result for the bulk modulus of certain composite materials which may be described by a matrix of a phase 'one' material in which spherical inclusions of a phase 'two' material are distributed in a particular way. Analogously, Equation 2.38 is the exact result when the matrix is of a phase 'two' material and the spherical inclusions are of a phase 'one' material. Also, when the shear moduli of the two phases are equal the bounds for the bulk modulus coincide, thus providing an exact result for this special case.

With the results obtained for the bulk and shear moduli, bounds for the Young's modulus and Poisson's ratio can be derived using the following expressions:

$$E = \frac{9KG}{3K + G} \tag{2.41}$$

$$\nu = \frac{3K - 2G}{2(3K + G)} \tag{2.42}$$

It is easily proved that the upper and lower bounds on the bulk and shear modulus give upper and lower bounds for the Young's modulus. For the Poisson's ratio the correspondence is reversed.

The separation of the Hashin and Shtrikman upper and lower bound is dependent upon the modulus ratio of inclusion to matrix (m=E_i/E_m). When the moduli of the constituent phases are closely matched, the bounds predict values within 10%. In the case of rigid polymeric-filled systems, where m approaches 20 or more, the bounds given by Equations 2.37-2.40 are still widely spaced, and therefore of limited predictive value (Ahmed and Jones 1990a). Nevertheless, the Hashin and Shtrikman bounds serve as a useful test for other approximate theories since any theoretical solution outside these bounds must be regarded as invalid.

In contrast to the previous theoretical treatments, the last expression to be considered has no physical meaning. Based on the Bache and Nepper-Christensen (BNC) model for strength, a simple and apparently effective model for the composite modulus of

a two-phase system has been proposed by analogy (Lydon and Balendran 1986) as follows:

$$E_c = E_m\left(\frac{E_i}{E_m}\right)^c \tag{2.43}$$

While completely empirical in its derivation it has been included here because it has been found to be sufficiently accurate for most types of concrete (Zhou et al. 1995).

2.4.2.4 Effective Medium Models

The last group of models to be discussed are known as effective medium models. This is because the composite properties of the two-phase heterogeneous material are obtained either by micro-structural transformation of the material into some mechanically equivalent effective medium, or by the transformation of the overall material into an effective homogeneous medium possessing the same average conditions of stress and strain as does some volume averaged representative volume element. The essential difference between the various effective medium methods lies in the treatment and evaluation of the interaction between the two phases, and that not all of them admit a physical description at the same level. This school of micro-mechanical modeling stems from the initial work of Kerner (1956) who introduced the composite sphere model as a method for determining the effective properties of a composite material, and has gone on to include contributions from numerous other authors. As such, only the original work of Kerner (1956) and three of the more promising effective medium models are presented in the following discussion. Comprehensive and insightful reviews on effective medium methods are provided by Christensen (1990) and Huang et al. (1995), and may serve as useful sources for further exploration on the subject matter.

Kerner (1956) presented an elaborate and apparently exact solution to the problem of determining the composite modulus of a suspension of spherical inclusions in an elastic matrix. For very rigid particles ($G_i >> G_m$), the Kerner equation simplifies to:

$$G_c = G_m\left(1+\frac{c}{(1-c)}\frac{15(1-\nu_m)}{(8-10\nu_m)}\right) \tag{2.44}$$

where ν_m is the Poisson's ratio of the matrix. In this model, the phase geometry is represented by a single spherical inclusion of radius a embedded in a sphere of the matrix material with a radius b. The ratio of a^3/b^3 is taken to be equal to the volume fraction of the filler. The composite sphere is in turn embedded in an infinite medium of unknown composite properties (Figure 2.42). By using averaging techniques an elasticity problem can be formulated for this simplified geometry such that a self-consistent stress field can be identified and the effective properties of the medium determined.

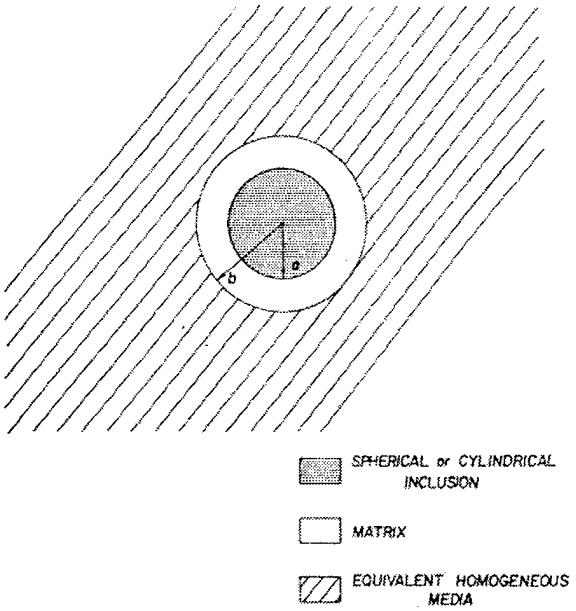

Figure 2.42: Effective medium model.

While many modifications have been proposed to the Kerner equation to describe the data of various authors, the treatment of Kerner (1956) was unfortunately found to be in error by Christensen and Lo (1979). While the explicit error in the Kerner equation cannot be "pinpointed because of the brevity of the derivation" (Christensen 1979) this casts doubts on the original Kerner equation and its subsequent modifications (e.g., Lewis and Nielsen 1970, Dickie 1973).

Based on the original geometric model developed by Kerner (1956), the Generalized Self Consistent Model (GSCM) (Christensen and Lo 1979) was developed to provide a solution for the effective modulus of a two phase system containing spherical inclusions which includes a physically realistic model of particle to particle interaction.

The GSCM has been described as simple in concept and complex in execution (Christensen 1990). The basic model is the same as that of Kerner (1956) given in Figure 2.42. A spherical inclusion is embedded in a concentric spherical annulus of the matrix material of the prescribed volume fraction, which is in turn embedded in an infinite medium possessing the unknown composite properties. The proper solution to this three phase problem along with proper averaging techniques yields the complete solution for the composite properties (K and G). A complete derivation of the solution, as well as an elaborate discussion of the model, can be found in Christensen and Lo (1979).

The exact solution to the effective medium problem is given by the solution of the following quadratic equation:

$$A\left(\frac{G_c}{G_m}\right)^2 + 2B\left(\frac{G_c}{G_m}\right) + C = 0 \tag{2.45}$$

where

$$A = 8\left(\frac{G_i}{G_m} - 1\right)(4 - 5\nu_m)\eta_1 c^{10/3} - 2\left[63\left(\frac{G_i}{G_m} - 1\right)\eta_2 + 2\eta_1\eta_3\right]c^{7/3} + 252\left(\frac{G_i}{G_m} - 1\right)\eta_2 c^{5/3}$$
$$- 50\left(\frac{G_i}{G_c} - 1\right)(7 - 12\nu_m + 8\nu_m^2)\eta_2 c + 4(7 - 10\nu_m)\eta_2\eta_3 ,$$

$$B = -2\left(\frac{G_i}{G_m} - 1\right)(1 - 5\nu_m)\eta_1 c^{10/3} + 2\left[63\left(\frac{G_i}{G_m} - 1\right)\eta_2 + 2\eta_1\eta_3\right]c^{7/3} - 252\left(\frac{G_i}{G_m} - 1\right)\eta_2 c^{5/3}$$
$$+ 75\left(\frac{G_i}{G_c} - 1\right)(3 - \nu_m)\eta_2\nu_m c + \frac{3}{2}(15\nu_m - 7)\eta_2\eta_3 ,$$

$$C = 4\left(\frac{G_i}{G_m} - 1\right)(5\nu_m - 7)\eta_1 c^{10/3} - 2\left[63\left(\frac{G_i}{G_m} - 1\right)\eta_2 + 2\eta_1\eta_3\right]c^{7/3} + 252\left(\frac{G_i}{G_m} - 1\right)\eta_2 c^{5/3}$$
$$+ 25\left(\frac{G_i}{G_m} - 1\right)(\nu_m^2 - 7)\eta_2 c - (7 + 5\nu_m)\eta_2\eta_3 ,$$

with

$$\eta_1 = \left(\frac{G_i}{G_m} - 1\right)(7 - 10\nu_m)(7 + 5\nu_i) + 105(\nu_i - \nu_m)$$

$$\eta_2 = \left(\frac{G_i}{G_m} - 1\right)(7 + 5\nu_i) + 35(1 - \nu_i)$$

$$\eta_3 = \left(\frac{G_i}{G_m} - 1\right)(8 - 10\nu_m) + 15(1 - \nu_m)$$

where c denotes the volume fraction of inclusions, and G_c refers to the composite shear modulus. The subscripts i and m again refer to the isotropic inclusion and the matrix phases respectively. The solution for the composite bulk modulus K_c is given by:

$$K_c = K_m + \frac{c(K_i - K_m)}{1 + (1-c)\dfrac{(K_i - K_m)}{\left(K_m + \dfrac{4}{3}G_m\right)}} \tag{2.46}$$

The GSCM not only provides a unique approach to exploring the matrix/inclusion interactions, but also yields the correct asymptotic behavior for rigid inclusions as the volume fraction of the rigid inclusions approaches unity (Dai et al. 1999). Accordingly, Christensen (1990) demonstrates that preference should be given to the GSCM over other effective medium models. However, the weak point of the GSCM is that it does not have a simple form of solution for the effective shear modulus which is inconvenient for engineering applications. Furthermore, the classical GSCM can only be made readily suitable for a two-phase composite material and there remain certain issues to be clarified regarding applications to multiphase composites. It does though recover reasonable physical behavior in the limiting case of a concentrated poly-disperse suspension of rigid spheres (Christensen 1990).

The Mori-Tanaka method (MTM) (Mori and Tanaka 1973) offers a completely different micromechanical analysis from the previous two models. Whereas the preceding models admit physical descriptions, the MTM does not, at least not at the same level. Rather the MTM in essence is an estimate of the solution form guided only by the requirement of the dilute solution at one end of the concentration scale, and at the opposite end of the scale by the requirement that as the volume fraction c increases, the effective property identifies with that of the inclusion phase.

This method has received much attention recently because it permits closed-form solutions for a series of problems ranging from the determination of composite elastic constants to the determination of stresses in and around inclusions. The outline given here follows the presentation of Christensen (1990) which highlights the underlying assumption

of the method. A rather mathematical description is necessary since the key to the method is essentially mathematical rather than physical.

For a two-phase composite experiencing far field conditions that give a uniform strain $\bar{\varepsilon}$, the average strain in the system is given by:

$$\bar{\varepsilon} = c_1\bar{\varepsilon}^{(1)} + c_2\bar{\varepsilon}^{(2)} \tag{2.47}$$

where c_1 and c_2 are the volume fractions of the two phases (c_1+c_2=1). Define a composite stiffness tensor **C** where average stress and strain are related by:

$$\bar{\sigma} = \mathbf{C}\bar{\varepsilon} \tag{2.48}$$

In composite material terminology, the following form is proven and often used:

$$\mathbf{C}\bar{\varepsilon} = \mathbf{C}_1\bar{\varepsilon} + c_2\left[\mathbf{C}_2\bar{\varepsilon}^{(2)} - \mathbf{C}_1\bar{\varepsilon}^{(2)}\right] \tag{2.49}$$

where $\mathbf{C}_1$ and $\mathbf{C}_2$ are the property tensors of the two phases. If phase 2 is taken as the inclusion phase then under dilute conditions it is possible to write:

$$\bar{\varepsilon}^{(2)} = \mathbf{T}\bar{\varepsilon} \tag{2.50}$$

where **T** is called the strain concentration tensor, considered here to be known. It results from the field variable solution of the dilute suspension problem. It is then possible to redefine **C**:

$$\mathbf{C} = \mathbf{C}_1 + c_2(\mathbf{C}_2 - \mathbf{C}_1)\mathbf{T} \tag{2.51}$$

Now the MTM can be used for generalizing the dilute solution form (Equation 2.51) to non-dilute conditions. Define the tensor **A** through:

$$\bar{\varepsilon}^{(2)} = \mathbf{A}\bar{\varepsilon} \tag{2.52}$$

Then using Equation 2.51 gives:

$$\mathbf{C} = \mathbf{C}_1 + c_2(\mathbf{C}_2 - \mathbf{C}_1)\mathbf{A} \tag{2.53}$$

In order to determine **A**, a new tensor **G** can be introduced such that:

$$\bar{\varepsilon}^{(2)} = \mathbf{G}\bar{\varepsilon}^{(1)} \tag{2.54}$$

where **G** is dependent upon the volume fraction of the inclusion phase (c_2). After some manipulation it can be revealed that:

$$\mathbf{A} = \left[c_1\mathbf{I} + c_2\mathbf{G}\right]^{-1}\mathbf{G} \tag{2.55}$$

Therefore, the solution for tensor **G** under non-dilute conditions will determine the composite property. It is seen that Equation 2.54 is the non-dilute counterpart of the dilute solution form given in Equation 2.50. Equation 2.54 can then be written as:

$$\bar{\varepsilon}^{(2)} = (c_1\mathbf{I} + c_2\mathbf{G})^{-1}\mathbf{G}\bar{\varepsilon} \tag{2.56}$$

or in a compact form as:

$$\bar{\varepsilon}^{(2)} = \mathbf{H}\bar{\varepsilon} \tag{2.57}$$

where

$$\mathbf{H} = \left[c_1\mathbf{I} + c_2\mathbf{G}(c_2)\right]^{-1}\mathbf{G}(c_2) \tag{2.58}$$

Considering the extreme values for c_2 it is clear that:

$$\mathbf{H}\big|_{c_2=0} = \mathbf{T} \tag{2.59}$$

and

$$\mathbf{H}\big|_{c_2=1} = \mathbf{I} \tag{2.60}$$

Thus the MTM assumes tensor **H** as:

$$\mathbf{H} = \left[c_1\mathbf{I} + c_2\mathbf{T}\right]^{-1}\mathbf{T} \tag{2.61}$$

where by assumption:

$$\mathbf{G}(c_2) \rightarrow \mathbf{T} \tag{2.62}$$

Now with **G** replaced by the known dilute solution form **T** in Equation 2.55 and then **A** in Equation 2.53, the determination of the composite property **C** is complete. Replacing the concentration dependent tensor $\mathbf{G}(c_2)$ by the concentration independent tensor **T** in Equation 2.62 amounts to the simplest form of **H** in Equation 2.58 that satisfies the endpoint conditions given in Equations 2.59 and 2.60.

Application of the MTM to the problem of determining the effective properties of a composite material containing a suspension of rigid spherical inclusions under non-dilute conditions yields the following expressions for the shear and bulk moduli:

$$G_c = G_m + c(G_i - G_m)\frac{1}{1 + (1-c)\left[\dfrac{G_i - G_m}{G_m + \dfrac{G_m(9K_m + 8G_m)}{6(K_m + 2G_m)}}\right]} \tag{2.63}$$

and

$$K_c = K_m + c(K_i - K_m)\frac{1}{1+(1-c)\left[\dfrac{K_i - K_m}{K_m + \frac{4}{3}G_m}\right]} \tag{2.64}$$

It should be noted that these Mori-Tanaka results correspond to the Hashin and Shtrikman lower bound solution (Willis 1977).

In a critical evaluation of the effective medium models (Christensen 1990), in which attention was focused on the analytical forms of the asymptotic, high concentration results, it was shown that the MTM predicts the same order of behavior for a suspension of rigid spherical inclusions in an isotropic elastic (compressible) matrix phase, as well as for the incompressible matrix case. The fact that the MTM does not capture the higher order effects associated with the incompressible matrix case indicates that the MTM completely misses the essential physics of the problem since higher order strain gradients necessarily occur in the incompressible case than in the compressible case. Similar analyses performed over the full volume fraction range also indicate that the full solution behavior is completely consistent with the asymptotic results. This means that overall the MTM has little justification other than its appealing simplicity since it consistently tends to underestimate the behavior of composite systems (Christensen 1990). In an effort to improve this methods prediction, Ju and Chen (1994) showed that by accounting for particle interaction effects, their model could reproduce experimental data more closely. Further evaluation of the improved Mori-Tanaka method for the prediction of the behavior of particulate-filled composites can be found in Wong and Ait-Kadi (1997).

One of the more recent effective medium approaches for predicting the Young's modulus of two-phase composites is based on the theory of topological transformation and mean field theory (Fan et al. 1992). This approach allows a two-phase microstructure with any combination of grain size, grain shape, and phase distribution, to be translated into an effective medium consisting of three well-defined microstructural elements which together are mechanically equivalent to the original body. This method for microstructural characterization combines the concept of contiguity, a description of the extent of particle

contact in dual phase microstructures, with Eshelby's continuum transformation theory (Eshelby 1957).

According to the theory of topological transformation, the two-phase microstructure, shown schematically in Figure 2.43a, can be transformed into a three microstructural element (3E) body (Figure 2.43b). It is important to point out that Figure 2.43 is only a schematic illustration of the idea of topological transformation and does not represent any quantitative information such as volume fraction, grain size, or grain shape. Element I (EI) consists only of α grains having an average grain size d_α. The volume fraction of EI is defined by the continuous volume of a phase $f_{\alpha c}$. This term is dependent on the degree of contiguity, which is in turn a function of inclusion grain size d, and volume fraction:

$$f_{\alpha c} = C_\alpha f_\alpha \tag{2.65}$$

where

$$C_\alpha = \frac{f_\alpha R}{f_\alpha R + f_\beta} \tag{2.66}$$

$$R = \frac{d_\beta}{d_\alpha} \tag{2.67}$$

Similar expressions can be written for Element II (EII) which consists only of β grains. Element III (EIII) consists of the long range α–β chains, and hence there are only phase boundaries in EIII. The volume fraction of EIII is defined by the degree of separation F_s:

$$F_s = \frac{f_\alpha f_\beta (1+R)}{f_\alpha R + f_\beta} \tag{2.68}$$

and the grain size is defined by the volume fraction weighted average grain size $\bar{d}_{III}$:

$$\bar{d}_{III} = d_\alpha f_{\alpha III} + d_\beta f_{\beta II} \tag{2.69}$$

where $f_{\alpha III}$ and $f_{\beta III}$ are the volume fraction of α and β in EIII, respectively, and can be expressed mathematically as:

$$f_{\alpha III} = \frac{f_\alpha - f_{\alpha c}}{F_s} \tag{2.70}$$

$$f_{\beta III} = \frac{f_\beta - f_{\beta c}}{F_s} \tag{2.71}$$

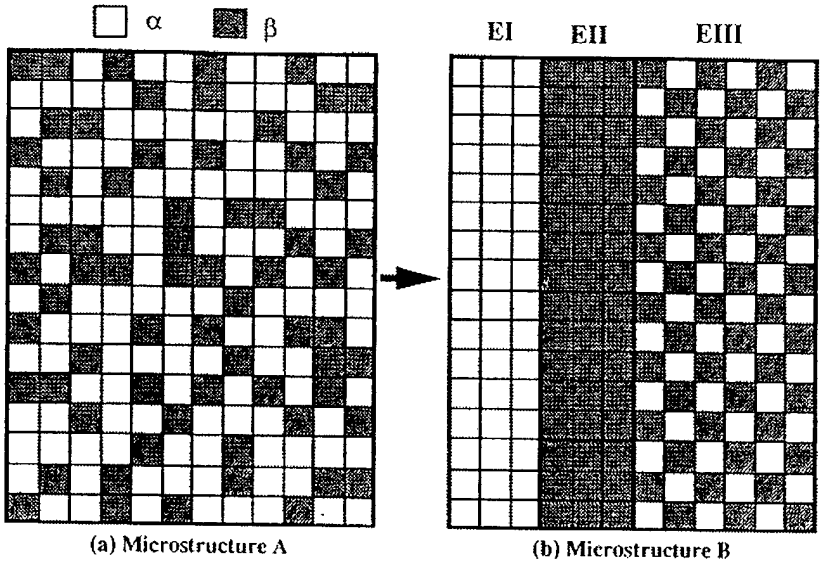

Figure 2.43: Topological transformation of a two-phase microstructure. (Fan et al. 1992)

As a consequence of this topological transformation, the determination of the mechanical properties of a complex two-phase microstructure can be replaced by an analysis of a simpler equivalent effective medium having three well-defined microstructural elements.

In the development of their approach, Fan et al. (1992) assume that if a uniaxial stress is applied along the aligned direction of the 3E body, strain compatibility requires that:

$$\varepsilon_I = \varepsilon_{II} = \varepsilon_{III} = \varepsilon_c \tag{2.72}$$

where ε_I, ε_{II}, ε_{III}, and ε_c are the elastic strains in EI, EII, EIII, and the whole 3E body respectively. Considering a subsequent elastic strain increment ($\delta\varepsilon_c$) in the 3E body, the elastic strain increments in EI, EII, and EIII can be written as $\delta\varepsilon_I$, $\delta\varepsilon_{II}$, $\delta\varepsilon_{III}$, respectively. Applying the principal of virtual work to the 3E body yields the expression:

$$\sigma_c \delta\varepsilon_c = \sigma_I \delta\varepsilon_I f_{\alpha c} + \sigma_{II} \delta\varepsilon_{II} f_{\beta c} + \sigma_{III} \delta\varepsilon_{III} F_s \tag{2.73}$$

where σ_I, σ_{II}, σ_{III}, and σ_c are the stresses in the three microstructural elements and the 3E body respectively. Since strain compatibility is also a requirement for the elastic strain increments, Equation 2.73 can be rewritten as:

$$\sigma_c = \sigma_I f_{\alpha c} + \sigma_{II} f_{\beta c} + \sigma_{III} F_s \tag{2.74}$$

Dividing through by ε_c, and noting that $\varepsilon_I=\varepsilon_{II}=\varepsilon_{III}=\varepsilon_c$ gives:

$$\frac{\sigma_c}{\varepsilon_c} = \frac{\sigma_I}{\varepsilon_I} f_{\alpha c} + \frac{\sigma_{II}}{\varepsilon_{II}} f_{\beta c} + \frac{\sigma_{III}}{\varepsilon_{III}} F_s \tag{2.75}$$

or, by applying Hooke's law:

$$E_c = E_I f_{\alpha c} + E_{II} f_{\beta c} + E_{III} F_s \tag{2.76}$$

where E_I, E_{II}, E_{III}, E_c refer to the Young's moduli of each microstructural element and the whole 3E body, respectively. Since EIII contains only phase boundaries, there is no direct contact between particles of the same phase, and therefore interactions between particles of the same phase can be neglected. Thus, a mean field approach (Pedersen 1983) can be applied to the EIII body. Pedersen developed the approach to describe the deformation behavior of inhomogeneous composites by assuming that the equivalent homogenous inclusion samples the mean matrix stresses. By applying this theory, the following equations can be derived:

$$G_{III} = \frac{G_\alpha}{1 + \dfrac{f_{\beta III} D}{1 - f_{\beta III} \gamma D}} \tag{2.77}$$

where

$$D = \frac{G_\alpha - G_\beta}{(G_\beta - G_\alpha)(1-\gamma) + G_\alpha} \tag{2.78}$$

$$\gamma = \frac{7 - 5\nu_\alpha}{15(1-\nu_\alpha)} \tag{2.79}$$

In Equations 2.78 and 2.79, G_α and G_β are the shear moduli of the α and β phase and G_{III} is the shear modulus of the EIII body, γ is the strain accommodation tensor for a sphere, and ν_α is the Poisson's ratio of the matrix. Once G_{III} is obtained, E_{III} can be calculated by:

$$E_{III} = 2G_{III}(1+\nu_{III}) \tag{2.80}$$

where ν_{III} can be approximated as:

$$\nu_{III} = \nu_{\alpha} f_{\alpha III} + \nu_{\beta} f_{\beta III} \tag{2.81}$$

From the above equations, the Young's modulus of a two-phase composite can be calculated.

The advantage of this approach over other continuum approaches is that it can predict not only the effect of volume fraction of the reinforcing phase, but also the effects of microstructural parameters such as grain shape and phase distribution on the stiffness of composites. It is shown (Fan et al. 1992) that in a particulate composite having a given volume fraction of reinforcement, the Young's modulus of the composite increases with increasing contiguity of the constituent phases, and this increment is dependent on the stiffness ratio of the constituent phases. Furthermore, the approach can provide a simple and effective solution to the problem of interaction between particles of the same phase.

2.4.3 Limitations of Theoretical Models for Young's Modulus

Having summarized some of the models available for the prediction of the modulus of two-phase particulate composites, a brief discussion of their applicability and limitations is warranted. Most of the theories discussed in the survey above assume that the composite modulus of a two-phase filled system can be adequately described in terms of the elastic properties of the constituents and the volume fraction of filler. The main difference between the various approaches then are the assumptions made in specifying the micro-geometry, and the simplifications made in the internal distribution of stress or strain.

The models presented in this discussion range from the completely empirical to those theoretically based in micro-mechanics. The assumptions that are made in simplifying the complex stress-strain distribution in a two-phase composite material offer the biggest limitation to the accurate prediction of the composite modulus. The upper and lower bound solutions given by Equation 2.37 and 2.38 assume that the individual phases are under a uniform strain or stress, respectively. The wide spacing of the bounds, and hence the limited predictive capability, results from oversimplifying the internal stress-strain field. While such simple models may give acceptable first estimates of composite material behavior, none of the models based on uniform stress or strain fields can be

strictly correct since interfacial forces are not in equilibrium for constant strain, and interfacial discontinuities must exist for constant stress. Only with higher mathematics can the exact solution for the effective properties of a particulate composite medium be evaluated. Therefore advanced micro-mechanical models offer the best level of prediction, but suffer from an increase in complexity. Clearly tradeoffs must be made between the level of detail and the resulting desired level of accuracy.

Theories that are used to explain the variation of the composite modulus for a two-phase system with volume fraction do not normally take into account the effect of particle size. There is, however, evidence that the modulus increases as the particle size decreases (Spanoudakis and Young 1984a), although this effect may be attributed to the testing method used. In contrast, the initial modulus was found to be independent of particle size in other particulate filled composites (Yilmazer and Farris 1983).

The properties of composites may also be affected by changes in particle shape. Early work by Bueche (1957) indicated that different filler shapes result in different mechanical properties. Furthermore, theoretical work by Wu (1966) proved that disc-shaped particles provided better reinforcement than needle or spherical shaped particles. However, the effect of anisotropy associated with non-spherical particles was ignored. Indeed, Brodnyan (1959) recognized that particle shape was important in concentrated suspensions and accordingly modified the Mooney equation (Equation 2.19) to account for the particle aspect ratio. Fairly recent experimental evidence by Ahmed and Jones (1990b) confirm that, in the absence of adhesion between particle and matrix, semi-angular shaped particle filled composites have higher moduli than their spherical counterparts.

One characteristic that has received very little attention is the preceding discussion is the effect of particle size distribution, which affects the maximum packing fraction. It is well-known that particles of different size can pack more densely than monodispersed particles because the small ones can fill the interstitial space between the closely packed large particles and form an agglomerate. These aggregated particles may be able to carry a larger portion of the load than the primary particles to yield a higher modulus at the same volume fraction predicted by most theories. This was confirmed by Ahmed and Jones (1990b) who showed that graded mixtures of particles can cause improved

reinforcement over narrowly distributed particle sizes. Efforts to account for particle gradation have been proposed by Lewis and Nielsen (1970) who proposed an empirical modification of the Kerner equation by introducing a curve fitting parameter, ϕ_m. A similarly modified Kerner equation was also proposed by Dickie (1973). Each of these equations appears to satisfactorily describe the data of the individual authors. A new approach to model the statistical distribution of the filler particles has been attempted by Guild and Young (1989). They applied finite element techniques to a statistical distribution of filler particles in a two-phase system and found a good correlation between the predicted and experimentally observed moduli. Its application to a wider range of data is, however, required to establish its full potential (Ahmed and Jones 1990a).

A common assumption in most of the theories which predict the reinforcing action of a filler in a composite material assume perfect adhesion to exist between the inclusion and the matrix so that slip does not occur at the boundary. Studies which have investigated the effect of particle adhesion offer conflicting results. Spanoudakis and Young (1984b) investigated glass-filled epoxy resin and found that composites containing spherical particles treated with release agents have significantly lower values of modulus than those treated with coupling agents. Yilmazer and Farris (1983) however concluded that the presence of a coupling agent in spherical glass bead-filled composites has no effect on modulus reinforcement. In both cases though, interface adhesion was found to affect the strength of the composite which may suggest that adhesion may not be an important factor as long as the frictional forces between the phases are not exceeded by the applied stress. The conflicting results may then be attributed to other factors such as particle shape or roughness. Furthermore, because in most filled systems there is a mismatch in the coefficients of thermal expansion, which is reflected as a mechanical bond resulting from thermally induced stresses, the assumption of perfect adhesion may be valid even if the bonding is poor.

Other factors which have largely been ignored in the composite material literature are the effects of external confinement, temperature, and strain rate. None of the models presented for modulus consider these variables in their formulations. One could argue that materials tested with confinement should display an increase in modulus due to the

restraining effect of the imposed stress. Temperature effects however are anticipated to be small and can easily be accounted for in the values of modulus chosen for the inclusion and matrix. This is especially important for polymeric composites since the modulus of most polymers vary strongly with temperature. Lastly, the effect of strain rate (i.e. crosshead speed) has been found to be important when dealing with viscoelastic matrix materials (i.e. polymers). In these cases, an increase in the composite modulus can be thought of as the normal strain rate behavior of a polymer (Spanoudakis and Young 1984a).

2.4.4 Strength of Particulate Composites

2.4.4.1 Introduction

Among the mechanical properties, the yield stress of composite materials is of primary importance, giving information on the maximum allowable load without considerable plastic deformation. Although a great number of theories have been developed for the prediction of the elastic modulus of particulate composites, a satisfactory treatment of the strength behavior of composites reinforced with rigid fillers has not yet been developed. This is mainly due to the great number of parameters upon which the strength depends. Such parameters include the properties of the constituent materials, the particle volume fraction, interfacial adhesion, and particle geometry (Papanicolaou and Bakos 1992). In a review of the mechanical properties of particulate-filled systems, Nielsen (1967) wrote: "Except in the case of filled rubbers, practically there is no good theory to guide one's thinking on the stress-strain properties of such materials. Empirically, it is known what will often happen, but the reasons for the observed behavior are often not clear". In the last 30 years there have been a number of attempts to correlate the strength of particulate-filled systems with some of the parameters that affect their behavior. However, much of the work has resulted in empirical or semi-empirical expressions, while little progress has been made in the development of theoretically-based or physically rigorous models for strength.

Furthermore, the majority of the work has concentrated on the tensile or fracture behavior of these materials. Few studies have looked at the behavior in compression.

Also, due to the above-mentioned difficulties, a great number of contradictory results may be found in the literature. The following discussion presents an overview of the existing strength models for particulate composite materials. Additional information regarding theories for the prediction of strength of particulate-filled polymeric composites can be found in Ahmed and Jones (1990a) and Liang and Li (1998).

2.4.4.2 Models for Strength in Tension and Compression

The various published experimental and theoretical strength relationships for rigid particulate filled polymeric materials have, in general, taken one of two main approaches in explaining the development of strength.

One approach, as developed by Sahu and Broutman (1972), is to assume that the composite fails in tension when one element is fractured as a result of a stress concentration around the filler particle. It follows from this assumption that the composite strength should decrease rapidly with the first addition of filler and remain essentially at that level with further additions of filler. With this assumption, a finite element analysis was used to model the composite and the results were correlated with experimental data obtained on glass bead filled epoxy and polyester resins. The theoretical predictions did not give a good fit to the experimental data, which was found to essentially be independent of volume fraction, yet highly dependent on the strength of the interfacial bond (Figure 2.44). The relatively poor fit probably resulted from the lack of consideration of particle interactions in the theoretical model. In addition, the composites may not have failed as a result of the failure of the first element (Ahmed and Jones 1990a).

The second approach is to assume that the tensile strength of a particulate-filled composite is determined by the effective decrease in the cross-sectional area of the load bearing matrix due to the presence of the filler (Nielsen 1967, Nicolais and Narkis 1971).

In the case of poor bonding between the matrix and the filler particles (i.e. no stress transfer), and the absence of stress concentrations at the particle-matrix interface, the yield strength of composites in tension depends only on the effective load bearing cross-sectional area fraction $(1-\psi)$ or:

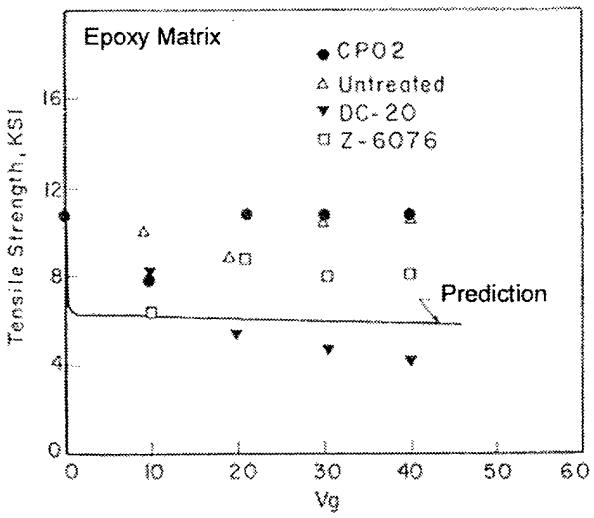

Figure 2.44: Tensile strength of glass bead filled epoxy composites plotted against volume fraction. Note: V_g = volume fraction of filler in percent (glass beads). (Sahu and Broutman 1972)

$$\sigma_{yt} = \sigma_{ym}(1-\psi) \tag{2.82}$$

where σ_{yt} is the tensile yield stress of the composite, σ_{ym} is the yield stress of the matrix. If it is assumed that ψ is a power law function of the volume fraction of filler c, then:

$$\sigma_{yt} = \sigma_{ym}(1-ac^b) \tag{2.83}$$

where a and b are constants depending on the assumed particle shape and plane of fracture.

A number of models have been based on the above expression, the most rigorous being that of Nicolais and Narkis (1971). They considered a unit cube with n^3 spherical particles of radius r uniformly dispersed throughout the matrix. Yielding was assumed to occur in the minimum cross section of the continuous phase which is perpendicular to the applied load, that is, in the cross section where stress is a maximum. The minimum cross section A_p is given by:

$$A_p = 1-\pi(nr)^2 \tag{2.84}$$

and the volume fraction of spheres c is equal to:

$$c = \frac{4}{3}\pi(nr)^3 \tag{2.85}$$

Substitution of $(nr)^2$ from Equation 2.85 in Equation 2.84 gives:

$$A_p = 1 - \pi\left(\frac{3}{4\pi}\right)^{2/3} c^{2/3} = 1 - 1.21c^{2/3} \tag{2.86}$$

and the resulting yield stress of the composite can be expressed as:

$$\sigma_{yt} = \sigma_{ym}(1 - 1.21c^{2/3}) \tag{2.87}$$

In Equation 2.87, $\sigma_{yt}=\sigma_{ym}$ for zero concentration of filler, and c is equal to 0.75 for $\sigma_{yt}=0$, which is the maximum theoretical packing where direct contacts are made between particles. In practice, the maximum packing that can be achieved by normal mixing techniques is about 0.64, while theoretically for hexagonal close-packed systems, the maximum packing is 0.74.

Equation 2.87 gives a lower bound for the tensile strength of a composite material (i.e. no adhesion). An upper bound is immediately obtained by considering that, in the case of perfect adhesion, the strength of the composite simply equals the strength of the polymer itself. This is shown in Figure 2.45.

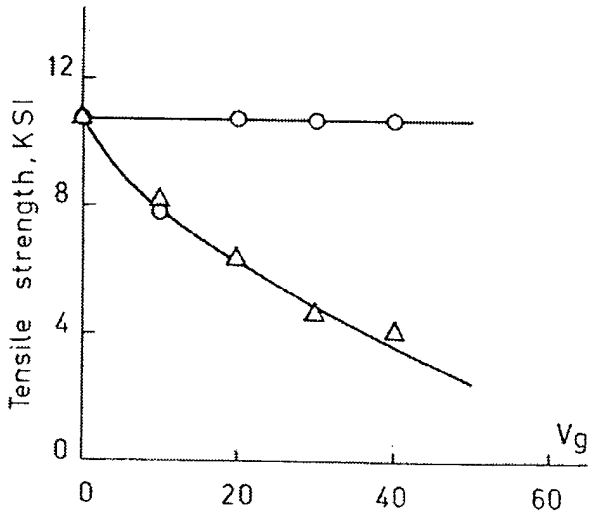

Figure 2.45: Upper and lower bounds as measured and predicted by Nicolais and Narkis (1971). (data from Sahu and Broutman 1972)

It can be seen by comparing Equations 2.82 and 2.87 that the matrix cross section is zero at a particle volume fraction of less than unity. Nicolais and Narkis (1971) justified this by the fact that at a certain filler content where the matrix loses its continuity (at the

maximum packing fraction), the strength of the composite material becomes very low. However, in reality, the cross section of the matrix can only be zero when c=1.

Considering the packing phenomenon of particles, Turcsanyi et al. (1988) chose a simple hyperbolic function to represent (1-ψ):

$$(1-\psi) = \frac{1-c}{1+A\cdot c} \tag{2.88}$$

where A is a constant related to the packing characteristics and shape of particles. For spherical particles the value of A is close to 2.5 for both hexagonal closed-packed and face-centered cubic structures (D'Almeida and Carvalho 1998). If A is taken as 2.5 then Equation 2.82 can be expressed approximately as:

$$\sigma_{yt} = \left(\frac{1-c}{1+A\cdot c}\right)\sigma_{ym} \tag{2.89}$$

where σ_{yt} and σ_{ym} are as defined as before. However, since some results in the literature show that σ_{yt} is an increasing function of c for filled composites with very strong interfacial adhesion, Turcsanyi et al. (1998) introduced a parameter B, which is proportional to the load carried by the dispersed component, and presented the empirical equation:

$$\sigma_{yt} = \left(\frac{1-c}{1+A\cdot c}\right)\sigma_{ym}\exp(B\cdot c) \tag{2.90}$$

The form of this equation, for various values of B, is shown in Figure 2.46.

An alternative representation for the upper bound tensile strength that accounts for reinforcement of the matrix by improved adhesion between the matrix and particles, and the competing loss in strength due to stress concentrations at the interface, was proposed by Bigg (1987):

$$\sigma_{yt} = \sigma_{ym}\left(1 - ac^{b} + mc^{n}\right) \tag{2.91}$$

where m and n are constants related to the interfacial adhesion. This empirical expression represents an extension of the lower bound equation given in Equation 2.87. With four constants it is sufficiently flexible to match a wide range of data, but because it does not have a theoretical basis, it cannot be used to predict the performance of untested compositions.

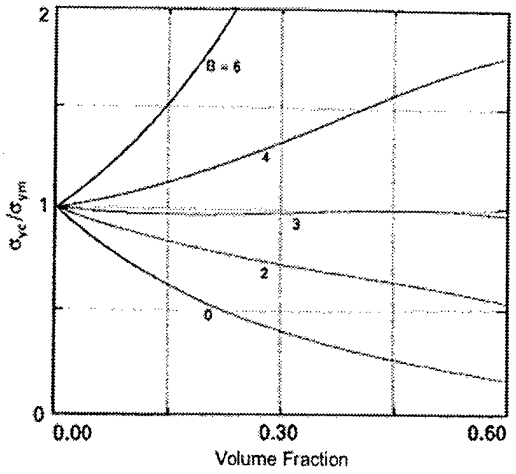

Figure 2.46: Variation of the yield stress ratio as a function of volume fraction for different values of B. Note: σ_{yc} = yield stress of composite in tension. (Turcsanyi et al. 1988)

Jancar et al. (1992) also studied the effects of particle volume fraction and strength of adhesion on the tensile strength of particulate-filled polymeric composites. Through the use of finite element simulations they found that where there is perfect adhesion between constituents, the upper bound for the tensile yield strength above a critical volume of particles is found to be 1.33 times the matrix yield strength. Below the critical volume fraction, the concentration dependence of the yield strength was determined to be proportional to the fraction of the yielded material, f_y:

$$f_y = F(a) \cdot c^2 \tag{2.92}$$

where c is the particle volume fraction and $F(a)$ is proportional to the average yielded area per particle as characterized by the parameter a:

$$F(a) = \left(\frac{9}{\pi}\right) a^4 \left[\frac{\sqrt{1-a^{-2}}}{2a\left(a^{-2}-0.25\right)\cos^{-1}(1/a)} + \left(\frac{1}{16}\right) \sin\left(4\cos^{-1}\left(\frac{1}{a}\right)\right) \right] \tag{2.93}$$

This leads to the following upper bound expression for the yield strength assuming perfect adhesion:

$$\sigma_{yt} = \sigma^*_{ym}\left(1 + 0.33\mathrm{F(a)} \cdot \mathrm{c}^2\right) \tag{2.94}$$

for $1/F(a) \geq c^2$ and

$$\sigma_{yt} = 1.33\sigma^{*}_{ym} \tag{2.95}$$

for $1/F(a) < c^2$ and where σ^{*}_{ym} is the matrix yield strength in the presence of a very small percentage of filler (generally less than the yield strength of the unfilled matrix).

A lower bound was similarly obtained by assuming no adhesion between components. In this case a modified form of the equation developed by Nicolais and Narkis (1971) was found to adequately represent the composite yield strength:

$$\sigma_{yt} = \sigma_{ym}(1 - 1.21c^{2/3}) \cdot S \tag{2.96}$$

where S is a strength reduction or concentration factor which was originally proposed by Nielsen (1966). Through finite element analysis S was determined to vary between 1.0 and 0.2, for low and high particle volume fraction, respectively. Although this method gives results that are in relatively good agreement with experiments, it is usually desirable to have not only a numerical solution, but also an analytical one related to the composite parameters.

Piggott and Leidner (1974) argued that the uniform filler arrangement assumed in most models was unlikely in practice and so proposed the empirical relationship:

$$\sigma_{yt} = A\sigma_{ym} - b \cdot c \tag{2.97}$$

where A is a factor expressing the stress concentration caused by the presence of spheres in the matrix, and b is a constant dependent upon the particle-matrix adhesion. They have shown that Equation 2.97 can give almost identical values to the two-thirds power law expression at volume fractions greater than 0.2.

There have also been a number of attempts to correlate the strength of a particulate-filled system at a constant volume fraction with the diameter of the filler particles. Alter (1965) found that the strength of a composite filled with spherical particles is related to the reciprocal of the diameter of the particle, namely:

$$\sigma_{yt} = \sigma_{ym} + k\frac{1}{d} \tag{2.98}$$

Hajo and Toyoshima (1973) later found that the strength is a linear function of the reciprocal of the square root of the particle diameter:

$$\sigma_{yt} = \sigma_{ym} + k\frac{1}{\sqrt{d}} \tag{2.99}$$

Finally, Landon et al. (1977) proposed that the strength of a particulate-filled composite can be described by the empirical relationship:

$$\sigma_{yt} = \sigma_{ym}(1 - c) - k(c)d \tag{2.100}$$

where in all cases d is the average particle diameter, and k is the slope of the plot of tensile strength against mean particle diameter at the particular volume fraction in question.

Thus, the difficulty in predicting the strength properties of particulate composites can be appreciated after considering these contradictory results reported in the literature.

In contrast to the highly empirical expressions above, Leidner and Woodhams (1974), using a comprehensive theoretical approach, related the strength of a composite containing spherical particles to the volume fraction, diameter, and degree of interfacial adhesion. They applied well-established theories for fiber reinforcement to the case of spheres (beads) in an elastic matrix after making certain modifications for geometry. In this way, the stress distribution in the spheres, and hence the maximum load carried by the particles at the breaking point of the composite, was obtained. In order to calculate the maximum load carried by the matrix, it was assumed that the strength of the matrix itself is affected by the presence of filler. This assumption was justified since the solid inclusions act as stress concentrators (Griffith's cracks).

In the case of non-bonded particles the stress is transferred from the matrix to the bead by frictional forces such that:

$$\tau = p \cdot \alpha \tag{2.101}$$

where τ is the frictional stress transferred to the matrix, p represents residual compressive stresses which act upon the particle-matrix interface and are due to differences in the coefficients of thermal expansion of the matrix and particle, and α is the coefficient of friction. The pressure p is identical to a hydrostatic pressure and therefore does not depend on the direction in which it is measured.

Computation of the average stress in the bead first requires approximating the bead by a series of cylinders and then applying fiber reinforcement theories to solve for the

distribution of load over the system of cylinders. The average stress in the bead can then be shown to be:

$$\sigma_{avg} = 0.83 \cdot p\alpha \tag{2.102}$$

This indicates that the average stress in the bead at the breaking point of the composite is a function of the frictional stress $p\alpha$ only and is independent of the diameter of the sphere.

If it is assumed that the cross-sectional area of the composite filled with randomly spaced spheres is equal to one, then the portion of the cross-sectional area attributed to the beads can be described by the volume fraction c. The maximum stress carried by the beads is then:

$$\sigma_b = \sigma_{avg} c = 0.83 \cdot p\alpha c \tag{2.103}$$

and the stress carried by the matrix at the breaking point of the composite is:

$$\sigma_m = K\sigma_{ym}(1-c) \tag{2.104}$$

where σ_b and σ_m are the stresses carried by the bead and matrix phase, respectively, σ_{ym} is the yield strength of the matrix, and K is the relative change of the strength of the matrix due to the presence of particles and depends on particle size. A modified version of the relationship of Hajo and Toyashima (1973) given in Equation 2.99 was found to satisfactorily describe the relative change of matrix strength in the presence of particles:

$$K = a + b\frac{1}{\sqrt{d}} \tag{2.105}$$

where a and b are constants. Equations 2.103 and 2.104 may then be combined to give an expression for the tensile strength of the composite (σ_{yt}):

$$\sigma_{yt} = \sigma_b + \sigma_m = 0.83p\alpha c + K\sigma_{ym}(1-c) \tag{2.106}$$

According to Equation 2.106, the tensile strength of the composite in the case of no adhesion between the matrix and the particle is a linear function of c, and for a constant volume fraction of filler, is inversely proportional to the square root of the particle diameter.

In the case of well-bonded particles the stress is transferred through adhesion shear stresses at the particle-matrix interface. The maximum stress in the particle is therefore dependent upon the shear strength of the matrix, and on the strength of the particle-matrix

bond. The maximum stress in the bead is reached when the shear stress reaches the shear strength of the matrix, and the tensile stress at the interface attains the particle-matrix bond strength. However, the behavior is governed by the volume fraction of particles, since at low fractions, the additional load placed on the matrix when the particle-matrix bond fails is small and therefore does not lead to catastrophic failure, whereas at higher fractions, the additional load is high and does lead to immediate failure. Only the case of high volume fractions needs to be discussed since the case of low particle volume fractions is similar to the previous case with no adhesion.

It is assumed that the maximum stress transferred to the bead is equal to the strength of the matrix-bead adhesion σ_a. The stress transferred from the matrix to the sphere by shearing can be calculated in a similar manner as in the case of no adhesion except that the shear strength of the matrix τ_m is substituted for the frictional stresses $p\alpha$. The stress carried by the beads at the point of failure of the composite is then given by:

$$\sigma_b = \left(\sigma_a + 0.83\tau_m\right)\cdot c \tag{2.107}$$

Due to stress concentrations, the average tensile stress in the matrix is usually lower than the stress at the particle-matrix interface. If the stress concentration is defined as:

$$S = \frac{\text{average tensile stress in the matrix at breaking point of the composite}}{\text{tensile stress at matrix - filler interface } (=\sigma_a)} \tag{2.108}$$

then the stress in the matrix is:

$$\sigma_m = \sigma_a S(1-c) \tag{2.109}$$

Equation 2.107 and Equation 2.109 give an expression for the ultimate strength of particulate-filled composites exhibiting adhesion:

$$\sigma_{yt} = \left(\sigma_a + 0.83\tau_m\right)\cdot c + \sigma_a S(1-c) \tag{2.110}$$

Thus, in the case of filler matrix adhesion the variation of the tensile strength of the composite is given by two straight lines: for small volume fraction of particles the strength of the composite decreases with increases in the volume fraction of the filler, whereas for high volume fractions, the strength increases with increasing volume fraction of filler.

Another more recent model for the prediction of the tensile strength of particulate-filled polymers has been developed by Papanicolaou and Bakos (1992). The model

follows a similar approach as that of Leidner and Woodhams (1974) by dividing the particle into an infinite number of coaxial cylinders and evaluating the overall stress σ_b carried by the particle (bead). The result is an expression of the form:

$$\sigma_b = B \cdot \sigma_{um} \tag{2.111}$$

where σ_{um} is the ultimate strength of the matrix material, and B is a constant of integration which depends directly on the difference between the particle and matrix modulus so that higher values of B correspond to higher values of the difference in moduli (E_p-E_m). Thus, since σ_b is proportional to B it is recommended to choose combinations of materials characterized by high values of (E_p-E_m).

In order to find the tensile strength of the composite (σ_{yt}) the well-known mixture law is applied and the yield strength:

$$\sigma_{yt} = \sigma_b c + \sigma_{um}(1-c) \tag{2.112}$$

where c is the particle volume fraction. However, in order to account for both the degree of adhesion between particle and matrix as well as the degradation of the matrix properties due to the presence of inclusions, Equation 2.112 has been modified:

$$\sigma_{yt} = \sigma_b K c^n + (1 - K c^n)\sigma_{um} \tag{2.113}$$

where K is a parameter which depends on the effective fraction of the inclusion, i.e. the percentage of particles that are well-bonded and can carry load, and n is a parameter that depends on the degradation of the matrix material due to the presence of inclusions. Combination of Equation 2.111 and 2.113 results in:

$$\sigma_{yt} = \sigma_{um}\left(1 + K c^n (B-1)\right) \tag{2.114}$$

Analytical investigation of Equation 2.114 indicates that since $B<1$ when the modulus of the particles exceeds that of the matrix, the expression decreases exponentially with a rate dependent on B and n. This implies that the tensile strength of the composite may never be greater than the strength of the unfilled matrix. For K=n=1, Equation 2.114 takes the form of Equation 2.112 and expresses the ideal situation where there is both perfect adhesion between the two phases and no degradation of the matrix properties. Similarly, K=0 indicates that all the load applied to the composite is carried by the matrix material.

Therefore when the properties of the particle and matrix are known, the tensile strength of a particulate-filled composite for specific values of the degree of adhesion, as well as of the matrix degradation, can be estimated.

Of course it is of interest to consider not only the effects of volume fraction and particle matrix adhesion on the strength of particulate composites, but to investigate the effects of temperature and strain rate. Although relatively few experimental studies are available, several trends may be discerned in the literature.

One of the earliest studies into the dependence of strain rate on the yielding behavior of particulate-filled composites was that of Ishai and Cohen (1968). Tests on quartz sand filled epoxy resins in compression indicated that the yield stress is a linear function of the logarithm of strain rate with a slope being independent of filler concentration, C_f (Figure 2.47).

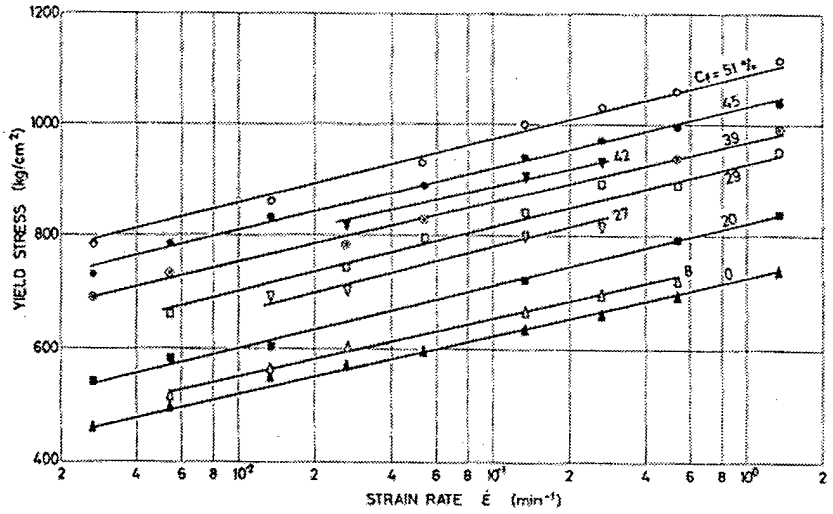

Figure 2.47: Unconfined compressive yield stress versus strain rate for different filler contents. (Ishai and Cohen 1968)

In contrast to the tensile strength results presented previously, Figure 2.47 shows that the compressive yield stress increases with increasing filler concentration. This suggests that the behavior of particulate-filled composites is very dependent of the mode of loading. This is because the tensile strength of relatively brittle materials is largely determined by flaws and sub-microscopic cracks, whereas in compression, these cracks are much less important since the stresses tend to close them rather than open them.

Thus, compression tests tend to be characteristic of the pure matrix material while tension tests are more characteristic of the flaws in the material (Nielsen 1974). For filled specimens, the quartz particles serve only a secondary role in the failure process, reducing the failure strain in tension, and increasing the compressive strength as shown in Figure 2.48 (Ishai and Bodner 1970).

Based on their results, Ishai and Cohen (1968) proposed that the variation in compressive yield stress with strain rate and volume fraction could be described by an equation of the form:

$$\sigma_{yc} = A_0 + A_1 \log \dot{\varepsilon} + A_2 c \tag{2.115}$$

where ε is the applied strain rate and c is the particle volume fraction as before. Figure 2.49 illustrates the model fit.

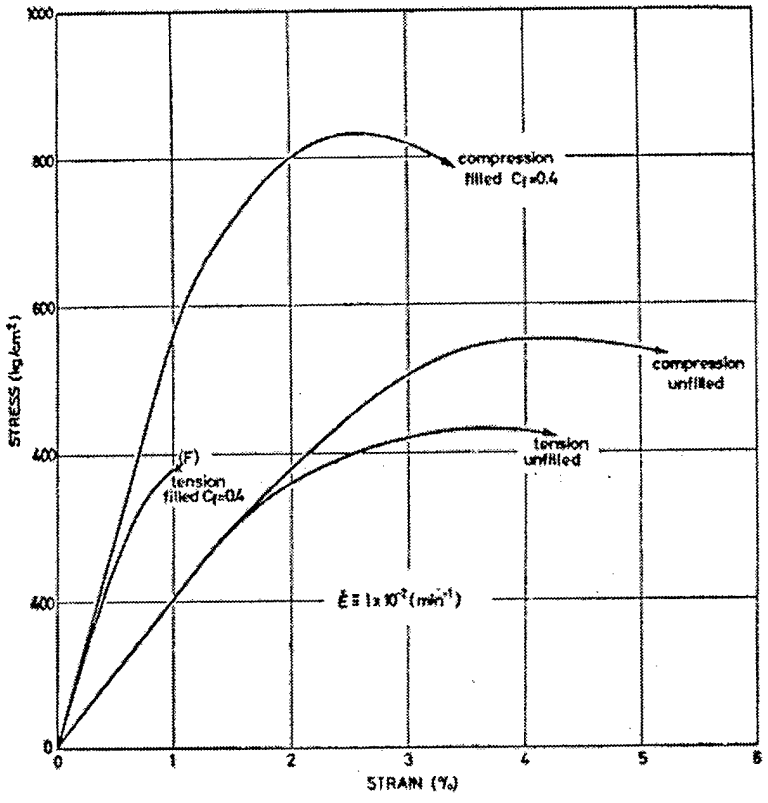

Figure 2.48: Typical stress-strain curves of filled and unfilled epoxy specimens in tension and compression for the same constant strain rate. (Ishai and Bodner 1970)

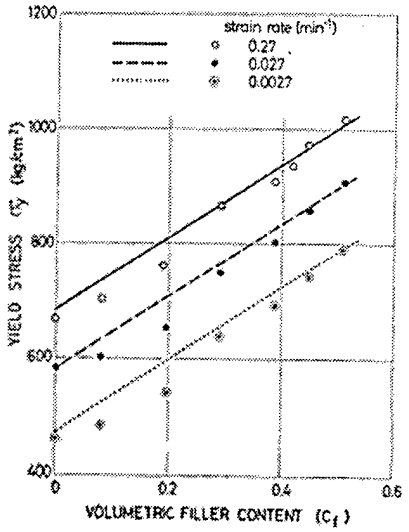

Figure 2.49: Compressive yield stress versus filler content for different strain rate levels illustrating model fit. (Ishai and Cohen 1968)

A similar linear dependence of the tensile yield stress on the logarithm of the strain rate was found by Moehlenpah et al. (1969) in a study of the yield stress of unfilled epoxy resins in both tension and compression at various temperatures. The temperature and strain rate dependence of the yield stress in compression is shown in Figure 2.50. This behavior suggests that the yield stress isotherms can be rather well superimposed by shifting along the log strain rate axis according to the time-temperature superposition principle first proposed by Williams et al. (1955). If this is done then all of the yield stress data can be adequately represented by the equation:

$$\sigma_y = K_1 + K_2 \log\left(\dot{\varepsilon} \cdot a_T\right) \tag{2.116}$$

where σ_y represents either the tensile or compressive yield stress, and a_T is the shift factor which is chosen as unity at the reference temperature T_0 and is generally a function of temperature.

Noting similar behavior for their glass bead filled composites and making use of Equation 2.87, Nicolais and Narkis (1971) proposed the following master curve equation to take account of both temperature and filler effects on the tensile yield stress as a function of strain rate:

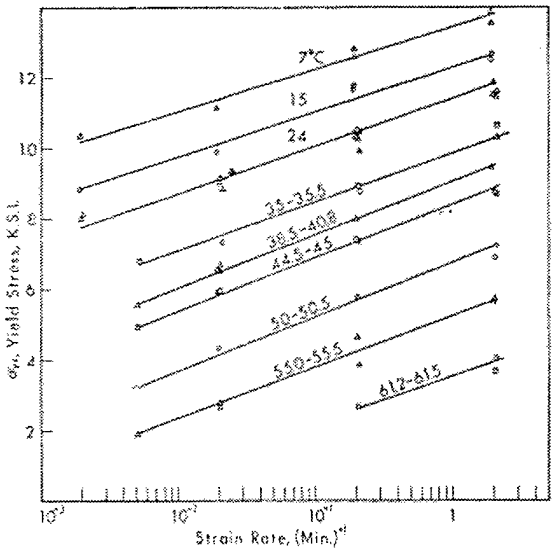

Figure 2.50: Compressive yield stress versus strain rate at various temperatures. (Moehlenpah et al. 1969)

$$\frac{\sigma_{yt}}{\left(1-1.21c^{2/3}\right)} = A + B\ln\left(\dot{\varepsilon}\cdot a_T\right) \tag{2.117}$$

where A and B are numerical constants. Reasonable agreement between prediction and theory was reported for a glass bead filled polymer in the glassy state (Figure 2.51). In effect, a double shift with respect to both temperature and filler content is performed.

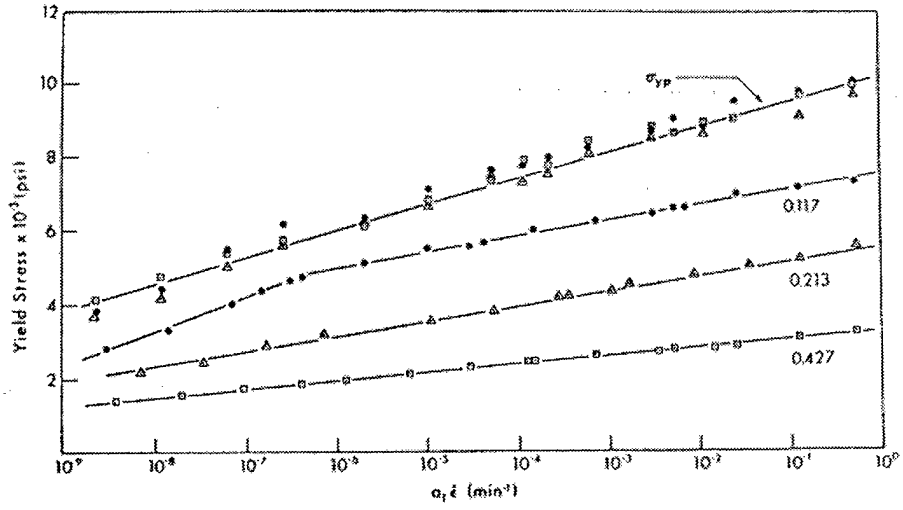

Figure 2.51: Yield stress versus $a_T\dot{\varepsilon}$ for different concentrations of glass beads. T_{ref} = 24°C. (Nicolais and Narkis 1971)

Finally, a review of composite modeling techniques for yielding would not be complete without reviewing the various predictive modeling techniques that exist in the literature. As was previously mentioned, many of the yielding models presented above have little theoretical basis. This limits their usefulness in a predictive sense since their application to poorly characterized systems are simply exercises in curve fitting and hence do not provide a true test of the models accuracy. As a result, a number of predictive models have been developed to predict the mechanical behavior of a composite without resorting to fabricating the composite first. This is particularly useful for the design of high-performance composite materials.

Anderson and Farris (1988) present a model that uses incremental linear elasticity theory and composite modulus calculations to predict the stress-strain and volumetric behavior of particulate-filled composites from constituent properties by relating the damage produced under stress to a quantifiable change in the composite properties such as modulus or effective concentration. This method was shown to satisfactorily predict the mechanical and dilatational behavior of elastic materials filled with spherical glass beads over a large range in strain under conditions of uniaxial tension and hydrostatic pressure.

The approach uses an energy balance to calculate the critical strain at which filler particles will debond when subjected to deformation under an applied stress. All deviations from linear behavior are assumed to be the effect of debonding. Repeated calculations of critical strain values using re-evaluated material properties, accounting for the damage caused by debonding, give highly non-linear stress-strain and dilation curves. Experimentally observed dependencies on particle size, particle volume fraction, adhesion, and particle and matrix properties are correctly predicted under conditions of uniaxial tension. Extensions to other modes of shearing and particle shapes was also shown to be straightforward. Agreement was found to be best for highly-filled materials, although adjustments to parameters that cannot be directly measured (e.g., energy of adhesion) improved the agreement somewhat at lower volume fractions. While a complete discussion of the theory behind the model is beyond the scope of this review, more information can be found in Anderson (1988) and in Anderson-Vratsanos and Farris (1993a, 1993b).

A similar micro-mechanical model for the prediction of the mechanical behavior of particulate-filled composites was advanced by Wong and Ait-Kadi (1997). Their evaluation of the Anderson-Vratsanos and Farris (1993a, 1993b) model indicated that, although it worked well for systems where material nonlinearity was mainly due to particle debonding, the model could not, however, account for the effects of localized straining or stress concentrations on the composite modulus or strength (Wong and Ait-Kadi 1995). Therefore, in systems where matrix nonlinearity dominated, predictions were less satisfactory.

The Anderson-Vratsanos and Farris model was then improved by implementing a modulus prediction routine based on the Mori-Tanaka method (Mori and Tanaka 1973), presented in Section 2.4.2.4, which permits closed-form solutions for multiphase anisotropic composites. By also including work from Ju and Chen (1994), particle interaction effects could be taken into account. This resulted in an improved modulus prediction routine and subsequently, an improved micromechanical model for the prediction of the mechanical behavior of particulate-filled composites.

Comparison of the new model with experimental data showed that modeling debonded particles by vacuoles (a spherical air pocket which surrounds a debonded inclusion) instead of voids, as in the original model, gave more representative results. However, the inability of the model to predict the stress-strain behavior of certain composites containing well-bonded particles suggests that it is still limited by the assumption of linear elastic matrix properties.

Using the concept of topological transformation and mean field theory, Fan and Miodownik (1993a) developed a new approach for calculating the deformation behavior of a two-phase microstructure with any combination of grain size, grain shape, and phase distribution. This method was introduced in Section 2.4.2.4 which discussed effective medium models for the prediction of Young's modulus of two-phase particulate composites.

The method first involves transforming the microstructure into a mechanically equivalent body consisting of three well-defined microstructural elements aligned along a particular direction of interest (Figure 2.43). The resultant three element body is shown to

be mechanically equivalent to the original body along this direction. The concept of contiguity and allied topological parameters is then combined with the continuum transformation theory of Eshelby (1957) to determine the stresses and strains in each of the three microstructural elements, and hence theoretically derive the stress-strain curve for the material. Interactions between particles of the same phase are also considered, as is the effect of volume fraction and phase distribution.

The approach predicts that there are four deformation stages in the total deformation process of two-phase composite materials. Furthermore, it predicts that there should always be a drop in the flow stress after the onset of the plastic deformation in the third microstructural element (EIII), which consists of a separated arrangement of the two individual phases. This drop in stress is thought to reflect the dramatic release of the elastic energy stored in EI after the onset of plastic deformation in EIII. It is also regarded as the start of macroscopic yielding in the composite, thus providing the first potential theoretical explanation for the upper yield stress in frozen sands.

This method was applied in a companion paper (Fan and Miodownik 1993b) to determine the deformation behavior of titanium alloys and dual-phase steels. It was shown that the theoretical predictions for these materials were in very good agreement with experimental results drawn from the literature. Although this method provides a rigorous treatment for the calculation of the overall deformation process in a two-phase composite material, it suffers from being somewhat complicated and involved.

2.4.5 Limitations of Theoretical Models for Strength

The yield failure of rigid particulate-filled polymeric composites has been shown to depend on a number of factors in both tension and compression. Most of the models presented above assume that the main factors affecting the yield strength of composites are the particle volume fraction, interfacial adhesion, and particle size. In general, the tensile strength decreases with increasing volume fraction (e.g., Nicolais and Narkis 1971), although a high interfacial bond strength has been shown to reverse this trend (e.g., Leidner and Woodhams 1974). Similarly, the tensile strength has also been shown to decrease with increasing particle size due to the decreased cross-sectional area of the

matrix available for load bearing (e.g., Landon et al. 1977, Yilmazer and Farris 1983). However, a number of contradictory results regarding the exact form of the dependence have been reported in the literature. Applied strain rate and temperature, although not having receiving as much attention, have also been definitively shown to affect the yield behavior of these materials (e.g., Ishai and Cohen 1968, Ishai and Bodner 1970). The importance of these variables is expected for viscoelastic systems and confirms that yielding is essentially a property of the matrix.

Few studies, however, have investigated the importance of particle modulus on the yielding behavior of particulate composites. Monette and Anderson (1993) conducted a preliminary study using an analytical spring-based model to investigate the effect of particle modulus on strength and found that stiffer particles provide a higher composite strength, especially at higher volume fractions. However, Zhou et al. (1995), investigating the effect of aggregate on the compressive strength on concrete, observed substantially different results. Aggregate particles of steel beads gave rise to lower strengths than similar specimens composed of gravel or glass beads. This may be partly attributable to a reduced bond strength, and partly to the high difference between the modulus of the steel and the mortar matrix. Too stiff an aggregate, while improving the composite Young's modulus, may cause stress concentrations and initiate micro-cracking causing a decrease in strength (Zhou et al. 1995).

In a similar fashion, the shape of the inclusion is expected to play an important role in determining the strength of the system (Ahmed and Jones 1990b). With non-regularly shaped inclusions, weakening of the system can occur as a result of stress concentrations, whereas, with rounded inclusions the effect of stress concentrations is much less severe. While comparisons between round and angular particles have not been detailed in the literature, Ishai and Bodner (1970) did notice that sand filled epoxy specimens in compression tended to turn milky as the maximum stress was approached indicating the cutting of the epoxy matrix by the filler (sand) particles.

The foregoing discussion in conjunction with the previous section alludes to the complexity of the yield behavior of particulate-filled composites. It is therefore not surprising that empirical approaches seem to be the most prevalent for describing the yield

stress of particulate composites. However, as the objective of the preceding review was to assess existing models for the strength of particulate composites in order to gain insights regarding the upper yield behavior of frozen soil, some of their limitations need to be discussed.

Certainly the majority of the models presented thus far have concentrated on the tensile strength of particulate-filled composites. Ishai and Bodner (1970) found that the failure mechanism causing gross yielding in sand filled polymers is essentially a property of the matrix, and that the presence of the sand particles serve only a secondary role in the failure process. Inclusions were found to reduce the failure strain in tension and increase the compressive strength. Such differences in behavior are expected, however, since in compression, rigid inclusions act to share the applied load. Furthermore, since they are usually stronger than the matrix, the yield strength is expected to increase with increasing volume fraction. In tension, however, non-bonded inclusions, which because of their dispersed nature cannot carry any load, serve only to decrease the cross-sectional area. This leads to the reduction in yield strength observed by many of the authors. In the case of well-bonded inclusions, an increase in strength can be expected and can be related to the actual bond strength if known.

Another issue which requires attention is the problem of determining the actual onset of yielding which may be different for different modes of loading. While the situation is relatively straightforward in metals, the basic viscoelastic nature of polymeric materials results in their stress-strain relation always being curved, so that the yield point is somewhat ambiguous (Figure 2.48). In most studies the yield stress is taken as the first point where the tangent of the force-deformation curve becomes zero, which in many cases also defines the peak stress or strength of the material. It is clear, however, that the onset of yielding occurs well before the peak as shown in Figure 2.48. Furthermore, other issues such as machine compliance and lack of on-specimen strain measurement may contribute in preventing the observation of a clear yield point.

Nicolais and Narkis (1971) however, in their comparison of stress-strain curves for a filled and unfilled polymer in tension at various volume fractions, temperatures and strain rates, noticed a sharp break in the stress-strain curves at about 0.35% strain (Figure 2.52).

This "stress at the point of discontinuity, σ_D" was found to be temperature dependent, decreasing with increasing temperature, and practically independent of particle concentration and strain rate (Figure 2.53). The associated strain at the point of discontinuity was also noted to be independent of temperature and particle volume fraction. It is thought to reflect the fact that the inclusions act as stress risers allowing multiple volume elements to reach a critical stress for craze formation. Once the matrix starts to craze, it contributes inhomogenous deformational mechanisms which lead to an increase in the work to break. The behavior of this point is very similar to the upper yield stress observed in frozen sands except for its lack of sensitivity to the applied strain rate. Although little additional characterization of this point is available, it at least suggests that the behavior of particulate-filled polymers in tension are somewhat similar to the behavior of frozen sands in compression and may be analyzed as such.

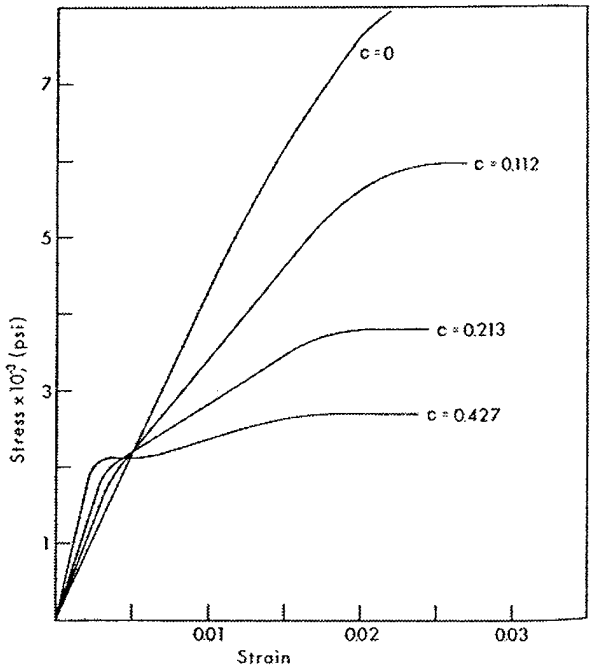

Figure 2.52: Tensile stress-strain curves for different concentrations of glass beads in a SAN matrix. Note: $T_{ref} = 48°C$, $\dot{\varepsilon} = 0.0262$ min^{-1}. (Nicolais and Narkis 1971)

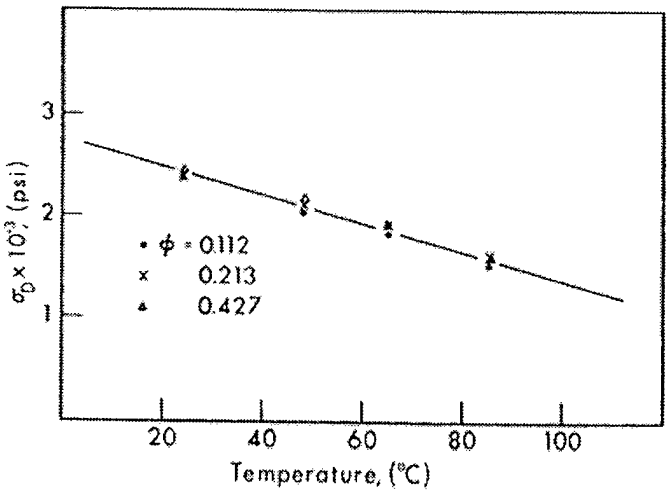

Figure 2.53: Tensile stress at the point of discontinuity (σ_D) versus temperature for different concentrations of glass beads. Note: $\dot{\varepsilon} = 0.0262\ min^{-1}$. (Nicolais and Narkis 1971)

2.5 REFERENCES

1. Ahmed, S. and Jones, F.R. (1990a), "A Review of Particulate Reinforcement Theories for Polymer Composites", *Journal of Materials Science*, v. 25, pp. 4933-4942.

2. Ahmed, S. and Jones, F.R. (1990b), "Effect of Particulate Agglomeration and the Residual Stress State on the Modulus of Filled Resin. Part II: Moduli of Untreated Sand and Glass Bead Filled Composites", *Composites*, v. 21, no. 1, pp. 81-84.

3. Alkire, B.D. and Andersland, O.B. (1973), "The Effect of Confining Pressure on the Mechanical Properties of Sand-Ice Materials", *Journal of Glaciology*, v. 12, no. 66, pp. 469-481.

4. Alter, H. (1965), "Filler Particle Size and Mechanical Properties of Polymers", *Journal of Applied Polymer Science*, v. 9, pp. 1525-1531.

5. Andersen, G.R. (1991), "Physical Mechanisms Controlling the Strength and Deformation Behavior of Frozen Sand", Sc.D Thesis, Department of Civil and Environmental Engineering, MIT, Cambridge, MA, 560 p.

6. Andersen, G.R., Swan, C.W., Ladd, C.C., Germaine, J.T. (1995), "Small-Strain Behavior of Frozen Sand in Triaxial Compression", *Canadian Geotechnical Journal*, v. 32, no. 3, pp. 428-451.

7. Andersland, O.B. and AlNouri, I. (1970), "Time-Dependent Strength Behavior of Frozen Soils", *ASCE Journal of the Soil Mechanics and Foundations Division*, v. 96, no. SM4, pp. 1249-1265.

8. Andersland, O.B. (1989), "General Report on Mechanical Properties of Frozen Soil", *Proc. 5th International Symposium on Ground Freezing*, Nottingham, England, pp. 433-441.

9. Anderson-Vratsanos, L. and Farris, R.J. (1993a), "A Predictive Model for the Mechanical Behavior of Particulate Composites. Part I: Model Derivation", *Polymer Engineering and Science*, v. 33, no. 22, pp. 1458-1465.

10. Anderson-Vratsanos, L. and Farris, R.J. (1993b), "A Predictive Model for the Mechanical Behavior of Particulate Composites. Part II: Comparison of Model Predictions to Literature Data", *Polymer Engineering and Science*, v. 33, no. 22, pp. 1466-1474.

11. Andeson, L. and Farris, R.J. (1988), "A Predictive Model for the Mechanical Behavior of Particulate Composites", *Polymer Engineering and Science*, v. 28, no.8, pp. 522-528.

12. Ashby, M.F. and Hallam, S.D. (1986), "The Failure of Brittle Solids Containing Small Cracks Under Compressive Stress States", *Acta Metallurgica*, v. 34, no. 3, pp. 497-510.

13. Baker, T.H.W. and Konrad, J.M. (1985), "Effect of Sample Preparation on the Strength of Artificially Frozen Sand", *Proc. 4th International Symposium on Ground Freezing*, Sapporo, Japan, pp. 171-176.

14. Baker, T.H.W. and Kurfurst, P.J. (1985), "Acoustic and Mechanical Properties of Frozen Sand", *Proc. 4th International Symposium on Ground Freezing*, Sapporo, Japan, pp. 227-234.

15. Barnes, P., Tabor, D., Walker, F.R.S., Walker, J.C.F. (1971), "The Friction and Creep of Polycrystalline Ice", *Proc. of the Royal Society of London, Series A*, v. 324, pp. 127-155.

16. Been, K., and Jefferies, M.G. (1985), "A State Parameter for Sands", *Geotechnique*, v. 35, no. 2, pp. 99-112.

17. Been, K., Jefferies, M.G., Hachey, J. (1991), "The Critical State of Sands", *Geotechnique*, v. 41, no. 3, pp. 365-381.

18. Bigg, D.M. (1987), "Mechanical Properties of Particulate Filled Polymers", *Polymer Composites*, v. 8, no. 2, pp. 115-122.

19. Bragg, R.A. and Andersland, O.B. (1980), "Strain Rate, Temperature, and Sample Size Effects on Compression and Tensile Properties of Frozen Sand", *Proc. 2nd International Symposium on Ground Freezing*, Trondheim, Norway, pp. 34-47.

20. Brodnyan, J.G. (1959), "The Concentration Dependence of the Newtonian Viscosity of Prolate Ellipsoids", *Transactions of the Society of Rheology*, v. 3, pp. 61-68.

21. Bueche, A.M. (1957), "Filler Reinforcement of Silicone Rubber", *Journal of Polymer Science*, v. 25, pp. 139-149.

22. Castro, G. and Poulos, S.J. (1977), "Factors Affecting Liquefaction and Cyclic Mobility", *ASCE Journal of Geotechnical Engineering*, v. 103, no. GT6, pp. 501-516.

23. Chamberlain, E., Groves, C., Perham, R. (1972), "The Mechanical Behavior of Frozen Earth Materials Under High Pressure Triaxial Test Conditions", *Geotechnique*, v. 22, no. 3, pp. 469-483.

24. Christensen, R.M. (1979), *Mechanics of Composite Materials*, John Wiley and Sons, New York.

25. Christensen, R.M. (1990), "A Critical Evaluation for a Class of Micromechanics Models", *Journal of the Mechanics and Physics of Solids*, v. 38, no. 3, pp. 379-404.

26. Christensen, R.M. and Lo, K.H. (1979), "Solutions for Effective Shear Properties in Three Phase Sphere and Cylinder Models", *Journal of the Mechanics and Physics of Solids*, v. 27, pp. 315-330.

27. Cole, D.M. (1985), "Grain Size and the Compressive Strength of Ice", *Journal of Energy Resources Technology*, v. 107, pp. 369-374.

28. Cole, D.M. (1986), "Effect of Grain Size on the Internal Fracturing of Polycrystalline Ice", CRREL Report No. 86-5.

29. Cole, D.M. (1987), "Strain-Rate and Grain-Size Effects in Ice", *Journal of Glaciology*, v. 33, no. 115, pp. 274-280.

30. Cole, D.M. (1988), "Crack Nucleation in Polycrystalline Ice", *Cold Regions Science and Technology*, v. 15, pp. 79-87.

31. Cole, D.M. (1990), "Reversed Direct-Stress Testing of Ice: Initial Experimental Results and Analysis", *Cold Regions Science and Technology*, v. 18, pp. 303-321.

32. Counto, U.J. (1964), "The Effect of the Elastic Modulus of the Aggregate on the Elastic Modulus, Creep, and Creep Recovery of Concrete", *Magazine of Concrete Research*, v. 16, n0. 48, pp. 129-138.

33. D'Almeida, J.R.M., and De Carvalho, L.H. (1998), "An Investigation on the Tensile Strength of Particulate Filled Polymeric Composites", *Journal of Materials Science*, v. 33, pp. 2215-2219.

34. Dai, L.H., Huang, Z.P., Wang, R. (1999), "Explicit Expressions for Bounds for the Effective Moduli of Multi-Phased Composites by the Generalized Self-Consistent Method", *Composites Science and Technology*, V. 59, pp. 1691-1699.

35. Dickie, R.W. (1973), "Heterogeneous Polymer-Polymer Composites. I: Theory of Viscoelastic Properties and Equivalent Mechanical Models", *Journal of Applied Polymer Science*, v. 17, pp. 45-63.

36. Duval, P. (1978), "Anelastic Behavior of Polycrystalline Ice", *Journal of Glaciology*, v. 21, no. 85, pp. 621-629.

37. Duval,P, Ashby, M.F., Anderman, I. (1983), "Rate Controlling Processes in the Creep of Polycrystalline Ice", *Journal of Physical Chemistry*, v. 87, no. 21, pp. 4066-4074.

38. Einstein, A. (1956), *Investigations on the Theory of Brownian Motion*, Dover Inc., New York. English translation of original work published in German, 1906 and 1911.

39. Eshelby, J.D. (1957), "The Determination of the Elastic Field of an Ellipsoidal Inclusion and Related Problems", *Proc. of The Royal Society of London, Series A*, v. 241, pp. 376-396.

40. Fan, Z. and Miodownik, A.P. (1993a), "The Deformation Behavior of Alloys Comprising Two Ductile Phases. I. Deformation Theory", *Acta Metallugica et Materialia*, v. 41, no. 8, pp. 2403-2413.

41. Fan, Z. and Miodownik, A.P. (1993b), "The Deformation Behavior of Alloys Comprising Two Ductile Phases. II. Application of the Theory", *Acta Metallugica et Materialia*, v. 41, no. 8, pp. 2415-2423.

42. Fan, Z., Tsakiropoulos, T., Miodownik, A.P. (1992), "Prediction of Young's Modulus of Particulate Two-Phase Composites", *Materials Science and Technology*, v. 8, pp. 922-929.

43. Goodman, D.J. (1979), "Critical Stress Intensity Factor Measurements at High Loading Rates for Polycrystalline Ice", *Proc. IUTAM Symposium on the Physics and Mechanics of Ice*, Copenhagen, Denmark, pp. 129-146.

44. Goodman, D.J., Frost, H.J., Ashby, M.F. (1981), "The Plasticity of Polycrystalline Ice", *Philosophical Magazine A*, v. 43, no. 3, pp. 665-695.

45. Goughnour, R.R. and Andersland, O.B. (1968), "Mechanical Properties of a Sand-Ice System", *ASCE Journal of the Soil Mechanics and Foundation Division*, v. 94, no. SM4, pp. 923-950.

46. Guild, F.J., Young, R.J. (1989), "A Predictive Model for Particulate-Filled Composite Materials", *Journal of Material Science*, v. 24, pp. 298-306.

47. Hojo, H. and Toyoshima, W. (1973), "Short and Long-Term Strength Characteristics of Particulate-Filled Cast Epoxy Resin", *Proc. 31st ANTEC, Society of Plastic Engineers*, Montreal, Canada, pp. 163-167.

48. Hallam, S.D. (1986), "The Role of Fracture in Limiting Ice Forces", *Proc. of the IAHR Symposium on Ice*, Iowa City, Iowa, v. 2, pp. 287-319.

49. Hashin, Z. (1962), "The Elastic Moduli of Heterogeneous Materials", *Journal of Applied Mechanics, Transactions of the ASME*, v. 29, pp. 143-150.

50. Hashin, Z. (1964), "Theory of Mechanical Behavior of Heterogeneous Media", *Applied Mechanics Reviews*, v. 17, no. 1, pp. 1-9.

51. Hashin, Z. and Shtrikman, S. (1963), "A Variational Approach to the Theory of the Elastic Behaviour of Mulitphase Materials", *Journal of the Mechanics and Physics of Solids*, v. 11, pp. 127-140.

52. Hawkes, I. and Mellor, M. (1972), Deformation and Fracture of Ice Under Uniaxial Stress, *Journal of Glaciology*, v. 11, no. 61, pp. 103-131.

53. Hirsch, T.J. (1962), "Modulus of Elasticity of Concrete Affected by Elastic Moduli of Cement Paste Matrix and Aggregate", *Journal of the American Concrete Institute*, v. 59, pp. 427-450.

54. Huang, Y., Hwang, K.C., Hu, K.X., Chandra, A. (1995), "A Unified Energy Approach to a Class of Micromechanical Models for Composite Materials", *Acta Mechanica Sinica*, v. 11, pp. 59-75.

55. Ishai, O. (1965), "The Effect of the Elastic Modulus of the Aggregate on the Elastic Modulus, Creep and Creep Recovery of Concrete; Discussion ", *Magazine of Concrete Research*, v. 17, pp. 148-149.

56. Ishai, O. and Bodner, S.R. (1970), "Limits of Linear Viscoelasticity and Yield of a Filled and Unfilled Epoxy Resin", *Transactions of the Society of Rheology*, v. 14, no. 2, pp. 253-273.

57. Ishai, O. and Cohen, L.J. (1967), "Elastic Properties of Filled and Porous Epoxy Composites", *International Journal of Mechanical Sciences*, v. 9, pp. 539-546.

58. Ishai, O. and Cohen, L.J. (1968), "Effect of Fillers and Voids on Compressive Yield of Epoxy Composites", *Journal of Composite Materials*, v. 2, no. 3, pp. 302-315.

59. Jancar, J., Dianselmo, A., DiBenedetto, A.T. (1992), "The Yield Strength of Particulate Reinforced Thermoplastic Composites", *Polymer Engineering and Science*, v. 32, no. 18, pp. 1394-1399.

60. Jellinek, H.H.G. (1962), "Ice Adhesion", *Canadian Journal of Physics*, v. 40, pp. 1294-1309.

61. Jones, S.J., and Parameswaran, V.R. (1983), "Deformation Behavior of Frozen Sand-Ice Materials under Triaxial Compression", *Proc. 4th International Conference on Permafrost*, Fairbanks, Alaska, pp. 560-565.

62. Jones, S.K. (1978), "Triaxial Testing of Polycrystalline Ice", *Proc. 3rd International Conference on Permafrost*, Edmonton, Canada, pp. 670-674.

63. Jones, S.K. (1982), "The Confined Compressive Strength of Polycrystalline Ice", *Journal of Glaciology*, v. 28, no. 98, pp. 171-177.

64. Ju, J.W., Chen, T.M. (1994), "Micromechanics and Effective Moduli of Elastic Composites Containing Randomly Dispersed Ellipsoidal Inhomogeneities", *Acta Mechanica*, v. 103, pp. 103-121.

65. Kaplar, C.W. (1963), "Laboratory Determination of the Dynamic Moduli of Frozen Soils and of Ice", *Proc. Permafrost International Conference*, Lafayette, Indiana, pp. 293-301.

66. Kerner, E.H. (1956), "The Elastic and Thermo-Elastic Properties of Composite Media", *Proceedings of the Physical Society of London, Series B*, v.69, pp. 808-813.

67. Ladanyi, B. (1981), "Mechanical Behavior of Frozen Soils", *Proc. International Symposium on Mechanical Behavior of Structured Media*, Ottawa, Canada, pp. 205-245.

68. Ladanyi, B. and Morel, J.F. (1990), "Effect of Internal Confinement on Compression Strength of Frozen Soil", *Canadian Geotechnical Journal*, v. 27, pp. 8-18.

69. Landon, G., Lewis, G., Boden, G.F. (1977), "The Influence of Particle Size on the Tensile Strength of Particulate-Filled Polymers", *Journal of Materials Science*, v. 12, pp. 1605-1613.

70. Langdon, T.G. (1973), "Creep Mechanisms in Ice", *Physics and Chemistry of Ice*, Royal Society of Canada, Ottawa, pp. 356-361.

71. Leidner, J., Woodhams, R.T. (1974), "The Strength of Polymeric Composites Containing Spherical Fillers", *Journal of Applied Polymer Science*, v. 18, pp. 1639-1654.

72. Lewis, T. and Nielsen, L. (1970), "Dynamic Mechanical Properties of Particulate Filled Composites", *Journal of Applied Polymer Science*, v. 14, pp. 1449-1471.

73. Liang, J.Z. and Li, R.K.Y. (1998), "Prediction of Tensile Strength of Rigid Inorganic Particulate Filled Thermoplastic Composites", *Journal of Materials Processing Technology*, v. 83, pp. 127-130.

74. Lo Presti, D.C.F. (1994), "General Report: Measurement of Shear Deformation of Geomaterials in the Laboratory", *Proc. 1st International Symposium on the Pre-Failure Deformation Characteristics of Geomaterials*, Hokkaido, Japan, v. 1, pp. 1097-1088.

75. Lydon, F.D. and Balendran, R.V. (1986), "Some Observations on Elastic Properties of Plain Concrete", *Cement and Concrete Research*, v. 16, pp. 314-324.

76. McGee, S. and McCullough, R.L. (1981), "Combining Rules for Predicting the Thermoelastic Properties of Particulate Filled Polymers, Polyblends, and Foams", *Polymer Composites*, v. 2, no. 4, pp. 149-161.

77. Mellor, M. (1980), "Mechanical Properties of Polycrystalline Ice", *Proc. IUTAM Symposium on the Physics and Mechanics of Ice*, Copenhagen, Denmark, pp. 217-245.

78. Mellor, M. and Testa, R. (1969), "Effect of Temperature on the Creep of Ice", *Journal of Glaciology*, v. 8, no. 52, pp. 131-145.

79. Michel, B. (1979), *Ice Mechanics*, University of Laval Press, Quebec, Canada.

80. Moehlenpah, A.E., Ishai, O., DiBenedetto, A.T. (1969), "The Effect of Time and Temperature on the Mechanical Behavior of a Plasticized Epoxy Resin Under Different Loading Modes", *Journal of Applied Polymer Science*, v. 13, pp. 1231-1245.

81. Monette, L. and Anderson, M.P. (1993), "Effect of Particle Modulus and Toughness on Strength and Toughness in Brittle Particulate Composites", *Scripta Metallurgica et Materialia*, v. 28, pp. 1095-1100.

82. Mooney, M. (1951), "The Viscosity of a Concentrated Suspension of Spherical Particles", *Journal of Colloid Science*, v. 6, pp. 162-170.

83. Mori, T. and Tanaka, K. (1973), "Average Stress in Matrix and Average Elastic Energy of Materials with Misfitting Inclusions", *Acta Metallurgica*, v. 21, pp. 571-574.

84. Nicolais, L. and Narkis, M. (1971), "Stress-Strain of Styrene-Acrylonitrile/Glass Bead Composites in the Glassy Region", *Polymer Engineering and Science*, v. 11, no. 3, pp. 194-199.

85. Nielsen, L.E. (1966), "Simple Theory of Stress-Strain Properties of Filled Polymers", *Journal of Applied Polymer Science*, v. 10, pp. 97-103.

86. Nielsen, L.E. (1967), "Mechanical Properties of Particulate-Filled Systems", *Journal of Composite Materials*, v. 1, pp. 100-119.

87. Nielsen, L.E. (1974), *Mechanical Properties of Polymers and Composites*, Marcel Dekker, New York.

88. Orth, W. (1985), "Deformation Behavior of Frozen Sand and its Physical Interpretation", *Proc. 4th International Symposium on Ground Freezing*", Sapporo, Japan, pp. 245-253.

89. Papanicolaou, G.C. and Bakos, D. (1992), "The Influence of the Adhesion Bond Between Matrix and Filler on the Tensile Strength of Particulate-Filled Polymers", *Journal of Reinforced Plastics and Composites*, v. 11, pp. 104-126.

90. Parameswaran, V.R. (1980), "Deformation Behavior and Strength of Frozen Sand", *Canadian Geotechnical Journal*, v. 17, pp. 74-78.

91. Parameswaran, V.R. and Jones, S.J. (1981), "Triaxial Testing on Frozen Sand", *Journal of Glaciology*, v. 27, no. 95, pp. 147-155.

92. Parameswaran, V.R. and Roy, M. (1982), "Strength and Deformation of Frozen Sand at -30°C", *Canadian Geotechnical Journal*, v. 19, pp. 104-107.

93. Paul, B. (1960), "Prediction of Elastic Constants of Multiphase Materials", *Transactions of the Metallurgical Society of AIME*, v. 218, no. 1, pp. 36-41.

94. Pedersen, O.B. (1983), "Thermoelasticity and Plasticity of Composites. Part I: Mean Field Theory", *Acta Metallurgica*, v.31, no. 11, pp. 1795-1808.

95. Piggott, M.R. and Leidner, J. (1974), "Misconceptions About Filled Polymers", *Journal of Applied Polymer Science*, v. 18, pp. 1619-1623.

96. Poulos, S.J. (1981), "The Steady State of Deformation", *Journal of Geotechnical Engineering Design*, v. 107, no. 5, pp. 553-562.

97. Poulos, S.J., Castro, G., France, J.W. (1985), "Liquefaction Evaluation Procedure", *ASCE Journal of Geotechnical Engineering*, v. 111, no. 6, pp. 772-792.

98. Ravichandran, K.S. (1994), "Elastic Properties of Two-Phase Composites", *Journal of the American Ceramics Society*, v. 5, pp. 1178-1184.

99. Reuss, A. (1929), "Calculation of Flow Limit in Mixed Crystals", *Z Angew Math. Mech.*, v. 9, pp. 49-58.

100. Rowe, P.W. (1962), "The Stress-Dilatancy Relation for Static Equilibrium of an Assembly of Particles in Contact", *Proc. of the Royal Society of London, Series A*, v. 269, pp. 500-527.

101. Sahu, S. and Broutman, L.J. (1972), "Mechanical Properties of Particulate Composites", *Polymer Engineering and Science*, v. 12, no. 2, pp. 91-100.

102. Sanderson, T.J.O. (1988), *Ice Mechanics: Risks to Offshore Structures*, Graham and Trotman, London.

103. Sayles, F.H. (1973), "Triaxial and Creep Tests on Frozen Ottawa Sand", *Proc. 2nd International Permafrost Conference*, Yakutsk, U.S.S.R, pp. 384-391.

104. Scholey, G.K., Frost, J.D., Lo Presti, D.C.F., Jamiolkowski, M. (1995), "A Review of Instrumentation for Measuring Small Strains During Triaxial Testing of Soil Specimens", *ASTM Geotechnical Testing Journal*, v. 18, no. 2, pp. 137-156.

105. Schulson, E.M., Lim, P.N., Lee, R.W. (1984), "A Brittle to Ductile Transition in Ice Under Tension", *Philosophical Magazine A*, v.49, no. 3, pp. 353-363.

106. Shibata, T., Adachi, T., Yashima, A., Takahashi, T., Yoshioka, I. (1985), " Time-Dependence and Volumetric Change Characteristics of Frozen Sand Under Triaxial Stress Condition", *Proc. 4th International Symposium of Ground Freezing*, Sapporo, Japan, pp. 173-179.

107. Shyam Sunder, S. and Wu, M.S. (1990), "Crack Nucleation due to Elastic Anisotropy in Polycrystalline Ice", *Cold Regions Science and Technology*, v. 18, pp. 29-47.

108. Sinha, N.K. (1982), "Delayed Elastic Strain Criterion for First Cracks in Ice", *Proc. Symposium on the Deformation and Failure of Granular Materials*, Delft, Netherlands, pp. 323-330.

109. Sinha, N.K. (1989), "Elasticity of Natural Types of Polycrystalline Ice", *Cold Regions Science and Technology*, v. 17, pp. 127-135.

110. Spanoudakis, J. and Young, R.J. (1984a), "Crack Propagation in a Glass Particle-Filled Epoxy Resin, Part 1: Effect of Particle Volume Fraction and Size", *Journal of Materials Science*, v. 19, pp. 473-486.

111. Spanoudakis, J. and Young, R.J. (1984b), "Crack Propagation in a Glass Particle-Filled Epoxy Resin, Part 2: Effect of Particle-Matrix Adhesion", *Journal of Materials Science*, v. 19, pp. 487-496.

112. Swan, C., Ladd, C.C., Germaine, J.T., Andersen, G.R. (1995), "Physical Mechanisms Controlling the Strength-Deformation Behavior of Frozen Sand: Part 2", Final Report to the U.S. Army Research Office, Department of Civil and Environmental Engineering, MIT, Cambridge, MA, 254p.

113. Swan, C. (1994), "Physical Mechanisms Controlling the Deformation and Strength Behavior of Unfrozen and Frozen Manchester Fine Sand", Sc.D Thesis, Department of Civil and Environmental Engineering, MIT, Cambridge, MA, 1044 p.

114. Ting, J.M., Martin, R.T., Ladd, C.C. (1983), "Mechanisms of Strength for Frozen Sand", *ASCE Journal of Geotechnical Engineering*, v. 109, no. 10, pp. 1286-1302.

115. Tsytovich, N.A. (1975), *The Mechanics of Frozen Ground*, McGraw-Hill, New York.

116. Turcsanyi, B., Pukanszky, B., Tudos, F. (1988), "Composition Dependence of Tensile Yield Stress in Filled Polymers", *Journal of Materials Science Letters*, v. 7, pp. 160-162.

117. Vinson, T.S. (1978), "Parameter Effects on Dynamic Properties of Frozen Soils", *ASCE Journal of the Geotechnical Engineering Division*, v. 104, no. GT10, pp. 1289-1302.

118. Voigt, W. (1910), *Lehrbuch der Kristallphysik*, Teubner, Leipzig.

119. Weeks, W.F. and Assur, A. (1967), "The Mechanical Properties of Sea Ice", CRREL Report No. 82-1, Hanover, NH.

120. Weeks, W.F. and Mellor, M. (1984), "Mechanical Properties of Ice in the Arctic Seas", *Proc. 2nd Annual MIT Sea Grant College Program Lecture and Seminar Series*, Washington, U.S.A, pp. 235-259.

121. Williams, M.L., Landel, R.F., Ferry, J.D. (1955), "The Temperature Dependence of Relaxation Mechanisms in Amorphous Polymers and Other Glass-Forming Liquids", *Journal of the American Chemical Society*, v. 77, pp. 3701-3707.

122. Willis, J.R. (1977), "Bounds and Self-Consistent Estimates for the Overall Properties of Anisotropic Composites", *Journal of the Mechanics and Physics of Solids*, v. 25, pp. 185-202.

123. Wong, F.C., Ait-Kadi, A. (1995), "Mechanical Behavior of Particulate Composites: Experiments and Micromechanical Predictions", *Journal of Applied Polymer Science*, v. 55, pp. 263-278.

124. Wong, F.C., Ait-Kadi, A. (1997), "On the Prediction of Mechanical Behavior of Particulate Composites Using an Improved Modulus Degradation Model", *Journal of Composite Materials*, v. 31, no. 2, pp. 105-127.

125. Wu, T.T. (1966), "The Effect of Inclusion Shape on the Elastic Moduli of a Two-Phase Material", *International Journal of Solids and Structures*, v. 2, pp.1-8.

126. Yilmazer, U., Farris, R.J. (1983), "Mechanical Behavior and Dilation of Particulate-Filled Thermosets in the Rubbery State", *Journal of Applied Polymer Science*, v. 28, pp. 3369-3386.

127. Youssef, H. (1988), "Volume Change Behavior of Frozen Sands", *ASCE Journal of Cold Regions Engineering*, v. 2, no. 2, pp. 49-64.

128. Zhou, F.P., Lydon, F.D., Barr, B.I.G. (1995), "Effect of Coarse Aggregate on Elastic Modulus and Compressive Strength of High-Performance Concrete", *Cement and Concrete Research*, v. 25, no. 1, pp. 177-186.

129. Zhu, Y. and Carbee, D.L. (1984), "Uniaxial Compressive Strength of Frozen Silt Under Constant Deformation Rates", *Cold Regions Science and Technology*, v. 9, pp. 3-15.

130. Zhu, Y., Jiayi, Z., Zhongyan, S. (1988), "Uniaxial Compressive Strength of Frozen Medium Sand Under Constant Deformation Rates", *Proc. 5th International Conference on Ground Freezing*, Nottingham, England, pp. 225-232.

CHAPTER 3

LABORATORY EQUIPMENT

3.1 INTRODUCTION

Successful investigation of the small strain behavior of frozen sands requires several types of specialized equipment that can withstand the harsh conditions imposed by the testing environment. This chapter describes the triaxial testing equipment and the associated electronics used to perform the experimental program on frozen soils. The current system is an improved version of the automated triaxial apparatus originally developed by Andersen (1991), and later modified by Swan (1994). Substantial innovations have been introduced to induce and observe the micron-level displacements necessary to quantify the small strain behavior of frozen geomaterials. These improvements are also described in this chapter.

The most significant contribution to the prior equipment was the improvement of the system for the on-specimen measurement of small strains which is based on miniature LVDT technology. Successful investigation of the small strain behavior of frozen soils in the triaxial apparatus relies, however, on a number of other components besides the availability of an effective measurement system. Other essential components include internal force measurement, stress path control, precise axial alignment, and a high-resolution data acquisition system (Santagata 1998). A system that can also quickly achieve a constant rate of strain during shear is also highly desirable.

Prior to discussing the characteristics and performance of the newly improved small strain measurement system, a brief overview of the dedicated laboratory used for frozen soil testing known as the Low Temperature Testing Facility is presented in Section 3.2. This is followed in Section 3.3 by a description of the MIT automated, high-pressure low-temperature triaxial apparatus for testing frozen soils. Particular emphasis is placed on the description of the chamber and on the load application system which was modified to improve the investigation of the small strain behavior. Since the level at which axial displacements can be resolved is affected by the precision of the data acquisition system, a

description of the data acquisition system used in the MIT Geotechnical Laboratory is also provided in Section 3.4.

A fairly detailed description of the small strain measuring system is given in Section 3.5 as it represents a major step forward in the measurement of the pre-failure deformation behavior of frozen sands. It represents the culmination of a joint effort between the author and other researchers in the MIT Geotechnical Laboratory, in particular Marika Santagata (Santagata 1998) who investigated the pre-failure behavior of cohesive soils. It involves the use of two miniature LVDT's mounted on a pair of Lucite yokes which clamp onto a standard sized triaxial specimen. Although the system is similar to that of Andersen (1991), who initiated small strain measurements at MIT, a number of innovations have been made to the original system such as a more refined mechanical design and a completely new signal conditioning system. Both are described in detail in Sections 3.5.3 and Section 3.5.4. Signal stability as a function of time, temperature, and pressure is also discussed. Finally, the performance of the system is presented based on proof tests conducted on aluminum and PMMA (polymethylmethacrylate), and on resedimented Boston blue clay and frozen Manchester fine sand.

3.2 LOW TEMPERATURE TESTING FACILITY

The Low Temperature Testing Facility consists of three separate rooms, each with independent temperature control. Constructed in 1988 originally for ice mechanics research, it has since been continuously used for the study of frozen soils. A plan view of the facility is shown in Figure 3.1. The vestibule serves as a buffer between the outside laboratory and the two other inner rooms. Its temperature is held constant at approximately -10°C. It contains the equipment used for the preparation of granular ice and for the trimming of ice and soil specimens. The growth room, located at the rear of the vestibule is somewhat smaller and is maintained at 0°C. It is mainly used for the preparation (i.e. de-airing, saturation, and freezing) of frozen soil specimens . The testing room, the largest room in the Low Temperature Testing Facility, contains the high-pressure triaxial apparatus and load frame inside an environmental enclosure. While this room has been designed to achieve temperatures down to -40°C, most testing for this

particular research program was conducted at much higher temperatures. The temperature inside the testing room fluctuates by ±1.5°C around the control point with a period of 400 to 600 seconds (Andersen 1991). Normally the temperature of the room is kept 5°C colder than the desired test temperature since the environmental enclosure is internally thermo-regulated and can provide only heat. This system works very well at dampening the temperature fluctuations in the room which result from the intermittent cooling and defrosting nature of the refrigeration units. More detail regarding the temperature variations within the testing room can be found in Andersen (1991).

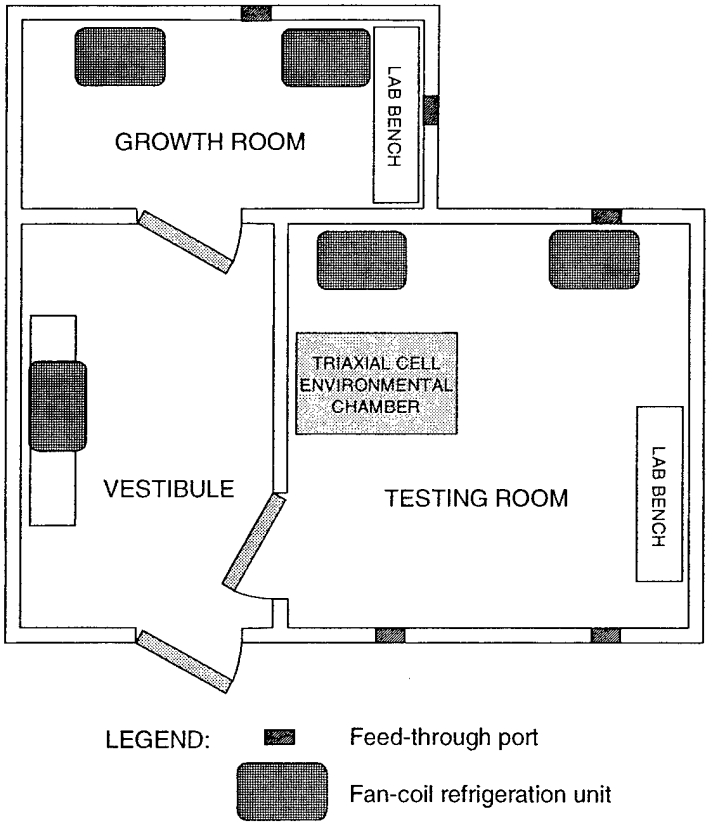

Figure 3.1: MIT Low Temperature Testing Facility (plan view).

3.3 SPECIMEN TESTING APPARATUS

3.3.1 Introduction

Two devices were employed in this study to investigate the properties of frozen soil and ice. The first device is the MIT automated, high-pressure low-temperature triaxial apparatus. This device was designed and built at MIT and represents the culmination of

many years of continuous improvement. It is dedicated to the strength testing of frozen soil and ice specimens under monotonic conditions. It is described in detail in the following section. The second device, designed and built specifically for this study, was used to gain insight into the mechanisms controlling ice adhesion. A complete description of the apparatus along with the results of the ice adhesion testing program is located in Appendix A since the results were not used directly in the analysis of the pre-failure behavior of frozen systems.

3.3.2 MIT Automated High-Pressure Low-Temperature Triaxial Cell

Over the past 10 years, a large effort has been invested by the MIT Geotechnical Laboratory into automating the strength testing equipment. The process of automating existing equipment, termed *adaptable automation* by Sheahan and Germaine (1992), involves the modification of system components, as well as the addition of innovative new components to increase flexibility and quality control. Automation also offers the added benefit of a dramatic reduction in labor. The first application of this concept, which resulted in the development of the MIT automated stress path triaxial cells, is described in detail by Sheahan (1991). The automation of other laboratory shear testing devices followed, in particular the high-pressure triaxial system used for testing frozen sands.

Figure 3.2 shows a schematic of the computer controlled triaxial testing apparatus used for testing frozen and unfrozen sands. The system combines existing MIT equipment (e.g., load frame and high-pressure triaxial cell) with some innovative components (e.g., analog-to-digital converter, electronic motor control system). The apparatus includes six basic components: 1) the triaxial chamber, 2) the system for load application consisting of the loading frame and actuators (pressure-volume controllers), 3) drive motors and control subsystem, 4) instrumentation package, 5) PC-based control system, and 6) the central data acquisition system (not shown).

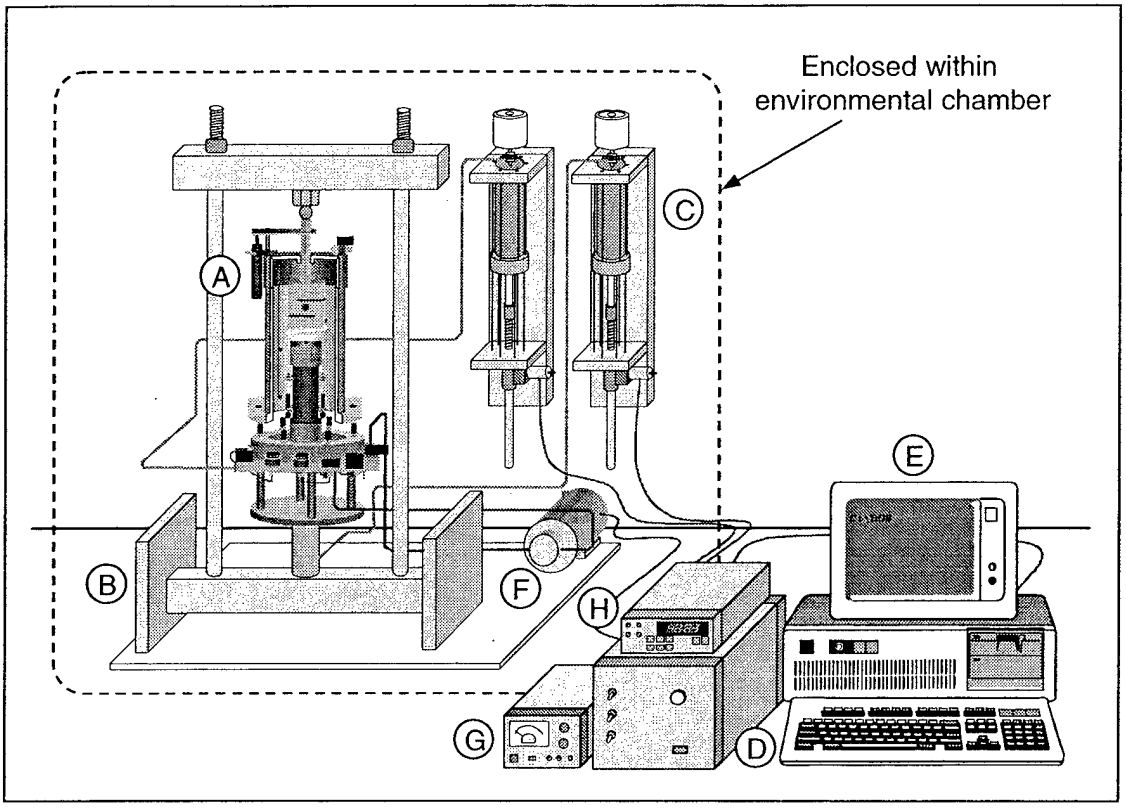

A: Triaxial cell
B: Load frame
C: Actuators (PVC's)
D: Motor control box
E: Personal Computer
F: Cell fluid pump
G: Power supply
H: Voltmeter

Figure 3.2: MIT automated high-pressure low-temperature triaxial system (connections between transducers and PC and remote data acquisition system not shown).

The high-pressure low-temperature triaxial testing apparatus (Figure 3.3) was originally built for previous frozen soil research at MIT (Andersen 1991) and subsequently modified by Swan (1994). The system, which is designed to operate at confining pressures up to 20 MPa, has a steel triaxial chamber which mates to the triaxial base containing the cell and pore fluid valving along with an enlarged base pedestal to accommodate at least 15% radial deformation of the specimen during shear. Stainless steel tubing and ball valves are employed to minimize compliance and limit pressure loss in the loading system. Pressures are measured using diaphragm-type bonded semiconductor strain gage pressure transducers (Data Instruments Inc., Model AB/HP2000, Acton, MA).

Since this system is dedicated to testing frozen soil specimens, it utilizes a floating top cap that is also oversized.

The axial load is applied to the specimen via a 2.54 cm diameter hardened steel piston to which a 45 kN (10,000 lb) shear-beam load cell (Data Instruments Inc., Model JP-10000, Acton, MA) is attached. The piston enters the top of the triaxial chamber through a double O-ring seal. Piston movement is continuously monitored by an externally mounted LVDT (Trans-Tek Inc., Series 240, Ellington, CT). The bottom of the load cell mates with the top cap on the specimen via an alignment device. All transducers are energized by a DC-regulated power supply. A summary of the calibration factors for each of the devices employed is given in Table 3.1.

Transducer	Model Number	Calibration Temperature	Calibration Factor
External axial LVDT	H-5 244-0000	-10°C	3.59333 cm/V/V
Cell pressure	AB/HP 5000	+20°C	1743.40 MPa/V/V
Load cell	JP-10000	+20°C	127943 kg/V/V
Volume change LVDT	0246-0000	-10°C	-39.6821 cm^3/V/V
Axial actuator LVDT	J-8 245-005	-10°C	8.15613 cm/V/V
Small strain LVDT1	#9354	-10°C	0.02533 cm/V
Small strain LVDT2	#9352	-10°C	0.02473 cm/V

Table 3.1: Summary of calibration details for devices used.

Two thermistors are located on the inside wall of the triaxial chamber to measure the temperature of the cell fluid (Dow-Corning Inc., #200-20 cs silicone oil) at the top and bottom of the specimen. The thermistors were calibrated using a portable Lauda refrigerating circulator (Brinkman Instruments Inc., Model RC-6, Westbury, NY). This particular silicone oil exhibits extremely low viscosity under a wide temperature range, and does not degrade the latex membranes used to seal the specimen during testing. This oil was initially selected to limit leakage over the course of a test, but also offers the added benefit of being nonconductive which is essential when locating electronic devices such as the load cell and the on-specimen strain measurement system within the triaxial chamber. A fluid circulation system utilizing a small stainless steel external magnetically-driven high-pressure pump (Micropump Inc., Model 219-56C, Vancouver, WA) helps to reduce the temperature gradient over the specimen to less than 0.1°C. This gradient is thought to be

caused by the heat released from the internal instrumentation (e.g. LVDTs, load cell). Information regarding the improvements made to the temperature control system is given in Section 3.3.3.3

In order to impose a triaxial state of stress to the specimen, the triaxial apparatus is linked to two MIT-designed actuators (pressure-volume controllers). These actuators consist of a DC analog motor driven ball-screw jack that converts the rotary motion of the motor into the linear motion of a piston that displaces fluid from a reservoir. In this configuration the actuator is capable of controlling either fluid pressure or volume.

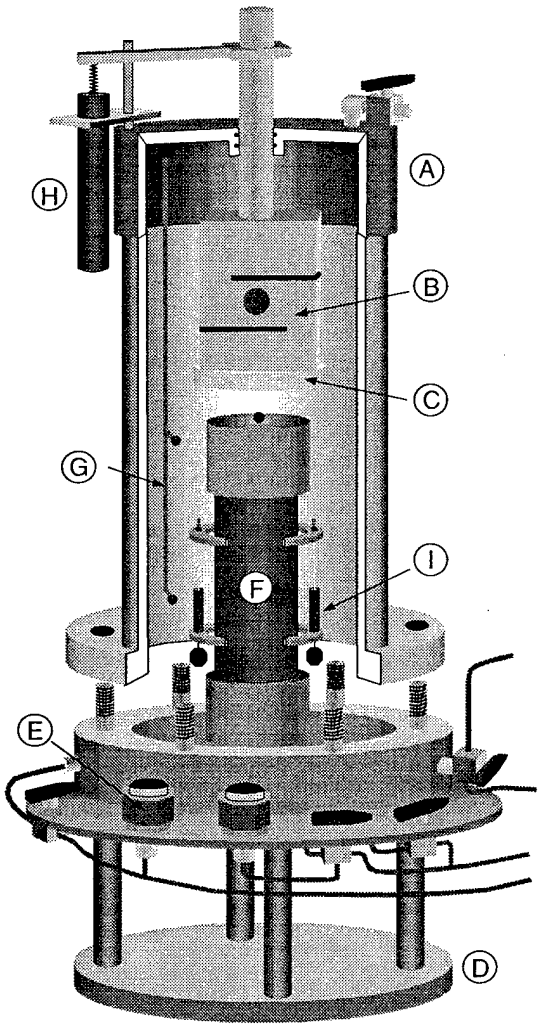

A: Triaxial chamber
B: Load cell
C: Alignment device
D: Triaxial base
E: Pressure sensor
F: Soil specimen
G: Thermistors
H: External LVDT
I: Internal LVDT's

Figure 3.3: High-pressure low-temperature triaxial chamber.

One actuator is directly linked to the triaxial chamber and pressurizes the cell fluid, thus applying a confining pressure to the soil specimen. The volume change of frozen specimens is computed from LVDT's monitoring the motion of this actuator and the triaxial cell loading piston. It is computed from these two direct measures using various corrections which account for leakage and compressibility of the cell fluid, and flexure of the triaxial cell base. This method of measurement results in a maximum volumetric strain error of ±0.2% (Swan 1994).

The other actuator is used to apply a vertical axial force to the specimen. It is directly attached to a 89 kN (10 ton) hydraulic ram (Templeton, Kenly & Co. Inc., Model HSR 102T, Broadview, IL) that converts fluid pressure to axial force, and thus moves the entire triaxial apparatus up against the load frame. In both actuators the same low viscosity silicone oil is used as the hydraulic fluid. In the case of unfrozen sand testing, a third actuator is added to control the pore (back) pressure within the test specimen. The actuators are used in conjunction with electronic control units that regulate the voltage provided to each DC motor. These motor control units determine the speed and direction of the piston movement and thus control the rate and direction of fluid movement. Improvements made to the loading system to achieve and maintain a constant rate of strain during shear are described in Section 3.3.3.4.

Automated control is carried out using a PC and a control program written is QBASIC. The control program is task specific and able to perform all phases of a standard triaxial test including initial pressure up, back-pressure saturation, stress path or K_0 consolidation, and (un)drained shear in compression or extension.

One of the main features of the triaxial testing system is the PC-based closed loop electro-hydraulic feedback control system shown in Figure 3.2. This system allows for the simultaneous control of the cell pressure, back pressure (not required for frozen tests), and axial force based on feedback signals from transducers which measure these quantities. The analog signals (continuous yet variable voltages) produced by the various sensors are fed into a PC fitted with a MIT-designed 22-bit analog-to-digital conversion card (ADC) which converts these voltages into discrete voltage levels that the computer can interpret. Triaxial testing control software written in QBASIC compares these voltages with user-

input target values which depend on the stage of the test. Digital signals (voltages) are computed and then sent out to the motor control units via a 12-bit digital-to-analog conversion card (DAC) also fitted within the PC (Strawberry Tree Computers, Model ACAO-12, Sunnyvale, CA). These voltages are interpreted by the motor controllers and then sent to the motors whereby they cause a perturbation in the system, either a change in pressure or force. The execution of these steps in a loop constitutes a feedback control system.

As mentioned previously, the complete testing system, aside from the computer and motor control unit, operates inside an environmental enclosure within the main testing room of the Low Temperature Testing Facility in order to help maintain the specimen and hydraulic fluids at a constant temperature.

3.3.3 Equipment Modifications

3.3.3.1 Introduction

A number of improvements have been made to the high-pressure low-temperature triaxial system for testing frozen soils over the course of this research in order to improve the measurement of small strain behavior. Some of these modifications resulted from recommendations given in Swan (1994) and most were made before the commencement of the experimental program. The modifications can be divided into three main categories: load application, temperature control, and strain rate control. These are discussed in detail in the following sections. Improvements made to the small strain measurement system are discussed separately in Section 3.5.

3.3.3.2 Load Application

Proof tests conducted on various materials (e.g., aluminum, PMMA, soil) indicated that minor eccentricities in load application led to significant differences in the strains measured by the LVDT's on opposite sides of the specimen thus limiting the reproducibility of small strain measurements. In fact, the development of the higher resolution small-strain measurement system showed that the difficulty in applying the load to the specimen in both a uniform and concentric fashion was the major limitation in

obtaining reliable measurements of the initial stiffness of frozen Manchester fine sand. Similar problems were noticed by Cuccovillo and Coop (1997b) in measuring the small strain behavior of structured sands in the triaxial cell. Perfect alignment of the loading axis with the center of the specimen and parallelism between the top cap surface and the specimen base are essential for minimizing non-uniform straining.

This problem of eccentric loading resulted mainly from the double O-ring seal surrounding the loading piston as it was a source of considerable amount of lateral play. Replacing this seal (bearing) with a high-pressure rolling diaphragm, combined with a linear ball bearing, would have necessitated extensive redesign of the triaxial chamber. It was therefore decided to incorporate a double moment break in the loading assembly: one between the top cap and the alignment device, and the other between the top of the loading piston and the upper crossbar on the load frame. The lower moment break is shown schematically in Figure 3.4. Both breaks consist of a hardened steel ball in a ball seat bearing against a flat hardened ceramic surface. This de-coupled any eccentricity caused by the O-ring seal and hence ensured repeatable concentric loading of the specimen in compression. Finally, the load frame uprights were pre-tensioned to increase stability as well as to reduce the amount of flexure upon loading, and the entire load frame was maintained completely vertical with the aid of a high-precision level. These small yet important modifications had a significant effect in reducing the amount of non-uniform straining that occurred during testing.

3.3.3.3 Temperature Control and Measurement

One of the main testing variables which was investigated in this and in the previous experimental programs was specimen temperature. Consistent temperature control was achieved by enclosing the triaxial testing system within an environmental enclosure inside the main testing room which was set a few degrees colder than the desired test temperature. This enclosure is regulated using a mercury contact switch (Princo Instruments Inc., Model T151, Southampton, PA) which controls two heat sources (i.e. light bulbs) and fans for circulation inside the enclosure. The air temperature surrounding the triaxial cell fluctuated by $\pm 0.17°C$ about the control point as set by the mercury

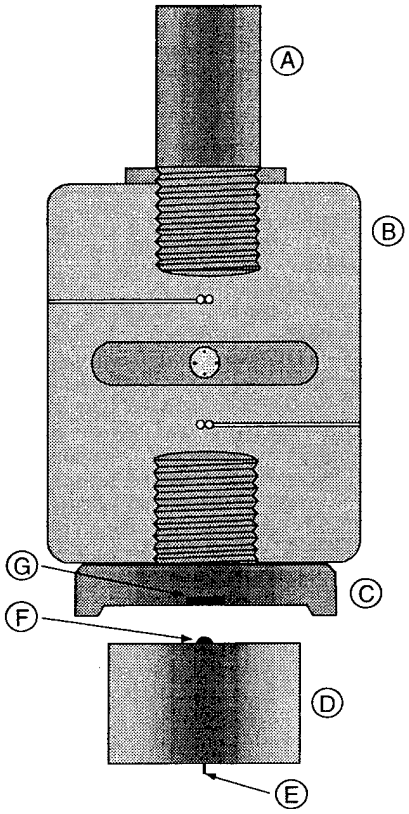

A: Loading piston B: Load Cell C: Alignment device
D: Specimen top cap E: Alignment pin F: Steel ball
G: Ceramic insert

Figure 3.4: Triaxial chamber loading assembly.

contact switch. Inside the triaxial cell the temperature of the oil was measured near the top and bottom of the specimen using two thermistors. Due to the presence of electronic devices within the triaxial cell a slight temperature gradient existed in the oil, with the oil near the top being warmer than the bottom. Table 3.2 summarizes the measured oil temperature (average of oil temperatures at the top and bottom of the specimen), as well as the temperature gradient for the temperatures investigated in the previous programs.

One of the main experimental objectives of this program was to reduce this temperature gradient since it might affect the results of tests at higher temperatures such as those important in permafrost research. In order to reduce this gradient, a small magnetically-driven high-pressure pump (Micropump Inc., Model 219-56C, Vancouver, WA) was used to circulate the confining fluid within the triaxial chamber. It withdraws

Nominal Temperature (°C)	Mean±S.D. (°C)	∇T (°C) (warmer near top)
-10	-9.55±0.05	0.35±0.05
-15	-15.60±0.10	0.40±0.10
-20	-20.25±0.20	0.55±0.20
-25	-25.35±0.20	0.30±0.15

Table 3.2: Summary of measured testing temperatures from previous experimental programs on frozen Manchester fine sand. (Andersen et al. 1995)

silicone oil at the bottom of the triaxial cell and injects it near the top of the triaxial chamber. The pump's housing, as well as all its internal components, are fabricated from 316 stainless steel and its unique design allows it to operate over a large range in temperature (-45°C to 120°C) and pressure (0 to 10 MPa) making it ideal for this application. Table 3.3 show the improvement in temperature control resulting from confining fluid circulation.

Nominal Temperature (°C)	Mean±S.D. (°C)	∇T (°C) (warmer near top)
-2	-2.21±0.16	0.03±0.05
-5	-4.97±0.35	0.04±0.09
-10	-9.34±0.52	0.00±0.14

Table 3.3: Improvement in temperature control in current testing program.

3.3.3.4 Strain Rate Control

Another important aspect of this work was developing a testing system that could apply a constant strain rate during shear. For the results reported by Andersen et al. (1995), the strain rate did not reach a constant value until approximately 0.5-1.0% axial strain. This is illustrated by tests 72 and 86 in Figure 3.5. This strain rate lag can be attributed to the use of the external LVDT for axial strain measurement, to the extensive compliance in the loading frame and triaxial cell base, and from using lubricated end platens.

The new system uses on-specimen axial deformation as the feedback source for a digital closed-loop PID (proportional-integral-derivative) control algorithm, and also

incorporates other modifications such as stiffer hydraulic lines and high-pressure valves to minimize the compliance in the system.

The objective of a PID control system is to maintain the controlled variable, in this case strain rate, equal to the target value specified by the user at all times regardless of changes in the environment. This requires the system to essentially respond to changes before an error occurs. However, this is impossible in the case of a feedback system since the controller requires a finite amount of error in order to produce changes in the manipulated variable. Thus control systems differ by the way they utilize an error signal to generate a control action. Proportional control generates a control action that is proportional to the difference between the reference value and the target value. Integral control changes the controller output by an amount related to the integral of the error signal. Derivative control bases the control response on the rate of change of the error signal. Combining these three forms of feedback control results in a PID control algorithm that can be implemented in the triaxial testing control program. This combination reduces the steady state error to zero and often yields satisfactory dynamic response. Additional information on this topic can be found in Perdikaris (1991).

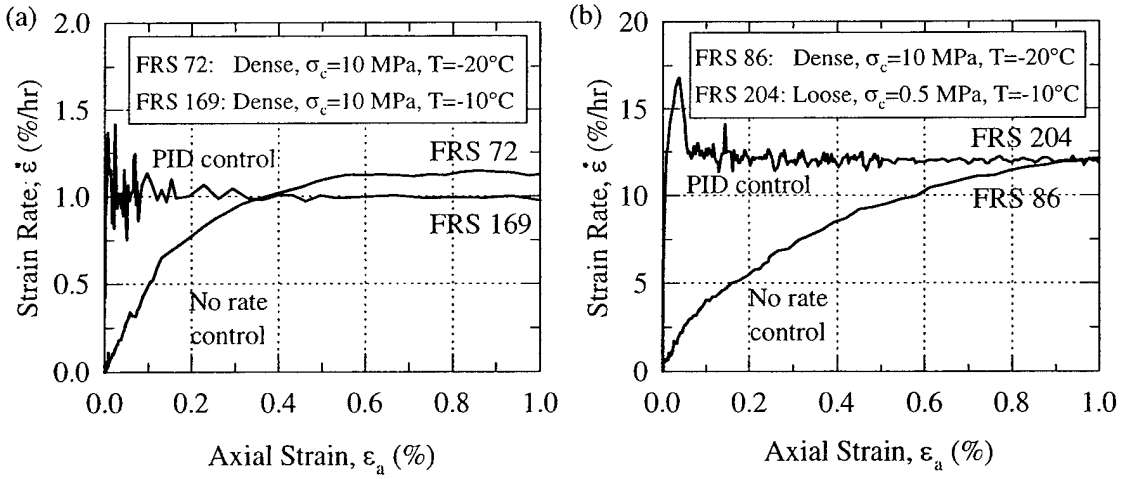

Figure 3.5: Improvement in strain rate as a result of PID algorithm and system modifications: (a) slow strain rate ($\dot{\varepsilon} = 3x10^{-6}$ s^{-1}), (b) moderate strain rate ($\dot{\varepsilon} = 3.5x10^{-5}$ s^{-1}).

Implementation of a PID control algorithm for strain rate allows the axial actuator to apply the desired constant deformation rate virtually from the start of the test for slow ($3x10^{-6}$ s^{-1}) and moderate ($3.5x10^{-5}$ s^{-1}) rates of strain, as shown in Figure 3.5 for tests 169 and 204.

3.4 DATA ACQUISITION SYSTEM

3.4.1 AD1170 Data Acquisition Card

The high-pressure triaxial apparatus described above include two data acquisition systems; a local one at the personal computer used for control purposes, and a central system used to collect all the data in the MIT Geotechnical Laboratory for subsequent analysis. The local data acquisition system makes use of a high quality MIT-designed (Sheahan 1991) analog-to-digital conversion (ADC) card which is built around Analog Devices model AD1170 high resolution, programmable integrating converter (Analog Devices Inc. 1994). The AD1170 offers independently programmable integration time (from 1 ms to 350 ms) and allows the user to specify any resolution from 7 to 22 bits. Usable resolution is typically limited to 18 bits due to measurement and calibration noise error. This translates into a maximum resolution of 0.0024 mV which provides ample sensitivity for closed-loop digital calculations. The high degree of signal averaging provided by the AD1170 helps eliminate anomalies in the signal due to noise and thus provides a more reliable and repeatable representation of the quantity to be measured.

3.4.2 Central Data Acquisition System

The central system is based on a 486 microprocessor PC driven by Windows NT software interfaced with an expanded channel Hewlett Packard HP3497A data acquisition unit which uses a very low noise integrating analog-to-digital converter. This system has a 5½ digit integrating analog-to-digital converter with auto-ranging amplification to four voltage scales (0.1, 1, 10, 100 V). This translates into an effective resolution, for example, of 0.001 mV on the 0.1 V range. Currently the system is configured to monitor 140 channels simultaneously while providing analog-to-digital conversion and data storage at rates up to 1 Hz. This high-quality low-noise system also makes its possible to directly

measure the output from the load cell, pressure transducers, and LVDT's without any signal amplification. The sensitivity of this system has been instrumental in observing levels of strain down to 10^{-6} since small displacements during shear correspond to extremely small changes in the output of both the LVDT's and load cell. The resolutions and the stability of transducers signals as measured by the central data acquisition system are summarized in Table 3.4.

Device	Range	Resolution	Stability
Axial Strain LVDT	5 cm (70%)	±0.001% (0.1 mV)	±0.01% (1 mV)
Volumetric Strain LVDT	45 cm^3 (65%)	±0.001% (0.1 mV)	±0.01% (1 mV)
Cell Pressure Transducer	35 MPa	0.0003 MPa (0.001 mV)	0.003 MPa (.01 mV)
Load Cell	4545 kg	25 g (0.001 mV)	250 g (0.01 mV)

Table 3.4: Transducer characteristics as measured by the central data acquisition system. Note: calculations based on dimensions of an average frozen triaxial specimen (H = 7.2 cm, D = 3.5 cm). (adapted from Sheahan 1991)

3.5 SMALL STRAIN MEASUREMENT SYSTEM

3.5.1 Introduction

Since the early 1980's when the first techniques for on-specimen strain measurement in the triaxial apparatus were employed (e.g., Brown et al. 1980, Burland and Symes 1982, Costa-Filho 1985, etc.), it has been recognized that the low stiffness values often measured in the laboratory, traditionally attributed to the effects of sample disturbance, were for the most part caused by bedding errors at the end platens. The development of new technologies which allows precise measurements of local strains in laboratory tests has since produced measures of stiffness much closer to the values measured in-situ and back-calculated from the field, and has assisted in closing the gap between the dynamic and static measurements of the initial modulus.

A number of devices have been developed over the past two decades for the measurement of the small strain behavior of soils in a triaxial state of stress. They include electrolevel displacement gages (e.g., Jardine et al. 1984), Hall effect semiconductors

(e.g., Clayton and Khatrush 1987), miniature LVDT's (e.g., Brown et al. 1980, CostaFilho 1985, Andersen et al. 1995, Cuccovillo and Coop 1997b), proximity sensors (e.g., Hird and Yung 1989, Lo Presti et al. 1994), and local deformation transducers (e.g., Goto et al. 1991). In many cases these technologies have allowed reliable measurement of axial strains as small as 10^{-5} . Scholey et al. (1995) presents a review of these methods and summarizes their capabilities and limitations.

The technology used for the measurement of the small strain behavior in the MIT Geotechnical Laboratory was first developed for the study of the behavior of frozen sand in triaxial compression (Andersen 1991). It was subsequently adapted, with minor modifications, to investigate the stress-strain properties of unfrozen and frozen sands (Swan 1994). The technology involves the use of two miniature submersible LVDT's mounted on a pair of yokes which clamp onto the soil specimen. The new measurement system, discussed in the following sections, is based on their original design although includes many new innovations. These include a refined mechanical design as well as a completely new MIT-designed signal conditioning system, which provides exceptional stability and noise reduction under a wide variety of stress and temperature conditions. Finally, a discussion of the performance of the system based on proof tests on various materials is given.

3.5.2 Design Requirements

The system for measurement of the small strains was designed to meet several requirements. The basic criterion was to develop a system that could be implemented without major modifications to the existing triaxial equipment and be capable of measuring strains as small as $5x10^{-6}$ or better. In general, the system had to possess the following properties:

- high resolution to measure strain as small as $5x10^{-6}$ or better
- operation over large range of strain
- DC output for compatibility with existing data acquisition system
- temperature and pressure insensitivity
- no influence on specimen loading as a result of displacement measurement

- compact design to facilitate mounting within the triaxial cell
- no interference with the pressure seals on the test specimen
- relative insensitivity to chamber pressure over the range of 0 to 10 MPa
- relative insensitivity to temperature over the range of -20 to +20°C
- ease of installation permitting rapid setup at low temperatures

While investigation of soil behavior at these small strains is necessarily associated with on-specimen measurement of the strains, many possibilities exist regarding the choice of instrumentation and setup configuration. Among the several constraints to be considered during the design of a measuring system, the most significant were the use of a standard size specimen, the space limitation imposed by the existing triaxial chamber, and that the same system be employed to measure, without major modifications, the small strain stiffness of a wide range of geomaterials. In particular, the design had to accommodate the requirements posed by two research projects: one dealing with a fundamental investigation of the small strain behavior of resedimented Boston blue clay (Santagata 1998); the second focusing on the pre-failure behavior of frozen Manchester fine sand, which is presented in this report. These two materials differ in their initial stiffness by more than two orders of magnitude, thus establishing a range in behavior that encompasses that of most soils.

The testing program for RBBC performed SHANSEP (Ladd and Foott 1974) type tests at a variety of stress levels and overconsolidation ratios (OCRs). In these tests, shear would occur in all cases after at least 5% consolidation strain. This constraint eliminated consideration of devices such as the LDT (Goto et al. 1991) which have an axial strain limit of about 2%, beyond which they cease to function. The testing program on RBBC also included multi-stage tests in which various small amplitude (ε_a<0.1%) shears, separated by consolidation phases with 1.5-2% axial strain, were performed on one specimen. This necessitated a device with a large enough linear range to accommodate measurement of strains over a range of approximately 0.5 cm, or to provide a means to adjust the position of the devices prior to each shear phase. In the investigation involving frozen MFS it was imperative that the measurement device be able to withstand confining

pressures of up to 10 MPa and temperatures as low as -25°C, yet still be able to resolve the displacements necessary to characterize the pre-failure deformation behavior.

Finally, the desire to make the measurement of pre-failure deformations a standard procedure in the MIT Geotechnical Laboratory necessitated that the measurement system be flexible, allowing it to be used on any type of specimen, and inexpensive such that a dedicated system could be implemented in each triaxial testing apparatus.

3.5.3 Mechanical Configuration

As previously mentioned, the small strain measurement system consists of two LVDT's set diametrically opposite to each other on two yokes, as shown schematically in Figure 3.6. The yokes are fabricated out of Lucite chosen for its strength and light weight. They are hinged and clamp onto the specimen at three points, each 120 degrees from the other. Currently, they are designed for standard sized triaxial specimens (3.56 cm in diameter), yet they can be scaled up for larger sized specimens. Due to their light weight, the clamping force needed to maintain stability is very small and can be adjusted through the use of a small spring placed across the hinge of both yokes. This type of clamping mechanism avoids mounting designs which rely on the insertion of pins in the specimen for stability (e.g., Cuccovillo and Coop 1997a) and therefore preserves the integrity of the membrane and eliminates the possibility of leakage. This is particularly important during long duration multi-stage tests such as those performed on RBBC. In addition, the "open" clamping mechanism accommodates radial deformation of the specimen while maintaining the alignment of the transducers. Barreling of the specimen at large strains is also not impeded.

As shown in Figure 3.6, the LVDT body is mounted on the lower yoke while the core assembly is suspended from the upper yoke using an adjustable screw. To allow for free movement of the core in the transducer body and to reduce friction, the LVDT core was extended using stainless steel rods such that the actual core length was longer than the transducer body. This was found to help eliminate stick-slip problems at extremely small displacements. To further reduce friction, particularly at the higher strains levels where non-uniform straining might occur, the extended core was connected to the upper yoke

screw assembly with a small length of woven Kevlar string. This allows the core to find its center within the LVDT body. A small lead weight (6-10 g) was attached to the other end of the core with another small length of Kevlar string to provide a small tensile force on the core assembly.

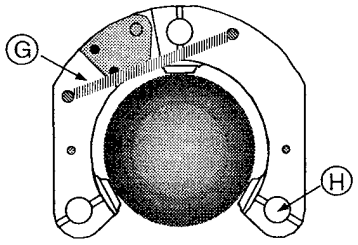

TOP VIEW

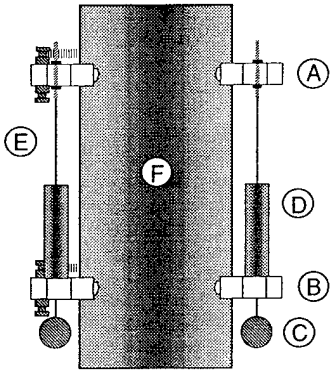

FRONT VIEW

A: Top yoke B: Bottom yoke C: Lead weights
D: Miniature LVDT E: Kelvar thread F: Soil specimen
G: Adjustable spring H: Alignment post holes

Figure 3.6: Schematic of yolks and mounting configuration.

Extensive proof testing on aluminum, PMMA, and soil (discussed in Section 3.5.7 and Section 3.5.8) indicates that this mechanical design eliminates the mounting, alignment, and friction problems traditionally associated with on-specimen measurements of strains using LVDT's (Scholey et al. 1995). Furthermore, the yoke system appears to have no influence on the integrity of the membrane surrounding the specimen.

The transducers chosen for this application are Schaevitz's XS-B Series sub-miniature LVDT's. These transducers, 22.4 mm in length and only 4.77 mm in diameter, have a mass of approximately 4.0 grams each. In addition to their small size, they offer a

number of additional features which make them particularly attractive for this type of application. They have a relatively large linear range of ±0.254 cm (±0.1 in.) and also exhibit an outstanding range of environmental compatibility. Operating temperatures can range from -55°C to 150°C, making them ideal for the low-temperature measurements on frozen sand. They can also operate continuously in fluids pressurized to 21 MPa (3000 psi).

3.5.4 Signal Conditioning Unit

An LVDT is an electromechanical transducer that has the mechanical displacement of a core as its input, and an AC voltage proportional to core position as its output. The induction principle by which the LVDT operates gives this device two outstanding characteristics. The first is truly infinite resolution, which means that the LVDT can respond to even the most minute motion of the core. Thus, the only limitation on the resolution is the capability of the data acquisition system. The inherent symmetry of the LVDT construction produces the other feature, null repeatability, meaning that the device's null position is extremely stable and repeatable.

The operation of the type of LVDT described above requires the use of signal conditioning on both its input and output. Although the standard signal conditioning units available for these transducers performed according to the manufacturers specifications, the resulting levels of stability and noise reduction did not permit resolution of the strains required for this program. For this reason a new signal conditioning system was developed in house to meet the required criteria. An LVDT signal conditioner must be capable of performing three tasks: 1) provide an appropriate amplitude-regulated AC voltage to energize the transducer at the appropriate frequency, 2) sense and then amplify the LVDT's AC output voltage since it is usually too low to be sensed accurately, and 3) convert (demodulate) the output signal, which is proportional to the core position, to filtered DC such that it can be read by the data acquisition system.

The signal conditioning unit was designed around the Analog Devices AD698 integrated circuit chip (Analog Devices Inc. 1994), which can be optimized for use with any LVDT including half-bridge and series opposed (4 wire) configurations, and the

AD826 operational amplifier. The AD698 integrated circuit provides a complete monolithic LVDT subsystem in a ceramic dipped package. It is powered by 30 V (±15 V) and has an operating temperature range of -55°C to +125°C, similar to that of the LVDT's employed. A functional block diagram of the integrated circuit is provided in Figure 3.7.

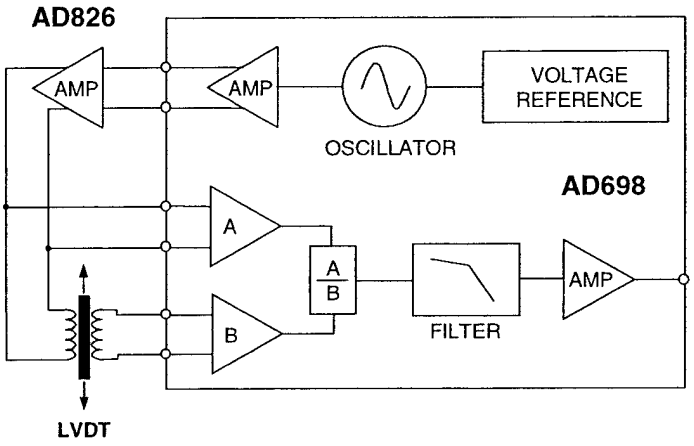

Figure 3.7: Functional block diagram of signal conditioning unit.

The AD698 energizes the LVDT primary coil through the use of a low-distortion sine wave oscillator and power amplifier. A single external resistor and capacitor determine frequency and amplitude. Output frequency can range from 20 Hz to 20 kHz and output amplitude from 2 V to 24 V. For the LVDT's described above, best performance was achieved through excitation at 1.8 V (rms) at 2.5 kHz. A high-speed low-power unity gain amplifier (AD826) was used on the output of the AD698 due to the extremely low impedance of this particular type of LVDT. The AD698 decodes the LVDT's by synchronously demodulating the amplitude-modulated input (secondary coils) and a fixed input reference. The ratio of the LVDT output to its input excitation is then filtered and amplified. This eliminates errors due to drift in the amplitude of the primary excitation thus improving temperature performance and stability.

The AD698 also includes a phase compensation network to add phase lead or lag to the LVDT output to compensate for the LVDT primary to secondary phase shift. Once both channels are demodulated and filtered, an output amplifier scales a reference current (by the ratio of LVDT output to input) converting it to a voltage. This voltage can then

be measured to determine the LVDT core displacement. This output ranges from -10 V to +10 V over the linear range of the transducer (0.508 cm).

3.5.5 Mounting the Small Strain System on the Triaxial Specimen

Mounting the yokes on the specimen occurs once the specimen is setup on the triaxial cell base. Alignment of the top and bottom yokes is ensured through the use of three alignment posts that also set the desired gage length (usually equal to 5.08 cm). Once the yokes are clamped onto the specimen the posts are removed by extracting six small brass pins, thus allowing the system to move freely as the specimen strains. Prior to set-up of frozen soil specimens, the position of the threaded rod in the top yoke is adjusted to ensure that each LVDT is in range at the beginning of the test. If pre-shear stress-path consolidation is required, as in the case of SHANSEP type tests on RBBC, then the position of the LVDT cores are adjusted such that they are initially out of range, but will come into range after a predetermined amount of axial consolidation strain. To ease positioning of the cores, additional holes were made in the vertical posts and an aluminum dummy specimen having the same diameter as the standard triaxial specimen was fabricated with a series of grooves cut into it every 0.127 cm (0.05 in). The yokes are placed on the grooves corresponding to the expected pre-shear height and the position of the threaded rod is adjusted to achieve the desired output. The initial gage length is then reset prior to clamping the yokes around the soil specimen.

3.5.6 LVDT Electrical Performance

3.5.6.1 Stability Characteristics

One of the most important characteristics of the LVDT signal conditioning system is the stability of its output over both the short term and the long term. Short term stability is necessary to accurately measure the stress-strain behavior of soils, whereas long term stability is essential for accurate measurements of creep behavior.

The electrical stability of the newly developed LVDT signal conditioning system was evaluated by monitoring the transducer output using the central data acquisition system described previously. Figures 3.8a and 3.8b present the results obtained at room

temperature (20° C) over periods of 300 seconds and 24 hours respectively. For these tests the LVDT was placed horizontally inside the triaxial chamber to avoid any possible creep in the Kevlar string. Both the yokes and signal conditioning electronics were located inside the environmental enclosure to ensure proper temperature control.

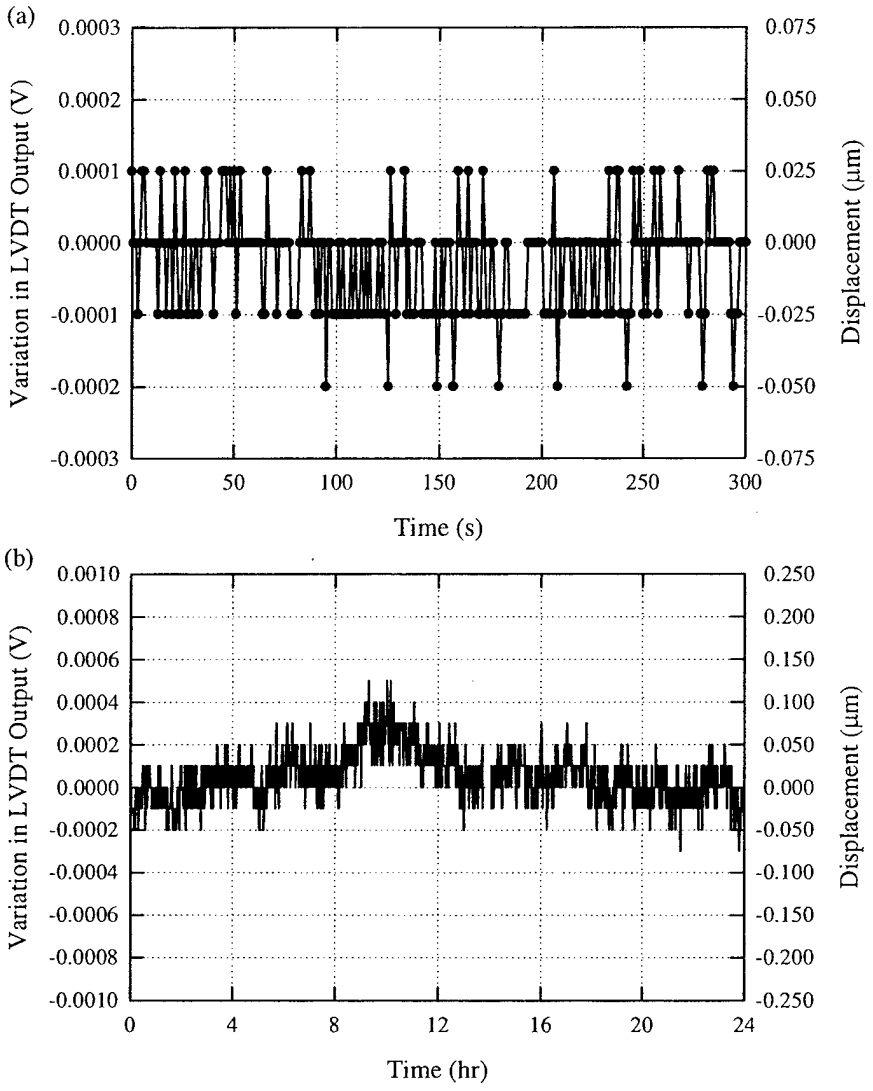

Figure 3.8: LVDT stability with new signal conditioning system at 20°C (a) over 300 s, (b) over 24 hours.

As shown in Figure 3.8a, the signal of the LVDT fluctuated by only ±0.15mV over a period of 300 seconds. This corresponds to 3 bits of digital noise (when the absolute value of the signal exceeds 1.000V). Based on the transducer's calibration factor this noise band corresponds to a displacement of 0.075 μm and translates into a strain of about

0.00015%, assuming a gage length of 5.08 cm. Note that even at the slowest strain rate employed in this program (1.0 %/hr), the entire linear region is crossed is less than 1 minute during shear. Figure 3.8b shows that over 24 hours the output signal of the LVDT fluctuates by approximately ±0.3mV without any appreciable signal drift.

The data shown in Figure 3.8 represent a marked improvement in electrical performance over that obtained using commercial signal conditioning units. While the performance of these units were well within their specifications they did not provide sufficient noise rejection for this particular application and suffered from excessive signal drift, especially over the long term.

3.5.6.2 Effect of Temperature on LVDT Output

As the instrumentation was also designed to measure the pre-failure behavior of frozen sands, its electrical performance was evaluated below room temperature. Figures 3.9a and 3.9b present stability data over 300 seconds and 24 hours, respectively, for three different temperatures: 20°C, -10°C and -20°C. These data indicate that there is no significant temperature effect on the short term (300 s) performance of the transducer at -10°C, while at -20°C the signal to noise band increases from ±0.15 mV to ±0.30 mV.

The data obtained over the long term (24 hours) show that the signal's noise band increases with decreasing temperature (from ±0.3 mV at 20°C to approximately ±1 mV at -10°C and ±2 mV at -20°C) and may have a tendency to drift slightly at lower temperatures. This behavior is believed to stem from difficulties associated with temperature control, which are enhanced at decreasing temperature, rather than from inherent deterioration of the device's performance at lower temperatures. Note that this drift is insignificant when compared to the strain occurring, for example, during secondary compression.

It is important to note that the magnitude of the output from the LVDT is temperature sensitive. This is due to changes in the resistance of the LVDT coils and signal conditioning circuitry which are all maintained at the same temperature as the test specimen. Fluctuations in temperature around the control point therefore may be responsible for the increased drift and noise observed in the LVDT output at the lower

temperatures. However, in the range of temperatures investigated (-20°C to +20°C), the LVDT still presents a linear calibration curve. Since frozen soil testing is conducted at a constant temperature, the variation in LVDT output with temperature does not represent a limit of the device, although it must be accounted for in some specific cases, such as during set-up of frozen sand specimens. In this case, part of the strain measured as the temperature equilibrates to the desired testing temperature is due to temperature induced changes in the LVDT output and not to the actual straining of the specimen.

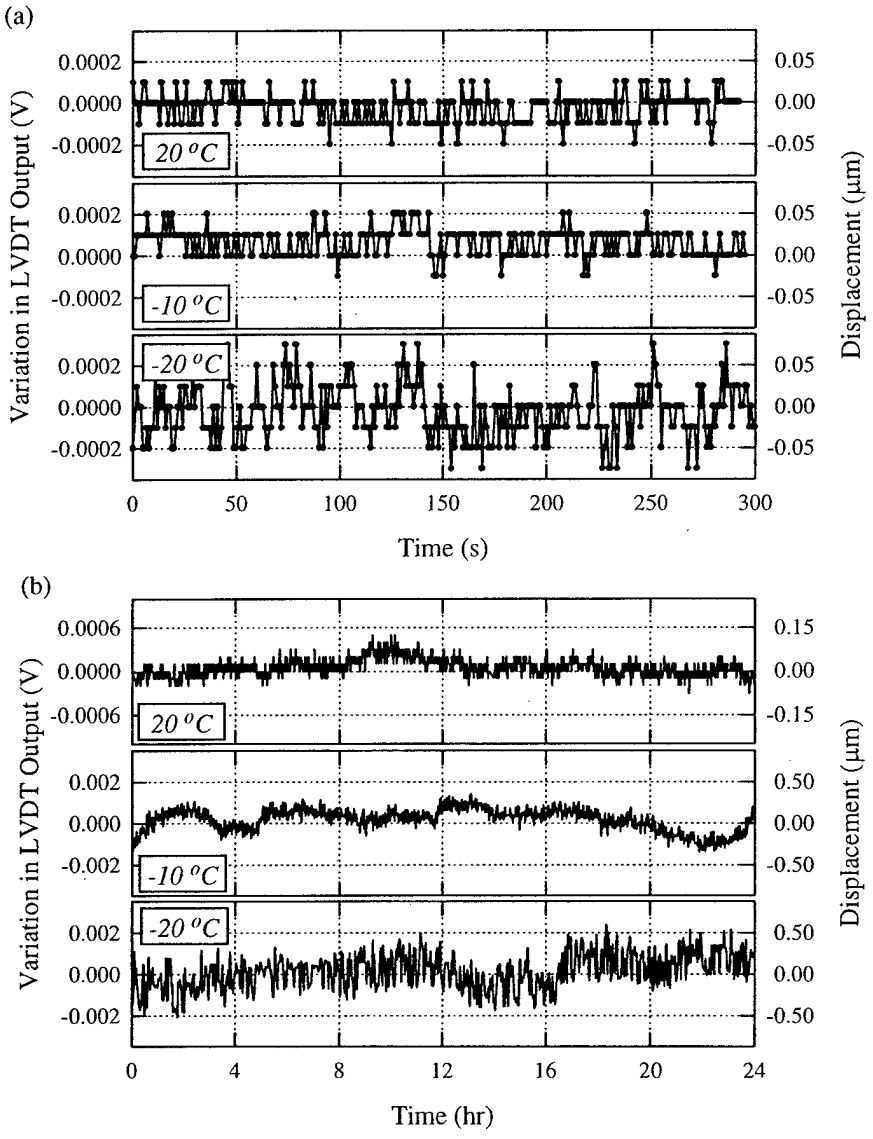

Figure 3.9: LVDT stability as a function of temperature (a) over 300 s, (b) over 24 hours.

3.5.6.3 Effect of Pressure on LVDT Output

Tests were also performed to verify the sensitivity of the LVDT's to variations in the chamber pressure inside the triaxial cell. Such tests were carried out by placing a LVDT inside the oil-filled high-pressure triaxial chamber, and then pressurizing it at a rate of 180 kPa/minute to a maximum of 10 MPa. This represents the maximum hydrostatic stress employed in this frozen sand program. The output of the transducer is plotted in Figure 3.10 versus the chamber pressure for one of these tests, which included two cycles of pressurization.

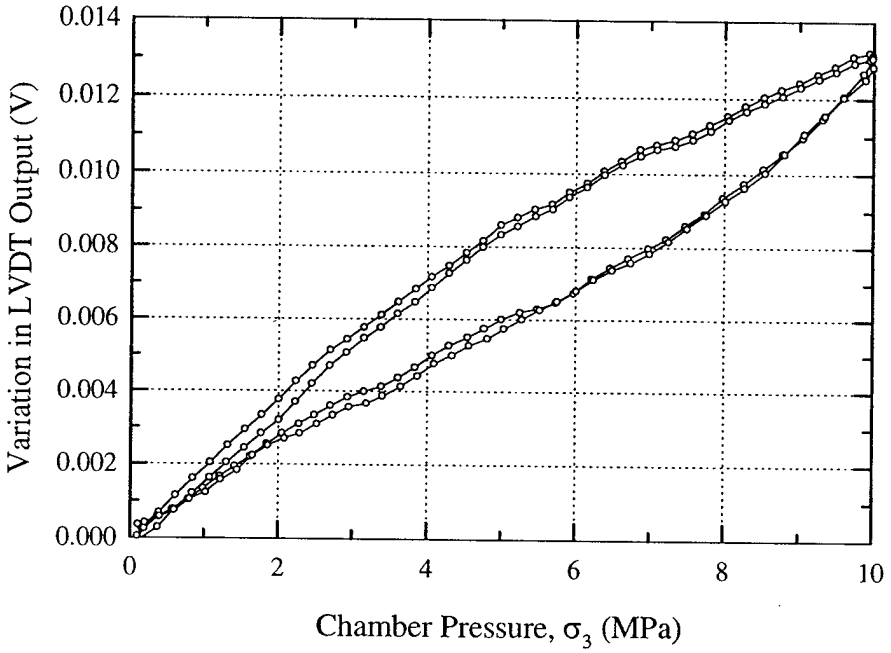

Figure 3.10: LVDT stability as a function of confining pressure (0-10 MPa) at T=20°C.

It is shown that over the range of pressure examined the output signal increases by approximately 14 mV and exhibits a hysteresis of 0.005% of the LVDT's full-scale output (±10 V). Some authors (e.g., Cuccovillo and Coop 1997a) have reported the necessity of using LVDT's with small pressure-relieving holes drilled in their casing in conjunction with non-conductive cell fluid for high-pressure applications. However, due to the particular construction of the miniature LVDT's used it was not possible to make a hole in its casing without causing the transducer to malfunction. Nonetheless, pressure sensitivity

should not present a problem since the on-specimen LVDT's are only employed to measure the deformation of the soil specimen only during undrained shear, and in some cases, during secondary compression. Since these processes occur at constant confining pressure, no correction is necessary. However, because the pressure effect is repeatable, it could be accounted for in the reduction of the test data for those processes that occur under varying mean stress (e.g., consolidation).

3.5.7 Proof Testing on Aluminum and PMMA

A series of tests were carried out using the new axial strain measurement system in order to confirm its ability to correctly measure the true axial strains experienced by the specimen during consolidation and shear. This was done by substituting various materials of known moduli in place of the regular soil specimen and measuring the strains that resulted from cycles of loading. The materials that were chosen were standard 6061 aluminum and PMMA (polymethylmethacrylate) since they are both extremely homogenous, readily available, and have well-known material properties. The quoted values of the Young's modulus in compression are 69 GPa for the aluminum, and 3.3 GPa for the PMMA specimen (Ashby 1992). The Young's modulus in compression of these two materials differ by more than two orders of magnitude and therefore allows for performance evaluation at two markedly different stiffness values. All proof tests were performed using two thin latex rubber membranes placed over each specimen to simulate actual soil testing conditions.

Figure 3.11 shows the stress-strain curve obtained by applying two cycles of load on the aluminum specimen in the high-pressure triaxial cell using the 45 kN load cell. The Young's modulus for this specimen calculated from a regression through the data over an axial strain range of 0.03% is 71.6 GPa.

Similar data for the PMMA specimen are presented in Figure 3.12. For this case the data were obtained using a 0.44 kN (100 lb) load cell in a similar apparatus used for testing cohesive soils. From these data a stiffness of 3.3 GPa is calculated over 0.01% axial strain. The stiffness of both the aluminum and PMMA specimen are in excellent agreement with the reference values available in the literature, thus indicating that the axial

strain measuring system can be used effectively to investigate the small strain stiffness of various materials in compression.

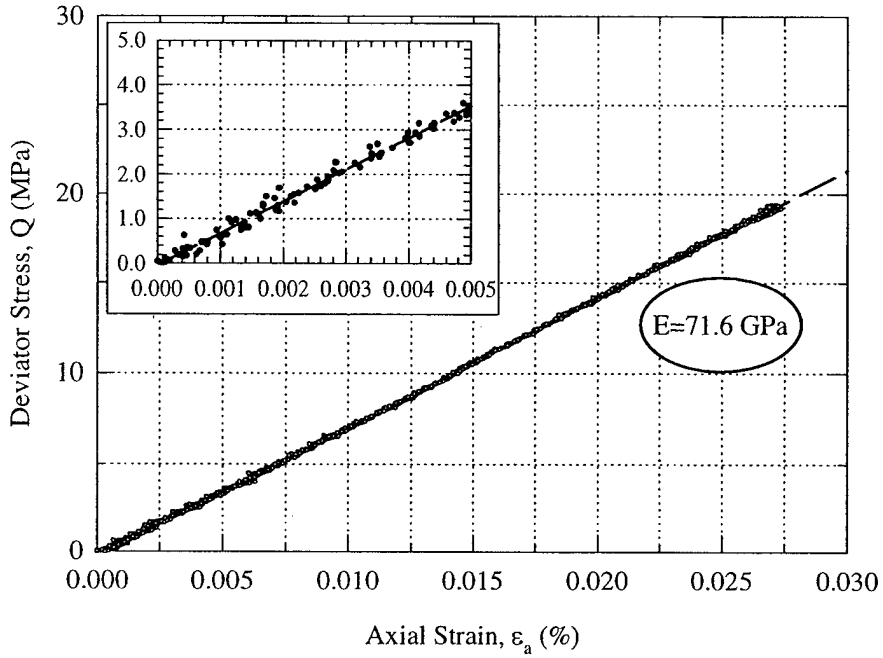

Figure 3.11: Stress-strain behavior of 6061 aluminum determined with the new MIT small strain measuring system.

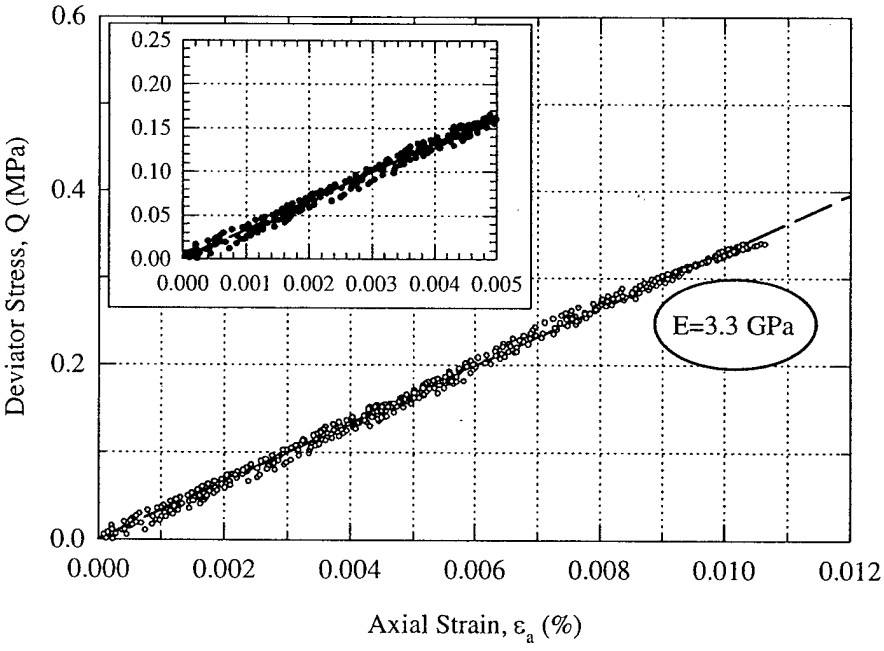

Figure 3.12: Stress-strain behavior of PMMA determined with the new MIT small strain measuring system.

3.5.8 Evaluation of Technology on Soil

3.5.8.1 Tests on Resedimented Boston Blue Clay

The first soil employed to evaluate the performance of the small strain measurement system presented above is resedimented Boston blue clay (RBBC), a soil resedimented in the laboratory from natural Boston blue clay, an illitic CL clay. A complete description of RBBC and its pre-failure deformation behavior can be found in Santagata (1998).

RBBC exhibits characteristics very similar to that of the original material, and to many natural cohesive soils, including stress-strain-strength anisotropy, low to medium sensitivity, and significant strain rate dependency. Its local relevance, uniform behavior, complete saturation, and virtually infinite supply make it, in fact, an ideal research tool to investigate fundamental aspects of soil behavior without having to take into account the variability of natural soils. Particularly in the normally consolidated (NC) state, RBBC exhibits fairly soft behavior and pronounced strain softening in undrained triaxial compression. Investigation of its small strain behavior poses challenges due to the expected low linear threshold and low stiffness. These aspects require extraordinary resolution in both the axial strain and load measurements.

Figure 3.13 shows an example of the quality of the small strain measurements obtained employing the system described in the previous sections. The data refer to a specimen of normally consolidated RBBC K_0-consolidated to about 0.17 MPa and sheared at a rate of 0.1%/hour after about 24 hours of secondary compression. Figure 3.13a shows the overall behavior of the soil under these conditions. The peak deviator stress is reached at approximately 0.1% axial strain after which the soil strain softens. Figures 3.13b-d present stress-strain curves in the range of 0-0.05%, 0-0.005% and 0-0.0005%, and illustrate the pre-failure behavior of the soil. As indicated in these figures, the measuring system captures the initial linear behavior (Figure 3.13d), and the onset of non-linearity at about 0.0015% axial strain.

The data presented in Figure 3.13a, b and d are obtained by averaging the displacements measured by the two LVDT's. A measure of the reliability of the results, particularly for a homogeneous material such as RBBC, is provided by the agreement

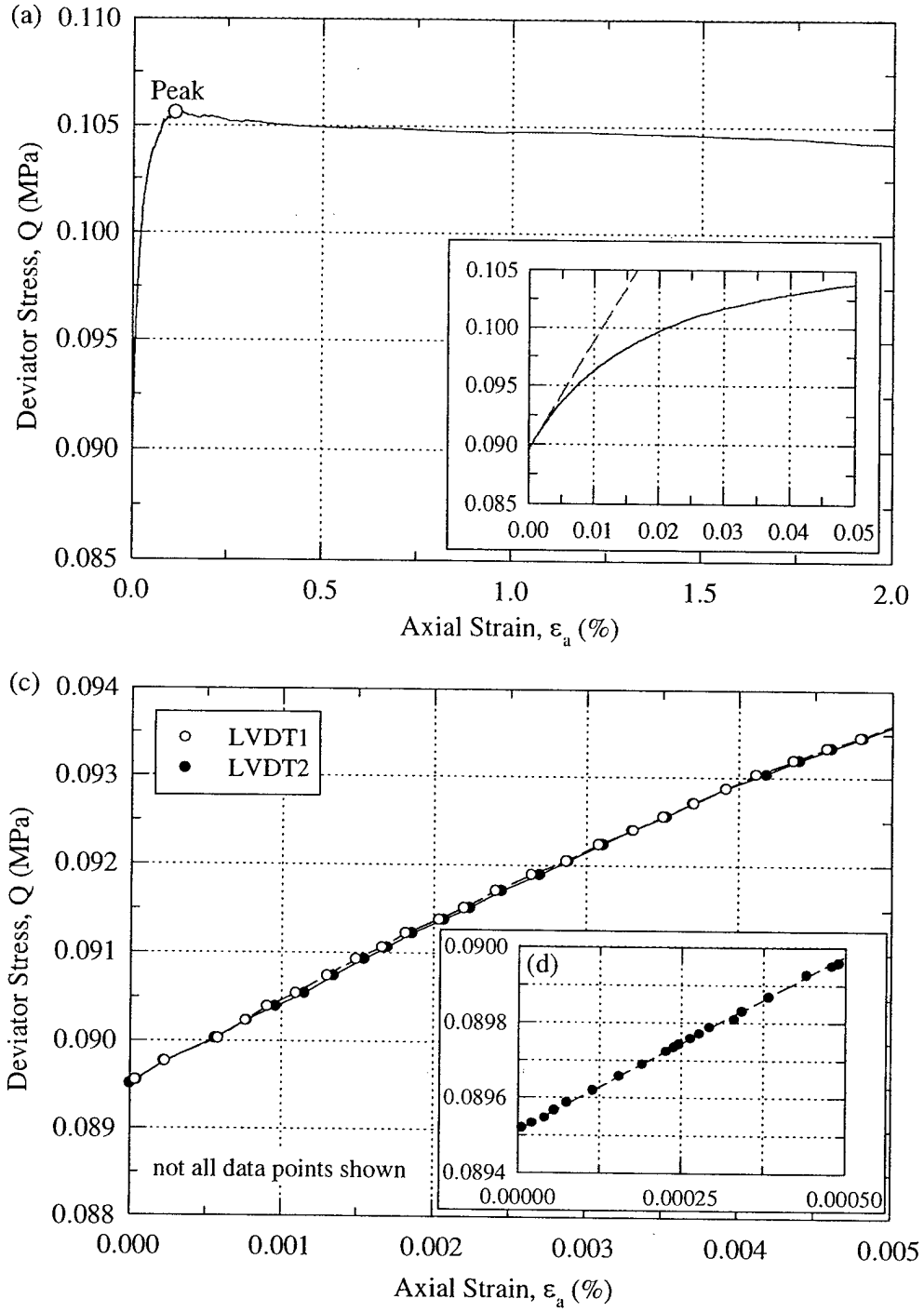

Figure 3.13: Undrained shear data on normally consolidated RBBC: (a) large strain region, 0.00-2.00%, (b) 0-0.05%, (c) small strain region, 0.00-0.005%, (d) 0.00-0.0005%. (Santagata 1998)

between the two transducers. Figure 3.13c shows a comparison of the stress–strain curves up to 0.005% axial strain obtained from each of the two LVDT's. The two curves are in excellent agreement over the entire strain range examined, and the difference in the initial stiffness measured with the two transducers is less than 5%.As shown in Figure 3.14, the method for measuring the pre-failure behavior of soils in the triaxial apparatus produces extremely repeatable results. The figure presents secant stiffness versus axial strain curves relative to the undrained shear, at 0.1%/hr after 24 hours of secondary compression, on four different specimens of RBBC all K_0-consolidated to the same stress level (~0.24 MPa). The figure shows that the large amount of high quality data collected allows precise description of the S-shaped curve of secant stiffness versus logarithm of axial strain, and demonstrates the excellent agreement of the data over the entire range of strain investigated.

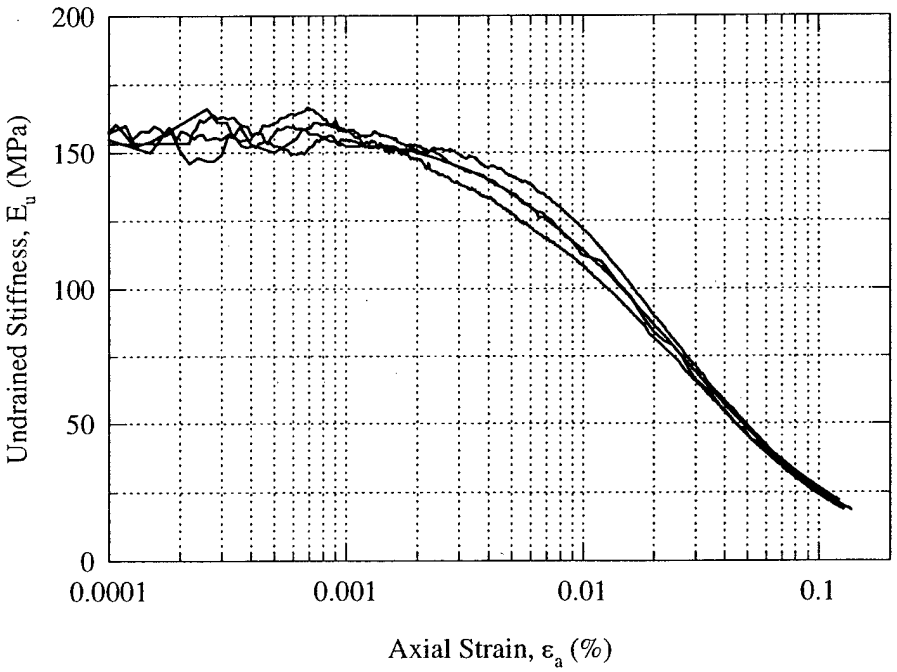

Figure 3.14: Repeatability of results on normally consolidated RBBC: stiffness versus logarithm of axial strain (σ'_{vc} = 0.24 MPa, K_0-consolidation). (Santagata 1998)

3.5.8.2 Tests on Frozen Manchester Fine Sand

Further evaluation of the performance of the small strain measurement system was performed on frozen specimens of saturated Manchester fine sand, a natural sand obtained from the banks of the Merrimack River in Manchester, New Hampshire. A complete description of this material is given in Chapter 4. Frozen sands exhibit complex stress-strain-time-temperature behavior due to interactions between the soil skeleton and pore ice matrix. The major problems encountered in testing this type of geomaterial stems from its high stiffness (~25 GPa) and from the particular design of the top cap in the testing apparatus which contributes to extensive seating errors.

Despite the fact that the previous studies on the behavior of frozen Manchester fine sand represented the state of the art at their time, the results of these efforts displayed, in general, unsatisfactory repeatability and limited strain resolution. This was mainly due to limitations in the previous small strain measurement system and inadequate control in the load application leading to non-uniformities in the strain field (discussed in Section 3.3.3.2).

The stress-strain data shown in Figure 3.15a-d were obtained from a specimen of frozen MFS sheared at a constant rate of strain (1.0%/hr) in triaxial compression using lubricated end conditions. Figure 3.15a shows the complete stress-strain curve for this material. In order to capture the upper yield stress, the small strain measuring system is used to measure strains up to 1-2% axial strain. Due to excessive system compliance in the early stages of shear, systems that use an external LVDT for axial strain measurement often fail to capture this point which typically occurs at around 0.3-0.5% axial strain (Figure 3.15b).

As with the data presented on RBBC, the data in Figure 3.15a, b and d represent the average strain of the two LVDT's, while Figure 3.15c shows the result for both transducers. This comparison shows that the two measurements of the initial stiffness differ by less than 5% for axial strains smaller than 0.005%, and that the agreement between the two LVDT's is very good. As the strain level increases, the two transducers tend to deviate somewhat, but their average is generally accurate up until 2% strain at which point the external LVDT is used to compute the strain of the specimen.

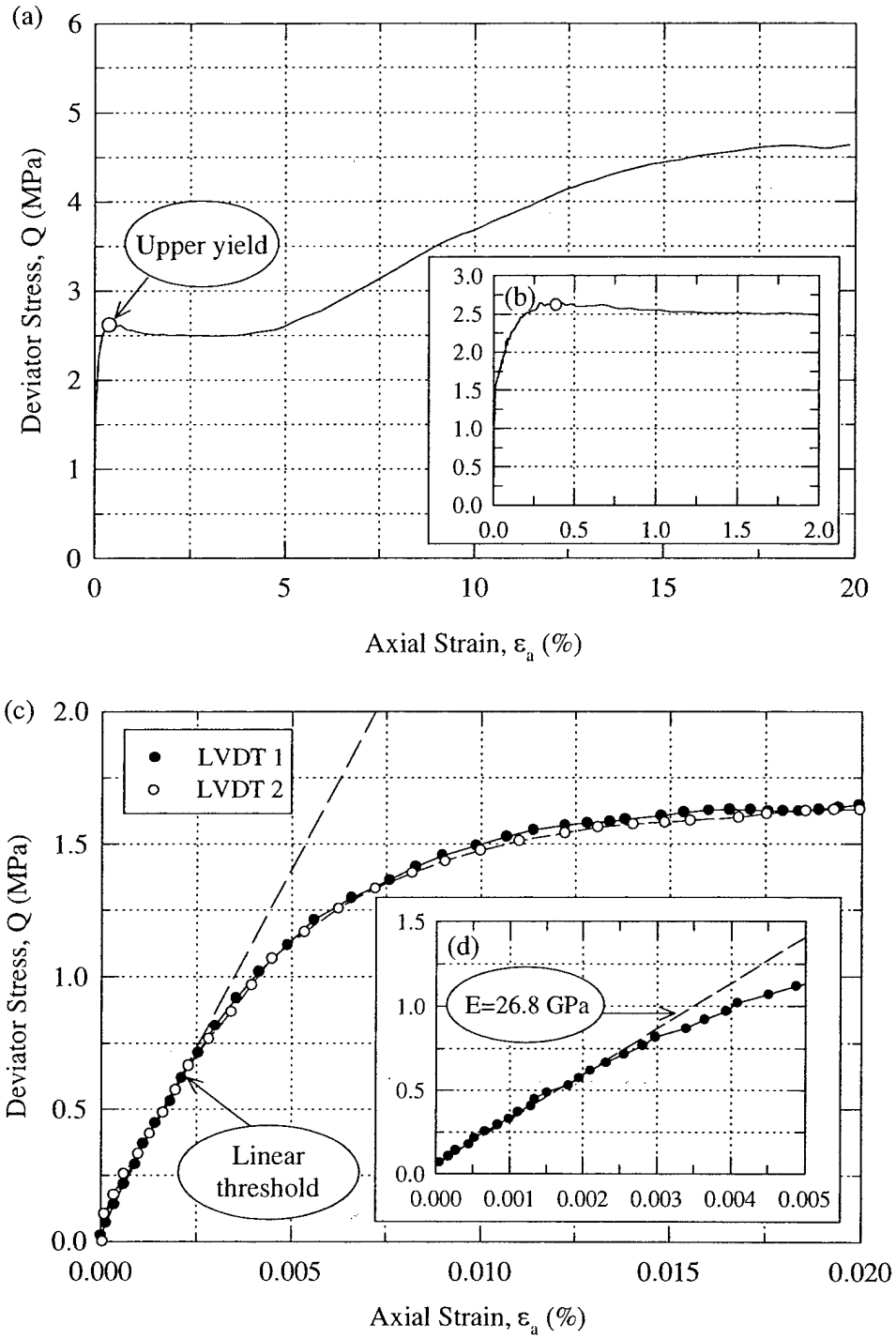

Figure 3.15: Shear data on frozen MFS: (a) large strain region, 0.00-20.0%, (b) 0.00-2.00%, (c) small strain region, 0.00-0.02%, (d) 0.00-0.005%. (FRS182: D_r=49.8%, σ_c=0.5 MPa, T=-5°C, $\dot{\varepsilon}$=3.0x10^{-6} s^{-1})

3.6 REFERENCES

1. Analog Devices Inc. (1994), *Design-In Reference Manual*, pp. 16-67 - 16-77.

2. Andersen, G.R. (1991), "Physical Mechanisms Controlling the Strength and Deformation Behavior of Frozen Sand", Sc.D Thesis, Department of Civil and Environmental Engineering, MIT, Cambridge, MA, 560 p.

3. Andersen, G.R., Swan, C.W., Ladd, C.C., Germaine, J.T. (1995), "Small-Strain Behavior of Frozen Sand in Triaxial Compression", *Canadian Geotechnical Journal*, v. 32, no. 3, pp. 428-451.

4. Ashby M.F. (1992), *Materials Selection in Mechanical Design*, Pergamon Press, Oxford.

5. Brown, S.F., Austin, G., Overy, R.F. (1980), "An Instrumented Triaxial Cell for Cyclic Loading of Clays", *Geotechnical Testing Journal*, v. 3, no. 4, pp. 145-152.

6. Burland, J.B. and Symes, M. (1982), "A Simple Axial Displacement Gauge for Use in the Triaxial Apparatus", *Geotechnique*, v. 32, no. 1, pp. 62-65.

7. Clayton, C.R.I and Khatrush, S.A. (1987), "A New Device for Measuring Local Axial Strains on Triaxial Specimens", *Geotechnique*, v. 36, no. 4, pp. 593-597.

8. Costa-Filho, L. (1985), "Measurement of Axial Strains in Triaxial Tests on London Clay", *ASTM Geotechnical Testing Journal*, v. 8, no. 1, pp. 3-13.

9. Cuccovillo, T. and Coop, M.R. (1997a), "The Measurement of Local Axial Strains in Triaxial Tests Using LVDTs", *Geotechnique*, v. 47, no. 1, pp. 167-171.

10. Cuccovillo, T. and Coop, M.R. (1997b), "Yielding and Pre-Failure Deformation of Structured Sands", *Geotechnique*, v. 47, no. 3, pp. 491-508.

11. Goto, S., Tatsuoka, F., Shibuya, S., Kim, Y-S., Sato, T. (1991), "A Simple Gauge for Local Small Strain Measurements in the Laboratory", *Soils and Foundations*, v. 31, no. 1, pp. 169-180.

12. Hird, C.C. and Yung, P.C.Y. (1989), "The Use of Proximity Transducers for Local Strain Measurements in Triaxial Cells", *ASTM Geotechnical Testing Journal*, v. 12, no. 1, pp. 292-296.

13. Jardine, R.J., Symes, M.J., Burland, J.B. (1984), "The Measurement of Soil Stiffness in the Triaxial Apparatus", *Geotechnique*, v. 34, no. 3, pp. 323-340.

14. Ladd, C.C. and Foott, R. (1974), "New Design Procedure for Stability of Soft Clays", *ASCE Journal of the Geotechnical Engineering Division*, v. 100, no. 7, pp. 763-786.

15. Lo Presti, D.C.F., Pallara, O., Costanzo, D., Impavido, M. (1994), "Small Strain Measurements During Triaxial Tests: Many Problems, Some Solutions", *Proc. 1st International Symposium on the Pre-Failure Deformation Characteristics of Geomaterials*, Hokkaido, Japan, v. 1, pp. 11-16.

16. Perdikaris, G.A. (1991), *Computer Controlled Systems: Theory and Applications*, Kluwer Academic, Boston.

17. Santagata, M.C. (1998), "Factors Affecting the Initial Stiffness and Stiffness Degradation of Cohesive Soils", Ph.D Thesis, Department of Civil and Environmental Engineering, MIT, Cambridge, MA, 336p.

18. Scholey, G.K, Frost, D.J., Lo Presti, D.C.F., Jamiolkowski, M. (1995), "A Review of Instrumentaion for Measuring Small Strains During Triaxial Testing of Soil Specimens", *ASTM Geotechnical Testing Journal*, v. 18, no. 2, pp. 137-156.

19. Sheahan, T.C. (1991), "An Experimental Study of the Time-Dependent Undrained Shear Behavior of Resedimented Clay Using Automated Stress-Path Triaxial Equipment", Sc.D Thesis, Department of Civil and Environmental Engineering, MIT, Cambridge, MA, 955p.

20. Sheahan, T.C. and Germaine, J.T. (1992), "Computer Automation of Conventional Triaxial Equipment", *ASTM Geotechnical Testing Journal*, v. 15, no. 4, pp. 311-322.

21. Swan, C.W. (1994), "Physical Mechanisms Controlling the Strength and Deformation Behavior of Unfrozen and Frozen Manchester Fine Sand", Sc.D Thesis, Department of Civil and Environmental Engineering, MIT, Cambridge, MA, 1044p.

CHAPTER 4

MATERIALS AND SPECIMEN PREPARATION

4.1 INTRODUCTION

This chapter presents a detailed characterization of the materials used in the experimental program and the techniques used in the preparation of test specimens. A number of experiments were performed in order to better understand the small strain behavior of frozen sands. In addition to triaxial compression tests on two types of sand and other granular materials, special shear tests were also performed to investigate the bond strength between ice and a quartz surface. The reasoning behind the selection of these materials is explained in detail in Chapter 5.

Sections 4.2 describes the nature of the various granular materials used throughout the experimental program while Section 4.3 outlines the techniques for preparing frozen specimens of soil and ice for testing in the high-pressure triaxial apparatus. Finally, references cited throughout this Chapter are listed in Section 4.4.

4.2 MATERIALS

4.2.1 Manchester Fine Sand

Manchester fine sand (MFS) was used by three previous MIT research programs on frozen sands and hence has been well characterized. It originates from the banks of the Merrimack River, approximately 16 km north of Manchester, New Hamsphire. A large supply was collected from the Plourde Sand and Gravel Company in Hooksett, New Hampshire and brought to MIT for subsequent processing to remove excess fines. The initial fines content, that is the percentage of material passing a No. 200 sieve (0.074 mm), was as high as 21% and this was subsequently reduced to approximately 9% by sieving and reblending. Mineralogical analysis indicates that this sand consists primarily of quartz and feldspar, but also contains traces of mica flakes (Martin et al. 1981). A typical SEM micrograph is shown in Figure 4.1. It indicates that the MFS grains are angular to subangular in nature and generally equi-dimensional.

(a)

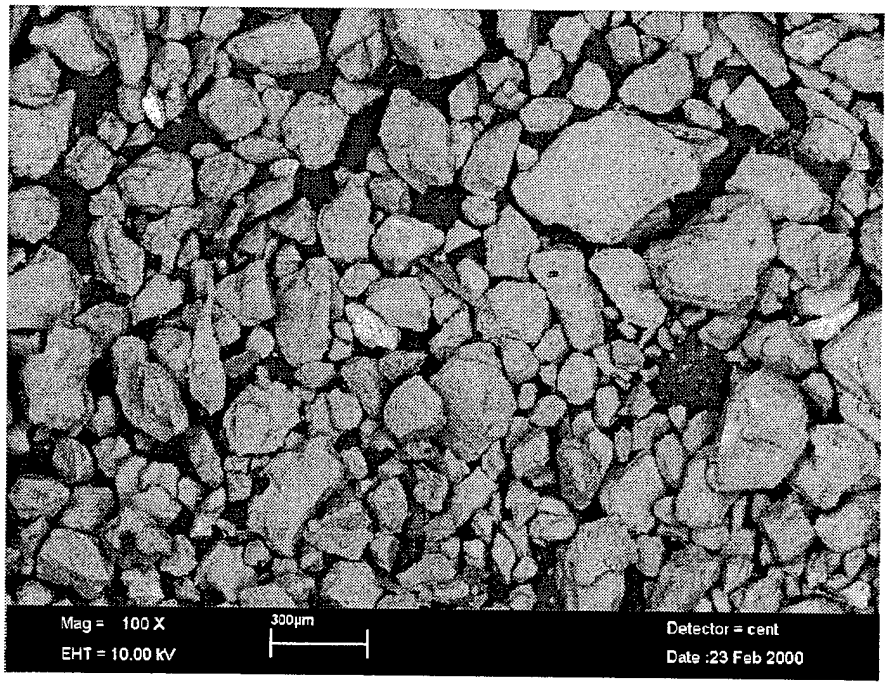

(b)

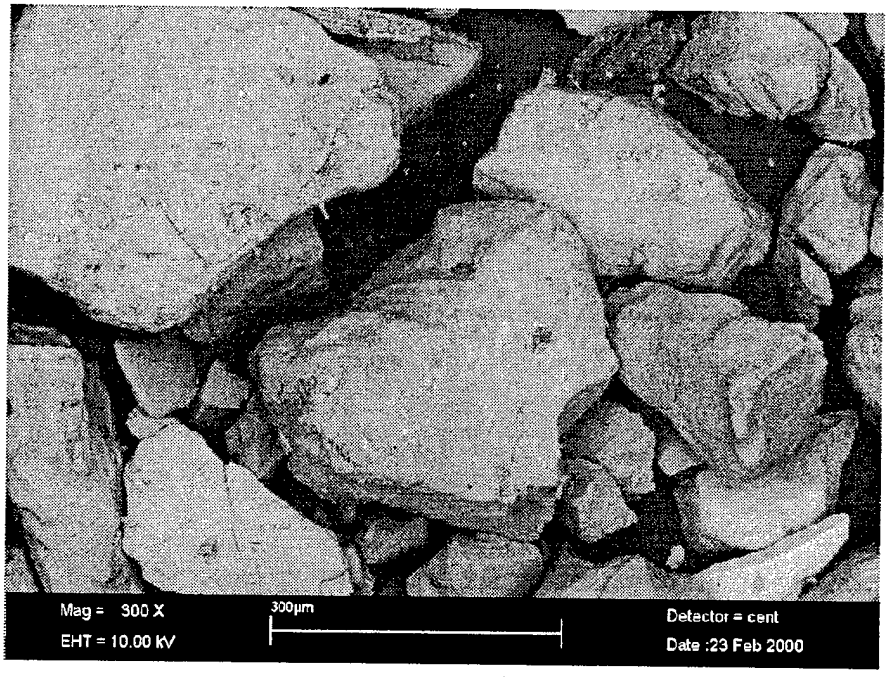

Figure 4.1: SEM image of untreated Manchester fine sand (a) Magnification 100X, (b) Magnification 300X.

Two sets of sieve and hydrometer analyses (ASTM D422-63, 1997a) were carried out on the MFS used for this research. The resulting grain size distribution is given in Figure 4.2 and shows that the material is a poorly graded medium to fine sand. It is classified according to the Unified Soil Classification System (USCS) system as a SP-SM. Manchester fine sand has a relatively low organic content (0.68%) as determined by ASTM D2974-87 (1997b) (Sinfield 1997).

From the grain size distribution chart given in Figure 4.2, the following parameters can be determined; $d_{10} = 0.077$ mm, $d_{30} = 0.11$ mm, $d_{50} = 0.145$ mm, and $d_{60} = 0.16$ mm. These are the particle diameters corresponding to 10%, 30%, 50% and 60% finer by mass. From these values the coefficient of uniformity C_u, and the coefficient of concavity C_c, can be calculated:

$$C_u = \frac{d_{60}}{d_{10}} = 2.08 \tag{4.1}$$

$$C_c = \frac{d_{30}^2}{d_{60} \cdot d_{10}} = 0.982 \tag{4.2}$$

These values match closely those presented by Andersen (1991) and by Swan (1994).

Andersen (1991) also carried out tests to determine the maximum and minimum dry density for this sand. The maximum dry density (ASTM D4253-93, 1997c) is ρ_{max} = 1701 kg/m^3 and corresponds to a minimum void ratio of $e_{min} = 0.580$. The minimum dry density (ASTM D4254-91, 1997d) was found to be ρ_{min} = 1408 kg/m^3 and corresponds to a maximum void ratio of $e_{max} = 0.909$. In addition, Andersen (1991) also carried out specific gravity determinations (ASTM D854-92, 1997e) and found it to be 2.688±0.003.

4.2.2 Polycrystalline Ice

Polycrystalline ice specimens were prepared in the laboratory from seed material obtained from a Hozisashu laboratory ice maker. It produced clean granular ice from a supply of distilled degassed water. This material was subsequently passed through a rotary grinder which reduced the mean particle size by a factor of 2 and then sieved on a #25 U.S. standard sieve (0.710 mm). This procedure was performed at an ambient temperature of -10°C to avoid adhesion or sintering of the grains.

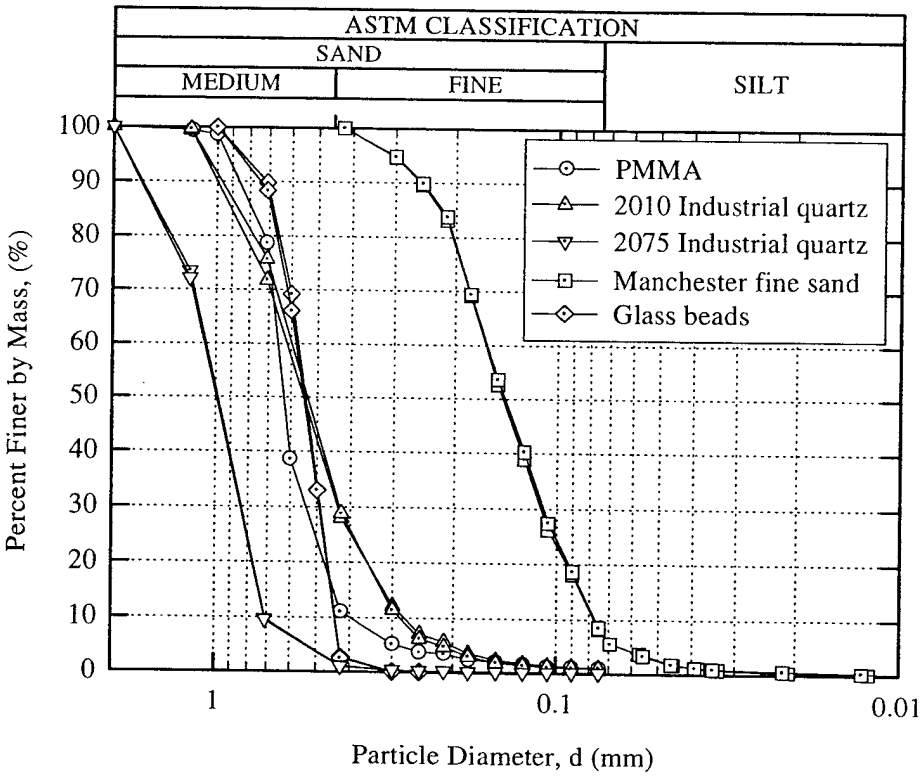

Figure 4.2: Grain size distributions for Manchester fine sand, industrial quartz, PMMA powder, and small glass beads.

A number of properties need to be controlled when preparing fine-grained ice specimens for experimental work. Grain size and orientation, homogeneity, density and physical dimensions are most important for studies concentrating on its mechanical properties. The general procedure for preparing ice specimens is to compact the seed material into a mold, evacuate the entrapped air, saturate with water, and freeze the resulting mixture. The procedure is described in more detail in subsequent sections. The compaction of fine grained ice particles yields randomly orientated freezing nuclei and limits the amount of water needing to be frozen, thus minimizing the freezing strains. Since the constituent crystals have a random orientation, the resulting ice is relatively homogeneous and isotropic.

The resulting specimens were generally optically clear with only a few very small bubbles evenly dispersed throughout. It has proven extremely difficult to reduce the porosity of this type of ice to zero. The reason lies in the difficulty in completely eliminating the gas molecules present in the seed material that lead to bubble formation

during the freezing process. Cole (1979) states that this preparation technique yields fine-grained specimens with equi-dimensional crystals of random c-axis orientation and average grain sizes of 1.2 mm and average bubble diameters of 0.1 mm. To verify the grain diameter of the specimens, thin sections of some specimens were taken. Figure 4.3 shows a thin section of typical untested polycrystalline ice. The grain size of a representative specimen was determined from this thin section photograph using the expression (Dieter 1976):

$$d = \sqrt{\frac{6}{\pi N_A}} \tag{4.3}$$

where N_A is the number of grains per unit area. The average grain size determined using this formula was approximately 1.08 mm. This corresponds very well to the values obtained by Cole (1979). In addition to characterizing the specimens by grain size, the density of each specimen was recorded and found to be 0.912±0.001 g/cc (n=8). This also compares well with the densities obtained on ice specimens prepared using the CRREL method (Cole 1979).

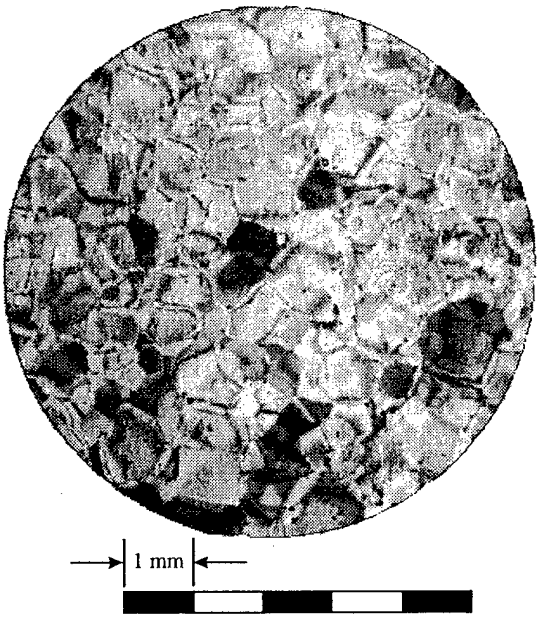

Figure 4.3: Thin section of typical untested polycrystalline ice.

4.2.3 Alternate Granular Materials

4.2.3.1 Industrial Quartz

Industrial quartz was chosen as a surrogate material for MFS for those tests which required a coarser-grained material with similar angularity and mineralogy characteristics. This material was quarried in Quebec and processed in Ontario, Canada. X-ray diffraction confirms that the material is essentially pure quartz (SiO_2). While five grades were available for use only the 2010 and 2075 grade were chosen for testing, with the majority of the tests being performed on the 2010 grade. The size, angular shape, and surface texture of these particles can be seen in the SEM micrograph in Figure 4.4.

Grain size distribution curves for these materials were shown in Figure 4.2. The four digit grade notation, XXYY, indicates that YY% of the material is retained on a number XX U.S. standard sieve. Therefore, for the 2010 grade, 10% of the material is larger than the number 20 sieve (0.850mm).

As with MFS, the following parameters are useful to describe the shape of the 2010 grain size distribution curve presented in Figure 4.2: $d_{10} = 0.29$ mm, $d_{30} = 0.43$ mm, $d_{50} = 0.54$ mm, and $d_{60} = 0.60$ mm. The coefficient of uniformity is 2.07, and the coefficient of concavity is 1.06. These coefficients are very similar to those for MFS indicating that the shape of the grain size curves are very similar, and that the mean particle size and shape are the only significant difference between these soils.

The maximum dry density of the 2010 industrial quartz, determined with a vibrating table and surcharge, is $\rho_{max} = 1616$ kg/m^3, which corresponds to a minimum void ratio of $e_{min} = 0.640$. The minimum dry density was found to be $\rho_{min} = 1355$ kg/m^3 and corresponds to a maximum void ratio of $e_{max} = 0.955$. The specific gravity is 2.65 (Sinfield 1997).

4.2.3.2 Hydrophobic Manchester Fine Sand

In an attempt to reduce the component of ice adhesion in frozen sands, a unique hydrophobic coating technique was developed and applied to MFS. The preparation of hydrophobic surfaces is readily accomplished through a process known as *silation*. This technique is widely used in various fields of analytical chemistry and is quite common in

(a)

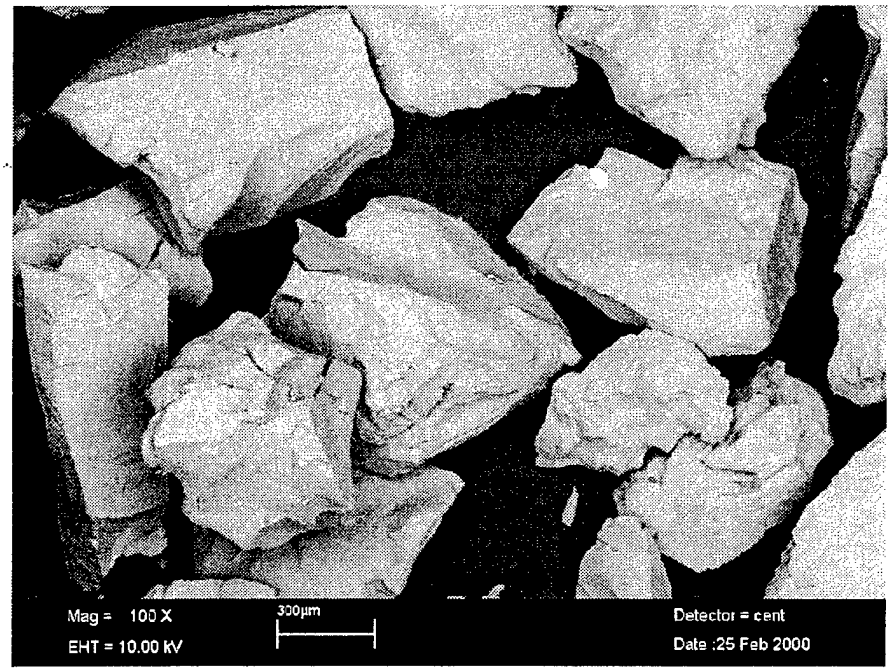

(b)

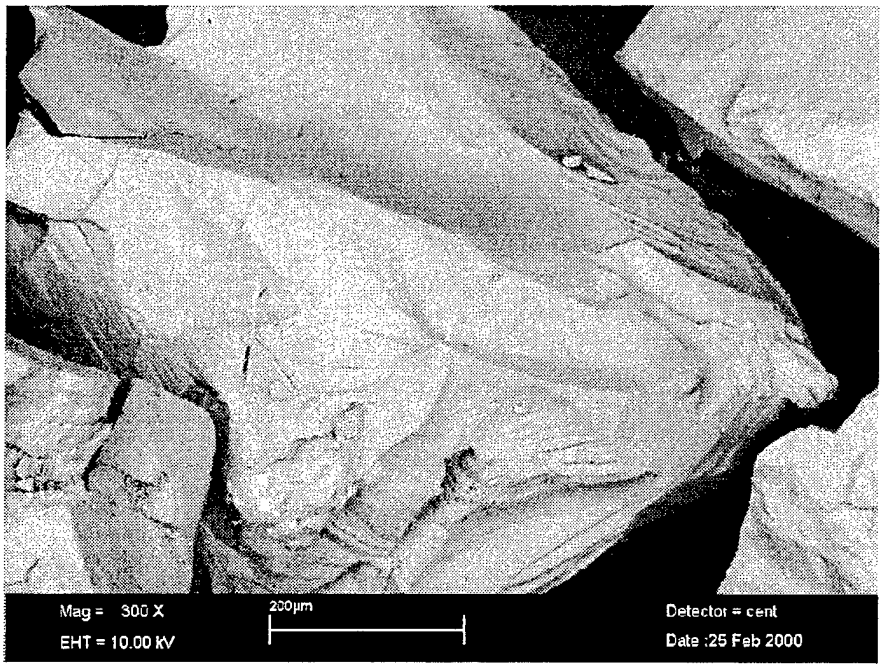

Figure 4.4: SEM image of 2010 industrial quartz (a) Magnification 100X, (b) Magnification 300X.

the HPLC (High-Pressure Liquid Chromatography) industry where it is used for the deactivation of column packing material (Runser 1981).

Silation involves the replacement of surface hydroxyl atoms with large non-polar functional groups at the molecular level. Quartz, which is the predominant mineral in natural Manchester fine sand, is a framework silicate composed entirely of silica tetrahedra where all four oxygen atoms are shared.

In natural environments surface hydroxyls form as protons are acquired to balance the negative charge from the oxygen atoms. These surface hydroxyls prefer to H-bond with water molecules that are usually present at the surface. This leads to the formation of a vicinal water layer on the surface of silicate minerals that is slightly acidic (excess of protons) at normal pH's. This arrangement is shown schematically in Figure 4.5. Silation of the silicate surface was accomplished through treatment with the silating agent Silquest A-137, which is a trade name for the chemical *octyl-triethoxysilane* (O-Si Specialties, Danbury, CT). This particular agent can deliver two ethoxy groups to each oxygen atom at the surface of the silicate. The reaction is qualitatively shown as:

$$\equiv Si-OH + C_8H_{17}Si(OC_2H_5)_3 \Rightarrow \equiv Si-O-Si(OC_2H_5)_2C_8H_{17} + C_2H_5OH \qquad (4.4)$$

Ethoxy groups are large non-polar groups consisting of an ethyl group bonded to a oxygen atom. The carrier molecule for this particular silating agent is an eight carbon chain which forms ethanol as a by-product of the reaction. As the silicon-oxygen bond formed is quite strong, the coating remains extremely stable. This accounts for the robust nature of the hydrophobic coating.

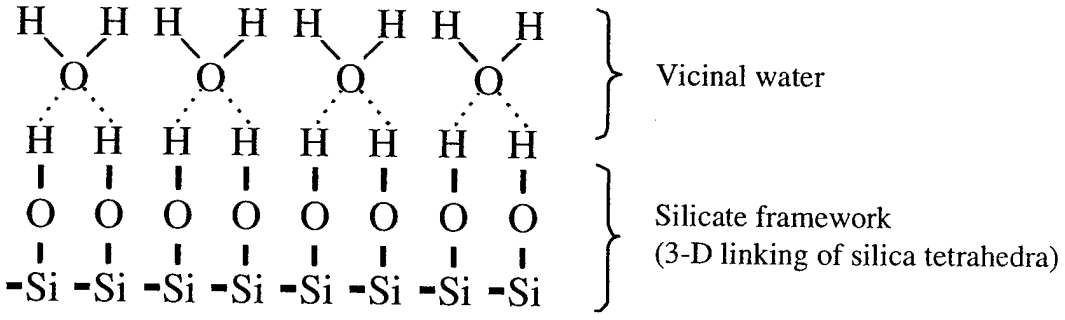

Figure 4.5: Schematic of quartz mineral surface.

The hydrophobic coating is achieved by combining 1 kg of sand in a 5% solution of octyl-triethoxysilane and ethanol and allowing it to react in a closed container for 24 hours. The sand is then allowed to air dry. No determination of the level of silane absorption was carried out although this may be done via a total carbon analysis.

The surface characteristics (i.e. roughness) of the sand were verified to be virtually unchanged from the original virgin sand through SEM analysis (Figure 4.6). It was therefore assumed that its maximum and minimum densities, as well as its specific gravity and particle size distribution, are unchanged from those for the original sand.

4.2.3.3 Polymethylmethacrylate (PMMA)

Polymethylmethacrylate (PMMA) powder was specifically chosen for tests that required a low particle modulus as compared to quartz. The quoted value of its Young's modulus in compression is 3.3 GPa (Ashby 1992). This material was obtained from its manufacturer, Goodfellow Corporation of Berwyn, PA. PMMA is an amorphous, transparent, and colorless thermoplastic that is hard and stiff, but brittle and notch sensitive. Although it is classified as a powder, its mean grain size is quoted to be 0.6 mm which is indicative of a fairly coarse granular material. Inspection under an SEM (Figure 4.7) reveals that the individual particles are almost spherical in shape and very smooth.

Figure 4.2 shows the results of a grain size analysis performed on the PMMA powder. The particle size distribution can be characterized by the following parameters: d_{10} = 0.40 mm, d_{30} = 0.53 mm, d_{50} = 0.62 mm, and d_{60} = 0.65 mm. The coefficient of uniformity is 1.625, and the coefficient of concavity is 1.080. The specific gravity of this material is 1.19 as quoted by Goodfellow Corporation. No determinations of the maximum and minimum dry densities were made due to the limited quantity and high price of this material.

4.2.3.4 Glass Beads

Two different types of glass beads were acquired for use in this program. The first type were small glass beads having a gradation similar to the industrial quartz and PMMA material described previously. These beads were manufactured by Ferro Corporation,

(a)

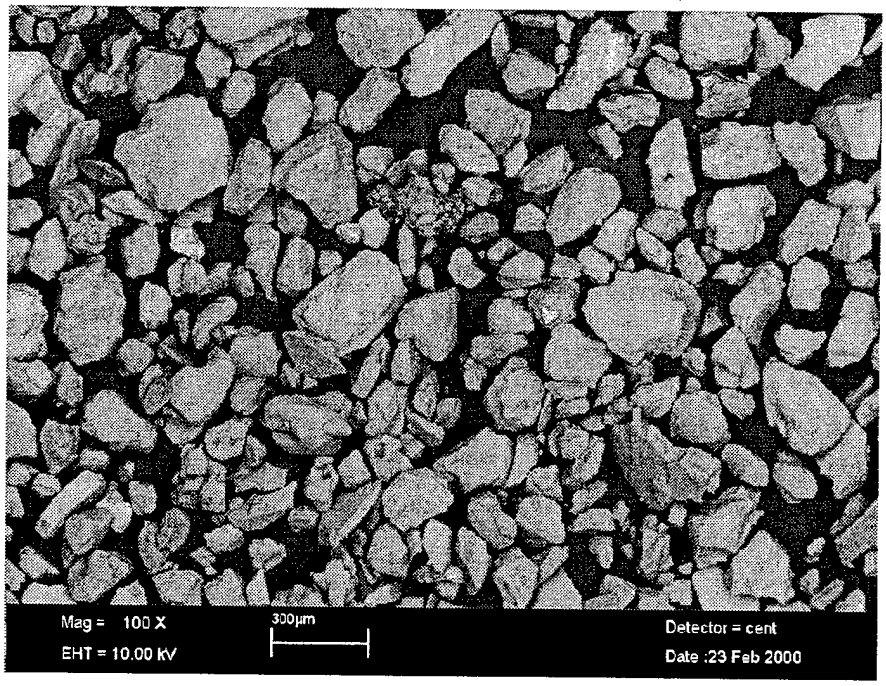

(b)

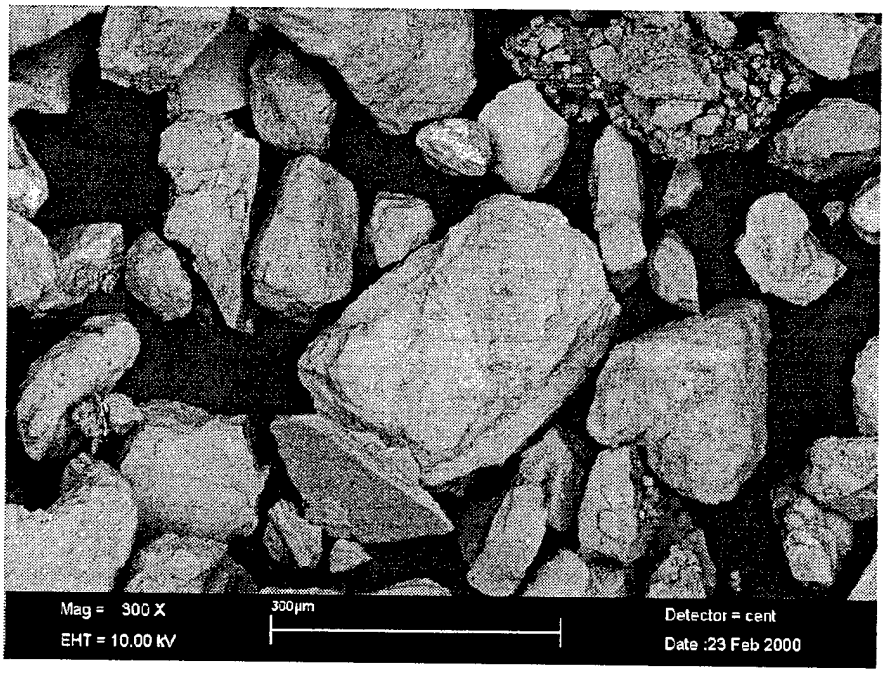

Figure 4.6: SEM image of hydrophobic Manchester fine sand (a) Magnification 100X, (b) Magnification 300X.

(a)

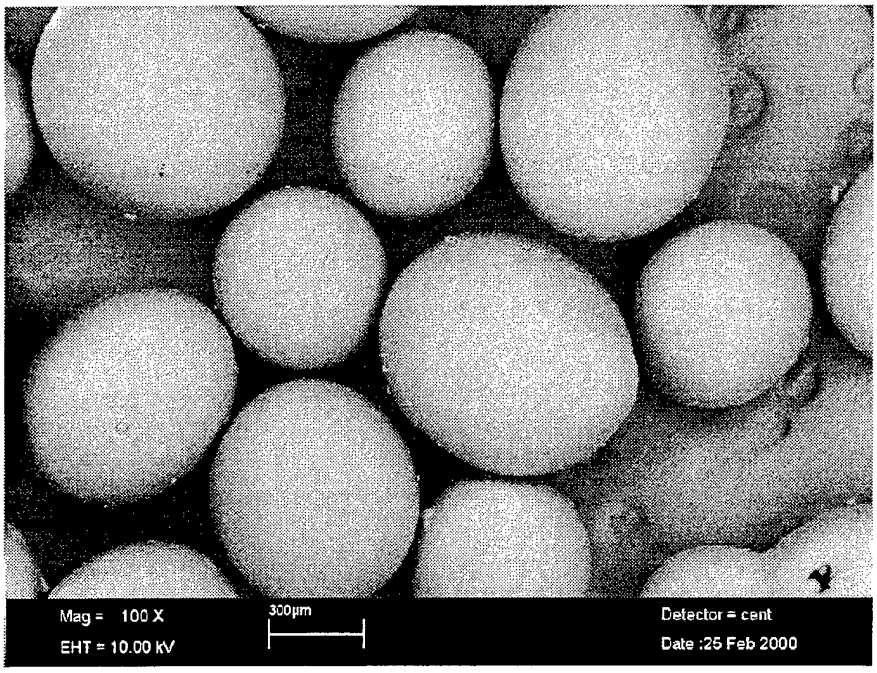

(b)

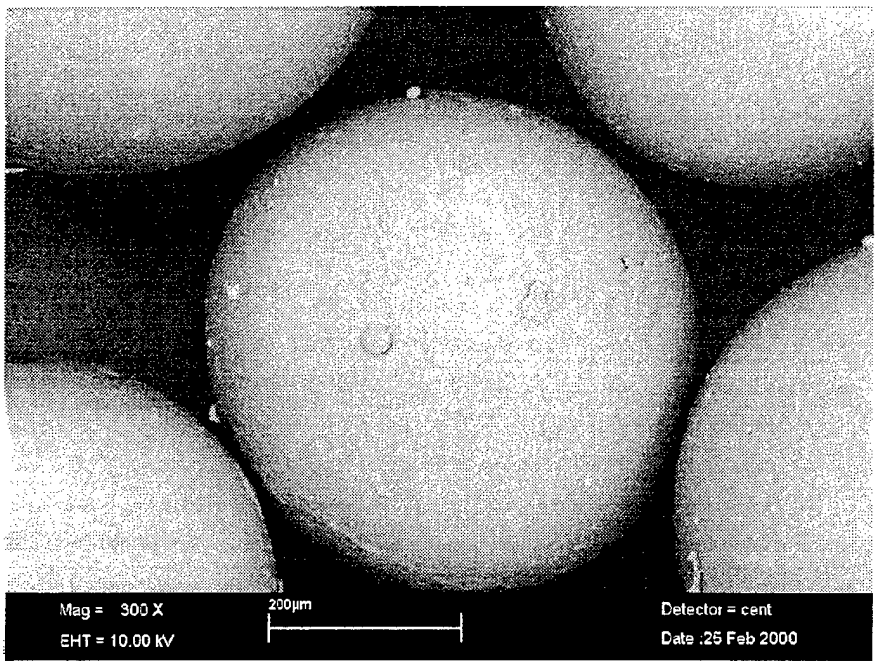

Figure 4.7: SEM image of PMMA powder (a) Magnification 100X, (b) Magnification 300X.

Cataphote Division in Jackson, Mississippi, and were originally obtained for the doctoral work of Ting (1981). The manufacturer classifies the beads as Class III Microbeads Glas-Shot (MS-XPX) and makes them from high-grade glass as an abrasive for blasting and cleaning. No information is available as to the composition of the glass. According to the manufacturers specifications, the beads are spherical in shape and contain not more than 15% of irregularly shaped particles and not more than 3% of angular particles. The size and surface texture of the beads can be seen in the SEM micrograph shown in Figure 4.8a-b.

The grain size distribution curve for this material was shown in Figure 4.2. From this curve the following parameters can be obtained: d_{10} = 0.44 mm, d_{30} = 0.49 mm, d_{50} = 0.54 mm, and d_{60} = 0.58 mm. The coefficient of uniformity is 1.32, and the coefficient of concavity is 0.94. These numbers indicate that this material is essentially mono-disperse. The specific gravity as quoted by the manufacturer is 2.51. As only a limited amount of this material was available, no determinations of the maximum and minimum dry densities were made.

In order to investigate the mechanisms controlling the modulus and strength of frozen particulate materials a number of surface treatments were applied to this material. A similar hydrophobic coating as that which was applied to the Manchester fine sand was also applied to these beads. Figure 4.8c-d shows that the application of this coating does not alter the surface roughness of the glass bead. These beads were also subject to surface roughening by acid-etching with a 48% hydrofluoric acid solution that was diluted 50/50 with distilled water. These roughened beads are shown in Figure 4.8e-f. Finally, these roughened beads were treated to make them hydrophobic (Figure 4.8g-h). As these SEM micrographs show, the hydrophobic roughened beads tend to pick up a number of the fines that were produced by the etching process.

The second type of glass beads used were obtained from VWR Scientific. These consisted of large high quality soda-lime glass beads, 3 mm in diameter, that were extremely spherical in shape. Their size and surface texture can be seen in Figure 4.9a-b. These beads were also subjected to surface modification. Surface roughening was performed by lightly grinding the beads between two abrasive corundum stones. The

(a)

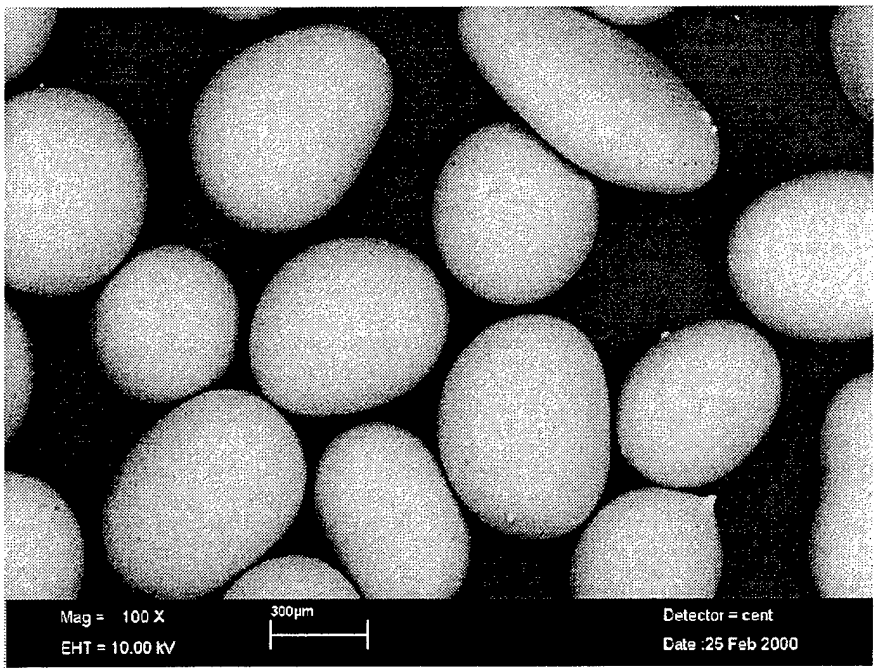

(b)

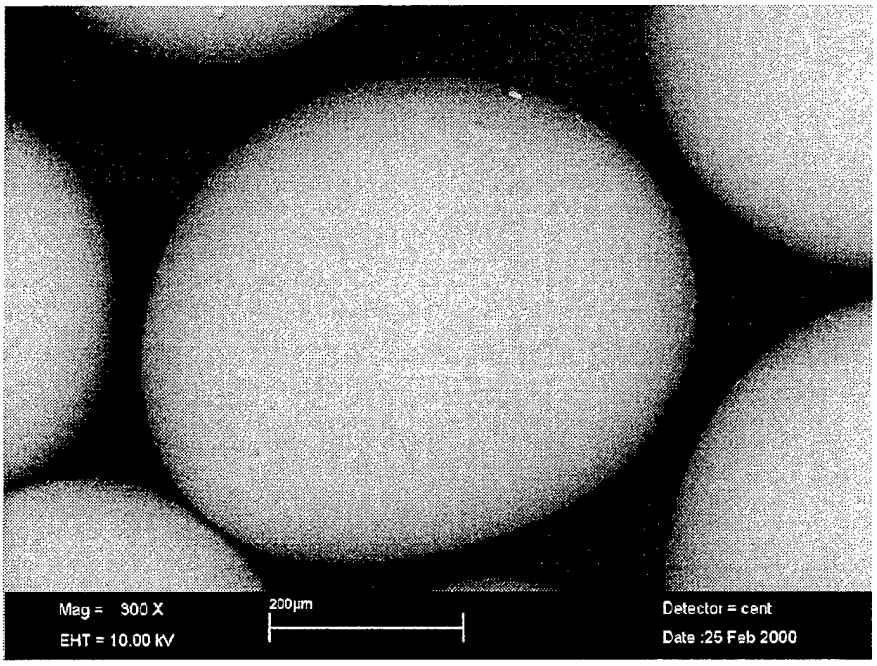

Figure 4.8: SEM image of small glass beads with various levels of treatment (a) untreated (Magnification 100X), (b) untreated (Magnification 300X).

(c)

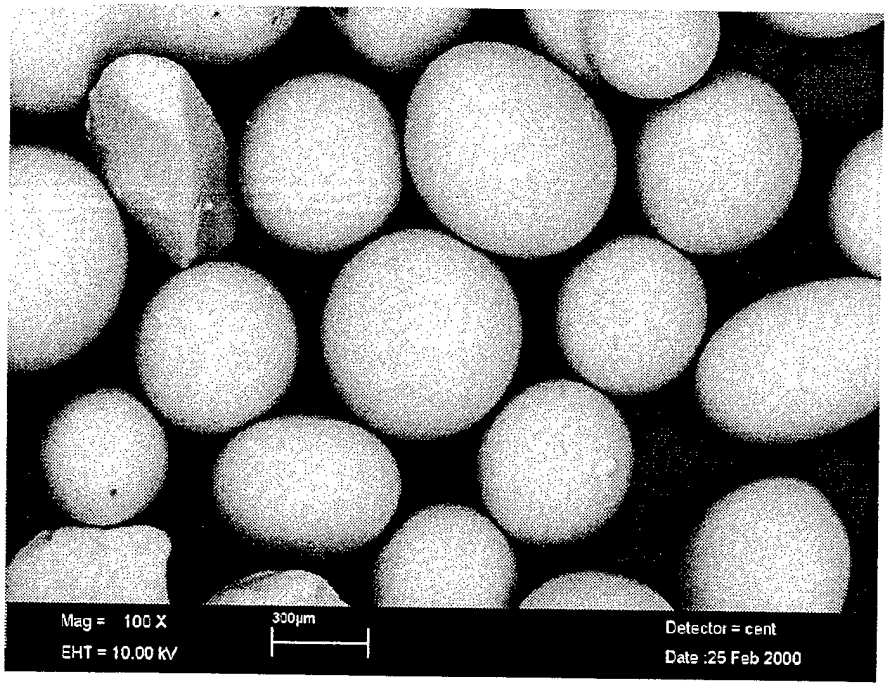

(d)

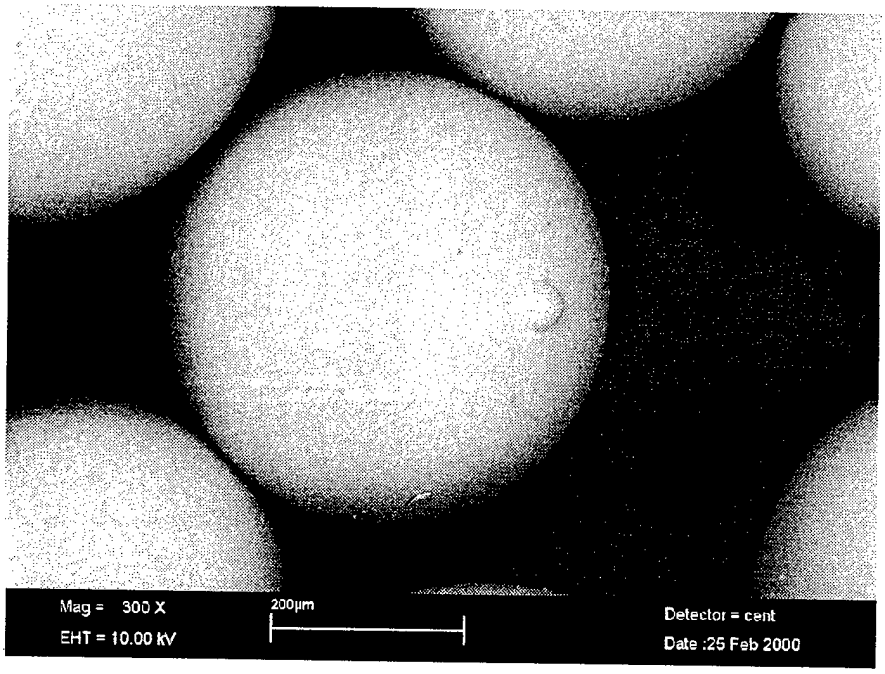

Figure 4.8: SEM image of small glass beads with various levels of treatment (c) hydrophobic (Magnification 100X), (d) hydrophobic (Magnification 300X).

(e)

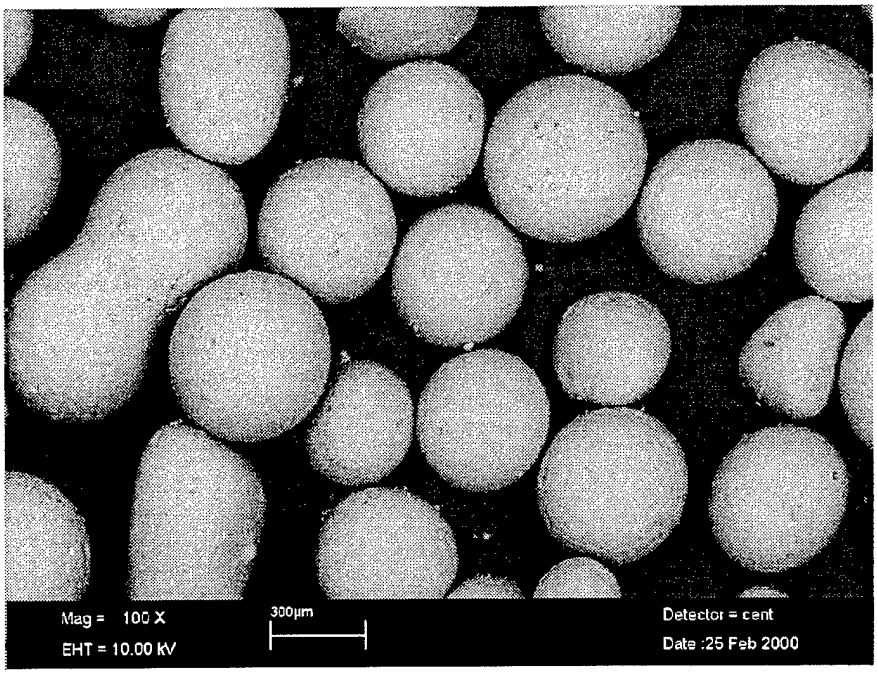

(f)

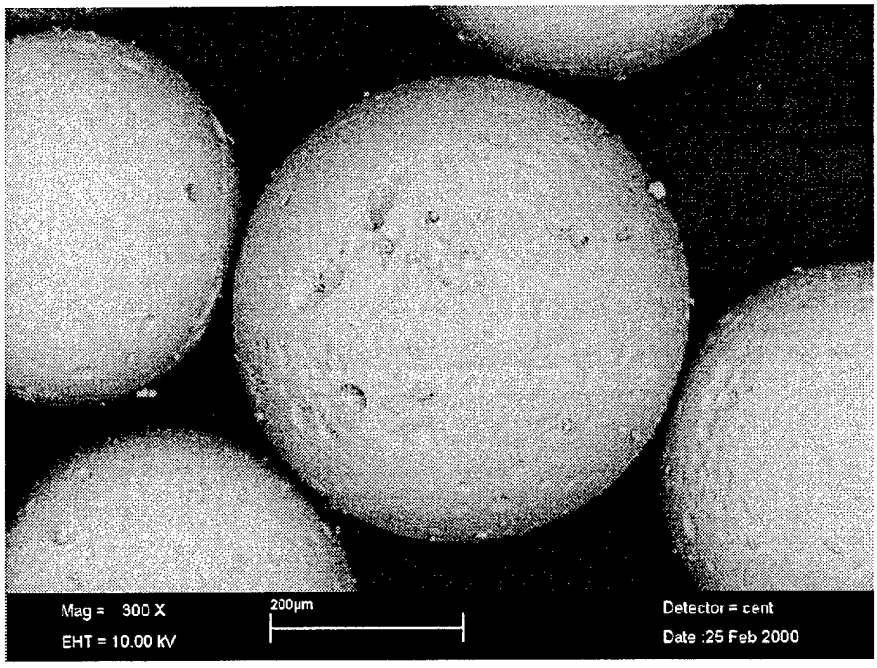

Figure 4.8: SEM image of small glass beads with various levels of treatment (e) surface roughened (Magnification 100X), (f) surface roughened (Magnification 300X).

(g)

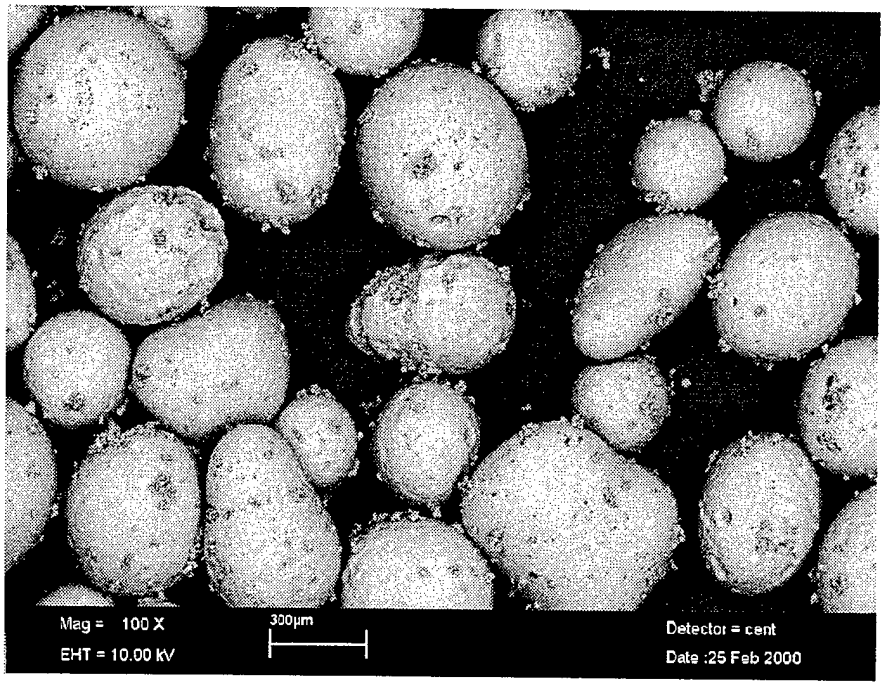

(h)

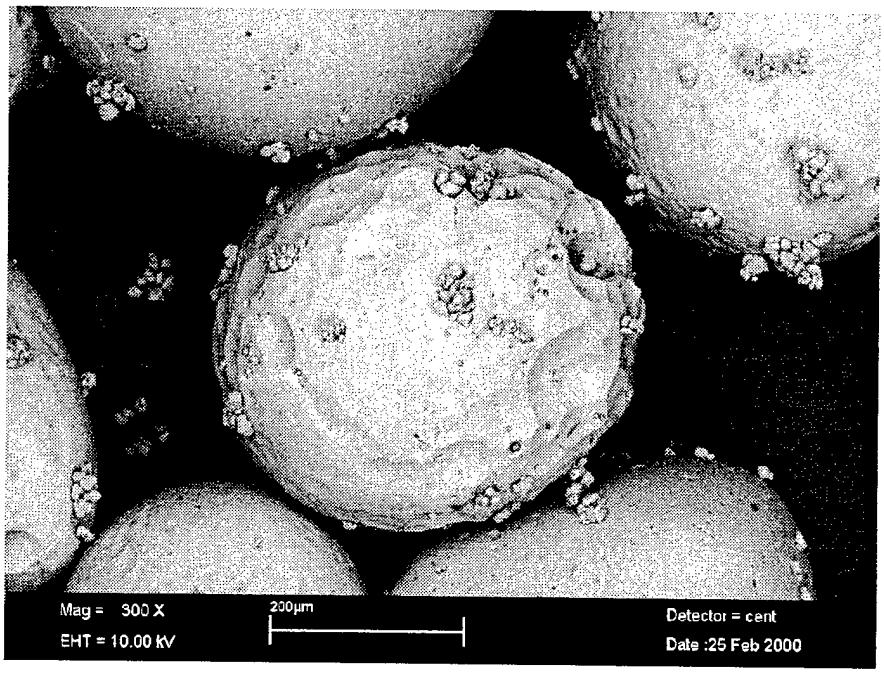

Figure 4.8: SEM image of small glass beads with various levels of treatment (g) hydrophobic surface roughened (Magnification 100X), (h) hydrophobic surface roughened (Magnification 300X).

(a)

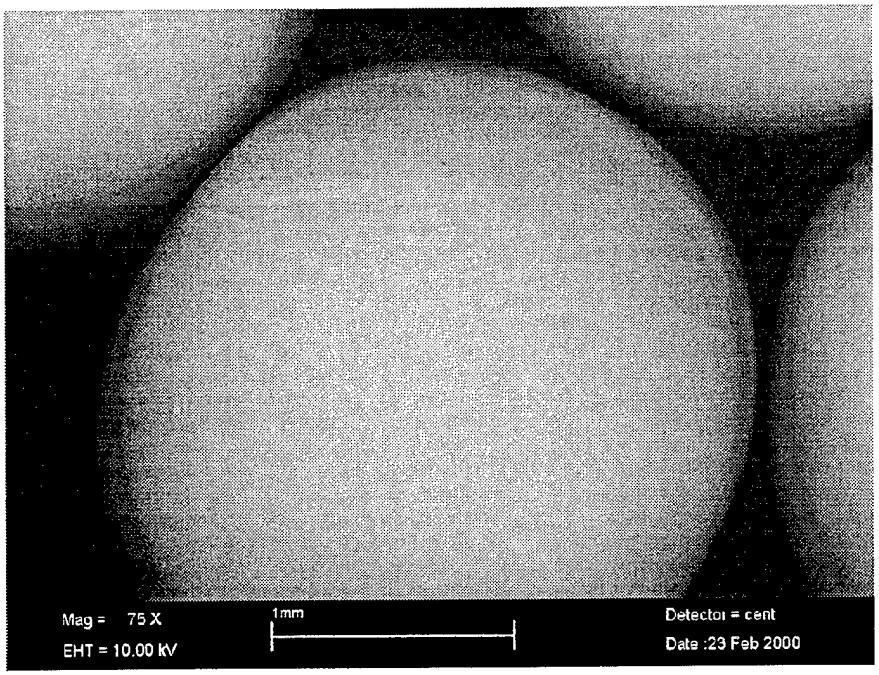

(b)

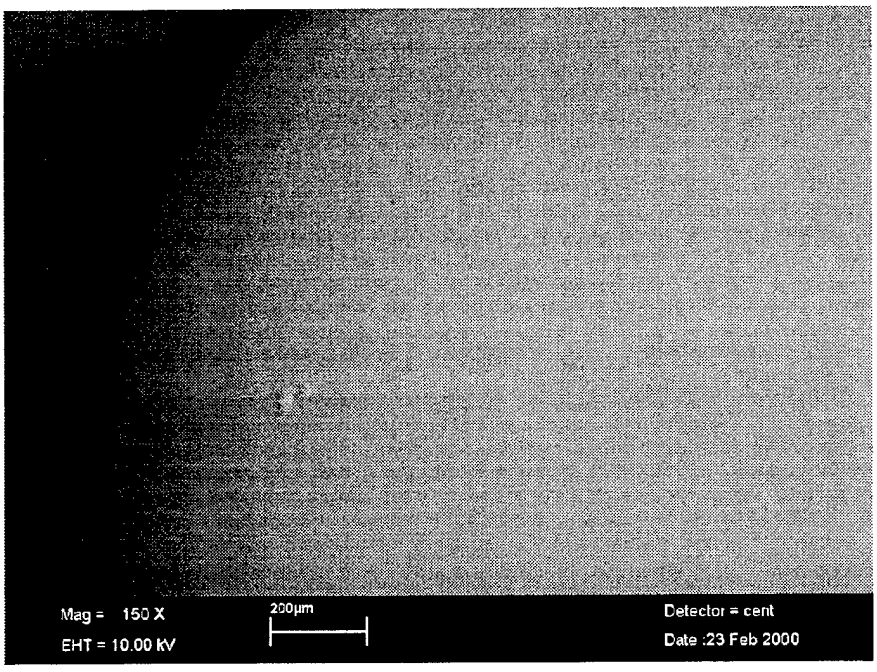

Figure 4.9: SEM image of large glass beads with various levels of treatment (a) untreated (Magnification 75X), (b) untreated (Magnification 150X).

(c)

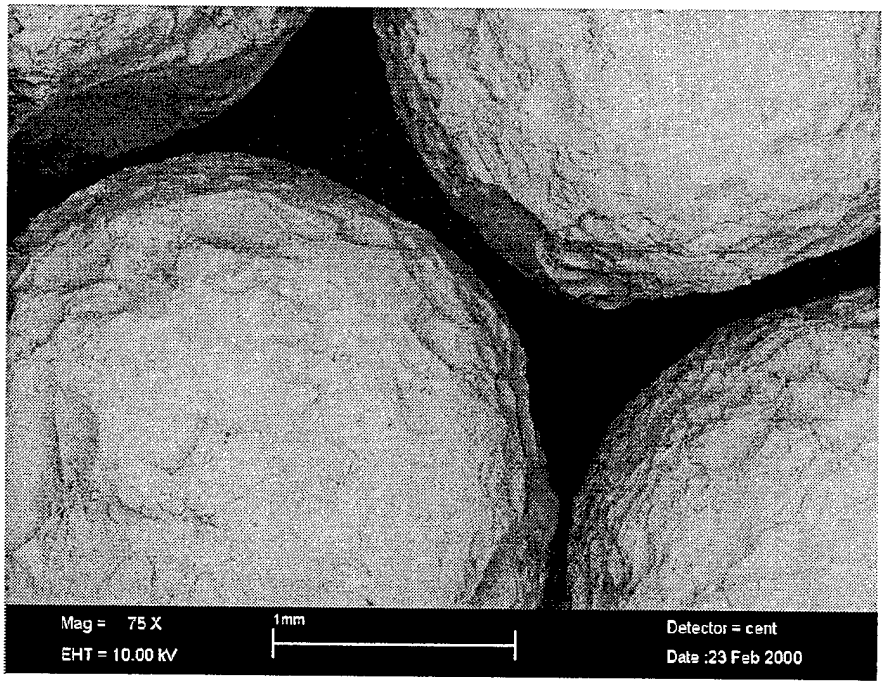

(d)

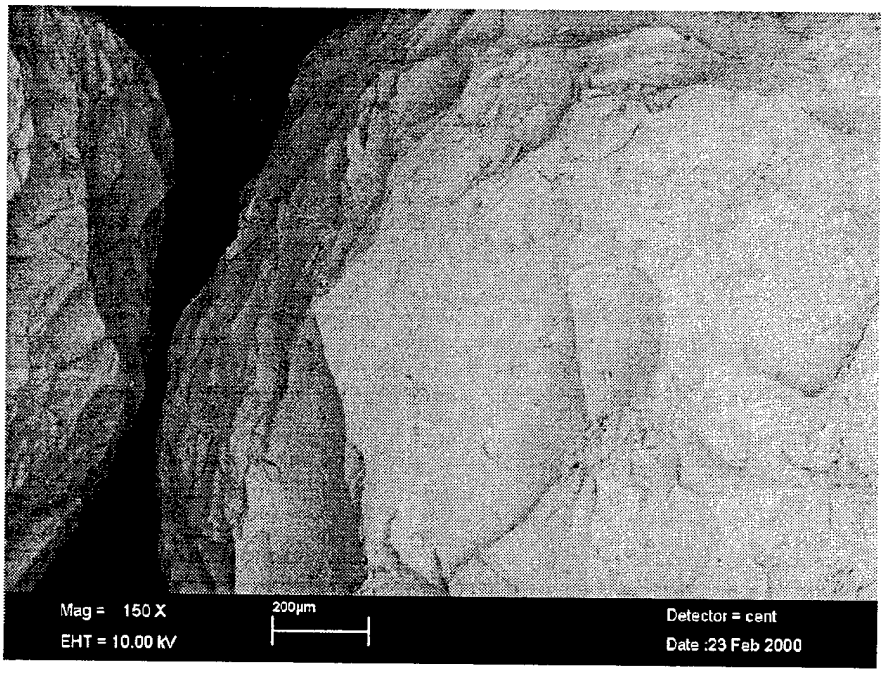

Figure 4.9: SEM image of large glass beads with various levels of treatment (c) surface roughened (Magnification 75X), (d) surface roughened (Magnification 150X).

resulting roughness is shown in Figure 4.9c-d. Subsequent hydrophobic treatment of these beads did not change the surface texture noticeably, as was shown previously for the small beads.

4.3 TRIAXIAL SPECIMEN PREPARATION TECHNIQUES

4.3.1 Introduction

The following sections provide a brief overview of both the equipment and various procedures which were followed to produce frozen specimens ready for testing in the high-pressure triaxial apparatus. While much of the procedure was adapted from previous research efforts (Andersen 1991, Swan 1994), a few alterations were made both to the apparatus and to the preparation procedures. Although the following techniques were generally applied to all the specimens, additional steps and/or method modifications were sometimes required to achieve specific results. For example, in the preparation of PMMA specimens, the freezing process generally lasted much longer due to its low thermal conductivity. Also, some specimens were put on a vibrating table after pluviation to increase their relative density. This was sometimes required as pluviation did not produce specimens of the required density. These and other minor modifications are discussed in detail in conjunction with the results of the specific testing series.

4.3.2 Equipment and Procedures

All specimens used in the frozen test program were prepared using a gang mold apparatus originally obtained from CRREL for use in earlier frozen soil research at MIT (Martin et al. 1981). Use of this particular apparatus allowed five frozen specimens to be prepared at one time. This configuration allows each specimen to be deposited, de-aired, saturated, and frozen in place. Figure 4.10 provides a detailed view of one of the molds. Prepared specimens are approximately 3.5 cm in diameter and 7.6 cm in length. Each mold consists of a thin inner split-sleeve made of Plexiglas, surrounded by a thick outer Plexiglas sleeve for stability. Soil is deposited and subsequently frozen in this inner split-sleeve. Both Plexiglas sleeves are compressed between a brass top ring and a bottom

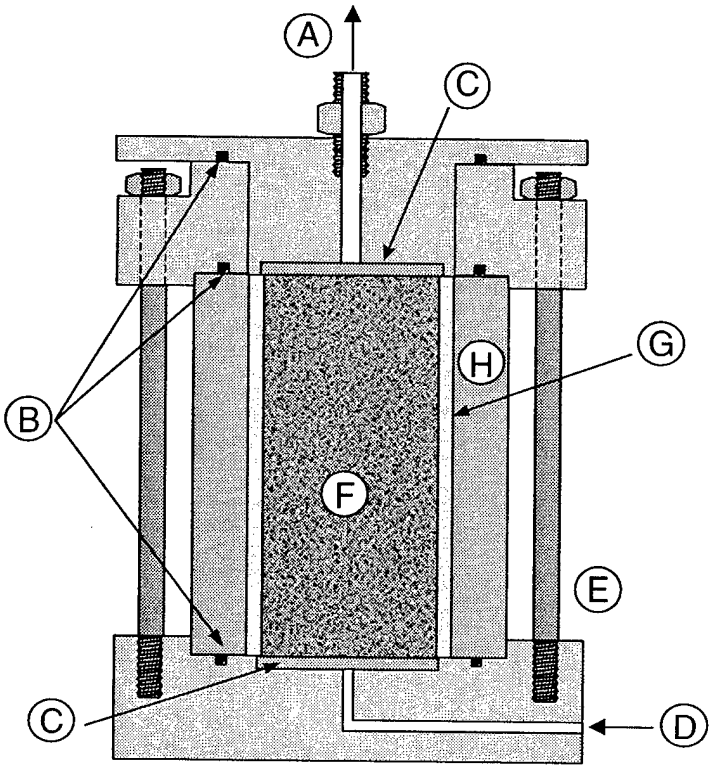

A: Water outflow C: Porous stone E: Threaded rods G: Split sleeve
B: O-rings D: Water inflow F: Soil specimen H: Lucite mold

Figure 4.10: Frozen specimen preparation mold detail.

base using four threaded rods. Rubber O-rings are used to ensure a tight fit and established a no-leak condition. The brass base holds a porous stone that supports the specimen as well as helps to distribute the water evenly throughout the specimen during saturation. The top ring provides coupling to the sand pluviation device and, once the sand is deposited, allows connection to the top cap which holds another porous stone and allows water and air to exit the specimen. Before the sand is deposited a small disc of filter paper is placed over the bottom stone in each mold to prevent the loss of fines during the saturation process, and to keep the porous stone from clogging. Most soil specimens were prepared using multiple sieve pluviation, a technique developed by Miura and Toki (1982). The pluviation setup is shown schematically in Figure 4.11. When preparing a soil specimen, oven dried material is allowed to fall freely through a small round opening in the soil reservoir (funnel) located on top of the pluviation device. The pluviation device

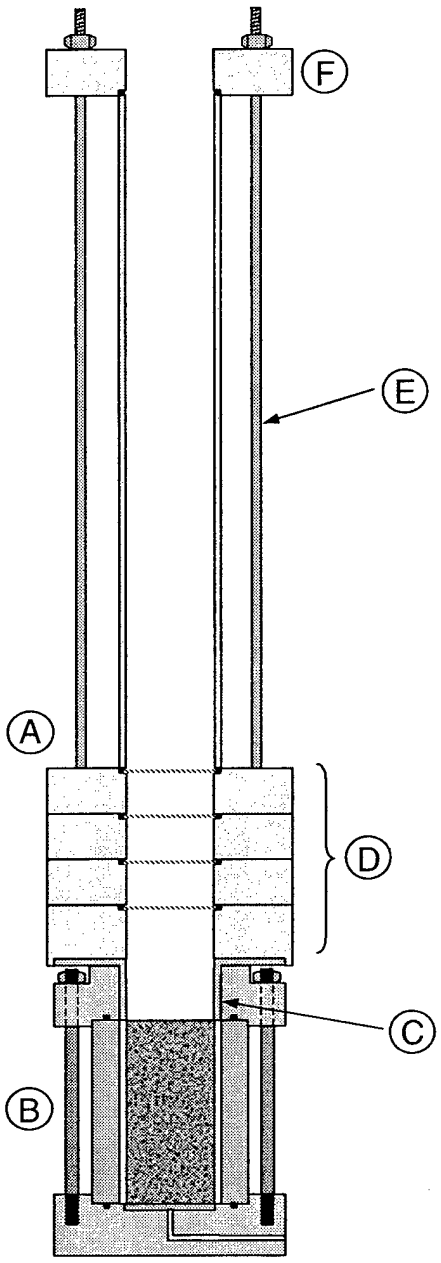

A: Pluviation device
B: Preparation mold
C: Alignment collar
D: #20 screens
E: Threaded rods (3)
F: Funnel rest

Figure 4.11: Multiple sieve pluviation technique.

consists of a hollow Plexiglas cylinder approximately 40 cm long that has four screens spaced 2 cm apart at the bottom. The four screens have openings corresponding to a No. 20 (0.850 mm) standard sieve. Soil that exits from the reservoir falls through the screens, randomly bouncing into the soil chamber to form the specimen. The rate at which the soil

falls from the reservoir determines the final density of the specimen. This rate can be altered by changing the size of the opening in the soil reservoir (funnel). Larger openings lead to faster deposition rates, and consequently to a less dense specimen.

Once the mold is filled, any excess soil is removed by vacuum until the level of the soil is flush with the top of the inner split-sleeve. A disc of filter paper is placed on top of the soil to prevent the migration of fines. The top cap of each mold is then gently connected to the top ring via four bolts. Once tightened, the gang is ready to be evacuated and subsequently saturated.

The procedure for the preparation of polycrystalline ice specimens was adapted from the CRREL technique (Cole 1979). Specimens were prepared in the same molds described above by compacting the sieved material in the molds from the bottom upwards in several layers or lifts, each about 1 cm in height. This was done inside the growth room of the Low Temperature Testing Facility at an ambient temperature of 0°C.

4.3.3 Specimen De-airing and Saturation

De-airing of the specimens is performed prior to saturation. In the preparation of soil and ice specimens the gang is taken into the growth room of the cold room facility, which is maintained at 0°C, and connected to the de-airing/saturation equipment as shown in Figure 4.12. A vacuum of 29 inches of mercury (25 torr) is drawn on the gang of five specimens and sustained for a period of 30 minutes. At this time distilled de-aired water at 0°C is introduced at the base of each mold from a reservoir of adjustable height while the specimens are maintained under vacuum. Water flow occurs upwards through the soil to a stationary collection reservoir. A total head of 50 cm is used for initial specimen saturation. After approximately 10 pore volumes have passed through each specimen, the movable reservoir is placed at the same elevation as the stationary collection reservoir. This no-flow condition is maintained for approximately 12 hours while the specimens remain under vacuum. This was found to help achieve high degrees of specimen saturation. When preparing ice specimens, this condition was maintained for only 30 minutes since longer periods led to significant ice grain melting.

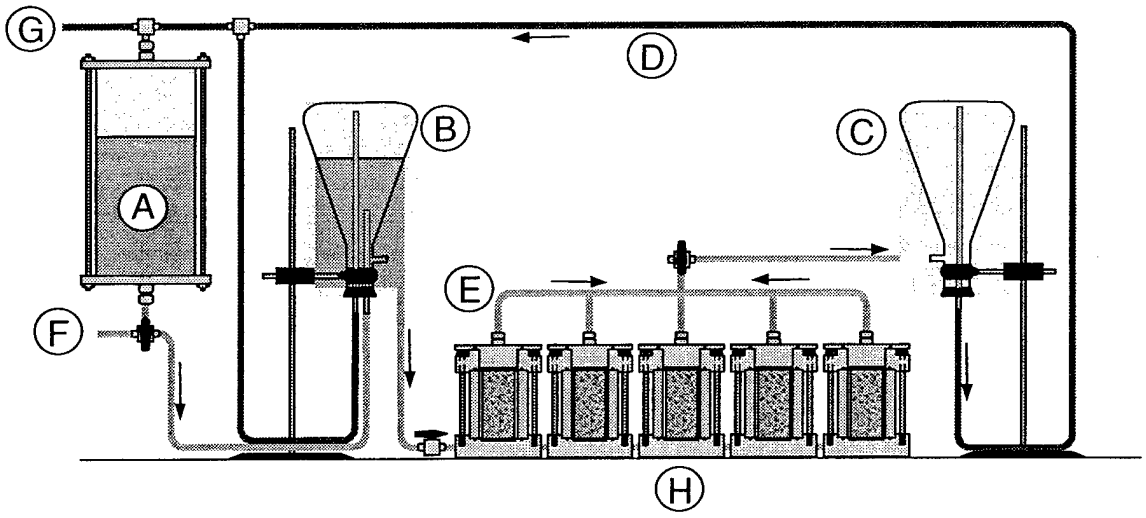

A: Deaired water reservoir
B: Movable reservoir
C: Exit reservoir
D: Vacuum line
E: Water lines
F: Water supply
G: To vacuum
H: Gang molds

Figure 4.12: Frozen specimen de-airing/saturation apparatus.

4.3.4 Specimen Freezing

Prior to freezing the movable reservoir is lowered to the level of the top of the specimens and the vacuum is slowly removed by exposing the specimens to the atmosphere through a valve connected in parallel with the top caps of the specimens. The brass top caps are removed and replaced with freezing caps (Figure 4.13). Care is taken to ensure that the top filter paper disc is retained and that the top of the specimen is kept under water to prevent de-saturation. The freezing caps are cooled internally by circulating a mixture of 75% ethylene glycol and 25% water at -15°C through them using an external Lauda refrigerating circulator (Brinkmann Instruments, Model RC-6, Westbury, NY). The specimens freeze from the top down. Drainage is allowed through the base of the molds into the movable reservoir to compensate for the increase in volume of water upon freezing. Freezing is assumed to be complete when water droplets on the outside of the brass base of each mold freeze. In general, the freezing process lasts six to eight hours.

The freezing process for ice specimens is very similar except that the freezing fluid from the circulator was maintained at -10°C instead of -15°C. This is recommended since

it promotes slow and even grain growth throughout the specimen. Even at this slightly higher temperature, freezing was generally completed within two to three hours.

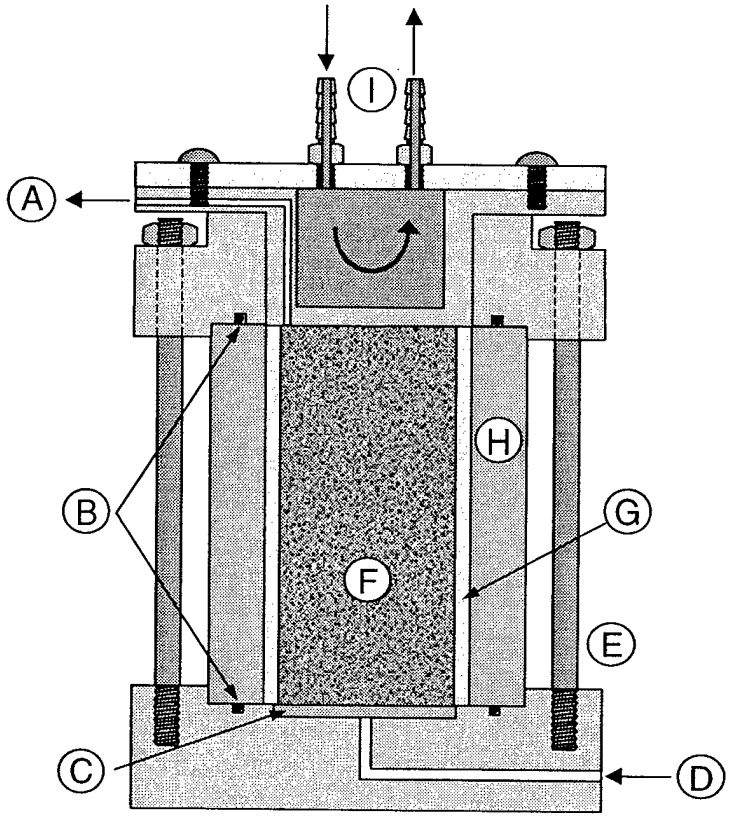

A: Vent (air/water)
B: O-rings
C: Porous stone
D: Water inlet
E: Threaded rods
F: Specimen
G: Split sleeve
H: Lucite mold
I: Glycol inlet/outlet

Figure 4.13: Freezing cap detail.

After the specimens are completely frozen, the freezing caps are removed, and the entire gang is moved into the vestibule of the Low Temperature Testing Facility where the temperature is held constant at -10°C. The top rings are unfastened and the specimens, along with their thin Plexiglas split-sleeve, are extruded from the thick outer sleeve using a Carver laboratory hydraulic jack. Each specimen and inner sleeve is wiped clean and then the exposed ends and the split-seam are covered with high-vacuum grease before being individually wrapped in aluminum foil and placed in a small plastic bag with ice. The specimens are then stored in a freezer set at -20°C until they are needed for testing. These

measures help protect the ice within the specimen from excessive sublimation while it remains in storage. Most specimens were tested within two weeks of preparation.

4.3.5 Trimming Procedures

Trimming is necessary before testing to bring the specimen to the desired length and to ensure that both ends of the sample are perpendicular to their longitudinal axis. Trimming is done by hand using sharp hardened steel knives in the vestibule of the Low Temperature Testing Facility which is maintained at -10°C. Extrusion of the specimen from the split-sleeve by hand allows both ends to be incrementally cut away, using the split-sleeve as a guide for parallelism, until the length is approximately 7.20 cm. The specimen's length is then measured at three locations with a digital caliper and then averaged to get the final length. The ends were said to be flat if the differences in length were less than 0.025 mm. Similarly, two measurements of the diameter are made at the top, middle, and bottom of the specimen. These are averaged as well to obtain the initial specimen area and hence the volume. Finally, the mass of the specimen is determined on an electronic scale sensitive to 0.01 g to obtain the initial unit weight.

To help maintain homogeneous radial deformation of the specimen during shear, lubricated end conditions were employed. These consisted of very thin ice caps that were frozen to each end of the specimen by open air freezing of distilled water. After freezing, which took approximately 20 minutes per cap, each ice cap was trimmed down to a thickness of about 0.5 mm using a sharp steel razor blade. The specimen's length was then measured again at three locations and re-trimmed if the same tolerance was not met. This new length was used to compute the average thickness of the ice caps, which generally ranged from 0.4-0.6 mm for most tests. The last step consisted of drilling a small hole, 1.5 mm in diameter and 3 mm deep, in the center of each end to allow mating with similar sized pins located on the triaxial base and top cap. This was found to greatly aid in aligning the specimen in the triaxial cell, which consequently increased the specimen's stability during shear.

4.4 REFERENCES

1. Andersen, G.R. (1991), "Physical Mechanisms Controlling the Strength and Deformation Behavior of Frozen Sand", Sc.D Thesis, Department of Civil and Environmental Engineering, MIT, Cambridge, MA, 560 p.

2. Ashby, M.F. (1992), *Materials Selection in Mechanical Design*, Pergamon Press, Oxford.

3. ASTM. (1997a), "Particle-Size Analysis for Soils (D 422-63)", *Annual Book of ASTM Standards*, v. 4.08, no. 4, pp. 10-16.

4. ASTM. (1997b), "Moisture, Ash, and Organic Matter of Peat and Other Organic Soils (D 2974-87)", *Annual Book of ASTM Standards*, v. 4.08, no. 4, pp. 285-287.

5. ASTM. (1997c), "Maximum Index Density and Unit Weight of Soils Using a Vibratory Table (D 4253-93)", *Annual Book of ASTM Standards*, v. 4.08, no. 4, pp. 501-513.

6. ASTM. (1997d), "Minimum Index Density and Unit Weight of Soils and Calculation of Relative Density (D 4254-91)", *Annual Book of ASTM Standards*, v. 4.08, no. 4, pp. 514-521.

7. ASTM. (1997e), "Specific Gravity of Soils (D 854-92)", *Annual Book of ASTM Standards*, v. 4.09, no. 4, pp. 337-343.

8. Cole, D.M. (1979), "Preparation of Polycrystalline Ice Specimens for Laboratory Experiments", *Cold Regions Science and Technology*, v.1, no.2, pp. 153-159.

9. Dieter, C.E. (1976), *Mechanical Metallurgy*, McGraw-Hill, New York.

10. Martin, R.T., Ting, J.M., Ladd, C.C. (1981), "Part I: Creep Behavior of Frozen Sand", Final Report No. R81-19, Department of Civil Engineering, MIT, Cambridge, MA, 253 p.

11. Miura, S. and Toki, S. (1982), "A Sample Preparation Method and Its Effect on Strength Properties of Sand", *Soils and Foundations*, v.22, no.1, pp. 61-77.

12. Runser, D.J. (1981), *Maintaining and Troubleshooting HPLC Systems: A User's Guide*, John Wiley and Sons, New York.

13. Sinfield, J.V. (1997), "Fluorescence of Contaminants in Soil and Groundwater Using a Time-Resolved Microchip Laser System", Sc.D Thesis, Department of Civil and Environmental Engineering, MIT, Cambridge, MA, 428 p.

14. Swan, C. (1994), "Physical Mechanisms Controlling the Deformation and Strength Behavior of Unfrozen and Frozen Manchester Fine Sand", Sc.D Thesis, Department of Civil and Environmental Engineering, MIT, Cambridge, MA, 1044 p.

15. Ting, J.M. (1981), "The Creep of Frozen Sands: Qualitative and Quantitative Models", Sc.D. Thesis, Department of Civil Engineering, MIT, Cambridge, MA, 432 p.

CHAPTER 5

RESEARCH METHODOLOGY

5.1 INTRODUCTION

The purpose of the experimental program is to obtain a better understanding of the physical mechanisms that control frozen sand behavior at small strains, and to extend the data set on the behavior of frozen systems for future modeling purposes. This chapter discusses the research methodology employed to obtain these objectives. This methodology had essentially three components: 1) *conduct* a comprehensive experimental program to precisely measure the behavior of frozen sand and other frozen particulate materials over a wide range of testing conditions, 2) *explain* the mechanisms responsible for the small strain behavior (Young's modulus and upper yield stress) of frozen sand from knowledge of the general behavior of polycrystalline ice and of the measured stress-strain behavior of the same sand in an unfrozen state, and 3) *employ* composite material models where possible to quantify the physical mechanisms responsible for the macro-behavior of frozen sands.

Section 5.2 discusses the variables investigated in the experimental program, the reasons behind their choice, and what is hoped to be gained by their study. This is followed in Section 5.3 by the general testing procedures which were followed for both the triaxial and adhesional testing programs. Section 5.4 summarizes the experimental program of triaxial compression tests. A description of the data handling techniques is presented in Section 5.5 to explain how pertinent test information was obtained in terms of engineering units. Finally, material referenced in this chapter is listed in Section 5.6.

5.2 VARIABLES INVESTIGATED

5.2.1 Introduction

Understanding of the mechanisms responsible for the small strain behavior of frozen sands first requires investigation of the variables that affect its stress-strain behavior. Andersen (1991) and Swan (1994) provided the first data set from conventional

frozen tests that completely characterize the behavior of Manchester fine sand in triaxial compression as a function of sand density, confining pressure, strain rate and temperature. Analysis of that unique set of experimental data has led to the development of several important conclusions and working hypotheses regarding the strength-deformation behavior of frozen sand systems, yet has also raised some questions regarding the mechanisms responsible for the observed behavior.

Thus, the focus of this experimental program was to develop a more comprehensive understanding of the physical mechanisms controlling the stress-strain-time-temperature behavior of frozen particulate systems. This involved investigating the impact of a number of additional parameters such as particle grain size, shape, roughness, and modulus, as well as interface adhesion. Table 5.1 outlines how each of the materials described in Chapter 4 was used to address these additional parameters. A detailed explanation of the significance of all the variables studied during this experimental program, as well the rationale behind their selection, is given in the following sections. Where appropriate, a description of the particular testing program (i.e. number of tests performed, materials used, test conditions, etc.) is also included.

Variable Investigated	Material Type
Void ratio/relative density	All materials
Confinement	MFS, industrial quartz (2010/2075)
Strain rate	All materials, but predominately MFS
Temperature	All materials, but predominately MFS
Particle modulus	PMMA
Particle grain size	Industrial quartz (2010/2075)
Interface adhesion	Hydrophobic MFS and glass beads
Particle roughness	Glass Beads (small and large)

Table 5.1: Summary of research approach for variables investigated during current research program.

5.2.2 Void Ratio/Relative Density

Perhaps the most important parameter which governs the stress-strain behavior of frozen sands, and composite materials in general, is the relative volume fraction of aggregate particles embedded within the matrix. This is often quoted in terms of relative density, if the maximum and minimum void ratios are known. Otherwise quantification in

terms of void ratio or porosity is most relevant. This is especially useful when comparing a number of different materials such as in this research program.

Previous experimental research in this area has shown that the Young's modulus of frozen sand increases with increasing sand density (Baker and Kurfurst 1985). This has been confirmed with the use of a composite material model (Counto 1964) by Andersen et al. (1995). Sand density has also been found to significantly affect the behavior at large strains by influencing whether the system strain hardens or strain softens after reaching the upper yield stress.

At the upper yield stress, however, conflicting results seem to exist since Zhu and Carbee (1984) found that the upper yield stress decreased with increasing sand density for a frozen silt, whereas Swan (1994) found no influence of any frictional component at this point for Manchester fine sand. Thus, the main goal of this aspect of the experimental program is to determine, via tests on a number of different particulate materials, if in fact the volume fraction does affect the upper yield stress.

Although this parameter was not systematically varied during the testing programs, efforts were taken to try to prepare specimens over as wide of a range as possible for each of the materials tested. However, due to the type of preparation method used, most of the specimens that resulted were somewhat dense. Nevertheless, for each material investigated, variations in void ratio did occur thereby allowing its influence on both the composite modulus and upper yield stress to be evaluated. Appendix B lists the void ratio, and relative density where appropriate, for each test performed.

5.2.3 Confinement Level

It is well-known that the frictional characteristics of the sand skeleton (i.e. density and confinement) play a major role in the undrained behavior of unfrozen sands. However, tests on frozen Manchester fine sand by Andersen (1991) and Swan (1994) indicated no evidence of a sand skeleton frictional component at the upper yield stress. Conversely, a number of other programs which tested coarser-grained sands observed some degree of pressure sensitivity at the upper yield stress (e.g., Sayles 1973, Chamberlain et al. 1972, Parameswaran and Jones 1981). The uncertainty surrounding the

influence of confinement at the upper yield stress may be due to particle size effects which may alter the ice grain size and strength. This is discussed in detail in Section 5.2.7.

While the role of confinement at small strains may be unclear, its role at larger strains is very clear. As Figure 2.21 shows, both relative density and confinement greatly affects the post-upper yield behavior. Moreover, confinement also affects the peak strength of bulk polycrystalline ice in the ductile to brittle regime by suppressing internal cracking. Therefore in an effort to better understand and quantify the effects of confinement on frozen sand it has been included as a major testing variable.

Table 5.2 summarizes the number of tests performed at each nominal confining pressure for each material investigated. Exact applied values are listed for each test in Appendix B. In most cases the average actual confining pressure used during a test did not deviate from the nominal value by more than 0.01 MPa. As the data in the table shows, the majority of the tests were performed at either low confinement (0.5 MPa) or high confinement (10 MPa) in order to bound the range of behavior.

	Confining Pressure, σ_c (MPa)							
Material Type	**0.1**	**0.5**	**1**	**2**	**5**	**7.5**	**10**	**12.5**
Manchester fine sand (MFS)	2	10	5	4	3	N/A	13	N/A
Hydrophobic MFS	N/A	7	N/A	N/A	N/A	N/A	7	N/A
Industrial quartz (2010/2075)	1	3	1	4	5	1	5	6
PMMA	N/A	10	N/A	N/A	1	N/A	7	N/A
Glass beads	N/A	2	N/A	N/A	N/A	N/A	3	N/A
Hydrophobic glass beads	N/A	2	N/A	N/A	N/A	N/A	2	N/A
Hydrophobic rough beads	N/A	5	N/A	N/A	N/A	N/A	4	N/A
Large glass beads (all)	N/A	5	N/A	N/A	N/A	N/A	N/A	N/A
Polycrystalline ice	N/A	4	N/A	N/A	N/A	N/A	4	N/A

Table 5.2: Number of tests performed for all materials at each confining pressure investigated.

5.2.4 Strain Rate

Investigation of the effects of strain rate was also performed as part of this research program with the goal of determining if the Young's modulus of frozen sands exhibits strain rate sensitivity. Most of the prior experimental programs that have investigated the effects of strain rate found that the Young's modulus increases with increasing strain rate (e.g., Parameswaran 1980, Zhu et al. 1988). Similarly, reverse

direct-stress testing of polycrystalline ice, one of the main components of frozen sands, at similar strain rates and temperatures show variations in Young's modulus with frequency of cyclic loading (Cole 1990). In contrast, prior research at MIT on Manchester fine sand by Andersen et al. (1995) showed that the Young's modulus of this material was independent of strain rate in the range of rates investigated. Hence, there is some discrepancy in the literature as to whether the Young's modulus of frozen granular materials exhibit strain rate sensitivity.

One potential reason why many of the previous programs found a strain rate dependency in Young's modulus is that they were made at much higher levels of strain and as a result include nonlinear plastic deformations, which have been shown to be rate dependent (Swan 1994). Hence, the author believes that those programs do not provide reliable values of the initial stiffness. Modulus determinations must be made with the use of on-specimen strain measurement devices capable of resolving the strains necessary to capture the initial linear response of frozen soil (approximately 0.002% for Manchester fine sand). Similarly, true measurements of strain rate must be made using on-specimen measured strains.

Due to limitations in the testing equipment, only a relatively small range of strain rates were investigated. The current testing program utilized only two rates, 3.0×10^{-6} s^{-1} (slow) and 3.5×10^{-5} s^{-1} (moderate), with the latter extending slightly into the ductile to brittle transition regime for polycrystalline ice as -10°C. Data from Andersen et al. (1995) also included strain rates extending approximately an order of magnitude higher (5×10^{-4} s^{-1}). At this rate ice behavior begins to exhibit brittle characteristics. Table 5.3 summarizes the number of tests performed at each strain rate for each material investigated during this experimental program.

The rates quoted within Table 5.3 should be interpreted as the nominal testing rates as the strain rates exhibited some variability during shear, especially during the initial portion of the test. This is primarily due to the implementation of the PID control algorithm that uses the on-specimen LVDT's as a feedback source. This was discussed in detail in Section 3.3.3.4. This has resulted in a marked decrease in the amount of strain (or time) needed to reach a constant strain rate, yet has led to small oscillations in the rate

during the initial stages of shear. An example of the improvement in strain rate control for the two strain rates investigated during this program was shown previously in Figure 3.5. Although nominal strain rates have been quoted in Table 5.3, instantaneous strain rates computed at the 0.01% yield offset stress have been used for subsequent analyses involving Young's modulus. Similarly, strain rates computed at the upper yield stress have been used in analyses involving the behavior in the upper yield region. These strain rates have been tabulated for each test in Appendix B.

	Strain Rate, $\dot{\varepsilon}$ (s^{-1})		
Material Type	**Slow**	**Moderate**	**Fast**
Manchester fine sand (MFS)	12	25	N/A
Hydrophobic MFS	6	8	N/A
Industrial quartz (2010/2075)	7	19	N/A
PMMA	9	9	N/A
Glass beads	2	3	N/A
Hydrophobic glass beads	2	2	N/A
Hydrophobic rough beads	3	6	N/A
Large glass beads (all)	N/A	5	N/A
Polycrystalline ice	4	4	N/A

Table 5.3: Range of strain rates examined during testing program. Note: slow = 3.0×10^{-6} s^{-1}, moderate = 3.5×10^{-5} s^{-1}, fast = 5×10^{-4} s^{-1} (number of tests shown for each condition).

5.2.5 Temperature

Test temperature was the last of the main testing variables which was investigated as part of this experimental program. An extensive characterization of the behavior of Manchester fine sand at -10°C was first undertaken by Andersen (1991). It was later extended by Swan (1994) to include tests at -15°C, -20°C, and -25°C.

One of the goals of this program was to extend the temperature database to include tests at warmer temperatures in order to encompass the conditions more representative of permafrost, and to where the behavior of bulk ice may differ from that at colder temperatures. Another goal was to check temperature dependent trends already obtained from lower temperature testing. Andersen et al. (1995) found that the Young's modulus of frozen Manchester fine sand is insensitive to temperature, whereas other

researchers (e.g., Zhu and Carbee 1984, Shibata et al. 1985) concluded that modulus increases with decreasing temperature in a manner similar to bulk polycrystalline ice.

As indicated in Table 5.4, tests were conducted at temperatures of -2°C, -5°C and -10°C during this experimental program. Most of the warmer temperature tests were restricted to Manchester fine sand while the majority of the tests performed on other materials were conducted at -10°C such that their results could be compared to the already extensive databases on Manchester fine sand and ice which exist in the literature. Table 5.4 lists the temperatures investigated for each material investigated during this program. The temperatures quoted in Table 5.4 should be interpreted as the nominal testing temperatures since the actual temperature varied from test to test. Table 3.3, presented previously, gives a summary of the actual testing temperatures.

	Temperature (°C)		
Material Type	**-2°C**	**-5°C**	**-10°C**
Manchester fine sand (MFS)	5	14	18
Hydrophobic MFS	N/A	4	10
Industrial quartz (2010/2075)	N/A	7	19
PMMA	N/A	7	11
Glass beads	N/A	N/A	5
Hydrophobic glass beads	N/A	N/A	4
Hydrophobic rough beads	N/A	N/A	9
Large glass beads (all)	N/A	N/A	5
Polycrystalline ice	N/A	4	4

Table 5.4: Number of tests performed for each material for each temperature investigated.

5.2.6 Particle Modulus

Another important aspect of this research program was to investigate the importance of particle modulus on the composite modulus and upper yield stress of frozen materials. An understanding of how the stiffness of composite materials is developed from its constituents is invaluable for predicting the stiffness and hence the engineering behavior of naturally occurring frozen soils. This aspect was initiated after Andersen et al. (1995) showed that Counto's (1964) isostrain composite material model, originally developed for predicting the Young's modulus of concrete, could describe the modulus of frozen sand quite well.

Counto's model neglects the structure of the overall skeleton and considers only the stiffness of the matrix and particles, the relative volume fraction of particles, and assumes full adhesion at the interface between phases. A complete description of this model was presented in Section 2.4.2. The model was shown to correctly predict the modulus of frozen Manchester fine sand and its trend with relative density by Andersen et al. (1995). In order to evaluate the accuracy of this and the other models presented in Section 2.4.2, a testing program was initiated on granular PMMA, a polymer with an extremely low modulus. This provided another composite system that could be used for model verification. Table 5.5 summarizes the experimental program on PMMA which consisted of 18 tests.

Confinement, σ_c	Temp. = -5°C		Temp. = -10°C	
(MPa)	Slow $\dot{\varepsilon}$	Moderate $\dot{\varepsilon}$	Slow $\dot{\varepsilon}$	Moderate $\dot{\varepsilon}$
0.5	2	1	2	5
10	3	1	2	2

Table 5.5: PMMA testing program (number of tests shown for each condition).

5.2.7 Particle Grain Size

As discussed in Section 2.3.4.1, good experimental evidence exists that shows that the upper yield behavior of frozen sand is dominated by the ice matrix. However, the strength of Manchester fine sand is much larger than the strength of bulk polycrystalline ice, as shown in Figure 2.27. Consequently the presence of the sand particles must cause a strengthening effect even though the frictional resistance of the sand skeleton appears to be unimportant as evidenced by the insensitivity of the upper yield to changes in relative density and confinement, and the negligible undrained shear resistance of unfrozen Manchester fine sand. It is also important to note that the peak strength of ice shows a confining pressure sensitivity (Figure 2.10) unlike the upper yield stress of frozen Manchester fine sand. Furthermore, other research (e.g., Sayles 1973, Parameswaran and Jones 1981) shows that some frozen coarse-grained sands behave differently than finer-grained materials, displaying a large pressure sensitivity in the upper yield region (Figure 2.24).

Since these differences may be related to the grain size of ice in frozen sands, this aspect of the experimental program involved testing industrial quartz (Figure 4.4), a coarser-grained quartz sand similar to the Ottawa sand tested in other programs. This assumes that ice within frozen soils is polycrystalline, and that grain size effects in frozen sands can be investigated by simply altering the sand particle size. While measurements of the ice fabric in frozen Manchester fine sand have not been made, Ting et al. (1983) suggest that, as long as no segregational freezing occurs, the maximum grain size is probably the pore size.

The goals of this testing program were to assess if these coarser-grained frozen sand specimens showed a pressure dependence at the upper yield stress, and to quantify the extent of ice matrix strengthening over that of bulk polycrystalline ice. Table 5.6 details the conditions of the industrial quartz testing program which consisted of 26 tests.

Confinement, σ_c	Temp. = -5°C		Temp. = -10°C	
(MPa)	Slow $\dot{\varepsilon}$	Moderate $\dot{\varepsilon}$	Slow $\dot{\varepsilon}$	Moderate $\dot{\varepsilon}$
0.1	N/A	N/A	N/A	1
0.5	N/A	1	1	1
1	N/A	N/A	N/A	1
2	N/A	1	1	2
5	N/A	1	1	3
7.5	N/A	N/A	N/A	1
10	N/A	1	2	2
12.5	1	2	1	2

Table 5.6: Industrial quartz testing program (number of tests shown for each condition).

5.2.8 Interface Adhesion

The primary goal of this program was to determine whether the presence of an adhesional bond is important to the composite modulus and upper yield stress of frozen particulate systems.

As discussed in Section 5.2.6, many of the composite material models that exist for predicting the modulus of a two-phase composite assume perfect bonding between phases, or in this case, between the ice matrix and individual particles. This implies that the adhesional strength is sufficient to transmit the shear stresses necessary to enable composite action, thus causing the frozen sand to behave as a composite material at very

small strains. This helps explain why the Young's modulus of frozen sand is much greater than either of its two components. In addition, bonding between the ice and the sand grains may be one of the physical mechanisms that causes the ice matrix to have an effective strength that is much larger than bulk polycrystalline ice.

In order to investigate and ideally quantify the importance of the adhesional strength between the particles and the ice matrix, a hydrophobic, and presumably icephobic, treatment was applied to systems of Manchester fine sand and glass beads (small and large). SEM analysis was used to confirm that the coating did not alter the surface texture of the particles, and hence the frictional behavior of the systems. Investigation of glass bead systems allows a more accurate assessment of the importance of adhesional strength, since strength due to particle interlocking is less prevalent. Table 5.7 summarizes the experimental program on these materials.

	Temp. = -5°C		Temp. = -10°C	
Material Type	**Slow $\dot{\varepsilon}$**	**Moderate $\dot{\varepsilon}$**	**Slow $\dot{\varepsilon}$**	**Moderate $\dot{\varepsilon}$**
Manchester fine sand (MFS)	3	11	7	11
Hydrophobic MFS	2	2	4	6
Small glass beads	N/A	N/A	2	3
Hydrophobic small beads	N/A	N/A	2	2
Large glass beads	N/A	N/A	N/A	1
Hydrophobic large beads	N/A	N/A	N/A	2

Table 5.7: Interface adhesion testing program (number of tests shown for each condition).

As part of this investigation 11 shear tests on treated and untreated quartz rods were also performed. The goal of these tests was to quantify in a controlled manner the reduction, if any, of the adhesional strength due to the application of a hydrophobic coating. In an effort to limit the scope of the program only the effects of strain rate (displacement rate) and temperature were investigated. The displacement rates used correspond to the "slow" and "moderate" strain rates used in the triaxial compression testing program. Test temperatures were limited to -5°C and -10°C. A complete description of the program including a description of the equipment, the procedures followed, and the results obtained, is given in Appendix A.

5.2.9 Particle Roughness

The last parameter which was investigated as part of this experimental program was particle roughness and shape, an important consideration to the strength of unfrozen sands. Rowe (1962) postulated that the drained strength of cohesionless sands results from a frictional component, dilatancy effects, and particle interference effects, which all depend on particle roughness or shape. Similarly, in frozen sands structural hindrance, resulting from the mechanical interaction between the ice matrix and soil skeleton which also depends on surface roughness and shape irregularity, was determined via creep tests to greatly increase the shear resistance of the soil skeleton (Ting et al. 1983).

To investigate this aspect of soil behavior, specimens of frozen glass beads (small and large) of varying degrees of imparted surface roughness were tested to specifically determine what influence particle shape has on the Young's modulus and upper yield characteristics of frozen sand. This is particularly important to the verification of many composite material models which do not account for particle shape in their determination of Young's modulus. Testing glass beads also allows for the quantification of the extent of structural hindrance in frozen Manchester fine sand which is thought to be minimal in the small strain region.

Additional tests were also performed on specimens made with hydrophobic glass beads, with and without surface roughening, in hopes of providing further information regarding the interplay between the ice bond strength and structural hindrance in frozen soils. These tests are also necessary to properly evaluate the data from the PMMA testing program, specifically the effect of particle modulus, since one type of glass beads that were tested are qualitatively similar to the PMMA particles in size and surface roughness. Details of the triaxial testing program which involved aspects of particle roughness are presented in Table 5.8.

Material Type	Regular	Hydrophobic	Hydrophobic Rough
Small glass beads	5	4	9
Large glass beads	1	2	2

Table 5.8: Materials examined for effects of particle roughness (number of tests shown for each condition).

5.3 GENERAL TESTING PROCEDURES

5.3.1 Frozen Testing Procedures

The high-pressure triaxial equipment described in Section 3.3.2 was used to perform a number of triaxial compression tests on a variety of different materials under a wide range of conditions. This warranted the development of a standardized testing procedure that could be followed for each test regardless of the type of specimen and test conditions. The following procedure outlines the steps that was followed for the majority of the triaxial compression tests performed over the course of this research.

1. Check to see if testing room and vestibule of the Low Temperature Testing Facility (LTTF) are at the proper temperature for the test being performed. The testing room should be at least 5°C colder than the desired test temperature, and the vestibule should be at approximately -10°C.

2. Clean and then apply a light coat of vacuum grease to the six O-rings used to seal the membranes around the specimen.

3. Apply a light coating of vacuum grease to the base pedestal of the triaxial cell located in the main testing room and then place the first membrane over the base pedestal. Secure with two O-rings spaced 5 mm apart. Place the second membrane over the first one and secure it with an additional O-ring placed in between the first two. Be careful not to expose the O-rings to the cold temperatures before placement since they tend to loose their flexibility when they become cold and then will not retract to their original diameter to fit tightly around the base pedestal.

4. Place the specimen alignment pin in the base pedestal.

5. Take a frozen specimen from the cube freezer (using gloves) and proceed to prepare it for testing following the procedure outlined in Section 4.3.5 of Chapter 4.

6. Reduce the specimen data to obtain the height and volume of the specimen. Transfer the readings to the testing log sheet and complete the other appropriate areas on the first page regarding the specific test conditions.

7. Start QBASIC and load MSET.bas. Press 'F5' to run the program. Use the name of the last test when prompted for a filename. Then change the name to the current test number, input the date, height, and area of the specimen.

8. Place the specimen on the base pedestal of the triaxial cell ensuring that the pin and alignment holes mate. Orient the specimen such that the seam from the

split-sleeve faces towards the rear of the triaxial cell. Also ensure that the specimen's orientation is correct (i.e. top up). Place the top cap complete with hardened steel ball on top of the specimen. Use the alignment device to hold the specimen in place.

9. Rub a small amount of vacuum grease around the top cap making sure that the entire circumference is covered. Roll the first membrane up and over the top cap. Ensure that it forms a good seal with the top cap and that there are no wrinkles.

10. Secure the first membrane with two O-rings as before, leaving a similar gap between them as on the base pedestal. Roll the second membrane up and secure it with an additional O-ring once all wrinkles in this membrane have been smoothed out.

11. Mount the small-strain yokes around the specimen and plug the LVDT's into the Amphenol connector in the base. Check their output on the voltmeter (should read between 4-5 V). Adjust yoke alignment until both LVDT's read approximately 4.5 V. This indicates proper alignment. Carefully remove the pins from the aluminum posts and recheck the output for both transducers. If they have changed substantially place the pins and posts back in and re-align the yokes. Record the two LVDT readings on the log sheet.

12. Carefully lift the triaxial chamber and place it over the triaxial cell base keeping the bolts and the bolt holes aligned. This should prevent the chamber from contacting the yokes. Should this happen, as indicated by a change in LVDT readings, the chamber will have to be removed and the yokes re-aligned.

13. Connect both the load cell and thermistor cables. Using the voltmeter, check to see that their outputs are reading correctly. Leave the voltmeter reading the load cell channel.

14. Tighten the six bolts which secure the chamber to the base and then lower the piston until it touches the top cap. Apply a slight pressure to the top and piston and watch the load cell output change. This will confirm that the load cell is in contact with the top cap. Place the hardened steel ball on top of the piston and adjust the moment break device until it just touches the steel ball.

15. Mount the external LVDT and manually adjust it until its output reads approximately -1.000 V.

16. Close the valve at the top of the AXIAL pressure-volume controller and open the valve to the hydraulic ram.

17. Turn on the air pressure near the LTTF control panel to 10 psi (69 kPa) by turning the regulator clockwise. Before filling the chamber do one last check of all transducer readings to ensure that they are reading correctly. Turn on the air valve inside the environmental enclosure to apply air pressure to the silicone oil reservoir.

18. Fill the triaxial chamber with silicone oil. This should take approximately 10-15 minutes. Once full, turn the air valve to the closed position, and reduce the air pressure using the regulator outside the LTTF. Close the valve at the top of the CELL pressure-volume controller and open the CELL valve on the triaxial manifold.

19. Record all of the transducer zero values on the test log sheet. Calculate a normalized zero value for each transducer by dividing its output by the input voltage and enter these values in the computer program. Turn the motor control box on, but first ensure that the motor control switches are in the off (middle) position.

20. Follow the instructions on the computer screen to start the test and then start data acquisition, and the temperature control within the environmental chamber. Also start the high-pressure pump (set speed to ~20 on the motor controller) to circulate the cell fluid.

21. Watch the values on the computer to ensure that the computer is reading the values correctly (i.e. the cell pressure and axial load are increasing to their target values). At this point the test has been successfully setup. Shearing can be initiated after approximately 12 hours have elapsed. This allows enough time for the specimen to equilibrate to the desired testing temperature, and to also assess a leakage rate.

22. Following shear, decrease the axial stress to the pre-shear value while maintaining the confining stress. Continue data collection for one hour in order to assess temperature fluctuations within the triaxial cell.

23. At the conclusion of the test de-pressurize the chamber and remove the specimen from the triaxial cell. Record the final dimensions of the specimen and draw its deformed shape. Also detail the presence of oil intrusion, tilting, and shear planes, and if the ice caps are intact. Finally, weigh the specimen before placing it in an oven set at 110°C. After 24 hours record the dry weight and calculate the ice saturation and dry density.

5.4 SUMMARY OF EXPERIMENTAL PROGRAM

A total of 126 triaxial compression tests were performed as part of this experimental program. Of these, 17 provided no useful data and hence have not been included in the accompanying Table 5.8 which summarizes each test that was performed. For each test, only the most pertinent test conditions have been given: material type, dry density, relative density, void ratio, ice saturation, confining stress, temperature, strain rate, and small strain rating (described in Section 5.5.2). A comprehensive summary of the data acquired from each test is provided in Appendix B.

In addition to these triaxial compression tests a series of 11 adhesion tests, described previously, were also performed to investigate the adhesional strength between ice and quartz. A detailed summary of the adhesional strength testing program along with the individual load-displacement curves can be found in Appendix A.

5.5 DATA HANDLING

5.5.1 Data Collection

As mentioned previously in Section 3.4.2, a central data acquisition unit was used for the bulk of the data collection used in this research program. A series of 12 channels were allocated to the frozen soil triaxial testing system in the LTTF. This allows a maximum of 11 sensing devices (e.g., pressure and force transducers, thermistors, displacement gauges) to be monitored and recorded simultaneously at a maximum frequency of 1 Hz. The other channel is dedicated to reading a common excitation voltage that powers all the sensors. The central data acquisition unit writes the information, in terms of voltages, directly to the hard disk of the PC controlling it. After the test is completed, the data files are copied to a 3.5 inch floppy diskette and processed as explained in Section 5.5.2.

For a typical frozen triaxial compression test, data from nine sensors are collected although only eight are needed to fully characterize the stress-strain-time-temperature behavior of the specimen (the axial actuator LVDT is monitored only to gage the position of the actuator piston during shear). Each of the sensors, along with their specifications,

Test #	Material	ρ_d (kg/m^3)	D_r (%)	e	S_i (%)	σ_c (MPa)	T (°C)	$\dot{\varepsilon}$ (%/hr)	LVDT Quality
151	MFS	1565	58.2	0.717	-	2	-10	1	Fair
152	MFS	1509	38.8	0.781	98.0	1	-10	1	Poor
160	MFS	1543	50.7	0.742	98.5	1	-10	1	Poor
161	MFS	1542	50.4	0.743	99.4	1	-10	12	Poor
162	MFS	1534	47.6	0.752	98.7	5	-10	12	Poor
163	MFS	1580	63.0	0.702	98.8	5	-10	12	Poor
164	MFS	1573	60.8	0.709	98.8	2	-10	12	Poor
166	MFS	1589	66.1	0.692	99.2	2	-10	12	Poor
167	MFS	1582	63.9	0.699	96.5	2	-10	12	Poor
168	MFS	1571	60.1	0.711	99.4	0.1	-10	1	Poor
169	MFS	1582	63.9	0.699	99.5	10	-10	1	Poor
170	MFS	1573	61.0	0.708	99.2	1	-10	12	Poor
171	MFS	1486	30.5	0.809	99.1	10	-10	12	Poor
174	MFS	1572	60.8	0.709	99.4	10	-10	12	Good
175	MFS	1519	42.5	0.769	95.0	10	-10	12	Good
176	MFS	1550	53.2	0.734	99.5	10	-10	1	Excellent
177	MFS	1551	53.6	0.733	99.3	0.5	-10	1	Excellent
178	MFS	1565	58.1	0.718	99.9	0.5	-5	1	Poor
180	MFS	1534	47.8	0.752	99.8	10	-5	1	Poor
182	MFS	1540	49.8	0.745	99.1	0.5	-5	1	Excellent
183	MFS	1597	68.5	0.684	99.2	0.5	-5	12	Excellent
185	MFS	1575	61.6	0.707	99.5	0.5	-5	12	Good
186	MFS	1591	66.7	0.690	98.7	10	-5	12	Good
191	MFS	1613	73.8	0.666	98.9	10	-5	12	Fair
192	MFS	1593	67.3	0.688	99.3	0.5	-5	12	Good
193	MFS	1611	73.0	0.669	98.9	10	-5	12	Good
194	MFS	1602	70.2	0.678	98.7	0.5	-10	12	Excellent
205	MFS	1629	78.8	0.650	98.6	10	-5	12	Fair
206	MFS	1655	86.6	0.624	97.2	5	-5	12	Poor
207	MFS	1618	75.2	0.662	98.3	2	-5	12	Good
208	MFS	1615	74.5	0.664	97.9	1	-5	12	Good
209	MFS	1635	80.6	0.644	96.0	10	-5	12	Poor
215	MFS	1640	82.0	0.639	97.6	0.5	-2	12	Poor
216	MFS	1609	72.5	0.671	97.1	0.5	-2	12	Fair
217	MFS	1638	81.5	0.641	97.2	0.5	-2	1	Good
218	MFS	1607	72.0	0.672	98.3	10	-2	12	Excellent
219	MFS	1610	72.9	0.669	98.6	10	-2	1	Poor
187	HP MFS	1599	69.5	0.681	96.8	0.5	-10	1	Good
188	HP MFS	1591	66.8	0.689	98.3	10	-10	1	Excellent
189	HP MFS	1592	67.1	0.688	97.6	10	-5	1	Excellent
190	HP MFS	1592	66.9	0.689	97.0	0.5	-5	1	Fair
195	HP MFS	1516	41.4	0.773	97.3	0.5	-10	12	Fair
196	HP MFS	1528	45.5	0.759	98.0	10	-10	12	Excellent
197	HP MFS	1535	47.9	0.752	98.2	0.5	-10	1	Good
198	HP MFS	1508	38.6	0.782	98.7	10	-10	1	Good
199	HP MFS	1659	87.8	0.620	87.8	0.5	-5	12	Good
200	HP MFS	1616	74.6	0.664	97.3	10	-5	12	Fair
201	HP MFS	1621	76.1	0.659	95.7	0.5	-10	12	Excellent
202	HP MFS	1622	76.5	0.657	94.8	10	-10	12	Excellent
203	HP MFS	1610	72.7	0.670	97.3	10	-10	12	Good
204	HP MFS	1552	53.9	0.732	93.9	0.5	-10	12	Excellent
210	Quartz	1557	91.5	0.702	95.3	0.5	-5	12	Good
211	Quartz	1590	109.6	0.667	94.2	2	-5	12	Excellent

Test #	Material	ρ_d (kg/m^3)	D_r (%)	e	S_i (%)	σ_c (MPa)	T (°C)	$\dot{\varepsilon}$ (%/hr)	LVDT Quality
212	Quartz	1605	117.4	0.651	90.5	5	-5	12	Good
213	Quartz	1568	97.5	0.690	91.9	10	-5	12	Excellent
220	Quartz	1609	98.0	0.647	96.1	0.5	-10	12	Good
221	Quartz	1625	102.9	0.631	96.4	10	-10	12	Good
222	Quartz	1624	102.6	0.632	97.3	0.5	-10	1	Good
223	Quartz	1602	95.5	0.655	97.5	10	-10	1	Good
224	Quartz	1531	71.2	0.731	97.1	2	-10	12	Good
225	Quartz	1612	99.0	0.644	98.0	5	-10	12	Excellent
226	Quartz	1597	94.0	0.659	97.3	5	-10	12	Fair
227	Quartz	1596	93.6	0.661	98.0	5	-10	12	Excellent
228	Quartz	1600	94.9	0.656	97.4	2	-10	1	Good
229	Quartz	1590	91.5	0.667	97.8	5	-10	1	Good
232	Quartz	1625	102.9	0.631	97.9	10	-10	12	Good
233	Quartz	1641	108.2	0.614	92.7	10	-10	1	Fair
242	Quartz	1566	83.3	0.693	96.6	12.5	-10	1	Good
243	Quartz	1569	84.3	0.690	96.6	12.5	-10	12	Good
244	Quartz	1544	75.7	0.717	98.1	12.5	-5	12	Excellent
245	Quartz	1575	86.7	0.682	97.4	12.5	-5	12	Excellent
246	Quartz	1584	89.6	0.673	98.1	12.5	-5	1	Fair
269	Quartz	1590	91.6	0.667	98.0	0.1	-10	12	Excellent
270	Quartz	1576	86.9	0.682	98.3	1	-10	12	Good
271	Quartz	1584	89.7	0.673	97.8	12.5	-10	12	Excellent
272	Quartz	1447	39.4	0.831	98.6	7.5	-10	12	Excellent
273	Quartz	1572	85.4	0.686	97.5	2	-10	12	Excellent
234	PMMA	823	-	0.446	91.2	0.5	-10	12	Excellent
235	PMMA	740	-	0.607	97.1	0.5	-10	12	Good
236	PMMA	821	-	0.449	93.2	0.5	-10	12	Excellent
237	PMMA	733	-	0.624	98.5	0.5	-10	1	Good
238	PMMA	751	-	0.585	98.7	10	-10	1	Fair
239	PMMA	764	-	0.558	98.4	0.5	-5	1	Excellent
240	PMMA	832	-	0.431	93.3	10	-5	1	Fair
241	PMMA	771	-	0.544	98.2	5	-5	1	Excellent
247	PMMA	738	-	0.613	98.4	0.5	-5	12	Good
248	PMMA	784	-	0.517	101.1	10	-5	12	Good
249	PMMA	782	-	0.522	98.5	0.5	-5	1	Excellent
250	PMMA	812	-	0.465	95.5	10	-10	12	Fair
251	PMMA	793	-	0.501	98.4	10	-5	1	Excellent
274	PMMA	765	-	0.559	99.7	0.5	-10	12	Good
275	PMMA	749	-	0.590	98.8	0.5	-10	12	Good
276	PMMA	749	-	0.589	100.8	10	-10	12	Good
277	PMMA	751	-	0.585	99.5	0.5	-10	1	Good
278	PMMA	745	-	0.568	98.4	10	-10	1	Fair
252	PC Ice	0.910	-	-	-	0.5	-10	1	Excellent
253	PC Ice	0.914	-	-	-	0.5	-10	12	Excellent
254	PC Ice	0.912	-	-	-	10	-10	1	Good
255	PC Ice	0.912	-	-	-	10	-10	12	Good
256	PC Ice	0.913	-	-	-	0.5	-5	1	Good
257	PC Ice	0.910	-	-	-	0.5	-5	12	Excellent
258	PC Ice	0.913	-	-	-	10	-5	1	Fair
259	PC Ice	0.912	-	-	-	10	-5	12	Good
260	Glass	1.618	-	0.552	95.8	0.5	-10	1	Good
261	Glass	1.642	-	0.528	89.0	0.5	-10	12	Good
262	Glass	1.618	-	0.551	94.7	10	-10	1	Excellent

Test #	Material	ρ_d (kg/m^3)	D_r (%)	e	S_i (%)	σ_c (MPa)	T (°C)	$\dot{\varepsilon}$ (%/hr)	LVDT Quality
263	Glass	1.597	-	0.572	96.4	10	-10	12	Excellent
264	Glass	1.638	-	0.533	90.6	10	-10	12	Excellent
265	HP Glass	1.550	-	0.619	96.0	0.5	-10	1	Good
266	HP Glass	1.539	-	0.631	95.9	0.5	-10	12	Good
267	HP Glass	1.568	-	0.601	92.1	10	-10	1	Fair
268	HP Glass	1.530	-	0.641	94.6	10	-10	12	Good
279	HPR Glass	1577	-	0.592	95.8	0.5	-10	12	Excellent
280	HPR Glass	1581	-	0.588	94.7	0.5	-10	12	Good
281	HPR Glass	1601	-	0.568	92.1	10	-10	12	Good
282	HPR Glass	1575	-	0.594	94.5	10	-10	12	Good
283	HPR Glass	1586	-	0.583	96.3	0.5	-10	1	Fair
284	HPR Glass	1592	-	0.576	95.6	10	-10	1	Excellent
285	HPR Glass	1544	-	0.626	96.5	0.5	-10	12	Excellent
286	HPR Glass	1540	-	0.630	96.0	0.5	-10	1	Good
287	HPR Glass	1572	-	0.596	91.5	10	-10	12	Good
288	Glass	1482	-	0.673	93.4	0.5	-10	12	Excellent
289	HP Glass	1494	-	0.660	94.9	0.5	-10	12	Good
290	HP Glass	1517	-	0.635	97.8	0.5	-10	12	Fair
291	HPR Glass	1478	-	0.678	93.7	0.5	-10	12	Good
292	HPR Glass	1486	-	0.669	96.6	0.5	-10	12	Excellent

Note: only nominal values for the degree of confinement, temperature, and strain rate are given.

Table 5.9: Summary of triaxial compression experimental program on frozen specimens.

were listed previously in Table 3.1. Each test consists of three stages, each with its own data requirements.

The first stage consists of a pressurizing and temperature equilibration stage. During this stage the confining stress on the specimen is gradually increased to its target value and the specimen is allowed to equilibrate to the desired test temperature. This stage generally lasts 12 hours. Data are collected on all nine sensors and stored to a file designated by the test type, number, and stage (e.g., FRS121P.dat denotes the data file for the pressure up stage of frozen soil test number 121). The reading rate throughout this stage is held constant at 0.0083 Hz (1 reading every two minutes).

Once the first stage of testing is complete, the second stage begins which consists of shearing the specimen by gradually increasing the axial load under constant rate of displacement control. Only the sensors which provide the stress-strain data are recorded (e.g., the external and internal LVDTs, the force and chamber pressure transducers, and the LVDT necessary for computing volume change). No temperature measurements are

made during this stage. The data are collected and stored to file (e.g., FRS121S.dat) at a variable rate to ensure that both the small and large strain behavior is captured without storing excessive amounts of data. The collection rate varies from 1 Hz during the initial portion of the test and gradually decreases to 0.0033 Hz at large axial strains (>10%).

After the maximum axial strain is reached (usually 10-20%), shearing is stopped and the axial load is decreased to its pre-shear level while the cell pressure remains constant. During this third stage, the system is allowed to hold this stress state for an additional hour while temperature data from the thermistors located at the top and bottom of the specimen are acquired and written to disk (e.g., FRS121T.dat) at a rate of 0.03 Hz.

5.5.2 Data Reduction

All data files generated by the central data acquisition system are stored in a similar format. The data acquisition system records each sensor's output (in Volts) and the time at which the readings were taken at the frequency specified by the operator. Once the data acquisition task is completed, the file is closed and written to disk. It is then used by the test reduction program to obtain the information about the test in terms of engineering units. Furthermore, the engineering output from the reduction program can then be imported by a variety of commercially available plotting and spreadsheet packages to enhance the visual presentation and analysis of the data.

The large number of triaxial compression tests performed over the course of this research necessitated an efficient method of data reduction. Templates were created in Microsoft Excel™ to assist in the reduction of the data. The templates facilitated the conversion of each sensor's output voltage into engineering units in a consistent and repeatable fashion. For the triaxial compression tests described above, each of the three data files were manipulated separately to extract pertinent test characteristics.

All sensors are monitored during the first phase of the test (i.e. the FRS121P.dat file). This is done mainly to ensure that the test is progressing normally during the pressure-up phase. Chamber fluid leakage rates as well as temperature gradient measurements over the height of the specimen are determined from these data. The leakage rate varies from test to test depending on the specific test conditions. The rate is

determined by observing the movement of the LVDT on the chamber fluid actuator over time at constant cell pressure once the pressurizing oil has reached a constant temperature as determined by the thermistors monitoring the chamber temperature. The leakage rate is then used to correct the volumetric strain measurements according to the following relation:

$$\Delta V_s = -\Delta V_{cp} - \Delta V_{lp} + LR \cdot \Delta t + F_{ax} C_{ax} \tag{5.1}$$

where ΔV_s is the volume change of specimen (positive means dilation), ΔV_{cp} is the change in volume computed from cell fluid actuator, ΔV_{lp} is the change in volume due to loading piston entering the chamber, LR is the leakage rate of fluid out of triaxial cell, Δt is the time from start of test, F_{ax} is the change in axial force during shear acting on the base of the triaxial cell, and C_{ax} is a coefficient relating the volume change due to base flexure to the applied axial load and is taken as 10.2 cc/MN (Andersen 1991).

The second or shear phase of testing provides all of the data needed to quantify the stress-strain behavior of the specimen. The triaxial testing reduction program, written in Microsoft VisualBASIC™ by Kurt Sjoblom, a Ph.D student in the Geotechnical Laboratory, and implemented in a spreadsheet as a executable macro, is an updated version of the original program used to reduce standard triaxial tests (Sheahan 1991). It takes the shear data file, makes the appropriate corrections to the data (e.g., for membrane stiffness, chamber fluid leakage, change in specimen area), and then computes the information required to define the stress-strain and volumetric strain behavior in the desired engineering units. Computation of axial strain is made using the average of the strains recorded by the two internal LVDT's up to 2.00% strain, and then switches to the external LVDT at larger strains. Based on the agreement between the two internal LVDT's a rating system was developed, similar to that of Andersen et al. (1995), to assess the quality of the calculated Young's modulus. Each shear was assigned one of four ratings: *poor, fair, good,* and *excellent.* This rating was based on the difference in slopes between the two transducers during the very early linear portion of the stress-strain curve. An example of each of the four categories is shown in Figure 5.1. Although tests classified as *poor* did not produce reliable and repeatable values of Young's modulus, they still provided meaningful data at larger strains, thus allowing quantification of the upper

yield stress and large strain behavior. Most of the tests performed in the early part of the experimental program resulted in *poor* ratings due to minor eccentricities in the load application. These results were the reason why modifications were made to the load application system described in Section 3.3.3.2. Internal LVDT quality ratings are summarized in the last column of Table 5.9.

After its reduction, the data, in the form of engineering units, are imported into a plotting package to allow for graphical representation and advanced statistical analysis.

Finally, the data file from the third stage are used as a final check on the temperature fluctuations and gradient at the end of the test. This step was added since limitations in the data acquisition system prevented the collection of temperature data during the early portions of shear.

After completion of the test and after the dry weight of the specimen is obtained, calculations of the specimen density (dry and total), void ratio, water content, and degree of ice saturation are performed. The degree of ice saturation was determined using the following equation (Andersen 1991):

$$S = \frac{\gamma_t\left(w_u + \frac{w_i}{G_i}\right)}{\gamma_w(w+1) - \frac{\gamma_t}{G_s}} \times 100\%$$

where S is the degree of saturation, γ_t is the total frozen density, γ_w is the density of water, w is the total water content, w_u is the unfrozen water content (<0.14% for MFS at T=-10°C), w_i is the ice content (the difference between the total and the unfrozen water content), and G_i and G_s are the specific gravity's of the ice and soil particles, respectively. It should be noted that the specific gravity of ice and the density of water are temperature dependent parameters. G_i has been found to range between 0.9164 and 0.9193 for 0°C>T>-30°C (Hobbs 1974), and γ_w between 0.9970 and 0.9895 g/cm^3 for -5°C>T> -25°C (Zheleznyi 1969).

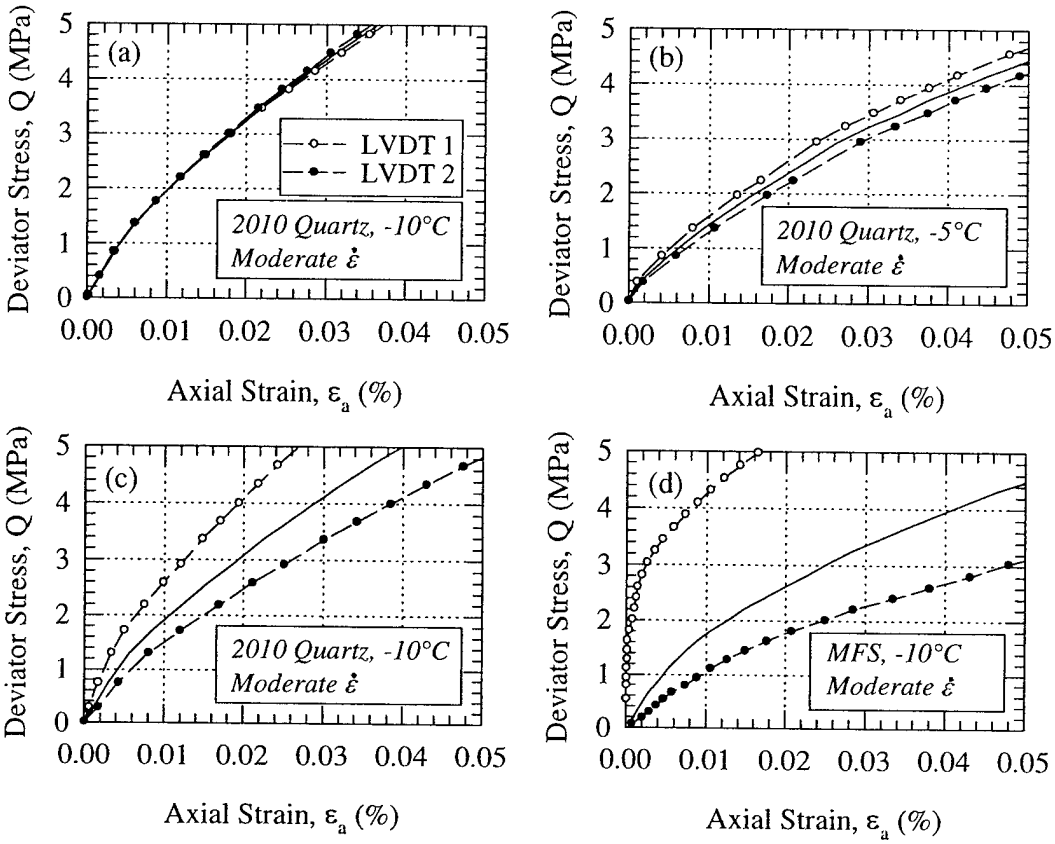

Figure 5.1: Comparison between on-specimen axial strain LVDT's showing (a) *excellent* agreement, (b) *good* agreement, (c) *fair* agreement, and (d) *poor* agreement. Note some data has been omitted for clarity.

5.6 REFERENCES

1. Andersen, G.R. (1991), "Physical Mechanisms Controlling the Strength and Deformation Behavior of Frozen Sand", Sc.D Thesis, Department of Civil and Environmental Engineering, MIT, Cambridge, MA, 560 p.

2. Andersen, G.R., Swan, C.W., Ladd, C.C., Germaine, J.T. (1995), "Small-Strain Behavior of Frozen Sand in Triaxial Compression", *Canadian Geotechnical Journal*, v. 32, no. 3, pp. 428-451.

3. Baker, T.H.W. and Kurfurst, P.J. (1985), "Acoustic and Mechanical Properties of Frozen Sand", *Proc. 4th International Symposium on Ground Freezing*, Sapporo, Japan, pp. 227-234.

4. Chamberlain, E., Groves, C., Perham, R. (1972), "The Mechanical Behavior of Frozen Earth Materials Under High Pressure Triaxial Test Conditions", *Geotechnique*, v. 22, no. 3, pp. 469-483.

5. Cole, D.M., 1990, "Reversed Direct-Stress Testing of Ice: Initial Experimental Results and Analysis", *Cold Regions Science and Technology*, v. 18, pp. 303-321.

6. Counto, U.J. (1964), "The Effect of the Elastic Modulus of the Aggregate on the Elastic Modulus, Creep and Creep Recovery of Concrete", *Magazine of Concrete Research*, v. 16, no. 48, pp. 129-138.

7. Hobbs, P.V. (1974), *Ice Physics*, Clarendon Press, Oxford.

8. Jones, S.K. (1982), "The Confined Compressive Strength of Polycrystalline Ice", *Journal of Glaciology*, v. 28, no. 98, pp. 171-177.

9. Parameswaran, V.R. (1980), "Deformation Behavior and Strength of Frozen Sand", *Canadian Geotechnical Journal*, v. 17, pp. 74-78.

10. Parameswaran, V.R. and Jones, S.J. (1981), "Triaxial Testing on Frozen Sand", *Journal of Glaciology*, v. 27, no. 95, pp. 147-155.

11. Rowe, P.W. (1962), "The Stress-Dilatancy Relation for Static Equilibrium of an Assembly of Particles in Contact", *Proc. of the Royal Society of London, Series A*, v. 269, pp. 500-527.

12. Sayles, F.H. (1973), "Triaxial and Creep Tests on Frozen Ottawa Sand", *Proc. 2nd International Permafrost Conference*, Yakutsk, U.S.S.R, pp. 384-391.

13. Sheahan, T.C. (1991), "An Experimental Study of the Time-Dependent Undrained Shear Behavior of Resedimented Clay Using Automated Stress-Path Triaxial Equipment", Sc.D Thesis, Department of Civil and Environmental Engineering, MIT, Cambridge, MA, 955p.

14. Shibata, T., Adachi, T., Yashima, A., Takahashi, T., Yoshioka, I. (1985), " Time-Dependence and Volumetric Change Characteristics of Frozen Sand Under Triaxial Stress Condition", *Proc. 4th International Symposium of Ground Freezing*, Sapporo, Japan, pp. 173-179.

15. Swan, C. (1994), "Physical Mechanisms Controlling the Deformation and Strength Behavior of Unfrozen and Frozen Manchester Fine Sand", Sc.D Thesis, Department of Civil and Environmental Engineering, MIT, Cambridge, MA, 1044 p.

16. Ting, J.M., Martin, R.T., Ladd, C.C. (1983), "Mechanisms of Strength for Frozen Sand", *ASCE Journal of Geotechnical Engineering*, v. 109, no. 10, pp. 1286-1302.

17. Zhu, Y. and Carbee, D.L. (1984), "Uniaxial Compressive Strength of Frozen Silt Under Constant Deformation Rates", *Cold Regions Science and Technology*, v. 9, pp. 3-15.

18. Zhu, Y., Jiayi, Z., Zhongyan, S. (1988), "Uniaxial Compressive Strength of Frozen Medium Sand Under Constant Deformation Rates", *Proc. 5th International Conference on Ground Freezing*, Nottingham, England, pp. 225-232.

19. Zheleznyi, B.V. (1969), "The Density of Supercooled Water", *Russian Journal of Physical Chemistry*, v. 43, no. 9, pp.1311-1315.

CHAPTER 6

BEHAVIOR OF FROZEN SYSTEMS IN THE ELASTIC REGION

6.1 INTRODUCTION

The first objective of this chapter is to develop an understanding of the mechanisms governing the initial stiffness or Young's modulus of frozen particulate systems. The second objective is to evaluate various composite material models for predicting Young's modulus of frozen sand. These objectives will be accomplished by investigating a number of variables which can potentially influence the behavior of unfrozen sands, ice, and particulate composites in general (e.g., relative density, confinement, strain rate, temperature, particle modulus, size, roughness, and interface adhesion). Their relative importance to the initial stiffness of frozen sand may be elucidated from the results of the experimental program. The chapter is organized to provide the reader first with a summary of the data obtained, then with a discussion of the mechanisms controlling the composite modulus, and finally with an evaluation of some models for its prediction. As such, Section 6.2 presents the results of the experimental program, treating the effects of each of the aforementioned variables separately. This is followed in Section 6.3 with a comprehensive analysis of the data and with a discussion of the relative importance of each of the parameters investigated. The application of predictive composite material models for Young's modulus of particulate composites is presented in Section 6.4. A methodology for the prediction of Young's modulus of frozen sand based on the analyses follows in Section 6.5. Finally, references for the literature cited throughout this chapter are listed in Section 6.6. This chapter will not present a discussion of the upper yield behavior as it is treated in detail in Chapter 7.

6.2 EVALUATION OF YOUNG'S MODULUS

This section presents the initial stiffness data obtained on the five materials (three of which has one or more types of surface treatment) investigated during this experimental

program. Each of the major variables outlined in Section 5.2 will be treated separately, but in the same order, in the discussion below. Data for Manchester fine sand are restricted to the results of this program, unless otherwise stated.

6.2.1 Effect of Void Ratio/Relative Density

The variation of Young's modulus with void ratio (e) or relative density (D_r) has been well established for frozen Manchester fine sand by the two previous experimental programs (Andersen 1991, Swan 1994). The recent improvements made to the axial strain measurement system and the addition of tests on other particulate materials during this program allows more accurate and more diverse characterization of the variation of the composite modulus with void ratio. Although this parameter was not systematically varied during the individual testing programs, efforts were taken to prepare specimens over as wide of a range as possible for each of the materials. However, most of the specimens that resulted were fairly dense due to the preparation method used. Nevertheless, for each material investigated, variations in void ratio did occur, thereby allowing its influence on the composite modulus to be evaluated. A summary of the void ratio range for each of the materials investigated at -10°C, excluding those systems having undergone surface modification, is given in Table 6.1 along with information on the number of tests performed at this temperature. The resulting modulus variation for each material is illustrated in Figure 6.1a-d, regardless of the ACDT agreement, strain rate, and confinement level used. Only the highest and lowest values of the "poor" tests have been omitted for purposes of clarity.

Material Type	Void Ratio Range	Number of Tests*
Manchester fine sand	0.678 - 0.809	18
Industrial quartz	0.614 - 0.831	19
PMMA	0.446 - 0.624	11
Small glass beads	0.528 - 0.572	5
Large glass beads	0.673	1

Note: * indicates regardless of ACDT agreement, confining pressure and strain rate.

Table 6.1: Summary of void ratio range and number of tests for each material investigated at -10°C.

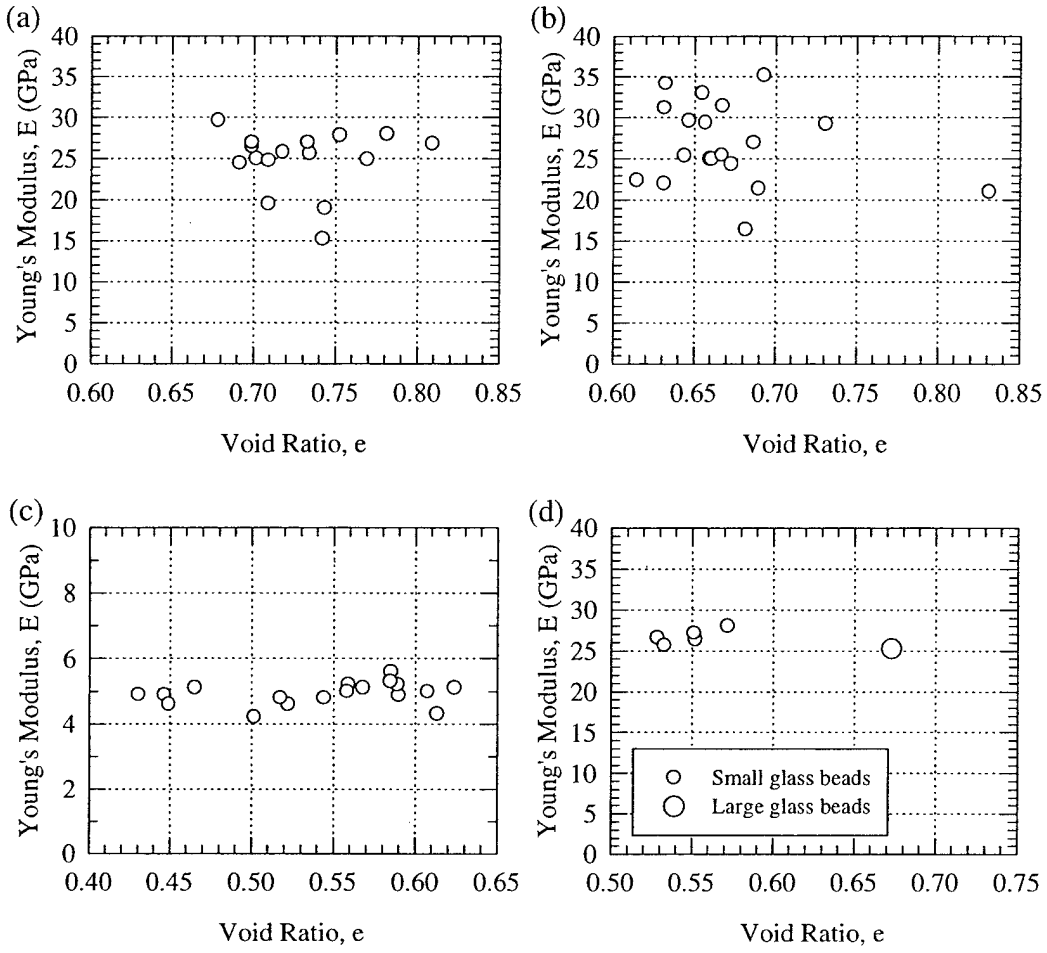

Figure 6.1: Effect of void ratio on Young's modulus of frozen systems at -10°C at varying confining pressures, and strain rates; (a) Manchester fine sand, (b) 2010 industrial quartz, (c) PMMA, (d) small and large glass beads.

As shown in Figure 6.1a, the modulus of frozen Manchester fine sand exhibits little dependence on void ratio at -10°C. Since it was possible to establish the maximum and minimum void ratios for this material, the data are also shown in terms of relative density in Figure 6.2. At this temperature, the mean and standard deviation for the modulus, excluding tests with "poor" ACDT agreement, is 26.3±1.8 GPa (n=6). For comparison, the data in Table 5 of Andersen et al. (1995) gives a value of 26.6±4.4 GPa (n=34) for the modulus for frozen MFS at -10°C, again excluding tests with "poor" ACDT agreement. The good agreement between the two data sets indicates consistency between the programs in terms of specimen preparation, testing, and data interpretation. The large

number of "poor" tests in the beginning of this program resulted from problems with the method of load application. This was described in detail in Section 3.3.3.2. After appropriate modifications were made, the overall percentage of "good" and "excellent" tests increased substantially.

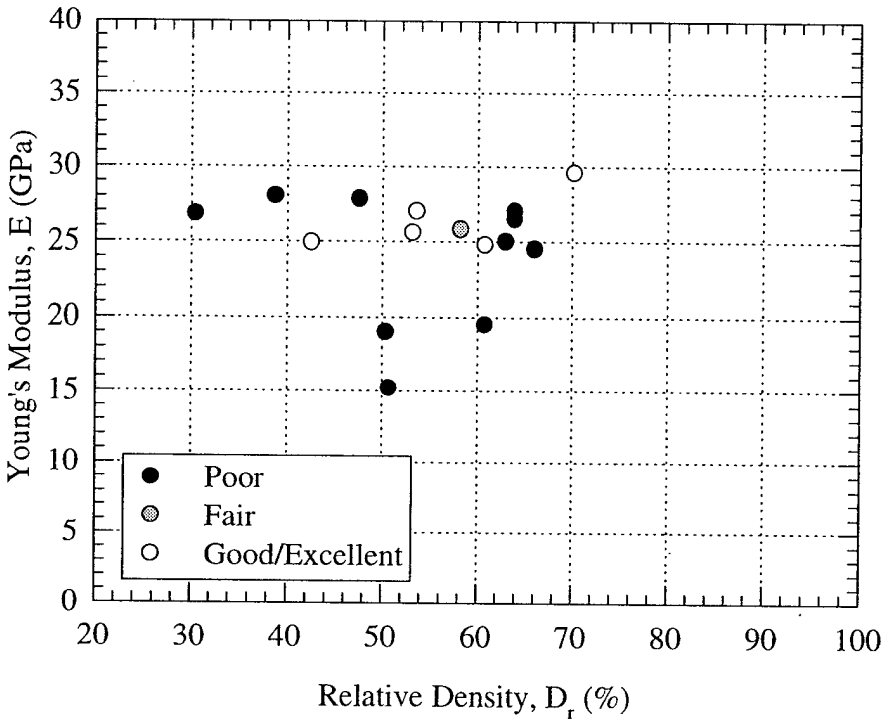

Figure 6.2: Effect of relative density on Young's modulus of frozen Manchester fine sand at -10°C.

The influence of high quality small strain measurements on the evaluation of Young's modulus is illustrated in Figure 6.3, which combines all of the data collected on Manchester fine sand at -10°C (including the data from previous experimental programs) and distinguishes it by ACDT agreement (i.e. poor, fair, good/excellent). The results of each group of measurements in terms of their mean, standard deviation, and coefficient of variation (COV) are given in Table 6.2. This comparison shows that tests characterized by fair, good, and excellent ACDT agreement have far less variation in modulus as reflected by a lower standard deviation and COV. Thus, for the analysis of the initial stiffness only tests with fair and good/excellent agreement have been used since they are judged to be the most reliable.

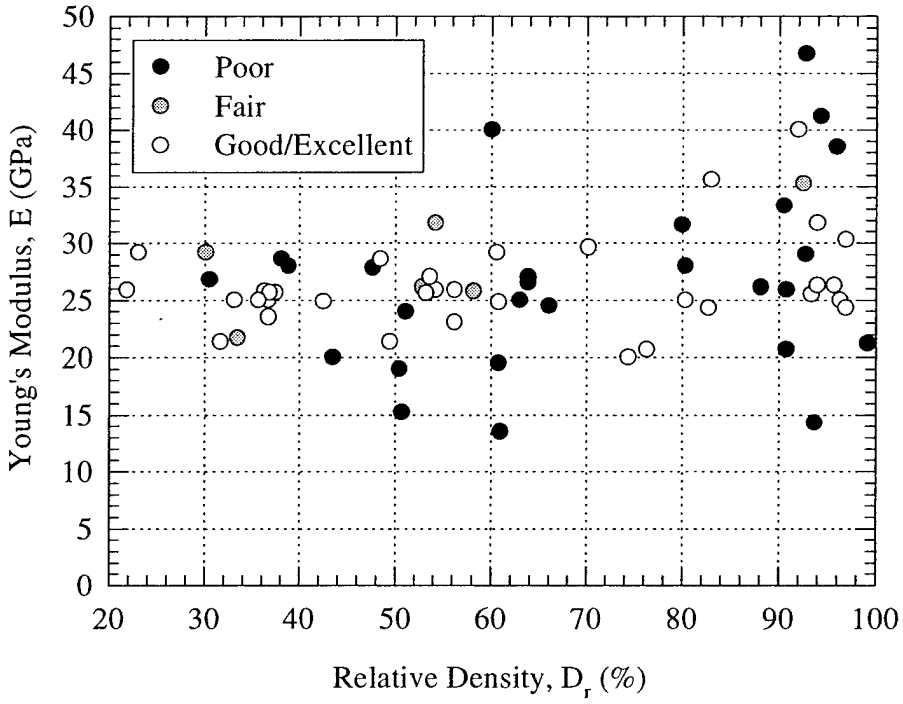

Figure 6.3: Variation of Young's modulus with ACDT agreement for Manchester fine sand at -10°C at varying confining pressures and strain rates. (includes data from Andersen 1991 and Swan 1994)

ACDT Agreement	Mean±S.D. (GPa)	Number of Tests	COV (%)
Poor	27.0±8.0	28	29.6
Fair	28.3±4.8	6	17.0
Good/Excellent	26.3±3.9	34	14.8

Table 6.2: Summary of variation of Young's modulus with ACDT agreement for Manchester fine sand at -10°C at all void ratios, confining pressures, and strain rates.

The other data shown in Figure 6.1 encompasses the rest of the particulate materials tested at -10°C in their natural state (prior to any surface modification). Systems that have been modified, either by surface treatment or by surface roughening, will be discussed in Sections 6.2.7 and 6.2.8. As with Manchester fine sand, the data shown in Figure 6.1b-d also show little variation in modulus over similar ranges of void ratio. An interesting and possibly more important observation is that the amount of scatter observed

in the data is substantially less for those systems composed of spherical particles (PMMA and glass beads). At the other extreme, the industrial quartz system (Figure 6.1b), which is characterized by similarly sized, yet extremely angular particles, exhibits substantially more scatter in the data than all of the other systems. A possible explanation for this apparent trend is discussed in Section 6.3. As a result of the limited dependence on void ratio, the mean modulus and standard deviation for each system are summarized in Table 6.3.

Material Type	Mean±Std. Dev. (GPa)	Number of Tests
Manchester fine sand	26.3±1.8	6
Industrial quartz	26.8±5.0	19
PMMA	5.1±0.3	11
Small glass beads	26.8±0.9	5
Large glass beads	25.2	1

Table 6.3: Summary of the mean Young's modulus and standard deviation for each material type at -10°C at varying void ratios, confining pressures, and strain rates. (excluding "poor" tests)

6.2.2 Effect of Confinement

Investigation of the physical mechanisms controlling the modulus of frozen particulate systems under triaxial stress conditions included the effect of confinement. Although the number of confinement levels (σ_c) used throughout the testing program ranged from 0.1 to 12.5 MPa, the majority of tests were performed at 0.5 and 10 MPa. These values correspond to low and high confinement when qualitatively describing the effect of confinement. Table 6.4 summarizes the confinement levels investigated at -10°C for each of the materials examined, as well as for the specimens of polycrystalline ice.

The values of Young's modulus versus confinement level at -10°C are shown in Figure 6.4a-f for all the materials listed in Table 6.4. Table 6.5 summarizes the modulus obtained for each material under low ($\sigma_c \leq 2$ MPa) and high confinement conditions. Little dependence is noted for these materials over the confinement range investigated. This is especially evident when looking at the systems composed of spherical particles, which show very little scatter in the measured modulus. Only the hydrophobic Manchester fine

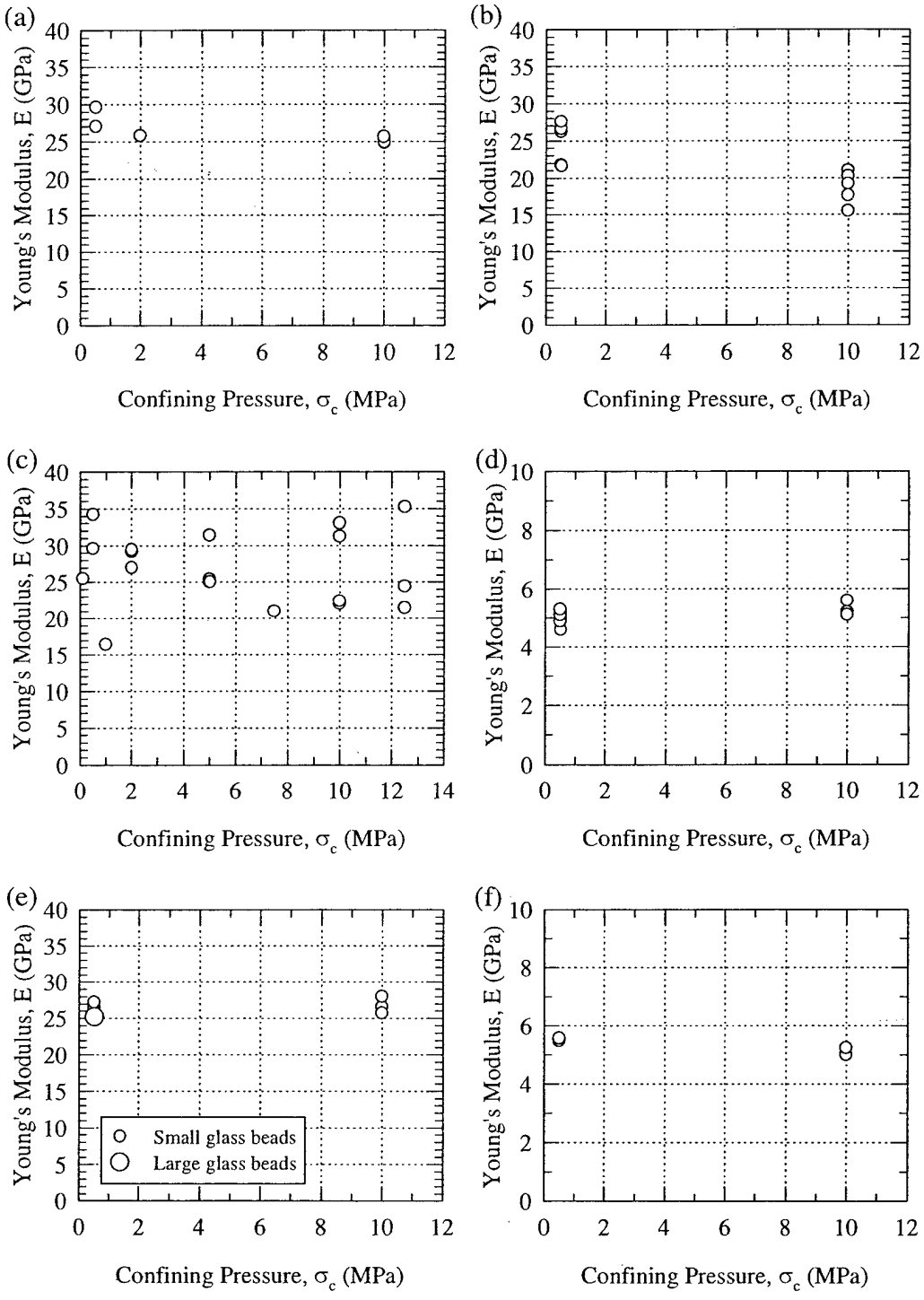

Figure 6.4: Effect of confinement on Young's modulus of frozen systems at -10°C at varying void ratios and confining pressures; (a) Manchester fine sand, (b) hydrophobic Manchester fine sand (c) 2010 industrial quartz, (d) PMMA, (e) small and large glass beads, (f) polycrystalline ice.

sand system (Figure 6.4b) has an obvious trend of decreasing modulus with increasing confinement level, which can be shown to be statistically significant. This directly contrasts, however, the slight increase in mean modulus observed in the PMMA specimens (Figure 6.4d).

Material Type	Confinement Levels (MPa)
Manchester fine sand (MFS)	0.1, 0.5, 1, 2, 5, 10
Hydrophobic MFS	0.5, 10
Industrial quartz	0.1, 0.5, 1, 2, 5, 7.5, 10, 12.5
PMMA	0.5, 10
Small glass beads (all treatments)	0.5, 10
Large glass beads (all treatments)	0.5
Polycrystalline ice	0.5, 10

Table 6.4: Summary of confinement levels investigated for each material type at -10°C at varying void ratios and strain rates.

Material Type	Mean±S.D. (GPa)	
	Low σ_c	High σ_c
Manchester fine sand (MFS)	27.5±1.9 (n=3)	25.1±0.4 (n=3)
Hydrophobic MFS	24.8±2.8 (n=5)	18.7±2.2 (n=5)
Industrial quartz	27.3±5.5 (n=7)	26.5±4.9 (n=12)
PMMA	5.00±0.2 (n=7)	5.30±0.2 (n=4)
Small glass beads	26.8±0.6 (n=2)	26.8±1.2 (n=3)
Large glass beads	25.2 (n=1)	N/A
Polycrystalline ice	5.50±0.1 (n=2)	5.10±0.2 (n=2)

Table 6.5: Summary of Young's modulus obtained at low ($\sigma_c \leq 2$ MPa) and high confinements for each material type at -10°C at varying void ratios and strain rates.

6.2.3 Effect of Strain Rate

Axial strain rate ($\dot{\varepsilon}$), or frequency of loading, is one of the most important variables influencing the measured modulus of polycrystalline ice (Cole 1990). However, previous research on frozen Manchester fine sand by Andersen et al. (1995) found its modulus to be relatively insensitive to strain rate. Hence an important aspect of this experimental program was to confirm the influence of strain rate on the modulus of frozen sand and other particulate composites. Only two nominal strain rates were used for all the tests: slow (3.0×10^{-6} s^{-1}) and moderate (3.5×10^{-5} s^{-1}) due to equipment limitations (i.e. ability to

impose a constant strain rate). The slow rate falls within the nominally ductile range of ice behavior at -10°C while the moderate rate falls within the ductile-to-brittle transition zone. A separate effort was directed at measuring the strain rate dependency of the modulus of polycrystalline ice specimens as it was recognized that the particular equipment and testing technique could influence the measured modulus dramatically.

Figure 6.5a-f illustrates the variation of Young's modulus with strain rate (calculated at a strain corresponding to the 0.01% yield offset stress) for each of the various materials tested at -10°C. Table 6.6 summarizes the means and standard deviation of the Young's modulus obtained at the two strain rates for each material tested. From the results shown in the figure there is no statistically significant dependency of Young's modulus with strain rate. This confirms the results reported by Andersen et al (1995) for Manchester fine sand at temperatures ranging from -10°C to -25°C.

The lack of rate dependency for the ice specimens tested, combined with a measured modulus that is substantially lower than the theoretical value of approximately 9 GPa (Sinha 1989), indicates that the testing procedure is probably measuring a relaxed modulus which can be as low as 5 GPa (Cole 2000). This most likely results from the procedure of subjecting the test specimens to the applied hydrostatic stress for a full 12 hours before shearing in order to allow the specimens to achieve temperature equilibrium. Therefore, it is not surprising that specimens of frozen sand tested in a similar manner also show no rate dependency.

	Mean±S.D. (GPa)	
Material Type	**Slow $\dot{\varepsilon}$**	**Moderate $\dot{\varepsilon}$**
Manchester fine sand (MFS)	26.1±0.8 (n=3)	26.4±2.7 (n=3)
Hydrophobic MFS	23.5±3.4 (n=4)	20.6±4.2 (n=6)
Industrial quartz	30.9±4.7 (n=6)	24.9±4.0 (n=13)
PMMA	5.30±0.2 (n=4)	5.00±0.2 (n=7)
Small glass beads	26.5±0.1 (n=2)	27.0±1.2 (n=3)
Large glass beads	N/A	25.2 (n=1)
Polycrystalline ice	5.20±0.3 (n=2)	5.40±0.2 (n=2)

Table 6.6: Summary of the Young's modulus obtained for each material type at the two strain rates investigated at -10°C at varying void ratios and confining pressures.

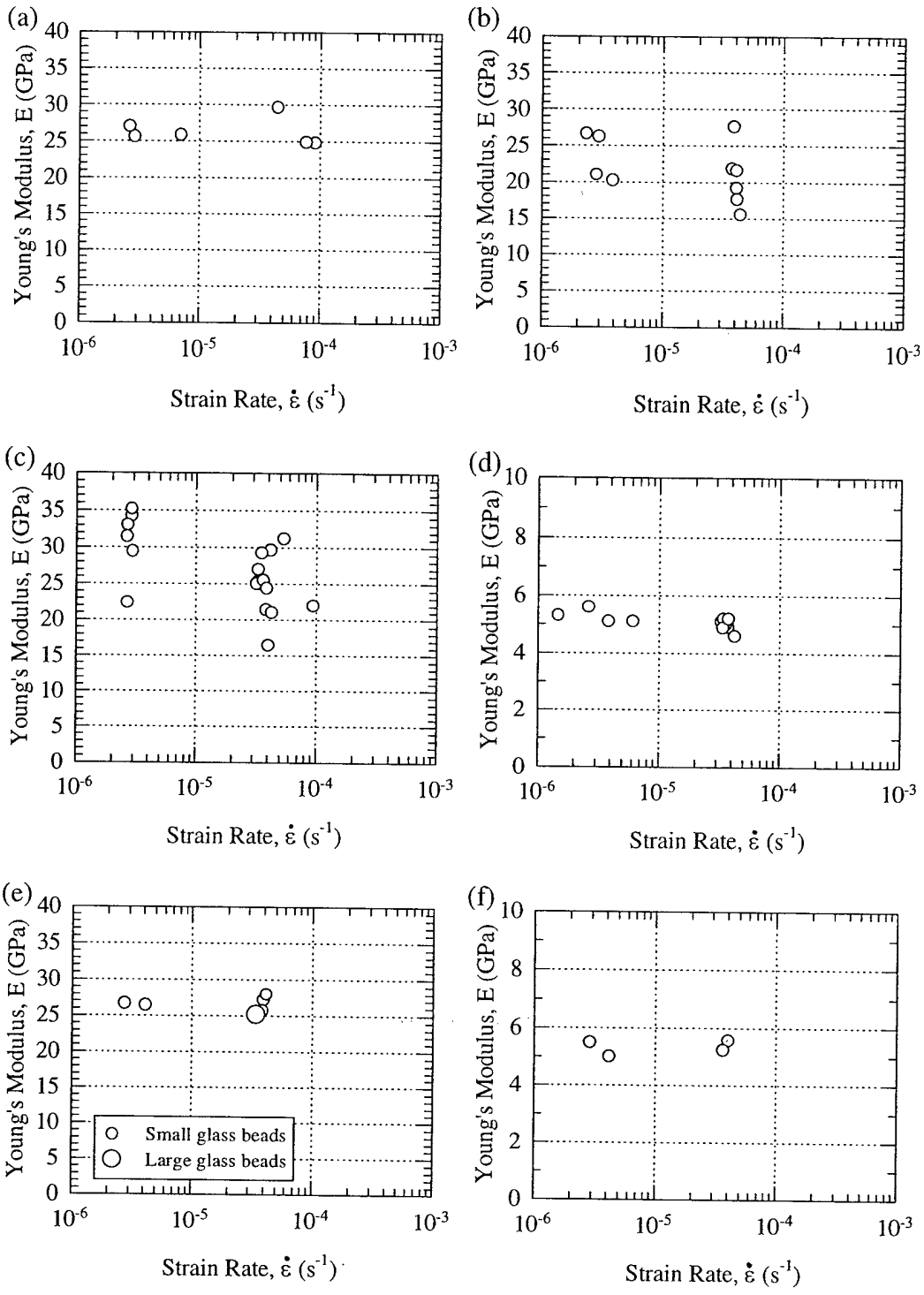

Figure 6.5: Effect of strain rate on Young's modulus of frozen systems at -10°C at varying void ratios and confining pressures; (a) Manchester fine sand, (b) hydrophobic Manchester fine sand (c) 2010 industrial quartz, (d) PMMA, (e) small and large glass beads, (f) polycrystalline ice.

6.2.4 Effect of Temperature

An extensive database encompassing the temperature range of -10°C to -25°C already exists on Manchester fine sand from the work of Andersen (1991) and Swan (1994). Therefore, one aspect of the experimental program was to augment this database by conducting a series of tests on Manchester fine sand at warmer temperatures to encompass a broader range of conditions of both practical and fundamental interest. Considering the difficulties in testing ice saturated specimens very close to its homologous temperature, it was decided to concentrate the majority of the tests at -5°C, and only perform a small sampling of tests at -2°C. In addition, since Swan (1994) found that the Young's modulus of frozen Manchester fine sand did not vary appreciably with temperature, even though it is reported to slightly influence the modulus of polycrystalline ice (Sinha 1989), it was then decided to investigate other particulate systems to see if any temperature dependence could be detected. Hence, a small number of tests were carried out on frozen systems of industrial quartz and PMMA over the relatively small temperature range of -5°C to -10°C.

The effect of temperature on the various materials tested during this program is shown in Figure 6.6a-e and summarized in Table 6.7. Only the modulus of ice (Figure 6.6e) and possibly the PMMA system (Figure 6.6d) show a clear dependence on temperature (i.e. becoming stiffer with decreasing temperature). Linear regression of the ice data reveals that this dependence is stronger than that which is theoretically predicted for the elastic behavior of pure polycrystalline ice over a similar temperature range (Sinha 1989). None of the other particulate materials tested show a similar dependence, although the scatter in the data from the angular systems may make it somewhat difficult to pick up a trend. There may be evidence however, as shown by the data on Manchester fine sand at -5°C and -2°C, that the variability in modulus increases at warmer temperatures. Clearly more tests need to be conducted at warmer temperatures to clarify the trend in modulus as the temperature approaches the melting point of ice.

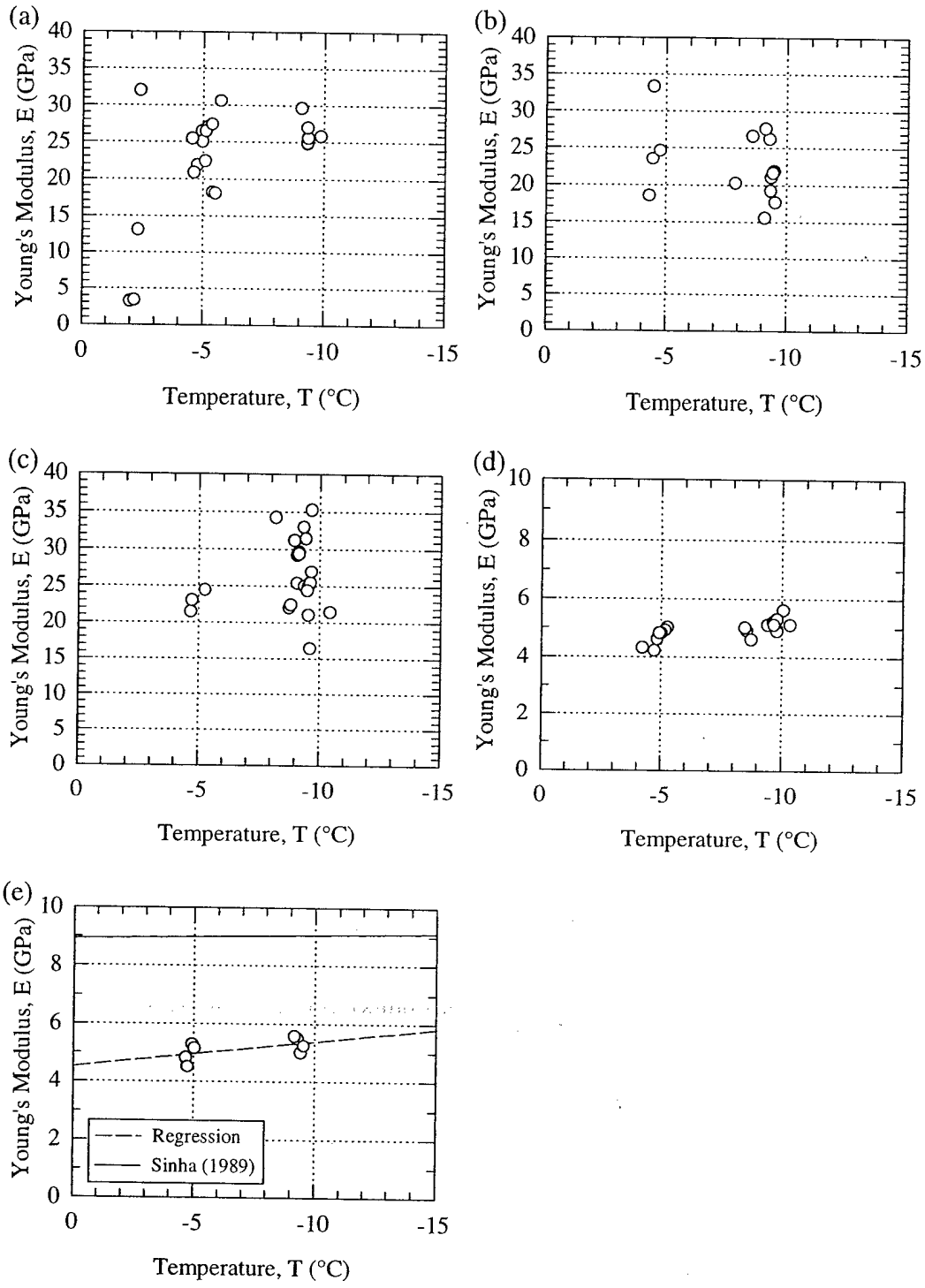

Figure 6.6: Effect of temperature on Young's modulus of frozen systems at varying void ratios, confining pressures and strain rates; (a) Manchester fine sand, (b) hydrophobic Manchester fine sand (c) 2010 industrial quartz, (d) PMMA, (e) polycrystalline ice.

Material Type	Mean±S.D. (GPa) T = -2°C	T = -5°C	T = -10°C
Manchester fine sand (MFS)	12.9±13.6 (n=4)	26.8±7.3 (n=10)	26.3±1.8 (n=6)
Hydrophobic MFS	N/A	25.0±6.2 (n=4)	21.7±4.0 (n=10)
Industrial quartz	N/A	22.9±1.5 (n=3)	26.8±5.0 (n=19)
PMMA	N/A	4.70±0.3 (n=7)	5.10±0.3 (n=11)
Polycrystalline ice	N/A	4.90±0.4 (n=4)	5.30±0.3 (n=4)

Table 6.7: Summary of the Young's modulus obtained for each material type at the various temperatures investigated.

6.2.5 Effect of Particle Modulus

Particle modulus is well-known to be an important variable to the resulting modulus of composite systems. Investigation of this parameter as part of the experimental program also provided an opportunity to validate a number of composite material models for direct application to frozen sand. This is described in detail in Section 6.4.

Manchester fine sand and industrial quartz, both being predominantly quartz-based, were assumed to have a mean particle modulus of 75 GPa based on their similarity to sands used in other programs (Counto 1964, Ishai and Cohen 1967, Ahmed and Jones 1990b). While this value is substantially lower than the 90 GPa assumed in the previous programs (Andersen et al. 1995), it was felt that it was more indicative of natural sands. In addition, the two types of glass beads used during this program were assumed to have the same modulus of 74 GPa, which is that for soda-lime glass (Gibson and Ashby 1988). This means that their behavior in frozen systems should emulate that of the Manchester fine sand and industrial quartz. This is indeed what has been observed and shown in the figures contained in the previous sections, but until now has not been formally explained. The similar particle moduli explain why the resulting composite moduli for all of these systems are approximately the same.

Therefore, in an effort to investigate the effect of changing this parameter, an alternative granular material with a substantially different modulus was sought. The polymer PMMA (polymethylmethacrylate) was chosen for its low modulus (3.3 GPa at 20°C) and relative abundance in granular form. However, the stiffness of polymers are very much affected by temperature and so a correction must be applied to this value. The

temperature dependence of the modulus of polymers in the glassy regime has been found to be well approximated by the linear equation (Gibson and Ashby 1988):

$$E_s = E_{so}\left(1 - \alpha_m \frac{T}{T_g}\right) \tag{6.1}$$

where E_{so} in the theoretical stiffness at 0°K, α_m accounts for the molecular relaxation processes that are temperature dependent, and T_g is the glass transition temperature. Substituting values for a typical amorphous polymer such as PMMA (E_{so}=7 GPa and α_m=0.5, T_g=378°K) results in a theoretical modulus of 4.5 GPa at -10°C.

The effect of particle modulus is shown in Figure 6.7 which presents the data on the systems described above as a function of void ratio for all confining pressures, strain rates, and temperatures investigated. Table 6.8 summarizes the average values of modulus for each of the materials and conditions shown in Figure 6.7. This figure clearly shows that the glass and quartz-based systems all have the same composite modulus of approximately 26 GPa. Furthermore, in comparing these systems to the PMMA system, it can be concluded that changing the particle modulus has a profound effect on the resulting composite modulus, since it dropped from 26 GPa to approximately 5 GPa.

Material Type	E_p (GPa)	Mean±S.D. (GPa) T = -5°C	Mean±S.D. (GPa) T = -10°C
Manchester fine sand (MFS)	75	26.8±7.3 (n=10)	26.3±1.8 (n=6)
Industrial quartz	75	22.9±1.5 (n=3)	26.8±5.0 (n=19)
PMMA	4.5*	4.70±0.3 (n=7)	5.10±0.3 (n=11)
Small glass beads	74	N/A	26.8±0.9 (n=5)
Large glass beads	74	N/A	25.2 (n=1)
Polycrystalline ice	N/A	4.90±0.4 (n=4)	5.30±0.3 (n=4)

Note: * indicates computed at -10°C

Table 6.8: Summary of the Young's modulus obtained for each material type at -5°C and -10°C at varying void ratios, confining pressures, and strain rates.

It is interesting to note the similarity between the data obtained on polycrystalline ice and the PMMA data at -5°C and -10°C. This similarity is shown in Figure 6.8 which compares these systems with respect to temperature. The fact that the PMMA data plots virtually on top of the polycrystalline ice data at both temperatures indicates that the

PMMA is not causing a stiffening effect leading to an increased modulus because the particles themselves have approximately the same stiffness as ice. Therefore, the measured temperature dependence described in Section 6.2.4 for the PMMA is primarily a reflection of ice behavior. As the stiffness of the particle increases (for a constant void ratio), this effect becomes masked as the system tends to become dominated by the temperature insensitivity of the much stiffer particles present.

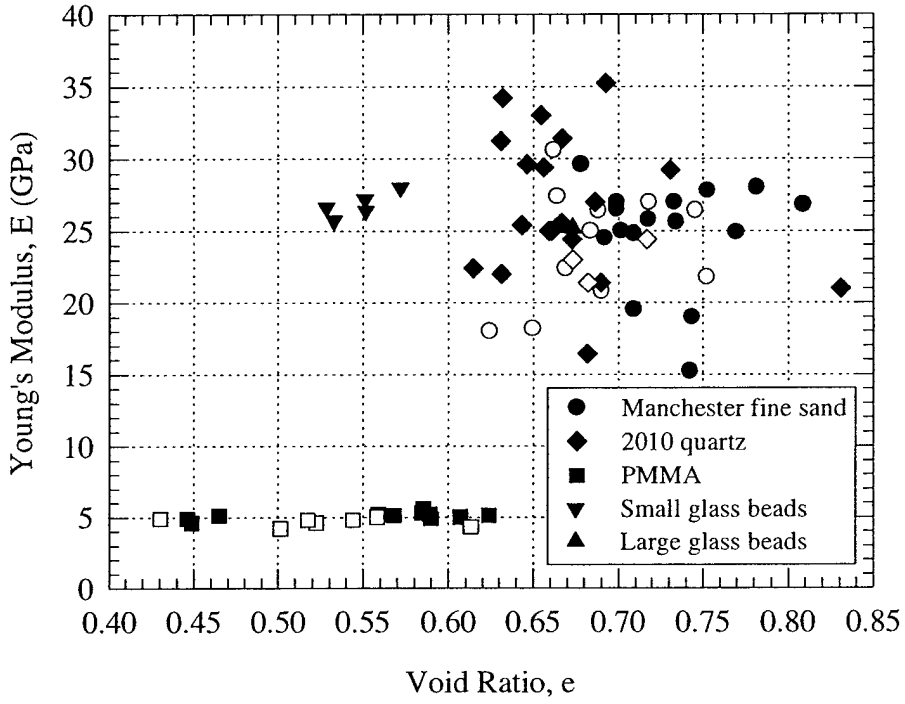

Figure 6.7: Effect of particle modulus on Young's modulus of frozen systems at -5°C and -10°C at varying confining pressures and strain rates. Note: open and closed symbols denote tests at -5°C and -10°C, respectively.

6.2.6 Effect of Particle Grain Size

The main motivation for undertaking a study of particle grain size was to investigate its influence on the upper yield behavior of frozen sands. However, it also provided an opportunity to investigate its influence on the Young's modulus of frozen particulate composites as well.

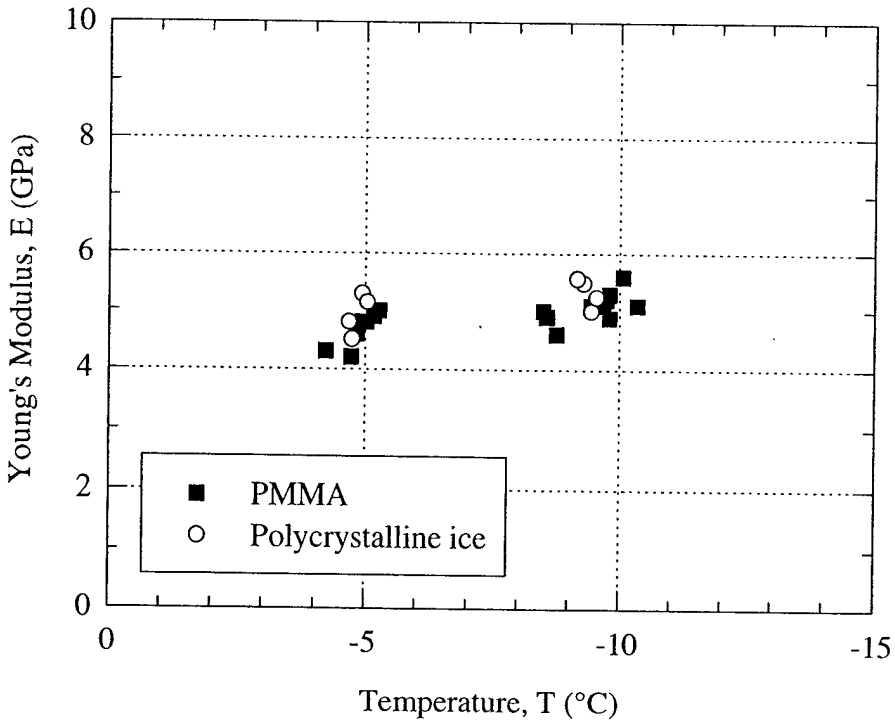

Figure 6.8: Comparison of Young's modulus of PMMA system with that of polycrystalline ice at varying void ratios, confining pressures, and strain rates.

Industrial quartz was the first material chosen for this purpose since it had similar angularity and mineralogical characteristics as those of Manchester fine sand. More importantly, since it is a quartz-based material, it is assumed to also have a similar particle modulus. As was just described in the previous section, the modulus of the particle has been shown to play a significant role on the overall composite modulus and so evaluating particle size effects using different materials necessitates the use of materials that have the same particle modulus. This fact also allows the consideration of data obtained from the glass bead systems since they too have a particle modulus similar to that of Manchester fine sand.

Most of the tests on the industrial quartz (22 out of 26) were conducted on the 2010 grade, which had a mean grain size of 0.54 mm as compared to 0.145 mm for Manchester fine sand. However, the 2075 grade, having a mean grain size of 1 mm (Sinfield 1997), was initially selected, and four specimens were tested at -5°C. The extreme angularity of the 2075 grade, however, caused problems with leakage through the

membranes and so it was decided to perform all the remaining tests on the finer 2010 grade. The glass bead testing program also involved two distinct particle sizes. The first system had an average particle size of 0.54 mm (Figure 4.2), while the other was composed of glass beads with a uniform diameter of 3 mm. Therefore, the influence of particle size on the composite modulus may be evaluated at five distinct grain sizes. Furthermore, since it was concluded in a previous section that temperature did not seem to affect the modulus of these frozen systems, it is possible to assess the effect of particle size using data obtained from tests performed at both -5°C and -10°C. The measured data for each of the five materials studied are plotted in Figure 6.9 and summarized in Table 6.9. It should be noted that only tests which had "fair" or "good/excellent" ACDT agreement have been used in this analysis in an effort to reduce the scatter in the data which may tend to mask a potential trend.

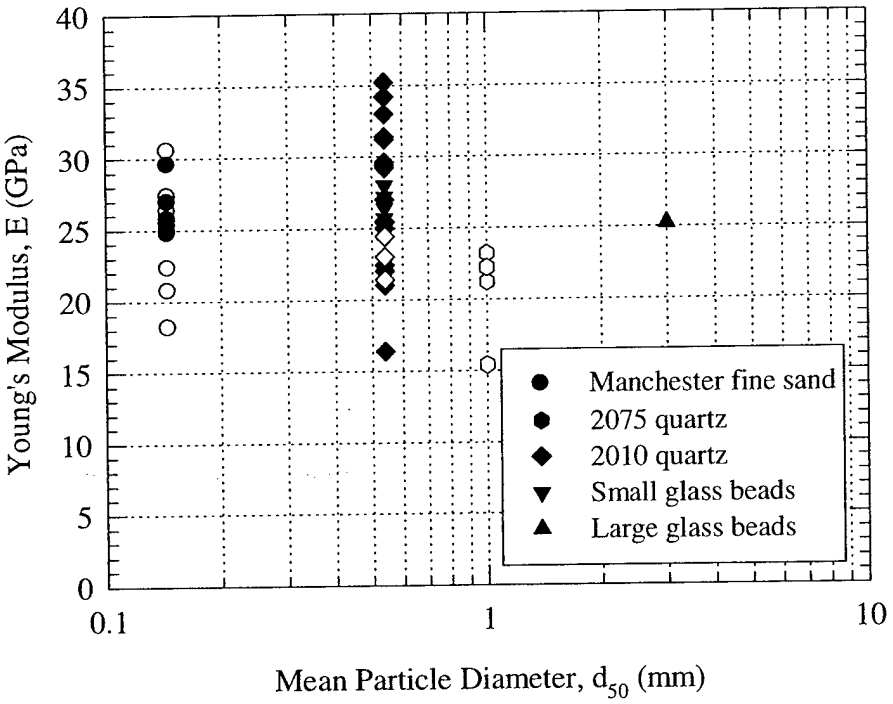

Figure 6.9: Effect of particle size on Young's modulus of frozen quartz based systems at -5°C and -10°C at varying void ratios, confining pressures, and strain rates. Note: open and closed symbols denote tests at -5°C and -10°C, respectively.

As Figure 6.9 and Table 6.9 show, there does not seem to be an influence of particle size on the Young's modulus of frozen sand, although more data are needed at the larger particle sizes in order to make a definitive statement. However, this observation agrees with the results of Ahmed and Jones (1990b) who found that particle size has little effect on the modulus of glass-filled resins.

Material Type	Grain Size d_{50} (mm)	Mean±S.D. (GPa) T = -5°C	Mean±S.D. (GPa) T = -10°C
Manchester fine sand	0.145	26.8±7.3 (n=10)	26.3±1.8 (n=6)
2010 industrial quartz	0.54	22.9±1.5 (n=3)	26.8±5.0 (n=19)
2075 industrial quartz	1.00	20.5±3.5 (n=4)	N/A
Small glass beads	0.54	N/A	26.8±0.9 (n=5)
Large glass beads	3.00	N/A	25.2 (n=1)

Table 6.9: Summary of the variation of Young's modulus with particle size at -5°C and -10°C at varying void ratios, confining pressures, and strain rates.

If a direct correlation is assumed between the particle size and the resulting ice grain size, then the insensitivity to particle size indicates that the modulus of the ice tested is also independent of grain size. This contradicts the findings of Cole (1990) who reported that the modulus of ice decreased with decreasing ice grain size. It is believed, however, that such a comparison may not be valid based on two reasons. The first being that the method of testing employed incurs substantial delayed elastic strains which prevent the true elastic response of ice to be observed; and the second being that the presence of particles have a substantial effect on the resulting composite modulus and hence may prevent small changes in the modulus of ice with decreasing grain size from being observed.

6.2.7 Effect of Interface Adhesion

A number of authors have alluded to the importance of the ice-silicate bond strength to the response of frozen sand systems (e.g., Ting et al. 1983, Baker and Kurfurst 1985, Andersen et al 1995). For example, Andersen et al. (1995) hypothesized that the bond which exists between the ice and the sand grains in frozen sand may be one of the physical mechanisms that cause the ice matrix to have an effective strength that is much

larger than bulk polycrystalline ice. Furthermore, most of the composite material models reviewed in Section 2.4 assume perfect bonding between the matrix and the inclusions, or that the adhesional strength is sufficient to transmit the shear stresses necessary to enable composite action. Interface adhesion characteristics were thus investigated during this experimental program by treating the material to make it hydrophobic in hopes that it would also become icephobic.

The two materials chosen for this investigation were Manchester fine sand and two sizes of spherical glass beads (Table 6.10). These materials were chosen since they represent extremes in both particle roughness and shape, which are properties that are known to be important in the behavior of unfrozen granular materials. Treatment of both materials was accomplished by the process outlined in Section 4.2.3.2. Although no unfrozen consolidated undrained triaxial compression (CIUC) tests were run on the treated materials to determine if the process caused changes in the frictional behavior of the particulate skeleton, the materials were qualitatively examined under a scanning electron microscope. Since no differences were observed between the SEM micrographs of the treated and untreated materials shown in Chapter 4, it was assumed that the frictional characteristics remained unchanged. Further support for this conclusion is provided by Ting et al. (1983) who found little difference in the drained friction angle between wetting and non-wetting glass beads tested in triaxial compression.

	Mean±S.D. (GPa)	
Material Type	**Regular**	**Hydrophobic**
Manchester fine sand	26.3±1.8 (n=6)	21.7±4.0 (n=10)
Small glass beads	26.8±0.9 (n=5)	5.70±0.2 (n=4)
Large glass beads	25.2 (n=1)	12.0±0.8 (n=2)

Table 6.10: Summary of the effect of interface adhesion on the Young's modulus of Manchester fine sand and glass bead systems at -10°C at varying void ratios, confining pressures, and strain rates.

Figure 6.10a-b shows the dependence of Young's modulus on void ratio for both materials in their treated and untreated states at -10°C. Figure 6.10a shows the behavior of treated and untreated Manchester fine sand. Not much difference can be seen in

comparing these data although it may be said that the hydrophobic system exhibits more scatter. The reason for this is unclear. Table 6.10 shows that the average value of the modulus of the hydrophobic Manchester fine sand system is lower than the untreated system by approximately 18% indicating either that the hydrophobic coating does not significantly alter the particle-matrix adhesional strength in a frozen two-phase system, or that the adhesional strength is not very important to the modulus of this particular system.

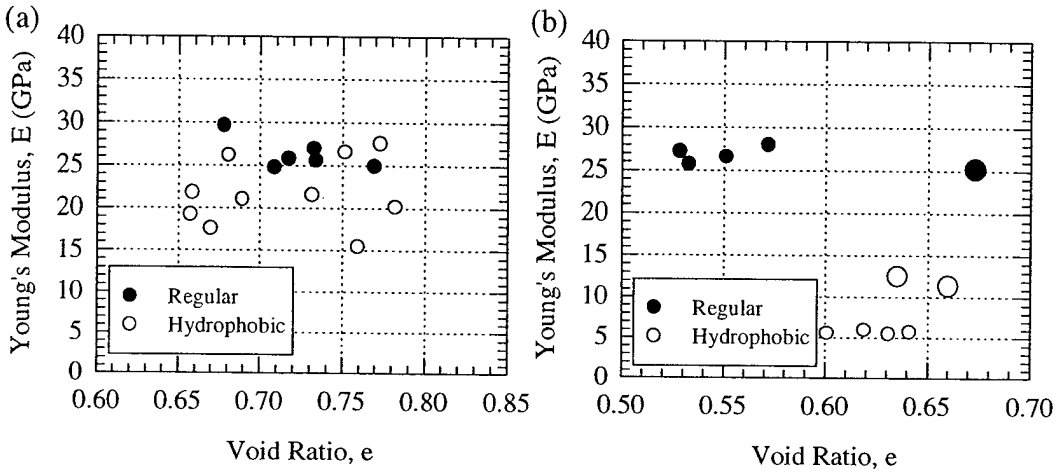

Figure 6.10: Effect of interface adhesion on Young's modulus results at -10°C at varying void ratios and strain rates for (a) Manchester fine sand, (b) small and large glass beads.

The uncertainty regarding the effectiveness of the hydrophobic coating at reducing ice adhesion in frozen MFS led to the investigation of the glass bead systems shown in Figure 6.10b. Spherical glass beads offer a more uniform mineralogical composition and reduce the potential effects of particle-ice interface interference resulting from the presence of surface roughness or shape. This makes them very attractive for use in the investigation of interface adhesion effects. The data shown in Figure 6.10b show that the hydrophobic coating has a very substantial effect as it decreases the modulus from an average of about 26 GPa to approximately 12 GPa for the large glass beads, and 6 GPa for the small glass beads (Table 6.10). This confirms that the hydrophobic treatment can change the adhesional characteristics of ice in frozen quartz-based particulate systems. Furthermore, these data shed some light on the mechanisms at work in frozen particulate systems. By comparing the Manchester fine sand and glass bead systems it appears that

particle roughness or angularity is extremely important to the observance of the bond strength effect. In rough angular systems (i.e. Manchester fine sand), surface treatment seems to have far less effect on the composite modulus due to the predominance of mechanical interference between the ice and the soil. In systems where little mechanical interlocking can develop, either because the particles are smooth or round, bond strength becomes very important. This hypothesis led to the investigation of particle roughness as discussed in the next section. A much more elaborate discussion of the importance of interface adhesion in particulate systems is given in Section 6.3.

6.2.8 Effect of Particle Roughness

The effect of particle shape or roughness is an important consideration in the strength of unfrozen sand. Similarly in frozen sand, structural hindrance, which depends on surface roughness and shape irregularity, greatly reduces creep susceptibility. The effect of particle shape was first noticed in the PMMA system (Figure 6.1c). Comparison of these data to that of Manchester fine sand or any other "natural" sand suggests that the presence of spherical particles leads to reduced scatter in the measured modulus. This observation is also confirmed by tests on spherical glass beads (Figure 6.1d).

As mentioned at the end of the previous section, the large effect of hydrophobic treatment on the glass bead systems compared to the relatively small effect for Manchester fine sand, initiated the investigation into the importance of particle roughness and particle shape. A small program was then performed using glass beads to determine whether the composite modulus in systems lacking adhesional strength could be increased by surface roughening.

The first tests were performed on acid-etched small glass beads. The process of acid-etching resulted in beads that were moderately roughened as shown in Figure 4.8g-h. The results of tests conducted at -10°C using these roughened glass beads, treated to make them hydrophobic, are shown in Figure 6.11 and summarized in Table 6.11. Particle roughening led to a 25% higher composite modulus, 7.1±1.0 GPa compared to 5.7±0.2 GPa for the hydrophobic smooth glass beads. This modest, yet significant, increase results from the increase in roughness imparted to the bead by the etching process.

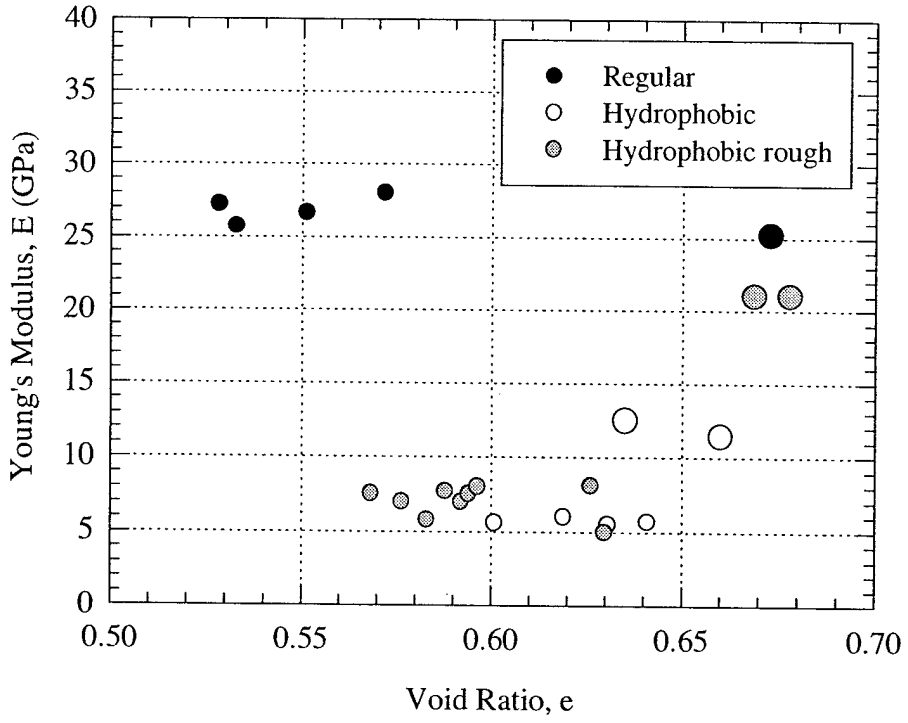

Figure 6.11: Effect of particle roughness on Young's modulus of small and large glass bead systems at -10°C at varying void ratios, confining pressures, and strain rates. Note: large symbols denote large glass beads.

	Mean±S.D. (GPa)		
Material Type	**Regular**	**Hydrophobic**	**Hydrophobic Rough**
Small glass beads	26.8±0.9 (n=5)	5.70±0.2 (n=4)	7.10±1.0 (n=9)
Large glass beads	25.2 (n=1)	12.0±0.8 (n=2)	21.0±0.0 (n=2)

Table 6.11: Summary of the effect of particle roughness on the Young's modulus of glass bead systems at -10°C and moderate strain rate at varying void ratios and confining pressures.

In an effort to obtain an extremely rough surface, large glass beads (3 mm) were individually mechanically roughened between two corundum grinding stones. The large beads were effectively roughened in a consistent manner using this technique, whereas the smaller beads could not be since they had a tendency to become pulverized in the process. Only a few tests were performed using these larger beads due to the amount of effort required to produce these roughened glass beads.

Only one test was performed on a system composed of large untreated smooth glass beads (before any surface treatment). This resulted in a modulus of 25.2 GPa which is consistent with the results in Table 6.9. The application of a hydrophobic treatment to these beads dropped the modulus to 12.0±0.8 GPa (Table 6.11). Although a value similar to that obtained for the small glass beads was expected, the smaller reduction may be due to less efficient surface treatment. Roughening the glass beads as described above and then applying the hydrophobic treatment resulted in a marked increase in the composite modulus to 21.0±0.0 GPa. This increase from 12.0 GPa shows that the degree of surface roughness is important in systems where reduced adhesional bonding exists between the ice and the soil. In addition, it appears that the degree of surface roughness, rather than particle shape, is the controlling variable affecting the composite modulus.

6.3 DISCUSSION OF MECHANISMS CONTROLLING YOUNG'S MODULUS OF FROZEN SAND

6.3.1 Introduction

The previous section presented the effects of the eight variables investigated (void ratio, confinement, strain rate, temperature, particle modulus, particle size, interface adhesion, and particle roughness) on the Young's modulus of frozen systems. The objective of this section is to synthesize those results in order to assess the relative importance of each variable, and to then take this information and build a qualitative framework for understanding the mechanisms controlling the Young's modulus of frozen sand. Ultimately, this information will be used in the development of a predictive technique for this parameter, as well as to guide assessment of predictive two-phase particulate composite material models for their suitability in describing the Young's modulus of frozen sand.

6.3.2 Summary of Observations on Young's Modulus

Before a discussion into the mechanisms controlling the development of stiffness in frozen particulate materials, it is useful to highlight the main findings of the experimental program. In order to better document the relative importance of the eight variables that

were investigated, data obtained from the previous experimental programs (i.e. Andersen et al. 1995) has been included in some of the summary plots that follow.

Section 6.2.1 presented the effect of void ratio (or relative density) on the Young's modulus of frozen particulate materials. Over the limited range of void ratios investigated during this research, it was concluded that the effect of this parameter was slight, even though it is well-known that this parameter is important to the stiffness of frozen soils as shown in Figure 2.22 (Baker and Kurfurst 1985) and in composite materials in general (Paul 1960, Ahmed and Jones 1990a). Furthermore, other data presented in Section 6.2 suggested that the stiffness is also relatively insensitive to the effects of confinement, strain rate, temperature, and particle size (Figures 6.4, 6.5, 6.6, 6.9) and hence confirm the results of Andersen et al. (1995). These observations are considered valid in light of the scatter which exists in the data, and the relatively small range investigated for each variable. The degree of confinement, while very important to the post-upper yield stress-strain behavior, is thought to have little impact on the elastic behavior of polycrystalline ice (Gold 1977, Singh and Jordaan 1996). Similarly, the temperature dependence of the modulus of polycrystalline ice over the range investigated is slight (Figure 2.7). Sinha (1989) calculates a 0.2 GPa increase in the theoretical modulus of ice from in going from -5°C to -25°C, the range in which data exists for Manchester fine sand. Data from Cole (1990) illustrates the existence of strain rate effects in polycrystalline ice, however, for the ranges investigated in this research program, the effect is small (2 GPa) and is probably masked by the scatter in these data. Finally, Ahmed and Jones (1990b) found that particle size has little effect on the modulus of glass-filled composites. However, in ice-filled systems where particle size effects are thought to manifest themselves as ice grain size effects, the dependence is difficult to evaluate mainly due to the inability to measure a truly unrelaxed modulus for ice.

The insensitivity to these parameters allows the investigation of the effect of void ratio over a larger range by permitting the inclusion of data at varying applied strain rates and temperatures. This has been done in Figure 6.12 which presents the variation of Young's modulus with relative density for Manchester fine sand for temperatures ranging

from -5°C to -25°C for all confining pressures and strain rates, however "poor" tests have been eliminated.

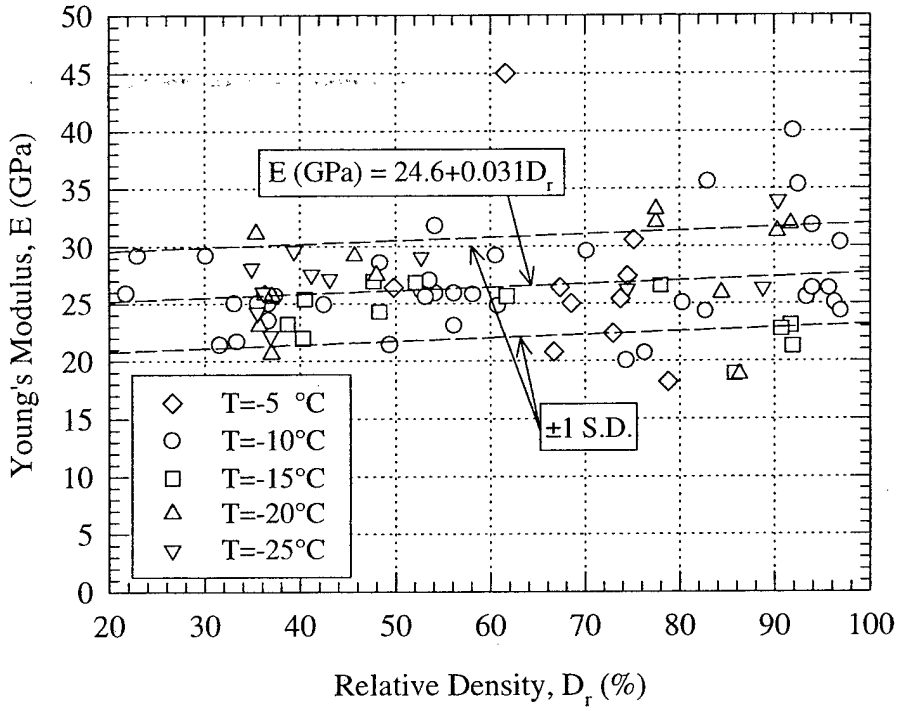

Figure 6.12: Variation of Young's modulus with relative density at varying temperatures for all confining pressures and strain rates. (adapted from Andersen et al. 1995)

Linear regression of the data in Figure 6.12 shows a slight increase in Young's modulus with increasing relative density. Although definitive verification of this effect is difficult, given the small range of particle volume fractions investigated and the scatter in the data, it is believed to be real based on the analyses presented in Section 6.4. However, from a practical viewpoint the modulus of frozen highly-filled particulate materials (where particles are in contact with one another) may be considered constant.

Another parameter that was shown to be important to the stiffness of frozen systems in the preceding section was particle modulus (Table 6.8). The importance of the modulus of the inclusions in particulate composite materials is well-known and their effect has been extensively studied (see Section 2.4). However, their importance to the stiffness of frozen systems has not yet been explicitly shown before this research.

The role of particle modulus was investigated by using granular PMMA, a polymer of low stiffness (~4.5 GPa), compared to natural sand particles which have a much higher stiffness (~75 GPa). The consequence of using lower modulus particles is a substantial decrease in the resulting composite modulus, as illustrated in Figure 6.7 and Table 6.8 by the drop in modulus from 26 GPa for the Manchester fine sand system to approximately 5 GPa for the system composed of PMMA. Furthermore, since systems having the same particle modulus as Manchester fine sand yet varying in particle size, shape, and origin (i.e. industrial quartz, glass beads) produced similar values for the composite modulus reinforces the importance of this parameter. This conclusion is shown in Figure 6.13 which illustrates the variation in the composite Young's modulus with particle modulus.

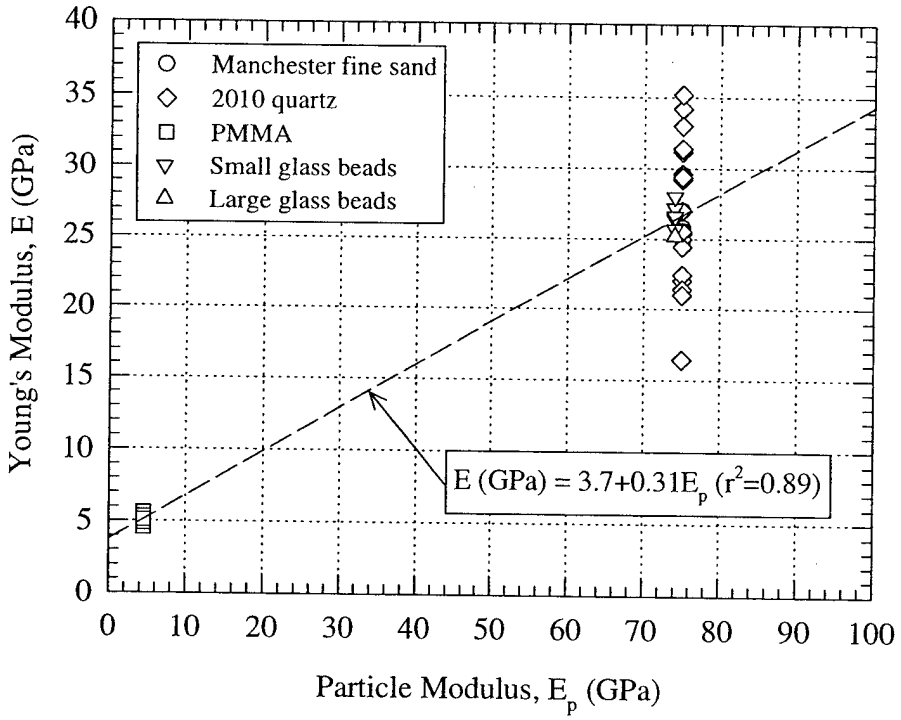

Figure 6.13: Variation of Young's modulus of frozen sand with particle modulus at -10°C at varying void ratios, confining pressures, and strain rates.

The insights gained from varying the particle modulus suggest that the modulus of the matrix material will have a profound impact on the resulting composite modulus, although tests to confirm this were not performed. This was predominately because of the difficulty in substantially altering the properties of ice. While substitution of various

polymeric materials for the ice matrix is possible, this was considered to be beyond the scope of this research program.

One of the key contributions of this research is the investigation into the importance of interface adhesion and particle roughness to the modulus of frozen systems. Most of the models that exist to describe the behavior of particulate composites assume that perfect bonding exists between the phases and that the adhesional strength is sufficient to enable composite action. This is especially important in the preparation of particulate polymer composites where two dissimilar materials are desgined to act together. Particle roughness, on the other hand, has not received much attention in the composite material literature, although it may affect the frictional characteristics and hence the development of strength in unfrozen granular materials. These two seemingly different variables are discussed together because they were found to be quite important to one another and to the overall stiffness of frozen particulate-filled materials.

As described in Section 6.2.7 and illustrated in Figure 6.10 and in Tables 6.10 and 6.11, the application of a hydrophobic coating to Manchester fine sand led to a modest drop in the resulting Young's modulus. However, a substantial drop in the modulus was observed for the hydrophobically treated glass bead systems. This observation confirmed the effectiveness of the treatment at reducing the bond strength, and of the importance of the adhesional bond in frozen granular materials. However, it also raised questions regarding the significance of particle shape and roughness, since a large bond strength effect was only noticed in the smooth spherical glass bead systems. Experiments on roughened glass beads, summarized in Table 6.11 and illustrated in Figure 6.11 indicate that in systems with little to no bond strength, particle roughness is extremely important and contributes to the development of stiffness by providing a source of mechanical interaction between the ice matrix and particle surface. It also eliminates the significance of particle shape, since the roughened particles were still very much spherical in shape (Figure 4.8e-f and Figure 4.9c-d).

A hypothesis to explain the interaction between particle roughness and interface adhesion is presented in Figure 6.14, which illustrates how these two parameters combine to affect stiffness. At low particle roughness, the stiffness is very much dependent on the

degree of adhesional bonding at the interface, whereas at higher values of particle roughness (denoted here by the symbol "ϕ" on an arbitrary scale ranging from 0 to 1) the importance of adhesion decreases due to the increase in mechanical interference that results between the rough particles and the matrix. This theory is illustrated using the concept of contours of adhesional bonding even though only the bounds have been established via experiments. However, it is reasonable to assume that degrees of adhesion may be present in particulate-filled systems depending on the effectiveness of the coupling or release agents used to modify the bond strength. Certainly the higher values for modulus measured in the tests on the large hydrophobic glass beads indicate that the hydrophobic coating did not completely eliminate the adhesional bond.

From the preceding presentation it can be concluded that of the eight variables investigated only void ratio (or particle volume fraction), particle modulus, interface adhesion, and particle roughness are important to the Young's modulus of frozen particulate systems. The other variables that were examined have been shown to be of minor importance over their respective ranges investigated confirming the results of earlier work (i.e. Andersen et al. 1995). However, the consideration of strain rate effects may become important if dynamic problems, such as those involving earthquake loadings, are to be investigated. Similarly, temperature considerations may also prove to be significant in problems involving the behavior of frozen soils at high temperatures. The next section will elaborate on the mechanisms behind the development of stiffness in frozen sands.

6.3.3 Development of Stiffness in Frozen Sand

Having concluded that the modulus of a two-phase composite is not only dependent on the moduli of the constituents and particle volume fraction, but also relies heavily on the extent of coupling between phases which is necessary for the effective transfer of stress, a conceptual qualitative model describing the mechanisms responsible for the stiffness of frozen sands can be developed.

Before discussing how the degree of coupling and hence transfer of stress occurs in a two-phase particulate system, which is considered to be the main contribution of this research, a short conceptual review of composite material behavior is warranted.

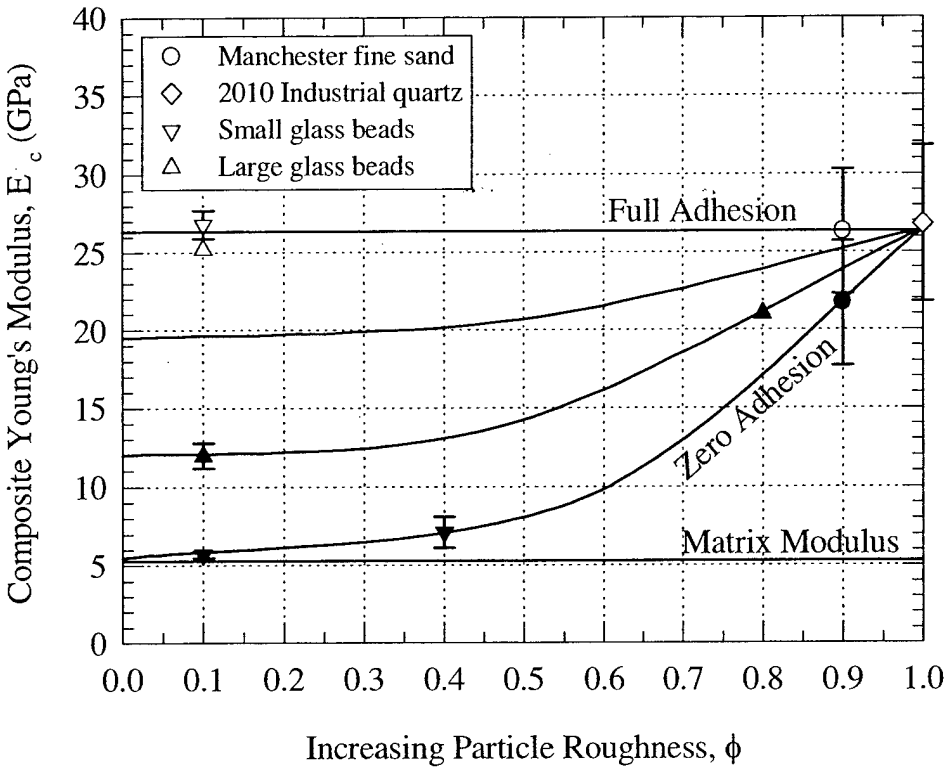

Figure 6.14: Interaction diagram for the influence of particle roughness and interface adhesion on the composite Young's modulus of frozen systems at -10°C. Note: open and closed symbols denote regular and hydrophobic systems, respectively.

In the development of a two-phase particulate composite material, it is well-known that its mechanical properties result from some combination of the material properties of the individual constituents. Therefore, focusing on the elastic properties, and namely the stiffness of frozen materials for this discussion, this requires that the resulting composite modulus must be that of ice modified by the presence of rigid inclusions. The trivial cases are those at the two extremes, which represent systems consisting of all matrix material (polycrystalline ice), or all inclusion material (quartz, if discussing frozen quartz-based sands). Therefore, the lowest modulus of a frozen sand must be that of ice and the highest possible value must be that of quartz. The difficulty lies in accurately predicting the variation of the composite modulus between these endpoints as a function of the amount or fraction of inclusion material present. This is not a trivial task as the consequence of this microstructural perturbation is a complex stress transfer mechanism involving higher

order particle interactions. Rigorous mathematical treatment of this type of problem in elasticity theory has not proved possible, however a number of approximate theories have been developed. These were discussed in Section 2.4 and their application to the systems investigated during this research is presented in the following section. Nevertheless, this simple thought experiment should confirm that the moduli of the individual constituents are of primary importance to the resulting composite modulus as is the volume fraction of inclusions which effectively controls the relative influence of each phase. Having established the reasons why the composite modulus is dependent on both the particle and matrix modulus, as well as the volume fraction of particles, it is necessary to explain the reasons for the observed dependence on the interfacial adhesion and particle roughness.

As alluded to in the previous discussion, the degree of coupling between phases is a prerequisite for stress transfer between the particle and matrix. It is well established that improving adhesion at the interface increases the fracture strength (Sahu and Broutman 1972, Leinder and Woodhams, 1974) and yield strength (Spanoudakis and Young 1984, Moloney et al 1983) of a composite. However, it is not entirely clear as to how this affects the Young's modulus of particulate-filled composites, especially when particles of different shape and roughness are considered.

There are a number of ways that the two phases in particulate materials may be coupled (bonded). Glass-filled polymeric materials usually rely on organic adhesion promoters such as silane-based compounds. In other systems, thermal compressive stresses resulting from a mismatch in the coefficients of thermal expansion can produce a substantial bonding effect. Finally, mechanical bonding can result due to the frictional characteristics of the particles and interparticle friction at the contacts (mechanical interactions). This last mechanism is well-known to be important in natural granular materials. In the natural (untreated) frozen systems that were investigated it is expected that bonding between phases is predominately due to some combination of the adhesive strength of ice, which is known to be very strong (Ryzhkin and Petrenko 1997), and the mechanical interactions between the ice matrix and the particle surface.

From the results presented in Sections 6.2.7 and 6.2.8 it is clear that in cases where the mechanical interactions are small (i.e. smooth round particles), the presence of an

adhesional bond is very important. This was shown for the glass bead system where a substantial drop in modulus was observed after treating the particles to make them hydrophobic. In contrast, in cases where the mechanical interactions are high, as in the system composed of Manchester fine sand, the internal shear stresses can be effectively transferred by friction at the interfaces and consequently the presence of an adhesional bond has little to no contribution on the stiffness of the system (Figure 6.14). A similar result was reported by other researchers who found that in the absence of chemical adhesion between particle and matrix, semi-angular shaped particulate-filled composites have higher moduli than their spherical counterparts (Ahmed and Jones 1990b). However, the author believes that it is the presence of particle surface roughness and not particle shape that is the reason for their observation of a higher modulus. This is based on the tests conducted on roughened glass bead systems, which by all accounts, were still very much spherical in shape after having undergone surface roughening. The fact that increasing surface roughness for the same particle shape leads to an increased modulus indicates that the Young's modulus is not particle shape dependent. Hence, this does not support the conclusion of Ahmed and Jones (1990b) who concluded that a composite with a higher degree of agglomeration is expected to have higher modulus.

Therefore, since it has been established that the presence of surface roughness dominates in frozen particulate systems, due to it providing effective mechanical interlocking, it will tend to override the presence of adhesional bonds. This means that even if the surface of a rough particle is made hydrophobic (for systems involving ice), the modulus will be little affected because of the mechanical coupling which already exists. This was confirmed by the tests on hydrophobic Manchester fine sand where the modulus dropped only by a modest amount.

Figure 6.15 schematically summarizes the main findings obtained from the analysis into the physical mechanisms controlling the Young's modulus of frozen sand. It is intended to give the reader an qualitative understanding of how the various parameters which have been shown to influence the modulus of frozen sands rank in terms of importance.

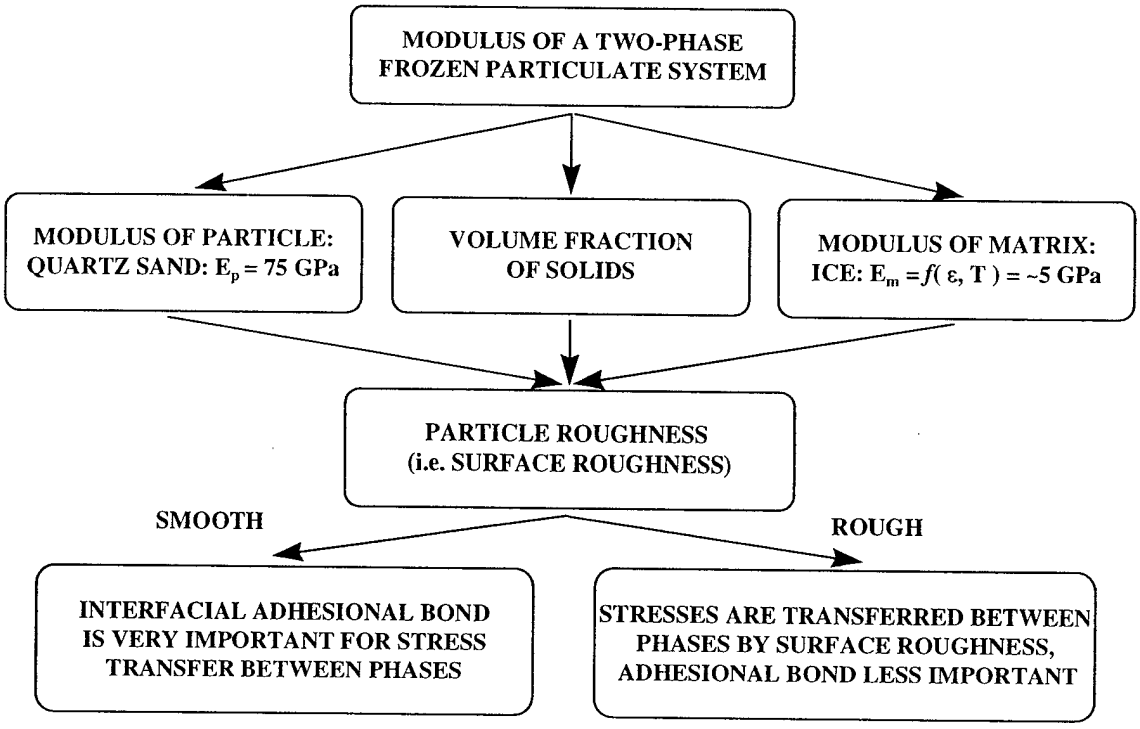

Figure 6.15: Proposed mechanism map for Young's modulus of frozen sand.

6.4 COMPARISON OF EXPERIMENTAL DATA WITH MODELS FOR TWO-PHASE PARTICULATE-FILLED SYSTEMS

6.4.1 Introduction

The discussion presented in the previous section has led to an improved understanding of the variables controlling the modulus of frozen sand and of particulate composite materials in general. The results indicate that the most important parameters contributing to the composite modulus of a two-phase system with perfect adhesion between phases are the moduli of the particle and matrix, and the volume fraction of solids (particle concentration).

The similarity between the factors controlling the modulus of frozen sand and those controlling the modulus of particulate composites in general suggests that frozen sand can be modeled as a two-phase composite material. This allows models already developed to predict the modulus of two-phase materials to be directly applied to frozen sand. Since one of the specific objectives of this research was to develop a practical methodology for predicting the Young's modulus of frozen sand, the purpose of this

section is to compare the experimental data obtained for Young's modulus with the various models available in the literature. Representative models developed for various composites ranging from plastics to concrete were presented in Section 2.4.2.

In the discussion that follows, model predictions are compared to the quartz-based systems, as well as to the PMMA system that was shown in Section 6.2.5 to produce a substantially lower composite modulus. The quartz-based data refer to all of the frozen systems with particles that were predominantly quartz, thus giving similar values for the composite modulus (~26 GPa). These included the systems composed of Manchester fine sand, industrial quartz, and small and large glass beads. These systems are characterized by a particle modulus of 75 GPa and a Poisson's ratio of 0.25 (Ahmed and Jones 1990b, Ishai and Cohen 1967, Counto 1964). The second system is composed of PMMA particles in an ice matrix and was included to provide another opportunity to test the predictive capability of the models. The spherical PMMA particles have a particle modulus of 4.5 GPa at -10°C (Gibson and Ashby 1988) and a Poisson's ratio of 0.30 (Miller 1996). The ice matrix in both cases is assumed to be described by the experimentally measured modulus for polycrystalline ice of 5.3 GPa (Table 6.7) and a Poisson's ratio of 0.31 (Sinha 1989). All comparisons are based on experimental data obtained at -10°C, however, data obtained at -5°C for the PMMA system has also been included for completeness. Furthermore, no attempt has been made to fit the various models to systems having undergone some type of surface treatment, since all the models that have been discussed assume perfect adhesion between phases and do not account for differences in particle roughness.

The following discussion is organized according to the three categories of predictive models presented in Section 2.4.2: models based on the theory of dilute suspensions, mechanistic models for composite materials, and effective medium models. The individual models comprising each category are then compared to the experimental data for the quartz-based and PMMA systems. Finally, a quantitative comparison of all the models presented in given in Section 6.4.5. This information will help in the development of a practical methodology for predicting the Young's modulus of frozen sand, outlined in Section 6.5.

6.4.2 Theory of Dilute Suspensions

As the name implies, models based on theories of dilute suspensions are strictly only applicable to those cases where the fractional volume of inclusions is very small. These models cannot be expected to capture the behavior of highly-filled systems such as those investigated, although they may be able to predict the correct behavior of bulk ice containing very low volume fractions of sand ("dirty ice"). In any case, these models serve as a useful starting point in the prediction of composite material behavior. A sampling of models based on the theory of dilute suspensions include those of Einstein (1906), Mooney (1951) and Brodnyan (1959). These were discussed in detail in Section 2.4.2.2.

A comparison of these models with the experimental data for both systems is given in Figure 6.16. The Einstein equation predicts a linear increase in modulus which clearly does not capture the behavior of either particulate system. This equation assumes no interaction between particles (i.e. a dilute system) and that the modulus of the particle is infinitely greater than the matrix. Both of these assumptions are not strictly correct for a rigid matrix. Mooney's attempt to account for particle interaction by incorporating a crowding factor (k=1.35) results in an expression that predicts considerably more reinforcing action than the Einstein equation. This is demonstrated by a modulus that tends to infinity at relatively low volume fractions. A similar result is predicted by Brodnyan who modified the Mooney equation to account for non-spherical particles through the inclusion of a particle aspect ratio ($1<p<15$). This solution predicts the development of higher stiffness at lower volume fractions for elongated particles (plotted for p=3). However, data collected on the quartz-based systems (e.g., the slightly elongated particles of Manchester fine sand) indicates that particle aspect ratio does not seem to be an important factor to the modulus of a frozen two-phase composite materials.

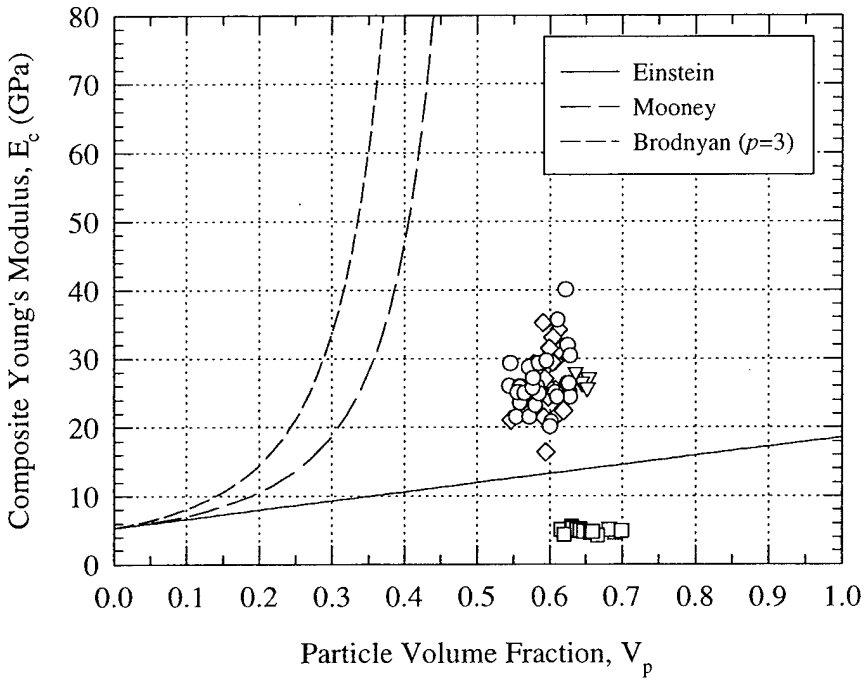

Figure 6.16: Comparison of dilute suspension models to experimental data on quartz and PMMA-based systems at -10°C at varying confining pressures and strain rates. Note: o Manchester fine sand, ◇ 2010 Industrial quartz, △ Small glass beads, ▽ Large glass beads, □ PMMA.

Clearly, none of these solutions offer satisfactory predictive capability for highly-filled particulate systems. Their simplistic formulation ignores many of the effects such as particle interaction and particle stiffness, which have been shown in the previous section to be very important. The lack of consideration of the particle modulus severely limits each models ability to describe the elastic behavior of systems composed of inclusions of different materials. Hence these models cannot account for the difference that exists between the sand and the PMMA-filled systems as shown in Figure 6.16. The correct predictive equation must therefore lie somewhere in between the solutions presented here.

The next category of models attempts to improve the predictive capability by considering the moduli of the constituents, the distribution of stresses and strains in the composite, and by making some assumptions regarding the geometry of the individual phases.

6.4.3 Mechanistic Models for Composite Materials

This second group of predictive models range from approximate approaches to sophisticated variational methods involving the theory of linear elasticity. Although the approaches vary widely in their treatment of the problem, all still must make simplifying assumptions in order to make the general analysis tractable. It is these assumptions that distinguish each of the models discussed below.

The simplest possible approach for determining the modulus of a two-phase system is to assume that the materials are either coupled in parallel or in series, as was shown in Figure 2.38. The solutions to these configurations are known as the classic results of Voigt (1910) and Reuss (1929) and are given below in Equation 6.2 and Equation 6.3, respectively.

$$E_c = E_i\, c + E_m\,(1-c) \tag{6.2}$$

$$\frac{1}{E_c} = \frac{c}{E_i} + \frac{(1-c)}{E_m} \tag{6.3}$$

As before, c refers to the volume fraction of inclusions (particles), and E_c, E_i, and E_m refer to the modulus of the composite, inclusion and matrix, respectively.

Examination of the Voigt and Reuss models shows that they represent extremes in material behavior, and if the Poisson's ratio of the two phases were equal, then Equations 6.2 and 6.3 actually provide the upper and lower bound solutions. In an attempt to account for the complex stress distribution in a two-phase system, Hirsch (1962) proposed a relation (Equation 6.4) which is basically a weighted average of Equations 6.2 and 6.3:

$$\frac{1}{E_c} = \left(1 - \frac{2Z}{\pi}\right)\left(\frac{c}{E_i} + \frac{(1-c)}{E_m}\right) + \frac{2Z}{\pi}\left(\frac{1}{E_i\, c + E_m(1-c)}\right) \tag{6.4}$$

where Z=0.785 as recommended by Hirsch (1962) based on tests from a series of concrete systems.

The theoretical curves predicted by these three models are compared in Figure 6.17a-b with the data for the quartz-based materials (i.e. Manchester fine sand, industrial quartz, glass beads). The curves were obtained using a inclusion (particle) modulus (E_i) of 75 GPa and an ice matrix modulus (E_m) of 5.3 GPa. The upper and lower bounds provided by Equation 6.2 and 6.3 are widely spaced and of limited predictive value,

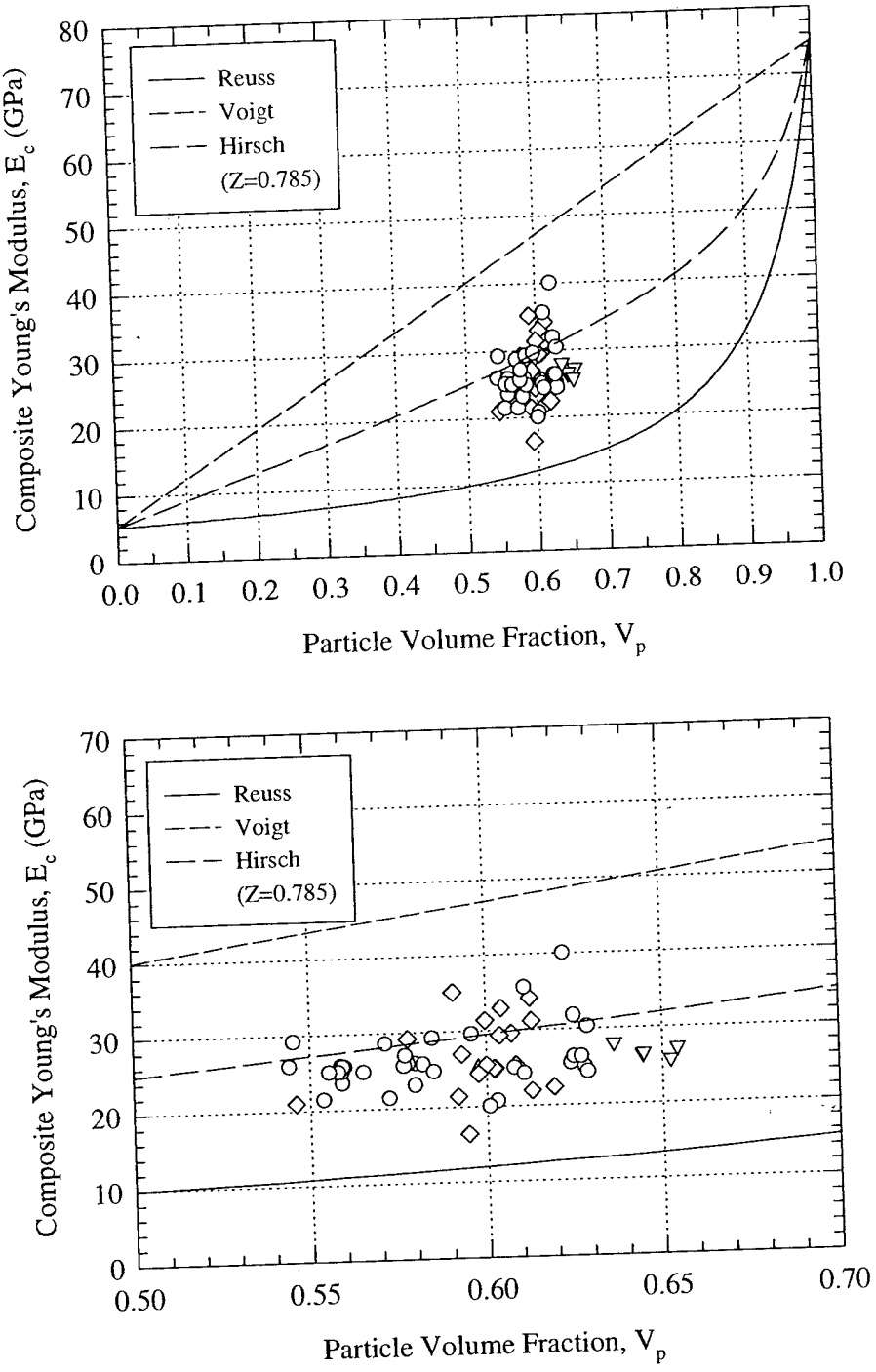

Figure 6.17: Comparison of Voigt, Reuss, and Hirsch models to experimental data for quartz-based systems at -10°C at varying confining pressures and strain rates for (a) V_p=0.00-1.00, (b) V_p=0.50-0.70. Note: o Manchester fine sand, ◇ 2010 Industrial quartz, △ Small glass beads, ▽ Large glass beads.

whereas the estimation by Hirsch (Equation 6.4) defines the average of the two bounds and thus provides an intermediate solution which, although somewhat high, provides an acceptable fit to the data (Figure 6.17b).

A further check on the ability of these models to describe the variation of the composite modulus is illustrated in Figure 6.18 for the data on the PMMA system. The small difference in modulus between the inclusion and matrix (E_i=4.5 GPa and E_m=5.3 GPa at -10°C) in this system results in the three models being essentially equal. This is expected as the spacing of the bounds is controlled by the modulus ratio between the two phases. Therefore, the PMMA system is of limited use for validating the fit of various models.

A number of other solutions for predicting the composite elastic modulus, which are neither upper nor lower bounds, have also been derived by various authors (e.g., Paul 1960, Counto 1964, Ishai 1965, Ravichandran 1994). These models assume that the macroscopic stress and strain can be reproduced in some average sense on a typical unit volume of a specified geometry (usually cubic) which contains a single inclusion of the second phase. Since most of these models assume the inclusion to be cubic, their different formulations are a result of the assumptions made in specifying the state of stress or strain at the boundary.

In Figure 6.19a the modulus of the quartz-based frozen composites are compared with three approximate solutions over the entire range of volume fraction using the values for the particle and matrix modulus given previously. The results show that all of these models tend to underestimate the experimental data, and that they do not differ greatly in their predictions. As discussed in Section 2.4.2.3, the upper and lower bound solutions provided by Ravichandran (1994) mimic the results of Paul (1960) and Ishai (1965) respectively and so are not shown in this figure. The inadequacy of the Counto model contrasts the findings of Andersen et al. (1995) which concluded that the Counto model provided a satisfactory fit to data on Manchester fine sand over a wide range of temperatures. The reasons for the disagreement are the values chosen for the particle and matrix modulus. They assumed a value of 90 GPa for the sand particles based on the value for quartzite quoted in Lambe and Whitman (1969). A value of 75 GPa was decided

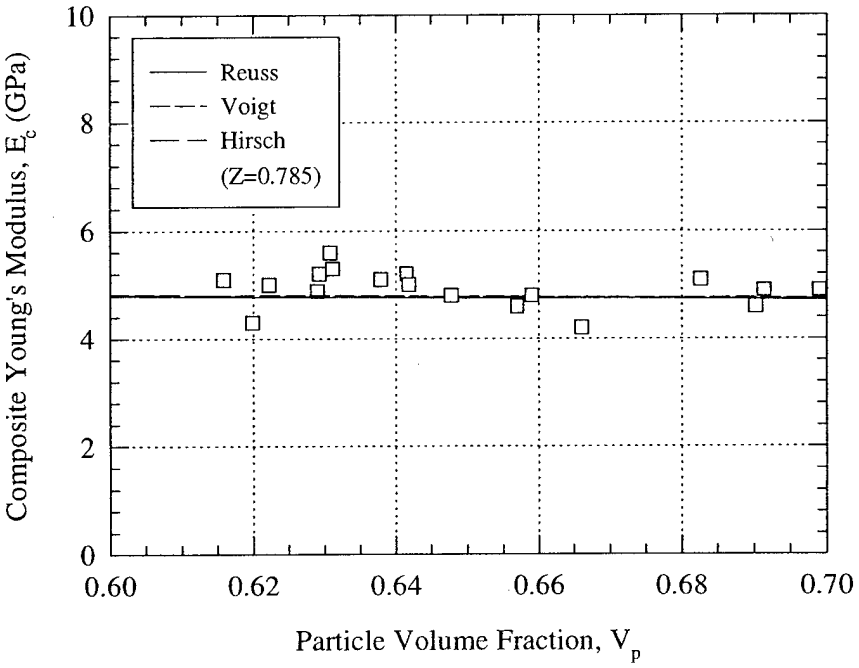

Figure 6.18: Comparison of Voigt, Reuss, and Hirsch models to experimental data for PMMA-based systems at -5°C and -10°C for V_p=0.60-0.70 at varying confining pressures and strain rates.

to be more realistic based on values taken from other programs studying particulate composites. Furthermore, Andersen et al. (1995) used the theoretical value of 9 GPa for the modulus of polycrystalline ice, whereas measurements performed during this research have found it to be substantially lower, around 5.3 GPa at -10°C as a result of delayed elastic strain effects induced by the testing procedure. It therefore seems unwarranted to use the theoretical modulus value for ice in a predictive model when the ice phase in the frozen composite most likely reflects this lower value.

Figure 6.19b provides a better idea of the fit of the three approximate solutions to the data on the quartz-based systems by focusing on the volume fraction range encompassing the data shown. Also given in Figure 6.19b are the various model fits to the data obtained on the PMMA system. Once again, it is very difficult to distinguish the various solutions for this system due to its small modulus ratio. As mentioned before, this results in very little variation between most models.

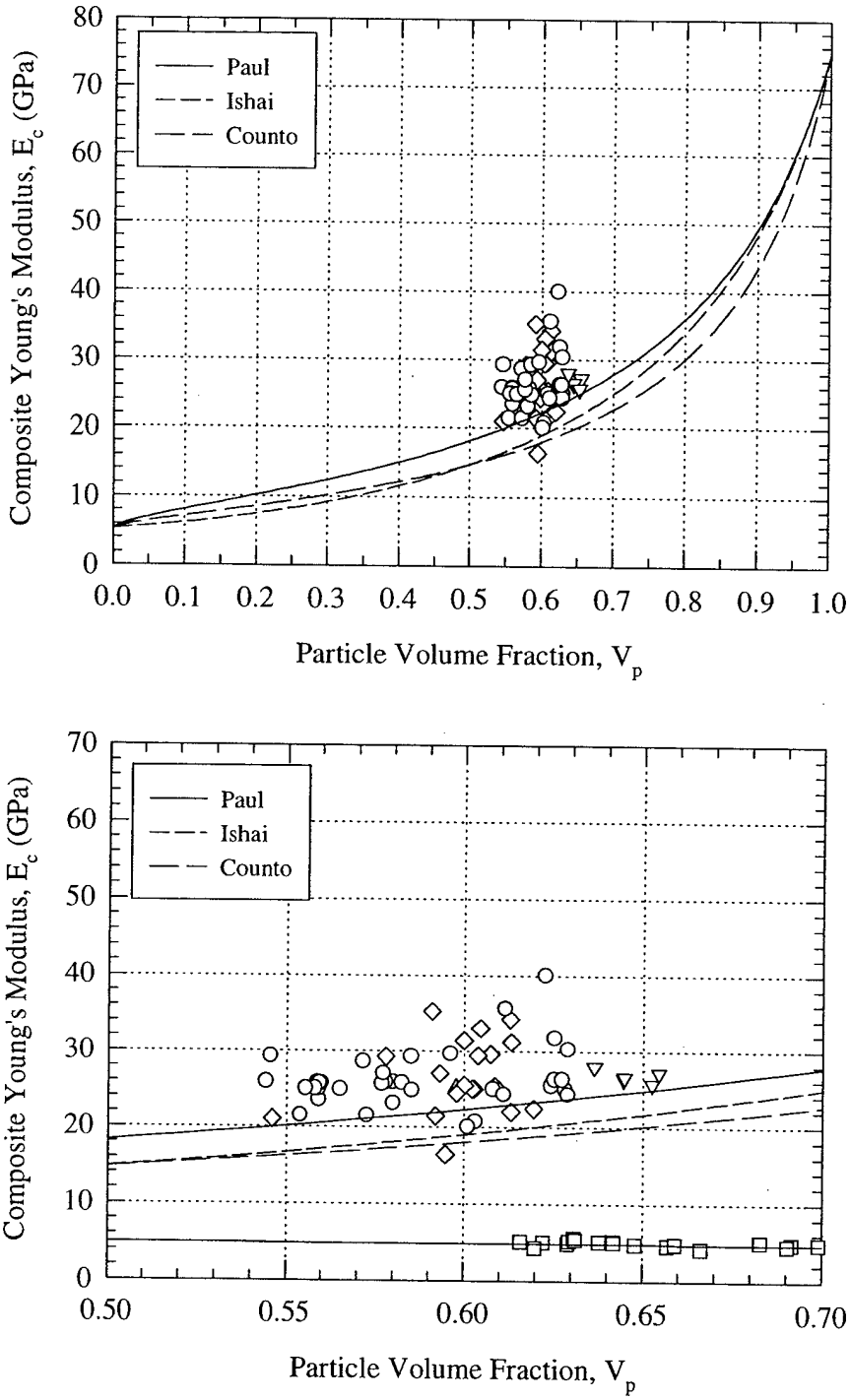

Figure 6.19: Comparison of Paul, Ishai, and Counto models to experimental data at -10°C at varying confining pressures and strain rates for (a) quartz-based systems, V_p=0.00-1.00, (b) quartz and PMMA-based systems, V_p=0.50-0.70. Note: o Manchester fine sand, ◇ 2010 Industrial quartz, △ Small glass beads, ▽ Large glass beads, □ PMMA.

Following the work of Paul (1960) and Hashin (1962), Hashin and Shtrikman (1963) derived upper and lower bounds for the effective elastic modulus of a two-phase material by invoking variational principles in the linear theory of elasticity and without making any assumptions about phase geometry. The determination of the Young's modulus of a composite using this formulation requires the calculation of the upper and lower limits of the bulk modulus K, and the shear modulus G. The equations which define the Hashin and Shtrikman upper and lower bounds have been given in Section 2.4.2.3 and, due to their length, have not been included again here. As Figure 6.20a-b shows, these bounds provide a much closer approximation than the Voigt and Reuss bounds given by Equations 6.2 and 6.3. The spacing of these bounds, however, is still dependent on the modulus ratio of particle to matrix which means that they are still rather widely spaced for the quartz-based systems. Nevertheless, for the quartz system shown in Figure 6.20a this formulation provides a solution that bounds the scatter in the data quite nicely. The fit to the PMMA system shown in Figure 6.20b is equally good, as would be expected.

In contrast to the theoretical treatment of the composite modulus provided by Hashin and Shtrikman, the Bache and Nepper-Christensen (BNC) model (Lydon and Balendran 1986), also presented in Section 2.4.2.3 and described by Equation 6.5, is completely empirical. However, it provides quite a satisfactory solution to the particulate-filled systems shown in Figure 6.20a-b, spanning the approximate mean of the Hashin and Shtrikman solution.

$$E_c = E_m\left(\frac{E_i}{E_m}\right)^c \tag{6.5}$$

Of all the models reviewed thus far, and although more tests over a larger range in volume fraction are needed to confirm its applicability, the BNC model seems to be the most attractive model for determining the composite modulus of frozen sands. Its simplicity also makes it potentially useful in design calculations.

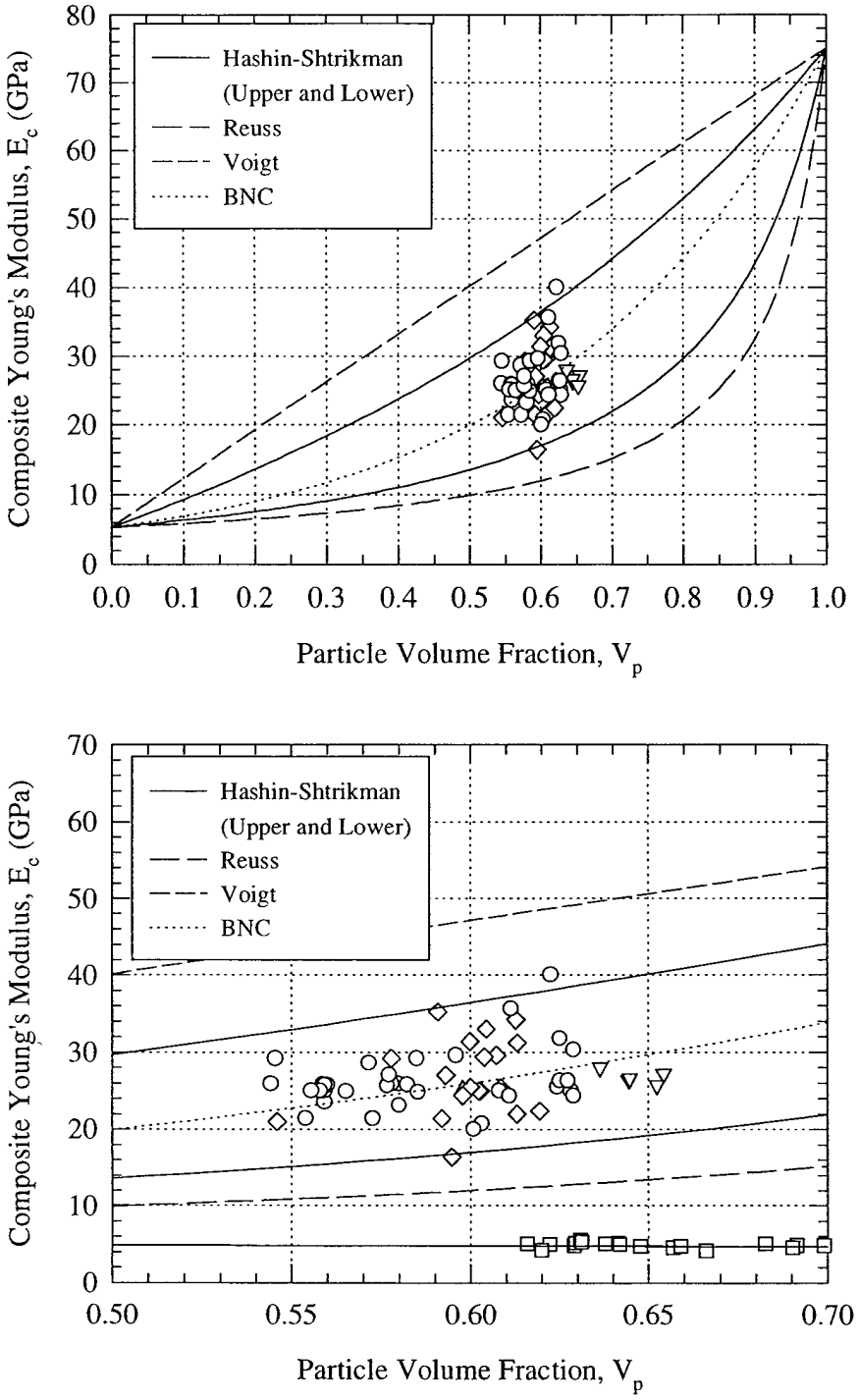

Figure 6.20: Comparison of Hashin-Shtrikman, Voigt, Reuss, and BNC models to experimental data at -10°C at varying confining pressures and strain rates for (a) quartz-based systems, V_p=0.00-1.00, (b) quartz and PMMA-based systems, V_p=0.50-0.70. Note: o Manchester fine sand, ◇ 2010 Industrial quartz, △ Small glass beads, ▽ Large glass beads, □ PMMA.

6.4.4 Effective Medium Models

The last group of predictive models are the effective medium models. These were discussed in Section 2.4.2.4 and are so named because they deduce the composite material properties either by a microstructural transformation of the material into some mechanically equivalent medium, or by the transformation of the overall material into an effective homogenous medium possessing the same average conditions of stress and strain as does some volume-averaged representative element. While a number of effective medium models exist in the literature, most stem from the original work of Kerner (1956). The ones discussed here are the Generalized Self Consistent Model (GSCM) developed by Christensen and Lo (1979), the Mori-Tanaka Method (Mori and Tanaka 1973), and that of Fan et al. (1992), which is based on a topological transformation and mean field theory.

The theoretical curves predicted by these effective medium models are shown in Figure 6.21a-b along with the BNC model that was presented in the previous section. The best prediction from this group of models is given by the field theory model of Fan et al. (1992) which agrees with the BNC model at low volume fractions, and only deviates slightly from it at higher concentrations. The other two models both follow the lower Hashin-Shtrikman bound and therefore underestimates the data. In fact, the MTM corresponds exactly to the lower Hashin-Shtrikman bound. This was first noticed by Willis (1977).

Figure 6.21b provides a detailed look at how well these models describe the various particulate systems. It is clearly evident that the effective medium model of Fan et al. (1992) along with the BNC model provide the best fit to the particulate systems that were investigated during this research. However, given the complexity of the mean field approach, described in Section 2.4.2.4, the BNC model remains the most attractive model for predicting the composite modulus of a two-phase material even though it has no physical basis. Should a bounded solution be desired then the Hashin-Shtrikman formulation provides upper and lower bound estimates with the least effort (Figure 6.20b).

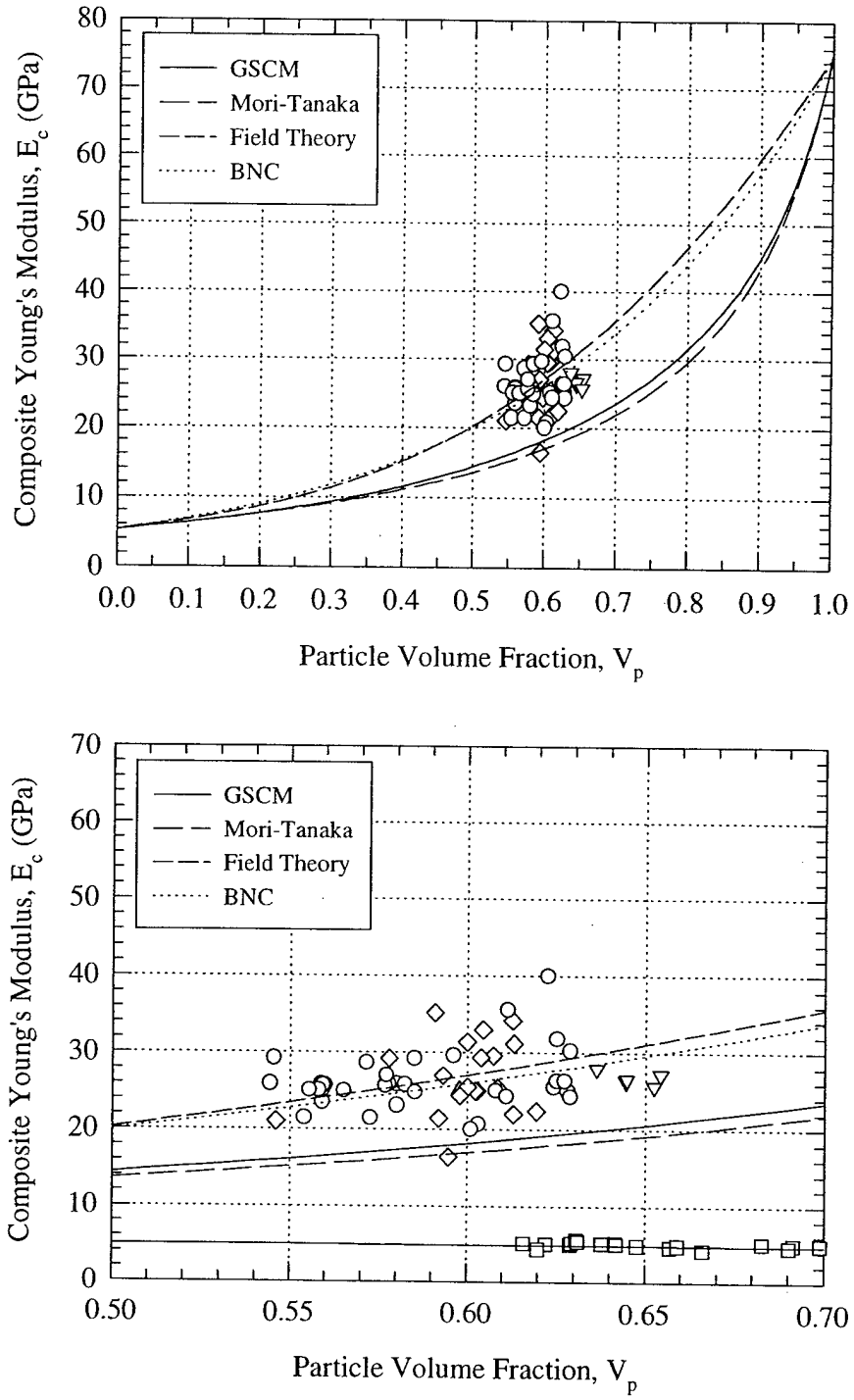

Figure 6.21: Comparison of Mori-Tanaka, GSCM, Field Theory, and BNC models to experimental data at -10°C at varying confining pressures and strain rates for (a) quartz-based systems, V_p=0.00-1.00, (b) quartz and PMMA-based systems, V_p=0.50-0.70. Note: o Manchester fine sand, ◇ 2010 Industrial quartz, △ Small glass beads, ▽ Large glass beads, □ PMMA.

6.4.5 Evaluation of Composite Material Models

Having presented a qualitative comparison of each of the models with the experimental data in the previous section, it is useful to establish a quantitative framework for their evaluation. Conceptually, it is assumed that each observation of the measured modulus is described by the product of the model prediction, some bias (β), and an error term (ε) resulting from the fact that each observation was experimentally measured. Mathematically, this can be expressed as:

$$E_{measured} = \frac{1}{\beta} \cdot E_{predicted} \cdot \varepsilon \tag{6.6}$$

The product of $(1/\beta)\cdot E_{predicted}$ in Equation 6.6 represents the true modulus for the value of volume fraction used in the experiments. In general the bias term β should be allowed to depend on the volume fraction. However, the range of volume fraction values in the experimental data is quite small and in this range β may be considered constant. Since the terms in the above expression are multiplicative and positive, it is convenient to rewrite the equation by expressing it in logarithmic form:

$$\log E_{measured} = -\log\beta + \log E_{predicted} + \log\varepsilon \tag{6.7}$$

The data can now be used to calculate the empirical log bias ($\underline{\log \beta}$), the variance of log ε (σ^2) and the root mean square error ($Error_{rms}$) of the log model. These parameters may be expressed mathematically as:

$$\underline{\log\beta} = -\frac{1}{n}\sum_{i}^{n}\left(\log E_{measured} - \log E_{predicted}\right) \tag{6.8}$$

$$\sigma^2 = \frac{1}{n-1}\sum_{i}^{n}\left(\log E_{measured} - \log E_{predicted} + \underline{\log\beta}\right)^2 \tag{6.9}$$

$$Error_{rms} = \sqrt{\frac{1}{n}\sum_{i}^{n}\left(\log E_{measured} - \log E_{predicted}\right)^2} \tag{6.10}$$

Notice that the empirical variance of log ε (σ^2) varies from model to model only due to variations in the slope of each model within the range of volume fractions investigated. These variations are very modest and therefore a comparison of the models

may be based on either the empirical log bias ($\underline{\log \beta}$) or the root mean squared error ($Error_{rms}$).

Considering the measurement error to be independent and identically distributed for different measurements, it is possible to use the experimental data to test the hypothesis that $\underline{\log \beta}$ for each of the given models is zero. In fact, under the null hypothesis that $\underline{\log \beta} = 0$, $\underline{\log \beta}$ has (with good approximation given the large sample size) a normal distribution with a mean value of zero and variance σ^2/n. From Table 6.12 the variance of the log ε (σ^2) is approximately 0.0043 for the quartz systems (n=60) and 0.0004 for the PMMA system (n=11). Hence σ^2/n is 7.1×10^{-6} and 3.6×10^{-5}, respectively. One would then accept the null hypothesis that $\underline{\log \beta} = 0$ at a significance level of 10% if:

$$\left| \underline{\log \beta} \right| < \sqrt{\left(\frac{\sigma^2}{n} \right)} \cdot Z_{0.05} \tag{6.11}$$

where $Z_{0.05}$ is the value exceeded by the standard normal variable with a probability of 0.05. This gives a critical value of 0.0139 (1.39%) for the quartz system and 0.0099 (0.99%) for the PMMA system. Models with empirical log bias values less then these values may be considered to be consistent with the data (unbiased) and hence plausibly correct. In addition, comparing the sign of this quantity in Table 6.12 gives an indication as to whether the model overpredicts or underpredicts the data.

Comparing the statistics for the dilute suspension models, it is clear that the Einstein equation provides the best fit of the three models presented in this category although it is far from being useful in a predictive sense due to its severe underestimation of the data. The poor fit of these models was expected, however, since they were originally developed to describe the behavior of dilute suspensions of rigid particles in a viscous matrix, and not the type of highly-filled systems presented here.

Of the mechanistic models presented, the best fit was clearly achieved by the Bache and Nepper-Christensen (BNC) model which is interesting given that it has no theoretical basis. Moreover, its simplicity and excellent fit to the experimental data makes it very attractive for computing the composite modulus of frozen sands in engineering practice. Of the remaining models in this category, only the formulation by Hirsch, which has been shown for equal weighting between the upper and lower bound solutions

Model Type	Variance of log ε (x100)		Empirical Log Bias (x100)		RMS Error (x100)	
	Quartz Systems	PMMA System	Quartz Systems	PMMA System	Quartz Systems	PMMA System
Dilute Suspension						
Einstein	0.41	.088	-29.72	43.53	30.39	43.62
Mooney	80.1	817.9	278.5	623.4	292.3	680.5
Brodnyan	108.6	1104.4	335.1	724.6	350.7	790.9
Mechanistic						
Reuss (Series)	0.42	0.044	-34.20	-2.90	34.80	3.52
Voigt (Parallel)	0.41	0.044	25.27	-2.64	26.06	3.31
Hirsch (Z=0.785)	0.41	0.044	5.01	-2.77	8.09	3.41
Paul	0.42	0.044	-7.32	-2.71	9.75	3.37
Ishai	0.44	0.044	-14.37	-2.74	15.81	3.39
Counto	0.42	0.044	-16.59	-2.75	17.79	3.40
BNC	0.44	0.044	-0.74	-2.77	6.62	3.42
Hashin-Shtrikman (LB)	0.43	0.044	-19.16	-2.77	20.23	3.41
Hashin-Shtrikman (UB)	0.42	0.044	14.00	-2.78	15.39	3.42
Effective Medium						
Mori-Tanaka	0.43	0.044	-19.16	-2.77	20.23	3.41
GSCM	0.43	0.044	-16.17	-2.77	17.43	3.41
Field Theory	0.45	0.044	0.92	-2.73	6.71	3.38

Table 6.12: Comparison of experimental data with predictive models for two-phase particulate systems at -10°C.

(Z=0.785) should be considered. Clearly, by adjusting the weighting factor an even better fit can be achieved. However, without a rational basis for adjusting this parameter, it is not possible to use this model in a predictive sense.

Special mention must be made of the bounding solution given by Hashin and Shtrikman. Due to the large separation of the bounds which result from the fact that frozen sand has a high modulus ratio of particle to matrix, it is difficult to recommend this model for predicting the composite modulus. Certainly the RMS errors in Table 6.12 do not support its use. However, since it is based on sound principles of linear elasticity and is expected to bound the experimental data quite well over the entire range of volume fraction, it would be appropriate to retain this model for validation purposes.

Finally, of the effective medium models compared in Table 6.12 and illustrated Figure 6.21 the model based on field theory and topological transformation by Fan et al. (1992) provides the best fit to the data. Comparison in terms of RMS error indicates that it is quantitatively similar to the BNC model described previously. However, even though the fits provided by these two models are comparable, the added mathematical complexity

of this model makes it far less attractive. The other two models presented in this category both underpredict the experimental data in the range of volume fraction investigated, and hence are not considered to be satisfactory for frozen sand in a predictive sense.

6.5 PREDICTION OF YOUNG'S MODULUS OF FROZEN SAND

One of the main objectives of this research was to develop a practical methodology for predicting the Young's modulus of frozen sands. Previous reliable data on natural sands have shown that the Young's modulus of frozen sand was essentially independent of the level of confinement, strain rate, temperature, and only moderately dependent on relative density or void ratio over the range tested (e.g., Kaplar 1963, Baker and Kurfurst 1985, Andersen et al. 1995). Results on a number of other frozen quartz-based particulate materials obtained during this research confirm this observation. Furthermore, they also have firmly established the importance of the stiffness of the particle and matrix, and of good bonding at the interface. It was shown that this bond can either be achieved through adhesional bonding, or by mechanical interactions that result when particles have significant surface roughness.

This relative insensitivity of the Young's modulus of frozen sand to the many variables known to affect ice behavior has allowed the application of composite material models originally developed for the prediction of the elastic properties of concrete and polymeric particulate-filled composites. From the analysis presented in the previous section it was found that the Bache and Nepper-Christensen (BNC) model, stated again in Equation 6.12, is sufficiently accurate at describing the data obtained over the range of volume fraction investigated during this research. The author therefore recommends the use of this expression to practicing engineers for estimating the Young's modulus of highly-filled frozen sands in addition to the following input parameters:

$$E_c = E_{ice}\left(\frac{E_p}{E_{ice}}\right)^{V_p} \tag{6.12}$$

with $E_p = 75$ GPa
$E_{ice} = 5\text{-}9$ GPa

This information has been compiled in a design chart covering the range of sand concentrations typically found in natural systems (Figure 6.22).

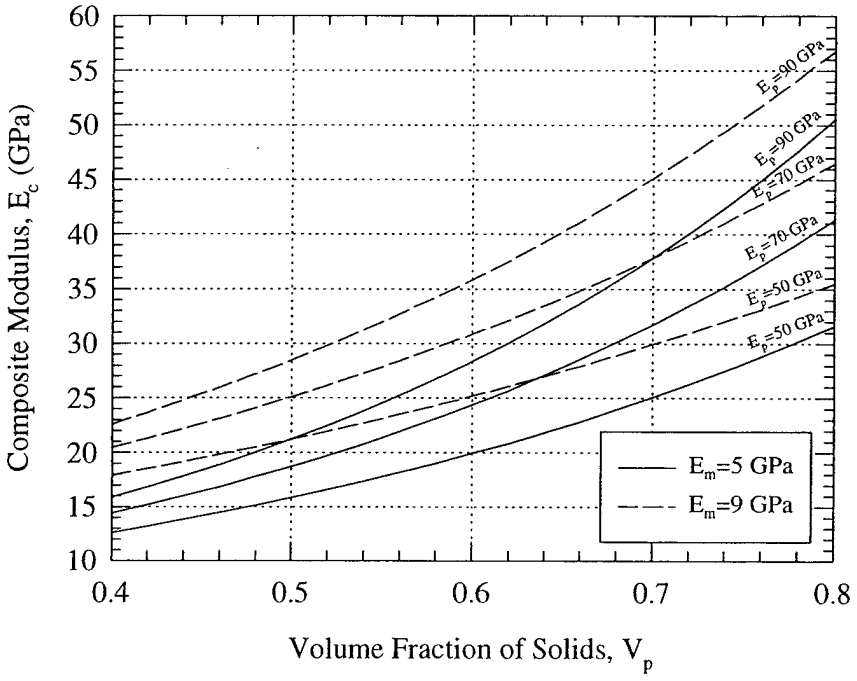

Figure 6.22: Design chart for estimation of the Young's modulus of frozen sand based on BNC model (Lydon and Balendran 1986).

The value for the particle modulus is based on average values for sands taken from the literature. However, if other natural granular materials are encountered then their moduli may be estimated based on the relationship between particle density and modulus given by Muller-Rochholz (1979) which takes the form:

$$E_p(\text{GPa}) = 8.1 \cdot \rho_p^2 \qquad (6.13)$$

where ρ_p has units of g/cc. Other relationships which correlate modulus to the product of Schmidt hardness and dry unit weight may also prove suitable (Deere and Miller 1966).

While considerable attention has been given in this thesis to which value is appropriate to use for the Young's modulus of ice, the choice very much depends on the frequency of loading, and to a lesser extent on temperature as shown in Figure 6.15. Hence a range of 5 to 9 GPa is recommended with the higher value being more appropriate at faster loading rates.

6.6 REFERENCES

1. Ahmed, S. and Jones, F.R. (1990a), "A Review of Particulate Reinforcement Theories for Polymer Composites", *Journal of Materials Science*, v. 25, pp. 4933-4942.

2. Ahmed, S. and Jones, F.R. (1990b), "Effect of Particulate Agglomeration and the Residual Stress State on the Modulus of Filled Resin. Part II: Moduli of Untreated Sand and Glass Bead Filled Composites", *Composites*, v. 21, no. 1, pp. 81-84.

3. Andersen, G.R. (1991), "Physical Mechanisms Controlling the Strength and Deformation Behavior of Frozen Sand", Sc.D Thesis, Department of Civil and Environmental Engineering, MIT, Cambridge, MA, 560 p.

4. Andersen, G.R., Swan, C.W., Ladd, C.C., Germaine, J.T. (1995), "Small-Strain Behavior of Frozen Sand in Triaxial Compression", *Canadian Geotechnical Journal*, v. 32, no. 3, pp. 428-451.

5. Baker, T.H.W. and Kurfurst, P.J. (1985), "Acoustic and Mechanical Properties of Frozen Sand", *Proc. 4th International Symposium on Ground Freezing*, Sapporo, Japan, pp. 227-234.

6. Brodnyan, J.G. (1959), "The Concentration Dependence of the Newtonian Viscosity of Prolate Ellipsoids", *Transactions of the Society of Rheology*, v. 3, pp. 61-68.

7. Christensen, R.M. and Lo, K.H. (1979), "Solutions for Effective Shear Properties in Three Phase Sphere and Cylinder Models", *Journal of the Mechanics and Physics of Solids*, v. 27, pp. 315-330.

8. Cole, D.M. (1979), "Preparation of Polycrystalline Ice Specimens for Laboratory Experiments", *Cold Regions Science and Technology*, v.1, no.2, pp. 153-159.

9. Cole, D.M. (1987), "Strain-Rate and Grain-Size Effects in Ice", *Journal of Glaciology*, v. 33, no. 115, pp. 274-280.

10. Cole, D.M. (1990), "Reversed Direct-Stress Testing of Ice: Initial Experimental Results and Analysis", *Cold Regions Science and Technology*, v. 18, pp. 303-321.

11. Cole, D.M. (2000), CRREL, Personal communication.

12. Counto, U.J. (1964), "The Effect of the Elastic Modulus of the Aggregate on the Elastic Modulus, Creep, and Creep Recovery of Concrete", *Magazine of Concrete Research*, v. 16, n0. 48, pp. 129-138.

13. Deere, D.U. and Miller, R.P. (1966), "Engineering Classification and Index Properties of Intact Rock", Technical Report No. AFWL-TR-65-116, Air Force Weapons Laboratory, Kirtland AFB, NM, 300 p.

14. Einstein, A. (1956), *Investigations on the Theory of Brownian Motion*, Dover Inc., New York. English translation of original work published in German, 1906 and 1911.

15. Fan, Z., Tsakiropoulos, T., Miodownik, A.P. (1992), "Prediction of Young's Modulus of Particulate Two-Phase Composites", *Materials Science and Technology*, v. 8, pp. 922-929.

16. Gibson, L.J. and Ashby, M.F. (1988), *Cellular Solids: Structure and Properties*, Pergamon Press, New York.

17. Gold, L.W. (1977), "Engineering Properties of Fresh-Water Ice", *Journal of Glaciology*, v. 19, no.81, pp. 197-212.

18. Hashin, Z. (1962), "The Elastic Moduli of Heterogeneous Materials", *Journal of Applied Mechanics, Transactions of the ASME*, v. 29, pp. 143-150.

19. Hashin, Z. and Shtrikman, S. (1963), "A Variational Approach to the Theory of the Elastic Behaviour of Mulitphase Materials", *Journal of the Mechanics and Physics of Solids*, v. 11, pp. 127-140.

20. Hirsch, T.J. (1962), "Modulus of Elasticity of Concrete Affected by Elastic Moduli of Cement Paste matrix and Aggregate", *Journal of the American Concrete Institute*, v. 59, pp. 427-450.

21. Ishai, O. (1965), "The Effect of the Elastic Modulus of the Aggregate on the Elastic Modulus, Creep and Creep Recovery of Concrete; Discussion ", *Magazine of Concrete Research*, v. 17, pp. 148-149.

22. Ishai, O. and Cohen, L.J. (1967), "Elastic Properties of Filled and Porous Epoxy Composites", *International Journal of Mechanical Sciences*, v. 9, pp. 539-546.

23. Kerner, E.H. (1956), "The Elastic and Thermo-elastic Properties of Composite Media", *Proceedings of the Physical Society of London*, v.69B, pp. 808-813.

24. Lambe, T.W. and Whitman, R.V. (1969) *Soil Mechanics*, John Wiley & Sons, New York.

25. Leinder, J. and Woodhams, R.T. (1974), "The Strength of Polymeric Composites Containing Spherical Fillers", *Journal of Applied Polymer Science*, v. 18, pp. 1639-1654.

26. Lydon, F.D. and Balendran, R.V. (1986), "Some Observations on Elastic Properties of Plain Concrete", *Cement and Concrete Research*, v. 16, pp. 314-324.

27. Miller, E. (1996), *Introduction to Plastics and Composites*, Marcel Dekker Inc. New York.

28. Moloney, A.C., Kausch, H.H., Stieger, H.R. (1983), "The Fracture of Particulate-Filled Epoxide Resins", *Journal of Materials Science*, v. 18, pp. 208-216.

29. Mooney, M. (1951), "The Viscosity of a Concentrated Suspension of Spherical Particles", *Journal of Colloid Science*, v. 6, pp. 162-170.

30. Mori, T. and Tanaka, K. (1973), "Average Stress in Matrix and Average Elastic Energy of Materials with Misfitting Inclusions", *Acta Metallurgica*, v. 21, pp. 571-574.

31. Muller-Rochholz, J. (1979), "Determination of the Elastic Properties of Lightweight Aggregate by Ultrasonic Pulse Velocity Measurement", *Journal of Lightweight Concrete*, v. 1, pp. 87-90.

32. Paul, B. (1960), "Prediction of Elastic Constants of Multiphase Materials", *Transactions of the Metallurgical Society of AIME*, v. 218, no. 1, pp. 36-41.

33. Ravichandran, K.S. (1994), "Elastic Properties of Two-Phase Composites", *Journal of the American Ceramics Society*, v. 5, pp. 1178-1184.

34. Reuss, A. (1929), "Calculation of Flow Limit in Mixed Crystals", *Z Angew Math. Mech.*, v. 9, pp. 49-58.

35. Ryzhkin, I.A. and Petrenko, V.F. (1997), "Physical Mechanisms Responsible for Ice Adhesion", *Journal of Physical Chemistry B*, v. 101, pp. 6267-6270.

36. Sahu, S. and Broutman, L.J. (1972), "Mechanical Properties of Particulate Composites", *Polymer Engineering and Science*, v. 12, no. 2, pp. 91-100.

37. Sinfield, J.V. (1997), "Fluorescence of Contaminants in Soil and Groundwater Using a Time-Resolved Microchip Laser System", Sc.D Thesis, Department of Civil and Environmental Engineering, MIT, Cambridge, MA, 428 p.

38. Singh, S.K. and Jordaan, I.J. (1996), "Triaxial Tests on Crushed Ice", *Cold Regions Science and Technology*, v. 24, pp. 153-165.

39. Sinha, N.K. (1989), "Elasticity of Natural Types of Polycrystalline Ice", *Cold Regions Science and Technology*, v. 17, pp. 127-135.

40. Spanoudakis, J. and Young, R.J. (1984), "Crack Propagation in a Glass Particle-Filled Epoxy Resin, Part 2: Effect of Particle-Matrix Adhesion", *Journal of Materials Science*, v. 19, pp. 487-496.

41. Swan, C. (1994), "Physical Mechanisms Controlling the Deformation and Strength Behavior of Unfrozen and Frozen Manchester Fine Sand", Sc.D Thesis, Department of Civil and Environmental Engineering, MIT, Cambridge, MA, 1044 p.

42. Ting, J.M., Martin, R.T., Ladd, C.C. (1983), "Mechanisms of Strength for Frozen Sand", *ASCE Journal of Geotechnical Engineering*, v. 109, no. 10, pp. 1286-1302.

43. Voigt, W. (1910), *Lehrbuch der Kristallphysik*, Teubner, Leipzig.

44. Willis, J.R. (1977), "Bounds and Self-Consistent Estimates for the Overall Properties of Anisotropic Composites", *Journal of the Mechanics and Physics of Solids*, v. 25, pp. 185-202.

CHAPTER 7

BEHAVIOR OF FROZEN SYSTEMS IN THE UPPER YIELD REGION

7.1 INTRODUCTION

This chapter provides the reader with a much improved understanding of the mechanisms controlling the upper yield stress observed to occur in frozen sands and other particulate materials under compressive triaxial loading. In addition, many of these findings may also apply to other composite systems, especially particulate-reinforced polymers. The upper yield stress represents the point in the stress-strain curve that signifies the onset of highly non-linear behavior and the development of significant plastic deformations. Characterization of this parameter, together with the Young's modulus presented in Chapter 6, provides a detailed description the small strain behavior of frozen sands.

A similar organizational format to that of Chapter 6 has been adopted for this chapter. Section 7.2 presents the data obtained for the upper yield stress as a function of the variables investigated (e.g., relative density or void ratio, confinement, strain rate, temperature, particle modulus, particle size, interface adhesion, and particle roughness), and identifies relative trends. A synthesis of the results is presented in Section 7.3 which culminates in a discussion of the mechanisms thought to control the upper yield stress of frozen sand. Based on the results obtained during this experimental program, an empirical model that predicts the upper yield behavior of frozen Manchester fine sand is proposed in Section 7.4. A methodology for estimating the upper yield stress of other frozen granular materials is also described. Finally, references cited are listed in Section 7.5

7.2 EVALUATION OF UPPER YIELD STRESS

This section presents the upper yield stress data obtained on each of the materials investigated during the experimental program and also includes, where applicable, results for Manchester fine sand from Andersen et al. (1995). It is organized according to each of

the variables outlined in Section 5.2. Along with a presentation of the data, the discussion in the following sections provides a detailed description of each of the variables influence on the upper yield stress.

7.2.1 Effect of Void Ratio/Relative Density

The variation of the upper yield stress with void ratio was not expected to be significant due to the limited range investigated, and based on the results of Andersen et al. (1995) which showed that the frictional resistance of the sand skeleton (i.e. void ratio and confinement) plays a minor role in the upper yield stress of frozen Manchester fine sand. Furthermore, Swan (1994) confirmed, via CIUC (isotropically consolidated-undrained triaxial compression) tests on unfrozen Manchester fine sand, that the undrained resistance of the sand skeleton at strain levels corresponding to the upper yield stress in frozen sands is negligible compared to measured values of the upper yield stress.

Although the void ratio was not systematically varied during the testing program, tests on various frozen particulate-filled systems do cover a modest density range. Figure 7.1a-e shows the variation of the upper yield stress with void ratio for each of the materials tested at -10°C. Very little variation with void ratio is noticed for each of the systems. However, the magnitude of the upper yield stress is shown to be clearly dependent on strain rate. This dependency is discussed in Section 7.2.3. A summary of the influence of void ratio for each material is given in Table 7.1.

	Slow $\dot{\varepsilon}$		Moderate $\dot{\varepsilon}$	
Material Type	**Void ratio range**	**Mean±S.D. (MPa)**	**Void ratio range**	**Mean±S.D. (MPa)**
Manchester fine sand	0.699 - 0.781	4.47±0.21	0.678 - 0.809	7.38±0.17
Hydrophobic MFS	0.681 - 0.782	3.93±0.20	0.657 - 0.773	7.45±0.89
2010 industrial quartz	0.614 - 0.693	7.36±0.46	0.631 - 0.731	12.70±0.54
PMMA	0.568 - 0.624	7.77±0.36	0.446 - 0.607	10.01±0.83
Small glass beads	0.551 - 0.552	7.12±0.64	0.528 - 0.572	10.45±0.67

Table 7.1: Summary of the effect of void ratio on the upper yield stress of each material tested at -10°C.

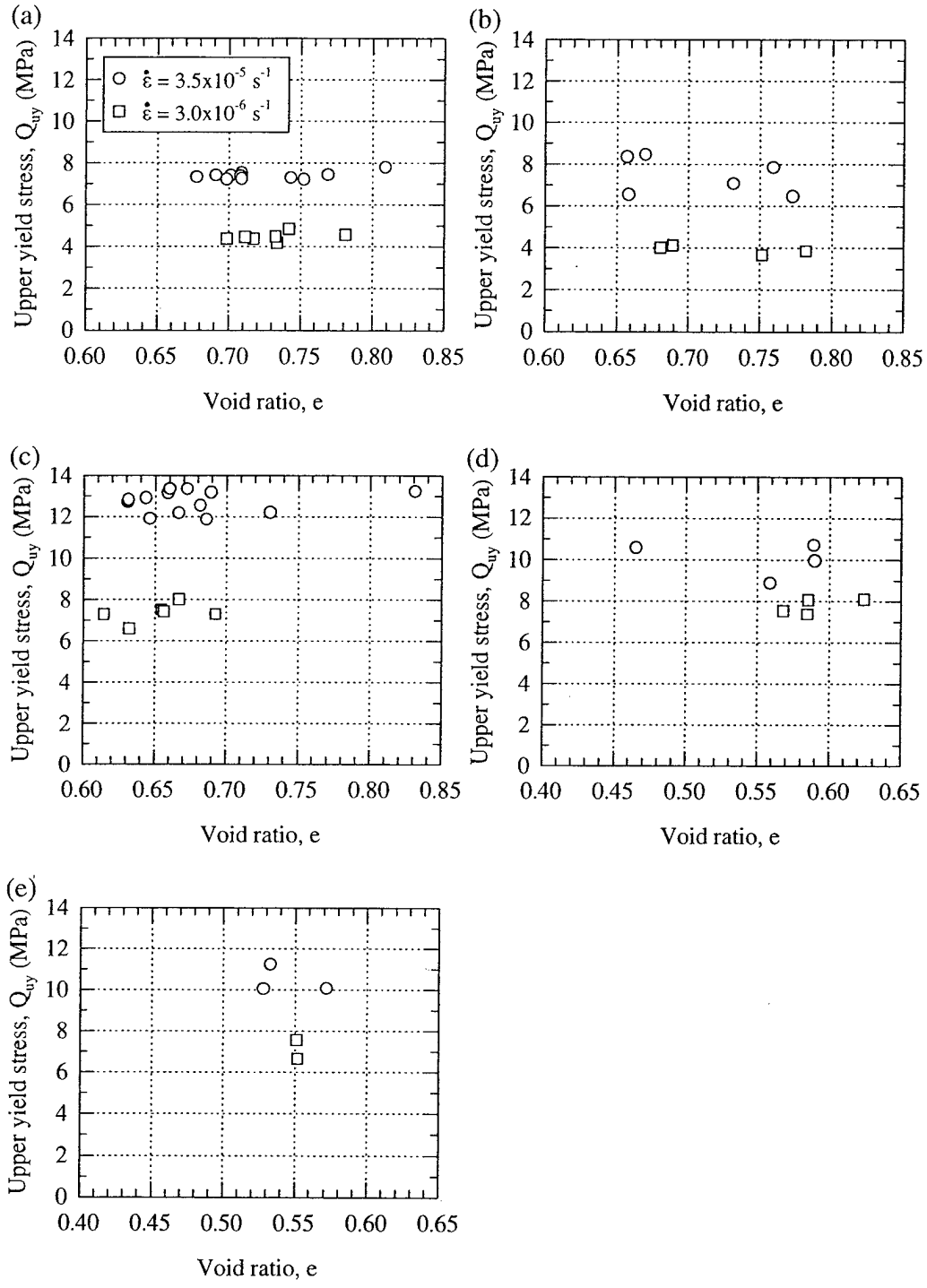

Figure 7.1: Effect of void ratio on the upper yield stress of frozen systems at -10°C at varying confining pressures and strain rates (a) Manchester fine sand, (b) hydrophobic Manchester fine sand, (c) 2010 industrial quartz, (d) PMMA, (e) small glass beads.

7.2.2 Effect of Confinement

As was mentioned previously, Andersen et al. (1995) found no evidence of a pressure sensitivity in the upper yield stress of Manchester fine sand. However, other programs reported that the upper yield stress in frozen sands is indeed pressure sensitive (e.g., Chamberlain et al. 1972, Sayles 1973, Parameswaran and Jones 1981). Since coarser-grained sands are reported to exhibit the highest degree of pressure sensitivity (i.e. the Chamberlain et al. 1972 and Sayles 1973 data in Figure 2.24), tests on coarser-grained materials were performed to investiage the circumstances under which confinement becomes important. Specimens were tested at confining pressures ranging from 0.1 MPa to 12.5 MPa, which was the maximum confinement that the triaxial testing system could sustain.

The effect of confinement is illustrated in Figure 7.2a-f for all the materials tested at -10°C for both the slow and moderate strain rates, including those treated with a hydrophobic coating. The data obtained on untreated Manchester fine sand (Figure 7.2a) agree well with the data reported by Andersen et al. (1995), indicating little to no pressure sensitivity at the two strain rates. In contrast, the data for the hydrophobic Manchester fine sand, shown in Figure 7.2b, show a significant increase (~23%) in the upper yield stress with confinement at the higher strain rate, but little to no sensitivity at the slower rate. The 2010 industrial quartz (Figure 7.2c), however, shows a slight pressure dependency in the upper yield stress for both strain rates up to about 5 MPa at which point no further change in the upper yield stress occurs with further increases in confinement. Similar sensitivity is seen at the moderate strain rate for both the PMMA and glass bead systems (regular and hydrophobic), although data at intermediate confining pressures are lacking to determine if the behavior is qualitatively similar to that observed in the 2010 industrial quartz system. Furthermore, the slight pressure sensitivity observed in ice at the moderate strain rate, illustrated in Figure 7.2e, indicates that these effects may simply be related to the pressure sensitivity of ice resulting from the suppression of cracking at faster strain rates.

The pressure sensitivity of the surface roughened hydrophobic small glass beads is shown in Figure 7.3. These data have been treated separately because they contain two

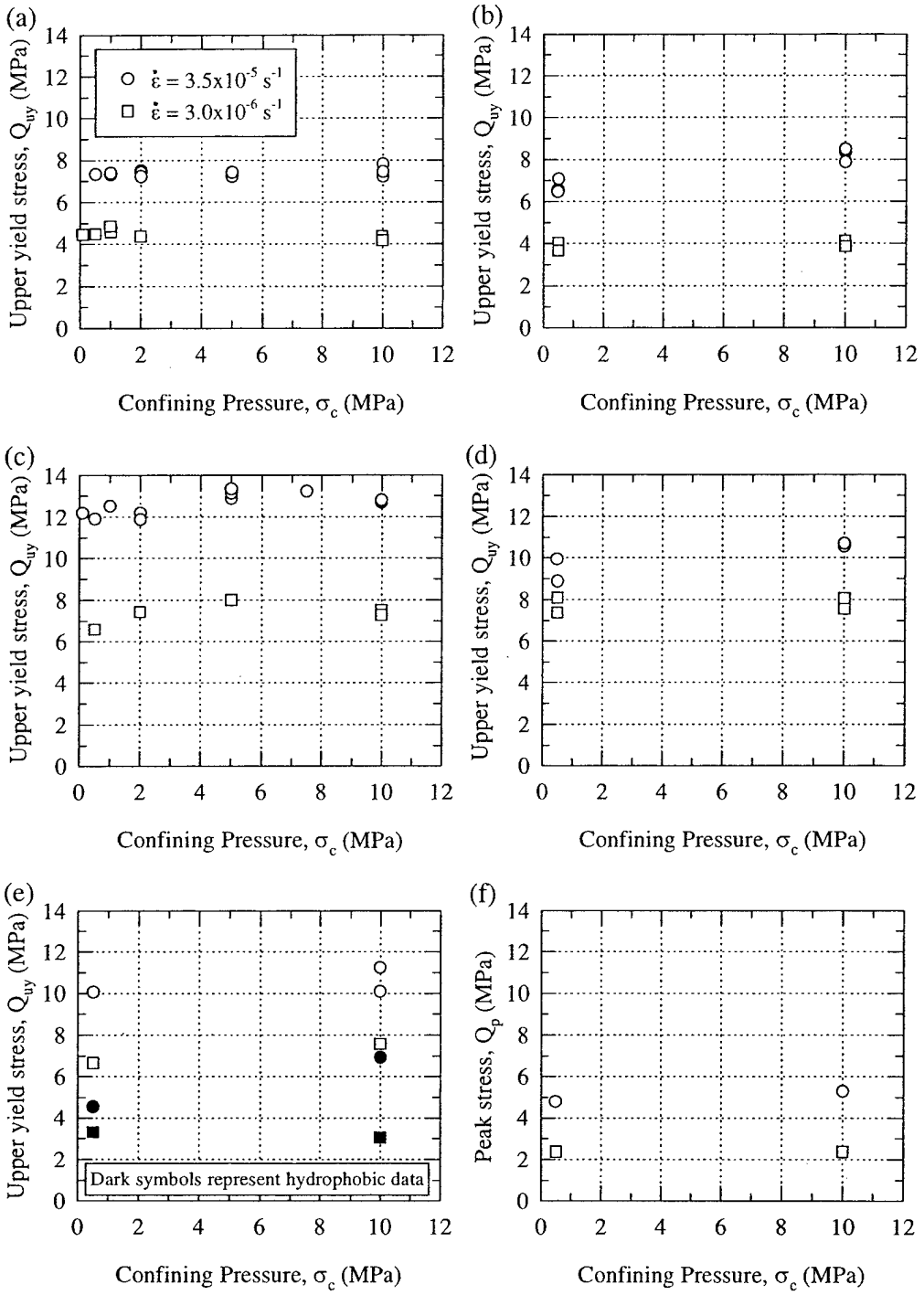

Figure 7.2: Effect of confinement on the upper yield stress of frozen systems at -10°C at varying void ratios and strain rates (a) Manchester fine sand, (b) hydrophobic Manchester fine sand, (c) 2010 industrial quartz, (d) PMMA, (e) small glass beads (regular and hydrophobic), (f) polycrystalline ice.

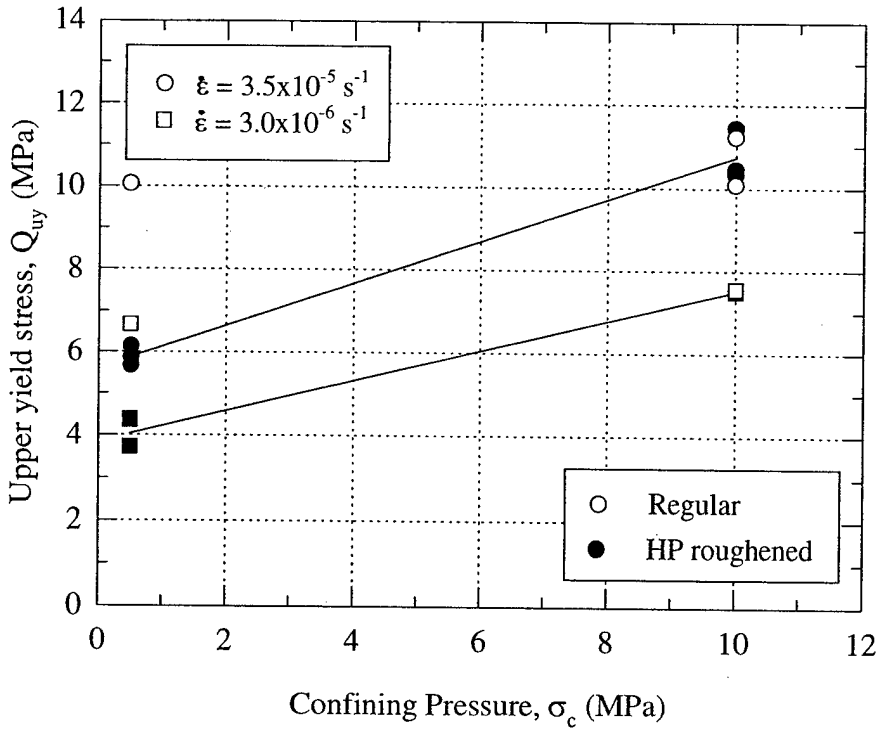

Figure 7.3: Effect of confinement for hydrophobic surface roughened small glass beads tested at -10°C at varying strain rates.

very important features regarding the effect of confinement. The first is that a large pressure sensitivity is seen at both strain rates, and the second is that the application of high confinement produces a system with the same upper yield stress as the original system of smooth fully bonded glass beads (whereas it had no effect on the Young's modulus). This second observation, which is thought to provide great insight into the mechanisms of strength generation in frozen sands, is discussed in more detail in Section 7.2.8, which focuses on the effect of particle roughness.

From these observations it is evident that confinement plays an important role in the upper yield stress of those materials that have undergone some sort of surface modification that alters the interaction between the particles and the ice matrix, yet is fairly unimportant in those systems tested in their natural state. A summary of the effect of confinement for those materials tested at -10°C is given in Table 7.2.

Material Type	Mean±S.D. (MPa) Slow $\dot{\varepsilon}$		Mean±S.D. (MPa) Moderate $\dot{\varepsilon}$	
	Low σ_c	High σ_c	Low σ_c	High σ_c
Manchester fine sand	4.55±0.18	4.28±0.14	7.35±0.10	7.41±0.24
Hydrophobic MFS	3.86±0.25	4.00±0.18	6.68±0.34	8.22±0.32
2010 industrial quartz	7.01±0.60	7.53±0.34	12.12±0.26	13.07±0.25
PMMA	7.74±0.50	7.81±0.37	9.40±0.76	10.61±0.11
Small glass beads	6.67	7.57	10.05	10.66±0.81
HP small glass beads	3.31	3.04	4.52	6.90
HPR small glass beads	4.04±0.46	7.51	5.87±0.23	10.74±0.61
Polycrystalline ice	2.37	2.37	4.79	5.29

Table 7.2: Summary of upper yield stress obtained at low ($\sigma_c \leq 2$ MPa) and high confinements for each material type tested at -10°C for varying void ratios.

In addition to affecting the upper yield stress of the coarser-grained materials at the moderate strain rate, confinement was also observed to be important to the upper yield strain (ε_{uy}). The effect is shown in Figure 7.4a-f for each of the materials investigated at -10°C, excluding the large glass beads. Although these data display some scatter, the Manchester fine sand (untreated and hydrophobic) and 2010 industrial quartz systems, shown in Figure 7.4a-c suggest that the yield strain decreases slightly with increasing confinement, and is essentially independent of void ratio and strain rate. In contrast, the yield strain for the PMMA system (Figure 7.4d) increases with increasing confinement. This in turn contrasts the system of small glass beads shown in Figure 7.4e, which shows essentially no dependence on confinement regardless of the level of adhesion even though the beads are very similar to the PMMA in size and shape. Finally, the polycrystalline ice data shown in Figure 7.4f indicate that the strain at its peak stress is also essentially independent of confinement, yet is substantially greater than for the frozen particulate-filled systems just mentioned.

7.2.3 Effect of Strain Rate

It is well-known that many linear viscoelastic materials (i.e. ice, polymers below their glass transition) exhibit a rate dependency. This dependency usually takes the form of a power law relationship (Equation 7.1) which defines a linear function between yield stress and strain rate on a log-log plot:

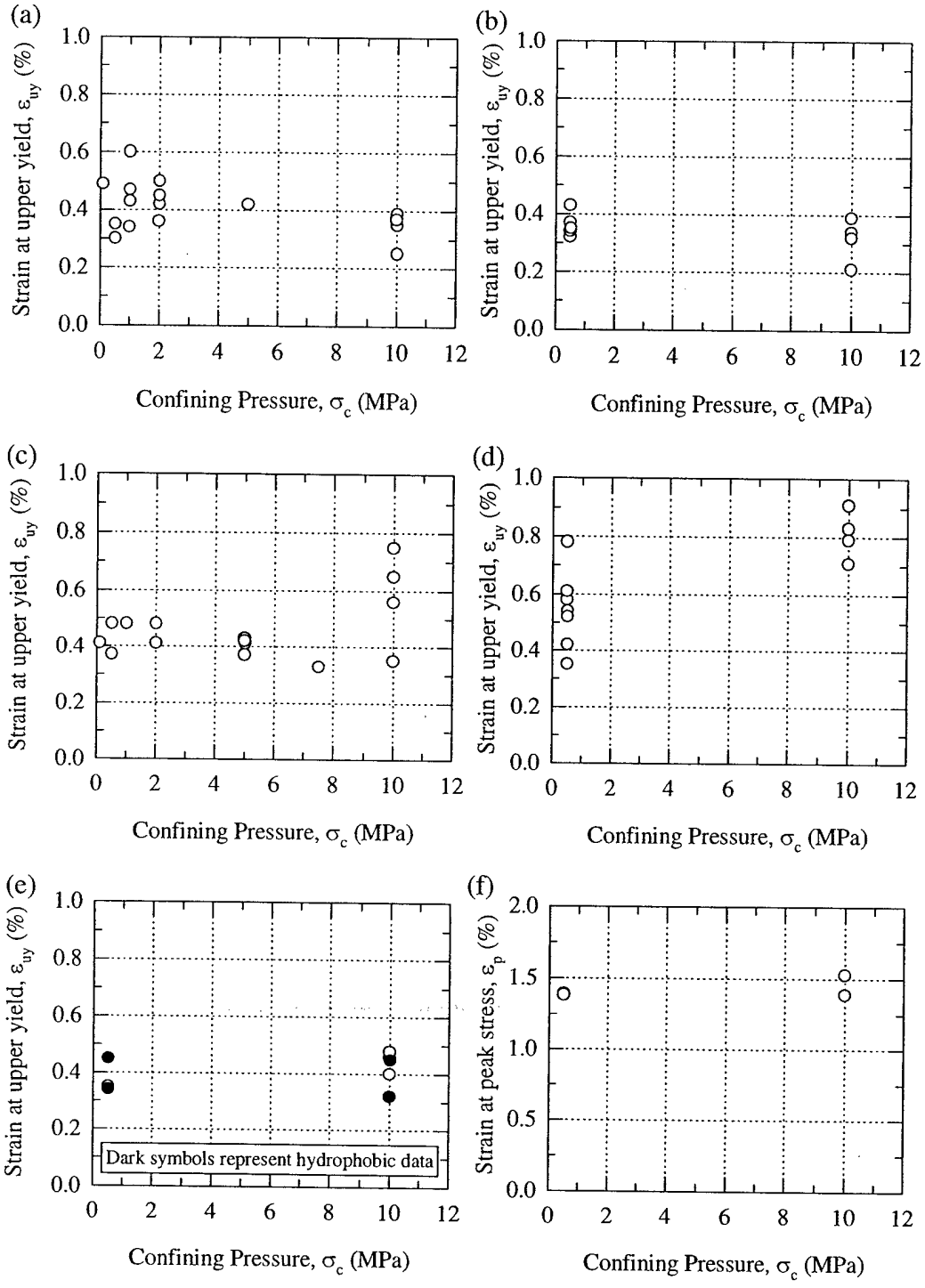

Figure 7.4: Effect of confinement on the strain at the upper yield stress (strain at peak stress for polycrystalline ice) at -10°C at varying void ratios and strain rates.

$$Q_{uy}(MPa) = A\dot{\varepsilon}^{\frac{1}{n}} \quad (7.1)$$

The behavior of polycrystalline ice in the ductile region at -10°C, which extends over a wide range of strain rates from 10^{-10} s^{-1} to about 10^{-5} s^{-1}, can be characterized quite well by a constant power law exponent (n) of approximately 3 (Sanderson 1988). A similar expression was used by Andersen et al. (1995) to quantify the strain rate dependency of the upper yield stress of Manchester fine sand at various temperatures. This suggests, at least qualitatively, that the behavior in this region is very much controlled by the behavior of the pore ice matrix.

Figure 7.5a-e illustrates the strain rate dependence of each of the non-modified materials investigated at -5°C and -10°C. A summary of the strain rate dependency coefficients for these materials is given in Table 7.3. Figure 7.5a presents the data for Manchester fine sand which has a power law exponent of 5.14 at -10°C. This is slightly higher than the value of 4.65 quoted by Andersen et al. (1995), however, their exponent was calculated over a larger range of strain rate (i.e. $3x10^{-6}$ s^{-1} to $5x10^{-4}$ s^{-1}) which may account for the slight difference between the two values. In examining the rest of the systems a number of observations become evident. The industrial quartz system (Figure 7.5b), the only other angular system tested, is characterized by a power law exponent that is very similar to the Manchester fine sand. In contrast, the systems characterized by smooth spherical particles (PMMA and glass beads) have a much lower strain rate sensitivity (higher power law exponents). Furthermore, all the systems tested exhibit a higher rate sensitivity with increasing temperature. This will be discussed in more detail in the next section. Finally, Figure 7.5e illustrates that the rate sensitivity of the polycrystalline ice specimens agree with those reported in the literature at comparable strain rates and temperatures.

7.2.4 Effect of Temperature

As a result of the collective work of Andersen (1991) and Swan (1994), the temperature dependence of the upper yield stress of frozen Manchester fine sand has already been well-defined in the temperature range from -25°C to -10°C. Collectively,

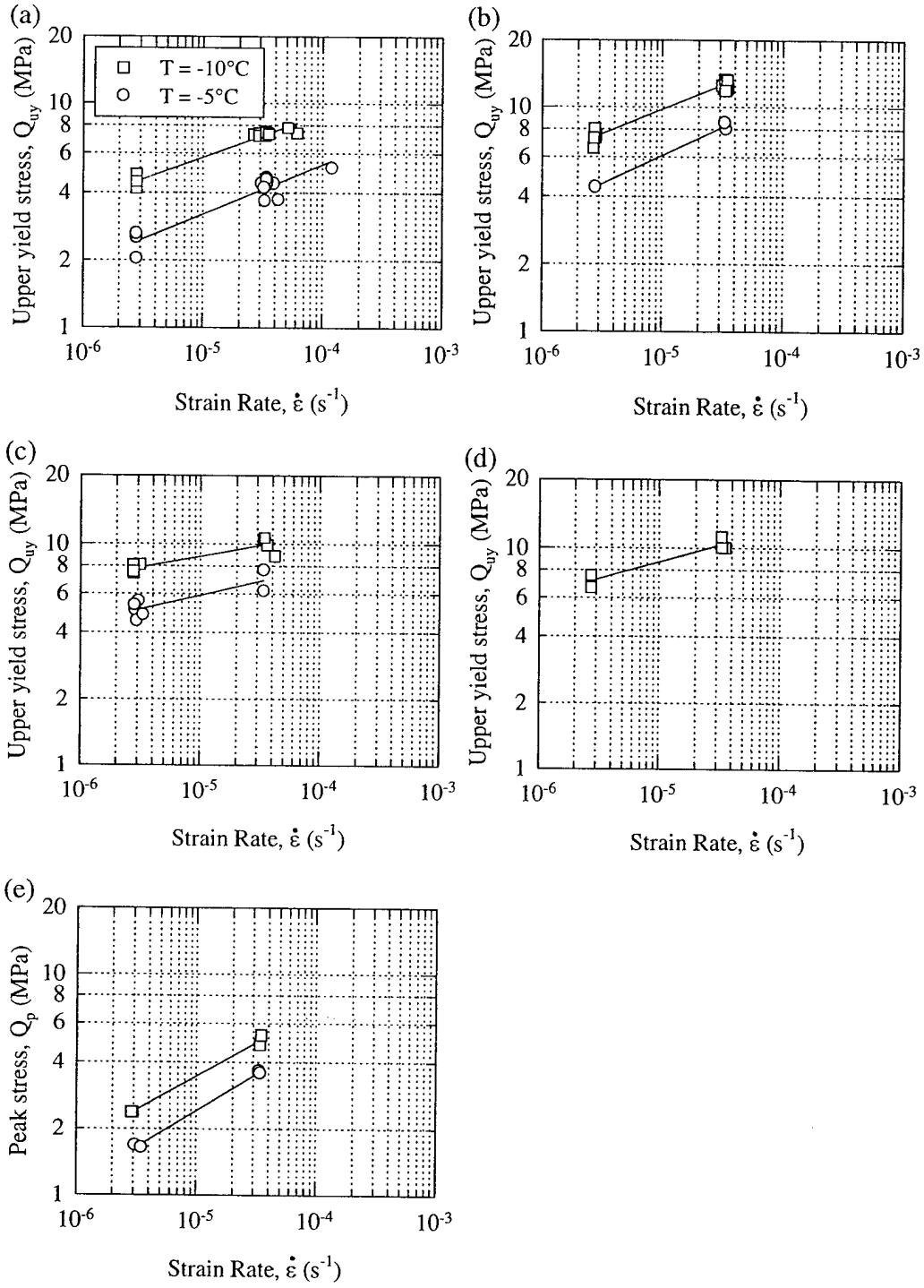

Figure 7.5: Effect of strain rate on the upper yield stress of untreated frozen systems at -5°C and -10°C at varying void ratios and confining pressures (a) Manchester fine sand, (b) 2010 industrial quartz, (c) PMMA, (d) small glass beads, (e) polycrystalline ice.

	T = -5°C		T = -10°C	
Material Type	Power Law n	Constant A	Power Law n	Constant A
Manchester fine sand	4.53	40.85	5.14	53.98
2010 industrial quartz	3.94	112.73	4.55	121.51
PMMA	7.84	25.61	10.38	26.65
Small glass beads	N/A	N/A	6.58	49.91
Polycrystalline ice	3.01	110.42	3.27	116.56

Table 7.3: Summary of strain rate dependency for each material type at -5°C and -10°C at varying void ratios and confining pressures.

their data represents the most comprehensive treatment of the small strain behavior of a frozen sand available in the literature.

In an effort to extend this database to include tests that encompass a broader range of conditions of both practical and fundamental interest, tests were performed on Manchester fine sand at -2°C and -5°C. These results are shown in Figure 7.6 in conjunction with data from Andersen et al. (1995) for comparison. This figure clearly shows that the upper yield stress of frozen sand increases with decreasing temperature and that the temperature dependency also increases with strain rate. This temperature dependency may be expressed using a linear relationship of the form:

$$Q_{uy}(\text{MPa}) = C + D(T) \tag{7.2}$$

where C and D are constants for a particular strain rate. Inclusion of the higher temperature data from this program does little to change the regression statistics as given in Andersen et al. (1995). This indicates that the upper yield behavior of frozen sand at temperatures approaching the melting point of ice can still be described by a linear dependence in temperature. Furthermore, this suggests that the processes responsible for the upper yield stress at higher temperatures are mechanistically similar to those at the lower temperatures.

The temperature dependence of the other materials is shown in Figures 7.7a-e and is quantified in Table 7.4 for each strain rate using the regression coefficients from Equation 7.2. This allows for the convenient comparison of temperature dependencies between materials and, in particular, to the polycrystalline ice data (Figure 7.6e) which is responsible for the inherent temperature dependence in these frozen systems. Figure 7.7a

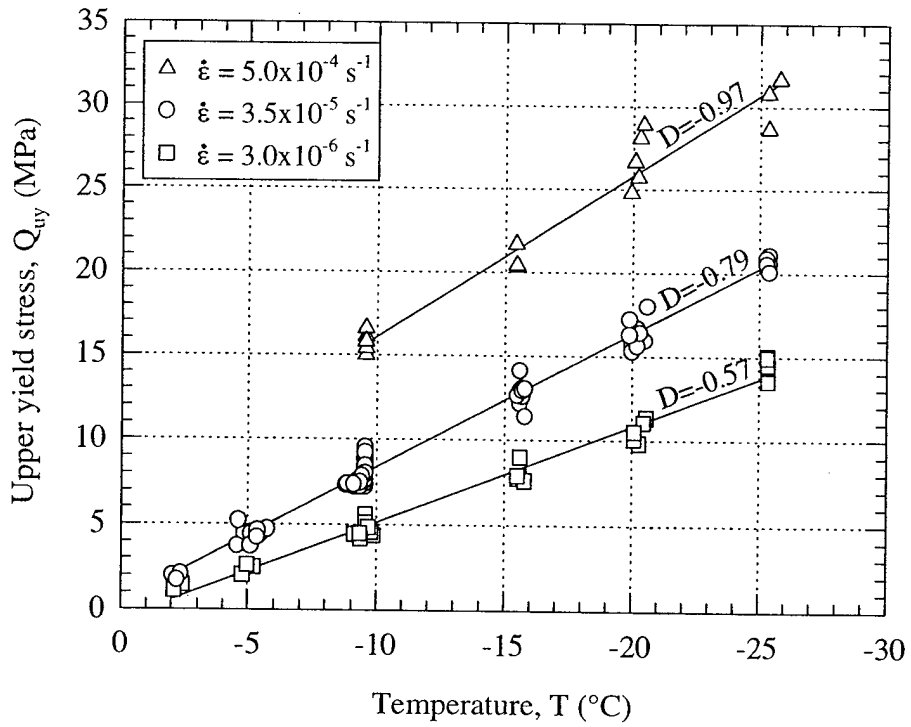

Figure 7.6: Temperature dependence of Manchester fine sand at slow, moderate, and fast strain rates.

shows the MFS system which was already discussed in conjunction with Figure 7.6. However, data in Figure 7.7b indicates that hydrophobic treatment of Manchester fine sand lowers the temperature dependence at both strain rates. Conversely, an increase in the temperature dependence is noticed for the two coarser-grained materials (i.e. 2010 industrial quartz and PMMA) shown in Figure 7.7c-d. In both cases the temperature dependency increases with increasing strain rate as observed for Manchester fine sand in Figure 7.6.

	Slow $\dot{\varepsilon}$		Moderate $\dot{\varepsilon}$	
Material Type	C (MPa)	D (MPa/°C)	C (MPa)	D (MPa/°C)
Manchester fine sand	0.24	-0.45	0.39	-0.76
Hydrophobic MFS	0.89	-0.34	2.28/2.17*	-0.47 / -0.65*
2010 industrial quartz	1.19	-0.68	3.78	-0.94
PMMA	2.30	-0.55	4.11	-0.61
Polycrystalline ice	0.91	-0.16	2.02	-0.32

Note: * indicates value obtained at high confinement levels

Table 7.4: Summary of temperature dependence for each material type investigated.

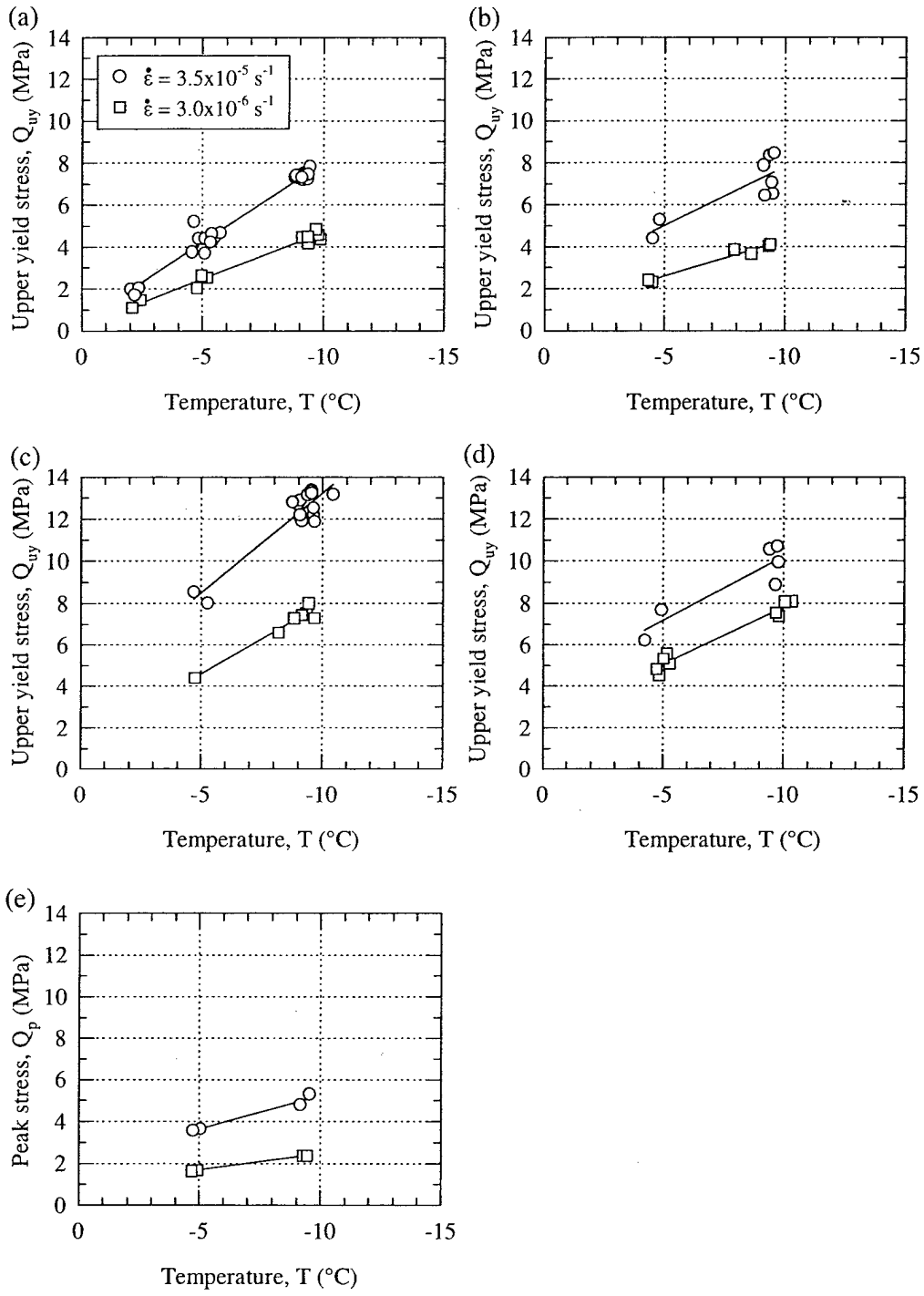

Figure 7.7: Effect of temperature on the upper yield stress of frozen systems for slow and moderate strain rates at varying void ratios and confining pressures (a) Manchester fine sand, (b) hydrophobic Manchester fine sand, (c) 2010 industrial quartz, (d) PMMA, (e) polycrystalline ice.

7.2.5 Effect of Particle Modulus

While the main reason for investigating particle modulus was to determine its influence on the Young's modulus of frozen particulate composite materials, the test program also shows its effect on the upper yield stress. As was discussed in Chapter 6, particle modulus is well known to play a very significant role in the resulting modulus of a two-phase composite material. Its role, however, in the yield and ultimate strength of particulate-filled composites in compression has been rather less well-defined in the literature on composite materials.

The effect of particle modulus can be shown by comparing the upper yield data for the PMMA system (E_p=4.5 GPa at -10°C) to that of the 2010 industrial quartz and small glass bead systems (E_p=~75 GPa). These materials were chosen since they all possess approximately the same particle size, therefore eliminating the effect of this variable in the comparison. Particle size effects will be discussed in the next section (Section 7.2.6).

Figure 7.8a and Figure 7.8b presents the results of the comparison at -10°C for the slow and moderate strain rate, respectively. Little difference can be seen in the upper yield stress of the three materials at the slow rate, i.e. particle modulus is unimportant at this rate. Similar results are observed at the moderate strain rate, although the regression is skewed by the 2010 industrial quartz data which has a yield stress at this strain rate that is clearly higher than the other two systems. If attention is focused strictly on the PMMA and glass bead data, which together provide the best comparison of particle modulus, since these systems also have the same shape in addition to particle size, virtually no difference in their upper yield stress can be seen. This confirms that the amount of ice matrix strengthening as described by the upper yield stress does not depend on the stiffness of the inclusion, although the shape or roughness of the particles may be important at the higher strain rates. This will be addressed in more detail in Section 7.2.8. Particles simply act as stress risers, or obstacles to propagating cracks within the pore ice matrix, thus allowing the system to sustain higher stresses. A summary of the upper yield stress behavior for each particle modulus is given in Table 7.5. This provides a quantitative comparison of the upper yield stress results in addition to the qualitative comparison in Figure 7.8a-b.

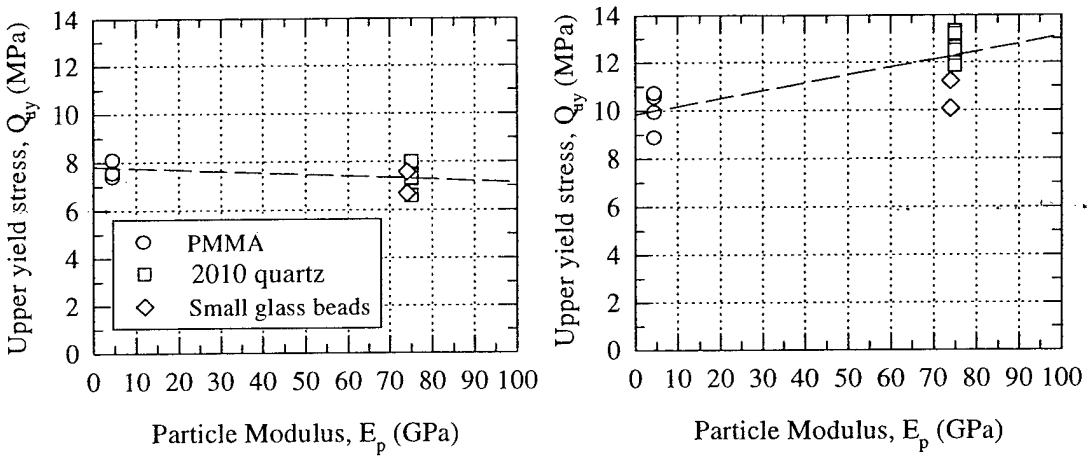

Figure 7.8: Effect of particle modulus on the upper yield stress of untreated frozen systems at -10°C at varying void ratios and confinements (a) slow rate ($3x10^{-6}$ s^{-1}), (b) moderate rate ($3.5x10^{-5}$ s^{-1}).

Material Type	E_p (GPa)	Mean±S.D. (MPa) Slow ε	Moderate ε
2010 industrial quartz	75	7.36±0.46	12.70±0.54
Small glass beads	74	7.12±0.64	10.45±0.67
PMMA	4.5*	7.77±0.36	10.01±0.83
Polycrystalline ice	5.3	2.37±0.00	5.04±0.35

Note: * indicates computed at -10°C

Table 7.5: Summary of the effect of particle modulus on the upper yield stress of frozen systems at -10°C at varying confining pressures.

7.2.6 Effect of Particle Grain Size

Having established that void ratio, confinement, and particle modulus do not play a significant role in the upper yield stress of frozen particulate materials, yet strain rate and temperature do, it is now possible to investigate the effect of particle grain size.

The effect of particle grain size on the yield characteristics of frozen sand has not been studied extensively in the literature. Most of the comparisons focus on the differences between sand and silt systems (Chamberlain et al. 1972, Zhu and Carbee 1988), and none have systematically characterized the influence of grain size on yielding or strength. This contrasts the enormous amount of information regarding the effect of

particle size in particulate-filled polymers. Most of that information, however, focuses on the tensile strength behavior, which although is not directly applicable to systems in compression, can nonetheless serve as a useful starting point for studying the effects of particle size.

As was shown in Figures 7.5 and 7.7, the magnitude of the upper yield stress at a given strain rate and temperature varied considerably between materials. Detailed examination of the data in these figures suggests that coarser-grained materials give higher values for the upper yield stress. Although a comprehensive evaluation of the effects of particle size is difficult due to the limited range of particle sizes investigated, it is nevertheless possible to quantitatively compare the experimental data. This is done in Figure 7.9a-b which shows the dependence of the upper yield stress on the mean particle diameter at both -5°C and -10°C for the moderate and slow strain rate.

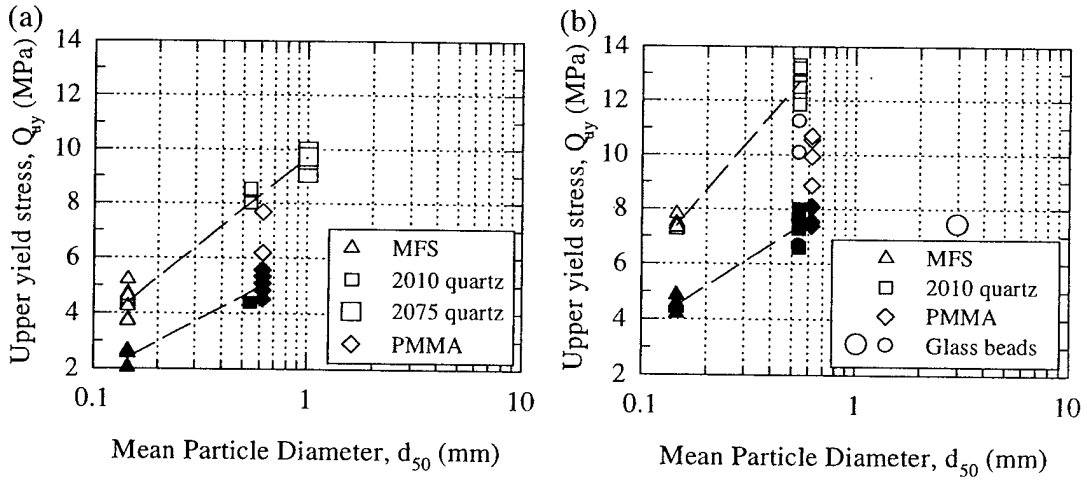

Figure 7.9: Effect of particle size on the upper yield stress of untreated frozen systems tested at slow (dark symbols) and moderate (open symbols) strain rates at (a) -5°C, (b) -10°C. Note: only the Manchester fine sand and quartz data are included in the regressions.

From the data shown in Figure 7.9a, which includes data from tests performed on Manchester fine sand, PMMA and both the 2010 and 2075 grades of industrial quartz, a definite trend of increasing upper yield stress with increasing particle diameter can be seen. A similar trend can be noticed for the data at -10°C (Figure 7.9b) if the data for the system

composed of large glass beads, which gave a much lower value, is discounted. This much lower stress is believed to have resulted from the fact that the 3 mm spheres were possibly too large for the test specimen size used (~35 mm). It is generally recommended that the minimum diameter of the test specimen be at least ten times the maximum soil particle size (ASTM D5520-94, 1996). While this standard suggests that the large beads are acceptable for use with this specimen size, it does not account for particle size gradation, and it does not consider systems that fracture. This may be an important consideration since the large glass beads tested were extremely uniform in size. As was shown in the previous section, the upper yield stress at the moderate strain rate exhibits a definite dependence on particle shape for similar grain sizes as shown by the difference in the yield stresses between the 2010 industrial quartz, and the PMMA and small glass bead systems. At this strain rate, the amount of strengthening does increase with particle size, but seemingly depends on the nature (i.e. roughness and shape) of the particle. A summary of the particle size dependence of the upper yield stress is given in Table 7.6 for both -5°C and -10°C.

Although far from a systematic characterization, this analysis presents strong evidence that the upper yield stress of frozen cohesionless materials is strongly dependent on the particle grain size, at least over the grain size (i.e. d_{50}) range tested during this experimental program. Further testing of materials having other values of d_{50} is necessary to fully document this trend.

		Mean±S.D. (MPa)			
	Grain Size	Slow $\dot{\varepsilon}$		Moderate $\dot{\varepsilon}$	
Material Type	d_{50} (mm)	T = -5°C	T = -10°C	T = -5°C	T = -10°C
2075 industrial quartz	1.00	N/A	N/A	9.59±0.35	N/A
2010 industrial quartz	0.54	4.4	7.36±0.46	8.27±0.37	12.70±0.54
Manchester fine sand	0.145	2.40±0.32	4.47±0.21	4.37±0.42	7.38±0.17
PMMA	0.62	5.10±0.41	7.77±0.36	6.93±1.04	10.01±0.83
Small glass beads	0.54	N/A	7.12±0.64	N/A	10.45±0.67
Large glass beads	3.00	N/A	N/A	N/A	7.46

Table 7.6: Summary of the particle size dependence of the upper yield stress of the frozen systems tested at -5°C and -10°C at the slow ($3.0\text{x}10^{-6}$ s^{-1}) and moderate ($3.5\text{x}10^{-5}$ s^{-1}) strain rates.

7.2.7 Effect of Interface Adhesion

The importance of interfacial adhesion to the yielding characteristics of a two-phase composite material is well-known (e.g., Ahmed and Jones 1990), having received a great deal of attention in the area of materials science concerning the manufacture of rigid particulate-filled thermoplastics (e.g., Leinder and Woodhams 1974, Papanicolaou and Bakos 1992, D'Almeida and De Carvalho 1998). Many of the models developed for the prediction of the yield strength, which were discussed in Section 2.4.4, account for interfacial bonding, although usually only in a descriptive way (i.e. poor, some, good). Furthermore, most of the effects of interfacial bonding have been investigated in tension tests where particulate composites behave much differently than in compression (Ishai and Bodner 1970). In frozen soils, the importance of ice-soil bonding has only been alluded to (e.g., Chamberlain et al. 1972, Parameswaran and Jones 1981), although Ting et al. (1983) did perform some creep tests on non-wetting glass beads.

The influence of interfacial bonding on the upper yield stress was investigated during this testing program by treating systems of frozen Manchester fine sand and both small and large glass beads to make them hydrophobic. Although a relatively large number of regular and hydrophobic specimens of Manchester fine sand were tested, material and time constraints resulted in substantially fewer tests being conducted on the small glass beads, and even fewer on the large glass beads. The results of the strain rate dependence of the upper yield stress of these materials at -10°C are shown in Figure 7.10a-c. A quantitative comparison of the systems is also given in Table 7.7.

Figure 7.10a illustrates the effect of interfacial bonding for the Manchester fine sand system at -10°C. The data for the regular and hydrophobic systems plot on top of one another indicating that interfacial adhesion is not important for this material. However, the hydrophobic system does exhibit a slightly higher rate sensitivity than the regular Manchester fine sand as shown in Table 7.7. Comparable results have also been found at -5°C, although they are not shown here. The Manchester fine sand results mirror those for Young's modulus (Chapter 6) which were also found to be relatively insensitive to the degree of particle-matrix bonding.

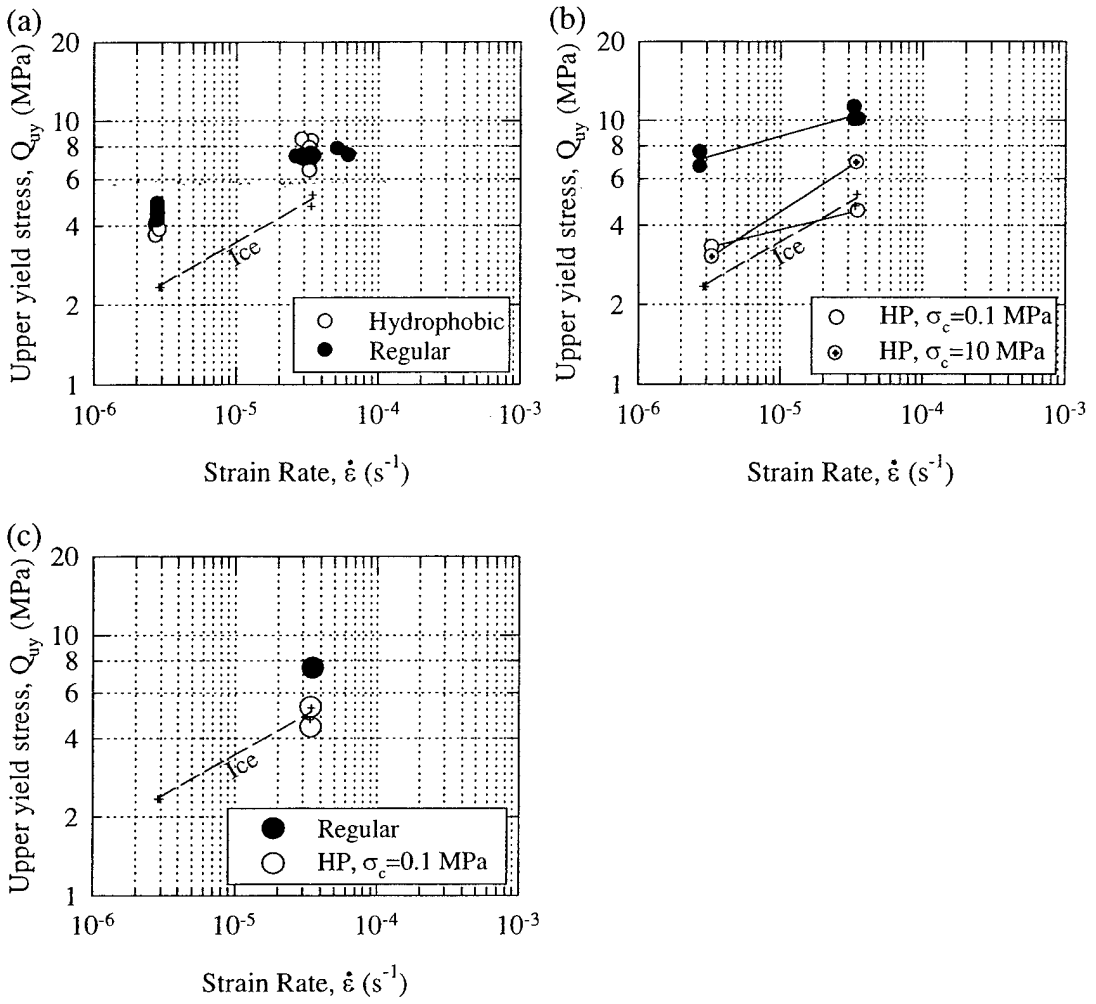

Figure 7.10: Effect of interface adhesion (hydrophobic coating) on the upper yield stress of frozen systems at -10°C at varying void ratios and confining pressures for (a) Manchester fine sand, (b) small glass beads, (c) large glass beads. Note: ice data plotted at the nominal strain rate.

In contrast to the data obtained for Manchester fine sand, the data presented in Figure 7.10b for the small glass beads shows that this system is very dependent on the degree of interfacial adhesion as evidenced by the large drop in the upper yield stress at both strain rates for the treated material. This system also displays a significant degree of pressure sensitivity as described earlier in Section 7.2.2. At low confinement this system is characterized by a similar rate sensitivity as that of the original untreated system. However, at high confinement there is a dramatic increase in the rate sensitivity. In fact,

the power law exponent for the small glass bead system at high confinement was 2.86, which is very close to that of polycrystalline ice. This further implies that the upper yield stress in frozen materials results from failure mechanisms occurring within the pore ice matrix.

Although limited data exist, the test results shown in Figure 7.10c for large glass beads substantiate the importance of particle-matrix bonding since the hydrophobic beads also have a substantially lower value for the upper yield stress than the untreated beads.

	Power Law Exponent 'n'		Mean±S.D. (MPa) Slow $\dot{\varepsilon}$		Mean±S.D. (MPa) Moderate $\dot{\varepsilon}$	
Material Type	**Reg.**	**HP**	**Reg.**	**HP**	**Reg.**	**HP**
Manchester fine sand	5.14	3.89	4.47±0.21	3.93±0.20	7.38±0.17	7.45±0.89
Small glass beads	6.58	7.60/2.86*	7.12±0.64	3.31/3.04*	10.45±0.67	4.52/6.90*
Large glass beads	N/A	N/A	N/A	N/A	7.46	4.84±0.60
Polycrystalline ice	3.27	N/A	2.37±0.00	N/A	5.04±0.35	N/A

Note: * indicates value obtained at high confinement levels

Table 7.7: Summary of the effect of interface adhesion on the upper yield stress of Manchester fine sand and glass bead systems at -10°C.

It is also interesting to point out that the system of small hydrophobic glass beads gave the lowest values for the upper yield stress of all the materials that were tested. They are, however, still greater than the values obtained for the polycrystalline ice specimens (except at low confinement at the moderate strain rate) even though the effects of particle bonding are minimal. If the upper yield of a frozen system is thought of as resulting from the summation of a number of individual strengthening mechanisms, then this higher strength can, in part, be due to the fact that the presence of particles will increase the strain rate in the ice matrix. This is discussed in much more detail in Section 7.3.

Finally, it is worth noting that interfacial adhesion also affects the post-upper yield behavior, only for those systems composed of spherical particles. As discussed in Section 2.3.4.2, which summarizes the behavior of frozen Manchester fine sand at large strains, the combination of high relative density and confinement leads to post-upper yield strain hardening (Type C and D curves). Conversely, strain softening behavior is expected for systems whose soil skeleton offers minimal frictional resistance. While these basic trends

were observed for the hydrophobic Manchester fine sand system, elimination of the interfacial bonding in the system of small glass beads led to strain softening behavior in all of the tests regardless of their relative density and degree of confinement. This is believed to be a significant observation with important engineering implications. It may also help in understanding the mechanisms operating in the upper yield region.

7.2.8 Effect of Particle Roughness

It is well-known that particle shape and roughness can affect the degree of structural hindrance between particles, which is an important mechanism of strength generation in unfrozen sands. Similarly, mechanical interaction between the ice and soil skeleton (which is affected by the adhesional bond at the interface) is thought to increase the peak shear strength of frozen sand (Ting et al. 1983), although little quantitative work has been performed to prove this hypothesis. Although much more information on this topic is available in the material science literature, most of the studies have concentrated on particle shape, and its impact on the fracture toughness (e.g., Moloney et al. 1984) and tensile strength (e.g., D'Almeida and Carvalho 1998) of polymeric particulate-filled composite materials, rather than on the broader issue of particle roughness. Most of the results conclude that particle shape is very important to the tensile strength of filled systems because irregularly shaped inclusions cause a weakening of the system due to the high stress concentrations that occur in their vicinity (Ahmed and Jones 1990). No information was found on the influence of particle shape on the strength of composites in compression.

As mentioned in the previous Chapter, investigation into the effects of particle roughness was initiated after a bond strength effect was observed for the modulus of the hydrophobic glass bead system, but not in the similarly treated system of Manchester fine sand. A small number of tests were then performed to see if the composite modulus in systems that lacked adhesional strength could be increased through surface roughening. In addition to providing great insights into the mechanisms controlling the Young's modulus of frozen materials, discussed in Section 6.3, these tests have also provided some

interesting results at the upper yield stress. The results, all obtained at -10°C, are summarized in Table 7.8 and shown in Figure 7.11.

Material Type	Power Law Exponent 'n'	Mean±S.D. (MPa)	
		Slow $\dot{\varepsilon}$	Moderate $\dot{\varepsilon}$
Small glass beads			
Regular	6.58	7.12±0.64	10.45±0.67
Hydrophobic (low σ_c)	7.60	3.31	4.52
Hydrophobic (high σ_c)	2.86	3.04	6.90
Hydrophobic rough (low σ_c)	6.27	4.04±0.46	5.87±0.23
Hydrophobic rough (high σ_c)	6.93	7.51	10.74±0.61
Large glass beads			
Regular	N/A	N/A	7.46
Hydrophobic (low σ_c)	N/A	N/A	4.84±1.64
Hydrophobic rough (low σ_c)	N/A	N/A	7.54±0.05

Table 7.8: Summary of the effect of particle roughness on the upper yield stress of hydrophobic glass bead systems at -10°C.

The first system shown (Figure 7.11a) is that of the small glass beads, made rough by acid-etching, and then treated to make them hydrophobic. At low confining pressure roughening leads to slightly higher yield stresses at both strain rates, as compared to the system of smooth hydrophobic beads, with little change in rate dependency. Application of high confinement on the other hand causes the system of hydrophobic roughened beads to behave in a similar manner as the original system composed of smooth fully-bonded particles, i.e. having the same upper yield stress and exhibiting the same rate dependency.

More information concerning the mechanisms controlling the upper yield stress can be obtained from the system of large glass beads shown in Figure 7.11b. These beads were made substantially rougher than the smaller beads through mechanical roughening techniques, as opposed to acid-etching. Figures 4.8e-f and 4.9c-d illustrate the end result for each system quite well. As Figure 7.11b shows, the limited number of tests performed make it impossible to assess any rate dependency, however, it is still possible to evaluate the results by comparing the individual data sets. Although tests have only been performed at low confinement on the large beads, the hydrophobic roughened system and the smooth fully-bonded system have almost identical values for the upper yield stress. This suggests an insensitivity to the level of confinement since the application of a high

confining stress was not necessary to cause the upper yield stress to increase to that of the original system, such as with the small glass beads. Furthermore, this indicates that, in the absence of particle adhesion, the upper yield stress is highly dependent on the degree of particle roughness. Hence, very significant particle roughness can fully counteract the lack of adhesion, whereas less rough particles require significant confinement to overcome the lack of adhesion. This will be discussed in greater detail in Section 7.3 which aims to summarize the mechanisms controlling the upper yield stress of frozen sand.

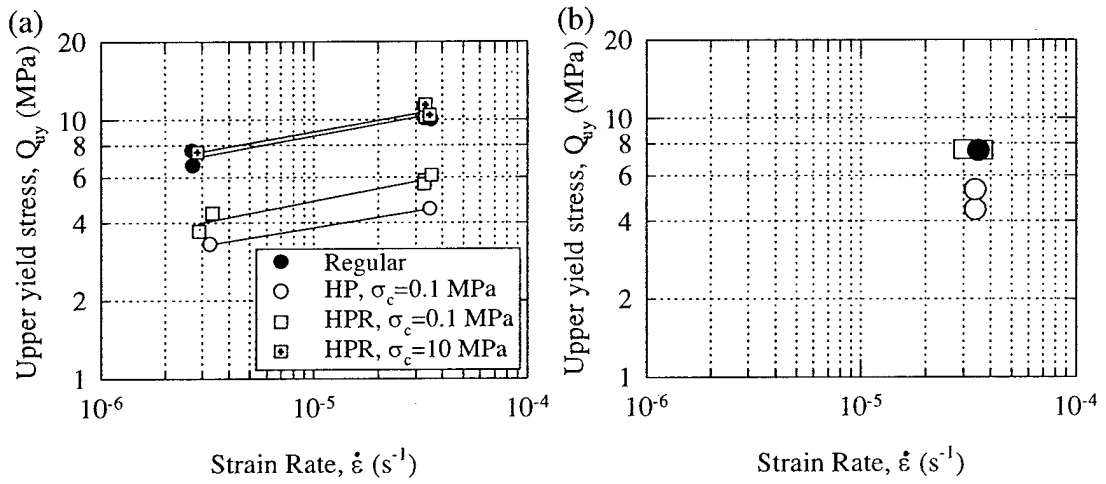

Figure 7.11: Effect of particle roughness on the upper yield stress of hydrophobic glass bead systems at -10°C at varying void ratios and confining pressures for (a) small glass beads, (b) large glass beads.

7.3 DISCUSSION OF MECHANISMS CONTROLLING THE UPPER YIELD BEHAVIOR OF FROZEN SAND

7.3.1 Introduction

This section develops a qualitative understanding of the mechanisms that operate in the upper yield region during the shearing of frozen materials in compression. By synthesizing the results presented in the previous section in a similar manner as done for the Young's modulus in Chapter 6, the relative importance of each parameter to the upper yield stress is inferred. This information is then used to construct a qualitative model in Section 7.3.3 for the mechanisms responsible for the upper yield stress in frozen sand. A

comprehensive understanding of the mechanisms controlling yielding in frozen materials is required for developing predictive techniques for frozen sands and in assessing the validity of existing yield models developed for particulate-filled composite materials. This will be the focus of the next two subsections.

7.3.2 Summary of Observations at the Upper Yield Stress

This section serves to clarify and highlight the main findings of the experimental program before a discussion on the mechanisms controlling the upper yield stress is presented in the next section. As was done for Chapter 6, data obtained from previous experimental programs have been included where necessary in order to further substantiate some of the trends.

In reviewing the data presented in the previous section, it is clear that the upper yield stress of frozen fully-bonded particulate materials is strongly dependent on the applied strain rate and temperature, and relatively insensitive to the volume fraction of solids and the degree of confinement. These results are qualitatively similar to those obtained on Manchester fine sand by Andersen et al. (1995). Based on their results, they concluded that the frictional resistance of the sand skeleton plays a very minor role in controlling the behavior of frozen sand in the upper yield region.

The importance of strain rate and temperature in the upper yield region has been clearly shown in Figures 7.5 and 7.7 for both fully-bonded and non-bonded systems. This dependency of the yield stress on these two parameters has also been well established for other frozen sands (e.g. Parameswaran 1980, Orth 1985, Shibata et al. 1985), and for a variety of two-phase composite materials in tension and compression (e.g. Ishai and Cohen 1968, Nicolais and Narkis 1971). In addition, it was also shown in Section 2.2 that the mechanical behavior of ice is highly dependent on both the applied strain rate and temperature.

The strain rate dependence of the strength of polycrystalline ice results from the movement of mobile dislocations and the stress dependence of the average dislocation velocity (Gold 1977, Goodman et al. 1981). This dependence can be well explained over a wide range of strain rates and temperatures using a power law relation as described

before (Equation 7.1) with a power law exponent of approximately 3. At higher strain rates, power law breakdown results as crack formation causes the ice to stop behaving as a continuum. Also, as shown in Figure 2.10, increasing the level of confinement can lead to higher strengths by suppressing crack formation and propagation.

Similarly, the temperature dependence of frozen systems can also be related to the strength of polycrystalline ice. Gold (1972) has shown that the number of cracks that form in polycrystalline ice at a given strain for the same compressive stress, decrease with decreasing temperature. For tests being carried out at a constant strain rate, this would have the effect of causing an increase in strength with a decrease in temperature (Gold 1977). This effect was shown in Figure 7.7 for all the systems tested. The temperature dependence of the strength of polycrystalline ice (Q_{ice}) in the ductile regime can be well described by incorporating the classical Arrhenius activation energy law into the power law expression (Equation 7.3). However, higher values for the Arrhenius parameters (i.e. Q_a, A) are required at temperatures warmer than -10°C to account for the non-linear temperature behavior of ice at these higher temperatures (Figure 2.9).

$$Q_{ice} = \left[\frac{1}{A}\cdot \exp\left(\frac{Q_a}{RT}\right)\dot{\varepsilon}\right]^{\frac{1}{3}} \tag{7.3}$$

The qualitatively similar behavior between polycrystalline ice and frozen soil has been summarized in Figure 7.12. This figure compares upper yield stress data for frozen Manchester fine sand at various temperatures and three strain rates to peak strength data for polycrystalline ice at temperatures ranging from -7°C to -12°C, and at confining stresses of 0 and 10 MPa. The power law exponents (*n* values) for the ice range from 4.3 to 5.4. For Manchester fine sand, however, they are higher and increase with decreasing temperature, which is in direct contrast to that which is observed for pure polycrystalline ice. As shown in Figure 2.8, the power law exponent for ice is relatively insensitive to temperature in the ductile regime.

Nevertheless, these similarities have led a number of authors to conclude that the upper yield stress is predominately due to yielding of the ice matrix (e.g., Sayles 1973, Bourbonnais and Ladanyi 1985, Andersen et al. 1995). Experimental data on the behavior of filled polymeric materials below their glass transition support this conclusion, since it

has been well established that their yield behavior is predominately due to the yielding characteristics of the matrix modified by the presence of inclusions (Ishai and Bodner 1970, Nicolais 1975). Therefore, it seems justified to believe that the onset of yielding in two-phase composites is controlled by the properties of the matrix material, although it is affected by the presence of the filler particles.

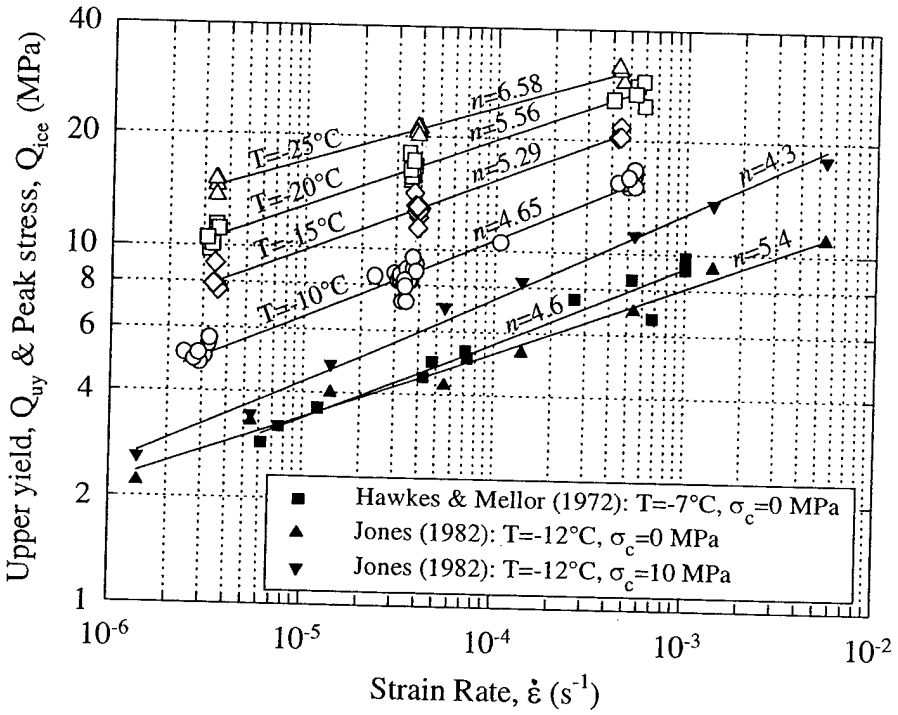

Figure 7.12: Upper yield stress of frozen Manchester fine sand and peak strength of polycrystalline ice. Ice data from Hawkes and Mellor 1972 and Jones 1982. (adapted from Andersen et al. 1995)

In addition to producing an increase and a temperature sensitivity in the power law exponent, the presence of inclusions also cause an important strengthening effect. This manifests itself by causing the upper yield stress in well-bonded frozen materials to be substantially greater than the peak strength of ice at comparable strain rates and temperatures. This strengthening effect was shown in Section 7.2.6 to be predominately related to the size of the inclusion, although particle roughness and interface adhesion have also been shown to be important. The positive dependency of the upper yield stress on particle size was shown in Figure 7.9, and although a definite trend is visible, more

testing needs to be done to fully characterize this effect and to determine the range over which this relationship is valid.

The effect of particle size on the tensile strength of particulate-filled polymers has been extensively studied and is well-known. At fixed volume fractions of fillers, there appears to be a linear relationship between tensile strength and particle diameter, the tensile strength decreasing for larger particle sizes (Landon et al. 1977). This is in direct contrast with the results obtained here for compression. The decrease in tensile strength for filled polymeric systems has simply been attributed to the resulting decrease in cross-sectional area of the load bearing polymer as the particle size is increased. Although this result is expected for tension, is not very helpful in explaining the behavior in compression where the filler actually sustains a portion of the load.

In contrast, the effect of particle size has not been extensively reported in the frozen soil literature. Rather, some discussions have focused on how soil particle size may affect the grain size of ice since some information is available for how the compressive strength of ice varies as a function of ice grain size. Cole (1985, 1987) shows that the peak strength of polycrystalline ice increases with decreasing grain size, although this effect is noticed to reverse itself at slower strain rates (i.e. $5x10^{-7}$ s^{-1} to $2x10^{-6}$ s^{-1}) for grain sizes in the 1-3 mm range (Figure 2.11). This reversal has been attributed to the intervention of dynamic recrystallization processes in the finer-grained material which serves to lower the peak stress of polycrystalline ice (Cole 1987). Although there is a clear lack of ice strength data in the range of grain sizes appropriate for frozen sand, data on other materials such as metals suggest that the strength generally increases with decreasing grain size due to a dramatic reduction in the number of dislocations per grain.

The results of the experimental program have helped to elucidate the importance of particle roughness and interfacial adhesion on the upper yield stress, which until now has only been alluded too in frozen soils. Chapter 6 described in detail how an increased composite modulus can result from either mechanical bonding, resulting from particle roughness, or from adhesional bonding between phases. This interaction was summarized in Figure 6.14. Examination of the results in Figure 7.10 and Figure 7.11 indicate that similar trends are evident in the upper yield region.

As illustrated in Figure 7.10a, the application of a hydrophobic coating to Manchester fine sand does little to alter its upper yield stress, whereas a substantial drop occurs in the hydrophobically treated glass bead systems (Figure 7.10b-c). Having already established the effectiveness of the hydrophobic coating at reducing ice adhesion, this observation strongly suggests that the differences in upper yield behavior are due to the differences in particle shape or roughness. Subsequent experiments using roughened spherical glass beads confirmed the importance of particle roughness over particle shape. In Figure 7.11a, a small increase in the upper yield stress was observed for the system of slightly roughened small hydrophobic glass beads sheared at low confinement. The application of a confining stress, however, caused this system to behave in an identical manner to the original fully-bonded system of smooth glass beads. The importance of the level of confinement in non-bonded systems indicates the operation of a mechanical interaction effect where resistance to shear between the ice matrix and the particles is controlled both by a friction coefficient (particle roughness) and an applied normal force (i.e. confinement). If the particle roughness is increased as in the system of large glass beads (Figure 7.11b), then effective mechanical interlocking dominates and the application of confining stress is not required. This explains why the system of roughened hydrophobic large glass beads tested at low confinement had the same yield stress as the original fully-bonded system.

Therefore, the degree of confinement does seem to be important in the upper yield region, however, its effects are usually concealed in typical tests on frozen materials. In tests on natural sands, the confinement effect is masked by the high degree of mechanical interlocking that results from their inherent roughness, whereas in tests on frozen glass beads, the existence of interfacial bonding is responsible for masking the effect.

From the preceding discussion it can be concluded that, for frozen systems with particles in contact, the most important parameters in the upper yield region are strain rate, temperature, particle grain size, interface adhesion, and particle roughness. All of the other variables that were examined (e.g., void ratio, confinement, particle modulus) have been shown to be of minor importance in fully-bonded systems. However, confinement

was shown to be very important when little to no bonding exists between ice and smooth spherical particles.

It should be mentioned that volume fraction would be expected to be an important factor based on the results of numerous studies on polymeric composite materials (e.g., Ishai and Cohen 1968, Nicolais and Narkis 1971, Landon et al. 1977). The ability to construct specimens over a wide range of volume fractions allowed those researchers to quantify the effects of volume fraction on the yielding behavior. However, in frozen soils, the preparation of specimens over a wide range of particle fractions has not been possible without also affecting the structure of the ice matrix (Goughnour and Andersland 1968). This has limited much of the work on frozen soils to highly-filled systems and consequently has led to the conclusion that volume faction is relatively unimportant in the upper yield region. Additional tests at lower volume fractions (i.e. at the upper end of the realm of "dirty ice") are needed to determine if indeed an effect of particle volume fraction exists in frozen soils similar to that observed in Figure 2.29. These results may be particularly important in understanding the strength of ice-rich soils such as permafrost.

The number of parameters that have been shown to be important to the upper yield stress means that the behavior of soils in this region is substantially more complex than the mechanisms controlling the Young's modulus of frozen soils. However, although there may be more factors influencing the upper yield stress, it seems that the effects of particle roughness and interface adhesion play a similar role as they did for Young's modulus, while the other parameters are simply artifacts of the behavior of polycrystalline ice under stress. The next section will elaborate on the ways the mechanisms interact to cause strength in frozen sands.

7.3.3 Development of Strength in Frozen Sand

Based on the test results and discussion presented in the previous section, it is possible to formulate a conceptual model similar to that developed by Ting et al. (1983) for how frozen sands develop strength. However, before incorporating the new findings of this research, it is useful to review the mechanisms originally proposed by Ting et al. (1983).

According to Ting et al. (1983) the peak strength of frozen sands can be thought of resulting from a combination of :

1. Ice strength and ice strengthening due to interaction with soil, which together account for a large percentage of the total strength, and is greater than that in normally tested ice due to deformational constraints, and different stress states and strain rates.

2. Soil strength and strengthening resulting from interparticle friction, particle interference (structural hindrance), and dilatancy effects, and is mainly a function of the effective confining stress level.

While these mechanisms have been proposed for the peak strength of frozen sands, they can in theory be applied to the strength in the upper yield region as well, with only the relative importance of each of the mechanisms changing. However, it is now known that the influence of the soil strength (i.e. the frictional resistance of the soil skeleton) in the upper yield region is negligible (Swan 1994), and that the behavior of frozen sand at the upper yield stress is qualitatively similar to the peak strength behavior of polycrystalline ice (Andersen et al. 1995). These observations propose that the upper yield stress is primarily controlled by the strength of the pore ice matrix and the factors which alter the stresses acting on it. Furthermore, it was concluded in Section 7.3.2 that the amount of strengthening over bulk polycrystalline ice is related to the particle size, the coupling between phases (adhesional or mechanical), and the particle shape at the higher rates of strain.

Therefore, based on the results obtained in this experimental program, it is proposed that the upper yield stress in frozen systems is predominantly due to an enhanced ice matrix strength that is controlled by the factors which affect the initiation and propagation of cracks within the pore ice matrix. Factors contributing to an enhanced ice matrix strength include an increase in the effective degree of confinement and mean strain rate within the pore ice matrix, and the added strengthening that results from adhesional bonding and/or mechanical interactions with the inclusions. The fracture behavior of the pore ice, however, is influenced by the applied strain rate and temperature, as well as by particle size, shape, and roughness. It is also highly dependent on the degree of interfacial adhesion, which in turn is affected by the level of confinement.

Using this framework it is possible to at least qualitatively explain the observed behavior at the upper yield stress for all of the particulate systems tested. This provides a better understanding of how frozen soils develop strength and ultimately aids in the development of physically-based models. In addition, the process of describing all of the various data with a plausible and consistent hypothesis is useful for identifying future research needs.

A convenient starting point for explaining strength generation in frozen sands is to compare the strengths of the bonded and non-bonded systems of smooth small glass beads at -10°C to that of polycrystalline ice, at a similar temperature, but at an increased strain rate to account for strain rate magnification within the pore ice matrix. This is shown in Figure 7.13. A magnification factor of 2.5, based on the average specimen porosity (~0.4), was used as a reasonable approximation for the increased strain rate within the pore ice matrix.

In explaining the data in Figure 7.13, concepts common to the fields of fracture mechanics and composite materials need to be applied. It is well-known that in systems lacking adhesional strength, debonding takes place at the particle interface. This is because a non-bonded interface offers the least resistance to crack propagation and hence the lowest debonding energy. Conversely, in the case of high adhesion, separation takes place in the matrix around the particle, and hence away from the interface (Mallick and Broutman 1975). Thus, the amount of energy (i.e. fracture energy) required to propagate a crack through the matrix is substantially higher. This explains the large difference in strengths between the bonded and non-bonded systems of glass beads.

Focusing on the system of non-bonded beads in Figure 7.13 it is evident that at the low strain rate (ductile regime), this system fails at the (modified) strength of ice regardless of the level of confinement. This is because at strain rates in the ductile regime, failure occurs by slow or non-propagating cracks that are essentially pressure insensitive (Figure 2.10). Furthermore, this suggests that there are no other mechanisms operating within the ice matrix of this system to cause its strength to be higher or lower than that of ice. However, at the moderate strain rate the strength of the non-bonded system is clearly increased by confinement. The application of high confinement suppresses cracking at the

particle interface and in the pore ice matrix, which results in the system yielding at a higher strength. In fact, it is similar to the strength of ice failing by ductile creep. However, in the absence of confinement, crack propagation is enhanced by the inclusions and, as a result, the system yields at a lower strength than ice.

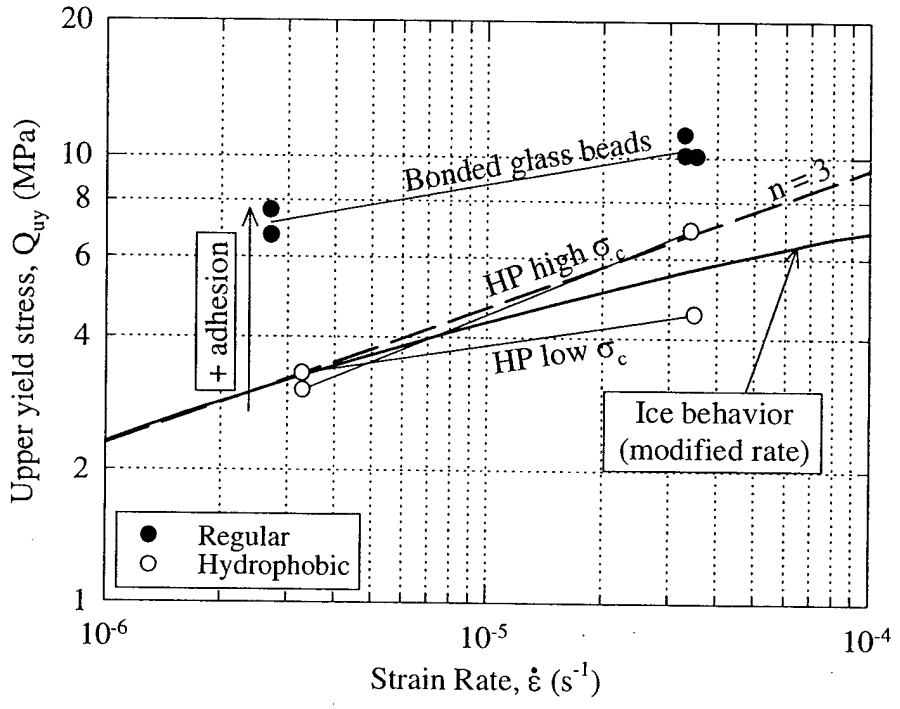

Figure 7.13: Effect of adhesional bonding and influence of confinement on frozen systems of small glass beads at -10°C at varying void ratios.

The fact that higher strengths can be realized at faster rates of strain by increasing the level of confinement is expected to occur in fully-bonded systems as well. Suppression of cracking is presumably the reason why the data of Chamberlain et al. (1972) and Sayles (1973) in Figure 2.24, which were conducted a high strain rates, show a pressure sensitivity at the upper yield stress. The other programs shown in Figure 2.24 show no effect of confinement because the data were obtained at strain rates where failure by crack propagation is not as prevalent.

The addition of surface roughness to the hydrophobic small glass beads was shown in Figure 7.11 to cause an increase in the upper yield strength. These data have been

reproduced in Figure 7.14, and compared with the strength of polycrystalline ice at the modified strain rate at -10°C. In this case, the strength is seen to depend both on roughness and confinement, that is, the debonding energy is a function of these two parameters. At low confinement, cracking at the interface is hindered by surface roughness. This added resistance results in the strength of this system being higher than that for the smooth hydrophobic glass beads. The combination of roughness and high confinement, however, effectively locks the system preventing the propagation of cracks at the interface. Cracks therefore are forced to propagate through the matrix leading to a dramatic increase in the fracture energy, and consequently the same strength as the original fully-bonded system, which also yields by cracks propagating through its matrix. Similarly, if the system has a high surface roughness, then only a small amount of confinement may be needed to propagate cracks through the matrix rather than at the interface. This was observed for the system of large glass beads which, upon roughening, exhibited a similar upper yield strength to the original system (Figure 7.11b).

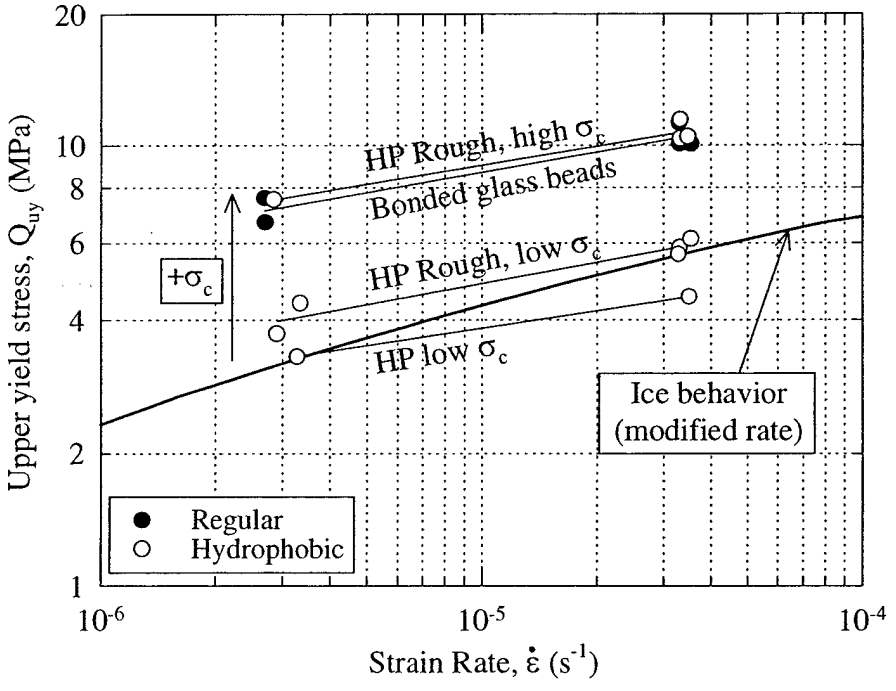

Figure 7.14: Effect of surface roughness and influence of confinement on frozen systems of small glass beads at -10°C at varying void ratios.

Having shown the importance of adhesional bonding in systems with minimal interfacial mechanical interlocking, and how particle roughness and confinement combine to produce strength, the impact of particle shape needs to be addressed in order to explain the upper yield strength for natural sand systems. Figure 7.15 compares the 2010 industrial quartz system with the PMMA and small glass bead systems at -10°C. These systems are all fully-bonded and have approximately the same particle size, thus eliminating the influence of this parameter. This figure shows that the 2010 industrial quartz system has a higher strength at the moderate strain rate, suggesting an influence of particle shape, whereas at the slow strain rate, all three systems give the same strength.

This behavior can be well explained through differences in fracture toughness (K_{Ic}), which quantifies the resistance encountered by propagating cracks. The lower strain rate sensitivity exhibited by the PMMA and glass bead systems indicates that spherical particles enhance cracking by offering the least resistance to propagating cracks. Conversely, systems composed of angular particles offer more resistance to propagating cracks which translates into greater strain rate sensitivity. However, explanations involving differences in fracture toughness are only applicable at higher strain rates where ice acts in a more brittle fashion and fails by rapid crack propagation. This explains why little difference is noticed between the three systems at the slow strain rate. At this rate, ice behaves as a predominantly ductile material and this allows propagating cracks to be pinned and blunted as they encounter inclusions in their path. As the strain rate increases, however, less time is available for crack blunting to occur and hence the resulting strength is determined by the resistance offered to propagating cracks (i.e. fracture toughness), which is affected by particle shape. Furthermore, no effect of confinement was noticed for these fully-bonded systems since it is believed that such systems provide a degree of "internal" confinement of sufficient magnitude that effectively causes the pore ice to behave as if it was confined regardless of the level of applied pressure.

Differences in particle shape and size were shown in Figure 7.4 to also affect the magnitude of the upper yield strain and its pressure sensitivity. This is expected since the ductility of the system (as characterized by the yield strain) depends heavily on the degree of interfacial mechanical interlocking which is dependent on particle shape. Spherical

particles exhibit a minimal amount of interlocking that effectively results in a ductile response to the applied stress. Furthermore, under high confinement the combination of minimal hindrance and suppression of cracking is expected to lead to a higher yield strain. In rough or angular systems, premature cracking and the higher resistance to particle movement would lead to a lower yield strain.

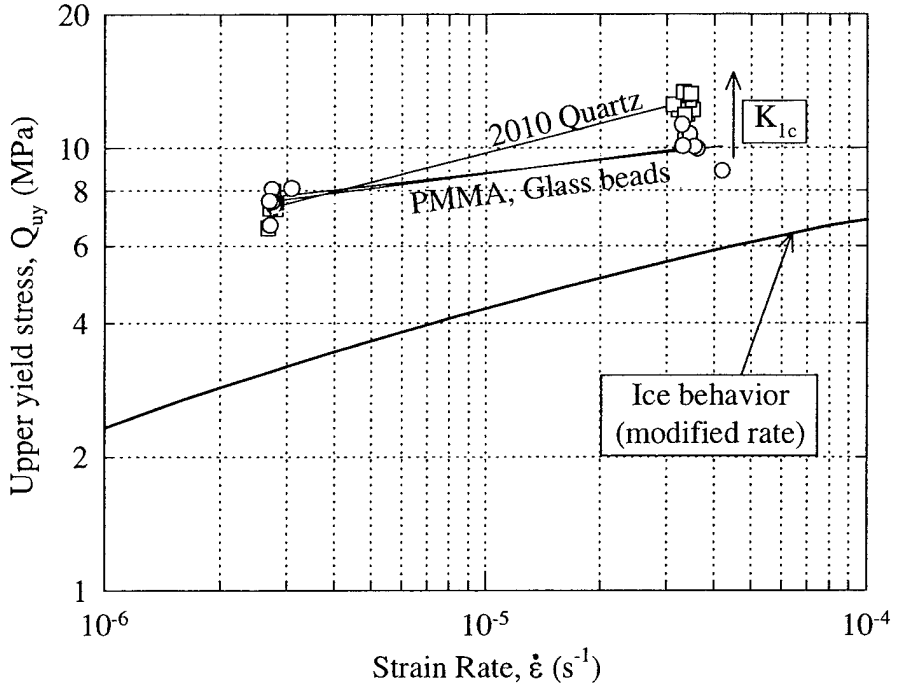

Figure 7.15: Comparison of 2010 industrial quartz, PMMA, and small glass beads at -10°C at varying void ratios and confining pressures showing the effect of particle shape (K_{1c}).

Examination of the nature of crack propagation within the ice matrix also provides a plausible explanation for the observed strengthening with increasing grain size that was discussed in Section 7.2.6 and illustrated for various fully-bonded materials in Figure 7.9. The effect of particle size is summarized in a slightly different way in Figure 7.16. It compares the strengths of the Manchester fine sand and 2010 industrial quartz systems to that of pure polycrystalline ice at a modified strain rate over the strain rate range investigated. If it is assumed that the application of stress to a frozen particulate system causes cracks to nucleate around each particle, and that yielding or failure is attributed to

crack coalescence, then the strengthening effect can be explained by relating the distance (or surface area) that nucleated cracks need to span before coalescing with the next crack to the grain size of the particle. Therefore, for a given applied stress that causes cracks to nucleate and then propagate, a system composed of smaller particles will fail or yield at a lower strength since more cracks, on average, will have coalesced than for a coarser-grained material.

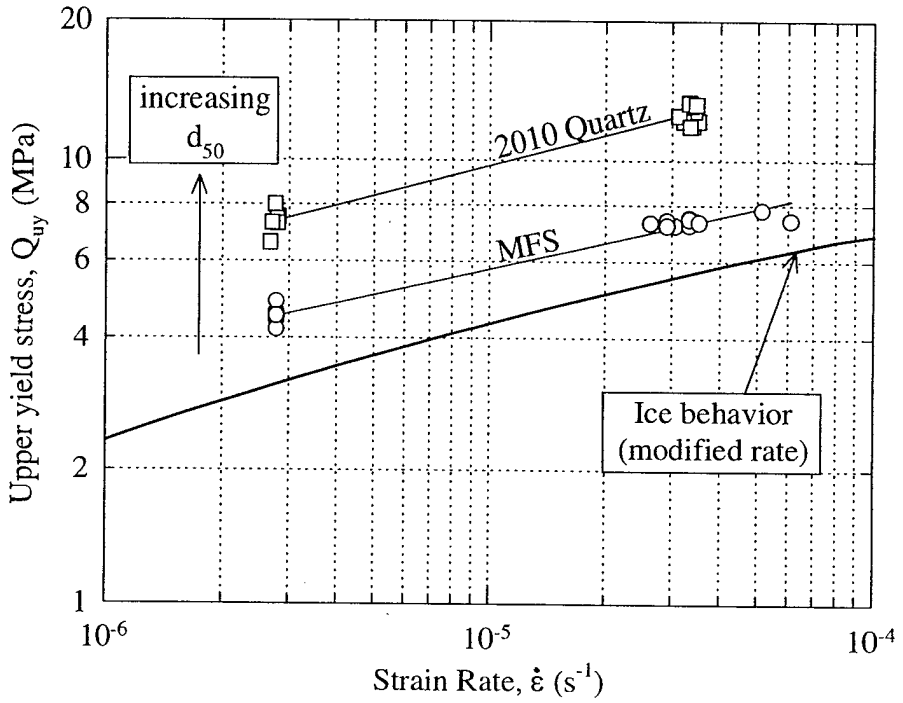

Figure 7.16: Comparison of 2010 industrial quartz and Manchester fine sand at -10°C at varying void ratios and confining pressures showing the effect of particle size.

Finally, it has been shown for various frozen systems that temperature affects both the degree of strengthening and the strain rate sensitivity at the upper yield stress (Figures 7.6, 7.7, 7.12). As mentioned in Section 7.3.2, the number of cracks that form in polycrystalline ice at a given strain for the same applied compressive stress, decrease with decreasing temperature, which leads to an increase in strength (Gold 1972). Assuming that the pore ice in a frozen soil system behaves similarly, this accounts for the positive dependence of the upper yield stress with decreasing temperature. However, as the

temperature decreases the ice matrix also becomes more brittle, thus crack propagation becomes easier (i.e. the fracture toughness decreases). This is reflected in the strain rate sensitivity decreasing (higher n value) with decreasing temperature. Thus the temperature dependence of frozen soil systems results from a complex interaction between crack initiation and crack propagation mechanisms within the pore ice matrix.

Figure 7.17 schematically summarizes the main findings obtained from the analysis into the mechanisms operating in the upper yield region. As with modulus, it is intended to illustrate how the various parameters which have been shown to be important to the strength of frozen systems rank in terms of importance.

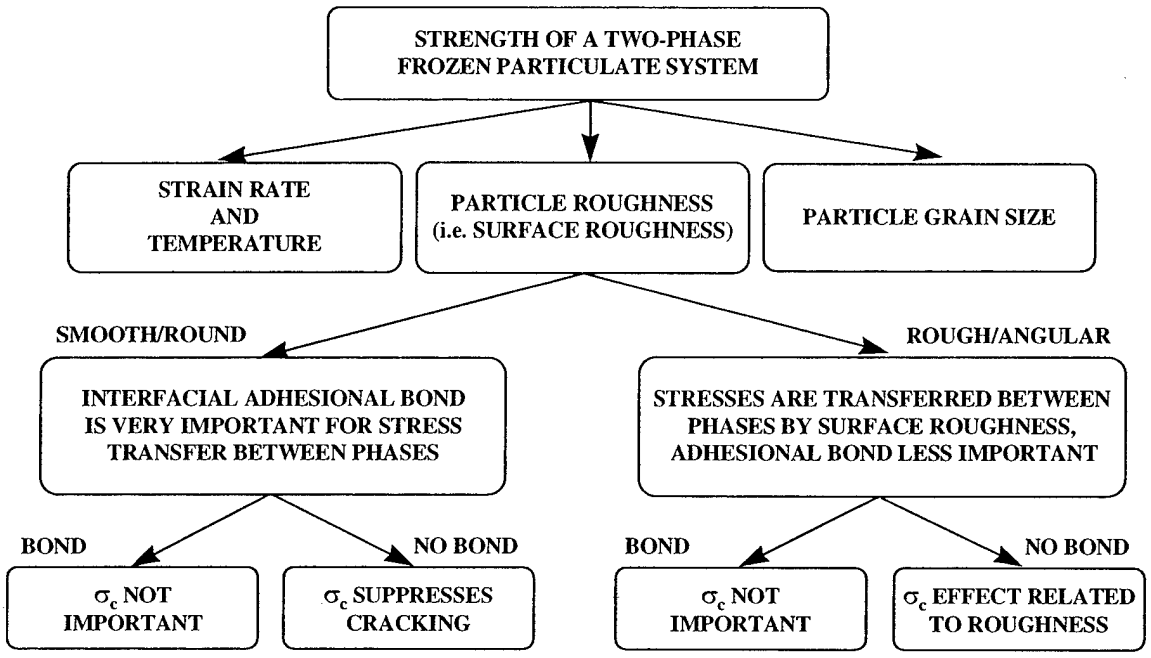

Figure 7.17: Proposed mechanism map for the upper yield stress of frozen sand.

7.4 PREDICTION OF THE UPPER YIELD BEHAVIOR OF FROZEN SAND

The results presented in the previous section confirm that the upper yield stress in frozen systems is primarily due to an enhanced pore ice matrix strength with little or no contributions from the soil (particle) skeleton and soil strengthening mechanisms.

Furthermore, through specialized tests conducted during this experimental program, the upper yield strength was also observed to be affected by factors that control the initiation and propagation of cracks within the pore ice matrix (e.g., strain rate, temperature, interface adhesion, particle size and shape).

This extremely complex behavior makes prediction of the upper yield behavior through physically-based mechanistic models rather difficult owing to numerous competing mechanisms that need to be accounted for. As was pointed out in Section 2.4.4, the theory for the strength of particulate-filled systems is less developed than that for modulus. As a result, no physically-based predictive models exist for describing the yielding behavior of composite materials, especially in compression. Although the situation is slightly better for yielding in tension, owing to the vast amount of experimental data available, most of the models offer little more than a correlation with volume fraction as this parameter is generally regarded to be the most important factor governing the yield strength in tension. Furthermore, the definition of yielding is usually taken as the peak stress, which is known to behave differently from the upper yield stress for frozen sands. These issues severely limit the application of the these models to describe the upper yield behavior of frozen sand.

While this experimental program has offered many insights into the mechanisms controlling the upper yield stress in frozen sands, the development of a physically-based model that considers all the factors that have been shown to be important is still rather premature. Before progress can be made, the hypotheses presented in the previous section need to be substantiated through further laboratory experimentation. Various recommendations for additional work are outlined in Section 8.3.2.

However, if attention is restricted to fully-bonded natural sand systems then prediction of the upper yield stress is greatly simplified. Using the data obtained for frozen Manchester fine sand in triaxial compression as a reference, since it represents the most comprehensive database of a natural sand available in the literature, an equation that describes its strain rate and temperature dependence can be written as:

$$Q_{uy} = \left(K_1 Q_{ice} + D\Delta T\right)\left(\frac{\dot{\varepsilon}}{\dot{\varepsilon}_0}\right)^{\frac{1}{\left(K_2 n_{ice} - \alpha \Delta T\right)}} \tag{7.4}$$

where: Q_{uy} = upper yield stress of frozen particulate system
Q_{ice} = peak strength of polycrystalline ice at T_0 and $\dot{\varepsilon}_0$
$\Delta T = (T-T_0)$
n = strain rate sensitivity of polycrystalline ice at T_0

The above equation relates the upper yield strength (Q_{uy}) of a frozen sand system to the strength of polycrystalline ice (Q_{ice}) at a specific strain rate ($\dot{\varepsilon}_0$) and temperature (T_0). Four fitting parameters (i.e. α, D, K_1, K_2) are necessary to modify the basic strength and strain rate sensitivity of ice to account for the various ice strengthening mechanisms described earlier. Particle grain size effects are incorporated into K_1, particle shape effects (i.e. toughness) into K_2, and D and α reflect changes in the amount of temperature induced strengthening (i.e. crack initiation) and rate sensitivity (i.e. crack propagation), respectively. Therefore, Equation 7.4 captures the most important parameters influencing the upper yield stress for fully-bonded materials.

Using the ice data obtained from this experimental program, the upper yield stress behavior of Manchester fine over a strain rate range of $3x10^{-6}$ s^{-1} to $5x10^{-4}$ s^{-1} and a temperature range of -2°C to -25°C can be adequately modeled using Equation 7.4 with the parameter values given in Table 7.9. This is shown in Figure 7.18.

	Fitting Coefficients for Equation 7.4			
Material	K_1	K_2	α	D
Polycrystalline ice	1.0	1.0	0.00	-0.15
Manchester fine sand	2.0	1.4	0.10	-0.53
2010 industrial quartz	3.1	1.4	0.14	-0.65
PMMA	3.2	3.0	0.55	-0.60
Glass beads (small)	3.0	2.0	0.55	-0.60

Note: Q_{ice}=2.37 MPa and n_{ice}=3.27 at $\dot{\varepsilon}_0=3x10^{-6}$ s^{-1} and T_0=-9.36°C

Table 7.9: Summary of fitting coefficients for Equation 7.4 for frozen systems investigated.

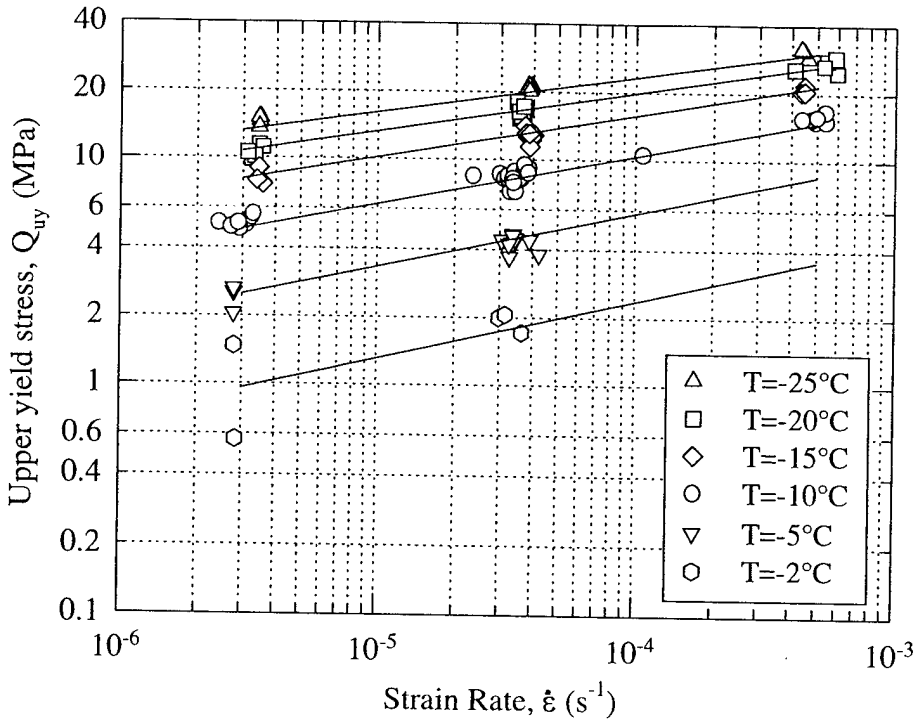

Figure 7.18: Comparison of upper yield model (Equation 7.4) and experimental data for Manchester fine sand at -2°C to -25°C using parameters given in Table 7.9. (T≤-10°C data from Andersen et al. 1995)

Further validation can be obtained by fitting Equation 7.4 to other frozen systems investigated during this research program (i.e. 2010 industrial quartz, PMMA, glass beads, polycrystalline ice). Since Equation 7.4 does not account for the effects of adhesion, no attempt was made to fit the data obtained on the hydrophobic systems. Figure 7.19a-d illustrates that excellent fits to these systems can be achieved with relatively minor adjustments in the four fitting parameters (Table 7.9).

Although Equation 7.4 cannot be used in a truly predictive sense, a very good estimate of the upper yield stress of a typical frozen natural granular material can be obtained by incorporating the additional information given in this Chapter regarding the relative significance of the parameters shown to be important to the upper yield stress. In particular, the information given in Figure 7.17 should be used as a guide when extrapolating Equation 7.4 to other frozen systems.

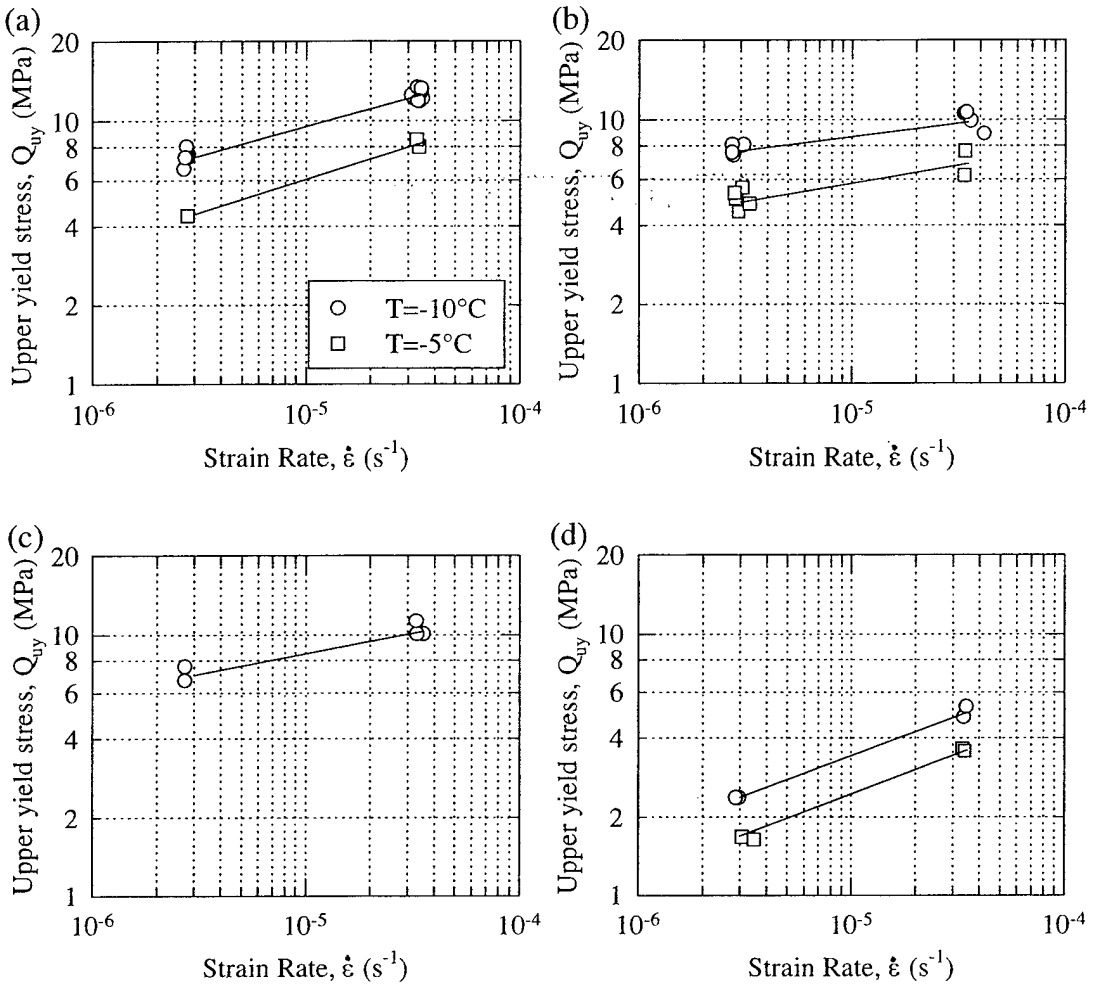

Figure 7.19: Comparison of upper yield model (Equation 7.4) and experimental data at -5°C and -10°C at varying void ratios and confining pressures for (a) 2010 industrial quartz, (b) PMMA, (c) small glass beads, (d) polycrystalline ice.

7.5 REFERENCES

1. Ahmed, S. and Jones, F.R. (1990), "A Review of Particulate Reinforcement Theories for Polymer Composites", *Journal of Materials Science*, v. 25, pp. 4933-4942.

2. Andersen, G.R. (1991), "Physical Mechanisms Controlling the Strength and Deformation Behavior of Frozen Sand", Sc.D Thesis, Department of Civil and Environmental Engineering, MIT, Cambridge, MA, 560 p.

3. Andersen, G.R., Swan, C.W., Ladd, C.C., Germaine, J.T. (1995), "Small-Strain Behavior of Frozen Sand in Triaxial Compression", *Canadian Geotechnical Journal*, v. 32, no. 3, pp. 428-451.

4. ASTM. (1996), "Laboratory Determination of Creep Properties of Frozen Soil Samples by Uniaxial Compression (D 5520-94)", *Annual Book of ASTM Standards*, v. 4.09, no. 4, pp. 337-343.

5. Bourbonnais, J. and Ladanyi, B. (1985), "The Mechanical Behavior of Frozen Sand Down to Cryogenic Temperatures", *Proc. 4th International Symposium on Ground Freezing*, Sapporo, Japan, pp. 235-244.

6. Chamberlain, E., Groves, C., Perham, R. (1972), "The Mechanical Behavior of Frozen Earth Materials Under High Pressure Triaxial Test Conditions", *Geotechnique*, v. 22, no. 3, pp. 469-483.

7. Cole, D.M. (1985), "Grain Size and the Compressive Strength of Ice", *Journal of Energy Resources Technology*, v. 107, pp. 369-374.

8. Cole, D.M. (1987), "Strain-Rate and Grain-Size Effects in Ice", *Journal of Glaciology*, v. 33, no. 115, pp. 274-280.

9. D'Almeida, J.R.M., and De Carvalho, L.H. (1998), "An Investigation on the Tensile Strength of Particulate-Filled Polymeric Composites", *Journal of Materials Science*, v. 33, pp. 2215-2219.

10. Gold, L.W. (1977), "Engineering Properties of Fresh-Water Ice", *Journal of Glaciology*, v. 19, no. 81, pp. 197-211.

11. Gold, L.W. (1972), "The Process of Failure of Columnar-Grained Ice", *Philosophical Magazine A*, v. 26, no. 2, pp. 311-328.

12. Goodman, D.J., Frost, H.J., Ashby, M.F. (1981), "The Plasticity of Polycrystalline Ice", *Philosophical Magazine A*, v. 43, no. 3, pp. 665-695.

13. Goughnour, R.R. and Andersland, O.B. (1968), "Mechanical Properties of a Sand-Ice System", *ASCE Journal of the Soil Mechanics and Foundation Division*, v. 94, no. SM4, pp. 923-950.

14. Hawkes, I. and Mellor, M. (1972), Deformation and Fracture of Ice Under Uniaxial Stress, *Journal of Glaciology*, v. 11, no. 61, pp. 103-131.

15. Ishai, O. and Bodner, S.R. (1970), "Limits of Linear Viscoelasticity and Yield of a Filled and Unfilled Epoxy Resin", *Transactions of the Society of Rheology*, v. 14, no. 2, pp. 253-273.

16. Ishai, O. and Cohen, L.J. (1968), "Effect of Fillers and Voids on Compressive Yield of Epoxy Composites", *Journal of Composite Materials*, v. 2, no. 3, pp. 302-315.

17. Jones, S.K. (1982), "The Confined Compressive Strength of Polycrystalline Ice", *Journal of Glaciology*, v. 28, no. 98, pp. 171-177.

18. Landon, G., Lewis, G., Boden, G.F. (1977), "The Influence of Particle Size on the Tensile Strength of Particulate-Filled Polymers", *Journal of Materials Science*, v. 12, pp. 1605-1613.

19. Leidner, J., Woodhams, R.T. (1974), "The Strength of Polymeric Composites Containing Spherical Fillers", *Journal of Applied Polymer Science*, v. 18, pp. 1639-1654.

20. Mallick, P.K. and Broutman, L.J. (1975), "Mechanical and Fracture Behavior of Glass Bead Filled Epoxy Composites", *Materials Science and Engineering*, v. 18, pp. 63-73.

21. Moloney, A.C., Kausch, H.H., Stieger, H.R. (1984), "The Fracture of Particulate-Filled Epoxide Resins", *Journal of Materials Science*, v. 19, pp. 1125-1130.

22. Nicolais, L. (1975), "Mechanics of Composites", *Polymer Science and Engineering*, v. 15, no. 3, pp. 137-149.

23. Nicolais, L. and Narkis, M. (1971), "Stress-Strain of Styrene-Acrylonitrile/Glass Bead Composites in the Glassy Region", *Polymer Engineering and Science*, v. 11, no. 3, pp. 194-199.

24. Nielsen, L.E. (1966), "Simple Theory of Stress-Strain Properties of Filled Polymers", *Journal of Applied Polymer Science*, v. 10, pp. 97-103.

25. Nielsen, L.E. (1974), *Mechanical Properties of Polymers and Composites*, Marcel Dekker, New York.

26. Orth, W. (1985), "Deformation Behavior of Frozen Sand and its Physical Interpretation", *Proc. 4th International Symposium on Ground Freezing*, Sapporo, Japan, pp. 245-253.

27. Papanicolaou, G.C. and Bakos, D. (1992), "The Influence of the Adhesion Bond Between Matrix and Filler on the Tensile Strength of Particulate-Filled Polymers", *Journal of Reinforced Plastics and Composites*, v. 11, pp. 104-126.

28. Parameswaran, V.R. and Jones, S.J. (1981), "Triaxial Testing on Frozen Sand", *Journal of Glaciology*, v. 27, no. 95, pp. 147-155.

29. Parameswaran, V.R. (1980), "Deformation Behavior and Strength of Frozen Sand", *Canadian Geotechnical Journal*, v. 17, pp. 74-78.

30. Sanderson, T.J.O. (1988), *Ice Mechanics: Risks to Offshore Structures*, Graham and Trotman, London.

31. Sayles, F.H. (1973), "Triaxial and Creep Tests on Frozen Ottawa Sand", *Proc. 2nd International Permafrost Conference*, Yakutsk, U.S.S.R, pp. 384-391.

32. Shibata, T., Adachi, T., Yashima, A., Takahashi, T., Yoshioka, I. (1985), " Time-Dependence and Volumetric Change Characteristics of Frozen Sand Under Triaxial Stress Condition", *Proc. 4th International Symposium of Ground Freezing*, Sapporo, Japan, pp. 173-179.

33. Swan, C., Ladd, C.C., Germaine, J.T., Andersen, G.R. (1995), "Physical Mechanisms Controlling the Strength-Deformation Behavior of Frozen Sand: Part II", Final Report to the U.S. Army Research Office, Department of Civil and Environmental Engineering, MIT, Cambridge, MA, 254p.

34. Swan, C. (1994), "Physical Mechanisms Controlling the Deformation and Strength Behavior of Unfrozen and Frozen Manchester Fine Sand", Sc.D Thesis, Department of Civil and Environmental Engineering, MIT, Cambridge, MA, 1044 p.

35. Ting, J.M., Martin, R.T., Ladd, C.C. (1983), "Mechanisms of Strength for Frozen Sand", *ASCE Journal of Geotechnical Engineering*, v. 109, no. 10, pp. 1286-1302.

36. Zhu, Y., and Carbee, D.L. (1988), "Triaxial Compressive Strength of Frozen Soils Under Constant Strain Rates", *Proc. 5th International Conference on Permafrost*, Trondheim, Norway, v. 5, no. 2, pp. 1200-1205.

CHAPTER 8

CONCLUSIONS AND RECOMMENDATIONS

8.1 OVERVIEW OF RESEARCH

The present study was undertaken to investigate the physical mechanisms affecting the pre-failure deformation characteristics of frozen sand in triaxial compression. The pre-failure deformation behavior must be well understood in order to make reliable predictions of deformations around geotechnical structures in cold regions and when artificial ground freezing is used as a construction aid. The pre-failure deformation behavior of frozen sand has been characterized in this study by the Young's modulus and by the upper yield stress, which represents the onset of highly non-linear behavior. The effects of particle (sand) volume fraction, degree of confinement (stress level), strain rate, and temperature were the primary variables investigated. This research also focused on the significance of particle size, shape, roughness, and modulus as well as the adhesional strength of the interface between the particle and the ice matrix. The primary focus of this study was to understand how these variables contribute to the stiffness and yielding behavior of frozen sand such that its constitutive behavior may be better understood and eventually modeled in a more rigorous manner.

In order to reliably quantify the pre-failure or small strain behavior of frozen geomaterials, a significant portion of the research was dedicated to the enhancement of the existing technology for the measurement of axial strains in the triaxial cell. The previous system employed for this purpose suffered from poor stability and noise rejection, and hence lacked the resolution to capture the extremely small strains necessary to more accurately define the initial stiffness. As a result, a new device was developed featuring two miniature LVDT's mounted on a pair of yokes that clamp to the specimen. In addition to not interfering with the pressure seals, this device also accommodates radial deformation and is quite compact in size. A highly stable, low-noise signal conditioning system was also developed to complete the design. Together, the system is easily capable

of resolving displacements of less than 0.1 microns, corresponding to strains less than 0.0002%, over a wide range in strain.

In conjunction with enhancing the axial strain measurement technology, a number of improvements to the triaxial testing system originally developed for testing frozen Manchester fine sand by Andersen (1991) were also implemented. These included systems for better temperature and strain rate control, as well as a number of small modifications to the load application system. These were described in detail in Section 3.3.3. Together they contributed to the accuracy and reliability of the small strain measurements achieved during this program.

An extensive compression testing program, utilizing the new strain measurement device, was then undertaken using the high-pressure low-temperature automated triaxial system originally developed for testing frozen Manchester fine sand by Andersen (1991). Although the pre-failure deformation behavior was of primary interest of this research, most of the specimens were strained to large strains (ε_a~10-20%) in order to provide information regarding the large strain behavior for future analysis. In addition to further tests on Manchester fine sand, whose properties and behavior (both unfrozen and frozen) have already been well documented, a number of other materials were also tested. These materials were used to investigate the importance of variables such as particle size and shape, interface adhesion, and particle modulus. Chapter 4 provides a comprehensive description of each of the materials used during this testing program

Finally, the results obtained during this experimental program have been analyzed and interpreted assuming that frozen soil acts as a two-phase particulate composite material, composed of a suspension of sand particles (inclusions) in a matrix of polycrystalline ice. This framework allows the stiffness and yielding behavior of frozen sand to be approached using theories that have been developed for other particulate-filled composite materials. This approach has proved to be very useful for understanding the mechanisms responsible for the stiffness of frozen sand and has led to a conceptual hypothesis for the yielding behavior as well.

8.2 RESULTS AND CONCLUSIONS

8.2.1 Introduction

As a result of an extensive triaxial compression program on a variety of frozen materials under varying conditions, an improved understanding has been achieved of the mechanisms controlling the stiffness and strength of frozen sands and of two-phase particulate composites in general.

Prior to highlighting the main conclusions from this research, a summary is presented of the effects of all the variables investigated with respect to the Young's modulus and the upper yield stress. This serves as a useful comparison of the effects of each variable and facilitates understanding the mechanisms underlying the observed behavior.

8.2.2 Summary of Important Variables

8.2.2.1 Effect of Void Ratio/Relative Density

Although a systematic characterization of void ratio was not performed during this research, efforts were taken to prepare specimens over as wide of a range as possible for each of the materials tested. However, due to the type of preparation method employed, the resulting void ratio range was quite narrow.

Figure 6.1 illustrated the effect of void ratio on the composite modulus. Although little to no dependence was observed for each of the materials tested, the composite modulus is expected to decrease with decreasing volume fraction of particles in a manner similar to other two-phase composite materials. The lack of any observed dependence on void ratio for both bonded and non-bonded systems can be attributed to the fact that over the small range of void ratios investigated, the composite modulus does not increase very much. This has been confirmed by models based on reinforcement theories for two-phase particulate-filled composite materials. Furthermore, the small increases were masked by the inherent scatter in the data, which was found to increase with particle angularity even though it has been substantially reduced as a result of the new axial strain measuring system.

Even less dependence on void ratio was found in the upper yield region regardless of the particle type and surface treatment (Figure 7.1). This agrees with the conclusions of Andersen et al. (1995) that the frictional characteristics of the sand skeleton play a minor role in the upper yield region. Qualitatively similar results have also been noticed for glass-filled polymers in tension over a relatively large range of volume fraction (Nicolais and Narkis 1971).

8.2.2.2 Effect of Confinement

The range of confining pressures or stress level investigated during this research varied from 0.1 MPa to 12.5 MPa, although, most tests were performed at either 0.5 MPa or 10 MPa. These values correspond to the low and high descriptors used when qualitatively describing the stress level in any particular test.

The Young's modulus of all the materials tested was observed to be virtually insensitive to the degree of confinement. This was especially evident when examining the systems composed of spherical particles which exhibit little scatter in the measured modulus. While the modulus was observed to decrease marginally in some systems and increase in others, these slight trends are not considered to be significant.

The effect of confinement in the upper yield region, however, varied depending on the level of interfacial adhesion. For Manchester fine sand, the effect was shown to be minimal over the range of stress levels investigated. Although the coarser-grained systems (i.e. 2010 industrial quartz, PMMA) did show a slight dependence on confinement, at least up to 5 MPa, the large pressure sensitivity reported by Chamberlain et al. (1972) and Sayles (1973) was not observed. In non-bonded systems the situation is much different and depends on the degree of surface roughness. For smooth non-bonded spherical particles, adding confinement causes the system to behave in a ductile manner, that is displaying a rate sensitivity similar to polycrystalline ice in the ductile regime (Figure 7.10b). The addition of surface roughness to a system lacking adhesional bonding, however, causes a similar strength gain at both strain rates upon the application of a confining stress (Figure 7.11). This observation indicates that mechanical interactions at the interface (frictional effects) are important to the upper yield stress of frozen materials.

8.2.2.3 Effect of Strain Rate

As a result of limitations in the control hardware, tests at strain rates greater than $3.5x10^{-5}$ s^{-1} were not possible while maintaining adequate control. Therefore, only the slow ($3x10^{-6}$ s^{-1}) and moderate rate ($3.5x10^{-5}$ s^{-1}), as described in Andersen et al. (1995), were used for this research.

Despite the fact that strain rate, or frequency of loading, is one of the most important variables influencing the measured modulus of polycrystalline ice, little dependence on this parameter was noticed for all the frozen systems. Furthermore, the lack of a rate dependency in the ice specimens indicates that the testing equipment is probably measuring a relaxed modulus, which can be as low at 5 GPa, rather than the unrelaxed modulus which is typically around 7 GPa (Cole 2000), or the theoretical value of 9 GPa (Sinha 1989). It is therefore not surprising that the modulus of frozen sand, tested in a similar manner, also shows no rate dependency.

In contrast, the upper yield stress is very dependent on strain rate as shown in Figure 7.5. The strain rate dependency of the upper yield stress can be well described by a simple power law relationship similar to the one used to express the rate dependency of ice. However, the upper yield stress of fully-bonded frozen systems is substantially greater than the peak strength of polycrystalline ice at similar temperatures and rates (Figure 7.12). These data also indicate that, in addition to causing a strengthening effect, the presence of particles in the ice matrix decreases the rate sensitivity (higher power law coefficients). Furthermore, the fact that systems composed of spherical particles have the lowest rate sensitivity indicates that these systems offer the least resistance to crack propagation.

8.2.2.4 Effect of Temperature

Investigation of the effects of temperature were limited to temperatures of -10°C and above since an extensive characterization of the behavior of Manchester fine sand at lower temperatures had already been performed by Swan (1994). The majority of the tests were performed at -10°C and -5°C although a small number of tests at -2°C were

conducted on specimens of frozen Manchester fine sand to assess its behavior at temperatures more representative of permafrost.

The temperature dependence of the composite modulus for all the systems that were investigated was shown in Figure 6.6. Only the modulus of polycrystalline ice, and possibly the PMMA system, show any dependence on temperature, in that they become stiffer with decreasing temperature. Although this behavior is expected for polycrystalline ice, its theoretical dependence on temperature has been reported to be much smaller than what was observed. It is therefore not surprising that little dependence on temperature was observed for the other systems since it would tend to be masked by the scatter in the data.

Conversely, the upper yield behavior is strongly dependent on temperature, increasing with decreasing temperature for all the materials tested. This reflects the fact that at a given strain rate, the number of cracks that form in polycrystalline ice decrease with decreasing temperature, thus leading to an increase in strength (Gold 1977). For the data shown in Figure 7.7, the temperature dependency at a given strain rate can be expressed through a simple linear relationship. The power law coefficients have also been shown to depend on temperature, increasing with decreasing temperature, as shown in Table 7.3. This indicates that lower temperatures facilitate crack propagation through the ice matrix.

8.2.2.5 Effect of Particle Modulus

The effects of particle modulus were investigated by comparing the behavior of systems composed of granular PMMA, which has a particle modulus of 4.5 GPa at -10°C, to the behavior of the traditional quartz-based systems (i.e. Manchester fine sand, 2010 industrial quartz, glass beads) which have a particle modulus of approximately 75 GPa. This value was found to be more realistic than the value of 90 GPa used by Andersen et al. (1995), which was based on the modulus of intact quartzite rock.

The composite modulus was found to be highly sensitive to the particle modulus. A value of 26 GPa was measured for the quartz-based systems, whereas a value of only 5 GPa was measured for the PMMA-based system. The fact that all of the systems based on

quartz particles gave approximately the same value for the composite modulus regardless of the particle shape or origin is significant.

The effect of particle modulus in the upper yield region was determined by comparing the data for the PMMA system to that of the 2010 industrial quartz and glass bead systems (Figure 7.8) as they all had the same particle size. Results at the slow strain rate show a slight decrease in the upper yield stress indicating that particle modulus has little to no effect. At the higher rates, however, analysis of particle modulus effects must account for particle shape since systems composed of angular particles display higher yield stresses than similarly sized spherical particles. Therefore, if attention is focused strictly on the PMMA and glass bead data, virtually no difference in their upper yield stress can be seen. This positively confirms that the amount of ice matrix strengthening does not depend on the stiffness of the inclusion.

8.2.2.6 Effect of Grain Size

Five frozen systems were available for evaluation of the influence of inclusion size (i.e. mean particle diameter) on the pre-failure behavior. Two sizes of industrial quartz along with two sizes of glass beads were used to compare with the data already obtained on Manchester fine sand. Furthermore, since it was concluded that the applied strain rate and temperature did not seem to affect the modulus of frozen systems, it was possible to assess the effect of particle size using data obtained from tests performed at both -5°C and -10°C, and at both strain rates.

Particle size effects on the composite modulus of frozen systems were shown in Figure 6.9. The data in this figure indicate little dependence on particle size, at least over the range of particle sizes tested (i.e. 0.145-3 mm). However, more data are needed at the larger particle sizes in order to make a definitive statement.

In contrast, the upper yield stress of frozen materials has been found to increase with mean particle grain size (Figure 7.9). However, it is important to note that the upper yield stress at the moderate rate was found to exhibit a definite dependence on particle shape for similar grain sizes. Furthermore, the rate of strengthening with particle size was found to be temperature dependent, at least over the small temperature range investigated.

While it has been reported that the strength of polycrystalline ice decreases with increasing grain size, the opposite effect observed in this research can be explained by examining how particles interfere with cracks propagating through the ice matrix

8.2.2.7 Effect of Interface Adhesion

Treatment of the surface of quartz-based particles through silation was found to produce an effective hydrophobic coating that was subsequently confirmed to alter the adhesional strength of ice. Three systems were made hydrophobic during this investigation: Manchester fine sand, and two sizes of glass beads.

Hydrophobic treatment of Manchester fine sand resulted in a lowering of the composite modulus from 26.3±1.8 GPa to 21.7±4.0 GPa, indicating very little effect for this material. In contrast, the hydrophobic coating had a substantial effect on the system of small glass beads where the modulus decreased from 26.8±0.9 GPa to 5.7±0.2 GPa. Similarly, the modulus decreased from 25.2 GPa to 12.0±0.8 GPa when the hydrophobic treatment was applied to the system of large glass beads.

Similar results were observed in the upper yield region (Figure 7.10). The upper yield stress of frozen hydrophobic Manchester fine sand was basically unchanged from that of the regular system indicating that interfacial adhesion is not very important for this material, however, the hydrophobic system exhibited slightly more rate sensitivity. In contrast, the glass bead systems are very dependent on the degree of interfacial adhesion as evidenced by the large drop in the upper yield stress for the treated systems at low confinement. In addition, the system of small glass beads also displayed a degree of pressure sensitivity. At low confinement this system displayed a similar rate sensitivity as for the original untreated system, whereas at high confinement the rate sensitivity approached that of polycrystalline ice in the ductile regime.

8.2.2.8 Effect of Particle Roughness

The effects of particle roughness on the pre-failure behavior of frozen materials were investigated by imparting various degrees of surface roughness to systems of smooth glass beads and then treating them to make them hydrophobic. This isolated the effects of

particle shape and particle roughness. Two degrees of surface roughness were attained by either acid-etching or mechanical roughening.

For the system of small glass beads, moderate particle roughening by acid-etching followed by hydrophobic treatment led to a moderately higher composite modulus, 7.1±1.0 GPa as compared to 5.7±0.2 GPa for the treated smooth glass beads. A much larger increase in the composite modulus was achieved for the larger glass beads which were individually mechanically roughened to produce an extremely rough surface while still maintaining a spherical shape. In this case the composite modulus increased from 12.0±0.8 GPa (the mean value for the large hydrophobic smooth glass beads) to 21.0±0.0 GPa, which is very close to the value obtained for the fully-bonded smooth large beads (25.2 GPa). These results indicate that it is the degree of surface roughness and not the particle shape which controls the modulus of non-bonded composites.

Similar results were obtained in the upper yield region, although the resulting yield stress was observed to be both a function of particle roughness and confinement level. For the system of hydrophobic small glass beads at low confining pressure, the slight roughening led to slightly higher yield stresses at both strain rates with little to no change in rate dependency. High stress levels, however, caused the system of hydrophobic roughened beads to have the same upper yield stress as the original system of smooth fully-bonded particles. However, if the degree of roughness was increased, as was done for the larger glass beads, then the original yield stress can be achieved at low confinement.

8.2.3 Conclusions on Young's Modulus

Based on an extensive laboratory study, the Young's modulus or initial stiffness of frozen sand has been found to increase with particle volume fraction and with the moduli of each of its constituents. The composite stiffness however relies heavily on the extent of coupling between phases for the effective transfer of shear stress. This coupling has been experimentally shown to take the form of either an adhesional bond or a frictional bond, indicating that the ice-soil bond strength and particle roughness are important variables.

In cases where the mechanical interaction at the ice-particle interface is small (i.e. smooth round particles), the presence of an adhesional bond is very important for the transfer of stress. In contrast, in cases where the mechanical interaction is high, as with natural sand particles or roughened glass beads, internal shear stresses can be effectively transferred by friction at the interfaces and consequently the presence of an adhesional bond offers little to no contribution to the composite stiffness. This means that even if the surface of a rough particle is made hydrophobic (for systems involving ice), the modulus will not be affected because of the mechanical coupling which already exists. Furthermore, since it has been shown that increasing the surface roughness for the same particle shape leads to an increased modulus, it is the particle roughness and not the particle shape which is the controlling variable.

The similarity between the factors controlling the modulus of frozen sand and those controlling the modulus of particulate composites in general suggest that frozen sand can be modeled as a two-phase composite material. After an extensive evaluation of a number of particulate composite material models the Bache and Nepper-Christensen (BNC) model (Lydon and Balendran 1986) was found to be the most suitable for describing the data obtained over the range of volume fraction investigated during this research, and indeed for most highly-filled natural frozen sand systems encountered in practice. However, should a bounding solution to the composite modulus be desired, the solution proposed by Hashin and Shtrikman (1963) offers excellent predictive capability. The BNC model can be written as follows:

$$E_c = E_{ice}\left(\frac{E_p}{E_{ice}}\right)^{V_p} \tag{8.1}$$

where: E_c = composite modulus
E_p = 75 GPa (for typical natural sands)
E_{ice} = 5-9 GPa
V_p = volume fraction of inclusions (particles)

Although this model does not account for particle roughness or adhesion, these considerations are not expected to be important for natural sands as they would exhibit natural angularity and roughness which, as described above, would make up for any lack of adhesional bonding.

While considerable attention has been given to which value is appropriate for the Young's modulus of ice, the choice very much depends on the frequency of loading, and to a lesser extent on temperature. Hence a range of 5 to 9 GPa is recommended with the higher value being more appropriate for dynamic problems, such as those involving earthquake loadings. Similarly, temperature considerations may also prove to be significant in problems involving the behavior of frozen soils at high temperatures (e.g., permafrost).

8.2.4 Conclusions on Upper Yield Behavior

The behavior in the upper yield region has been found to be primarily controlled by the applied strain rate, temperature, particle grain size, and particle shape, and for fully bonded materials is essentially independent of volume fraction and stress level. These findings are in agreement with those of Andersen et al. (1995). However, this research has firmly established that particle grain size and shape are important considerations as well. The upper yield stress increases substantially with particle grain size as a result of cracks having to propagate over a distance proportional to the surface area of the particle before joining to cause global yielding. Particle shape was shown to influence the fracture toughness of the system (i.e. the resistance encountered by propagating cracks). However, it only becomes important at the faster rates of strain where ice acts as a brittle solid and fails by rapid crack propagation.

While the frictional characteristics of the soil skeleton (i.e. volume fraction and stress level) are unimportant in fully-bonded materials, tests on hydrophobic materials indicate that the upper yield stress also relies heavily on the extent of coupling between phases. This suggests that similar bonding mechanisms to those governing the Young's modulus (i.e. adhesional bonding and mechanical interactions), also operate in the upper yield region. In the absence of an adhesional bond, the degree of surface roughness and stress level affect the upper yield stress behavior of the system. This complex behavior has been analyzed by examining the nature of crack propagation within the ice matrix.

In non-bonded systems, debonding takes place at the particle interface and the lower strengths observed for systems of low mechanical interaction simply reflect the

strength of ice at an adjusted strain rate to account for strain rate magnification within the pore ice matrix. Confinement acts to suppress cracking and causes the system to exhibit behavior similar to ice in the ductile regime.

The addition of a frictional component (i.e. roughness) to non-bonded systems increases the shear resistance at the interface manifesting itself as an increase in composite strength. The shear resistance can be further increased by adding confinement to the system. In this case, cracking at the interface is effectively inhibited and is forced to take place in the matrix. This leads to a large increase in the upper yield strength.

For fully-bonded systems, crack propagation also occurs away from the interface. At slow strain rates, crack blunting by the filler particles occurs which hinders crack propagation. The strength therefore is only controlled by the particle size, and not the particle shape or roughness. However, at higher rates particle shape becomes important as it influences the ease with which a crack may propagate through the matrix. This effect may be described by the lower fracture toughness of a system composed or smooth round particles.

Similarly, the effect of temperature on the degree of strengthening and strain rate sensitivity at the upper yield stress can also be related to cracking mechanisms. The number of cracks that form (initiate) within the pore ice at a given strain decreases with decreasing temperature, thus resulting in an increase in strength. However, as the temperature decreases, the ice matrix also becomes more brittle, thus crack propagation becomes easier (i.e. the fracture toughness decreases). This is reflected in the strain rate sensitivity decreasing (higher n value) with decreasing temperature. Thus, the temperature dependence of frozen soil systems results from a complex interaction between *crack initiation* and *crack propagation* mechanisms.

Although a number of models exist to predict the yielding behavior of two-phase composite materials in tension, no satisfactory models exist to explain the behavior in compression where numerous competing mechanisms need to be accounted for. While this experimental program has offered many insights into the mechanisms controlling the upper yield stress in frozen particulate-filled materials, the development of a physically-based model is still premature. However, based on the results presented herein an

empirical model for the upper yield stress of fully-bonded natural sand systems has been presented:

$$Q_{uy} = \left(K_1 Q_{ice} + D\Delta T\right)\left(\frac{\dot{\varepsilon}}{\dot{\varepsilon}_0}\right)^{\frac{1}{\left(K_2 n_{ice} - \alpha \Delta T\right)}} \qquad (8.2)$$

where: Q_{uy} = upper yield stress of frozen particulate system
Q_{ice} = peak strength of polycrystalline ice at T_0 and $\dot{\varepsilon}_0$
$\Delta T = (T\text{-}T_0)$
n = strain rate sensitivity of polycrystalline ice at T_0

This model relies on four fitting parameters (i.e. α, D, K_1, K_2) which modify the basic strength and strain rate sensitivity of ice to account for the various ice strengthening mechanisms (Table 7.9). Furthermore, it was shown that Equation 8.2 can satisfactorily describe the temperature and strain rate behavior of all of the fully-bonded systems tested during this research.

8.3 RECOMMENDATIONS FOR FUTURE RESEARCH

Although this research has contributed to the understanding of the pre-failure behavior of frozen materials by investigating a number of the physical mechanisms important to similar two-phase composite materials, several questions remain before the level of understanding is advanced to the point where physically-based constitutive relationships to describe frozen soil behavior can be formulated. In addition, several improvements to the equipment used to investigate the pre-failure behavior of frozen sands can be made that will improve the quality of the equipment as a whole, and hence improve the quality of the data obtained. Therefore recommendations for future research in this area have been divided accordingly into equipment enhancements and additional investigations.

8.3.1 Equipment Enhancement

The performance of the existing high-pressure low-temperature triaxial cell may be enhanced through a series of relatively small improvements that will ultimately improve

the ability to measure the pre-failure behavior of frozen soils and other higher strength materials with greater confidence and ease.

One of the main limitations with the current equipment arises from the inability of the load application system to consistently apply load evenly to the specimen. Even the slightest unbalanced loading results in poor small strain measurements that translate into uncertainties in the calculation of modulus. Although redesign of the top cap and load cell connection has improved the results dramatically, the installation of a high-pressure linear bearing for the loading piston would immediately help to eliminate eccentricities in the load application. Furthermore, increasing the stiffness of the loading frame and triaxial cell base would also prove fruitful.

As was mentioned in Chapter 3, the implementation of a PID feedback control system for the load application system has greatly reduced the time lag that it takes the system to reach a constant strain rate. A consequence of this improvement, however, has been the inability to test at faster strain rates. This is predominately due to the low sampling frequency of the current ADC card. If faster rate tests are desired, an ADC card with a sampling frequency in the kilohertz (kHz) range would need to be implemented. Of course, testing at much faster rates would also require the redesign of the axial actuator to withstand the higher forces.

A faster data acquisition system, either locally or remotely, is also required before higher rate tests can be performed. Currently, it is not possible to take readings at rates greater than 1 Hz which severely limits the amount of data available to define the Young's modulus at the moderate strain rate (3.5×10^{-5} s^{-1}) used during this research.

The current system also suffers from a lack of sensitivity in the measurement of volumetric strains which, if improved, would help to define Poisson's ratio for frozen sands. A more sensitive system may also be able to detect the onset of cracking in the pore ice matrix. Although a device for the measurement of radial strains based on the current LVDT technology was attempted in the early phases of this research, sufficient sensitivity could not be consistently achieved. However, if a larger triaxial cell was constructed, other devices to measure radial strains such as proximity sensors (e.g., Brown et al. 1980, Hird and Yung 1989), Hall effect semiconductor gages (e.g., Clayton

et al. 1989), or resistance wire transducers (e.g., Skopek and Cyre 1994) could be implemented with relative ease.

Finally, if an effort to reduce the number of tests in which leakage through the membranes occurred, a relatively simple modification to the top cap is proposed. Since the rolling of the second membrane over the two O-rings which seal the first membrane to the top cap often resulted in the formation of wrinkles in the membrane, which are detrimental to a good pressure seal, adding two grooves to the top cap to recess the O-rings slightly would help alleviate the difficulty in getting the second membrane past the first two O-rings.

8.3.2 Additional Investigations

Overall, the results of this study have provided many insights into the physical mechanisms controlling the pre-failure deformation of frozen sands while simultaneously illustrating the similarities between frozen sands and other two-phase particulate composite materials. However, there are many more issues that can and should be studied that would greatly help in clarifying the present understanding of frozen sand behavior. Some of the more pertinent ones that can readily be investigated with the current equipment are summarized below.

Detailed characterization of the pre-failure behavior of polycrystalline ice in a triaxial state of stress is clearly needed in order to better understand the nature of the pore ice matrix within frozen soils. A small testing program over typical ranges of strain rates, temperatures, and confining pressures would be invaluable to the cold regions community, and would greatly aid in the analysis of frozen soil data.

In a similar program, quantification of the effects of delayed elastic strains, both in specimens of pure polycrystalline ice and frozen Manchester fine sand, could be helpful in explaining the discrepancy between the modulus measured in the triaxial cell under monotonic loading, and the modulus derived using the fully reversed direct-stress testing technique (Cole 1990). As a first step in reducing the effects of delayed elastic strains, the testing procedure should be modified such that specimens are not subjected to any deviator stress during acclimatization to the desired test temperature.

While the applicability of composite material models to describe the modulus of frozen materials has been confirmed during this study, further validation of their applicability especially at low volume fractions is both desired and necessary. Although the ability to manufacture specimens at low volume fractions has proven to be very difficult thus far, this information would be very useful for the permafrost engineering community.

Further exploration of particle size effects is also warranted given the relatively surprising and unexpected results obtained in the upper yield region. It is recommended that this program use relatively uniform distributions of glass beads to investigate this effect as they are readily available, and because the results of this research have also shown that spherical particles tend to exhibit less scatter in the measured modulus.

In Chapter 7 results were shown that indicated that fully-bonded systems composed of angular particles tend to exhibit higher strengths in the upper yield region than similarly sized systems of spherical particles. This difference, which manifested itself only at the faster rates of strain, was attributed to differences in fracture toughness. Measurements of the fracture toughness of frozen systems composed of particles of varying shape and degrees of roughness would be very useful in confirming this hypothesis, and in furthering our understanding of how crack propagation within frozen materials lead to yielding and failure.

Future tests on frozen soils should also include measurements of acoustic emissions to capture the pore ice cracking activity. This information would be especially useful in confirming differences in the nature and extent of crack propagation in the non-bonded materials used during this experimental program as described in Section 7.3.3.

Potentially one of the most promising areas of research that would dramatically help in the understanding of the pre-failure behavior of frozen sands is the numerical modeling of the interactions at the pore scale. For example, a relatively simple finite element scheme could be used to compute the stress and deformation fields in the ice matrix around two interacting particles. This type of simulation would allow investigation of the effects of particle shape, roughness, and adhesion, in addition to the other variables that were investigated during this experimental program. The author believes that this

type of analysis would be invaluable in understanding the micromechanical aspects of frozen soil behavior.

Finally, although considerable progress has been made in understanding the mechanisms controlling the upper yield stress in frozen soils, the development of a quantitative model for its prediction is still premature. However, the author believes that micromechanical models already developed for polymeric particulate composites (e.g., Wong and Ait-Kadi 1995 and 1997) may provide further insights for understanding the pre-failure behavior of frozen soils, and for modeling its behavior as well.

8.4 REFERENCES

1. Andersen, G.R., Swan, C.W., Ladd, C.C., Germaine, J.T. (1995), "Small-Strain Behavior of Frozen Sand in Triaxial Compression", *Canadian Geotechnical Journal*, v. 32, no. 3, pp. 428-451.

2. Brown, S.F., Austin, G., Overy, R.F. (1980), "An Instrumented Triaxial Cell for Cyclic Loading of Clays", *ASTM Geotechnical Testing Journal*, c. 3., no. 4, 145-152.

3. Chamberlain, E., Groves, C., Perham, R. (1972), "The Mechanical Behavior of Frozen Earth Materials Under High Pressure Triaxial Test Conditions", *Geotechnique*, v. 22, no. 3, pp. 469-483.

4. Clayton, C.R.I., Khatrush, S.A., Bica, A.V.D., Siddique, A. (1989), "The Use of Hall Effect Semiconductors in Geotechnical Instrumentation", *ASTM Geotechnical Testing Journal*, v. 12, no. 1, pp. 69-76.

5. Cole, D.M. (1990), "Reversed Direct-Stress Testing of Ice: Initial Experimental Results and Analysis", *Cold Regions Science and Technology*, v. 18, pp. 303-321.

6. Cole, D.M. (2000), CRREL, Personal communication.

7. Hird, C.C. and Yung, P.C.Y. (1989), "The Use of Proximity Transducers for Local Strain Measurements in Triaxial Tests", *ASTM Geotechnical Testing Journal*, v. 12, no. 4, pp. 292-296.

8. Lydon, F.D. and Balendran, R.V. (1986), "Some Observations on Elastic Properties of Plain Concrete", *Cement and Concrete Research*, v. 16, pp. 314-324.

9. Nicolais, L. and Narkis, M. (1971), "Stress-Strain of Styrene-Acrylonitrile/Glass Bead Composites in the Glassy Region", *Polymer Engineering and Science*, v. 11, no. 3, pp. 194-199.

10. Sayles, F.H. (1973), "Triaxial and Creep Tests on Frozen Ottawa Sand", *Proc. 2nd International Permafrost Conference*, Yakutsk, U.S.S.R, pp. 384-391.

11. Sinha, N.K. (1989), "Elasticity of Natural Types of Polycrystalline Ice", *Cold Regions Science and Technology*, v. 17, pp. 127-135.

12. Skopek, P. and Cyre, G.P. (1994), "A Resistance Wire Transducer for Circumferential Strain Measurement in Triaxial Tests", *ASTM Geotechnical Testing Journal*, v. 18, no. 1, pp. 106-111.

13. Swan, C. (1994), "Physical Mechanisms Controlling the Deformation and Strength Behavior of Unfrozen and Frozen Manchester Fine Sand", Sc.D Thesis, Department of Civil and Environmental Engineering, MIT, Cambridge, MA, 1044 p.

14. Wong, F.C., Ait-Kadi, A. (1995), "Mechanical Behavior of Particulate Composites: Experiments and Micromechanical Predictions", *Journal of Applied Polymer Science*, v. 55, pp. 263-278.

15. Wong, F.C., Ait-Kadi, A. (1997), "On the Prediction of Mechanical Behavior of Particulate Composites Using an Improved Modulus Degradation Model", *Journal of Composite Materials*, v. 31, no. 2, pp. 105-127.

Appendix A

MEASUREMENT OF ICE ADHESION IN THE LABORATORY

MEASUREMENT OF ICE ADHESION IN THE LABORATORY

OUTLINE

A.1 Introduction
A.2 Ice Adhesion Apparatus
A.3 Specimen Preparation
A.4 Testing Procedures and Data Handling
A.5 Summary of Adhesion Test Results
A.6 Measurement of Contact Angles
A.7 Bibliography

A.1 INTRODUCTION

In addition to the experimental program on frozen particulate materials, two initiatives to quantify the effectiveness of the hydrophobic coating at reducing ice adhesion in the various particulate systems described in Chapter 4 were also undertaken.

The first program involved performing a number of shear tests on treated and untreated quartz rods. The goal of these tests was to quantify in a controlled manner the reduction in the adhesional strength of polycrystalline ice to a quartz surface that had been treated to make its surface hydrophobic. This program only investigated the effects of displacement rate and temperature. The range of displacement rates corresponded to the "slow" and "moderate" load frame settings used for the triaxial compression tests of Andersen (1991) and Swan (1994). Test temperatures were limited to -5°C and -10°C. Table A.1 summarizes the adhesional strength testing program.

	Temp. = -5°C		Temp. = -10°C	
Material	**Slow**	**Moderate**	**Slow**	**Moderate**
Regular quartz rod	-	1	3	2
Hydrophobic quartz rod	-	1	2	2

Table A.1: Adhesional strength shear test program. Note: slow = 0.0137 mm/min, moderate = 0.1600 mm/min. (number of tests shown for each condition)

The second program involved measuring the difference in contact angles between water and treated and untreated quartz surfaces. This method is widely used for providing a quantitative assessment of the degree of hydrophobicity, but unfortunately does not

provide any information as to the potential reduction of ice adhesion. Nevertheless, it was thought that such a test would provide valuable information as to the effectiveness of the surface treatment, and hence could be used in the future as a measure of the consistency of treatment between treated batches of sand. Although many sophisticated methods exist for the measurement of contact angles, simple optical measurements were found to yield values of sufficient accuracy. A complete description of the technique along with the results obtained is given in Section A.6.

A.2 ICE ADHESION APPARATUS

Ice adhesion tests were conducted in the Low Temperature Testing Facility using a modified triaxial apparatus and load frame. The equipment design was patterned after an apparatus used to test the effectiveness of various coatings at reducing the adfreeze strength of ice and frozen soil to coated foundation piles (Parameswaran 1981). The apparatus determines the peak adfreeze strength of a 15 mm diameter circular rod embedded in polycrystalline ice by subjecting it to an increasing load under a constant rate of displacement (Figure A.1).

The apparatus consists of three components: a triaxial cell base with a modified base pedestal, a Lucite chamber, and a gear-driven load frame. The cell base is similar in design to the high-pressure low temperature triaxial base with the exception of the base pedestal. The standard pedestal was replaced with a similarly sized insert bored out to a diameter of 17 mm and then fitted with a removable brass plug that acted to support and center the rod during the freezing process. Removal of the plug after freezing exposes the bottom of the rod and allows the vertical displacement of the rod to be measured using a LVDT (Hewlett Packard Inc., Model 7DCDT-5000, Waltham, MA). A detail of the base pedestal is given in Figure A.2.

In place of the triaxial chamber, a circular Lucite cylinder is used to contain the polycrystalline ice around the rod. This cylinder has a diameter of 11 cm and a height of 20 cm and rests on an O-ring seal in the triaxial base. This configuration helps prevent leaks once the cylinder is full of ice and saturated with water. The rod is kept centered within the cylinder through the use of a top plate that rests on the top of the cylinder. The

plate keeps the rod vertical and centered in the ice throughout the freezing process. It also forms an airtight seal that allows the ice to be de-aired before it is saturated with water.

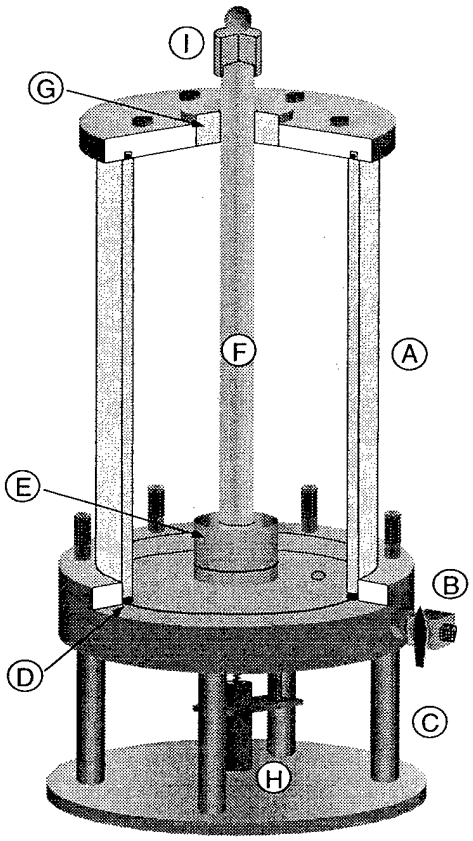

A: Lucite mold
B: Fill/drain valve
C: Triaxial base
D: O-ring seal
E: Base pedestal
F: Quartz rod
G: Top plate
H: LVDT
I: Loading cap and ball

Figure A.1: Ice adhesion testing apparatus.

The last component consists of a screw-driven variable speed 45 kN loading frame (Wykeham Farrance, Model T-57, Slough, England). This device was kept in the testing room in the Low Temperature Testing Facility and allowed ice adhesion tests to proceed independently of the triaxial tests on frozen soil. Load is applied to the rod through a brass cap containing a hardened steel ball as a moment break. This cap also serves to protect the end of the rod from damage. Load is measured with a 45 kN shear-beam load

cell (Data Instruments Inc., Model JP-10000, Acton, MA) attached to the upper crossbar of the loading frame.

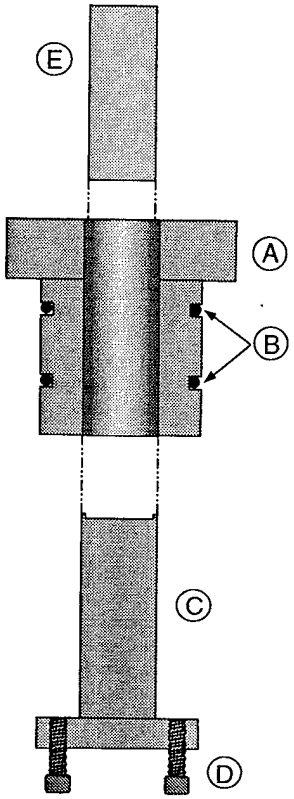

A: Base pedestal B: O-rings C: Removable plug
D: Screws E: Quartz rod

Figure A.2: Detail of base pedestal of ice adhesion testing apparatus.

A.3 SPECIMEN PREPARATION

Once the quartz rod to be tested is centered within the apparatus described above, sieved granular ice, prepared using the technique described in Section 4.2.2, is then uniformly compacted around the rod in approximately 5 cm lifts. As with the preparation of ice specimens, this procedure was performed in the growth room of the LTTF at an ambient temperature of 0°C. This procedure was continued until the level of the compacted ice was approximately 5 cm from the top of the Lucite cylinder. At this point the top plate (with a greased O-ring) is placed on the cylinder and the rod aligned using its Lucite insert. The system is then placed under a vacuum of 29 in. Hg (25 torr) and left to

de-gas for approximately 20 minutes. After this time, distilled de-aired water is allowed to enter the specimen by opening a valve at the bottom of the mold. Once the water level reached the top of the ice surface, the valve was closed and the vacuum released slowly. The entire apparatus is then moved into the main testing room, wrapped in fiberglass insulation, and placed on a massive steel block to promote uniaxial freezing from the bottom to the top at the ambient test temperature. On average, the entire freezing process lasted about 8-12 hours and produced a relatively clear polycrystalline ice mass with little to no air bubbles. In general, the -10°C shear tests were performed 24 hours after initiation of the freezing process, while the -5°C tests were performed after 48 hours to ensure that they were completely frozen before testing.

A.4 TESTING PROCEDURES AND DATA HANDLING

Tests that investigated the role of ice adhesion in the overall strength of frozen sand were performed in the modified triaxial apparatus described previously in Section A.2. The procedure detailed below outlines the steps followed during each test.

1. Clean all the parts of the triaxial base including the Lucite cylinder with alcohol and rinse with distilled de-ionized water. Also wipe clean the large O-ring which seals the cylinder to the base.

2. Apply a light coating of petroleum jelly to the brass plug and insert it into the base pedestal and secure it using a small screw-jack.

3. Apply a light coating of vacuum grease to the large O-ring and mate the Lucite cylinder to the triaxial base. Ensure a watertight seal has been made.

4. Install the quartz rod to be tested vertically in the center of the apparatus. Bring the entire apparatus into the growth room of the LTTF (set at 0°C) and leave it to equilibrate for 12-24 hours.

5. Ensure that the testing room of the LTTF is set to the desired test temperature.

6. Prepare the polycrystalline ice specimen following the procedure outlined in Section A.3 while it is still in the growth room. It is important that the rod be kept as vertical as possible during the preparation process since it must mate with the top plate once the desired ice level has been achieved.

7. After 24 hours from the onset of freezing remove the insulation from around the apparatus. The ice should be completely frozen at this time.

8. Measure the length of rod protruding from the ice surface in three locations. This will be used to calculate the ice contact area.

9. Remove the brass plug from the base pedestal exposing the bottom of the rod. Turn the two screws into the pedestal helps to free the plug from the rod base.

10. Move the entire apparatus onto the loading frame. Place the small brass loading cap, complete with hardened steel ball, over the exposed top of the rod. This device protects the end of the rod from possible fracture and eliminates the application of moments to the rod.

11. Fix the LVDT that measures rod displacement to the triaxial base using the specifically designed clamp making sure that the core of the displacement transducer be aligned with the center of the rod.

12. Adjust the load frame such that the ball is in contact with the load cell. Check the output of both the load cell and LVDT to ensure that they are operating correctly. Record the zero values of both devices on the test log sheet before starting the test.

13. Check to make sure that the gear settings for the load frame correspond to the desired displacement rate for the test. Correct if necessary.

14. Start data acquisition and then turn the load frame power switch to the "reverse" position.

15. Stop the test after 5 mm of displacement has occurred by turning the load frame power switch to the "off" position. Back off the load using the load frame's manual control, disconnect the LVDT from the triaxial cell base, and remove the apparatus from the load frame.

16. Measure the height of rod above the ice surface in three locations as a check to the displacement measured by the LVDT. Bring the entire apparatus out of the cold environment and let the ice melt.

17. Carefully remove the rod using gloves, wash with alcohol and then rinse with distilled de-ionized water. Store the rod in a container filled with distilled de-ionized water to prevent surface contamination until the next test.

The data requirements associated with the ice adhesion testing program were much less intensive than for the triaxial testing program. For these shear tests, only load (force)

and displacement data were collected. No temperature measurements were made since these tests were performed in the main testing room without any strict temperature control. Therefore, the actual test temperature may have varied by an estimated ±2°C. In addition, since the apparatus is already at the desired test temperature before the start of loading, only one data file is required (e.g., ICEADH01.dat) to capture the load-displacement behavior. Data acquisition is commenced immediately before the start of loading at a frequency of 1 Hz. This rate can be gradually decreased as the rod displacement increases.

Reduction of the limited amount of data obtained from the ice adhesion tests was relatively straight-forward. A spreadsheet package was used for processing the data to obtain the engineering values needed to construct the load-displacement curves. From this curve, the peak adhesional strength was calculated by dividing the peak force by the surface area of ice in contact with the rod which varied from test to test.

A.5 SUMMARY OF ADHESION TEST RESULTS

Eleven successful adhesion tests were performed in total. The pertinent results of the testing program have been summarized in Table A.2. The individual load-displacement curves can be found at the end of this Appendix.

Test	Rod Type	Machine Disp. Rate (mm/min)	Nom. Test Temp. (°C)	Rod Adfreeze Area** (mm^2)	Peak Load Q_p (kg)	Disp. at Peak δ_p (mm)	Peak Adfreeze Strength (MPa)
1	Quartz	0.0137	-10	7146	226.23	0.0105	0.311
2	Quartz	0.0137	-10	6827	149.64	0.0098	0.215
3	Quartz	0.0137	-10	7093	222.53	0.0152	0.308
4	HP Quartz	0.0137	-10	6582	127.27	0.0137	0.190
5	Quartz	0.1600	-10	6953	159.39	0.0148	0.226
6	HP Quartz	0.0137	-10	7063	122.85	0.0094	0.171
7	Quartz	0.1600	-10	7713	183.55	0.0202	0.233
8	HP Quartz	0.1600	-10	6952	100.03	0.0195	0.141
9	HP Quartz	0.1600	-10	7321	157.41	0.0119	0.211
10	Quartz	0.1600	-5	7509	33.90	0.0000	0.044
11	HP Quartz	0.1600	-5	7360	29.47	0.0000	0.039

** Quartz rod diameter = 15.04 mm, HP Quartz rod diameter = 14.87 mm

Table A.2: Summary of adhesional testing program.

A.6 MEASUREMENT OF CONTACT ANGLES

Measurement of contact angles was performed at room temperature using a two-axis optical comparator (R.S. Wilder Inc., Model Varibeam, Waltham, MA) with 20X magnification, modified for the measurement of contact angles. This instrument projects the magnified image of a droplet of liquid on a surface onto a viewing screen that allows direct measurement of the contact angle. In this case the projections were traced onto a sheet of tracing paper allowing the angles to be measured at a later time. Although the precision in angle measurement was not directly evaluated, it is believed to be approximately 2-3° which is more than adequate for assessing the impact of the hydrophobic treatment.

Specimens of quartz were obtained from the rods used in the previously described adhesion experiments. Discs, approximately 5 mm is thickness, were cut from each rod and then wet polished using progressively finer grits of silicon carbide powder to obtain as smooth a surface as possible. One of the discs was then treated to make its surface hydrophobic, as outlined in Section 4.2.3.2. All specimens were cleaned with acetone before testing and then thoroughly rinsed with distilled de-ionized water. In between trials they were stored under water to prevent contamination from airborne dust particles. Only one drop of liquid was used for the determination of the contact angle (i.e. placed on the test surface) thus eliminating potential discrepancies resulting from differences in drop volume. Consistency in this parameter was achieved using a precision micro-syringe.

In order to determine the accuracy of this method, contact angles of a number of systems were measured and compared to values found in the literature (e.g., Adamson 1976, Janczuk and Zdziennicka 1994). This information, along with the measurements made on the treated and untreated quartz discs, are summarized in Table A.3. Angles were determined from both the left and right hand sides of the projected image of the droplet in order to eliminate any bias induced from leveling of the device. The angles determined with this technique are generally very close to the values obtained from the literature, however, on average the measurement method tends to under-predict the contact angle.

	SiO_2-H_2O		$HPSiO_2$-H_2O		PTFE-H_2O		PTFE-Hg		Glass-Hg	
	Left	Right	Left	Right	Left	Right	Left	Right	Left	Right
Trial 1	29.5	36	77.5	75.5	102.5	106.5	130	121	127	130.5
	25.5	31	85.5	90.5	86	79	139	122	128.5	128
	40	35.5	80.5	87	92	94.5	136.5	130	134	126
	31.5	39.5	83	86					128	128
Trial 2	31	29.5	88.5	91	98.5	105	125.5	121.5	135	132
	35	42.5	89	94.5	95.5	100	127	128	136.5	140.5
	31.5	31.5	92	90	95.5	103	126.5	132	138	140
	41.5	39	94	93	93	96	126.5	133.5	134.5	136.5
Mean	33.2	35.6	86.3	88.4	94.7	97.7	130.1	126.9	132.7	132.7
Mean	34.4		87.3		96.2		128.5		132.7	
S.D.	5.0		5.7		7.4		5.4		4.8	
Publis.	26.8[1]		N/A		98-112[2]		150[2]		128-148[2]	

Note: all measurements in degrees.
[1] Janczuk and Zdziennicka 1994
[2] Adamson 1976

Table A.3: Summary of contact angle measurements.

In addition to the these measurements, subsequent tests to assess the degree of hydrophobicity imparted by the silation process were performed. These involved treating glass slides with varying percentages of the silating agent, Silquest A-137 (octyl-triethoxysilane), and measuring the resulting contact angle that a droplet of water makes when placed on the treated slide. The results of two independent trials (of four measurements per system) are summarized in Table A.4.

The results generally show that treatment with a 2-5% silating solution yields the highest value for the contact angle, and consequently the highest degree of hydrophobicity for the percentages investigated. Furthermore, comparison of the mean contact angles from both trials indicates excellent repeatability at least for the treated slides, whereas a somewhat substantial difference is noticed for the untreated glass slide. This difference can most likely be attributed to inadequate cleaning of the slide before testing. As was mentioned before, the presence of dust particles and especially fingerprints can lead to substantial errors in the contact angle.

	Glass-H_20 (0%)		Glass-H_20 (2%)		Glass-H_20 (5%)		Glass-H_20 (10%)	
	Left	Right	Left	Right	Left	Right	Left	Right
Trial 1	35	35	53.5	55.5	53	51	45	47.5
	34	33.5	53	54.5	56	53	45	45
	29.5	32.5	53	54	53.5	56	46	44.5
	29.5	31	54.5	55	49	56.5	45.5	44
Mean	32.0	33.0	53.5	54.8	52.9	54.1	45.4	45.3
Mean	32.5		54.1		53.5		45.3	
S.D.	2.3		0.9		2.6		1.1	
Trial 2	39.5	40.5	50	57	45	44	46	46
	43.5	43	53.5	54	47.5	51	46	45
	43.5	41.5	54	56	57.5	53.5	43	42
	35	34.5	55	55	56	53.5	43	48
Mean	40.4	39.9	53.1	55.5	51.5	50.5	44.5	45.3
Mean	40.1		54.3		51.0		44.9	
S.D.	3.6		2.1		5.0		2.0	

Note: all measurements in degrees.

Table A.4: Summary of contact angle measurements of water on glass slides of varying degrees of hydrophobicity (A-137 silation).

A.7 BIBLIOGRAPHY

1. Adamson, A.W. (1976), *Physical Chemistry of Surfaces, 3rd Ed.*, John Wiley and Sons, New York.

2. Andersen, G.R. (1991), "Physical Mechanisms Controlling the Strength and Deformation Behavior of Frozen Sand", Sc.D Thesis, Department of Civil and Environmental Engineering, MIT, Cambridge, MA, 560 p.

3. Drelich, J. and Miller, J.D. (1994), "The Effect of Solid Surface Heterogeneity and Roughness on the Contact Angle/Drop Size Relationship", *Journal of Colloid Science and Interface Science*, v. 164, pp. 252-259.

4. Janczuk, B. and Zdziennicka, A. (1994), "A Study on the Components of Surface Free Energy of Quartz from Contact Angle Measurements", *Journal of Materials Science*, v. 29, no. 13, pp. 3559-3564.

5. Jellinek, H.H.G. (1962), "Ice Adhesion", *Canadian Journal of Physics*, v. 40, pp. 1294-1309.

6. Minsk, L.D. (1983), "How Effective are Icephobic Coatings?", *Proc. 1st International Workshop on Atmospheric Icing of Structures, CRREL Special Report 83-17*, pp. 93-95.

7. Mulherin, N.D., Richter-Menge, J.A., Tantillo, T.J., Gould, L.D., Durrell, G.D., Elder, B.C. (1990), "Laboratory Test for Measurement of Adhesion Strength of Spray Ice to Coated Flat Plates", *CRREL Special Report 90-2*, 44p.

8. Parameswaran, V.R. (1981), "Adfreeze Strength of Model Piles in Ice", *Canadian Geotechnical Journal*, v.18, no. 1, pp. 8-16.

9. Parameswaran, V.R. (1987), "Adfreezing Strength of Ice to Model Piles", *Canadian Geotechnical Journal*, v.24, pp. 446-452.

10. Ryzhkin, I.A. and Petrenko, V.F. (1997), "Physical Mechanisms Responsible for Ice Adhesion", *Journal of Physical Chemistry B*, v. 101, pp. 6267-6270.

11. Seaver, A.E. and Berg, J.C. (1994), "Spreading of a Droplet on a Solid Surface", *Journal of Applied Polymer Science*, v.52, no. 3, pp. 431-435.

12. Swan, C. (1994), "Physical Mechanisms Controlling the Deformation and Strength Behavior of Unfrozen and Frozen Manchester Fine Sand", Sc.D Thesis, Department of Civil and Environmental Engineering, MIT, Cambridge, MA, 1044 p.

13. Yasuda, T., Okuno, T., Yasuda, H. (1994), "Contact Angle of Water on Polymer Surfaces", *Langmuir*, v. 10, no. 7, pp. 2435-2439.

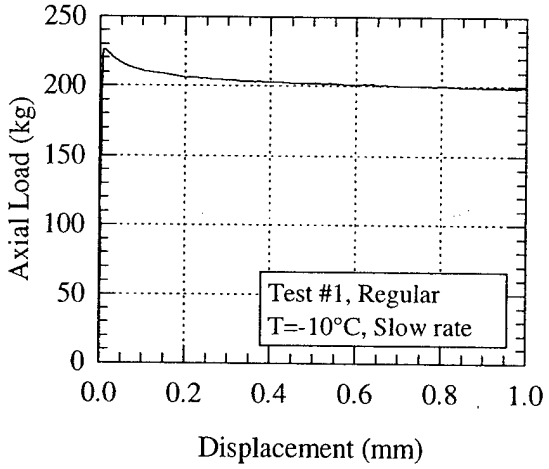
Axial Load (kg)
250
200
150
100
50
0
0.0
0.2
0.4
0.6
0.8
1.0
Displacement (mm)
Test #1, Regular
T=-10°C, Slow rate

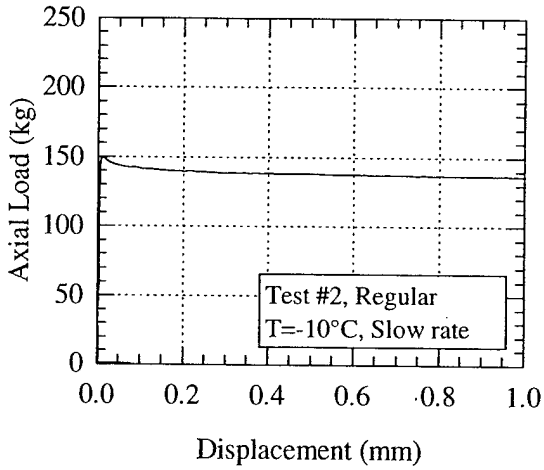
Axial Load (kg)
250
200
150
100
50
0
0.0
0.2
0.4
0.6
0.8
1.0
Displacement (mm)
Test #2, Regular
T=-10°C, Slow rate

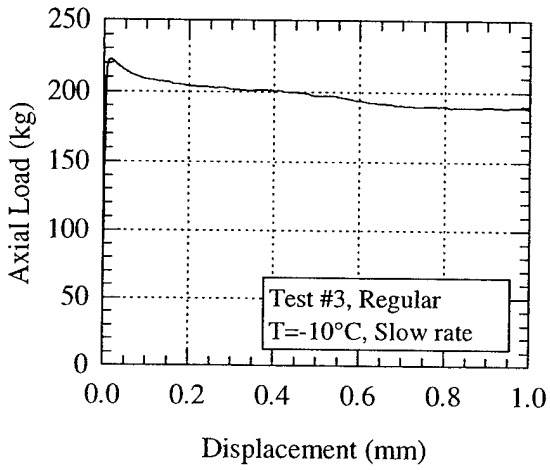
Axial Load (kg)
250
200
150
100
50
0
0.0
0.2
0.4
0.6
0.8
1.0
Displacement (mm)
Test #3, Regular
T=-10°C, Slow rate

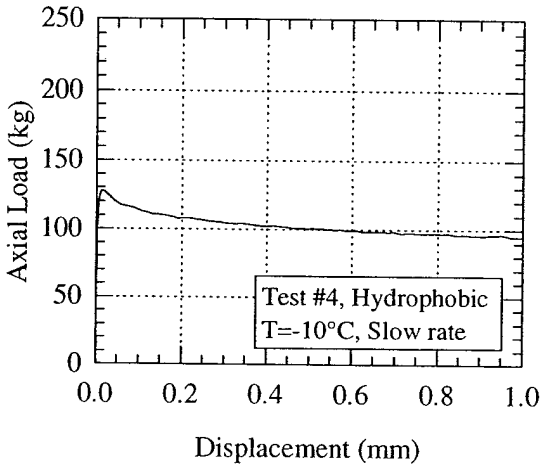
Axial Load (kg)
250
200
150
100
50
0
0.0
0.2
0.4
0.6
0.8
1.0
Displacement (mm)
Test #4, Hydrophobic
T=-10°C, Slow rate

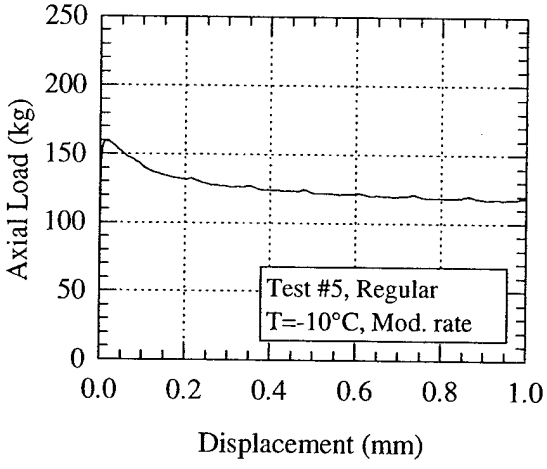
Axial Load (kg)
250
200
150
100
50
0
0.0
0.2
0.4
0.6
0.8
1.0
Displacement (mm)
Test #5, Regular
T=-10°C, Mod. rate

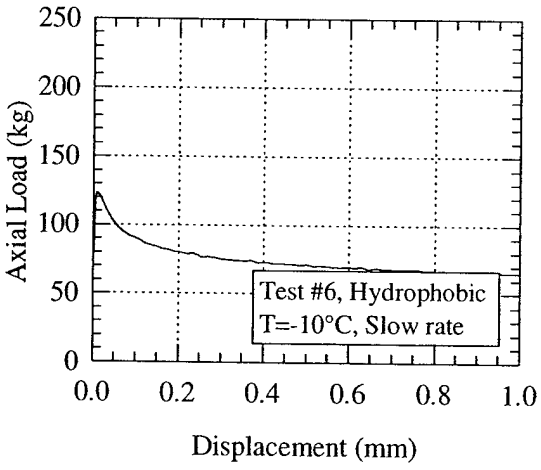
Axial Load (kg)
250
200
150
100
50
0
0.0
0.2
0.4
0.6
0.8
1.0
Displacement (mm)
Test #6, Hydrophobic
T=-10°C, Slow rate

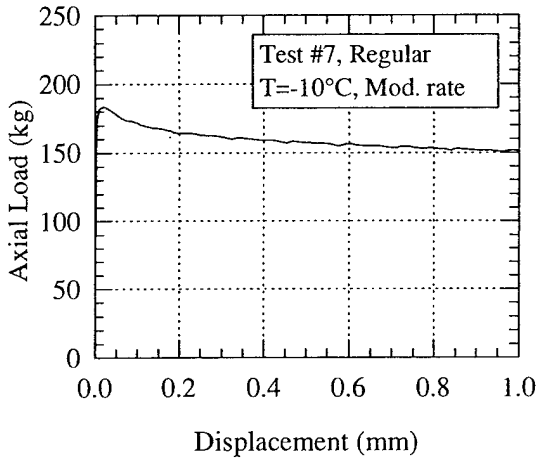
Test #7, Regular
T=-10°C, Mod. rate
Axial Load (kg)
Displacement (mm)

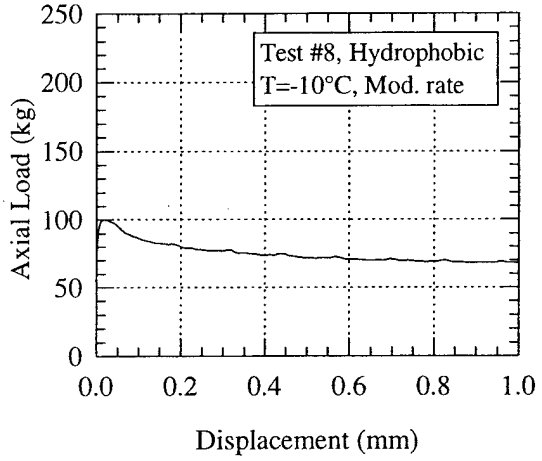
Test #8, Hydrophobic
T=-10°C, Mod. rate
Axial Load (kg)
Displacement (mm)

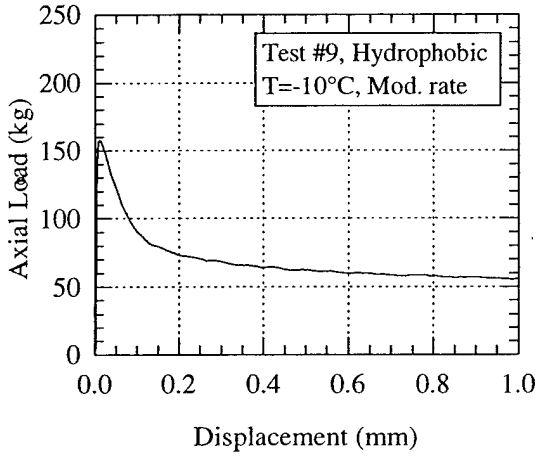
Test #9, Hydrophobic
T=-10°C, Mod. rate
Axial Load (kg)
Displacement (mm)

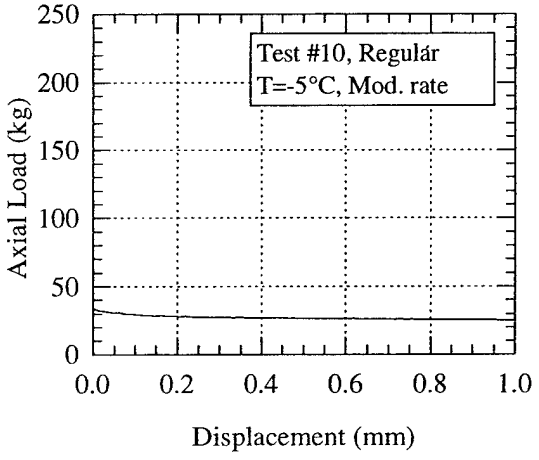
Test #10, Regular
T=-5°C, Mod. rate
Axial Load (kg)
Displacement (mm)

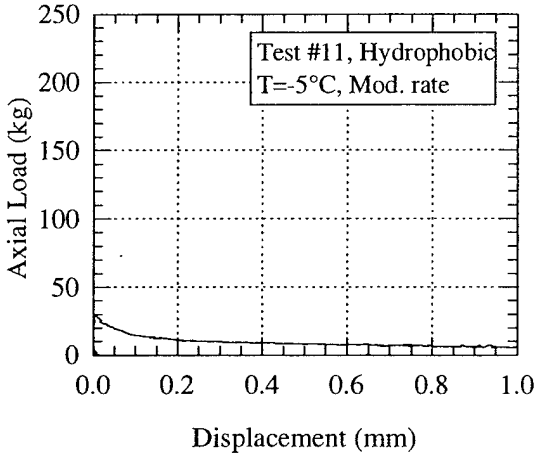
Test #11, Hydrophobic
T=-5°C, Mod. rate
Axial Load (kg)
Displacement (mm)

Appendix B

SUMMARY OF FROZEN TESTING PROGRAM

Frozen Test Summary. Part 1: *Test Conditions*

Test Number	Test Material	Initial Length [cm]	Initial Diameter [cm]	Initial Volume [cc]	γ_t [g/cc]	γ_d [g/cc]	D_r [%]	e [-]	w_c [%]	S_i [%]	σ_c [MPa]	Strain Rate [-]	Nominal Temp [°C]	Average Temp [°C]	ΔT (top-base) [°C]	Leakage Rate [cc/hr]	Comments
FRS150	MFS	7.355	3.552	72.893	N/A	1.528	45.7	N/A	N/A	N/A	N/A	N/A	N/A	N/A	N/A	N/A	Failed during setup
FRS151	MFS	7.173	3.511	69.450	1.962	1.565	58.2	0.7174	N/A	N/A	2	S	-10	-9.88	0.36	N/A	
FRS152	MFS	7.252	3.518	70.492	1.903	1.509	38.8	0.7812	26.1	99.0	1	S	-10	-9.78	0.15	N/A	
FRS153	MFS	7.188	3.510	69.549	2.016	1.594	67.7	0.6863	26.5	114.4	1	S	-10	-9.72	0.20	0.029	Poor strain rate control
FRS154	MFS	7.224	3.512	69.961	1.927	1.558	55.7	0.7256	23.7	96.9	N/A	N/A	N/A	N/A	N/A	0.061	No shear data
FRS155	MFS	7.224	3.518	70.211	1.949	1.574	61.3	0.7075	23.8	99.6	N/A	N/A	N/A	N/A	N/A	N/A	No shear data
FRS156	MFS	7.242	3.510	70.082	1.969	1.569	59.7	0.7127	25.5	106.0	1	S	-10	-10.51	0.19	0.050	Oscillations
FRS157	MFS	7.258	3.546	71.672	1.935	1.596	68.5	0.6838	21.2	91.9	1	S	-10	-10.46	0.46	0.056	Poor strain rate control
FRS158	MFS	7.252	3.513	70.282	1.905	1.508	38.3	0.7831	26.4	99.7	1	S	-10	-10.67	0.18	0.003	Poor strain rate control
FRS159	MFS	7.220	3.511	69.909	1.918	1.531	46.5	0.7560	25.3	99.0	1	S	-10	-10.60	0.27	0.003	Poor strain rate control
FRS160	MFS	7.249	3.508	70.071	1.927	1.543	50.7	0.7422	24.9	99.5	1	S	-10	-9.67	0.09	0.039	
FRS161	MFS	7.249	3.512	70.225	1.930	1.542	50.4	0.7433	25.2	100.4	1	M	-10	-8.81	-0.05	0.026	Obscured upper yield
FRS162	MFS	7.219	3.508	69.784	1.923	1.534	47.6	0.7523	25.3	99.8	5	M	-10	-9.18	-0.01	0.091	Obscured upper yield
FRS163	MFS	7.250	3.515	70.369	1.953	1.580	63.0	0.7016	23.7	99.9	5	M	-10	-9.26	-0.02	0.102	Obscured upper yield
FRS164	MFS	7.247	3.509	70.063	1.949	1.573	60.8	0.7090	23.9	99.9	2	M	-10	-9.17	0.01	0.031	Obscured upper yield
FRS165	MFS	7.211	3.517	70.039	1.956	1.583	64.2	0.6978	23.6	100.2	2	M	-10	-9.17	-0.01	0.031	Change in strain rate
FRS166	MFS	7.239	3.514	70.209	1.961	1.589	66.1	0.6915	23.4	100.3	2	M	-10	-9.12	-0.04	0.018	Obscured upper yield
FRS167	MFS	7.227	3.548	71.429	1.946	1.582	63.9	0.6987	23.0	97.6	2	M	-10	-9.10	0.07	0.019	Obscured upper yield
FRS168	MFS	7.249	3.514	70.309	1.950	1.571	60.1	0.7114	24.1	100.5	0.1	S	-10	-9.12	-0.05	0.116	
FRS169	MFS	7.219	3.512	69.916	1.958	1.582	63.9	0.6988	23.7	100.7	10	S	-10	-9.34	0.12	0.222	
FRS170	MFS	7.231	3.514	70.141	1.950	1.573	61.0	0.7084	24.0	100.3	1	M	-10	-8.85	-0.06	0.015	
FRS171	MFS	7.234	3.515	70.194	1.892	1.486	30.5	0.8088	27.4	100.1	10	M	-10	-9.42	-0.05	0.095	Obscured upper yield
FRS172	MFS	7.248	3.507	70.008	1.958	1.580	63.2	0.7010	23.9	101.1	0.1	M	-10	-9.38	0.09	0.133	Poor strain rate control
FRS173	MFS	7.217	3.520	70.219	1.958	1.588	65.8	0.6924	23.3	99.7	10	M	-10	-9.34	-0.15	N/A	Poor strain rate control
FRS174	MFS	7.224	3.512	69.977	1.951	1.572	60.8	0.7089	24.0	100.5	10	M	-10	-9.33	-0.13	0.177	
FRS175	MFS	7.201	3.518	69.975	1.912	1.519	42.5	0.7693	24.9	97.7	10	M	-10	-9.35	-0.11	0.127	
FRS176	MFS	7.230	3.510	69.974	1.936	1.550	53.2	0.7339	24.9	100.5	10	S	-10	-9.36	-0.07	0.223	
FRS177	MFS	7.247	3.513	70.240	1.936	1.551	53.6	0.7328	24.8	100.4	0.5	S	-10	-9.34	0.00	0.050	
FRS178	MFS	7.215	3.508	69.722	1.948	1.565	58.1	0.7178	24.5	100.6	0.5	S	-5	-5.20	-0.02	0.022	
FRS179	MFS	7.221	3.512	69.964	1.940	1.555	54.7	0.7292	24.8	100.4	0.5	M	-5	-5.22	-0.01	0.011	Erratic to 2% strain
FRS180	MFS	7.249	3.509	70.083	1.927	1.534	47.8	0.7519	25.6	100.5	10	S	-5	-4.77	-0.03	0.039	
FRS181	MFS	7.246	3.507	70.005	1.941	1.560	56.6	0.7229	26.7	104.4	10	M	-5	-4.62	-0.18	0.071	Erratic to 2% strain
FRS182	MFS	7.243	3.513	70.212	1.928	1.540	49.8	0.7452	25.2	99.7	0.5	S	-5	-4.97	-0.06	0.012	
FRS183	MFS	7.254	3.503	69.917	1.966	1.597	68.5	0.6836	25.8	105.8	0.5	M	-5	-4.99	-0.04	0.026	
FRS184	MFS	7.193	3.515	69.809	1.959	1.600	69.5	0.6804	25.1	103.3	N/A	N/A	N/A	N/A	N/A	N/A	Lost temp. control
FRS185	MFS	7.244	3.507	69.954	1.953	1.575	61.6	0.7065	24.0	100.2	0.5	M	-5	-4.84	0.00	0.016	
FRS186	MFS	7.256	3.509	70.149	1.960	1.591	66.7	0.6896	23.2	99.3	10	M	-5	-4.64	0.03	0.007	Obscured upper yield
FRS191	MFS	7.231	3.515	70.164	1.976	1.613	73.8	0.6661	22.5	99.6	10	M	-5	-4.57	-0.06	0.037	Obscured upper yield
FRS192	MFS	7.206	3.517	69.990	1.964	1.593	67.3	0.6877	23.3	100.1	0.5	M	-5	-5.13	0.01	0.039	
FRS193	MFS	7.218	3.515	70.022	1.974	1.611	73.0	0.6689	22.6	99.6	10	M	-5	-5.10	0.04	0.008	
FRS194	MFS	7.242	3.511	70.120	1.967	1.602	70.2	0.6779	22.8	99.7	0.5	M	-10	-9.09	-0.12	0.034	Odd jumps
FRS205	MFS	7.258	3.517	70.498	1.985	1.629	78.8	0.6497	21.8	99.2	10	M	-5	-5.42	0.01	0.005	
FRS206	MFS	7.234	3.508	69.928	1.998	1.655	86.6	0.6242	20.7	98.0	5	M	-5	-5.53	0.04	0.008	
FRS207	MFS	7.163	3.523	69.822	1.977	1.618	75.2	0.6616	22.2	99.1	2	M	-5	-5.74	0.00	0.055	
FRS208	MFS	7.234	3.520	70.394	1.974	1.615	74.5	0.6640	22.2	98.7	1	M	-5	-5.38	0.02	0.059	No ice caps
FRS209	MFS	7.244	3.562	70.340	1.980	1.635	80.6	0.6437	21.1	96.7	10	M	-5	-5.34	0.02	0.056	No ice caps
FRS214	MFS	N/A	N/A	N/A	N/A	N/A	N/A	N/A	N/A	N/A	N/A	N/A	N/A	N/A	N/A	N/A	No test data
FRS215	MFS	7.263	3.512	70.344	1.989	1.640	82.0	0.6391	21.3	98.3	0.5	M	-2	-2.02	-0.10	0.053	Low temperature

Frozen Test Summary. Part 1: *Test Conditions*

Test Number	Test Material	Initial Length [cm]	Initial Diameter [cm]	Initial Volume [cc]	γ_t [g/cc]	γ_d [g/cc]	D_r [%]	e [-]	w_o [%]	S_r [%]	σ_c [MPa]	Strain Rate [-]	Nominal Temp [°C]	Average Temp [°C]	ΔT (top-base) [°C]	Leakage Rate [cc/hr]	Comments
FRS216	MFS	7.252	3.512	70.233	1.966	1.609	72.5	0.6705	22.2	97.7	0.5	M	-2	-2.35	0.01	0.015	Low temperature
FRS217	MFS	7.247	3.511	70.148	1.986	1.638	81.5	0.6408	21.2	97.9	0.5	S	-2	-2.41	0.00	0.012	Low temperature
FRS218	MFS	7.244	3.520	70.513	1.970	1.607	72.0	0.6723	22.5	99.0	10	M	-2	-2.20	0.01	0.003	Low temperature
FRS219	MFS	7.248	3.509	70.095	1.973	1.610	72.9	0.6692	22.5	99.3	10	S	-2	-2.09	-0.09	0.017	Low temperature
FRS187	HP MFS	7.225	3.505	69.703	1.959	1.599	69.5	0.6805	22.5	97.9	0.5	S	-10	-9.32	-0.11	0.029	Odd jump
FRS188	HP MFS	7.249	3.507	70.021	1.959	1.591	66.8	0.6891	23.1	99.4	10	S	-10	-9.39	-0.10	0.053	
FRS189	HP MFS	7.244	3.503	69.802	1.957	1.592	67.1	0.6884	25.5	103.9	10	S	-5	-4.48	0.08	0.039	Odd jump
FRS190	HP MFS	7.235	3.516	70.257	1.955	1.592	66.9	0.6889	25.5	103.7	0.5	S	-5	-4.32	-0.05	0.006	
FRS195	HP MFS	7.233	3.507	69.844	1.905	1.516	41.4	0.7728	25.7	98.3	0.5	M	-10	-9.16	-0.08	0.033	
FRS196	HP MFS	7.215	3.502	69.487	1.916	1.528	45.5	0.7594	25.4	99.1	10	M	-10	-9.12	-0.24	0.022	
FRS197	HP MFS	7.256	3.502	69.898	1.921	1.535	47.9	0.7515	25.2	99.3	0.5	S	-10	-8.62	-0.12	0.040	Odd jump
FRS198	HP MFS	7.255	3.507	70.091	1.905	1.508	38.6	0.7821	26.3	99.6	10	S	-10	-7.91	-0.15	0.010	
FRS199	HP MFS	7.255	3.506	70.026	1.967	1.659	87.8	0.6202	18.6	88.4	0.5	M	-5	-4.50	0.06	N/A	No temp. equil.
FRS200	HP MFS	7.244	3.514	70.259	1.972	1.616	74.6	0.6635	22.0	98.0	10	M	-5	-4.78	0.12	0.048	
FRS201	HP MFS	7.257	3.507	70.111	1.969	1.621	76.1	0.6585	21.5	96.8	0.5	M	-10	-9.50	-0.03	0.042	
FRS202	HP MFS	7.247	3.515	70.324	1.967	1.622	76.5	0.6574	21.3	96.0	10	M	-10	-9.35	-0.07	0.043	
FRS203	HP MFS	7.244	3.509	70.056	1.968	1.610	72.7	0.6699	22.2	98.5	10	M	-10	-9.54	-0.02	0.032	End at 2%
FRS204	HP MFS	7.228	3.501	69.598	1.916	1.552	53.9	0.7316	23.5	94.9	0.5	M	-10	-9.46	-0.04	0.023	
FRS210	2075 Quartz	7.212	3.519	70.147	1.917	1.557	91.5	0.7020	23.1	95.9	0.5	M	-5	-5.33	-0.02	0.040	2075 Quartz
FRS211	2075 Quartz	7.222	3.525	70.483	1.936	1.590	109.6	0.6665	21.7	94.9	2	M	-5	-5.44	0.39	0.023	2075 Quartz
FRS212	2075 Quartz	7.219	3.523	70.373	1.932	1.605	117.4	0.6511	20.4	91.1	5	M	-5	-5.29	0.04	0.031	2075 Quartz
FRS213	2075 Quartz	7.187	3.527	70.226	1.912	1.568	97.5	0.6903	22.0	92.6	10	M	-5	-5.16	0.12	0.017	2075 Quartz
FRS220	2010 Quartz	7.239	3.512	70.122	1.955	1.609	98.0	0.6465	21.5	97.1	0.5	M	-10	-9.15	-0.21	0.019	
FRS221	2010 Quartz	7.252	3.522	70.640	1.967	1.625	102.9	0.6311	21.1	97.6	10	M	-10	-8.98	-0.26	0.051	
FRS222	2010 Quartz	7.222	3.515	70.074	1.969	1.624	102.6	0.6321	21.3	98.4	0.5	S	-10	-8.19	-0.22	0.018	
FRS223	2010 Quartz	7.253	3.519	70.550	1.956	1.602	95.5	0.6545	22.1	98.6	10	S	-10	-9.33	-0.18	0.115	
FRS224	2010 Quartz	7.247	3.516	70.370	1.907	1.531	71.2	0.7308	24.6	98.2	2	M	-10	-9.08	-0.11	0.059	
FRS225	2010 Quartz	7.247	3.511	70.168	1.964	1.612	99.0	0.6435	21.8	99.1	5	M	-10	-9.09	-0.05	0.024	
FRS226	2010 Quartz	7.250	3.509	70.093	1.952	1.597	94.0	0.6592	22.2	98.5	5	M	-10	-9.39	-0.09	0.067	
FRS227	2010 Quartz	7.243	3.517	70.366	1.953	1.596	93.6	0.6605	22.4	99.1	5	M	-10	-9.55	-0.17	0.090	
FRS228	2010 Quartz	7.222	3.514	70.047	1.954	1.600	94.9	0.6563	22.1	98.5	2	S	-10	-9.15	-0.10	0.053	
FRS229	2010 Quartz	7.221	3.508	69.781	1.948	1.590	91.5	0.6670	22.6	98.8	5	S	-10	-9.43	-0.05	0.050	
FRS230	2010 Quartz	7.235	3.512	70.087	1.968	1.617	100.5	0.6386	21.7	99.3	12.5	M	-10	-8.87	-0.04	0.033	No load data
FRS231	2010 Quartz	7.212	3.517	70.049	1.976	1.634	105.8	0.6221	21.0	98.6	12.5	S	-10	-8.63	-0.11	0.029	No load data
FRS232	2010 Quartz	7.221	3.519	70.233	1.972	1.625	102.9	0.6312	21.4	99.1	10	M	-10	-8.75	-0.11	0.035	
FRS233	2010 Quartz	7.231	3.516	70.195	1.965	1.641	108.2	0.6144	19.7	93.8	10	S	-10	-8.83	-0.05	0.041	
FRS242	2010 Quartz	7.223	3.517	70.167	1.928	1.566	83.3	0.6927	23.2	97.7	12.5	S	-10	-9.67	0.05	0.107	
FRS243	2010 Quartz	7.250	3.513	70.269	1.930	1.569	84.3	0.6895	23.0	97.7	12.5	M	-10	-10.45	0.22	0.060	
FRS244	2010 Quartz	7.259	3.508	70.152	1.919	1.544	75.7	0.7167	24.3	99.2	12.5	M	-5	-5.26	0.02	0.060	
FRS245	2010 Quartz	7.233	3.515	70.198	1.938	1.575	86.7	0.6821	23.0	98.5	12.5	M	-5	-4.68	0.02	0.025	
FRS246	2010 Quartz	7.264	3.508	70.227	1.946	1.584	89.6	0.6730	22.8	99.2	12.5	S	-5	-4.74	0.03	0.069	
FRS269	2010 Quartz	7.249	3.513	70.249	1.950	1.590	91.6	0.6666	22.6	99.1	0.1	M	-10	-9.62	-0.03	0.019	
FRS270	2010 Quartz	7.244	3.511	70.115	1.941	1.576	86.9	0.6816	23.2	99.5	1	M	-10	-9.62	-0.02	0.024	
FRS271	2010 Quartz	7.261	3.510	70.241	1.945	1.584	89.7	0.6727	22.8	98.9	12.5	M	-10	-9.52	-0.07	0.058	
FRS272	2010 Quartz	7.234	3.514	70.160	1.858	1.447	39.4	0.8310	28.4	99.6	7.5	M	-10	-9.56	-0.05	0.018	
FRS273	2010 Quartz	7.238	3.515	70.239	1.936	1.572	85.4	0.6861	23.2	98.6	2	M	-10	-9.67	-0.02	0.026	
FRS234	PMMA	7.226	3.507	69.798	1.081	0.823	N/A	0.4463	31.4	92.6	0.5	M	-10	-8.57	0.13	0.038	
FRS235	PMMA	7.259	3.512	70.339	1.077	0.740	N/A	0.6072	45.5	98.4	0.5	M	-10	-8.50	0.17	0.078	

Frozen Test Summary. Part 1: *Test Conditions*

Test Number	Test Material	Initial Length [cm]	Initial Diameter [cm]	Initial Volume [cc]	γ_i [g/cc]	γ_d [g/cc]	D_r [%]	e [-]	w_o [%]	S_i [%]	σ_c [MPa]	Strain Rate [-]	Nominal Temp [°C]	Average Temp [°C]	ΔT (top-base) [°C]	Leakage Rate [cc/hr]	Comments
FRS236	PMMA	7.245	3.503	69.840	1.086	0.821	N/A	0.4489	32.2	94.6	0.5	M	-10	-8.76	-0.06	0.065	
FRS237	PMMA	7.295	3.509	70.549	1.080	0.733	N/A	0.6238	47.4	99.8	0.5	S	-10	-10.35	0.11	0.023	
FRS238	PMMA	7.328	3.508	70.815	1.085	0.751	N/A	0.5852	44.5	99.9	10	S	-10	-10.06	0.07	0.057	
FRS239	PMMA	7.201	3.510	69.672	1.087	0.764	N/A	0.5582	42.3	99.2	0.5	S	-5	-5.27	0.02	0.023	
FRS240	PMMA	7.249	3.520	70.528	1.089	0.832	N/A	0.4305	31.0	94.2	10	S	-5	-5.17	0.03	0.014	
FRS241	PMMA	7.249	3.514	70.283	1.088	0.771	N/A	0.5440	41.2	99.0	5	S	-5	-5.02	0.16	0.025	
FRS247	PMMA	7.249	3.505	69.953	1.081	0.738	N/A	0.6132	46.5	99.2	0.5	M	-5	-4.23	0.16	0.082	
FRS248	PMMA	7.256	3.496	69.634	1.100	0.784	N/A	0.5174	40.3	102.0	10	M	-5	-4.94	0.09	0.062	
FRS249	PMMA	7.220	3.509	69.831	1.092	0.782	N/A	0.5222	39.6	99.4	0.5	S	-5	-4.83	0.11	0.085	
FRS250	PMMA	7.207	3.518	70.036	1.090	0.812	N/A	0.4650	34.2	96.9	10	M	-10	-9.44	0.00	0.190	
FRS251	PMMA	7.270	3.513	70.445	1.094	0.793	N/A	0.5013	38.0	99.3	10	S	-5	-4.73	-0.03	0.056	
FRS274	PMMA	7.242	3.508	69.980	1.091	0.765	N/A	0.5589	42.9	101.0	0.5	M	-10	-9.67	-0.07	0.052	
FRS275	PMMA	7.198	3.508	69.580	1.085	0.749	N/A	0.5899	44.9	100.0	0.5	M	-10	-9.80	-0.02	0.032	
FRS276	PMMA	7.234	3.506	69.822	1.092	0.749	N/A	0.5890	45.8	102.1	10	M	-10	-9.74	-0.06	0.091	
FRS277	PMMA	7.254	3.510	70.188	1.088	0.751	N/A	0.5846	44.8	100.7	0.5	S	-10	-9.80	-0.03	0.056	
FRS278	PMMA	7.250	3.509	70.134	1.086	0.745	N/A	0.5679	43.1	99.7	10	S	-10	-9.68	-0.09	0.094	
FRS252	PC Ice	7.235	3.509	69.978	0.910	N/A	N/A	N/A	N/A	N/A	0.5	S	-10	-9.29	-0.15	0.046	
FRS253	PC Ice	7.211	3.506	69.627	0.914	N/A	N/A	N/A	N/A	N/A	0.5	M	-10	-9.17	-0.15	0.051	
FRS254	PC Ice	7.257	3.505	70.018	0.912	N/A	N/A	N/A	N/A	N/A	10	S	-10	-9.44	-0.04	0.137	
FRS255	PC Ice	7.205	3.511	69.759	0.912	N/A	N/A	N/A	N/A	N/A	10	M	-10	-9.54	0.19	0.046	
FRS256	PC Ice	7.244	3.510	70.089	0.913	N/A	N/A	N/A	N/A	N/A	0.5	S	-5	-4.94	0.13	0.001	
FRS257	PC Ice	7.231	3.513	70.076	0.910	N/A	N/A	N/A	N/A	N/A	0.5	M	-5	-5.04	0.11	0.001	
FRS258	PC Ice	7.229	3.510	69.942	0.913	N/A	N/A	N/A	N/A	N/A	10	S	-5	-4.68	0.11	0.014	
FRS259	PC Ice	7.211	3.516	70.031	0.912	N/A	N/A	N/A	N/A	N/A	10	M	-5	-4.75	0.08	0.028	
FRS260	Glass	7.267	3.507	70.175	1.930	1.618	N/A	0.5517	19.3	97.1	0.5	S	-10	-8.81	0.00	0.108	
FRS261	Glass	7.233	3.506	69.827	1.924	1.642	N/A	0.5283	17.2	90.1	0.5	M	-10	-9.32	0.16	0.040	
FRS262	Glass	7.228	3.510	69.921	1.927	1.618	N/A	0.5511	19.1	95.9	10	S	-10	-9.38	0.07	0.048	
FRS263	Glass	7.248	3.517	70.406	1.918	1.597	N/A	0.5717	20.1	97.5	10	M	-10	-9.33	0.09	0.025	
FRS264	Glass	7.244	3.516	70.318	1.926	1.638	N/A	0.5328	17.6	91.8	10	M	-10	-9.21	0.05	0.022	
FRS265	HP Glass	7.197	3.519	69.626	1.888	1.550	N/A	0.6189	21.7	97.3	0.5	S	-10	-9.65	0.11	0.049	
FRS266	HP Glass	7.268	3.511	70.348	1.879	1.539	N/A	0.6306	22.1	97.0	0.5	M	-10	-9.71	0.12	0.033	
FRS267	HP Glass	7.229	3.515	70.153	1.885	1.568	N/A	0.6008	20.2	93.3	10	S	-10	-9.78	0.21	0.034	
FRS268	HP Glass	7.188	3.516	69.792	1.868	1.530	N/A	0.6410	22.2	95.7	10	M	-10	-9.66	0.14	0.066	
FRS279	HPR Glass	7.235	3.509	69.970	1.903	1.577	N/A	0.5919	20.7	97.0	0.5	M	-10	-10.27	0.10	0.076	
FRS280	HPR Glass	7.271	3.508	70.254	1.902	1.581	N/A	0.5878	20.3	95.9	0.5	M	-10	-10.01	0.02	0.105	
FRS281	HPR Glass	7.234	3.515	70.202	1.907	1.601	N/A	0.5682	19.1	93.3	10	M	-10	-9.75	-0.01	0.060	
FRS282	HPR Glass	7.252	3.516	70.400	1.897	1.575	N/A	0.5939	20.5	95.6	10	M	-10	-10.22	0.08	0.060	
FRS283	HPR Glass	7.220	3.510	69.847	1.911	1.586	N/A	0.5829	20.5	97.5	0.5	S	-10	-10.06	0.04	0.180	
FRS284	HPR Glass	7.203	3.518	70.024	1.913	1.592	N/A	0.5763	20.1	96.8	10	S	-10	-9.67	-0.05	0.045	
FRS285	HPR Glass	6.980	3.516	67.754	1.884	1.544	N/A	0.6261	22.1	97.7	0.5	M	-10	-10.33	0.05	0.060	
FRS286	HPR Glass	7.183	3.520	69.919	1.880	1.540	N/A	0.6298	22.1	97.1	0.5	S	-10	-10.28	0.03	0.039	
FRS287	HPR Glass	7.273	3.517	70.644	1.886	1.572	N/A	0.5963	19.9	92.6	10	M	-10	-10.23	0.01	0.010	
FRS288	Glass	7.348	3.510	71.097	1.827	1.482	N/A	0.6730	23.3	92.8	0.5	M	-10	-10.33	0.03	0.040	3 mm Beads
FRS289	HP Glass	7.388	3.510	71.478	1.840	1.494	N/A	0.6601	23.2	94.3	0.5	M	-10	-10.31	0.04	0.040	3 mm Beads
FRS290	HP Glass	7.379	3.514	71.556	1.865	1.517	N/A	0.6351	23.0	97.1	0.5	M	-10	-10.24	0.01	0.039	3 mm Beads
FRS291	HPR Glass	7.327	3.520	71.316	1.825	1.478	N/A	0.6780	23.5	93.1	0.5	M	-10	-10.33	0.05	0.036	3 mm Beads
FRS292	HPR Glass	7.219	3.513	69.953	1.841	1.486	N/A	0.6688	23.9	96.0	0.5	M	-10	-10.34	0.04	0.050	3 mm Beads

** **Note:** Tests in italics were not used in analysis

Frozen Test Summary. Part 2: *Engineering Properties*

Test Number	Test Material	D_t [%]	S_t [%]	σ_c [MPa]	Average Temp [°C]	Strain Rate @Q_{yo} [%/hr]	Strain Rate @Q_{uy} [%/hr]	Strain Rate Nom. [%/hr]	Small Strain Region E [GPa]	Small Strain Region Q_{yo} [MPa]	Upper Yield Region Q_{uy} [MPa]	Upper Yield Region ε_{uy} [%]	Peak Strength Q_p [MPa]	Peak Strength ε_p [%]	Curve Type	ACDT Quality	ε_v @ Q_{uy} [%]
FRS150	MFS	N/A	N/A	N/A	N/A	N/A	N/A	N/A	N/A	N/A	N/A	N/A	N/A	N/A	N/A	N/A	N/A
FRS151	MFS	58.2	N/A	1.99	-9.88	2.52	1.00	1.00	25.8	3.10	4.38	0.36	8.60	15.70	D	Fair	0.373
FRS152	MFS	38.8	98.98	1.01	-9.78	2.58	1.00	0.97	28.0	2.70	4.58	0.43	7.30	20.00	D	Poor	0.525
FRS153	MFS	67.7	114.36	1.00	-9.72	2.30	1.00	1.15	30.0	2.55	4.49	0.25	7.30	11.50	C	Poor	-0.012
FRS154	MFS	N/A	N/A	N/A	N/A	N/A	N/A	N/A	N/A	N/A	N/A	N/A	N/A	N/A	N/A	N/A	N/A
FRS155	MFS	N/A	N/A	N/A	N/A	N/A	N/A	N/A	N/A	N/A	N/A	N/A	N/A	N/A	N/A	N/A	N/A
FRS156	MFS	59.7	105.96	1.00	-10.51	2.55	1.00	0.99	17.9	3.20	4.93	0.49	8.10	15.00	C	Poor	-0.189
FRS157	MFS	68.5	91.92	1.00	-10.46	2.50	1.00	1.06	22.5	2.55	4.90	0.45	7.70	12.56	C	Poor	-0.165
FRS158	MFS	38.3	99.71	1.01	-10.67	2.62	1.00	1.03	20.5	2.75	4.80	0.40	7.08	13.99	C	Poor	-0.268
FRS159	MFS	46.5	99.04	0.99	-10.60	2.45	1.00	1.01	25.4	2.21	5.07	0.48	7.57	12.78	D	Poor	-0.379
FRS160	MFS	50.7	99.52	0.99	-9.67	2.75	1.00	0.97	15.2	2.60	4.85	0.34	7.52	15.02	D	Poor	-0.092
FRS161	MFS	50.4	100.43	1.01	-8.81	11.00	9.50	12.20	19.0	3.35	7.30	0.60	9.46	13.12	C	Poor	-0.288
FRS162	MFS	47.6	99.77	5.00	-9.18	9.00	11.00	12.10	27.8	2.60	7.20	0.42	11.50	18.34	D	Poor	0.011
FRS163	MFS	63.0	99.92	5.00	-9.26	5.40	22.00	12.33	25.0	2.92	7.40	0.42	13.00	19.51	D	Poor	-0.257
FRS164	MFS	60.8	99.88	2.00	-9.17	14.80	12.00	12.04	19.5	3.80	7.50	0.50	11.21	15.60	D	Poor	-0.288
FRS165	MFS	64.2	100.17	2.01	-9.17	2.45	17.20	15.09	21.5	2.60	8.23	0.49	11.90	12.79	C	Poor	-0.301
FRS166	MFS	66.1	100.32	2.00	-9.12	10.30	10.50	12.10	24.5	3.50	7.40	0.42	11.36	16.90	D	Poor	-0.211
FRS167	MFS	63.9	97.59	2.00	-9.10	9.60	10.50	12.30	26.5	3.00	7.20	0.45	11.21	9.41	D	Poor	-0.233
FRS168	MFS	60.1	100.50	0.09	-9.12	2.20	1.00	0.98	40.0	2.60	4.46	0.49	7.21	10.50	C	Poor	-0.360
FRS169	MFS	63.9	100.66	9.99	-9.34	1.56	1.00	0.97	27.0	1.90	4.38	0.38	10.23	19.33	D	Poor	1.334
FRS170	MFS	61.0	100.29	1.01	-8.85	18.70	12.50	12.14	13.5	4.45	7.38	0.47	10.25	12.51	C	Poor	-0.373
FRS171	MFS	30.5	100.14	10.01	-9.42	22.50	18.50	12.40	26.8	3.58	7.80	0.25	9.86	19.68	B	Poor	-0.128
FRS172	MFS	63.2	101.06	0.11	-9.38	21.70	12.00	12.04	27.0	3.60	7.72	0.43	9.77	10.03	B	Poor	-0.388
FRS173	MFS	65.8	99.69	10.00	-9.34	19.70	18.00	N/A	25.6	3.50	7.90	0.40	N/A	N/A	N/A	Excellent	-0.238
FRS174	MFS	60.8	100.48	10.01	-9.33	33.00	12.00	12.02	24.8	3.60	7.22	0.35	12.44	18.63	D	Good	-0.083
FRS175	MFS	42.5	97.68	10.01	-9.35	27.80	12.00	12.26	24.9	3.60	7.44	0.39	10.38	15.30	C	Good	0.022
FRS176	MFS	53.2	100.51	10.00	-9.36	1.05	1.00	1.00	25.6	2.38	4.18	0.37	8.81	19.73	D	Excellent	0.056
FRS177	MFS	53.6	100.36	0.50	-9.34	0.95	1.00	0.99	27.0	2.68	4.49	0.35	7.02	16.21	C	Excellent	-0.345
FRS178	MFS	58.1	100.64	0.50	-5.20	2.40	1.00	1.06	27.0	1.60	2.53	0.41	5.33	14.82	C	Poor	-0.094
FRS179	MFS	54.7	100.37	0.51	-5.22	25.70	12.00	12.57	25.0	2.05	4.23	0.40	6.93	12.88	C	Good	-0.334
FRS180	MFS	47.8	100.47	9.99	-4.77	1.85	1.00	1.10	21.8	0.98	2.04	0.40	5.73	18.72	D	Poor	-0.015
FRS181	MFS	56.6	104.38	10.00	-4.62	38.00	12.00	12.94	21.0	1.59	3.50	0.30	8.80	19.87	D	Good	-0.166
FRS182	MFS	49.8	99.74	0.50	-4.97	1.20	1.00	1.02	26.4	1.64	2.63	0.36	4.62	19.35	D	Excellent	-0.083
FRS183	MFS	68.5	105.80	0.50	-4.99	41.00	14.00	12.26	25.0	2.72	4.40	0.16	7.02	10.91	C	Excellent	-0.154
FRS184	MFS	N/A	N/A	N/A	N/A	N/A	N/A	N/A	N/A	N/A	N/A	N/A	N/A	N/A	N/A	N/A	N/A
FRS185	MFS	61.6	100.23	0.50	-4.84	32.00	11.00	12.16	45.0	2.16	4.40	0.33	6.65	12.43	C	Good	-0.194
FRS186	MFS	66.7	99.35	10.00	-4.64	40.00	46.00	13.35	20.8	2.08	3.60	0.20	10.84	19.99	D	Good	-0.031
FRS191	MFS	73.8	99.60	10.00	-4.57	37.20	18.64	13.44	25.4	1.60	3.80	0.14	10.94	20.28	D	Fair	0.025
FRS192	MFS	67.3	100.08	0.50	-5.13	15.61	12.35	12.17	26.4	1.96	4.40	0.32	7.57	10.06	C	Good	0.013
FRS193	MFS	73.0	99.61	9.99	-5.10	17.70	11.77	11.95	22.4	1.71	3.70	0.34	12.10	20.07	D	Good	0.039
FRS194	MFS	70.2	99.73	0.50	-9.09	16.10	12.72	11.92	29.6	3.61	7.32	0.30	10.76	7.23	C	Excellent	-0.193
FRS205	MFS	78.8	99.24	10.00	-5.42	7.82	12.08	10.40	18.2	1.95	4.29	0.41	11.23	19.34	D	Fair	0.073
FRS206	MFS	86.6	98.00	5.01	-5.53	13.82	12.40	11.95	18.0	2.24	4.48	0.38	10.99	12.41	C	Poor	0.054
FRS207	MFS	75.2	99.10	2.01	-5.74	17.18	12.19	12.00	30.6	2.12	4.68	0.27	9.95	11.37	D	Good	-0.112
FRS208	MFS	74.5	98.67	1.01	-5.38	17.61	12.13	12.13	27.4	2.11	4.61	0.33	9.13	7.81	C	Good	-0.160
FRS209	MFS	80.6	96.73	10.00	-5.34	N/A	11.70	12.03	N/A	N/A	4.23	0.32	12.04	15.89	D	Poor	-0.008
FRS214	MFS	N/A	N/A	N/A	N/A	N/A	N/A	N/A	N/A	N/A	N/A	N/A	N/A	N/A	N/A	N/A	N/A
FRS215	MFS	82.0	98.34	0.51	-2.02	8.70	10.74	12.15	3.2	0.56	1.99	0.35	6.14	9.31	C	Poor	-0.225

Frozen Test Summary. Part 2: *Engineering Properties*

Test Number	Test Material	D_f [%]	S_f [%]	σ_c [MPa]	Average Temp [°C]	Strain Rate @Q_{yo} [%/hr]	Strain Rate @Q_{uy} [%/hr]	Strain Rate Nom. [%/hr]	Small Strain Region E [GPa]	Upper Yield Region Q_{yo} [MPa]	Upper Yield Region Q_{uy} [MPa]	Upper Yield Region ε_{uy} [%]	Peak Strength Q_p [MPa]	Peak Strength ε_p [%]	Curve Type	ACDT Quality	ε_v @ Q_{uy} [%]
FRS216	MFS	72.5	97.72	0.51	-2.35	12.21	11.37	12.23	13.0	1.30	2.05	0.25	5.43	11.38	C	Fair	-0.113
FRS217	MFS	81.5	97.86	0.51	-2.41	2.73	1.01	1.07	32.0	0.48	1.47	0.44	4.41	2.87	C	Good	0.037
FRS218	MFS	72.0	99.03	10.00	-2.20	12.02	13.17	12.20	3.3	0.92	1.71	0.43	6.59	18.13	D	Excellent	-0.002
FRS219	MFS	72.9	99.31	10.00	-2.09	N/A	1.02	1.04	N/A	N/A	0.57	0.08	4.24	11.64	D	Poor	0.014
FRS187	HP MFS	69.5	97.91	0.50	-9.32	1.07	0.97	1.00	26.2	1.56	4.03	0.32	4.89	3.00	C	Good	-0.280
FRS188	HP MFS	66.8	99.43	9.99	-9.39	1.02	0.98	1.00	21.0	1.69	4.13	0.21	9.98	19.90	D	Excellent	-0.131
FRS189	HP MFS	67.1	103.93	10.00	-4.48	1.55	1.00	1.03	23.5	0.80	2.33	0.16	6.59	19.89	D	Excellent	-0.040
FRS190	HP MFS	66.9	103.74	0.50	-4.32	1.10	0.99	1.00	18.5	0.75	2.41	0.34	3.30	6.04	C	Fair	-0.142
FRS195	HP MFS	41.4	98.30	0.50	-9.16	14.10	11.73	11.97	27.6	1.98	6.45	0.43	6.49	0.50	A	Fair	-0.167
FRS196	HP MFS	45.5	99.11	10.00	-9.12	15.97	11.80	12.06	15.5	3.06	7.86	0.34	11.03	20.04	D	Excellent	-0.075
FRS197	HP MFS	47.9	99.28	0.50	-8.62	0.84	0.97	1.00	26.6	1.42	3.68	0.34	4.06	6.22	C	Good	-0.226
FRS198	HP MFS	38.6	99.65	10.00	-7.91	1.40	1.03	1.04	20.2	1.38	3.87	0.39	6.57	18.58	D	Good	-0.035
FRS199	HP MFS	87.8	88.42	0.51	-4.50	14.79	11.93	11.94	33.3	1.33	4.40	0.42	5.13	2.01	C	Good	0.124
FRS200	HP MFS	74.6	98.01	10.00	-4.78	15.32	12.31	12.10	24.6	1.75	5.29	0.35	11.53	19.44	D	Fair	-0.035
FRS201	HP MFS	76.1	96.77	0.50	-9.50	13.60	11.74	11.92	21.8	2.37	6.53	0.37	6.99	2.00	C	Excellent	0.016
FRS202	HP MFS	76.5	95.95	10.00	-9.35	14.84	12.16	12.00	19.2	2.36	8.34	0.34	13.25	13.15	D	Excellent	-0.022
FRS203	HP MFS	72.7	98.48	10.00	-9.54	15.04	10.43	12.02	17.6	2.74	8.47	0.32	N/A	N/A	D	Good	-0.084
FRS204	HP MFS	53.9	94.94	0.51	-9.46	14.77	11.87	12.07	21.6	2.28	7.07	0.35	7.09	0.38	A	Excellent	-0.069
FRS210	2075 Quartz	91.5	95.90	0.51	-5.33	10.04	12.44	11.58	23.2	3.41	9.11	0.22	9.11	0.23	B	Good	-0.167
FRS211	2075 Quartz	109.6	94.94	2.00	-5.44	13.83	13.40	12.17	21.2	4.38	9.61	0.20	9.62	0.20	B	Excellent	-0.112
FRS212	2075 Quartz	117.4	91.14	5.00	-5.29	12.83	11.53	12.17	22.2	4.06	9.94	0.25	9.99	0.26	B	Good	-0.025
FRS213	2075 Quartz	97.5	92.56	10.00	-5.16	12.00	12.13	12.21	15.4	4.15	9.72	0.24	9.72	0.24	B	Excellent	-0.077
FRS220	2010 Quartz	98.0	97.15	0.50	-9.15	15.17	12.20	12.20	29.6	3.49	11.89	0.37	11.90	0.43	A	Good	-0.278
FRS221	2010 Quartz	102.9	97.61	10.00	-8.98	19.55	11.94	11.46	31.2	3.10	12.69	0.75	13.70	7.79	D	Good	-0.359
FRS222	2010 Quartz	102.6	98.43	0.50	-8.19	1.05	0.96	1.01	34.2	2.29	6.59	0.48	7.75	5.54	C	Good	-0.227
FRS223	2010 Quartz	95.5	98.57	10.00	-9.33	0.97	1.01	1.00	33.0	2.16	7.52	0.65	11.18	10.95	D	Good	0.174
FRS224	2010 Quartz	71.2	98.17	2.01	-9.08	12.77	12.60	11.50	29.2	3.41	12.18	0.41	12.18	0.41	A	Good	0.067
FRS225	2010 Quartz	99.0	99.10	5.00	-9.08	12.05	12.06	12.10	25.4	3.55	12.88	0.37	12.88	0.37	B	Excellent	0.020
FRS226	2010 Quartz	94.0	98.47	5.00	-9.39	12.37	12.07	12.04	25.0	3.57	13.12	0.43	13.12	0.43	A	Fair	-0.189
FRS227	2010 Quartz	93.6	99.10	5.01	-9.55	11.64	11.97	12.05	25.0	3.94	13.34	0.41	13.34	0.41	B	Excellent	-0.114
FRS228	2010 Quartz	94.9	98.53	2.00	-9.15	1.07	1.00	1.00	29.4	2.45	7.43	0.48	8.66	4.24	B	Good	-0.110
FRS229	2010 Quartz	91.5	98.84	5.00	-9.43	0.96	0.99	1.00	31.4	2.54	8.01	0.42	9.10	6.12	B	Good	0.077
FRS230	2010 Quartz	N/A	N/A	N/A	-8.87	N/A	N/A	N/A	N/A	N/A	N/A	N/A	N/A	N/A	N/A	N/A	N/A
FRS231	2010 Quartz	N/A	N/A	N/A	-8.63	N/A	N/A	N/A	N/A	N/A	N/A	N/A	N/A	N/A	N/A	N/A	N/A
FRS232	2010 Quartz	102.9	99.07	10.00	-8.75	34.20	12.34	12.41	22.0	4.20	12.79	0.56	12.79	0.56	B	Good	0.182
FRS233	2010 Quartz	108.2	93.83	10.00	-8.83	0.97	1.00	0.99	22.4	2.34	7.28	0.35	10.56	6.40	C	Fair	-0.147
FRS242	2010 Quartz	83.32	97.71	12.50	-9.67	1.04	0.97	1.00	35.2	2.10	7.30	0.39	9.65	5.90	D	Good	-0.046
FRS243	2010 Quartz	84.34	97.67	12.50	-10.45	13.93	12.09	12.05	21.4	3.95	13.16	0.44	13.16	0.44	B	Good	-0.025
FRS244	2010 Quartz	75.70	99.16	12.50	-5.26	12.51	12.19	12.75	24.4	2.35	8.01	0.41	10.33	11.04	B	Excellent	-0.039
FRS245	2010 Quartz	86.69	98.50	12.50	-4.68	13.08	11.83	12.21	21.4	2.20	6.53	0.42	12.64	11.92	D	Excellent	-0.005
FRS246	2010 Quartz	89.58	99.17	12.50	-4.74	2.20	1.00	0.99	23	1.32	4.40	0.36	8.53	10.04	D	Fair	-0.013
FRS269	2010 Quartz	91.61	99.15	0.10	-9.62	13.22	11.55	12.27	25.5	3.9	12.17	0.41	12.17	0.41	B	Excellent	-0.208
FRS270	2010 Quartz	86.85	99.48	1.00	-9.62	14.52	11.24	12.26	16.4	4.82	12.51	0.48	12.51	0.48	B	Good	-0.001
FRS271	2010 Quartz	89.68	98.95	12.50	-9.52	14.07	11.92	12.32	24.4	3.65	13.33	0.44	14.24	10.42	B	Excellent	0.083
FRS272	2010 Quartz	39.39	99.63	7.50	-9.56	15.48	12.46	12.22	21	3.86	13.22	0.33	13.22	0.33	A	Excellent	-0.189
FRS273	2010 Quartz	85.42	98.62	2.00	-9.67	12.01	12.02	12.10	27	3.72	11.87	0.41	11.87	0.41	A	Excellent	0.062
FRS234	PMMA	N/A	92.64	0.51	-8.57	13.44	12.55	12.17	4.9	2.28	5.99	0.35	6.70	5.82	D	Excellent	-0.009
FRS235	PMMA	N/A	98.37	0.51	-8.50	12.92	11.91	12.10	5.0	2.90	5.71	0.54	7.07	4.96	D	Good	0.092

Frozen Test Summary. Part 2: *Engineering Properties*

Test Number	Test Material	D_i [%]	S_i [%]	σ_c [MPa]	Average Temp [°C]	Strain Rate @Q_{yo} [%/hr]	Strain Rate @Q_{uy} [%/hr]	Nom. [%/hr]	Small Strain Region E [GPa]	Small Strain Region Q_{yo} [MPa]	Upper Yield Region Q_{uy} [MPa]	Upper Yield Region ε_{uy} [%]	Peak Strength Q_p [MPa]	Peak Strength ε_p [%]	Curve Type	ACDT Quality	ε_v @ Q_{uy} [%]
FRS236	PMMA	N/A	94.60	0.51	-8.76	15.36	12.37	12.27	4.6	3.10	6.83	0.42	6.91	5.00	B	Excellent	0.191
FRS237	PMMA	N/A	99.75	0.50	-10.35	1.39	1.11	1.04	5.1	1.87	8.09	0.78	8.09	0.78	B	Good	-0.152
FRS238	PMMA	N/A	99.92	10.00	-10.06	0.95	0.99	1.12	5.6	1.97	8.07	0.71	10.32	10.19	D	Fair	-0.133
FRS239	PMMA	N/A	99.22	0.51	-5.27	0.93	1.02	1.03	5.0	1.20	5.07	0.64	7.28	10.04	D	Excellent	0.069
FRS240	PMMA	N/A	94.22	10.00	-5.17	0.89	1.09	1.04	4.9	1.27	5.57	0.98	9.47	12.53	D	Fair	0.001
FRS241	PMMA	N/A	99.04	5.00	-5.02	1.40	1.01	1.03	4.8	1.38	5.33	0.80	5.46	5.12	D	Excellent	-0.017
FRS247	PMMA	N/A	99.19	0.50	-4.23	8.81	12.13	12.39	4.3	1.95	6.20	0.58	6.20	0.58	B	Good	-0.014
FRS248	PMMA	N/A	101.97	10.00	-4.94	11.62	12.21	12.22	4.8	1.84	7.67	0.88	10.68	10.45	D	Good	-0.045
FRS249	PMMA	N/A	99.35	0.50	-4.83	2.11	1.05	1.10	4.6	1.15	4.51	0.67	6.59	10.02	D	Excellent	0.038
FRS250	PMMA	N/A	96.91	10.00	-9.44	11.80	12.11	12.32	5.1	3.56	10.54	0.91	12.32	12.40	D	Fair	-0.007
FRS251	PMMA	N/A	99.30	10.00	-4.73	1.00	1.19	1.07	4.2	1.35	4.83	0.78	8.32	10.12	D	Excellent	0.038
FRS274	PMMA	N/A	100.98	0.51	-9.67	12.37	15.08	12.52	5.2	2.7	8.86	0.52	8.86	0.52	C	Good	-0.004
FRS275	PMMA	N/A	100.02	0.50	-9.80	12.24	13.00	12.60	4.88	3.85	9.93	0.58	9.93	0.58	B	Good	-0.070
FRS276	PMMA	N/A	102.11	10.00	-9.74	13.56	12.40	12.79	5.2	3.36	10.69	0.83	10.69	0.83	B	Good	0.026
FRS277	PMMA	N/A	100.75	0.50	-9.80	0.53	1.00	1.13	5.3	2.45	7.38	0.61	7.83	7.74	D	Good	-0.018
FRS278	PMMA	N/A	99.72	10.00	-9.68	2.19	0.99	1.08	5.1	2.3	7.54	0.79	8.54	7.88	D	Fair	-0.014
FRS252	PC Ice	N/A	N/A	0.50	-9.29	1.04	0.96	1.07	5.48	1.22	1.64	0.10	2.37	1.39	C	Excellent	-0.041
FRS253	PC Ice	N/A	N/A	0.50	-9.17	14.58	12.59	12.16	5.56	2.75	3.14	0.09	4.79	1.38	C	Excellent	-0.106
FRS254	PC Ice	N/A	N/A	9.99	-9.44	1.51	0.88	1.03	5	0.74	1.60	0.11	2.37	1.53	C	Good	0.030
FRS255	PC Ice	N/A	N/A	10.00	-9.54	13.18	11.96	12.44	5.24	2.63	2.61	0.07	5.29	1.39	C	Good	-0.120
FRS256	PC Ice	N/A	N/A	0.50	-4.94	0.93	1.18	1.11	5.28	0.96	1.37	0.12	1.68	1.52	C	Good	0.000
FRS257	PC Ice	N/A	N/A	0.50	-5.04	16.02	13.94	11.96	5.14	2.57	2.71	0.08	3.65	1.23	C	Excellent	0.093
FRS258	PC Ice	N/A	N/A	10.00	-4.68	1.78	1.03	1.26	4.8	0.77	1.32	0.11	1.64	0.92	C	Fair	0.056
FRS259	PC Ice	N/A	N/A	10.00	-4.75	13.50	12.33	12.25	4.5	1.38	2.21	0.13	3.57	1.27	C	Good	0.079
FRS260	Glass	N/A	97.07	0.50	-8.81	1.48	0.98	1.01	26.4	2.25	6.67	0.34	11.95	3.41	C	Good	-0.010
FRS261	Glass	N/A	90.14	0.50	-9.32	14.28	12.79	12.33	27.2	3.13	10.05	0.35	12.33	3.30	C	Good	-0.021
FRS262	Glass	N/A	95.93	10.00	-9.38	1.00	0.97	1.00	26.6	2.2	7.57	0.46	18.14	4.96	D	Excellent	-0.008
FRS263	Glass	N/A	97.55	10.00	-9.33	14.95	11.90	12.02	28	2.8	10.08	0.40	11.54	2.00	D	Excellent	-0.034
FRS264	Glass	N/A	91.75	10.00	-9.21	13.99	11.84	12.08	25.7	3.05	11.23	0.48	14.79	2.00	D	Excellent	-0.018
FRS265	HP Glass	N/A	97.29	0.50	-9.65	0.96	1.18	1.07	6	0.94	3.31	0.34	3.31	0.34	A	Good	0.070
FRS266	HP Glass	N/A	96.99	0.51	-9.71	13.29	12.60	12.16	5.5	2.8	4.52	0.45	4.52	0.45	A	Good	0.376
FRS267	HP Glass	N/A	93.26	10.00	-9.78	0.82	1.18	1.05	5.6	0.65	3.04	0.32	3.04	0.32	A	Fair	0.006
FRS268	HP Glass	N/A	95.66	10.01	-9.66	13.20	12.30	12.39	5.7	2.96	6.90	0.45	6.90	0.45	A	Good	0.047
FRS279	HPR Glass	N/A	97.01	0.51	-10.27	15.05	11.89	14.34	7	4.85	5.86	0.35	5.86	0.35	A	Excellent	0.266
FRS280	HPR Glass	N/A	95.86	0.51	-10.01	14.12	11.80	12.12	7.7	3.7	5.65	0.40	5.65	0.40	A	Good	0.518
FRS281	HPR Glass	N/A	93.32	10.00	-9.75	12.60	11.97	12.31	7.5	3.75	10.33	0.55	11.26	1.24	A	Good	0.006
FRS282	HPR Glass	N/A	95.61	10.00	-10.22	13.41	11.96	12.28	7.5	3.54	11.45	0.65	16.13	6.82	C	Good	-0.234
FRS283	HPR Glass	N/A	97.54	0.50	-10.06	1.28	1.05	1.02	5.8	1.05	3.72	0.56	3.72	0.56	A	Fair	0.534
FRS284	HPR Glass	N/A	96.83	10.00	-9.67	1.35	1.03	1.05	7	0.95	7.51	0.82	13.53	6.41	D	Excellent	-0.084
FRS285	HPR Glass	N/A	97.68	0.51	-10.33	12.94	12.78	12.15	8.1	3.3	6.12	0.32	6.12	0.32	A	Excellent	0.324
FRS286	HPR Glass	N/A	97.13	0.50	-10.28	0.95	1.20	1.08	5.0	1.62	4.37	0.41	4.37	0.41	A	Good	0.228
FRS287	HPR Glass	N/A	92.63	10.00	-10.23	12.09	12.51	12.37	8.0	3.65	10.45	0.64	10.45	0.64	A	Good	0.050
FRS288	Glass	N/A	92.82	0.51	-10.33	12.28	12.69	12.08	25.2	4.03	7.46	0.22	7.46	0.22	A	Excellent	0.068
FRS289	HP Glass	N/A	94.31	0.51	-10.31	17.19	12.28	12.20	11.4	3.35	4.41	0.28	4.41	0.28	A	Good	0.365
FRS290	HP Glass	N/A	97.12	0.50	-10.24	16.86	12.27	12.13	12.5	3.75	5.26	0.17	5.26	0.17	A	Fair	0.130
FRS291	HPR Glass	N/A	93.08	0.51	-10.33	16.90	10.73	12.15	21	5.62	7.58	0.11	7.58	0.11	A	Good	0.027
FRS292	HPR Glass	N/A	95.97	0.51	-10.34	16.98	13.25	12.24	21	4.35	7.51	0.13	7.51	0.13	A	Excellent	0.024

** **Note:** Tests in italics were not used in analysis